



Journal of Turbomachinery

Published Quarterly by ASME

VOLUME 131 • NUMBER 4 • OCTOBER 2009

RESEARCH PAPERS

- 041001 **Boundary Layer Separation Control With Fluidic Oscillators**
Ciro Cerretelli and Kevin Kirtley
- 041002 **Superposition Predictions of the Reduction of Hot Streaks by Coolant From a Film-Cooled Guide Vane**
Sean C. Jenkins and David G. Bogard
- 041003 **Prediction of Film Cooling and Heat Transfer on a Rotating Blade Platform With Stator-Rotor Purge and Discrete Film-Hole Flows in a 1- $\frac{1}{2}$ Turbine Stage**
H. Yang, Z. Gao, H. C. Chen, J. C. Han, and M. T. Schobeir
- 041004 **Turbine Blade Platform Film Cooling With Typical Stator-Rotor Purge Flow and Discrete-Hole Film Cooling**
Zhihong Gao, Diganta Narzary, and Je-Chin Han
- 041005 **Heat Transfer Coefficients of Film Cooling on a Rotating Turbine Blade Model—Part I: Effect of Blowing Ratio**
Zhi Tao, Zhenming Zhao, Shuiting Ding, Guoqiang Xu, Bin Yang, and Hongwei Wu
- 041007 **Film-Cooling Flowfields With Trenched Holes on an Endwall**
N. Sundaram and K. A. Thole
- 041008 **The Effects of Aerodynamic Asymmetric Perturbations on Forced Response of Bladed Disks**
Tomokazu Miyakozawa, Robert E. Kielb, and Kenneth C. Hall
- 041009 **Investigations on the Discharge and Total Temperature Increase Characteristics of the Labyrinth Seals With Honeycomb and Smooth Lands**
Xin Yan, Jun Li, Liming Song, and Zhenping Feng
- 041010 **Sensitization of the SST Turbulence Model to Rotation and Curvature by Applying the Spalart–Shur Correction Term**
Pavel E. Smirnov and Florian R. Menter
- 041011 **Effect of Unsteadiness on the Performance of a Transonic Centrifugal Compressor Stage**
Isabelle Trébinjac, Pascale Kulisa, Nicolas Bulot, and Nicolas Rochuon
- 041012 **Effect of Wakes and Secondary Flow on Re-attachment of Turbine Exit Annular Diffuser Flow**
David Kluß, Horst Stoff, and Alexander Wiedermann
- 041013 **The Effect of Leading-Edge Geometry on Wake Interactions in Compressors**
Andrew P. S. Wheeler, Alessandro Sofia, and Robert J. Miller
- 041014 **Shorten the Intermediate Turbine Duct Length by Applying an Integrated Concept**
A. Marn, E. Göttlich, D. Cadrecha, and H. P. Pirker
- 041015 **Aerothermal Performance of Streamwise and Compound Angled Pulsating Film Cooling Jets**
Vipluv Aga, Michel Mansour, and Reza S. Abhari
- 041016 **Influence of Wake Structure on Unsteady Flow in a Low Pressure Turbine Blade Passage**
S. Sarkar

(Contents continued on inside back cover)

This journal is printed on acid-free paper, which exceeds the ANSI Z39.48-1992 specification for permanence of paper and library materials. ©™

♻️ 85% recycled content, including 10% post-consumer fibers.

Editor, **DAVID C. WISLER** (2013)
Assistant to the Editor: **ELIZABETH WISLER**
Associate Editors
Gas Turbine (Review Chairs)
K. BRUN (2009)
T. SATTELMAYER (2009)
Aeromechanics
M. MONTGOMERY (2009)
A. SINHA (2009)
Boundary Layers and Turbulence
G. WALKER (2009)
Compressor Aero
ZOLTAN S. SPAKOVSKY (2011)
Computational Fluid Dynamics
J. ADAMCZYK (2009)
M. CASEY (2009)
Experimental Methods
W.-F. NG (2009)
Heat Transfer
R. BUNKER (2009)
J.-C. HAN (2009)
Radial Turbomachinery
R. VAN DEN BRAEMBUSSCHE (2009)
Turbomachinery Aero
S. GALLIMORE (2009)
D. PRASAD (2009)
A. R. WADIA (2009)

PUBLICATIONS COMMITTEE
Chair, **BAHRAM RAVANI**

OFFICERS OF THE ASME
President, **AMOS E. HOLT**
Executive Director, **THOMAS G. LOUGHLIN**
Treasurer, **WILBUR MARNER**

PUBLISHING STAFF
Managing Director, Publishing
PHILIP DI VIETRO
Manager, Journals
COLIN MCATEER
Production Coordinator
JUDITH SIERANT

Transactions of the ASME, Journal of Turbomachinery (ISSN 0889-504X) is published quarterly (Jan., Apr., July, Oct.) by The American Society of Mechanical Engineers, Three Park Avenue, New York, NY 10016. Periodicals postage paid at New York, NY and additional mailing offices.

POSTMASTER: Send address changes to Transactions of the ASME, Journal of Turbomachinery, c/o THE AMERICAN SOCIETY OF MECHANICAL ENGINEERS, 22 Law Drive, Box 2300, Fairfield, NJ 07007-2300.

CHANGES OF ADDRESS must be received at Society headquarters seven weeks before they are to be effective. Please send old label and new address.

STATEMENT from By-Laws. The Society shall not be responsible for statements or opinions advanced in papers or ... printed in its publications (B7.1, Par. 3).

COPYRIGHT © 2009 by the American Society of Mechanical Engineers. For authorization to photocopy material for internal or personal use under those circumstances not falling within the fair use provisions of the Copyright Act, contact the Copyright Clearance Center (CCC), 222 Rosewood Drive, Danvers, MA 01923, tel: 978-750-8400, www.copyright.com. Request for special permission or bulk copying should be addressed to Reprints/Permission Department. Canadian Goods & Services Tax Registration #126148048

- 041017 Heat Transfer in Leading Edge, Triangular Shaped Cooling Channels With Angled Ribs Under High Rotation Numbers
Yao-Hsien Liu, Michael Huh, Dong-Ho Rhee, Je-Chin Han, and Hee-Koo Moon
- 041018 The Effects of Manufacturing Tolerances on Gas Turbine Cooling
Ronald S. Bunker
- 041019 Windage Power Losses From Spiral Bevel Gears With Varying Oil Flows and Shroud Configurations
Graham Johnson, Budi Chandra, Colin Foord, and Kathy Simmons
- 041020 Simplified Approach to Predicting Rough Surface Transition
R. J. Boyle and M. Stripf

TECHNICAL BRIEFS

- 044501 Experimental Study of Heat Transfer Augmentation Near the Entrance to a Film Cooling Hole in a Turbine Blade Cooling Passage
Gerard Scheepers and R. M. Morris

i Author Index

The ASME Journal of Turbomachinery is abstracted and indexed in the following:

Aluminum Industry Abstracts, Aquatic Science and Fisheries Abstracts, Ceramics Abstracts, Chemical Abstracts, Civil Engineering Abstracts, Compendex (The electronic equivalent of Engineering Index), Corrosion Abstracts, Current Contents, Ei EncompassLit, Electronics & Communications Abstracts, Energy Information Abstracts, Engineered Materials Abstracts, Engineering Index, Environmental Science and Pollution Management, Excerpta Medica, Fluidex, Fuel and Energy Abstracts, INSPEC, Index to Scientific Reviews, Materials Science Citation Index, Mechanical & Transportation Engineering Abstracts, Mechanical Engineering Abstracts, METADEX (The electronic equivalent of Metals Abstracts and Alloys Index), Metals Abstracts, Oceanic Abstracts, Pollution Abstracts, Referativnyi Zhurnal, Shock & Vibration Digest, Steels Alert

Boundary Layer Separation Control With Fluidic Oscillators

Ciro Cerretelli

Kiepe Electric S.p.A.,
Cernusco S.N. (MI), 20063, Italy
e-mail: cirissimo@yahoo.com

Kevin Kirtley

GE Energy,
Greenville, SC 29515
e-mail: kevin.kirtley@ge.com

Fluidic oscillating valves have been used in order to apply unsteady boundary layer injection to “repair” the separated flow of a model diffuser, where the hump pressure gradient represents that of the suction surface of a highly loaded stator vane. The fluidic actuators employed in this study consist of a fluidic oscillator that has no moving parts or temperature limitations and is therefore more attractive for implementation on production turbomachinery. The fluidic oscillators developed in this study generate an unsteady velocity with amplitudes up to 60% rms of the average operating at nondimensional blowing frequencies (F^+) in the range of $0.6 < F^+ < 6$. These actuators are able to fully reattach the flow and achieve maximum pressure recovery with a 60% reduction of injection momentum required and a 30% reduction in blowing power compared with optimal steady blowing. Particle image velocimetry velocity and vorticity measurements have been performed, which show no large-scale unsteadiness in the controlled boundary layer flow. [DOI: 10.1115/1.3066242]

1 Introduction

A great emphasis has recently been placed on assessing the merits of fluidic flow control in overcoming boundary layer separation [1–5]. This situation presents itself throughout the compression system of aircraft engines in highly loaded turbomachinery passages and transition ducts and is a limiter in engine performance and efficiency [1]. By injecting small amounts of air taken from high-pressure engine sources into the near wall region upstream of a separated flow, the boundary layer may be sufficiently energized to overcome the downstream adverse pressure gradient and avoid flow separation in aggressive engine components. Because the extraction of this high-pressure air results in a penalty on overall aircraft engine performance and efficiency, it is necessary to implement boundary layer injection as efficiently as possible and minimize the flow requirements in order to achieve a net positive impact on engine performance.

In a recent study, Luedke et al. [6] investigated steady blowing flow control in a hump diffuser as a means of preventing boundary layer separation due to an adverse pressure gradient. Discrete hole injection has been analyzed to determine the optimum injection configuration in terms of hole diameter, hole spacing, and hole orientation (yaw angle). Yawed injection ($\theta=45$ deg) has been shown to be the most effective configuration, with significantly higher pressure recovery arguably due to enhanced shear layer mixing induced by large-scale corotating vortices resulting from the jet-main flow interaction.

The focus of the present effort is to investigate possible ways of improving the effectiveness of fluidic injection schemes to levels beyond the previously optimized techniques for steady blowing. It is very well known [7,8] that pulsing the boundary layer greatly reduces the amount of injected mass flow, which is necessary for the control of separated flow, and a great deal of attention has been paid to the quantification of the benefits of pulsing in the previous 2 decades [9]. This research has provided great insight upon the physics of large coherent structures. It has also achieved impressive results in the control, or rather the manipulation, of turbulent shear flows, with reduction of more than two orders of magnitude in the required mass flow to repair flow separation. The vast majority of these studies, however, generate unsteady blow-

ing by means of mechanical or piezoelectric actuators, which are often large in size, employ numerous moving parts, have reliability issues and limited lifetime, or are extremely difficult to implement in high temperature turbomachinery components. Therefore, the most urgent issue that is pertinent to the engineer who is looking to successfully implement unsteady flow control is the development of an actuation mechanism that can meet gas turbine engine requirements. For this purpose, in recent years there has been a renewed interest in the field of fluidics [10,11], in particular to fluidic oscillators for flow control application. There have been attempts [12] to incorporate these devices in turbomachinery components such as stator vanes. The results, however, have not been entirely positive up to this point. The reasons for this are probably related to the high-pressure drop and the consequential injected mass flow penalty that these actuators require to generate unsteadiness. It is necessary to operate these devices close to the point of their maximum efficiency and in a way that is the most effective on repairing the separated boundary layer flow. Because of the highly complicated vane design and the narrow spaces associated with turbomachinery applications, this is not a trivial exercise.

The intent of this study is to demonstrate the viability of passive fluidic actuators to perform unsteady blowing and to quantify their benefit. These actuators consist essentially of a fluidic bistable switch, have no moving parts or temperature limitations, and are therefore more attractive for implementation on production turbomachinery.

2 Experimental Setup

A picture of the GE GRC diffuser rig model, aft looking forward, is shown in Fig. 1. The lower wall contour of the test model under investigation (Fig. 2) is designed to produce a streamwise pressure distribution representative of that found on the suction surface of a highly loaded compressor stator blade. This distribution provides an unanchored, naturally separated flow pattern downstream of the crest and includes the streamline curvature seen in compressor blades. Seifert and Pack [13] and Viken et al. [14] studied a similar hump model; however the separated flow over the hump was anchored by a highly convex surface. The rig is an open circuit flow system, exhausting into ambient. The upper and sidewalls of the model are flat and result in a cross section at the crest of the lower hump with an aspect ratio of 6. Fences are placed 0.25 chord lengths from the sidewalls to minimize the effects of sidewall boundary layers and therefore reduce flow three-dimensionalities along the span. Flow control is introduced

Contributed by the Turbomachinery Division of ASME for publication in the JOURNAL OF VIBRATION AND ACOUSTICS. Manuscript received October 27, 2006; final manuscript received July 22, 2008; published online June 30, 2009. Review conducted by Matthew Montgomery. Paper presented at the ASME Turbo Expo 2006: Land, Sea and Air (GT2006), Barcelona, Spain, May 8–11, 2006.

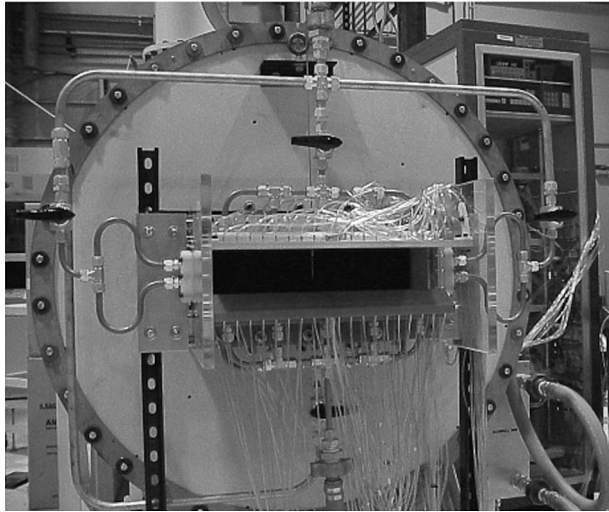


Fig. 1 GE GRC diffuser test rig, aft looking forward

along the span of the model at the location of the crest of the hump, just upstream of the line of natural separation. The stream-wise pressure gradient is adjusted by changing the configuration of the model upper wall, which is hinged above the crest of the lower surface (Fig. 2). This allows for comparison of the effectiveness of injection configurations in the presence of a progressively stronger adverse pressure gradient downstream of the crest.

The model has been designed to allow for easy implementation of various flow control configurations. The surface area along the crest of the hump where flow control in the form of steady or unsteady blowing is applied consists of a removable insert that completes the contour of the hump. By making this portion of the lower surface removable, injection patterns may be changed without requiring any alterations to the overall rig. A plenum, which is fed by five equally distributed 2.54 cm diameter pipes, is fixed to the bottom of the flow control insert to provide a uniform flow source.

A direct current blower is used to supply the main flow to the diffuser. Secondary air for flow control is supplied by 6 bar house air. The main flow is delivered to a settling chamber through a shallow angle diffuser, designed with an expansion angle of 7 deg to avoid boundary layer separation. The 1.219 m diameter settling chamber is fitted with a layer of aluminum honeycomb to suppress any swirl and lateral mean velocity variations exiting the diffuser. Immediately downstream of the honeycomb are two rows of 3.2 mm thick perforated plates to suppress longitudinal mean velocity variations and to reduce the inlet turbulence intensity [15]. Downstream of the plates, an elliptical bell mouth transitions to the 12.2×50.8 cm² rectangular cross section. Because of the large aspect ratio of the duct cross section, an optimized bell mouth

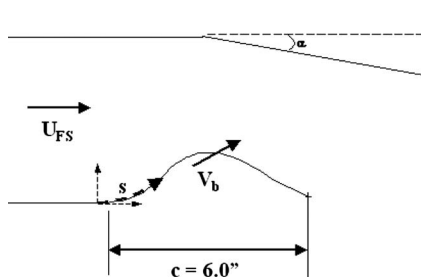
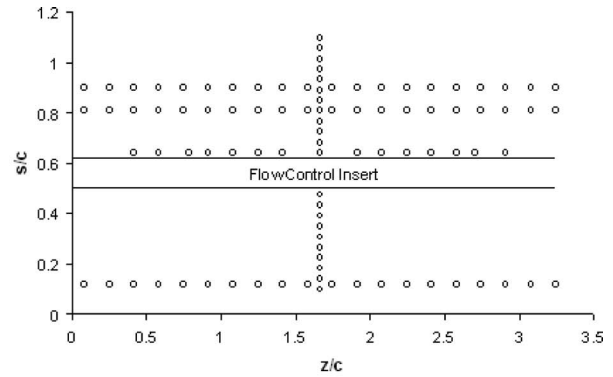
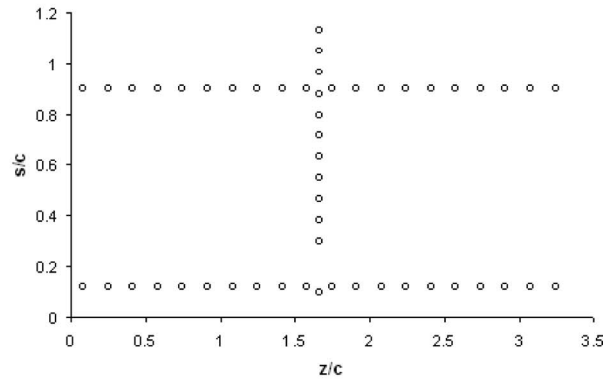


Fig. 2 Hump diffuser cross section



a)



b)

Fig. 3 Layout of wall static pressure taps on (a) lower and (b) upper model walls

design is not practical. An inlet wire mesh is located at the exit of the bell mouth to reduce any spanwise nonuniformities resulting from the design.

Baseline, no-flow-control test conditions correspond to a freestream velocity of 25.9 m/s and Re_c of 300,000. The freestream condition is defined at center span, center height, and 0.3 chord lengths upstream of the hump model leading edge (origin of coordinate system in Fig. 2). Trip wires made of 0.25 mm diameter wires are placed along the perimeter of the duct upstream of the test section to ensure turbulent transition for the incoming low Reynolds number flow.

3 Diffuser Measurements

3.1 Measurements and Performance Metrics. The diffuser test rig is instrumented with 164 static pressure taps along the upper and lower flow path walls. A schematic of the locations of the pressure taps is provided in Fig. 3, with $s/c=0$ defined at the hump leading edge (Fig. 2). Four rows of spanwise taps with 2.54 cm spacing are located along the lower wall at 0.12, 0.64, 0.81, and 0.90 chord lengths downstream of the hump leading edge. Two rows of spanwise taps are located along the upper wall at 0.12 and 0.90 chord lengths (measured with an upper wall at $\alpha = 0$ deg). An axial row of taps equally spaced at an arc length of 6.35 mm is located along the centerline of both the upper and lower walls. The freestream flow condition, as identified in Sec. 2, is monitored through a Pitot-static pressure probe and a subsonic Venturi-meter located in the upstream supply piping. The mass flow rate and pressure of the secondary flow control air are also monitored during the tests.

Two key performance metrics are considered, the local pressure recovery coefficient (Cp_s) and the overall diffuser pressure recovery

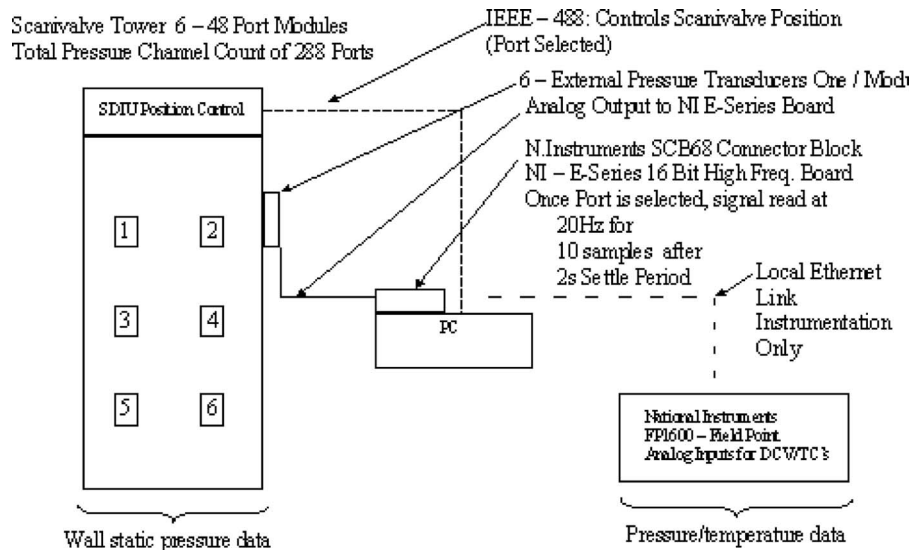


Fig. 4 Schematic of data acquisition system

ery coefficient (C_p), as defined in Eqs. (1) and (2). C_{p_s} is calculated along the centerline of the lower wall to monitor the pressure recovery distribution along the hump contour, while C_p provides a measure of the overall diffuser performance. The crest dynamic head is approximated in these quantities by the difference between the freestream total pressure measured upstream of the test section and the spanwise averaged crest static pressure. Because C_{p_s} and C_p are relative performance measures and are consistently defined throughout the study, this approximation is deemed adequate,

$$C_{p_s} = \frac{P_{s,s} - \bar{P}_{s,\text{crest}}}{P_{t,\text{FS}} - \bar{P}_{s,\text{crest}}} \quad (1)$$

$$C_p = \frac{P_{s,\text{exit}} - \bar{P}_{s,\text{crest}}}{P_{t,\text{FS}} - \bar{P}_{s,\text{crest}}} \quad (2)$$

3.2 Data Acquisition. A Scanivalve system with six 48-port modules, each with a dedicated differential pressure transducer, is used to monitor the pressure signals from the 164-wall static pressure taps as well as the freestream Pitot-static probe. Scanivalve data are sampled through a National Instruments E-Series 16 bit high-frequency data acquisition board at a rate of 20 Hz for a period of ten samples after a 2 s settling time. The frequency content cutoff of measured pressure signals in the separated flow region has been experimentally shown to be less than 5 Hz, indicating that sampling rates greater than 10 Hz are free from aliasing. This low-frequency content is likely due to the damping provided by the length of small diameter plastic tubing connecting each pressure tap to the measurement port and is not related to the actual frequency content of the flow unsteadiness. The effect of the number of samples on the measurements has been studied, and ten samples have been shown to be adequate to determine the actual mean pressure values. The 2 s settling time has been shown through testing to be adequate for allowing the pressure port volume to equilibrate. Additional differential pressure transducers monitoring Venturi-meter and settling chamber temperatures and pressures are channeled through a Validyne CD280 carrier demodulator and sampled through a National Instruments FP1600 Field Point system. Statistics from the Field Point measurements are recorded and phased with the mean and standard deviation of pressures measured for each Scanivalve port. By setting the statistics time interval for the Field Point data to some time less than the total time of one complete Scanivalve rotation (48 ports), each set of statistical Field Point data is guaranteed to be representative

of the same flow condition of the corresponding Scanivalve rotation data. A schematic detailing the configuration of the data acquisition system is shown in Fig. 4.

3.3 Measurement Error. An analysis of measurement capabilities has been performed on the measurement system of the current study to assess the repeatability and reproducibility of pressure measurements. For this assessment, each flow control insert is assembled in the diffuser rig, tested, removed, and then reassembled and retested to determine the random error due to the measurement system and the part-to-part variability. This assessment has been performed for the $\alpha = -5$ deg diffuser configuration in terms of overall pressure recovery levels, C_p , for the baseline, no-flow-control condition. A one-way analysis of variance of the test data gives a measurement standard deviation due to repeatability error of $\pm 0.01 C_p$, with a ratio of part-to-part variability to measurement variability of about 27. These results indicate that measured differences in C_p due to different characteristics are well above the level of expected measurement noise. Geometric tolerances are specified as ± 0.08 mm.

3.4 PIV Measurements. A TSI Insight particle image velocimetry (PIV) system has been used to obtain quantitative measurements of velocity. The experimental arrangement is shown in Figs. 5(a) and 5(b). Atomized olive oil particles have been used to seed the flow. These particles were illuminated by a laser sheet, of 3 mm thickness, from two pulsed yttrium aluminum garnet (YAG) lasers. Images of the particles were captured using a Kodak Megaplug (1008 \times 1018 pixels) camera and were transferred in real time to a PC at an image rate of 15 Hz. Pairs of images were analyzed using cross-correlation of subimages and were digitally implemented. Further details of this experimental technique can be found in the TSI Insight user manual. The measurement standard deviation of the velocities in the highly separated flow area is $\pm 0.05 U$.

4 Hump Diffuser Performance Without Flow Control

As reported by Luedke et al. [6], no-flow-control tests have been performed in order to assess the reference pressure distribution through the model in the presence of separated flow. These tests are run at a mass flow rate of 1.9 kg/s, corresponding to a freestream velocity of 25.9 m/s. The midspan streamwise lower surface pressure distribution is plotted in terms of C_{p_s} in Fig. 6(a) for both the $\alpha = 0$ deg and $\alpha = -5$ deg diffuser configurations. Because the $\alpha = 0$ deg configuration has a larger expansion area dis-

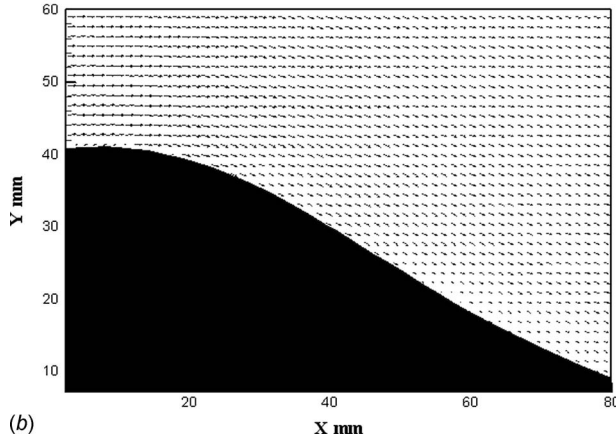
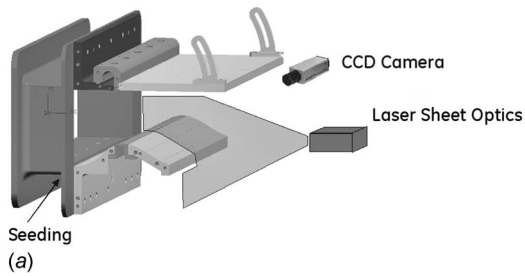


Fig. 5 (a) Schematic of PIV setup. (b) Example of a full-resolution PIV velocity field.

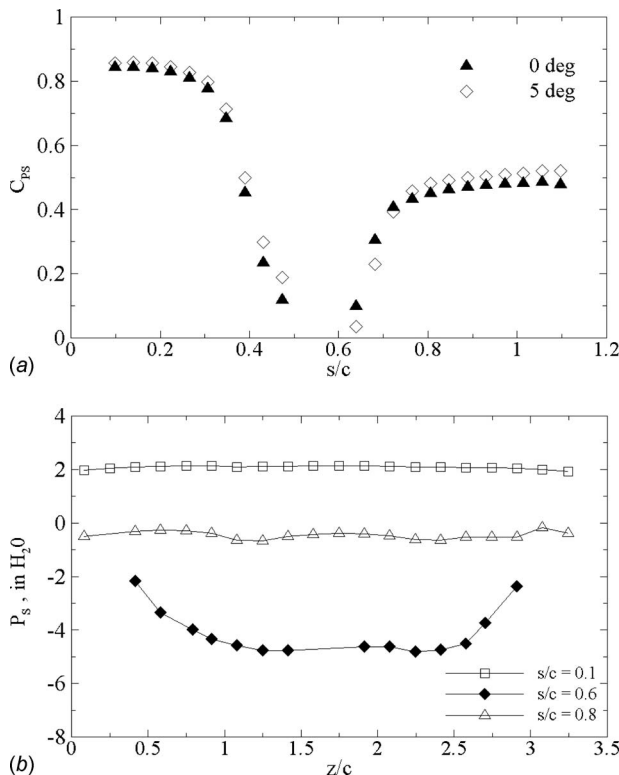


Fig. 6 (a) Baseline local pressure recovery curves along the lower surface for $\alpha=0$ deg and -5 deg. Flow control insert is located between $0.5 \leq s/c \leq 0.62$. (b) Spanwise lower wall pressure distribution at $s/c=0.12$, 0.64 , and 0.81 ($\alpha=-5$ deg).

Table 1 Geometric features of optimal discrete hole insert

Discrete hole insert	
d	1.905 mm
b	7.620 mm
N	54
θ	45 deg
l/d	6.5
A_{open}	1.568 cm ²

tribution, the associated pressure recovery increases at a slightly steeper rate than the $\alpha=-5$ deg configuration just downstream of the crest ($0.64 < s/c < 0.75$). However, this larger expansion area also creates a stronger adverse pressure gradient in the diffuser, and therefore the separation point moves upstream relative to the $\alpha=-5$ deg configuration, resulting in a lower exit pressure recovery level. Shown in Fig. 6(b) are the spanwise pressure distributions for the lower wall pressure tap rows located in the accelerating region of the hump ($s/c=0.12$), at the crest ($s/c=0.64$), and in the decelerating region ($s/c=0.81$). The lower surface inlet flow appears quite uniform across the span, whereas the distribution at the crest shows significant sidewall pressure deficits. This sidewall deficit is likely due to the fact that the weak corner flow along the base of the fences separates earlier than the midspan flow. This nonuniformity is seen to have dissipated by $s/c=0.81$ where a near constant pressure distribution is found across the span within the separated region.

When comparing the effectiveness of unsteady blowing with respect to steady blowing, the strongest adverse pressure gradient $\alpha=0$ deg configuration was employed to have a sharper quantification of the benefits of flow control.

5 Steady Injection Characterization

In a previous investigation on the same experimental rig, Luedke et al. [6] tested a series of discrete steady injection flow control configurations to determine the effect that each of a series of flow and geometric parameters has on the lower wall pressure recovery distribution. The parameters considered in the study are injection hole diameter (d), injection hole spacing (b), injection hole yaw orientation (θ), injection momentum coefficient (C_μ), and velocity ratio (V_R), where (C_μ) and (V_R) are defined as in Eqs. (3) and (4), respectively. Each combination of flow control parameters is tested under both the $\alpha=0$ deg and -5 deg upper wall configurations to determine their relative effectiveness in a progressively stronger adverse pressure gradient,

$$C_\mu = \frac{m_b V_b}{\left(\frac{1}{2} \rho U_{FS}^2 c_w\right)_{baseline}} \quad (3)$$

$$V_R = \frac{V_b}{(U_{FS})_{baseline}} \quad (4)$$

Yawed injection ($\theta=45$ deg) has been shown to be the most effective configuration, with significantly higher pressure recovery arguably due to enhanced shear layer mixing induced by large-scale corotating vortices resulting from the jet-main flow interaction. Both hole and slot injections have been tested, with discrete injection capable of achieving increased pressure recovery at reduced levels of momentum injection.

While the reader should refer to the original paper for the complete details of this study, the most effective configuration for steady blowing constitutes the baseline for the present work, and the pertinent results are summarized here. The geometric characteristics of this configuration are summarized in Table 1, and the diffuser pressure recovery is plotted in Fig. 7. It is interesting to note that as soon as injection is initiated, the pressure recovery coefficient falls to lower values. This drop in performance is likely

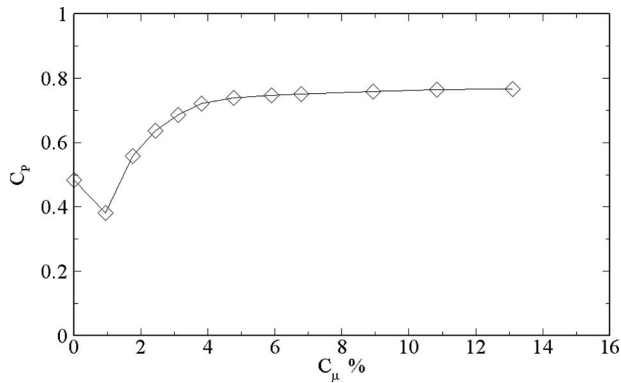


Fig. 7 Diffuser pressure recovery for discrete injection insert as a function of C_μ for $\alpha=0$ deg

due to the fact that at very low velocity ratios injection perturbs the flow stream and may promote earlier separation. However, as the injected mass flow is augmented, the diffuser recovery rapidly increases above the no-flow-control levels. While the initial increase in C_p is rather steep, the slope of the pressure recovery curve strongly decreases as the maximum value of $C_p=0.77$ is approached. Therefore, a question arises on the definition of the C_p level at which we can consider the flow to be fully reattached.

In Fig. 8 the centerline hump pressure distributions are plotted as flow control is progressively increased, and it is possible to notice that the separation is not completely suppressed until $C_p \approx 0.75$. This information will be of paramount importance when the benefits of unsteady flow control are quantified in the following sections.

6 Fluidic Actuators for Pulsing

Fluidic oscillators have been employed for the past 4 decades, and a review of the most common configurations can be found in Campagnuolo and Lee [16]. A feedback oscillator constitutes the core of the no-moving-part actuator that has been conceived for this study. The working mechanism of such oscillators is shown in Fig. 9. This device consists of a high-gain bistable fluid amplifier in which part of each output signal is fed back and applied as a negative signal at the amplifier's control port to switch the jet. The frequency of the feedback oscillator is determined by the transport time of the stream in the feedback path and by the filling time of the feedback capacitance and is therefore governed by volume and length. The oscillatory mode is excited only at pressure ratios for

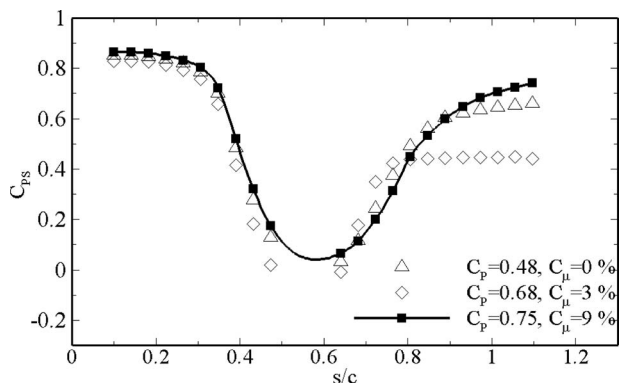


Fig. 8 Centerline pressure for 1.905 mm discrete injection at different recovery levels as per Fig. 6. Flow control insert is located between $0.5 \leq s/c \leq 0.62$.

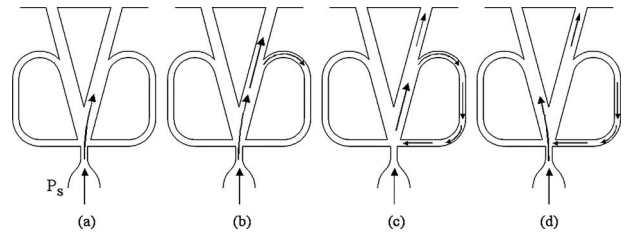


Fig. 9 Feedback fluidic oscillator: switching mechanism. P_s indicates the supply plenum pressure.

which the jet occupies the full downstream channel width. Feedback oscillators can be made insensitive to temperature, pressure, or both [16].

Unsteady blowing has been implemented upon the baseline configuration summarized in Table 1, where flow control jets are yawed at $\theta=45$ deg. In this way, a direct comparison with the most efficient steady blowing is made possible. Feedback oscillators are applied such that the output channels connect directly to two adjacent jet holes in the flow control insert, and the hydraulic diameter of the oscillator outputs is matched to the diameter of the yawed holes. In this way, the unsteady flow control insert is constituted by a row of holes, where pairs of adjacent holes are pulsed in opposition of phase with each other, at a frequency (f) that is set by the oscillators. The phase difference between hole pairs is not controlled.

Nishri and Wagnanski [17] and McManus et al. [18], together with numerous other authors employing electromechanic actuators such as solenoid and siren valves [9], found that the most effective forcing frequency for flow control $F^+=fL/U_{FS}$ lies between $0.4 \leq F^+ \leq 1$ where the actuation period scales with the advection time of the separated shear layer vortices. However, Glezer et al. [19] suggested that at these frequencies the coupling between unsteady actuation and wake vortex shedding might trigger large-scale global instabilities resulting in unsteady aerodynamic forces, which would be highly undesirable for obvious reasons. Therefore, they proposed a radically different approach that emphasizes fluidic modification of the apparent aerodynamic shape of the surface upstream of the separation point with the objective of altering the streamwise adverse pressure gradient in order to suppress separation. For this purpose, surface-mounted high-frequency piezoelectric actuators (i.e., synthetic jets) are employed at frequencies that are at least one order of magnitude higher than the vortex shedding frequency in the separated boundary layer, decoupling unsteady actuation from global instabilities of the base flow.

In order to provide insight into these two different regimes of flow control, two unsteady blowing inserts (A) and (B) have been designed for our experiments. The fluid amplifier is identical in both devices, but the feedback path geometry differs, thus changing the frequency characteristic between the two inserts. Insert (A) has been designed to operate at a constant frequency $F^+ \approx 0.7$, and insert (B) has been designed to operate at a pressure-controlled frequency in the range of $3 \leq F^+ \leq 6$. Examples of the unsteady velocity waveforms measured with a hotwire anemometer at the output of the oscillators are given in Figs. 10 and 11, together with the frequency response curve as a function of the driving pressure. The hotwire probe was placed one nozzle diameter downstream of the exit surface. The modulation is very strong, with the rms velocity component ranging from 35% to 60% of the average value of the outlet velocity.

It is somewhat difficult to quantify the "pressure drop" and the "efficiency" of a fluidic oscillator since it is an unsteady device and it requires pressure ratio significantly greater than 1 to operate in the bistable mode. An ideal oscillator would have a maximum velocity equal to the ideal frictionless velocity, a minimum velocity equal to zero (complete shutoff), and a rms velocity component of $1/\sqrt{2}$ of the average value. In practice, oscillators can never

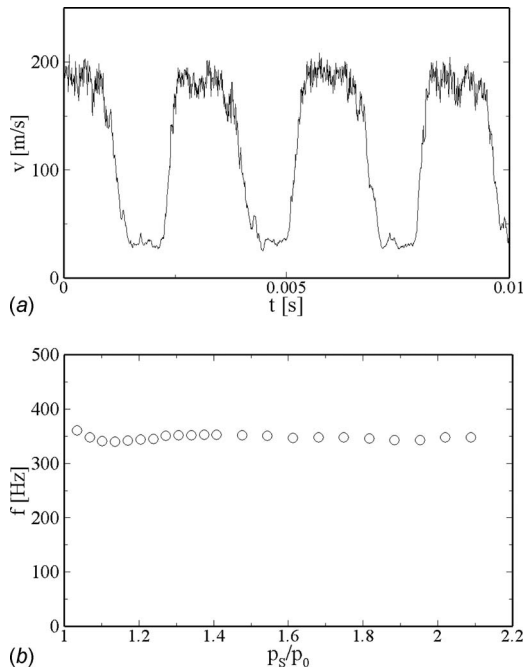


Fig. 10 Feedback fluidic oscillator in insert A, $F^+ \approx 0.7$. (a) Velocity waveform. (b) Frequency response as a function of supply pressure.

attain complete shutoff because of the inherent leakage that is present in any fluidic bistable switch [20]. Figure 12 gives an indication of the efficiency of the oscillators employed in this work by plotting the velocity of an ideal frictionless nozzle, the maximum velocity, and the minimum velocity from the oscillator outlets. It can be noticed that the devices have a relatively small minimum velocity, and the maximum velocities often exceed 80% of the ideal values.

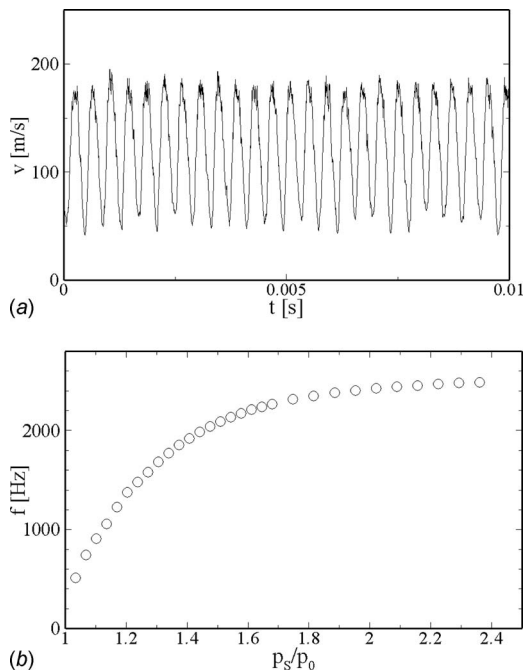


Fig. 11 Feedback fluidic oscillator in insert B, $3 \leq F^+ \leq 6$. (a) Velocity waveform. (b) Frequency response as a function of supply pressure.

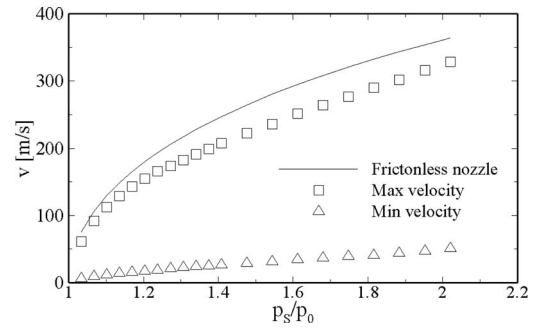


Fig. 12 Frictionless nozzle velocity and oscillator maximum and minimum velocities as functions of the supply pressure

7 Unsteady Injection Characterization

The diffuser pressure recovery coefficients (C_p) resulting from steady blowing and unsteady blowing are plotted in Fig. 13 as a function of injected momentum for the diffuser configuration at $\alpha = 0$ deg. The geometry of the optimal injection configuration is summarized in Table 1, and the frequency characteristics of the two unsteady injection manifolds are illustrated in Figs. 10(b) and 11(b), respectively. The resulting nondimensional frequency (F^+) is indicated in the plot. Note that for the unsteady flow control the momentum coefficient is computed as in Eq. (5), where the oscillatory injected flow control momentum is averaged. This is the most widely used definition of oscillatory momentum coefficient and allows for a meaningful comparison with the steady injection coefficient computed in Eq. (3),

$$C_\mu = \frac{\overline{m_b V_b}}{\left(\frac{1}{2} \rho U_{FS}^2 c w\right)_{\text{baseline}}} \quad (5)$$

Unsteady injection achieves the same full recovery levels as steady blowing but requires less than half the injected momentum. It is found that insert (A) performs significantly better than insert (B), suggesting that for these experiments the most efficient regime is where the unsteady forcing period scales with the advection time of the shear layer vortices. The inability of repeating the results of the synthetic jet experiments of Glezer et al. [19] for $F^+ \gg 1$ might be due to the fundamental operational difference between fluidic oscillators and piezoelectric synthetic jets. While synthetic jets are zero net mass flow devices and operate in both suction and blowing modes, fluidic actuators produce a velocity waveform that is similar to the one produced by more classic forms of actuation such as solenoid and siren valves. Therefore, it is plausible that the most effective forcing frequency for fluidic oscillators lies between $0.4 \leq F^+ \leq 1$.

In this experiment, the coupling between unsteady actuation at $F^+ \approx 0.7$ and the boundary layer does not trigger global large-scale instabilities in the flow. No unsteadiness in the reattached flow has been observed in the pressure measurements, and PIV velocity measurements have been taken in order to capture any possible large-scale structure in the flow field. A word of caution is necessary here, as the time resolution of the PIV system that was employed in this work is not high enough to detect the paths of the vortices separating from the diffuser hump. However, the authors feel confident that the measurement time was large enough to detect large-scale unsteadiness and any possible higher rms velocity component that would result from a prolonged undersampling of higher-frequency velocity fluctuations due to small-scale coherent structures.

The evolution of the average flow field and streamlines over the hump diffuser is shown in Fig. 14. It is interesting to note that as soon as injection is initiated, the size of separated flow area actually grows, corresponding to the drop in performance seen in Figs. 7 and 13. At this stage, the pressure recovery coefficients are

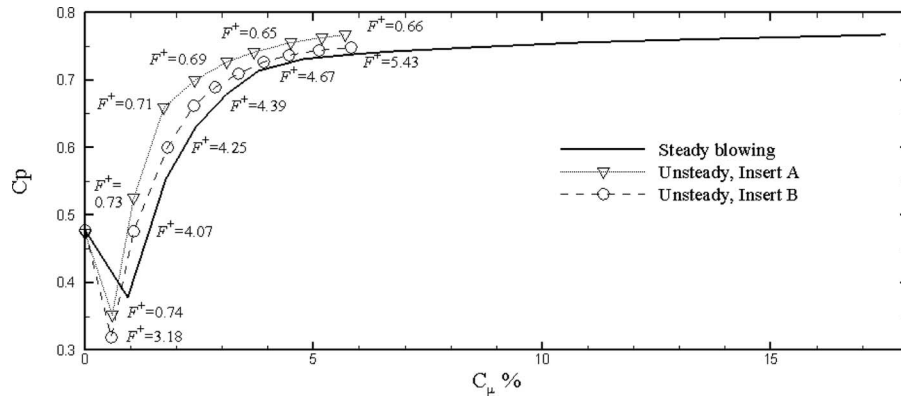


Fig. 13 Diffuser pressure recovery curves for steady and unsteady blowing as a function of C_μ for $\alpha=0$ deg

apparently below the one associated with steady blowing. However, this is probably associated with the lower values of C_μ for the oscillator experiment when flow control is initiated. Further investigations are recommended when control is initiated. Further investigation is recommended in order to better assess the differences between steady and unsteady blowing at very low values of the momentum coefficient C_μ .

As flow control is progressively implemented in the model, the separation streamline moves aft until the flow is fully reattached. In Fig. 14(f), it is possible to see that when the flow is fully reattached, there is no sign of flow instability, and the flow struc-

ture appears to be essentially the same as it would be had the separation been repaired by steady blowing. In order to corroborate this observation with quantitative data, in Fig. 15 we plot a comparison of the total rms velocity profile for steady and unsteady blowing at the exit of the diffuser and the relative velocity profiles extrapolated from PIV measurements. The velocity and \bar{U}_{rms} profiles are plotted for the no-flow-control scenario and at a correspondent fully repaired flow for a $C_p=0.76$. Small differences between the two curves without flow control are due to the strong unsteady and three-dimensional features of the separated

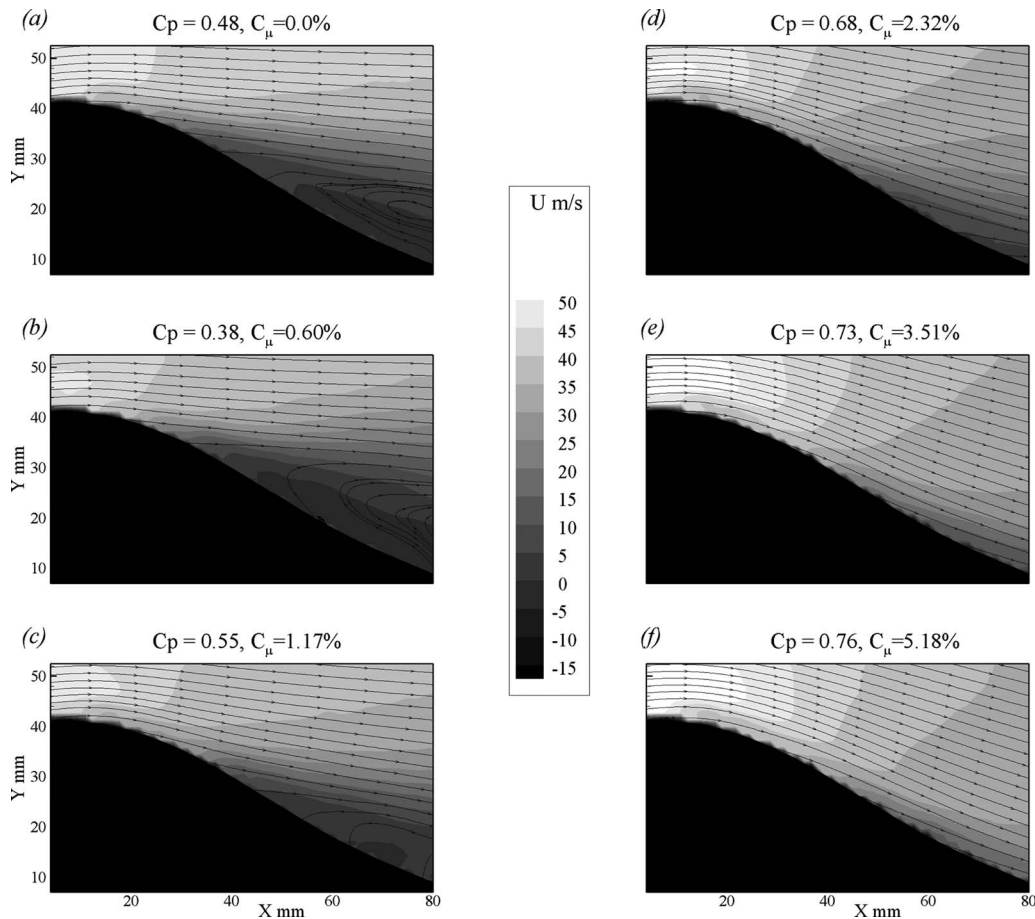


Fig. 14 U velocity fields and streamlines for unsteady flow control applied by insert A over the hump diffuser

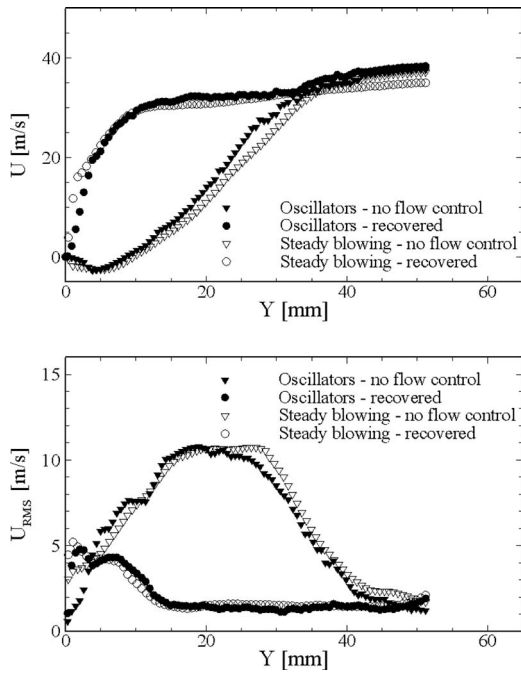


Fig. 15 U velocity and \bar{U}_{rms} profiles for steady blowing and fluidic oscillators

flow field. The PIV averaged two-dimensional velocity measurements necessarily do not capture the whole amplitude and frequency content of the flow.

From the U velocity profile, it is interesting to see how the flow control recovers a fully attached boundary layer. Also, flow control suppresses the high fluctuations that were present in the base flow especially in the separated shear layer where the velocity gradients are stronger (see also Fig. 14(a)). The unsteadiness level seems to be very similar for steady blowing and fluidic oscillators.

8 Quantification of the Benefits of Unsteady Flow Control

In order to quantify the benefits of unsteady blowing, in Fig. 16 we plot the relative reduction in the required momentum, mass flow, and blowing velocity that are required to obtain a specific pressure recovery (C_p) in the diffuser. It is interesting to see that the fluidic oscillator's performance increases with the recovery level, with higher benefits for higher pressure coefficients

(C_p). When the flow is fully reattached ($C_p \approx 0.75$), fluidic oscillators allow for a 60% reduction in injected momentum, 30% reduction in blowing power, and 35% reduction in blowing ratio.

9 Conclusions

Fluidic valves have been used in order to apply unsteady boundary layer injection to the separated flow of a model diffuser, where the hump pressure gradient represents that of the suction surface of a highly loaded stator vane. It is well known that oscillatory blowing greatly reduces the injected momentum required by steady blowing in order to repair a separated boundary layer. In the previous 2 decades, a great deal of attention has been paid to the quantification of the benefits of pulsing, and many authors have demonstrated reductions up to two orders of magnitude in injected mass flow by using unsteady injection rather than steady injection. The vast majority of these studies, however, generate unsteady blowing by means of mechanical or piezoelectric actuators that employ moving parts, have reliability issues and limited lifetime, and are difficult to implement in high temperature turbomachinery components.

The focus of the present effort is to demonstrate the viability of fluidic actuators to perform unsteady blowing. These actuators essentially consist of a fluidic oscillator, have no moving parts or temperature limitations, and are therefore more attractive for implementation on production turbomachinery. The fluidic oscillators developed generate an unsteady velocity with an amplitude of up to 60% rms of the average at frequencies (f) ranging from 350 Hz to 2500 Hz. The nondimensional blowing frequency (F^+) of the current experiment lies in the range of $0.6 < F^+ < 6$ based on the shedding of the large-scale vortices in the separated boundary layer downstream of the diffuser hump.

In order to demonstrate the effectiveness of this unsteady injection technique, the overall pressure recovery of the diffuser (C_p) was compared with the optimal steady injection configuration previously achieved in the same rig with the same discrete hole injection geometry. Fluidic oscillators show a strong net reduction in the penalty associated with flow control when separation is fully repaired. These actuators are able to fully reattach the flow and achieve maximum pressure recovery at $F^+ \approx 0.7$ with a 60% reduction of injection momentum required and a 30% reduction in blowing power over the optimal steady injectors.

Whenever high-pressure recovery is achieved with pulsed blowing, questions arise on the emergence of large-scale fluctuations that would be disruptive in any turbomachinery application. In this study, we performed velocity and vorticity PIV measurements that show no large-scale unsteadiness in the flow, exhibiting the same streamlines as when the boundary layer is reattached by steady blowing.

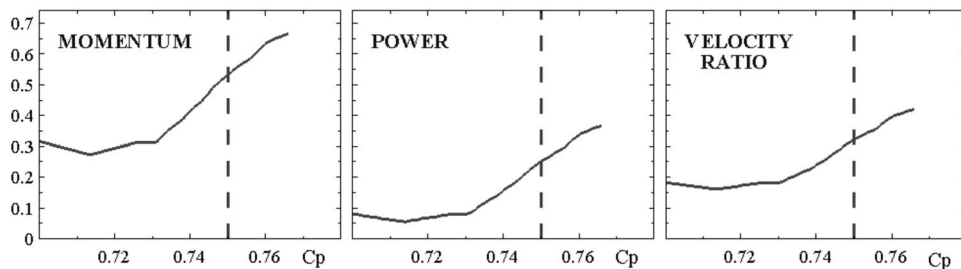


Fig. 16 Diffuser pressure recovery curves for steady and unsteady blowing as a function of C_μ for $\alpha=0$ deg

Acknowledgment

We are indebted to Dr. Paolo Graziosi for the enormous enthusiasm, help, and guidance he provided in the early stage of the project. We have very much benefited from many discussions with John Luedke, and we owe a great deal of thanks to Ron Capello, whose technical skills and dedication actually made the measurements happen. General Electric Co.'s financial support is gratefully acknowledged.

Nomenclature

C_p	=	diffuser pressure recovery coefficient
C_{p_s}	=	local pressure recovery coefficient
C_μ	=	injected momentum coefficient
c	=	hump chord
d	=	injection hole diameter
h	=	height
l	=	injection hole length
m_b	=	injection mass flow
Re_c	=	chord based Reynolds number
b	=	injection hole spacing
U, U_{FS}	=	x -velocity component, freestream velocity
V_b	=	injection jet absolute velocity
V_R	=	injection velocity ratio
P_t, P_t	=	pressure, total or static
f	=	oscillator frequency
F^+	=	nondimensional injection frequency
L	=	distance between the injection location and the diffuser trailing edge
N	=	number of injection holes
w	=	span
s	=	hump arc length
z	=	spanwise coordinate
a	=	upper diffuser wall angle
θ	=	injection hole streamwise angle
ρ	=	density

References

- [1] Lord, W. K., MacMartin, D. G., and Tillman, T. G., 2000, "Flow Control Opportunities in Gas Turbine Engines," AIAA Fluids Conference, AIAA, Reston, VA.
- [2] Jenkins, L., Althoff Gorton, S., and Anders, S., 2002, "Flow Control Device Evaluation for an Internal Flow With an Adverse Pressure Gradient," 40th Aerospace Sciences Meeting and Exhibit, AIAA, Reston, VA.
- [3] Lin, J. C., Howard, F. G., Bushnell, D. M., and Selby, G. V., 1990, "Investigation of Several Passive and Active Methods for Turbulent Flow Separation Control," 21st Fluid Dynamics, Plasma Dynamics and Lasers Conference, AIAA, Washington, D.C.
- [4] Walker, S., 1997, "Lessons Learned in the Development of a National Cooperative Program," 33rd AIAA/ASME/SAE/ASEE Joint Propulsion Conference and Exhibit, AIAA, Reston, VA.
- [5] Washburn, A. E., Althoff Gorton, S., and Anders, S., 2002, "Snapshot of Active Flow Control Research at NASA Langley," First Flow Control Conference, AIAA, Reston, VA.
- [6] Luedke, J., Graziosi, P., Kirtley, K., and Cerretelli, C., 2005, "Characterization of Steady Blowing for Flow Control in a Hump Diffuser," AIAA J., **43**(8), pp. 1644–1652.
- [7] Seifert, A., and Pack, L. G., 1999, "Active Control of Separated Flows on Generic Configurations at High Reynolds Numbers," AIAA Paper No. 99-3403.
- [8] Wignanski, I., 1997, "Boundary Layer and Flow Control by Periodic Addition of Momentum," AIAA Paper No. 97-2117.
- [9] Greenblatt, D., and Wignanski, I., 2000, "The Control of Flow Separation by Periodic Addition of Momentum," Prog. Aerosp. Sci., **36**, pp. 487–545.
- [10] Gregory, J., Sullivan, J., Raman, G., and Raghu, S., 2004, "Characterization of a Micro Fluidic Oscillator for Flow Control," AIAA Paper No. 2004-2692.
- [11] Kim, B., Williams, D., Emo, S., and Acharya, M., 2002, "Large Amplitude Pneumatic Oscillator for Pulsed-Blowing Actuators," AIAA Paper No. 2002-2704.
- [12] Culley, D. E., Prahst, P. S., Bright, M. M., and Strazisar, A. J., 2003, "Active Flow Separation Control of a Stator Vane Using Surface Injection in a Multi-stage Compressor Experiment," ASME Paper No. GT2003-38863.
- [13] Seifert, A., and Pack, L. G., 1999, "Active Control of Separated Flows on Generic Configurations at High Reynolds Numbers," AIAA Paper No. 99-3403.
- [14] Viken, S. A., Vatsa, V. N., Rumsey, C. L., and Carpenter, M. H., 2003, "Flow Control Analysis on the Hump Model With RANS Tools," 41st Aerospace Sciences Meeting and Exhibit, AIAA, Reston, VA.
- [15] Mehta, R. D., and Bradshaw, P., 1979, "Design Rules for Small Low Speed Wind Tunnels," Aeronaut. J., pp. 443–449.
- [16] Campagnuolo, C. J., and Lee, H. C., 1970, "Fluidic Oscillators," Instrum. Control Syst., June, pp. 99–103.
- [17] Nishri, B., and Wignanski, I., 1998, "Effects of Periodic Excitation on Turbulent Flow Separation From a Flap," AIAA J., **36**(4), pp. 547–556.
- [18] McManus, K., Legner, H., and Davis, S., 1994, "Pulsed Vortex Generator Jets for Active Control of Flow Separation," AIAA Paper No. 94-2218.
- [19] Glezer, A., Amitay, M., and Honohan, A. M., 2003, "Aspects of Low- and High-Frequency Aerodynamic Flow Control," AIAA Paper No. 2003-533.
- [20] Kirshner, J. M., and Katz, S., 1975, *Design Theory of Fluidic Components*, Academic, New York.

Superposition Predictions of the Reduction of Hot Streaks by Coolant From a Film-Cooled Guide Vane

Sean C. Jenkins

e-mail: sjenkins@mail.utexas.edu

David G. Bogard

e-mail: dbogard@mail.utexas.edu

Mechanical Engineering Department,
The University of Texas at Austin,
Austin, TX 78712

The turbine section of a gas turbine engine is subjected to hot gases flowing from the combustor that typically have high temperature regions known as "hot streaks." These hot streaks pass through the nozzle guide vanes, either impacting the vanes or passing through the passages between vanes. Generally the vanes are highly film cooled, and the coolant from the vanes interacts with the hot streak resulting in a reduction of the hot streak temperature. In this study, predictions of the reduction of hot streaks were made using superposition of measured temperature distributions due to coolant injection and measured temperature distributions of hot streaks. These predictions were compared to the measured hot streak reduction to determine the accuracy of the superposition technique. Results showed that the superposition predictions generally underpredicted the reduction of the peak hot streak temperature, but were within at least 20% of the peak temperature value. The superposition technique was also found to be useful for determining the hot streak reduction for different hot streak locations, and different coolant and hot streak operating conditions. [DOI: 10.1115/1.2948964]

Keywords: film cooling, hot streak, superposition

Introduction

Modeling of "hot streaks" downstream of the combustor in the turbine section of a gas turbine engine has been a subject of research for some time. The temperature nonuniformities, or hot streaks, in the flow field are due to the discrete number of circumferentially positioned combustors upstream of the first stage nozzle guide vanes. A majority of the modeling efforts have been computational fluid dynamics (CFD) simulations of the hot streak impinging on a first stage nozzle guide vane or passing between vanes. However, the estimation of the hot streak temperatures downstream of the first stage nozzle guide vanes involves consideration of cooling flows from those guide vanes.

The first investigations of hot streaks combined with vane coolant flows were by Roback and Dring [1,2]. In their first paper [1], Roback and Dring made separate measurements of a simulated hot streak and a coolant flow from the trailing edge of a stator. They used CO₂ as a trace gas to track the progress of a hot streak introduced through a pipe in the middle of the vane passage and to track the trailing edge coolant. In a companion paper [2], they made measurements of the combined hot streak and coolant flow, and evaluated whether the combined effects were predictable from the additive effects of the separate measurements of the hot streak and coolant, i.e., superposition. However, in their study the hot streak was positioned to pass through the middle of the passage between two stators, so the interaction between the hot streak and coolant would be expected to be small, if any. Furthermore, the description of their facility suggests that turbulence levels were very low, while for actual engine conditions the turbulence levels are very large. Finally, results from the study are difficult to inter-

pret because of their focus on the effects on the surface of the downstream rotor airfoils rather than the flow and thermal field approaching the rotor.

A recent study from our laboratory [3] showed that coolant from a fully film-cooled vane can cause a significant reduction of a hot streak impacting the vane. A more detailed study of the film cooling effects on hot streak reduction is presented in the companion paper [4]. This study shows the effects of varying coolant blowing ratio and density ratio on the reduction of the hot streak. In the current paper, measurements of the separate hot streak and coolant temperature profiles are used along with the measurements of the combined hot streak and coolant profiles to evaluate the predictive capability of superposition of the independent hot streak and coolant profiles. We then develop models capable of predicting a variety of hot streak and coolant conditions and their interactions. Finally, these models are used to predict the maximum reduction of the hot streak and the expected reduction of higher temperature hot streaks.

Facilities and Experimental Conditions

The test facility used to make the experimental measurements was a closed-loop, low-speed wind tunnel, driven by a 50 hp variable pitch, variable speed fan. The test section, shown in Fig. 1, was a simulated three vane, two passage cascade with adjustable bleed and adjustable walls to maintain the proper flow around the test airfoil. A full description of the facility is given in Polanka [5].

The test airfoil was a scaled up model of a first stage turbine guide vane, with the Reynolds number matched to actual engine operating conditions. The vane had a true chord length of $C=594$ mm and a span of $S=550$ mm, and the pitch between airfoils was $P=460$ mm. The mainstream approach velocity was $U_0=5.8$ m/s for all experiments, resulting in a Reynolds number of $Re=1.2 \times 10^6$ based on chord length and exit velocity. The test vane was constructed of polyurethane foam selected for strength and low thermal conductivity, with a value of $k=0.048$ W/(m K). For all coolant regions, the coolant hole di-

Contributed by the International Gas Turbine Institute of ASME for publication in the JOURNAL OF TURBOMACHINERY. Manuscript received September 26, 2006; final manuscript received August 3, 2007; published online June 30, 2009. Review conducted by David Wisler. Paper presented at the ASME Turbo Expo 2005: Land, Sea and Air (GT2005), Reno, NV, June 6–9, 2005.

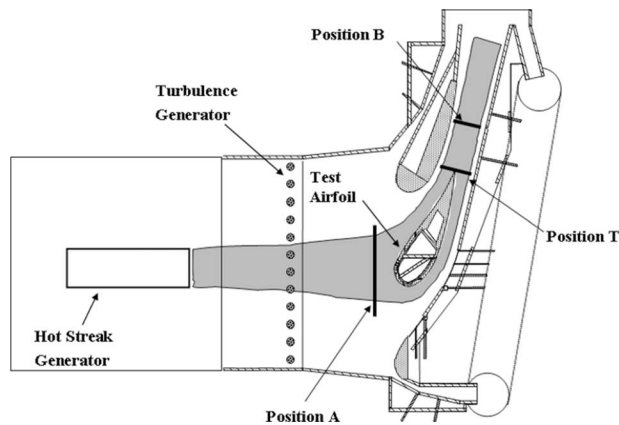


Fig. 1 Simulated vane cascade with hot streak generator

anometer was $d=4.11$ mm and the pitch in the vertical, or spanwise, direction between coolant hole centerlines was $5.55d$.

Three separate regions of coolant holes were used in the present study (shown in Fig. 2). The showerhead region had six rows of coolant holes with a row spacing of $3.33d$. These holes were oriented laterally, i.e., 90 deg to the streamwise direction, and had an injection angle of 25 deg relative to the surface. The pressure side film cooling holes consisted of two rows of coolant holes. These rows were located at $s/d=-25$ and $s/d=-45$, where $s/d=0$ is located at the stagnation line at the leading edge of the airfoil. The pressure side coolant holes had an injection angle of $\phi=30$ deg and a streamwise angle of $\theta=45$ deg. The three rows of suction side holes are also shown in this figure. Their locations with respect to the stagnation line were $s/d=30$, $s/d=53$, and $s/d=84$. The injection angles were $\phi=50$ deg, 45 deg, and 35 deg, respectively and the streamwise angles were $\theta=0$ deg, 45 deg, and 45 deg, respectively. The nominal mainstream temperature was $T_\infty=300$ K and the coolant consisted of cryogenically cooled air supplied at $T_C=187.5$ K, resulting in a density ratio of $DR=1.6$ for a majority of the results. Each coolant region had a separate pressure plenum providing coolant supply, as shown in Fig. 2. A full description of the film cooling supply and of the construction of the film cooling holes is given in Cutbirth and Bogard [6].

The hot streak generator section was installed upstream of the test section, as shown in Fig. 1. The exit of the hot streak genera-

tor was located $1.7C$ upstream of the vane leading edge and was designed to provide a nominal temperature ratio of $T_{0,HS}/T_\infty=1.1$ under both low and high turbulence conditions at a location $0.21C$ upstream of the vane, noted as Position A in Fig. 1. Given the nominal mainstream temperature of $T_\infty=300$ K, the nominal peak hot streak temperature was $T_{0,HS}=330$ K. The hot streak generator was designed to be continuously adjustable across the pitch of the vane cascade. The construction and adjustment of the hot streak generator section is fully described in Jenkins et al. [3].

Turbulence intensity and integral length scales were established using hot-wire anemometer measurements at Position A. For the low turbulence condition, the turbulence intensity was $Tu=3.5\%$ and the integral length scale was large, $\Lambda_f=19-30$ mm. High mainstream turbulence was generated using an array of 38 mm diameter vertical rods, spaced 85 mm apart, and located $0.88C$ upstream of the stagnation line, as shown in Fig. 1. The turbulence generator produced a turbulence intensity of $Tu=20\%$ with an integral length scale of $\Lambda_f=33$ mm at Position A. Additional details regarding the turbulence field and turbulence generator are available in Cutbirth [7].

Measured hot streak and coolant temperature profiles were acquired using a thermocouple rake consisting of 22 K-type thermocouples spaced 7.8 mm apart. Measurements were taken normal to the flow direction, as shown in Fig. 1, in measurement planes at Positions A, T, and B. Temperature readings from the thermocouple rake and thermocouples placed in the mainstream were acquired using a National Instruments multiplexer, an analog/digital (A/D) module, and the LABVIEW software and were time averaged over a 6 s time span.

A normalized temperature ratio, Θ_R , was used to define the "strength" of the hot streak. The normalized temperature ratio, Θ_R , was defined based on the peak hot streak temperature, $T_{0,HS}$, measured at the standard reference position (Position A) upstream of the vane leading edge. Since the local temperature is scaled by the peak value upstream, Θ_R may be thought of as the hot streak reduction, or as a percentage of the original hot streak. It is shown in the following equation:

$$\Theta_R = \frac{T_{ij} - T_\infty}{T_{0,HS} - T_\infty} \quad (1)$$

where Θ_R is computed at a point (ij) based on the temperature at that point, T_{ij} , and the mainstream temperature at the measurement plane, T_∞ .

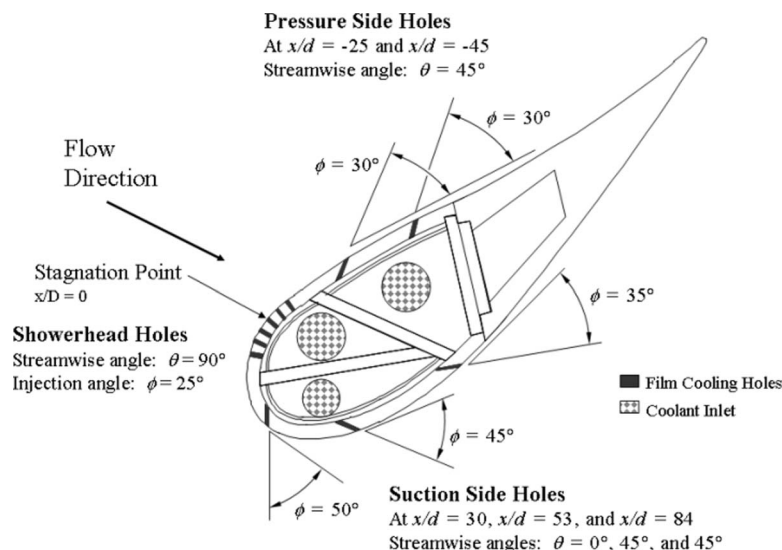


Fig. 2 Schematic of film cooling hole configuration

To eliminate bias uncertainty of the measurements for the thermocouple rake, the equipment was tested against a known standard, i.e., an ice bath, and repeatable bias errors were computed. The bias errors between thermocouples were eliminated by adjusting the raw data according to the bias error previously determined. In this way, biases between thermocouples and thermocouple channels were removed, leaving only random or precision error. Based on a statistical analysis of the temperature measurements, the precision uncertainty (95% confidence interval) of the time averaged temperature values ranged from ± 0.1 K at the mainstream temperature to ± 0.4 K at the peak hot streak temperature. This error was a random error resulting from the data acquisition system. Based on the temperature uncertainties, the uncertainty in the temperature ratio, T/T_∞ , was calculated to be ± 0.001 and the uncertainty in the normalized temperature ratio, Θ_R , was calculated to be ± 0.02 .

Derivation of the Superposition Equation

An energy balance at a point in the flow shows that the energy contained at that point is a function of the mass flow rate, specific heat, and temperature difference with respect to a reference temperature, in this case the mainstream temperature. This may be expressed as a superposition of energy levels at that point for the coolant profile and hot streak profile separately, shown in

$$(\rho U d A) c_p (T_{ij} - T_\infty)_{SP} = (\rho U d A) c_p (T_{ij} - T_\infty)_C + (\rho U d A) c_p (T_{ij} - T_\infty)_{HS} \quad (2)$$

where the subscript SP refers to the superposition result, and the subscripts C and HS refer to measurements of the coolant and hot streak temperatures, respectively. The specific heat varied only slightly for the full range of temperatures during the experiments, so this may be considered as constant. At a point in the flow, the velocity field is relatively unaffected by the presence of the hot streak, as shown by Dorney [8], and previous measurements in the facility showed that coolant flows had a negligible effect on the velocity field downstream of the vane. Thus the velocity was considered invariant for a given position. At the measurement plane (i.e., Position T or B), for the range of temperatures observed, the density varied by no more than about 5%, so it too may be considered nearly constant. Therefore, this equation may be written as the superposition of fluid temperature differences from the mainstream as

$$(T_f - T_\infty)_{SP} = (T_f - T_\infty)_C + (T_f - T_\infty)_{HS} \quad (3)$$

Dividing both sides by the peak hot streak-to-mainstream temperature difference results in

$$\frac{(T_f - T_\infty)_{SP}}{(T_{0,HS} - T_\infty)} = \frac{(T_f - T_\infty)_C}{(T_{0,HS} - T_\infty)} + \frac{(T_f - T_\infty)_{HS}}{(T_{0,HS} - T_\infty)} \quad (4)$$

which can be quickly related to the normalized temperature ratio, Θ_R , using its definition from Eq. (1) to obtain the superposition equation

$$\Theta_{R,SP} = \Theta_{R,C,exp} + \Theta_{R,HS,exp} \quad (5)$$

where the subscripts C and HS refer to coolant only and hot streak only experimental results and the subscript SP refers to the superposition result. This equation is used to predict hot streak reduction due to coolant flow under various conditions.

Results

The goal of superposition analysis is to predict the effect of coolant on the hot streak by adding coolant profiles to hot streak profiles. First, the capability of superposition was evaluated by comparing these predictions with measured data. Following this validation, the method was used to estimate the effect of coolant on the hot streak for different hot streak pitch positions and determine the ideal hot streak pitch position based on these predictions. A numerical simulation by Dorney [8] showed that increasing the

hot streak temperature ratio from $T/T_\infty=1.5$ to 2.0 had very little effect on the predicted kinematics of the hot streak. Thus, scaling of the hot streak temperature profiles by a different peak hot streak temperature ratio was also possible. The results shown in a concurrent paper [4] indicated that coolant profiles could be scaled by the coolant hole exit to mainstream temperature difference, so coolant profiles with different density ratios could be estimated as well. Superposition of these coolant profiles with the scaled hot streak profiles made it possible to predict the reduction of hot streaks for other combinations of hot streak temperature ratios and coolant density ratios not attainable in the present facility.

Validation of Superposition Predictions. The following evaluation of superposition in predicting hot streak and coolant interaction is presented for a range of conditions. These include results for individual blowing regions, different blowing ratios, density ratios at DR=1.2 and 1.6, and low and high mainstream turbulence levels (Tu=3.5% and 20%). While the majority of results are shown for midspan profiles, where the hot streak was the strongest, full field comparisons are also shown for selected cases.

The following comparisons are made under conditions of high mainstream turbulence (Tu=20%). A comparison of the measured and predicted midspan profiles of the hot streak is presented in Fig. 3 for the case of showerhead coolant injection at $M^*=1.6$ and a density ratio of DR=1.6 at Position T, i.e., at the trailing edge of the vane, as shown in Fig. 1. Also shown in Fig. 3 are the measured profiles for the hot streak alone and the showerhead coolant alone. These data were used to compute the superposition profile using Eq. (5). The superposition prediction matched the overall shape of the experimental profile fairly well but underpredicted the reduction in the peak Θ_R value, showing a hot streak reduction of 21% (dotted line) compared with the measured 33% peak hot streak reduction (solid line). At blowing ratios of $M^*=1.4$ and 2.0, not shown in the figure, superposition also underpredicted the benefit of showerhead coolant by similar amounts. Error bars are shown for this figure to indicate the levels of uncertainty for the measured values.

For suction side film cooling, with a blowing ratio of $M_{av}=0.7$, shown in Fig. 4, superposition predicted the near wall dip in hot streak temperature well and did a reasonable job of capturing the shape of the rise in hot streak temperature farther away but also underpredicted the benefit of coolant in reducing the hot streak on the suction side. The superposition model does not account for the influence of strong temperature gradients or changes in the flow field due to coolant/hot streak interaction, which resulted in stronger deviations in the predicted results in

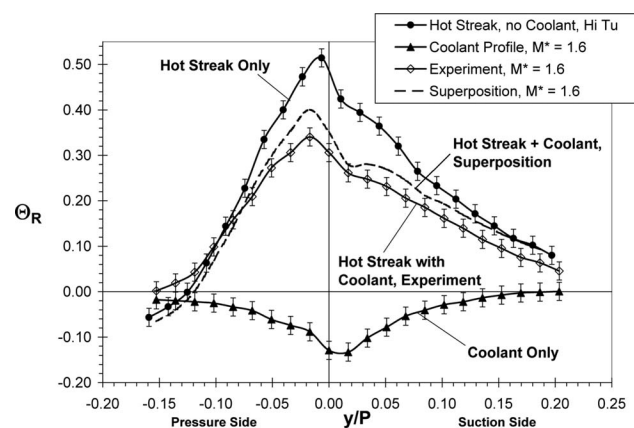


Fig. 3 Comparison of experimental and superposition normalized temperature ratio (Θ_R) profiles at Position T at midspan ($z/S=0.50$) for the hot streak at the stagnation line with showerhead blowing at $M^*=1.6$ and high mainstream turbulence ($T_u=20\%$)

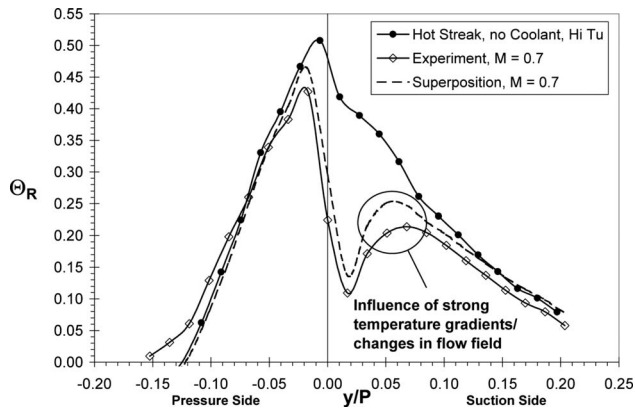
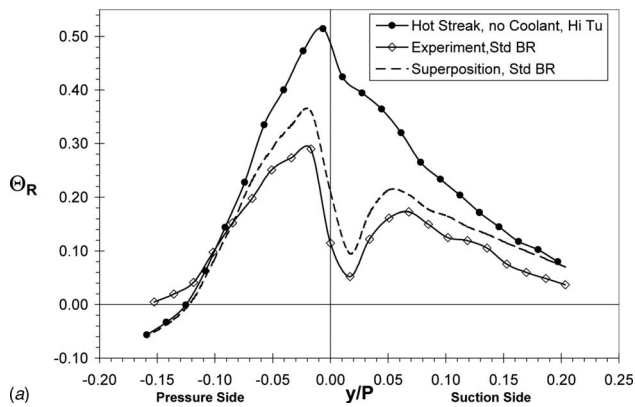


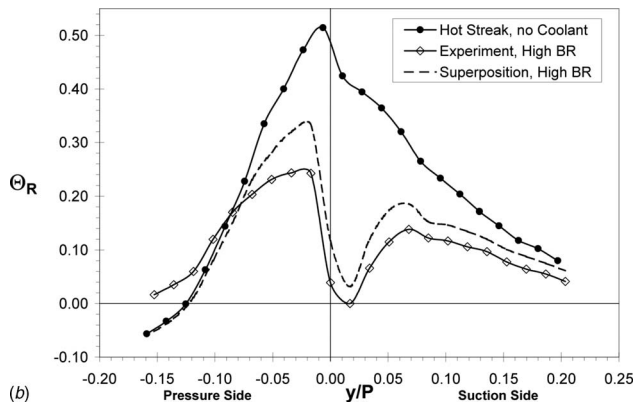
Fig. 4 Comparison of experimental and superposition normalized temperature ratio (Θ_R) profiles at Position T at midspan ($z/S=0.50$) for the hot streak at the stagnation line with suction side blowing at $M_{av}=0.7$ and high mainstream turbulence ($Tu=20\%$)

some locations. One such example is pointed out in Fig. 4.

The superposition prediction with full coverage film cooling with blowing ratios of $M^*=1.6$ from the showerhead, $M_{av}=0.7$ from the suction side, and $M_{av}=0.6$ from the pressure side is shown in Fig. 5(a). Again superposition predicts the general shape of the temperature profile but underpredicts the decrease in hot

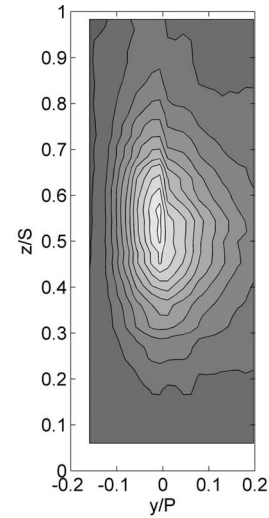


(a)

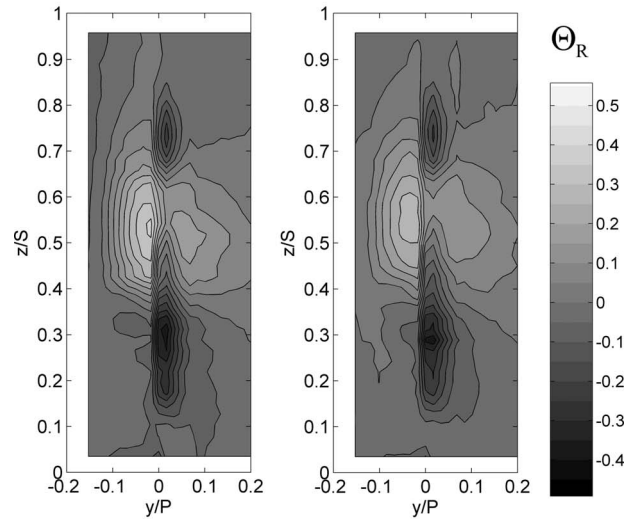


(b)

Fig. 5 Comparison of experimental and superposition prediction normalized temperature ratio (Θ_R) profiles at Position T at midspan ($z/S=0.50$), for the hot streak at the stagnation line with full coverage blowing and high mainstream turbulence ($Tu=20\%$) at (a) standard blowing ratios ($M^*_{showerhead}=1.6$, $M_{av,suction}=0.7$, and $M_{av,pressure}=0.6$) and (b) high blowing ratios ($M^*_{showerhead}=2.0$, $M_{av,suction}=1.0$, and $M_{av,pressure}=1.0$)



a.



b.

c.

Fig. 6 Normalized temperature ratio (Θ_R) contours at Position T with the hot streak at the stagnation line and high mainstream turbulence ($Tu=20\%$) with (a) no coolant, (b) superposition prediction of full coverage blowing at $M^*_{showerhead}=2.0$, $M_{av,suction}=1.0$, and $M_{av,pressure}=1.0$, and (c) measured values for full coverage blowing at $M^*_{showerhead}=2.0$, $M_{av,suction}=1.0$, and $M_{av,pressure}=1.0$

streak peak temperature caused by coolant injection. While the measured hot streak reduction was over 40% compared with no film cooling, superposition predicted that it would be a little less than 30%. At higher full coverage blowing ratios ($M^*_{showerhead}=2.0$, $M_{av,suction}=1.0$, and $M_{av,pressure}=1.0$) in Fig. 5(b), overall agreement was also good. Here the measured hot streak reduction was just over 50% while superposition predicted that it would be about 35%.

The superposition prediction of the temperature distribution across the two-dimensional $y-z$ plane at the trailing edge of the vane is shown in Fig. 6(b) along with the measured temperature distribution (Fig. 6(c)). The two-dimensional hot streak contours with no film cooling are shown as a reference (Fig. 6(a)). Full coverage coolant injection was used in this case with $M^*=2.0$ from the showerhead, $M_{av}=1.0$ from the suction side, and $M_{av}=1.0$ from the pressure side. The most important observation when comparing the measured and predicted temperature profiles

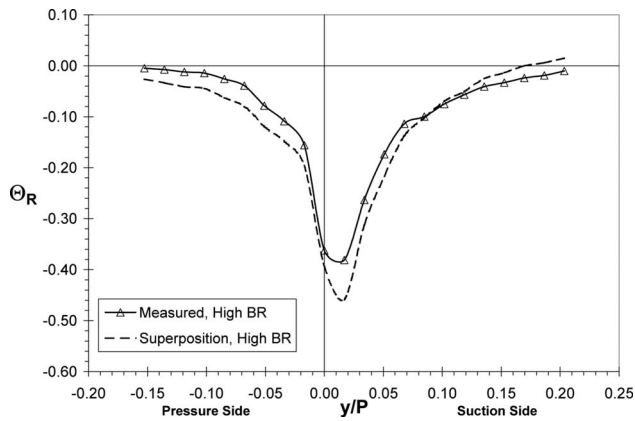


Fig. 7 Comparison of measured coolant temperature (Θ_R) profiles at Position T at midspan ($z/S=0.50$) for full coverage film cooling at high blowing ratios ($M_{\text{showerhead}}^*=2.0$, $M_{\text{av,suction}}=1.0$, and $M_{\text{av,pressure}}=1.0$) and superposition of individual region coolant temperature (Θ_R) profiles at the same blowing ratios and high mainstream turbulence ($Tu=20\%$)

is that the superposition prediction gives a good representation of the complete temperature distribution. A closer inspection of the temperature contours reveals that the measured temperature contours are more widely dispersed than the predicted temperature contours, while the peak values of Θ_R are slightly higher for the prediction.

It was also possible to estimate the full coverage coolant profile by superposition of individual region coolant profiles. As shown in Fig. 7, superposition predicted a coolant profile peak at Position T that was more than 20% colder than the measured profile.

Comparisons were also made under conditions of high mainstream turbulence with coolant at low density ratio ($DR=1.2$). Here, superposition predicted higher values over the width of the hot streak with full coverage blowing (Fig. 8). The peak of the hot streak was predicted to be $\Theta_R=0.43$, while the measured peak was $\Theta_R=0.40$ (from $\Theta_R=0.51$ for no film cooling). Therefore, the measured reduction of the peak ($\Delta\Theta_R=-0.11$) was about 30% greater than predicted ($\Delta\Theta_R=-0.08$).

At low mainstream turbulence levels ($Tu=3.5\%$), hot streak reduction was also possible to predict, as shown in Fig. 9. This comparison was also made with full coverage film cooling and

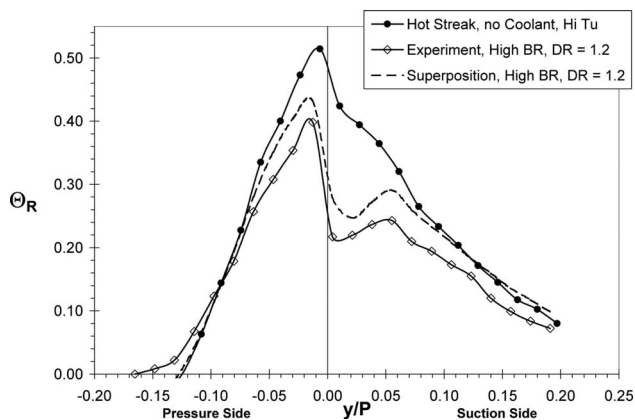


Fig. 8 Comparison of experimental and superposition normalized temperature ratio (Θ_R) profiles at Position T at midspan ($z/S=0.50$) for the hot streak at the stagnation line with full coverage blowing at high blowing ratios ($M_{\text{showerhead}}^*=2.0$, $M_{\text{av,suction}}=1.0$, and $M_{\text{av,pressure}}=1.0$) at a density ratio of $DR=1.2$ and high mainstream turbulence ($Tu=20\%$)

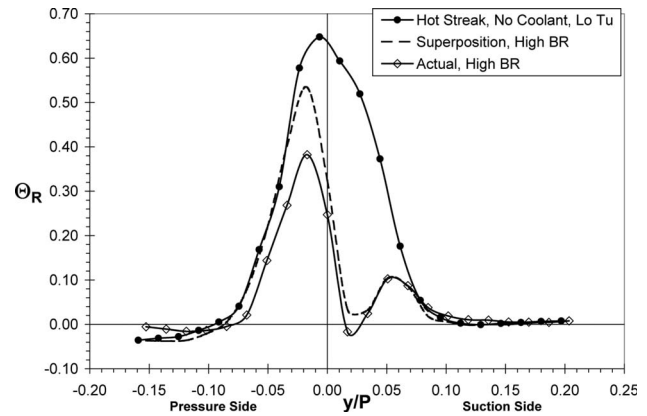


Fig. 9 Comparison of experimental and superposition normalized temperature ratio (Θ_R) profiles at Position T at midspan ($z/S=0.50$) for the hot streak at the stagnation line with full coverage blowing at $M_{\text{showerhead}}^*=2.0$, $M_{\text{av,suction}}=1.0$, and $M_{\text{av,pressure}}=1.0$, low mainstream turbulence ($Tu=3.5\%$)

may be compared with Fig. 5(b) at high turbulence. The general shape of the profile was predicted well, but the prediction of the reduction of the peak was not as good as under conditions of high mainstream turbulence, as superposition predicted only about half of the total reduction measured. However, this result shows that superposition works over a wide range of turbulence levels, so the prediction of profiles at other turbulence levels should also be possible.

Predictions made further downstream of the vane at Position B (0.34C downstream of the trailing edge) were fairly similar to those at Position T. Figure 10 shows the results of these predictions at high mainstream turbulence ($Tu=20\%$) for showerhead cooling only at a blowing ratio of $M^*=2.0$. The shape of the profile was predicted well, but the reduction in the hot streak peak was underpredicted.

For suction side cooling at $M_{\text{av}}=1.0$, superposition predicted more dispersion of the temperature gradient at $0.0P$, while the experimental profile showed a steeper gradient (Fig. 11). This resulted in a lower predicted peak, but higher values to the suction side of $0.0P$.

For full coverage film cooling at Position B, superposition predictions gave better estimates of the reduction in peak strength of the hot streak compared to the trailing edge. As shown in Fig. 12,

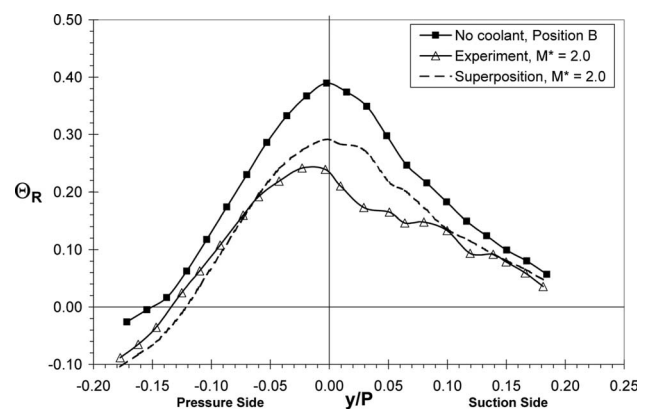


Fig. 10 Comparison of experimental and superposition normalized temperature ratio (Θ_R) profiles at Position B at midspan ($z/S=0.50$) for the hot streak at the stagnation line with showerhead blowing at $M^*=2.0$ and high mainstream turbulence ($Tu=20\%$)

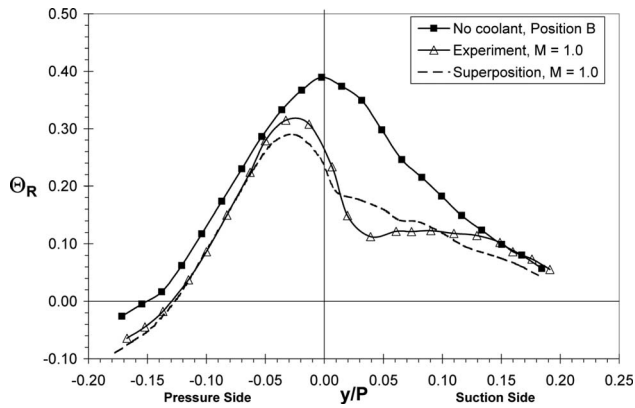


Fig. 11 Comparison of experimental and superposition normalized temperature ratio (Θ_R) profiles at Position B at mid-span ($z/S=0.50$) for the hot streak at the stagnation line with suction side blowing at $M_{av}=1.0$ and high mainstream turbulence ($Tu=20\%$)

the prediction of the hot streak peak was fairly accurate. Superposition predicted a reduction of about 45% compared to 55% measured. The improved predictions at Position B relative to predictions at the trailing edge may be due to the dispersion that occurs between the trailing edge and Position B.

The superposition prediction of the temperature distribution across the two-dimensional plane at position B is shown in Fig. 13(b) for full coverage blowing with the measured temperature distributions in Fig. 13(c). The hot streak contours at Position B without coolant injection are provided as a reference (Fig. 13(a)). Coolant injection in this case was $M^*=2.0$ from the showerhead, $M_{av}=1.0$ from the suction side, and $M_{av}=1.0$ from the pressure side. Again the superposition prediction gives a good representation of the complete temperature distribution although the dispersion of the temperature contours is slightly less than the measured temperature contours. The predicted peak value for the hot streak was very similar to the measured peak value.

Prediction of Coolant From Adjacent Vanes. Although the facility contained only one film-cooled test vane, superposition allows the effect of coolant from adjacent vanes to be predicted. The computed coolant profile for Position T under conditions of high mainstream turbulence is shown in Fig. 14 for high blowing

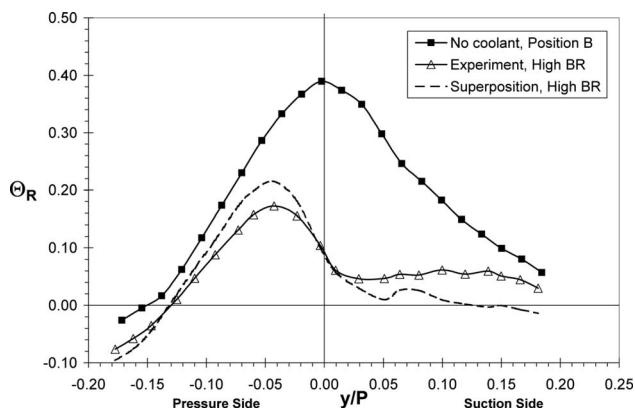
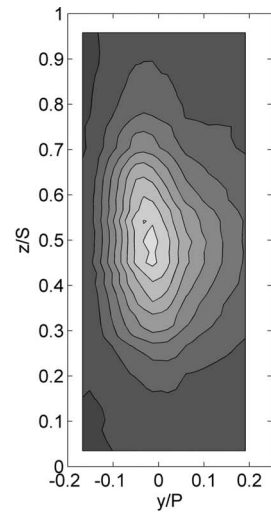
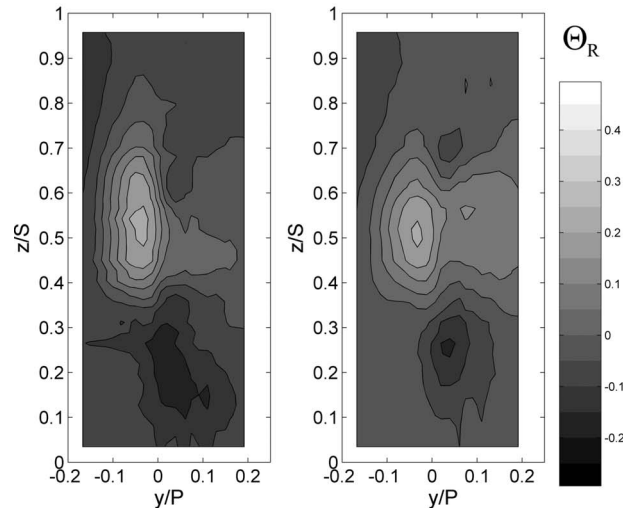


Fig. 12 Comparison of experimental and superposition normalized temperature ratio (Θ_R) profiles in the wake at Position B at midspan ($z/S=0.50$) for the hot streak at the stagnation line with full coverage blowing at $M_{showerhead}^*=2.0$, $M_{av,suction}=1.0$, and $M_{av,pressure}=1.0$ and high mainstream turbulence ($Tu=20\%$)



a.



b.

c.

Fig. 13 Normalized temperature ratio (Θ_R) contours in the wake at Position B with the hot streak at the stagnation line and high mainstream turbulence ($Tu=20\%$) with (a) no coolant, (b) superposition prediction of full coverage blowing at $M_{showerhead}^*=2.0$, $M_{av,suction}=1.0$, and $M_{av,pressure}=1.0$, and (c) measured values for full coverage blowing at $M_{showerhead}^*=2.0$, $M_{av,suction}=1.0$, and $M_{av,pressure}=1.0$

ratios. The figure indicates the overlapping coolant profiles from vanes to the suction and pressure sides of the test vane and the predicted combined profile.

Figure 15 shows a superposition prediction of the effect of this coolant profile for a hot streak centered at the stagnation line. The comparison shows that although there was some effect on the hot streak peak, the majority of the effect was well away from the peak toward the edges of the hot streak. This effect would clearly be much greater for a hot streak positioned at midpassage to either side of the vane.

At Position B, the dispersion of coolant was much greater and a prediction of coolant from adjacent vanes resulted in a profile that was much flatter, as shown in Fig. 16. The combined profile had a somewhat lower negative peak due to coolant spreading well away from the simulated adjacent vanes toward $y/P=0.0$, but the primary effect was to the edges of the profile. The enhanced levels of cooling in the simulated profile at midpassage positions indi-

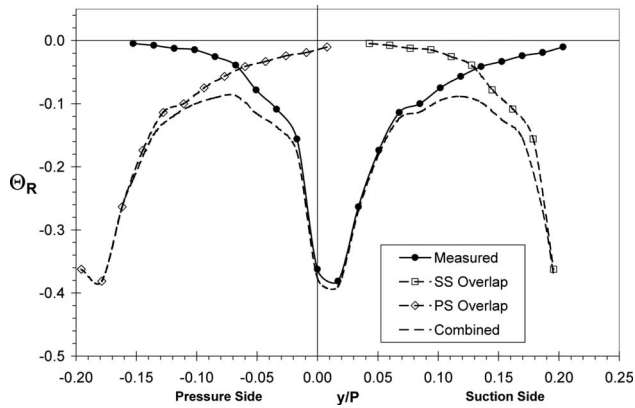


Fig. 14 Prediction of coolant profile including coolant from adjacent vanes for full coverage at high blowing ratios ($M_{showerhead}^* = 2.0$, $M_{av,suction} = 1.0$, and $M_{av,pressure} = 1.0$) and high mainstream turbulence ($Tu = 20\%$)

cate that the hot streak would be greatly reduced if the hot streak were positioned at midpassage as well as at the stagnation line.

Prediction of the Ideal Hot Streak Pitch Position With Film Cooling. Given the verification of the predictive capabilities of superposition, this tool was used to estimate the ideal hot streak pitch position with film cooling. An analysis was performed using hot streak pitch position data from a paper by the same authors [9] along with coolant profiles under conditions of high mainstream turbulence at the trailing edge (Position T) and farther downstream at Position B. A coolant profile including coolant from adjacent vanes was used in the predictions, as shown in Fig. 14 previously. A minimum hot streak peak was identified for full coverage film cooling at Positions T and B.

Since the coolant had the strongest effect for the individual regions and for full coverage to the suction side (see Figs. 3–5), superposition was expected to predict an ideal hot streak position to the suction side of the stagnation line. This ideal hot streak position was found to be $+0.043P$. With full coverage film cooling at high blowing ratios, superposition predicted an additional reduction of the hot streak peak to the pressure side of a little more than 20% compared with the hot streak at the stagnation line. A comparison between the reduction in hot streak strength for the

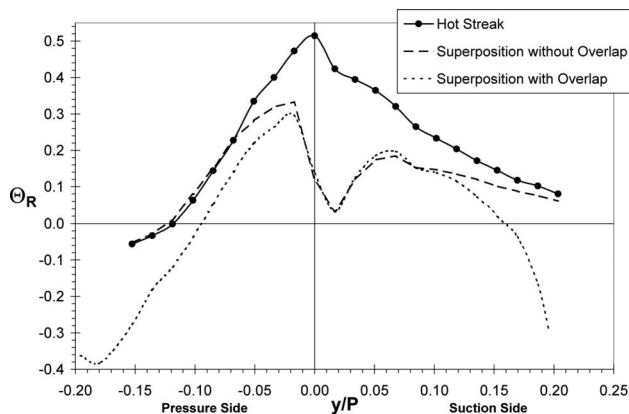


Fig. 15 Comparison of experimental and superposition normalized temperature ratio (Θ_R) profiles at Position T at mid-span ($z/S = 0.50$) for the hot streak at the stagnation line with full coverage blowing at ($M_{showerhead}^* = 2.0$, $M_{av,suction} = 1.0$, and $M_{av,pressure} = 1.0$), high mainstream turbulence ($Tu = 20\%$) including a prediction for the reduction with coolant from adjacent vanes

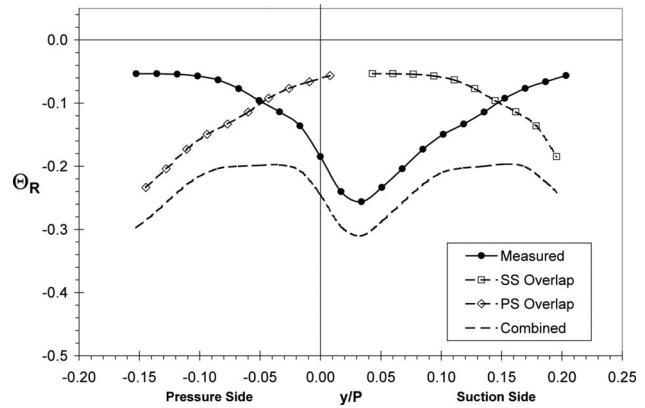


Fig. 16 Prediction of coolant profile including coolant from adjacent vanes for full coverage at high blowing ratios ($M_{showerhead}^* = 2.0$, $M_{av,suction} = 1.0$, and $M_{av,pressure} = 1.0$) at Position B and high mainstream turbulence ($Tu = 20\%$)

hot streak positioned at $0.0P$ and $+0.043P$ is shown in Fig. 17. Both hot streak curves without coolant are shown as a reference, while predicted values indicate that coolant interaction would result in a lower peak value for the hot streak position at $+0.043P$. As shown in the figure, this is due to a change in the shape of the resulting profile with full coverage film cooling.

An analysis was performed to determine how sensitive the hot streak reduction was to the hot streak pitch position. The predicted ideal hot streak pitch position is clearly shown in Fig. 18 at $+0.043P$. This figure also shows the effect of hot streak pitch position without film cooling as presented in a previous paper by the same authors [9] for comparison. With film cooling, there was a distinctly lower hot streak peak at $+0.043P$ compared to all other hot streak pitch positions even though the total predicted reduction due to film cooling was similar for other hot streak locations. Moving the hot streak to the pressure side away from the ideal position resulted in a nearly linear trend of the peak value up to a pitch position of $-0.065P$ with a predicted peak nearly 60% higher at $\Theta_R = 0.39$. From this point farther to the pressure side, the increase in predicted peak was less steep due to the interaction of the hot streak with simulated coolant from adjacent vanes. Moving the hot streak to the suction side resulted in an increase in hot streak temperature as well, but not as great as to the pressure side. To the suction side, the prediction of the hot

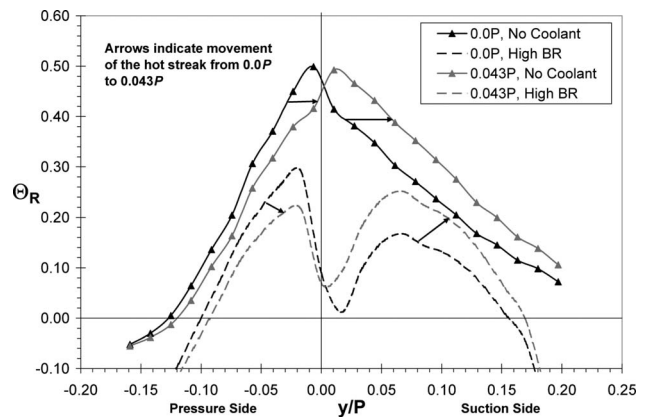


Fig. 17 Comparison of normalized temperature ratio (Θ_R) profiles at Position T for pitch positions of $0.0P$ (base line) and $+0.043P$ (ideal) without coolant (measured) and with full coverage blowing at $M_{showerhead}^* = 2.0$, $M_{av,suction} = 1.0$, and $M_{av,pressure} = 1.0$ (predicted)

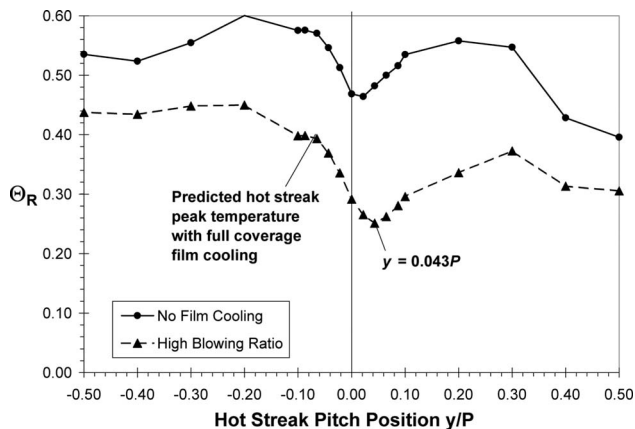


Fig. 18 Peak hot streak temperature ratio (Θ_R) predictions versus hot streak pitch position at Position T for full coverage film cooling at $M_{showerhead}^* = 2.0$, $M_{av,suction} = 1.0$, and $M_{av,pressure} = 1.0$, including adjacent vane overlap predictions

streak peak with simulated coolant from adjacent vanes resulted in peak values decreasing with the movement of the hot streak toward midpassage. Focusing in on a range between $0.00P$ and $+0.10P$, which surrounds the ideal predicted pitch position, the predictions suggested that the hot streak peak temperature would rise about 20% up to about $\Theta_R = 0.29$ on either side of the range, compared with $\Theta_R = 0.25$ at $+0.043P$.

At Position B downstream of the trailing edge, the ideal pitch position was slightly different, at $+0.022P$, as shown in Fig. 19. This prediction also utilized a predicted coolant profile including coolant from adjacent vanes. Due to the extensive spreading of coolant by Position B, the peak hot streak value was reduced by about the same amount for the full range of hot streak pitch positions. Compared with Position T, superposition predicted a small improvement in additional reduction for the ideal pitch position at Position B compared with $y = 0.0P$.

Predictions of Aeroengine Scaled Hot Streak Reduction. In a concurrent paper by the same authors [4], coolant temperature profiles with variations in the coolant density ratio were shown to scale well using the normalized coolant temperature, Θ_C . This, along with superposition, allowed for predictions under conditions of high mainstream turbulence ($Tu = 20\%$) of combinations of coolant density ratio and hot streak temperature ratio unattainable in the current facility. It was also noted that aerospace engines

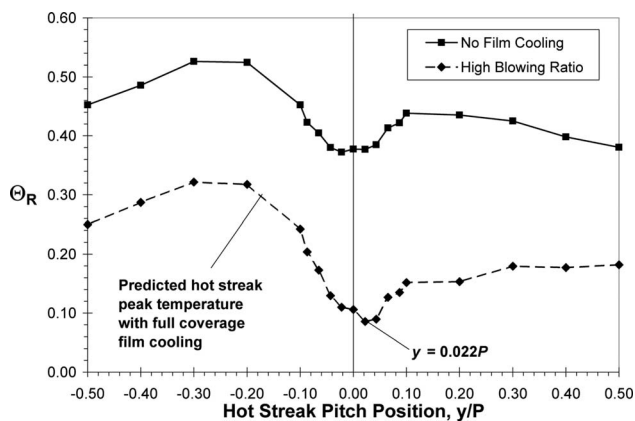


Fig. 19 Peak hot streak temperature ratio (Θ_R) predictions vs hot streak pitch position at Position B for full coverage film cooling at $M_{showerhead}^* = 2.0$, $M_{av,suction} = 1.0$, and $M_{av,pressure} = 1.0$

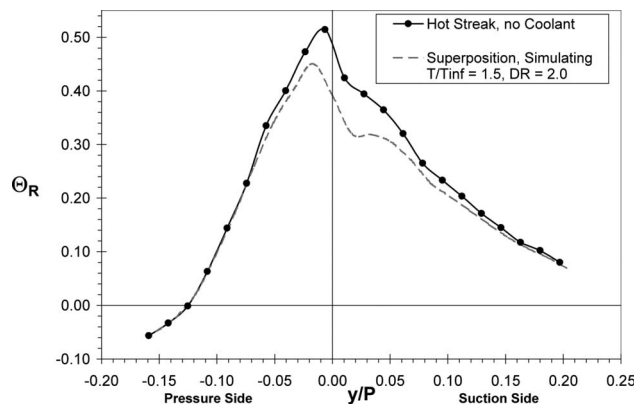


Fig. 20 Comparison of normalized temperature ratio (Θ_R) profiles at Position T at midspan ($z/S = 0.50$) for the hot streak at a simulated temperature ratio of $T/T_\infty = 1.5$ at the stagnation line without cooling and with full coverage blowing at a simulated coolant density ratio of $DR = 2.0$ at $M_{showerhead}^* = 2.0$, $M_{av,suction} = 1.0$, and $M_{av,pressure} = 1.0$ and high mainstream turbulence ($Tu = 20\%$)

may have hot streak temperature ratios as high as $T/T_\infty = 1.5$.

An appropriate hot streak profile at the trailing edge was calculated by scaling measured values at $T_{0,HS}/T_\infty = 1.09$ to a temperature ratio of $T_{0,p}/T_\infty = 1.5$. As such, the shape of the hot streak at the trailing edge was assumed to be invariant with upstream temperature ratio. This assumption is substantiated by looking at numerical simulations by Dorney et al. [8] who investigated the effect of the hot streak temperature ratio for a range of $T/T_\infty = 1.5 - 2.5$. Increasing the temperature ratio from $T/T_\infty = 1.5$ to 2.0 was found to have very little effect on the predicted kinematics of the hot streak, so it is unlikely that the hot streak shape would be significantly different between hot streak temperature ratios of $T/T_\infty = 1.09$ and 1.5.

For an aeroengine, density ratios tend to be somewhat higher as well. Using experimental coolant profile data in terms of the normalized coolant temperature, Θ_C , a profile in terms of Θ_R with a density ratio of $DR = 2.0$ was computed. Superposition of these results with the predicted hot streak profile estimated the probable effect of full coverage film cooling at high blowing ratios for aeroengine specific conditions of $T_{0,p}/T_\infty = 1.5$ and a density ratio of $DR = 2.0$. In Fig. 20, it is clear that the hot streak would be reduced much less for aerospace engine conditions than ground-based engine conditions. These predictions suggest that the hot streak peak would be reduced by about 10% compared with no film cooling. For an estimated peak turbine inlet temperature of 1900 K [10], this translates into nearly a 40°C drop in peak fluid temperature. Since the fluid temperature field has a strong influence on the surface temperatures of the downstream components, and the life of a component has been shown to double with a surface temperature decrease of only 50°C , this fluid temperature reduction is significant. The fluid temperature reduction predicted is much less than the nearly 40% reduction with ground-based engine representative conditions but indicates that film cooling could still assist in hot streak reduction for aerospace applications.

Conclusions

Superposition of coolant profiles and hot streak profiles was compared with measured data to evaluate the capability of additive superposition in predicting hot streak reduction due to film cooling. This method was used to predict other combinations of hot streak temperatures and coolant density ratios not attainable in the current facility.

This method proved to be fairly capable of predicting film-cooled hot streak profiles. Errors in predicting the peak of the

cooled hot streak were generally below 20%, with some much lower. The predictive capacity of the superposition method was also used to determine the ideal pitch position of the hot streak relative to the stagnation line of the vane. This predicted position was just to the suction side with full coverage film cooling, with a predicted additional reduction in the hot streak peak temperature of about 20%. The same ideal hot streak pitch position was predicted at Position B for full coverage film cooling, and additional reductions due to the pitch position were predicted to be on the order of about 10%. However, the nature of errors in using superposition at Position B shown earlier makes it unclear how much improvement would be realized. Superposition was also used to predict the effect of film cooling for aerospesific engine conditions. These predictions indicated that film cooling would reduce the hot streak by about 10% compared with no film cooling. As such, the coolant would be less effective at reducing the hot streak under these conditions, but could reduce the peak fluid temperatures by as much as 40°C, possibly increasing the life of some components.

Acknowledgment

We would like to thank Jay Rutledge and Dave Robertson for their assistance in running experiments and developing a new data acquisition system for the facility.

Nomenclature

C	= vane chord length, 594 mm
d	= film cooling hole diameter, 4.11 mm
DR	= density ratio of coolant to mainstream, ρ_c/ρ_∞
k	= thermal conductivity
M	= blowing ratio for the suction and pressure sides, where U_∞ is the local freestream velocity at the hole location, $\rho_c U_c/\rho_\infty U_\infty$
M^*	= blowing ratio for the showerhead region, where U_0 is the approach velocity to the vane, $\rho_c U_c/\rho_0 U_0$
p	= film cooling hole pitch in the spanwise direction
P	= pitch between vanes, 460 mm
S	= span length of vane, 550 mm
s	= surface length from the leading edge stagnation line
T_{ij}	= fluid temperature at a point in the flow
$T_{0,HS}$	= upstream peak hot streak temperature at the reference location, Position A
T_∞	= mainstream temperature
Tu	= turbulence intensity, $u_{rms}/U \times 100\%$
U_0	= approach velocity to the vane
U_∞	= local freestream velocity

y = flow normal coordinate originating at the trailing edge (positive for the suction side of the test vane; negative for the pressure side of the test vane)
 z = spanwise coordinate

Greek Symbols

ϕ	= injection angle with respect to the surface plane
θ	= streamwise injection angle
ρ	= density
Λ_f	= turbulence integral length scale
Θ_C	= normalized coolant temperature ratio, $(T_{ij}-T_\infty)/(T_\infty-T_{0,C})$
Θ_R	= normalized hot streak temperature ratio, $(T_{ij}-T_\infty)/(T_{0,HS}-T_\infty)$

Subscripts

C	= coolant
HS	= hot streak value
p	= predicted value
R	= normalized
SP	= superposition result
∞	= mainstream
0	= approach condition

Superscripts

* = showerhead (blowing ratio)

References

- [1] Roback, R. J., and Dring, R. P., 1993, "Hot Streaks and Phantom Cooling in a Turbine Rotor Passage: Part 1—Separate Effects," *ASME J. Turbomach.*, **115**(4), pp. 657–666.
- [2] Roback, R. J., and Dring, R. P., 1993, "Hot Streaks and Phantom Cooling in a Turbine Rotor Passage: Part 2—Combined Effects and Analytical Modeling," *ASME J. Turbomach.*, **115**(4), 667–674.
- [3] Jenkins, S. C., Varadarajan, K., and Bogard, D. G., 2003, "The Effects of High Mainstream Turbulence and Turbine Vane Film Cooling on the Dispersion of a Simulated Hot Streak," *ASME J. Turbomach.*, **126**(1), pp. 203–211.
- [4] Jenkins, S. C., and Bogard, D. G., 2007, "Scaling of Guide Vane Coolant Profiles and the Reduction of a Simulated Hot Streak," *ASME J. Turbomach.*, **129**(3), pp. 619–627.
- [5] Polanka, M. D., 1999, "Detailed Film Cooling Effectiveness and Three Component Velocity Field Measurements on a First Stage Turbine Vane Subject to High Freestream Turbulence," Ph.D. thesis, The University of Texas at Austin.
- [6] Cutbirth, J. M., and Bogard, D. G., 2002, "Evaluation of Pressure Side Film Cooling With Flow and Thermal Field Measurements, Part I: Showerhead Effects," ASME Paper No. GT-2002-30174.
- [7] Cutbirth, J. M., 2000, "Turbulence and Three-Dimensional Effects on the Film Cooling of a Turbine Vane," Ph.D. thesis, The University of Texas at Austin.
- [8] Dorney, D. J., 1997, "Investigation of Hot Streak Temperature Ratio Scaling Effects," *Int. J. Turbo Jet Engines*, **14**, pp. 217–227.
- [9] Jenkins, S. C., and Bogard, D. G., 2005, "The Effects of the Vane and Mainstream Turbulence Level on Hot Streak Attenuation," *ASME J. Turbomach.*, **127**(1), pp. 215–221.
- [10] Han, J. C., Dutta, S., and Ekkad, S. V., 2000, *Gas Turbine Heat Transfer and Cooling Technology*, Taylor & Francis, New York.

Prediction of Film Cooling and Heat Transfer on a Rotating Blade Platform With Stator-Rotor Purge and Discrete Film-Hole Flows in a $1\frac{1}{2}$ Turbine Stage

H. Yang¹

Z. Gao²

Department of Mechanical Engineering,
Texas A&M University,
College Station, TX 77843-3123

H. C. Chen

Department of Civil Engineering,
Texas A&M University,
College Station, TX 77843-3136

J. C. Han

e-mail: jc-han@tamu.edu

M. T. Schobeir

Department of Mechanical Engineering,
Texas A&M University,
College Station, TX 77843-3123

Numerical simulations were performed to predict the film cooling effectiveness and heat transfer coefficient distributions on a rotating blade platform with stator-rotor purge flow and downstream discrete film-hole flows in a $1\frac{1}{2}$ turbine stage using a Reynolds stress turbulence model together with a nonequilibrium wall function. Simulations were carried out with sliding mesh for the rotor under three rotating speeds (2000 rpm, 2550 rpm, and 3000 rpm) to investigate the effects of rotation and stator-rotor interaction on the rotor blade-platform purge flow cooling and discrete-hole film cooling and heat transfer. The adiabatic film cooling effectiveness and heat transfer coefficients were calculated using the adiabatic wall temperatures with and without coolant to examine the true coolant protection excluding the effect of turbine work process. The stator-rotor interaction strongly impacts the purge slot film cooling and heat transfer at the platform leading portion while only slightly affects the downstream discrete-hole film cooling near the platform trailing portion. In addition, the effect of turbine work process on the film cooling effectiveness and the associated heat transfer coefficients have been reported.

[DOI: 10.1115/1.3068325]

1 Introduction

The inlet temperature of a modern gas turbine has continually increased to achieve high thrust power and high thermal efficiency. Most often, the film cooling needs to be applied on the platform to protect the material from high heat load. Platform film cooling has gained significant attention due to the usage of low-aspect ratio and low-solidity turbine designs. Film cooling effectiveness and the associated heat transfer are strongly influenced by the stator-rotor interactions. A turbine stage consists of one row of nozzle guide vanes (i.e., stators) and one row of rotating blades called rotors, and transfers the gas total energy into rotating mechanical work. Although the film cooling slightly increases the heat transfer coefficient, the driving temperature difference ($T_{aw} - T_w$) is reduced significantly; therefore, the overall heat load decreases.

Han et al. [1] provided a detailed review of advanced cooling techniques for the turbine blade. Harasgama and Burton [2,3] reported heat transfer measurements on film-cooled endwalls of an annular cascade of turbine nozzle guide vanes, and they found that the Nusselt number gradually increases from the leading edge to the trailing edge on the endwall. Friedrichs et al. [4] presented adiabatic film cooling effectiveness distributions on the endwall of a large scale low speed linear turbine cascade using the ammonia-diazo technique. They found that the horseshoe vortex from the pressure side moving across the passage pushes most of the cool-

ant from the middle of the passage toward the suction surface. Recently, Roy et al. [5] used experimental and numerical methods to study the flow and heat transfer on the vane hub. They found that the flow field predicted by the FLUENT computational fluid dynamics (CFD) code is in good agreement with the experimental data. Burd and Simon [6,7] experimentally studied the effects of slot bleed injection on a contoured endwall of nozzle guide vane and found that the coolant accumulates near the suction surface for the low bleed flow rate. Radomsky and Thole [8] employed laser Doppler velocimeter (LDV) and infrared (IR) camera to study the effect of turbulence intensity on the endwall heat transfer. They concluded that the leading edge horseshoe vortices are similar for low and high turbulence intensity conditions, and the high turbulence intensity produces high St number. Lin and Shih [9] used CFL3D (version 5) code with the shear-stress-transport (SST) $k-\omega$ turbulence model to study the gap leakage flow on contouring endwall. They found that all types of the contour endwalls will reduce the secondary flow, but only the through blade contour endwall increases the film cooling effectiveness. Nicklas [10] used an IR camera to study the film-cooled turbine endwall in a transonic cascade and suggested to shift the slot upstream of the rotor leading edge to avoid increasing the horseshoe vortex. Knost and Thole [11] used the FLUENT CFD code to predict the endwall film cooling for a first-stage vane and indicated that the superposition overpredicts the film cooling effectiveness along the endwall for the combined endwall film cooling and slot cooling configurations. Zhang and Moon [12] used the pressure sensitive paint (PSP) technique to study the effect of back-facing step on the endwall film cooling and found that the back-facing step causes an unstable boundary layer and damages the film coverage. Han and Goldstein [13] used mass transfer technique to study the leading edge fillet effect on the endwall heat transfer and summarized that the fillet significantly reduces the horseshoe vortex for the low turbulence intensity conditions but increases the leading edge corner vortices. Cardwell et al. [14] measured the endwall

¹Present address: Compressor Development, Tech Center, Trane Co., La Crosse, WI 54601.

²Present address: Siemens Energy, 11842 Corporate Boulevard, Orlando, FL 32817.

Contributed by the International Gas Turbine Institute of ASME for publication in the JOURNAL OF TURBO MACHINERY. Manuscript received April 1, 2008; final manuscript received November 20, 2008; published online June 30, 2009. Review conducted by David Wisler. Paper presented at the ASME Turbo Expo 2007: Land, Sea and Air (GT2007), Montreal, QC, Canada, May 14–17, 2007.

film cooling adiabatic effectiveness with realistic features including a combustor to turbine interface gap, a vane to vane midpassage gap, and a platform misalignment and surface roughness.

Recently, Yang et al. [15] numerically investigated the film cooling produced by slot purge flow on the rotating platform in a $1\frac{1}{2}$ turbine stage, which is closer to the real engine working conditions compared with other studies. They concluded that the stator-rotor interaction yields unsteady film cooling and heat transfer, and the cooling effectiveness increase with increasing rpm until the rotating speed reaches the best performance point. They calculated both the overall and adiabatic film cooling effectiveness and heat transfer coefficients and demonstrated that the turbine work process has a strong impact on the film cooling and heat transfer patterns inside the turbine stage. Suryanarayanan et al. [16] employed the PSP technique to measure the film cooling on the rotating platform in a complete turbine stage. PSP is a mass transfer technique, which eliminates the heat conduction error near the film holes and the turbine work effect in the measurement of film cooling effectiveness. They found that the film cooling effectiveness on the rotating blade platform increases with increasing coolant purge rate. In addition, increasing rpm also enhanced the film cooling effectiveness for the range of rotating speeds (1500 rpm, 2000 rpm, and 2550 rpm) considered in their study. Until now, very few researchers reported in the literature the effect of stator-rotor interaction on detailed film cooling effectiveness and heat transfer coefficients of the purge slot and discrete holes on the rotating platform in a complete turbine stage. In the present study, numerical simulations were performed to investigate the detailed unsteady film cooling and heat transfer on the rotating platform in a $1\frac{1}{2}$ turbine stage with combined stator-rotor purge flow and downstream discrete-hole film cooling under various working conditions. The geometry considered in the present numerical simulations is similar to the turbine stage studied experimentally by Suryanarayanan et al. [17].

2 Computational Details

The present three-dimensional calculations were carried out for a $1\frac{1}{2}$ turbine stage, which includes the first-stage stator (stator 1), the first-stage rotor (rotor), and the second-stage stator (stator 2), as shown in Fig. 1. There are two different film cooling configurations on the rotating platform; one is the purge slot on the rotor leading edge and the other consists of nine discrete film holes on the platform trailing portion. For the purge slot cooling, the film coolant enters the disk cavity of the first-stage stator and purges through the inclined slot in the hub junction between the first-stage stator and the rotor, as shown in Fig. 1(a). For discrete-hole film cooling, the coolant flows into a plenum and discharges through nine tubes with compound angle to the platform trailing portion. In Fig. 1(a), the portions outlined in gray are nonrotating domains, which include stator 1, disk cavity of stator 1, and stator 2, while the black represents the rotating domains such as the rotor and its disk cavity, coolant plenum, and nine connecting tubes for discharge of coolant jets. The axial width of the slot is 7 mm with 25 deg inclined angle to the rotor platform. The slot length is 16.5 mm and the slot bottom is connected to both the stator 1 and the rotor disk cavity. The length of the disk cavity for stator 1 is 25.4 mm (1 in.), and 12.7 mm (0.5 in.) for the rotor. The height of the disk cavity is 144.8 mm (5.7 in.). A matrix of nine discrete compound angled coolant holes of 1 mm in diameter is placed on the rotor platform at about 50% downstream of the blade passage. The pitch to diameter ratio for the discrete holes is approximately 5 and the compound angles for all nine holes were given in Ref. [17]. Figure 1(b) shows the surface grids for stators, rotor, platform, and disk cavity. Calculations were performed for one row of stators and rotor passages with periodic boundary conditions in the circumferential direction, as shown in Fig. 1(a), but the numerical grids were repeated in Fig. 1(b) to provide a clear view of the blade passage. Only the rotor platform (indicated in Fig. 1(b)) is film cooled in the present study. The blade height is

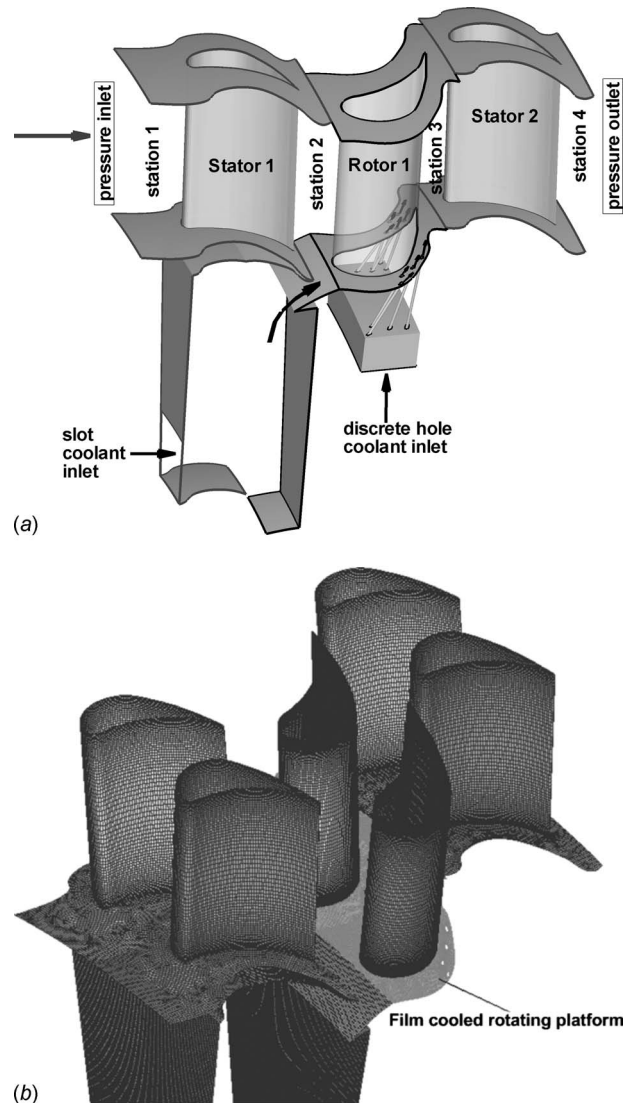


Fig. 1 (a) Computational domain of purge slot and discrete holes film-cooled platform in a $1\frac{1}{2}$ turbine stage and (b) numerical grids (repeated two times)

63.5 mm (2.5 in.), the root diameter is 558.8 mm (22 in.), and the shroud diameter is 685.8 mm (27 in.). Both the stator and rotor blades are two dimensional with the same blade profiles in the spanwise direction. The present blade profiles are exactly the same as the experimental blades used by Suryanarayanan et al. [16]. In their experiment, there were 58 first-stage stator blades, 46 rotor blades, and 52 second-stage stator blades. To simulate the experimental conditions exactly, it is necessary to use 29 first-stage stator blades, 23 rotor blades, and 26 s-stage stator blades with periodic boundary conditions along the circumferential direction. In order to significantly reduce the computer memory and CPU time requirements, it is desirable to use the same number of blades for both the rotor and stators in the present $1\frac{1}{2}$ turbine stage. This enables us to simulate only one flow passage with periodic boundary conditions in the circumferential direction. Since this paper focuses on the film cooling on the rotor platform, it is reasonable to simplify the turbine stage by using 46 blades for both the first- and second-stage stators while maintaining the correct number of rotor blades, as shown in Fig. 1(b). Additional information of the turbine rig and the two-dimensional blades can be found in Refs. [18,19].

The simulations were performed using the CFD software pack-

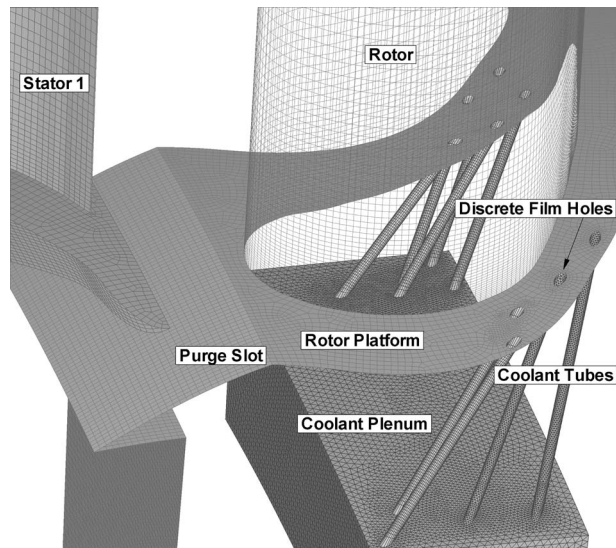


Fig. 2 Detailed grid distributions of the platform purge slot and discrete film holes on the rotating platform

age FLUENT (version 6.2) [20]. The solutions were obtained by solving the compressible Reynolds-averaged Navier–Stokes (RANS) equations together with a Reynolds stress model (RSM) using a finite volume method to discretize the continuity, momentum, and energy equations. The GAMBIT software with Turbo function was used to generate the unstructured hexahedral grids. The computational domain consists of fluid around the first-stage stator and its disk cavity, film-cooled rotor platform with its leading edge disk cavity, trailing portion discrete holes and coolant plenum, and the second-stage stator. The computational domain is mostly composed of the hexahedral cells, which gives higher numerical accuracy for the same number of cells. A sliding mesh was used in conjunction with an interface technique to facilitate the information exchange between the stators and rotor domains. Relatively coarse grids were used for the majority of the $1\text{--}1\frac{1}{2}$ turbine stage, while the angled purge slot, the discrete film holes, the platform of rotor, and the boundary layer of the stator and rotor blades were covered with much finer grids to provide accurate resolution of the film cooling effectiveness and heat transfer. The total number of grid cells used is about 2.4×10^6 . Nonequilibrium wall function based on the two-layer concept is adopted to compute the kinetic energy equations in the wall-neighboring cells. It provides better representation of the near-wall flow than the standard wall function, and is more appropriate for complex three-dimensional flow involving separations. Our previous studies [21,22] show that the nonequilibrium wall function provides good prediction of heat transfer coefficients while overpredicts the film cooling effectiveness. In the present study, the $y^* = \rho C_{\mu}^{1/4} k_p^{1/2} y_p / \mu$ value of near-wall cells falls between 30 and 100 for most of the regions, where k is the turbulent kinetic energy and the subscript p denotes the near-wall grid point. The geometry and detailed numerical grids around the purge slot, nine discrete film holes, and rotor platform are shown in Fig. 2.

Calculations were performed for three different rotating speeds of 2000 rpm, 2550 rpm, and 3000 rpm, where 2550 rpm is the design condition while 3000 rpm is the best performance point for the highest turbine efficiency for the test rig considered in the present study. Note that the design rpm is lower than the best performance rpm in this test rig. The inlet total and exit static pressures of the turbine stage are $P_{in}=101,356$ Pa and $P_{ex}=85$ kPa, respectively, with a pressure ratio of 1.19. At the inlet of the first-stage stator, the total temperature (323 K) and turbulence intensity (5%) are specified with an inlet flow angle of 0 deg.

The absolute velocity at the stator 1 inlet is about 30 m/s. The coolant temperature is 300 K for both the purge slot flow and the discrete-hole film cooling, which is identical to the experimental conditions. The amount of coolant entering the purge slot and discrete holes were specified independently to achieve the desirable local blowing ratios for purge flow and coolant jets. For the purge slot, the overall coolant mass flow rate is $MFR=1\%$ of mainstream flow, which corresponds to a local blowing ratio of $M=0.184$. For the discrete holes film cooling, the blowing ratio based on the rotor exiting velocity is $M=1$.

In this paper, three sets of calculations with different thermal boundary conditions were performed to evaluate the adiabatic film cooling effectiveness $\eta_{aw}=(T_{aw,0}-T_{aw,f})/(T_{aw,0}-T_{t,c})$ and the heat transfer coefficient $h_{aw}=q_w/(T_w-T_{aw,0})$. The h_{aw} is based on the adiabatic wall temperature. For the calculation of $T_{aw,f}$, the turbine inlet total temperature is specified at $T_{t,\infty}=323$ K and the coolant total temperature is $T_{t,c}=300$ K. The adiabatic wall boundary condition is used for the platform and blade surfaces to obtain $T_{aw,f}$. It should be noted that $T_{aw,f}$ includes not only the effects of film cooling but also the temperature decrease due to the turbine work process. In order to determine the true film cooling effectiveness η_{aw} without the complication caused by turbine work process, it is necessary to calculate another adiabatic wall temperature $T_{aw,0}$ for the same configurations in the absence of film coolant injection. This enables us to obtain the true effect of coolant protection by comparing the temperature differences between the two cases with and without the presence of the coolant. For the calculation of heat transfer coefficient, the coolant total temperature is kept the same as the turbine inlet total temperature of 323 K, while the wall temperature is fixed as 300 K to evaluate the heat flux q_w'' . The heat transfer coefficient is calculated from $h_{aw}=q_w''/(T_w-T_{aw,0})$, which depends only on the turbine flow condition but not the turbine work process. For completeness, the overall heat transfer coefficient $h=q_w''/(T_w-T_{t,\infty})$ is also given in this paper to quantify the effects of turbine work process.

At the initial stage of each simulation, the rotor rotates with a rather large time increment of 100 time steps per revolution for ten revolutions. This enables us to quickly build up the swirling flow inside the disk cavity and purge slot. However, this time increment is too large to resolve the detailed blade-to-blade flow since the rotor moves through the wakes of 46 first-stage stator blades in one complete revolution. After the swirling flow inside the disk cavity is fully established in ten revolutions, the time increment was reduced drastically to provide accurate resolution of the blade-to-blade flow induced by stator-rotor interactions. Based on our previous study [15] for cavity purge flow, a much smaller time increment with 100 time steps per passing period was used for accurate resolution of the stator-rotor interactions. Here, the passing period T is defined as the time it takes the rotor to move from one stator row to another. To achieve good periodic results for the blade passage flow, simulations were performed for ten passing periods and the numerical results were recorded and analyzed once every 25 time steps (i.e., every $\frac{1}{4}$ passing period). In Secs. 3–6, the numerical results at four different time phases with $t/T=9\frac{1}{4}, 9\frac{1}{2}, 9\frac{3}{4},$ and 10 will be presented. The present simulations are computationally intensive since they involve unsteady three-dimensional flow sliding rotor mesh, and about 2.4×10^6 cells. Each simulation was performed using the parallel version of FLUENT on two processors, and requires about one month of CPU time on the SGI Altix 3700 supercomputer at Texas A&M University. A total of nine simulations were performed to determine the adiabatic wall temperature, film cooling effectiveness, and heat transfer coefficients for three different rotating speeds of 2000 rpm, 2550 rpm, and 3000 rpm, respectively.

3 Flow Structure Study

Figure 3 shows a vertical cross section and the corresponding streamlines and dimensionless temperature (θ) contours for the

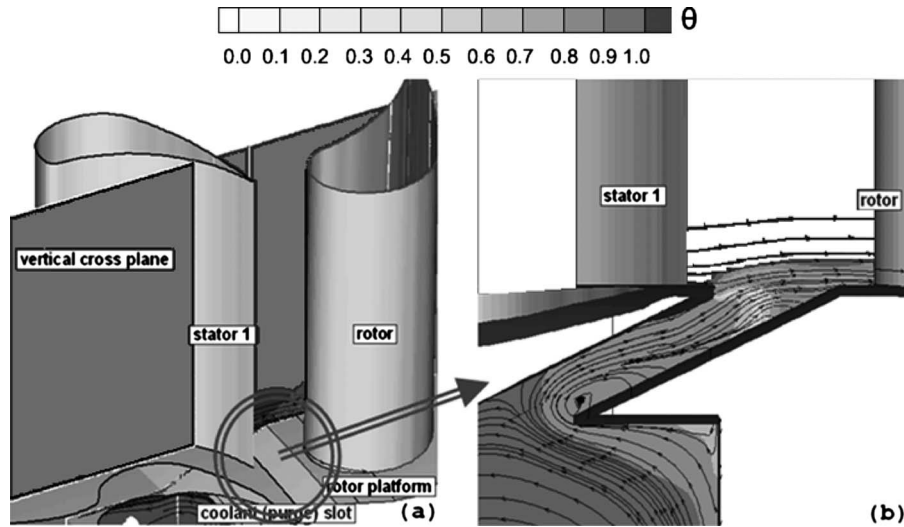


Fig. 3 (a) Vertical cross section and (b) corresponding dimensionless temperature contours and streamlines, 2550 rpm, MFR=1%

purged coolant slot. Due to the rotation of the rotor blade, a swirling flow is induced inside the disk cavity. The swirling coolant is pushed (purged) out of the disk cavity through the inclined coolant slot into the rotor blade passage at a prescribed mass flow rate of MFR=1%. It is seen that there is a small recirculation region near the slot entrance due to the sharp turn. In addition, a small portion of the mainstream flow in the blade passage is entrained into the coolant slot as seen from the relatively high temperature (low dimensionless temperature θ) fluid near the slot exit. It should also be remarked that the coolant flow in the slot is highly three dimensional (not shown in the figure) with significant variations in the circumferential directions.

Figure 4 shows the conceptual rotor velocity diagram, inlet velocity triangle, and outlet velocity. The previous studies [21,22] show that the rotor inlet absolute velocity V_2 is nearly constant since it depends primarily on the turbine inlet/outlet pressure ratio, while rotor relative velocity W_2 varies significantly with the rotating speed U_2 . When the rotating speed U_2 increases from the low-rpm condition to the intermediate-rpm, and then to the high-rpm condition, the flow angle (β_2) of the relative velocity W_2 changes correspondingly. Consequently, the stagnation points on the rotor leading portion shifts gradually from the pressure side (denoted by the dashed line) to the suction side (solid line), and the incident flow angle changes significantly, as shown in the middle of Fig. 4(a). It should also be noted that the rotor relative exit flow angle is nearly independent of the rotating speed, since it is determined mainly by the rotor blade profile.

Figure 4(b) compares the predicted rotor relative velocity on an annular (constant-radius) cross section, which is located at 1% of the blade span above the hub and parallel to the platform. The lowest velocity magnitude region denotes the stagnation point of the rotor leading edge. For the low rotating speed (2000 rpm) condition, the stagnation point (lowest velocity region) was observed on the pressure side of the leading edge. The stagnation point gradually shifts from the pressure side to the blade leading edge with increasing rotating speed to 2550 rpm. When the rotating speed further increases to 3000 rpm, the stagnation point moves to the suction side, and the incident angle becomes negative, as noted in Fig. 4(a). It is interesting to note that the relative velocity decreases with increasing rpm, especially in the trailing portion, because the high rotating speed rotor extract more energy from the gas.

Figure 5 shows the streamlines and dimensionless temperature (θ) contours on two annular cross sections located at 1% and 2% of the blade span to provide a detailed description of the flow and

film cooling characteristics under various rotating conditions. It should be noted that the dimensionless temperature θ is defined in the same way as the adiabatic film cooling effectiveness η_{aw} . Therefore, the dimensionless temperature is identical to the adiabatic cooling effectiveness on the platform surface. The arrow with double solid line denotes the incident flow angle of rotor relative velocity under the design condition, while the dashed line indicates the relative inflow direction for the low rpm, and the single solid line for the high-rpm conditions. The denotations are the same as those shown earlier in Fig. 4. The coolant from the purge slot is strongly affected by the rotation and the coolant traces can be clearly detected by the high values of dimensionless temperature θ near the leading portion of the rotor blade. For the low rotating speed of 2000 rpm, the dividing streamline impinges on the leading edge pressure side with a positive inflow angle. The coolant flow structure is rather complex due to the influence of horseshoe vortices. At the design condition 2550 rpm, the stagnation point shifts to the leading edge and the coolant purge flow is driven from the pressure side to the suction side. For the high rotation condition of 3000 rpm, the rotor inlet relative velocity directs to the suction side of the leading edge with a negative angle of attack and the coolant penetration is significantly weaker comparing to the design condition. It is clearly seen that the design condition produces the highest dimensionless temperature around the rotor leading edge since the platform purge slot coolant impinges directly on the leading edge.

In general, the dimensionless temperatures at 1% cross section are higher than those observed at 2% cross section since the purged coolant flow is confined to a fairly thin layer above the platform. It is also worthwhile to note that the temperature contours at 1% and 2% annular cross sections are not significantly affected by the discrete-hole coolant jets since the coolant mass flow rate from each film hole is considerably smaller than the mass flow rate from the purge slot.

Figure 6 shows a comparison of the static pressure contours around the rotor blade hub region with and without platform purge flow. For the blade without purge flow shown in Fig. 6(a), high pressure is confined to pressure side while a low static pressure region exists on the suction side rotor region. For the rotor blade with platform purge flow shown in Fig. 6(b), the high pressure region extends from the pressure side to the suction side due to the impingement of purged coolant flow on the blade leading edge. It can also be clearly seen that the effect of the purged coolant is confined to the root region of the rotor blade.

For completeness, the three-dimensional coolant flow structures

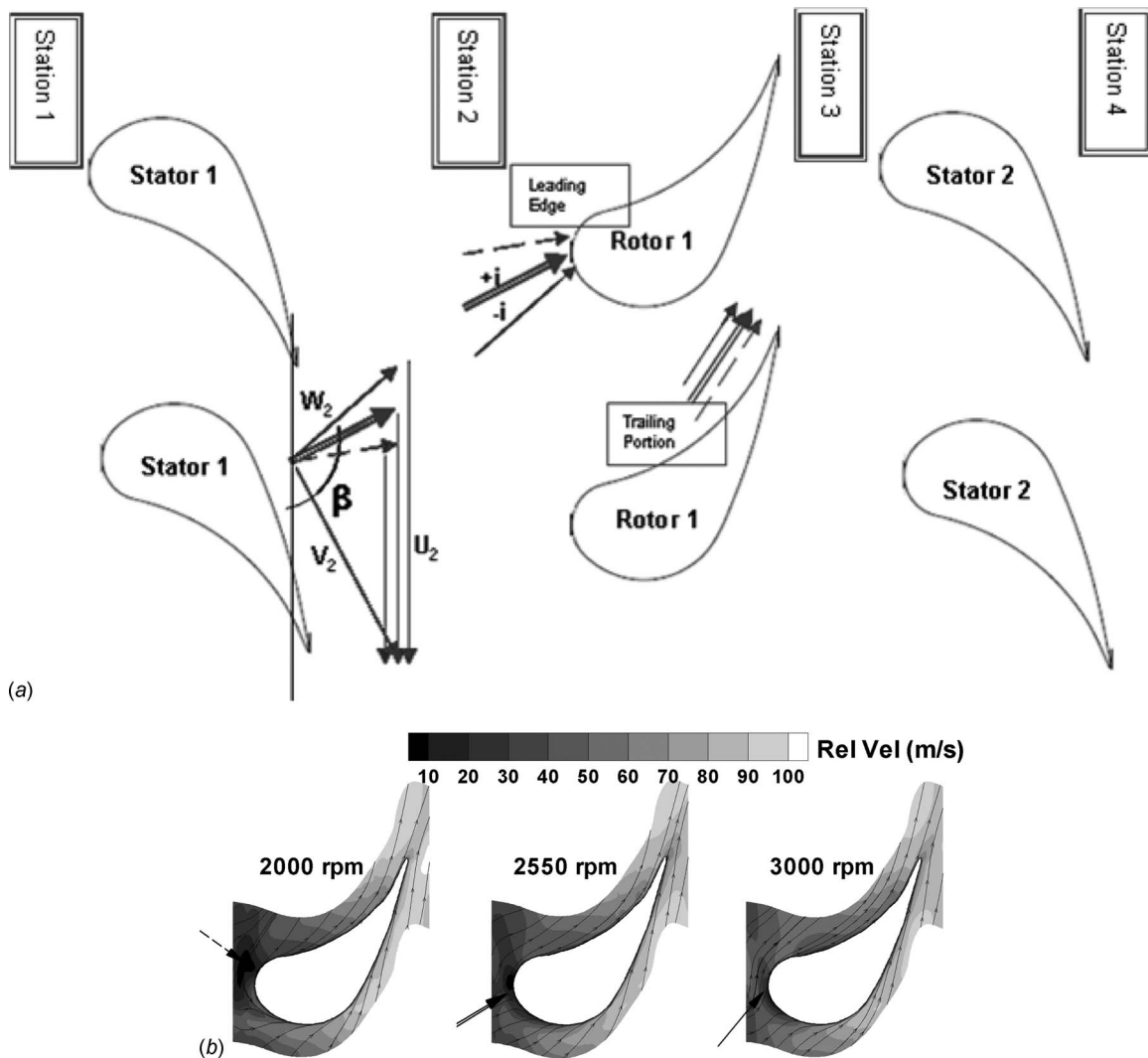


Fig. 4 (a) Conceptual rotor inlet velocity triangle and (b) predicted rotor relative velocity for various working conditions

in the rotor blade passage and the associated adiabatic film cooling effectiveness contours on the platform are also plotted in Fig. 7 to provide more detailed understanding of the coolant flow and heat transfer characteristics at various rotating speeds. It should be noted that the streamlines in the rotor inlet region shown in Fig. 7(a) are plotted in rotating reference frame using the relative velocity, while the absolute velocity is used for streamlines in the outlet sections shown in Fig. 7(b). For the purge slot coolant flow structure in Fig. 7(a), the coolant accumulates on the blade suction side with very little protection of the pressure side of the rotor platform except in the leading edge region. The coolant traces diminish gradually downstream of the purge slot and vanish completely toward the trailing portion after mixing with the mainstream flow. In the midchord region (i.e., third cross section from the blade leading edge), the purged coolant flow is driven by the blade passage vortex from the pressure side toward the suction side, leaving the pressure side of the platform unprotected. For the 2000 rpm condition, a pair of horseshoe vortices is clearly visible in the blade root region and the suction side vortex is much stronger than that on the pressure side. With increasing rotation speed, the strength of the suction side horseshoe vortex reduces quickly and the pressure side vortex disappeared completely. For the design condition at 2550 rpm, the mainstream flow impinges directly on the rotor leading edge. Consequently, the coolant from the purge slot accumulates around the blade leading edge region.

When the rotating speed is further increased to the best performance point at 3000 rpm, the horseshoe vortex is very weak and the coolant is pushed away from the suction side root region into the middle section of the rotor blade passage.

Figure 7(b) shows the downstream coolant flow structures and the corresponding adiabatic film cooling effectiveness distributions. The streamlines are plotted using the tangential components of the absolute velocity at each cross section. It is interesting to note that there are two distinctive coolant strips on the rotor suction side. The upper coolant strip is produced by the platform purge slot, while the bottom one along the blade-platform junction is produced by the discrete-hole coolant jets. The coolant from the platform purge slot covers a fairly wide section of the blade suction side up to about 25% of the blade span but provides very limited coverage for the pressure side of the platform, as noted earlier in Fig. 7(a). On the other hand, the discrete-hole coolant jets protect a wide region of the platform passage but provide very limited protection of the blade suction along the blade-platform junction. It is worthwhile to note that the passage vortex develops from the midchord portion to the trailing portion with increasing rpm.

4 Adiabatic Film Cooling Effectiveness Study

Figure 8 shows detailed comparisons of the instantaneous adiabatic film cooling effectiveness at four time phases for various

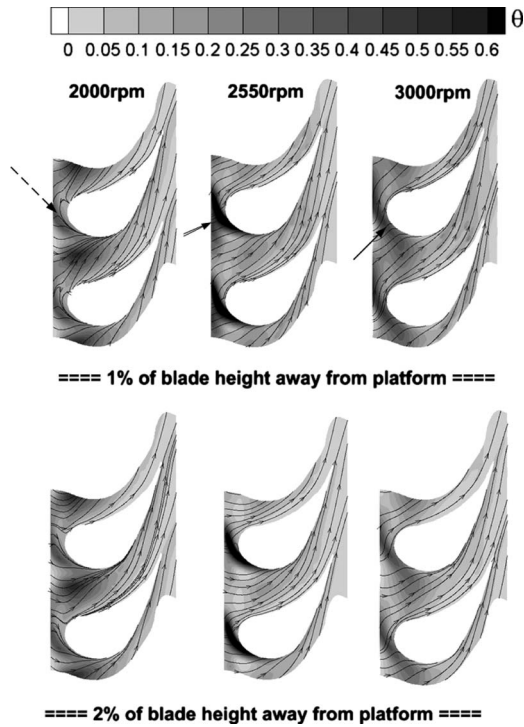


Fig. 5 Comparison of streamlines and dimensionless temperature (θ) contours on the annular cross sections for various rotating speeds, time phase $\frac{1}{4}$

rotating speeds. In general, the film cooling effectiveness decreases along the flow direction due to the mixing of the coolant with the mainstream in turbine blade passage. The purge slot film cooling is strongly affected by the stator-rotor interactions in the leading edge region, while the discrete-hole film cooling is not significantly influenced by the unsteady intensity of the stator wake flow. As mentioned earlier in Fig. 7, the coolant from purge slot is driven by the blade passage vortex away from the pressure side and accumulates on the suction side. Consequently, most of the coolant coverage is confined to a curved triangular region adjacent to the blade suction side with diminishing protection for the blade pressure side in the midchord and downstream areas.

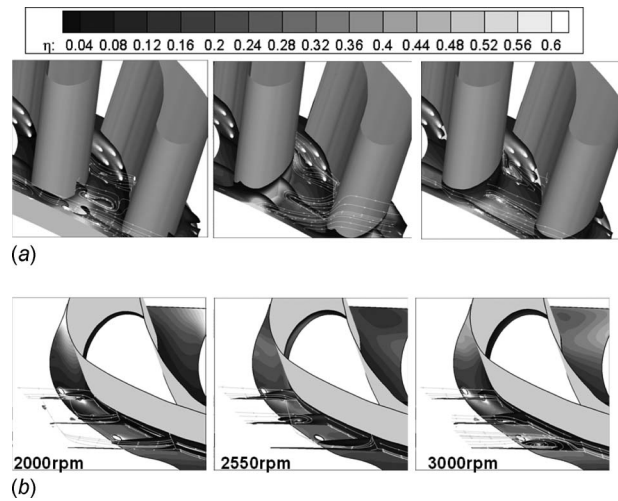


Fig. 7 Coolant flow structures for (a) purge slot at leading portion based on the rotor relative velocity and (b) discrete holes at trailing portion based on the rotor absolute velocity

For the low-rpm case at 2000 rpm, the slot coolant is pushed away from the suction side by the positive incident flow angle. The film cooling effectiveness fluctuates significantly among four different time phases in the leading edge region due to the strong stator-rotor interactions. The effects of stator-rotor interaction reduce rapidly in the midchord and downstream regions. Therefore, the discrete-hole film cooling tends to be more stable with relatively small fluctuations. For the intermediate rotating speed of 2550 rpm, the purge slot coolant impinges directly on the rotor leading edge and produces a high level of adiabatic film cooling effectiveness around the leading edge and spread out over a fairly wide area. In addition, the film cooling effectiveness is highly unsteady around the blade leading edge region due to the strong stator-rotor interactions. However, the film cooling effectiveness and unsteady intensity of the purge flow diminishes rather quickly in the rotor blade passage. Therefore, it is desirable to place the discrete holes in the midchord region in order to provide necessary protection of the platform surface in the midchord and trailing edge regions. For the high rotating condition at 3000 rpm, the purge slot coolant spreads more uniformly across the blade passage with a decrease in the peak value of film cooling effectiveness, but the overall

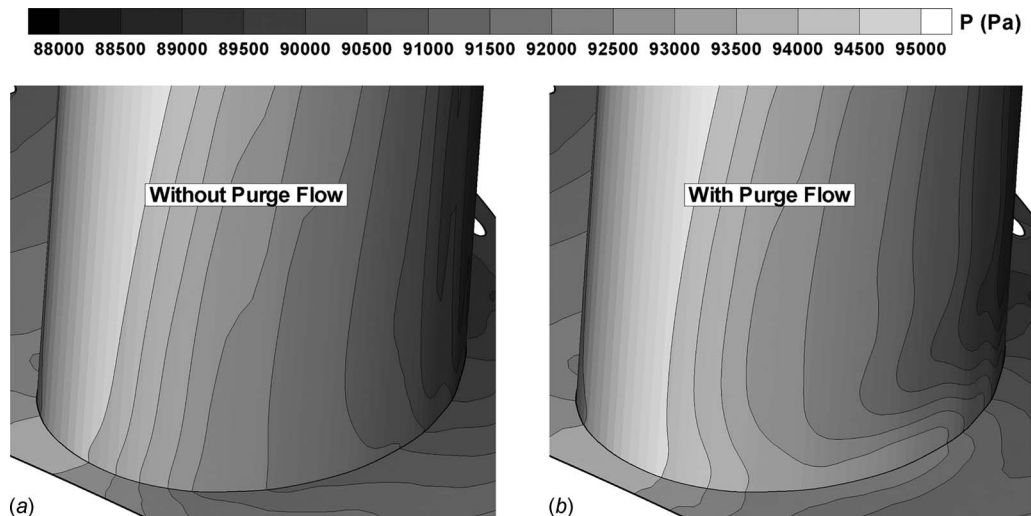


Fig. 6 Comparison of static pressure contours on the rotor blade hub region: (a) without platform purge flow and (b) with platform purge flow; 2550 rpm, time phase $\frac{1}{4}$, MFR=1%

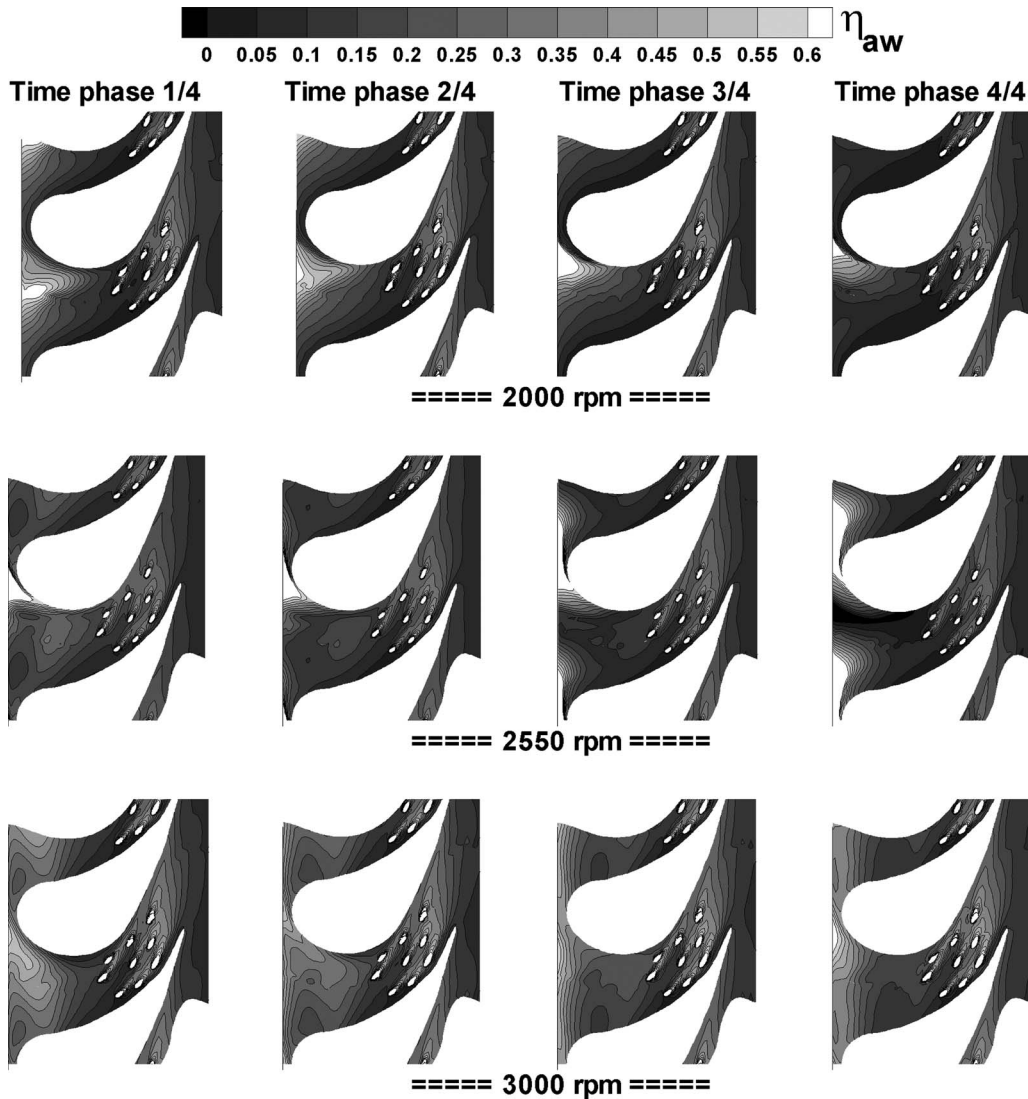


Fig. 8 Comparison of adiabatic film cooling effectiveness on the rotating blade platform for various rotating speeds, platform purge slot MFR=1%, discrete film holes $M=1$

adiabatic film cooling effectiveness level is somewhat higher compared to the design condition. The reduction in platform purge flow cooling effectiveness may be attributed to (1) shift of the stagnation point to suction side and (2) stronger wake effect of the first-stage stator.

Figure 9 shows the laterally averaged cooling effectiveness and unsteady intensity on the rotating platform for various rotating speeds with a purge flow rate MFR=1% and discrete holes blowing ratio $M=1$. In the upstream section of the blade passage ($0 < X/Cx < 0.5$), the film cooling effectiveness decreases along the turbine passage due to the mixing of purged coolant with mainstream flow. With increasing rotating speed, the purge slot cooling effectiveness increases slightly because high rpm decreases the rotor relative velocity and reduce the strength of the horseshoe vortex. At the trailing portion ($0.5 < X/Cx < 1$), the cooling effectiveness varies in a sawtooth pattern due to the superposition of staggered coolant jets from the nine discrete holes. It is further noted that the laterally averaged film cooling effectiveness at the design condition is somewhat lower than those observed for the 2000 rpm and 3000 rpm conditions. This can be attributed to the rapid decay of the film cooling effectiveness for purge slot flow at 2550 rpm as noted earlier in Fig. 8.

Figure 9(b) shows the instantaneous and time-averaged adia-

batic cooling effectiveness for the design condition with slot mass flow ratio MFR=1% and discrete-hole blowing ratio $M=1$. It is clearly seen that the fluctuation of cooling effectiveness increases from the leading edge and reaches the peak value at 20% of the blade axial chord length (i.e., $X/Cx=0.2$), and then decreases toward the trailing edge since the effect of stator-rotor interaction diminishes rapidly after the midchord section. The film cooling effectiveness pattern due to the discrete-hole coolant jets is fairly steady with relatively small fluctuations. In order to quantify the level of unsteady fluctuations, we evaluate the unsteady intensity of the film cooling effectiveness using the following definition:

$$Tu_{\eta} = \sqrt{\frac{1}{N} \sum_{i=1}^N (\eta_i - \bar{\eta})^2 / \bar{\eta}}$$

where η_i is the cooling effectiveness for time step i and $\bar{\eta}$ is the averaged cooling effectiveness over N time steps. Figure 9(c) shows the comparison of cooling effectiveness unsteady intensity for various rotating speeds. In general, the purge slot film cooling shows a high level of unsteady intensity for all the rotating speeds over the first half of the rotor blade passage due to strong rotor-stator interactions at the rotor inlet. In the midchord and trailing edge regions, the discrete-hole coolant jets produce high film

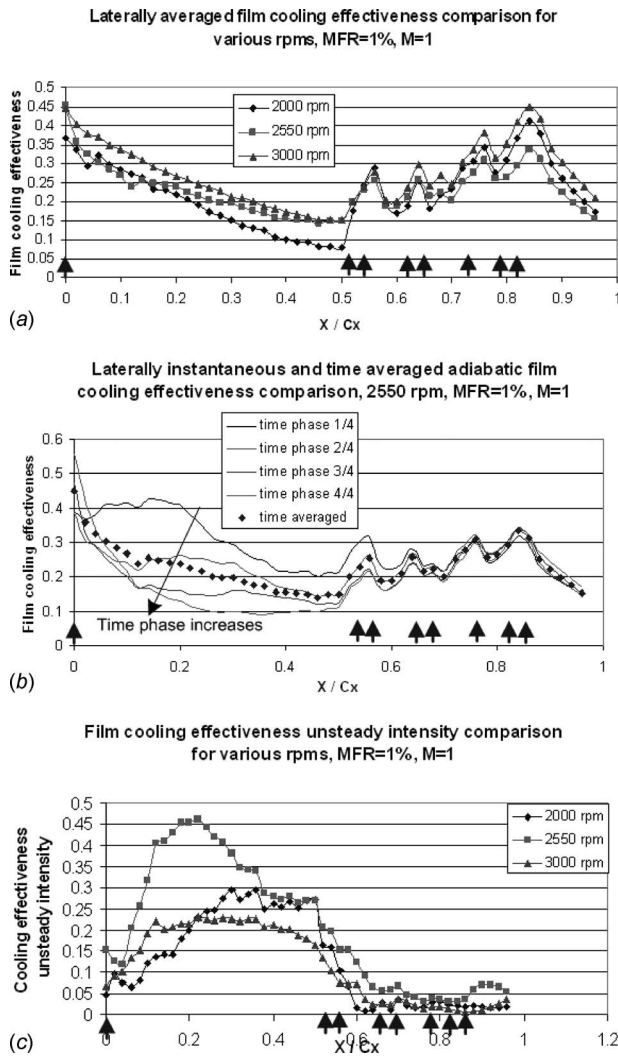


Fig. 9 (a) Laterally averaged adiabatic cooling effectiveness for various rotating speeds. (b) Instantaneous and time averaged adiabatic film cooling effectiveness for 2550 rpm. (c) Laterally averaged unsteady intensity of adiabatic cooling effectiveness for various rotating speeds, with platform purge slot MFR=1%, discrete film holes $M=1$.

cooling effectiveness but the corresponding unsteady intensity is relatively low since the influence of stator-rotor interactions diminishes rapidly downstream of the midchord section.

Figure 10 shows a comparison of the measured [17] and calculated adiabatic cooling effectiveness for 2550 rpm and 3000 rpm, respectively, with a purge flow rate MFR=1% and discrete holes blowing ratio $M=1$. Please be noted that the normal slot width for the current study is 3 mm; however, it is 2.3 mm in the measurement by Suryanarayanan et al. [17]. Therefore, the low blowing ratio for the purge flow in the prediction is about 23% lower than the experiment. The predicted film cooling effectiveness patterns are in reasonably good agreement with the corresponding measurement, but the discrete-hole film cooling effectiveness is somewhat overpredicted. Both the simulation and experiment indicate that the purge slot cooling covers the leading portion of the rotor platform and the purged coolant tends to accumulate on the suction side with diminishing coverage of the pressure side beyond 25% of the axial chord length. Both the measurement and prediction show that the passage vortex drives cooling traces from discrete holes from the pressure side to the suction side. Although the purge slot film cooling MFR is 1%, the corresponding local blowing ratio (M) is only 0.184, which is far below the blowing ratio

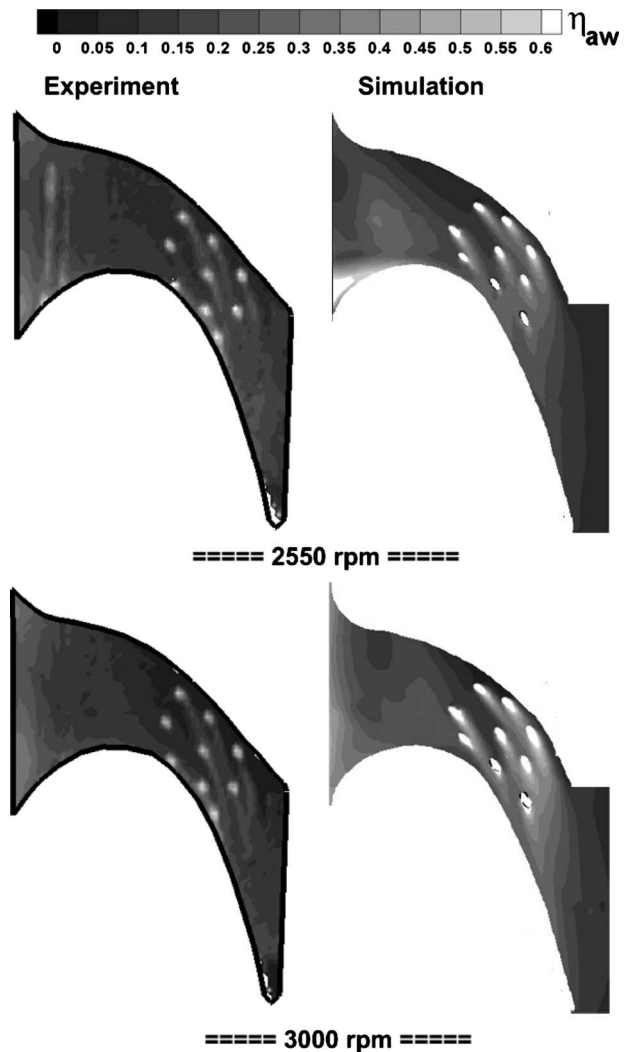


Fig. 10 Comparison of adiabatic film cooling effectiveness on the rotating blade platform between experiment [17] and simulation for 2550 rpm and 3000 rpm, purge slot MFR=1%, discrete holes $M=1$

for discrete holes film cooling of $M=1$. Therefore, the simulation predicted higher local cooling effectiveness downstream of the discrete holes than that of the purge slot, which is confirmed by the experimental data. However, the predicted discrete-hole film cooling effectiveness levels are considerably higher than the corresponding measurements. The measured film cooling effectiveness reduces slightly when the rotating speed increases from 2550 rpm to 3000 rpm. The simulation also shows a reduction in purge slot cooling effectiveness at the rotor inlet at 3000 rpm, but the laterally averaged effectiveness increases significantly in the mid-chord and downstream regions, as shown earlier in Fig. 9(a).

5 Adiabatic Heat Transfer Study

Figure 11 shows the heat transfer coefficients, based on the adiabatic wall temperature, $h_{aw} = q_w / (T_w - T_{aw,0})$, on the rotor platform at four time phases for three rotating speeds. The high heat transfer coefficient region develops from the leading portion pressure side and increases along the mainstream flow direction toward the trailing edge due to the flow acceleration in the rotor passage, which is confirmed by the experiment studies of Harasgama and Burton [2,3]. Downstream of the rotor trailing edge, the heat transfer coefficient decreases due to the deceleration of mainstream flow in the rotor wake region. The heat transfer coefficient

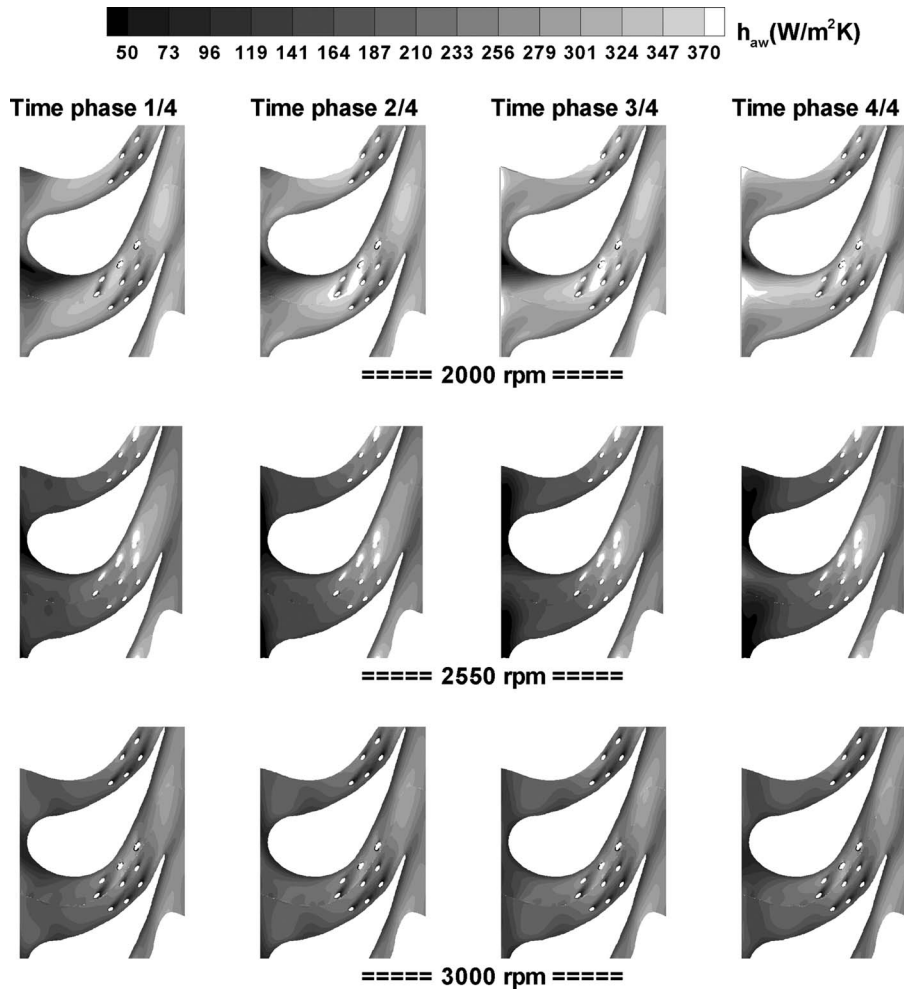


Fig. 11 Heat transfer coefficients (based on the adiabatic wall temperature) on the rotating platform for various rotating speeds, purge slot MFR=1%, discrete holes $M=1$

is also low in the leading edge region because purge slot coolant is slower than the mainstream flow and acts as a blockage to reduce the heat transfer coefficient. Similarly, the heat transfer coefficient also decreases downstream of the discrete-hole coolant jets since the blowing ratio ($M=1$) for the coolant jets is defined based on the rotor exit velocity, which is lower than the mainstream velocity in the midchord region where the discrete holes are located.

As noted earlier in Fig. 4(b), the rotor relative velocities decrease with increasing rotating speed for the fixed inlet/outlet pressure ratio considered in the present study. It is clearly seen that the heat transfer coefficient is quite high for 2000 rpm case due to high rotor relative velocity. When the rotating speed was increased to 2550 rpm and then to 3000 rpm, the heat transfer coefficients decrease sharply since the rotor relative velocities are significantly lower for high-rpm conditions. Similar to the adiabatic film cooling effectiveness, the heat transfer coefficients also fluctuate significantly among four different time phases. In general, the unsteady intensity of heat transfer coefficient is high in the platform leading portion but diminishes in the midchord and downstream regions where the discrete film holes are located.

6 Overall Heat Transfer Coefficients and Film Cooling Effectiveness

In order to evaluate h_{aw} as shown earlier in Fig. 11, it is necessary to determine the adiabatic wall temperature $T_{aw,0}$ separately with additional measurements or calculations. On the other hand, the overall heat transfer coefficient $h = q_w'' / (T_w - T_{t,\infty})$ can be easily

evaluated since the turbine inlet total temperature $T_{t,\infty}$ can be measured directly. However, the overall heat transfer coefficient h involves not only the effects of the velocity field but also the turbine work process while h_{aw} depends only on the flow field. In general, the turbine work process reduces the mainstream temperature since a portion of the thermal energy is converted to mechanical work to turn the rotor blades. Therefore, the local adiabatic wall temperature $T_{aw,0}$ in the rotor passage is lower than the inlet total temperature $T_{t,\infty}$ for the turbine stage and closer to the wall temperature T_w on rotor blade surface. It is clearly seen from Fig. 12 that the overall heat transfer coefficient h is significantly lower than the h_{aw} based on adiabatic wall temperature (note for different scales in Figs. 11 and 12) since the denominator $T_w - T_{t,\infty}$ is larger than $T_w - T_{aw,0}$ for the same wall heat flux q_w'' .

To study the impact of turbine work process on the film cooling effectiveness, the overall film cooling effectiveness, defined as $\eta = (T_{t,\infty} - T_{aw,f}) / (T_{t,\infty} - T_{t,c})$, is also presented in Fig. 13 using the same scale as the adiabatic cooling effectiveness in Fig. 8. As noted earlier, the turbine work reduces the mainstream temperature and produces an overall film cooling effectiveness even without the presence of coolant in platform purge slot or discrete film holes. This results in a high overall cooling effectiveness η near the trailing edge since the mainstream temperature reduces along the rotor blade passage as a result of the turbine work. Compared to the adiabatic film cooling effectiveness η_{aw} in Fig. 8, it is clearly seen that the overall film cooling effectiveness η is much higher than the corresponding true film cooling effectiveness η_{aw}

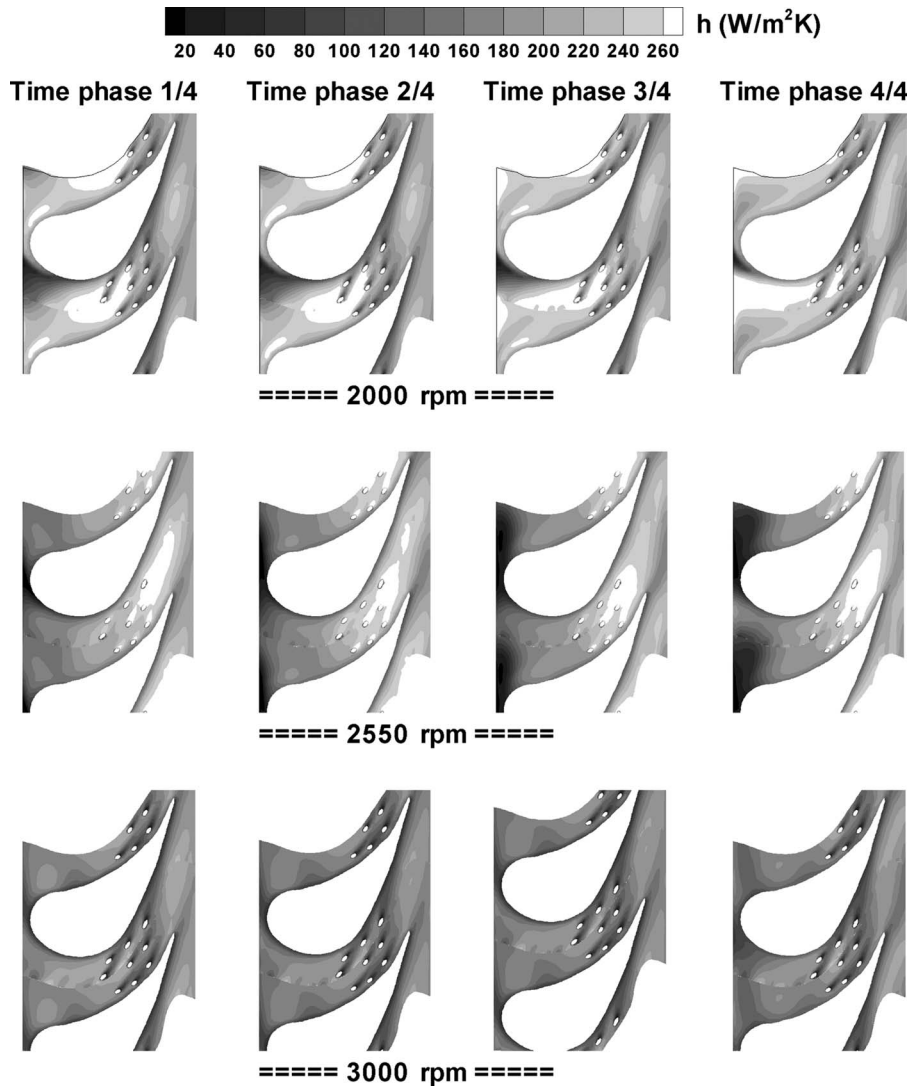


Fig. 12 Overall heat transfer coefficients on the rotating platform for various rotating speeds, purge slot MFR=1%, discrete holes $M=1$

for all three rotating speeds. Furthermore, the overall film cooling effectiveness tends to increase with increasing rotating speed since more turbine work is produced at higher rpm for the range of rotating speeds considered in the present study.

7 Conclusions

Numerical simulations were performed for the three-dimensional $1\frac{1}{2}$ turbine stage to determine the effect of stator-rotor interaction on platform purge slot and discrete holes film cooling and heat transfer. The platform purge slot with overall coolant mass flow rate MFR=1% and discrete film holes with blowing ratio $M=1$ were investigated for low, intermediate, and high rotating speeds. Both the adiabatic film cooling effectiveness and heat transfer coefficient based on adiabatic wall temperature were evaluated to determine the true effect of film cooling. The overall film cooling effectiveness and heat transfer coefficient were also presented to determine the influence of turbine work process. The primary findings from this study are summarized as follows.

(1) The stator-rotor interaction produced high unsteady intensities for platform purge slot film cooling and heat transfer, while the discrete holes film cooling is only slightly affected.

- (2) With increasing rotating speed, the flow incidence angle changed significantly and the stagnation point shifts gradually from the pressure side to the suction side on the rotor leading edge. Higher rotating speed also reduces the rotor relative velocity and increases the local blowing ratio for platform purge flow.
- (3) At the design condition of 2550 rpm, the film cooling effectiveness is very high in the upstream section of rotor passage since the platform purge coolant impinges directly on the rotor leading edge. For lower rotating speed of 2000 rpm, the purge flow cooling effectiveness reduces due to the lower blowing ratio (higher rotor relative inlet velocity) and the shift of stagnation point to the blade pressure side. The trend is reversed in the midchord and downstream sections with lower discrete holes film cooling effectiveness for the design condition. At 3000 rpm, the peak value of purge flow cooling effectiveness is lower than the design condition due to the stronger wake effect from the first-stage stator blades and the shift of stagnation point to the blade suction side, but the overall film cooling effectiveness is somewhat higher than low-rpm cases.
- (4) With increasing rotating speed, the heat transfer coefficients (based on adiabatic wall temperature) decrease sharply

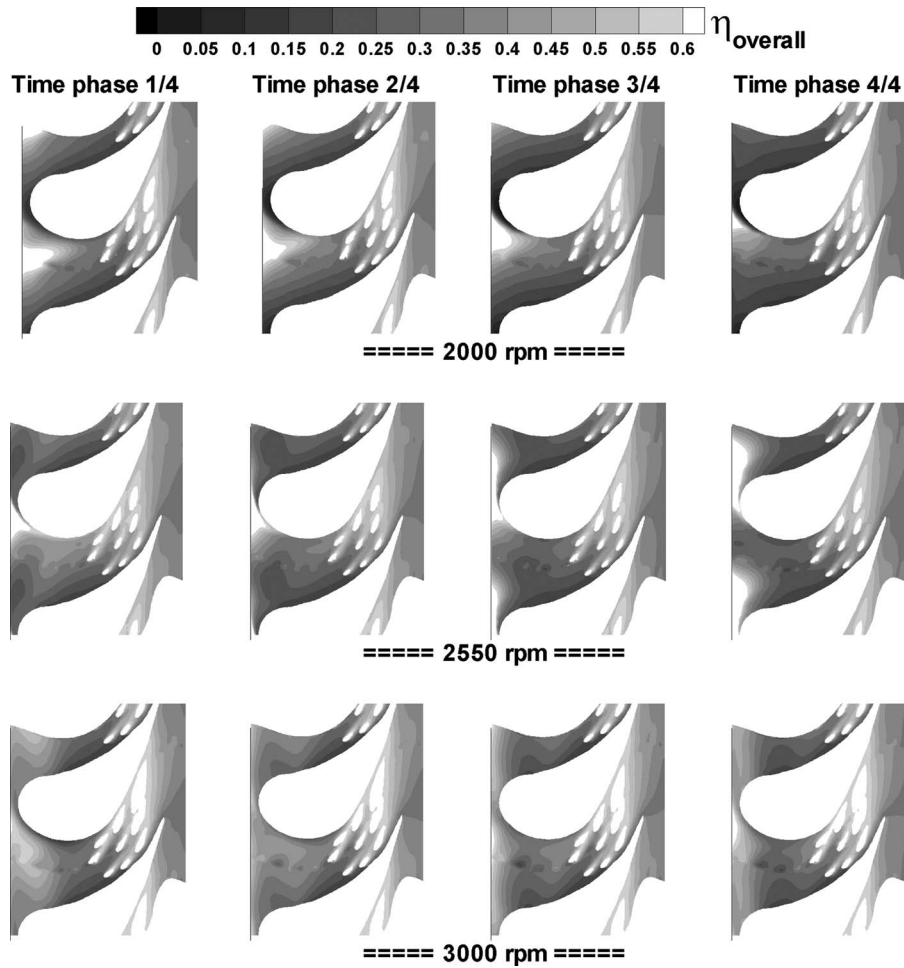


Fig. 13 Overall film cooling effectiveness on the rotating blade platform for various rotating speeds at four time phases, purge slot MFR=1%, discrete holes M=1

since the rotor relative velocities are significantly lower for high-rpm conditions.

- (5) The turbine work process reduces the mainstream temperature in the rotor blade passage. This results in a significant increase in the overall film cooling effectiveness and a reduction in the overall heat transfer coefficients.
- (6) The predicted adiabatic film cooling effectiveness is in reasonably good agreement with the corresponding experiment data, but the effectiveness of the discrete film holes was overpredicted.

Acknowledgment

This publication is partially supported by the U.S. Department of Energy. The authors would like to thank the supercomputer center in Texas A&M University for providing the computing resources.

Nomenclature

A = area (m²)
 C_x = axial chord length of the rotor blade
 h = overall heat transfer coefficient, $q_w''/(T_w - T_{t,c})$ (W/m² K)
 h_{aw} = heat transfer coefficient based on the adiabatic wall temperature, $q_w''/(T_w - T_{aw,0})$ (W/m² K)
 P = local static pressure (Pa)
 r = radius of turbine
 Tu = turbulence intensity

Tu_η = unsteady intensity of film cooling effectiveness, $\sqrt{(\sum(\eta_i - \bar{\eta})^2/N)/\bar{\eta}}$

M = blowing ratio, $(\rho_c V_c)/(\rho_\infty W_{local})$

MFR = purge-to-mainstream mass flow ratio, $M_c/M_\infty = (A_c \rho_c V_c)/(A_\infty \rho_\infty V_\infty)$

U = rotor rotating speed (m/s)

V = absolute inlet velocity of rotor (m/s)

W = relative inlet velocity of rotor (m/s)

X = axial distance (cm)

η = overall film cooling effectiveness $(T_{i,\infty} - T_{aw,f})/(T_{i,\infty} - T_{t,c})$

η_{aw} = adiabatic film cooling effectiveness $(T_{aw,0} - T_{aw,f})/(T_{aw,0} - T_{t,c})$

α = absolute flow angle

β = relative flow angle

i = flow incidence angle

θ = dimensionless temperature $(T_{aw,0} - T_{aw,f})/(T_{aw,0} - T_{t,c})$

Subscripts

0 = without film cooling

2 = station 2

3 = station 3

aw = adiabatic wall

c = coolant

f = with film cooling

t = total or stagnation value

w = wall of blade
 ∞ = inlet stream of turbine stage

References

- [1] Han, J. C., Dutta, S., and Ekkad, S. V., 2000, *Gas Turbine Heat Transfer and Cooling Technology*, Taylor & Francis, New York.
- [2] Harasgama, S. P., and Burton, C. D., 1992, "Film Cooling Research on the Endwall of a Turbine Nozzle Guide Vane in a Short-Duration Annular Cascade, Part I: Experimental Technique and Results," *ASME J. Turbomach.*, **114**, pp. 734–740.
- [3] Harasgama, S. P., and Burton, C. D., 1992, "Film Cooling Research on the Endwall of a Turbine Nozzle Guide Vane in a Short-Duration Annular Cascade, Part II: Analysis and Correlation of Results," *ASME J. Turbomach.*, **114**, pp. 741–746.
- [4] Friedrichs, S., Hodson, H. P., and Dawes, W. N., 1996, "Distribution of Film-Cooling Effectiveness on a Turbine Endwall Measured Using the Ammonia and Diazo Technique," *ASME J. Turbomach.*, **118**, pp. 613–621.
- [5] Roy, R. P., Squires, K. D., and Song, S., 2000, "Flow and Heat Transfer at the Hub Endwall of Inlet Vane Passages—Experiments and Simulations," *ASME Paper No. 2000-GT-198*.
- [6] Burd, S. W., and Simon T. W., 2000, "Effects of Slot Bleed Injection Over a Contoured Endwall on Nozzle Guide Vane Cooling Performance: Part I—Flow Filed Measurements," *ASME Paper No. 2000-GT-199*.
- [7] Burd, S. W., Satterness, C. J., and Simon, T. W., 2000, "Effects of Slot Bleed Injection Over a Contoured Endwall on Nozzle Guide Vane Cooling Performance: Part II—Thermal Measurements," *ASME Paper No. 2000-GT-200*.
- [8] Radomsky, R. W., and Thole K. A., 2000, "High Free Stream Turbulence Effects on End Wall Heat Transfer for a Gas Turbine Stator Vane," *ASME Paper No. 2000-GT-2001*.
- [9] Lin, Y.-L., and Shih, T. I.-P., 2000, "Effects of Gap Leakage on Fluid Flow in a Contoured Turbine Nozzle Guide Vane," *ASME Paper No. 2000-GT-0555*.
- [10] Nicklas, M., 2001, "Film-Cooled Turbine Endwall in a Transonic Flow Field: Part II—Heat Transfer and Film-Cooling Effectiveness," *ASME Paper No. 2001-GT-0146*.
- [11] Knost, D. G., and Thole, K. A., 2003, "Computational Predictions of Endwall Film-Cooling for a First Stage Vane," *ASME Paper No. GT2003-38252*.
- [12] Zhang, L., and Moon, H. K., 2003, "Turbine Nozzle Endwall Inlet Film Cooling—The Effect of a Back-Facing Step," *ASME Paper No. GT2003-38319*.
- [13] Han, S., and Goldstein, R. J., 2005, "Influence of Blade Leading Edge Geometry on Turbine Endwall Heat/Mass Transfer," *ASME Paper No. GT2005-68590*.
- [14] Cardwell, N. D., Sundaram, N., and Thole, K. A., 2005, "Effects of Mid-Passage Gap, Endwall Misalignment and Roughness on Endwall Film-Cooling," *ASME Paper No. GT2005-68900*.
- [15] Yang, H., Chen, H. C., and Han, J. C., 2006, "Numerical Study of a Rotating Blade Platform With Film Cooling From Cavity Purge Flow in a $1\frac{1}{2}$ Turbine Stage," *ASME Paper No. GT2006-90322*.
- [16] Suryanarayanan, A., Mhetras, S. P., Schobeiri, M. T., and Han, J. C., 2006, "Film-Cooling Effectiveness on a Rotating Blade Platform," *ASME Paper No. GT2006-90034*.
- [17] Suryanarayanan, A., Ozturk, B., Schobeiri, M. T., and Han, J. C., 2007, "Film-Cooling Effectiveness on a Rotating Turbine Platform using Pressure Sensitive Paint Technique," *ASME Paper No. GT2007-27122*.
- [18] Schobeiri, M. T., Suryanarayanan, A., Jermann, C., and Neuenschwander, T., 2004, "A Comparative Aerodynamic and Performance Study of a Three-Stage High Pressure Turbine With 3-d Bowed Blades and Cylindrical Blades," *ASME Paper No. GT2004-53650*.
- [19] Schobeiri, M. T., Gilaranz, J. L., and Johansen, E. S., 2000, "Aerodynamic and Performance Studies of a Three Stage High Pressure Research Turbine With 3-D-Blades, Design Points and Off-Design Experimental Investigations," *ASME Paper No. 2000-GT-484*.
- [20] Fluent Inc., 2002, *FLUENT Version 6.0*.
- [21] Yang, H., Chen, H. C., and Han, J. C., 2004, "Numerical Prediction of Film Cooling and Heat Transfer on the Leading Edge of a Rotating Blade in a $1\frac{1}{2}$ Turbine Stage," *ASME Paper No. IMECE2004-59599*.
- [22] Yang, H., Chen, H. C., and Han, J. C., 2005, "Numerical Prediction of Film Cooling and Heat Transfer on the Leading Edge of a Rotating Blade With Two Rows Holes in a $1\frac{1}{2}$ Turbine Stage at Design and Off Design Conditions," *ASME Paper No. 2005-GT-683*.

Turbine Blade Platform Film Cooling With Typical Stator-Rotor Purge Flow and Discrete-Hole Film Cooling

Zhihong Gao

Diganta Narzary

Je-Chin Han

e-mail: jc-han@tamu.edu

Department of Mechanical Engineering,
Turbine Heat Transfer Laboratory,
Texas A&M University,
College Station, TX 77843-3123

This paper is focused on the effect of film-hole configurations on platform film cooling. The platform is cooled by purge flow from a simulated stator-rotor seal combined with discrete-hole film cooling within the blade passage. The cylindrical holes and laidback fan-shaped holes are assessed in terms of film-cooling effectiveness and total pressure loss. Lined up with the freestream streamwise direction, the film holes are arranged on the platform with two different layouts. In one layout, the film-cooling holes are divided into two rows and more concentrated on the pressure side of the passage. In the other layout, the film-cooling holes are divided into four rows and loosely distributed on the platform. Four film-cooling hole configurations are investigated totally. Testing was done in a five-blade cascade with medium high Mach number condition (0.27 and 0.44 at the inlet and the exit, respectively). The detailed film-cooling effectiveness distributions on the platform were obtained using pressure sensitive paint technique. Results show that the combined cooling scheme (slot purge flow cooling combined with discrete-hole film cooling) is able to provide full film coverage on the platform. The shaped holes present higher film-cooling effectiveness and wider film coverage than the cylindrical holes, particularly at higher blowing ratios. The hole layout affects the local film-cooling effectiveness. The shaped holes also show the advantage over the cylindrical holes with lower total pressure loss. [DOI: 10.1115/1.3068327]

1 Introduction

The ability of today's gas turbine engines to withstand increasingly higher turbine-inlet temperatures has been largely due to the advancement in cooling technology. One technique heavily relied on is film cooling. With film cooling, relatively cool air forms a protective film on the outer surface of the airfoil, creating an additional layer of resistance between the hot mainstream gas and the metallic airfoil. With the platform of the blade comprising a large percentage of the area directly exposed to the hot gas, it is vital that this area is adequately protected from the hot gases. Several reviews have been published by Han et al. [1], Langston [2], Chyu [3], and Simon and Piggush [4], which gave an overview of the fluid flow, heat transfer, and film cooling near the endwall and platform regions. Studies by Langston et al. [5,6] revealed some secondary flow structures. When a boundary layer flow approaches a blade or vane, a vortex forms at the leading edge and continues along each side of the airfoil forming a horseshoe vortex. The pressure distribution within the passage causes the suction side leg of the horseshoe vortex to follow the suction side of the airfoil. The pressure side leg of the horseshoe vortex is carried across the passage and gains strength. This large vortex is often called passage vortex. The passage vortex meets the suction side of the airfoil and climbs up to the airfoil surface. Goldstein and Spores [7] and Wang et al. [8] found several "corner" vortices that formed near the intersection of the airfoil surface and the endwall. The secondary flows increase the heat transfer between the mainstream gases and the uncooled platform. They also make film cooling on the platform difficult.

Many researchers have investigated film cooling on endwalls

with discrete cylindrical holes. Takeishi et al. [9] obtained heat transfer and film effectiveness distributions on a vane endwall with film holes placed at three locations in the passage. Harasgama and Burton [10] used film cooling near the leading edge, just inside the passage, with the film-cooling holes located along an iso-Mach line. The film-cooling configuration used by Jabbari et al. [11] consisted of discrete holes placed on the downstream half of the passage. Friedrichs et al. [12,13] studied the film-cooling effectiveness and aerodynamic loss on a fully film cooled endwall. Friedrichs et al. [14] also improved the endwall film-cooling configurations. From the above studies, it is found that the film cooling is strongly affected by the endwall secondary flows. The cross flow transports the coolant from the pressure side to the suction side of the passage. If a film hole is located at separation lines of the secondary flows, the coolant will be lifted off and results in little film protection on the surface. The leading edge region of the endwall is very hard to be cooled by the discrete holes because of the rollup of the horseshoe vortex.

Recently, researchers attempted to employ the shaped hole on the endwall film cooling. Barigozzi et al. [15,16] studied the film-cooling effectiveness and aerothermal performance on a passage endwall with four rows of cylindrical holes or fan-shaped holes. Similar to flat plate film cooling, shaped film-cooling holes offer better film protection than cylindrical holes. The thermodynamic secondary loss increases for the holes with larger area ratios. In the film-cooling design by Colban et al. [17], two rows of cylindrical holes were arranged upstream of passage. The hole configurations varied within the passage—either cylindrical holes or fan-shaped holes. The fan-shaped holes show much higher effectiveness and lower aerodynamic loss than the cylindrical holes. Little benefit was seen from the cylindrical holes upstream of the passage.

Upstream of the inlet guide vane, a gap commonly exists between the combustion chamber and the vane endwall. A similar gap exists between the vane endwall and the rotor platform, en-

Contributed by the International Gas Turbine Institute of ASME for publication in the JOURNAL OF TURBOMACHINERY. Manuscript received August 18, 2008; final manuscript received August 29, 2008; published online July 1, 2009. Review conducted by David Wisler. Paper presented at the ASME Turbo Expo 2008: Land, Sea and Air (GT2008), Berlin, Germany, June 9–13, 2008.

suring the rotor can move freely. Coolant air is often expelled through these gaps or slots to prevent hot mainstream gases from entering the engine cavity. This coolant air has a secondary effect of protecting the platform region. An early study by Blair [18] showed that the film-cooling effectiveness for upstream slot injection varies greatly through the passage due to the secondary flows. Many researchers, including Granser and Schulenberg [19], Roy et al. [20], Burd et al. [21], Simon and co-workers [22,23], Zhang and Jaiswal [24], Zhang and Moon [25], Wright et al. [26–28], and Gao et al. [29], documented the characteristic of slot cooling on endwalls or platforms. The studies showed that coolant from an upstream slot reduces the secondary flows in the passage by increasing the momentum of the boundary layer. The areas that are typically difficult to cool, including the area near the leading edge, can be cooled effectively with the upstream slot injection. The heat transfer near the leading edge is reduced as well. The upstream slot configurations and flow conditions (such as vane passage vortex, etc.) influence the endwall film-cooling effectiveness. Suryanarayanan et al. [30] investigated platform slot purge flow cooling in a three-stage turbine rotating facility. They found that the stator-rotor interaction has a significant impact on the platform film-cooling effectiveness.

In order to provide adequate film coverage for the entire endwall or platform, an upstream slot cooling can be combined with discrete-hole film cooling. Nicklas [31] measured the heat transfer coefficients and film-cooling effectiveness on a nozzle guide vane (NGV) endwall with the combined cooling scheme. The film-cooling holes were concentrated on the entrance region of the passage, so the trailing edge region is hardly cooled. In the design of Wright et al. [32], the film holes were close to the throat region of a blade platform. The entire platform is cooled at the cost of a large amount of purge flow coolant consumption. Suryanarayanan et al. [33] studied rotating platform film cooling by stator-rotor purge flow combined with discrete-hole film cooling in the same rotating facilities as Ref. [30]. The film-cooling holes in Refs. [31–33] were all cylindrical holes.

Taking advantage of the slot purge flow cooling, this paper is aimed to implement discrete-hole film-cooling designs within a blade passage to provide complete film protection for the blade platform. The leading edge region of the platform, which is hard to be cooled by discrete holes, is cooled by slot purge flow. To minimize the purge flow coolant, the downstream region of the platform is cooled by discrete holes. The performance of cylindrical holes and shaped holes are assessed in terms of film-cooling effectiveness and total pressure loss. Taking the three dimensional nature of the platform flow into account, different hole layouts on the platform are also studied. Totally, four discrete-hole film-cooling configurations (2 hole shapes \times 2 hole layouts) are investigated. Testing was done in a cascade with medium high Mach number conditions. The freestream inlet and exit Mach numbers are 0.27 and 0.44, respectively. The film-cooling effectiveness is measured using pressure sensitive paint (PSP) techniques. The total pressure on an exit plane of the cascade is measured with Pitot tubes.

2 Experimental Facility

Figure 1 schematically shows the five-blade linear cascade with a platform test section cooled by upstream purge flow and discrete-hole film cooling. The same cascade facility was used by Gao et al. [29] for the upstream purge flow cooling study. Some of the important parameters of the cascade and mainstream flow conditions are listed in Table 1. The inlet cross section of the test section is 19.6 cm (width) \times 12.7 cm (height, H) while the exit cross section is 12.9 cm (width) \times 12.7 cm (height). The top plate, which acts as the shroud for the blades, was machined out of 1.27 cm thick acrylic sheets for optical access. The three middle blades in the cascade have a span of 12.64 cm and an axial chord length of 8.13 cm. The blades have a turning angle of 116.9 deg. The blade-to-platform interface is 90 deg, i.e., there is no fillet at the

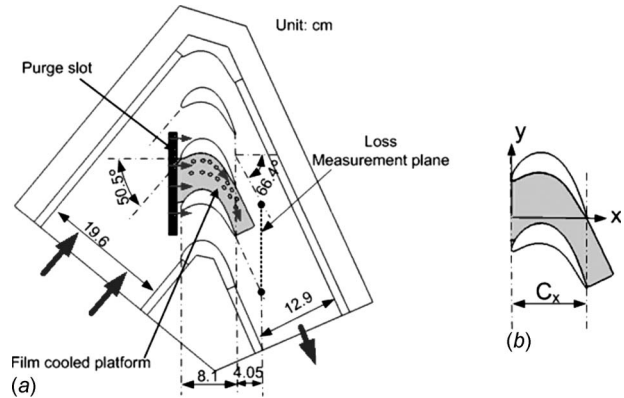


Fig. 1 (a) Schematic of the cascade blade platform with upstream slot purge flow cooling and downstream discrete-hole film cooling. (b) Definition of platform coordinates.

interface. A honeycomb mesh, 7.62 cm long with a cell size of 1.27 cm, is placed 1.78 m upstream of the blade passage to uniform the velocity distribution. Downstream flow periodicity is ensured by adjusting the cascade tailboards. The mainstream air is supplied by a centrifugal compressor that can deliver a volume flow rate up to 6.2 m³/s. The cascade inlet and exit velocities are set to be 96 m/s and 156 m/s, corresponding to inlet and exit Mach numbers of 0.27 and 0.44, respectively. The Reynolds number based on the axial chord length and exit velocity is 750,000. The overall pressure ratio (cascade inlet total pressure to exit static pressure) is 1.14. Turbulence intensity and boundary layer thickness were recorded 6.3 cm upstream of the middle blade. Turbulence intensity, which was measured by a hot wire anemometer in the center of channel, is 1.75% with integral length scale of 5 cm. The boundary layer thickness, based on 99% of mainstream velocity, is about 25 mm. A traversing plane, located 0.5C_x downstream of the trailing edge, for the total pressure measurement is also indicated in Fig. 1(a). The definition of the coordinate, which will be used to present the data, is shown in Fig. 1(b).

2.1 Platform Film-Cooling Design. Gao et al. [29] showed that the purge flow from the stator-rotor seal can be effectively used to cool the upstream regions of the platform. Nonetheless,

Table 1 Cascade geometry and mainstream flow conditions

Cascade geometry	
Blade span (cm)	12.64
Tip clearance (cm)	0.064
Axial chord length (cm)	8.13
Pitch (cm)	7.69
Aspect ratio (H/C_x)	1.55
Leading edge diameter (mm)	4.8
Inlet area (cm ²)	249
Exit area (cm ²)	164
Inlet angle (deg)	50.5
Exit angle (deg)	66.4
Total turning angle (deg)	116.9
Convergence ratio	1.5
Mainstream flow conditions	
Inlet Mach No.	0.27
Exit Mach No.	0.44
Re _{in}	465,000
Re _{ex}	750,000
Pressure ratio (P_t/P)	1.14
Turbulence intensity	1.75%
Boundary layer thickness (cm)	2.5

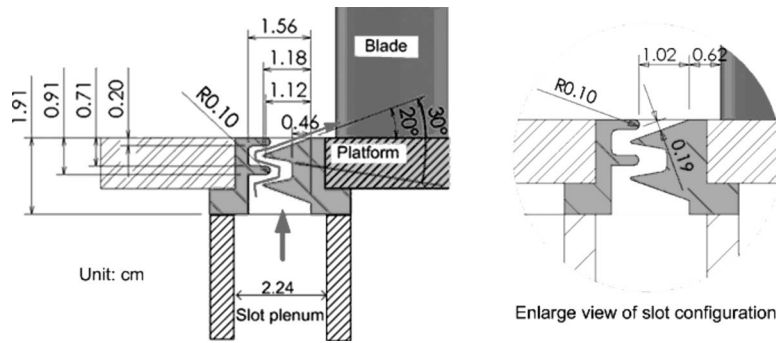


Fig. 2 Configuration of upstream labyrinthlike stator-rotor seal in Ref. [29]

the strong passage vortex sweeps the coolant off the platform; the area downstream of passage vortex separation line is left unprotected. In the current study, the same stator-rotor seal configuration [29] is used to cool the upstream region of the platform. The discrete-hole film-cooling design is implemented to cool the rest area of the platform. Figure 2 shows the slot configuration. The double-tooth labyrinthlike slot simulates a typical stator-rotor seal in real engines. The seal consists of two parts, an upstream (stator) part with round teeth and a downstream (rotor) part with sharp teeth. The seal breaks at $0.076C_x$ upstream of passage with a breakout width of 1.02 cm. The downstream part of the slot is inclined 20 deg to the platform surface with a throat width of 0.19 cm. The seal covers 1.5 pitches of passage. Coolant is supplied via a coolant plenum underneath the purge slot. Detailed description on the slot configuration can be found in Ref. [29].

Additional platform film cooling is provided by discrete holes. Figure 3 shows the hole configurations. This paper is focused on assessing the film-cooling performance from the shaped holes. To serve this purpose, the designs with cylindrical holes are also provided as baseline. The film-cooling holes in the current studies are lined up with the freestream streamwise direction. Past studies in the open literature have confirmed that the passage cross flow sweeps the film coolant from pressure side to suction side. Studies on the flat plates show that coolant from compound angle holes covers wider area due to jet deflection. It is anticipated that the passage cross flow would turn the coolant jet and a wider surface area would be covered with the inline design. The film-cooling holes are arranged on the platform with two layouts. With one layout, the film-cooling holes are divided into two rows and more concentrated on the pressure side of the passage. In the other layout, the film-cooling holes are divided into four rows and loosely distributed on the entire platform. With the two film-hole shapes and two layouts, four film-hole configurations are implemented. Among the four configurations, Configurations A and B have cylindrical holes; while Configurations C and D laidback fan-shaped holes. Configurations A and C are arranged in two rows, while Configurations B and D are arranged in four rows. Sixteen film holes, inclined 30 deg to the platform surface, are used in all configurations. The cylindrical holes have a diameter (d) of 1.588 mm with a hole length of $8d$. The laidback fan-shaped holes are featured with a lateral expansion of 10 deg from the hole axis and forward expansion of 5 deg into the platform surface. The hole diameter in metering part (cylindrical part) of the shaped holes is the same as that for the cylindrical holes. The expansion starts at $4d$, resulting in a cross sectional area ratio of 3.85 between the hole exit and hole inlet. For the two-row designs (Configurations A and C), one row is located along the midpassage line and the other row is located along a curve 6.35 mm offset from the pressure side of the blade surface. There are eight holes in each row. The first hole in each row is located at the axial location $x/C_x=0.36$. The hole to hole spacing along the curve is about $4d$. The four-row designs B and D are achieved by shifting the alternative holes in Configurations A and C, respectively. Four

holes in the midpassage are shifted to the middle of midpassage and suction side surface. Four holes offset of pressure side are shifted to the middle of the two original curves. Due to the large variation of pressure on the platform, it is hard to control the local blowing ratios for the multiple holes with one common coolant plenum chamber. In the current study, three coolant cavities are used for the discrete holes. The coolant supplied to each cavity is independently controlled by a rotameter dedicated to that cavity. Cavity 1 feeds holes 1–4, cavity 2 feeds holes 5–11, and the rest five holes are fed by cavity 3.

The coolant purge flow rate is generally considered as a percentage of the mainstream mass flow rate. From the previous study [29], it is found that the film coverage and effectiveness increase when the coolant mass flow ratio (MFR) increases from 0.25% to 1.0%. However, the increment in effectiveness is not

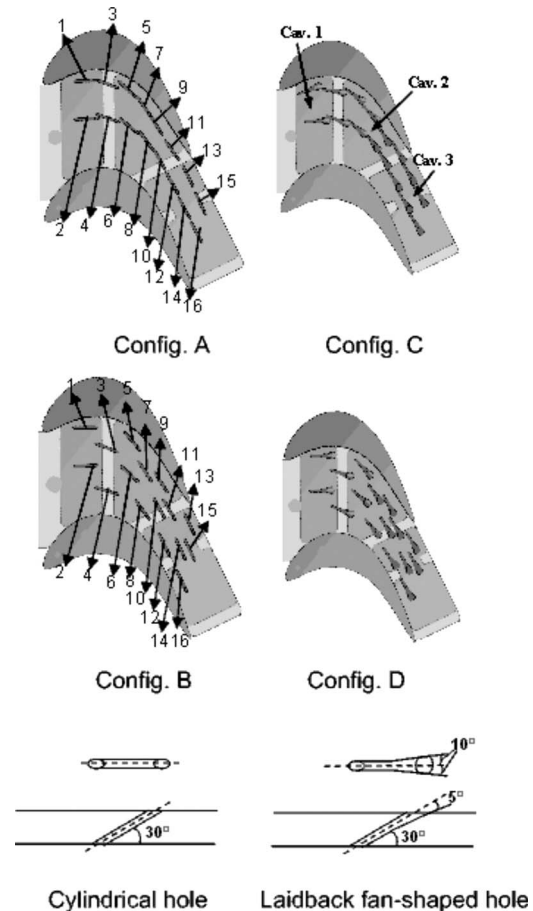


Fig. 3 Discrete hole configuration on platform

significant from $MFR=0.75\%$ to $MFR=1.0\%$. The strong passage vortex lifts the coolant off from the platform resulting in a large unprotected area in the downstream region of the platform. Further increasing the coolant mass flow rate from the slot purge flow may reduce the strength of passage vortex and increase the protected area on the platform. However, the coolant consumption will substantially increase. Therefore, the mass flow ratio of 0.75% (equivalent to a blowing ratio of 0.33), which can sufficiently cool the hard-to-cool leading edge region, is chosen in the current study. The area, which is not protected by the purge flow cooling, is expected to be cooled by the discrete-hole film cooling. Four averaged blowing ratios are tested for the film holes, i.e., $M=0.5, 1.0, 1.5,$ and 2.0 . The average blowing ratios are defined as $M=(\rho_c V_c)/(\rho_m V_m)$. The density ratio is 1 in the current study; therefore, the mass flux ratio is reduced to velocity ratio. The local mainstream velocity at film-hole locations is used as V_m in the M calculation. V_m is obtained from P/P_t , where P is local static pressure, measured by PSP; and P_t is inlet total pressure, measured with Pitot tube. The nominal blowing ratio $M=1.0$ corresponds to 0.54% of freestream flow at the inlet. The local blowing ratio distribution will be discussed in the later part of this paper.

3 Film-Cooling Effectiveness Measurement Theory and Data Analysis

Data for film-cooling effectiveness were obtained using the PSP technique. PSP is a photoluminescent material that emits light when excited, with the emitted light intensity inversely proportional to the partial pressure of oxygen. This light intensity is recorded using a charge-coupled device (CCD) camera. The image intensity obtained from PSP by the camera during data acquisition is normalized with a reference image intensity (I_{ref}) taken under no-flow condition. Background noise in the optical setup is removed by subtracting the image intensities with the image intensity obtained under no-flow conditions and without light excitation (I_{blk}). The resulting intensity ratio can be converted to pressure ratio using a predetermined calibration curve and can be expressed as

$$\frac{I_{ref} - I_{blk}}{I - I_{blk}} = f\left(\frac{(P_{O_2})_{air}}{(P_{O_2})_{ref}}\right) = f(P_{ratio}) \quad (1)$$

where I denotes the intensity obtained for each pixel and $f(P_{ratio})$ is the relationship between intensity ratio and pressure ratio obtained after calibration.

Calibration of the PSP system was performed using a vacuum chamber at several known pressures varying from 0 atm to 1.8 atm. The same optical setup that was used during experiments was chosen for calibration. The calibration curve is shown in Fig. 4. PSP is also sensitive to temperature with higher temperatures resulting in lower light emission. Hence, the paint was also calibrated at different temperatures. It is observed that if the emitted light intensity at a certain temperature is normalized with the reference image intensity taken at the same temperature, the temperature sensitivity can be minimized as shown in Fig. 4(b). Hence, during experiments, the coolant was heated to the same temperature as the mainstream air (approximately 35°C) before supplying through the seal; the reference (I_{ref}) and black (I_{blk}) images were acquired immediately after stopping the mainstream flow so that the test surface temperature did not change appreciably.

To obtain film-cooling effectiveness, air and nitrogen are used alternately as coolant. Nitrogen, which has nearly the same molecular weight as that of air, displaces the oxygen molecules on the surface causing a change in the emitted light intensity from PSP. By noting the difference in partial pressure between the air and nitrogen injection cases, the film-cooling effectiveness can be determined using the following equation:

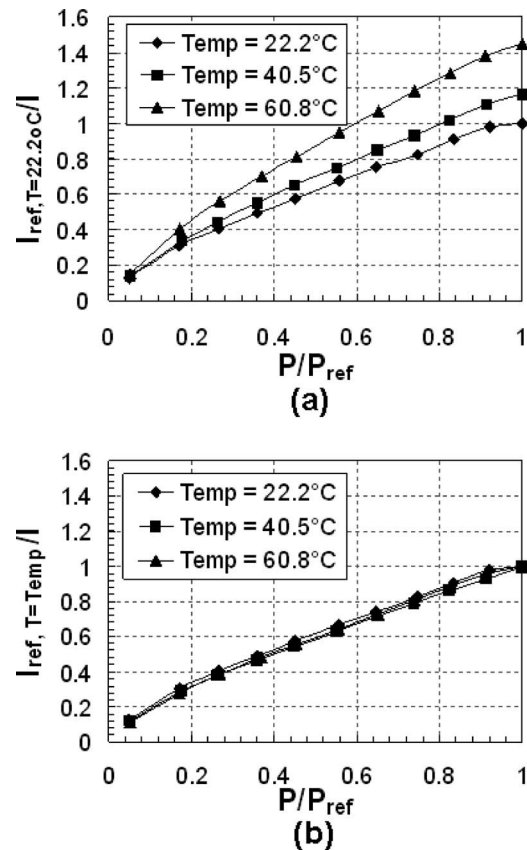


Fig. 4 (a) PSP calibration at single reference temperature, and (b) PSP calibration at corresponding reference temperature

$$\eta = \frac{C_{mix} - C_{air}}{C_{N_2} - C_{air}} = \frac{C_{air} - C_{mix}}{C_{air}} = \frac{(P_{O_2})_{air} - (P_{O_2})_{mix}}{(P_{O_2})_{air}} \quad (2)$$

where C_{air} , C_{mix} , and C_{N_2} are the oxygen concentrations of mainstream air, air/nitrogen mixture, and nitrogen on the test surface, respectively. The definition of the film-cooling effectiveness in Eq. (2) based on mass transfer analogy assumes similar form as that of adiabatic film-cooling effectiveness given in

$$\eta = \frac{T_{mix} - T_m}{T_c - T_m} \quad (3)$$

The film cooled platform was coated with PSP using an air brush. It was excited by a strobe light fitted with a narrow band-pass interference filter (optical wavelength=520 nm). A flexible dual fiber optic guide was used to get a uniform incident light distribution on the test surface. Upon excitation, the PSP coated surface emits light with a wavelength higher than 600 nm. A 12 bit scientific grade CCD camera (Cooke Sencam QE with CCD temperature maintained at -15°C using a two-stage Peltier cooler), fitted with a 35 mm lens and a 600 nm long-pass filter, recorded images. The filter mounted on the camera is chosen such that it does not allow any reflected light from the illumination source to pass through. The camera and the strobe light were triggered simultaneously using a TTL signal from a function generator. A total of 200 TIF images were captured and ensemble-averaged to get the individual intensities. The spatial resolution of each image is 0.6 mm/pixel. A computer program was used to convert these pixel intensities into pressure using the calibration curve and then into film-cooling effectiveness.

Uncertainty calculations were performed based on a confidence level of 95% and were based on the uncertainty analysis method of Coleman and Steele [34]. Lower effectiveness magnitudes have

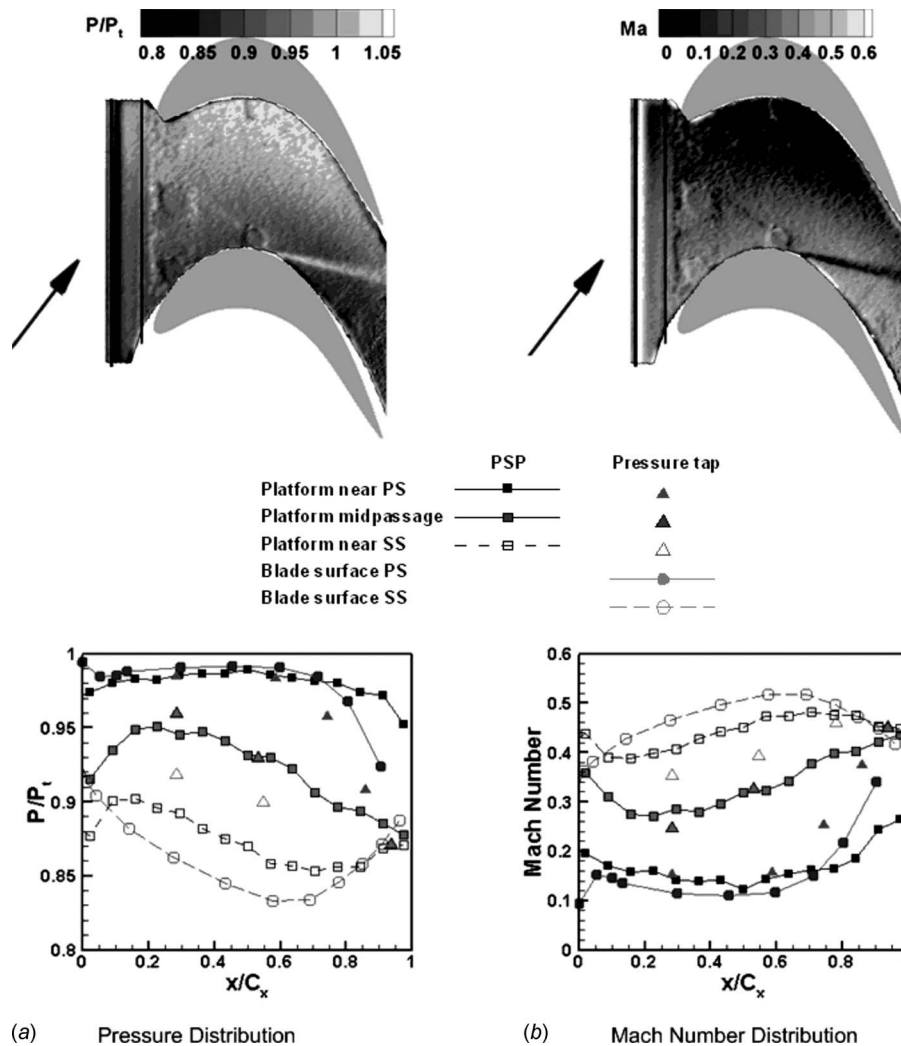


Fig. 5 Pressure and Mach number distribution without coolant injection. (a) Pressure distribution and (b) Mach number distribution.

higher uncertainties. For an effectiveness magnitude of 0.3 or larger, uncertainty is around $\pm 4.8\%$ while for effectiveness magnitude of 0.05, uncertainty is as high as $\pm 8\%$. This uncertainty was the result of uncertainties in calibration (4%) and image capture (1%). Uncertainty for the pressure measurement was 3%; uncertainty for the coolant mass flow rate was 4%.

4 Results and Discussion

4.1 Pressure Measurement on Platform and Local Blowing Ratio Distributions.

Prior to presenting the film effectiveness data, the pressure and Mach number distribution on the platform are examined and shown in Fig. 5. The pressure distribution is represented by the ratio of local static pressure and inlet total pressure. The local static pressure was measured by PSP while the inlet total pressure was measured by Pitot tube placed upstream of the cascade inlet. Eleven pressure taps were instrumented along three curves on the platform to verify the PSP data. One curve is offset of the blade pressure side by 10% of pitch distance, and the other is offset of suction side by 10%. The third curve is along the midpassage. The pressure and Mach number data obtained from PSP measurement were extracted along three curves and compared with pressure tap data. Pressure distribution along the midspan of the blade surface, measured by pressure taps, is also presented for comparison. It can be seen from the contour plot that the static pressure near the pressure side is higher than that near

the suction side. This is the driving force of turbine work as well as the passage cross flow. From the leading edge to the trailing edge, the pressure gradually decreases; the mainstream flow is accelerated; Mach number increases. It can be seen from the line plots that the PSP data matched well with pressure tap data; the maximum deviation between PSP data and pressure tap data is less than 6%. Near the pressure side, the pressure on the platform is very close to the pressure on the blade midspan. However, near the suction side, the pressure on platform is higher than that on the blade midspan. This results in a reduced driving force (pressure differential between pressure side and suction side) near the platform. It can be seen from Fig. 5(b) that the velocity near the suction side on the platform is lower than the freestream velocity.

This nonuniform outer pressure distribution affects purge flow distribution along the slot as well as the local blowing ratio distribution from the discrete holes. Based on the pressure differential between the total pressure inside the plenums and static pressure on the surface, the local coolant flow is calculated. The purge flow distribution, discussed by Gao et al. [29], is shown in Fig. 6(a). From the suction side to the pressure side along the purge slot, the outer pressure increases and the local coolant mass flow rate decreases. The high outer pressure near the pressure side of the passage prohibits the coolant exiting from this region. Detailed discussion on the purge flow distribution can be found in Ref. [29]. The local blowing ratio for the discrete holes is defined as

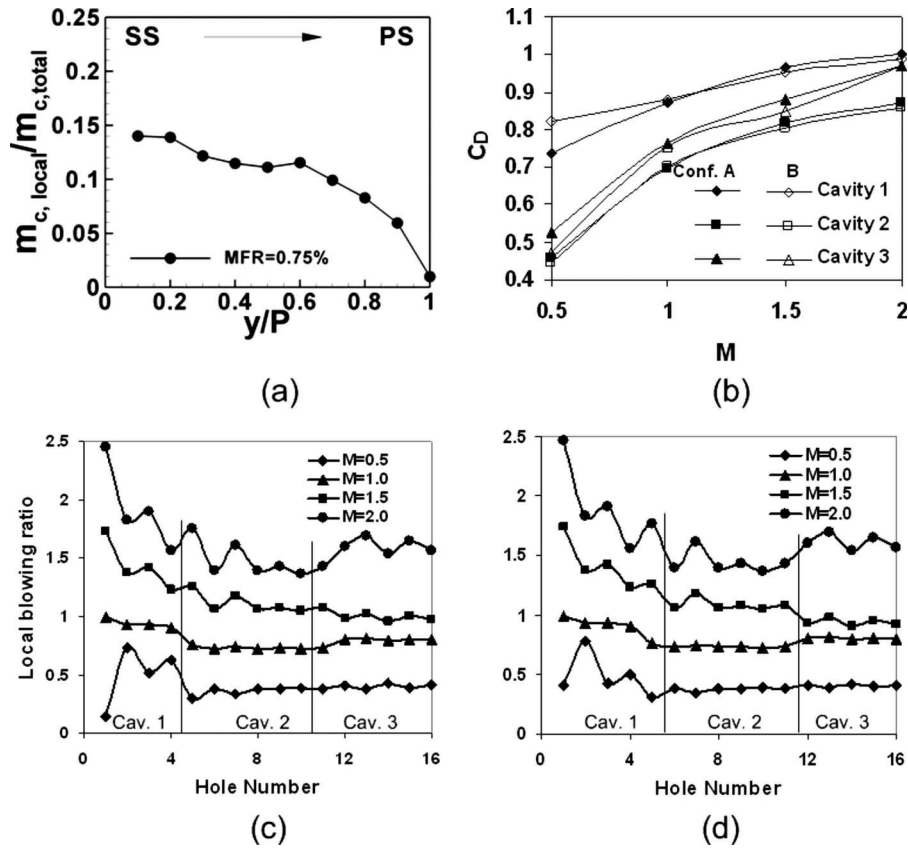


Fig. 6 (a) Local coolant mass flow rate distribution along the purge slot [29], (b) discharge coefficient distribution, (c) local blowing ratio distribution for Configuration A, and (d) local blowing ratio distribution for Configuration B

$M_{local} = \rho_c V_{c,local} / \rho_m V_m$. Same as in the definition of M , V_m is the local mainstream velocity near the film-cooling holes. Whereas $V_{c,local}$ is the actual coolant velocity from the film-cooling hole. To obtain the actual coolant mass flow rate from each hole, the discharge coefficient C_D is calculated by

$$C_D = \dot{m}_{hole} / \left(\frac{\pi}{4} d^2 \right) \times \left(P_{t,cav} \left(\frac{P}{P_{t,cav}} \right)^{(y+1)/2y} \right) \sqrt{\frac{2y}{(y-1)RT_c} \left(\left(\frac{P_{t,cav}}{P} \right)^{(y-1)/y} - 1 \right)} \quad (4)$$

The total pressure inside the coolant cavity $P_{t,cav}$ was measured with pressure taps instrumented on the plenum cavities. The discharge coefficient C_D is assumed to be constant for all holes in the cavity for a given average blowing ratio M . It should be noted that the constant assumption of C_D may not be true as C_D depends on not only the geometry but also the external and internal flow conditions. It is assumed that the deviation in the discharge coefficients from hole to hole is not significant and hence an average value can be used without introducing a significant error. Once the C_D for a given M is determined, the coolant velocity from each hole is calculated and the local blowing ratio for the hole is computed. It can be seen from Fig. 6(b) that the discharge coefficients increase with M , but the gradient gradually reduces. The values of C_D are about the same for Configurations A and B at a given M . As shown in Figs. 6(c) and 6(d), the local blowing ratio distribution in the first cavity has a larger variation than the other two. The local blowing ratios for the holes in cavity 2 or cavity 3 are close to each other. The multiple coolant supply cavity helps to

control the local blowing ratios. The difference in local blowing ratios for Configurations A and B is small.

4.2 Film-Cooling Effectiveness on Platform. Film-cooling effectiveness measurements were done for the four hole configurations. As stated earlier, a typical coolant mass flow ratio (MFR=0.75%) is chosen for the slot purge flow, while the average blowing ratios for the downstream discrete holes vary from $M=0.5-2.0$.

Before considering the realistic cooling schemes of combined purge flow cooling and discrete-hole film cooling, the isolated effects from discrete holes are understood first. Figure 7 shows the film-cooling effectiveness distribution for Configurations A and C. Some common features of platform film cooling are observed regardless of hole shapes. It is clear that the coolant is deflected to the suction side of passage by the cross flow within the passage. From the leading edge to the trailing edge, the deflection reduces. Increasing the blowing ratio, the jet momentum increases, resulting in less jet deflection. Due to the jet deflection, the jets from holes 1 and 3 are unable to impinge to the blade pressure surface. Therefore, the junction area between the platform and the blade pressure side is unprotected by the film cooling. The coolant from upstream holes extends to the downstream region. With the upstream coolant accumulation, the film-cooling effectiveness in the downstream region is higher than that in the upstream region. At $M=0.5$, the pressure inside the plenum chamber is relatively low. The coolant is prohibited ejecting through holes 1, 3, and 5, where the outer pressure is high. In this case, the mainstream ingestion may occur to the three holes. On the other hand, more coolant ejects from holes 2 and 4 and results in a higher local blowing ratio for these two holes. Therefore, the jets from holes 2 and 4 lift

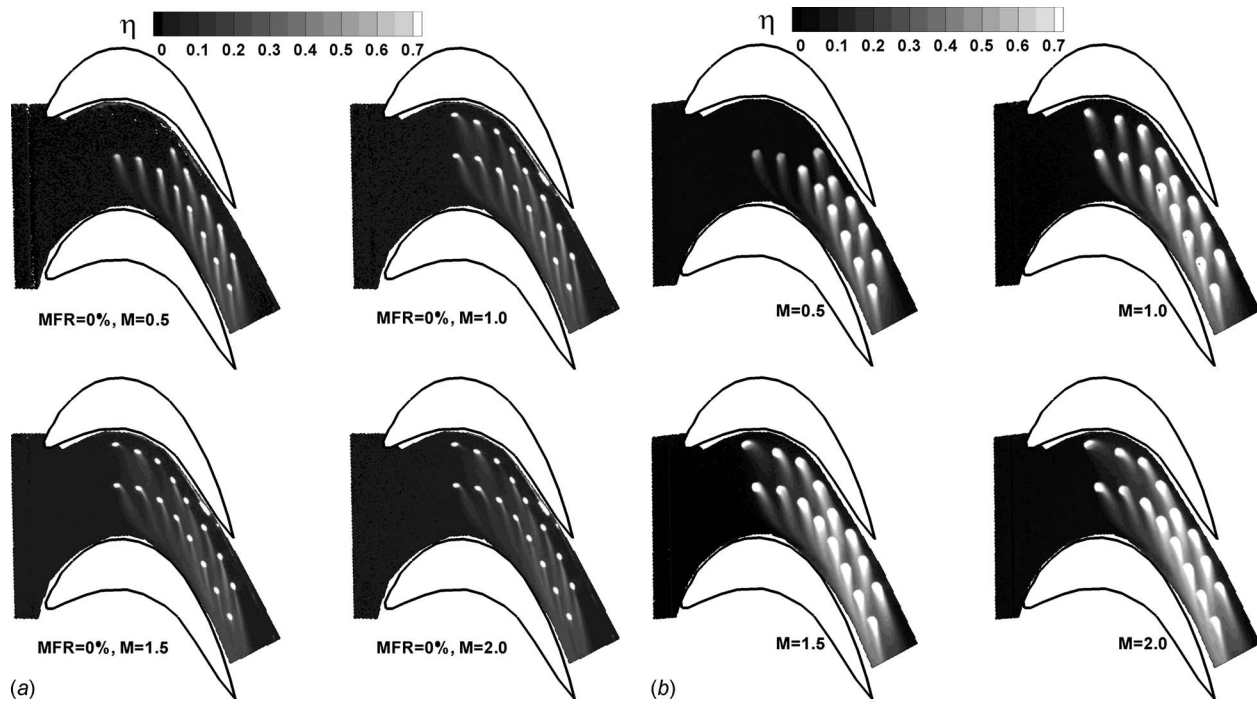


Fig. 7 Film-cooling effectiveness distribution on platform with discrete holes. (a) Configuration A and (b) Configuration C.

off from the surface and quickly mix with mainstream. It should be noted that the effectiveness reduction from holes 2 and 4 may be also caused by the mixing between ingested air (from holes 1, 3, and 5) and coolant inside the cavity. Comparing Figs. 7(a) and 7(b), it can be seen that the shaped holes offer a larger film coverage and higher effectiveness magnitude. The best film-cooling effectiveness for cylindrical holes is obtained at $M=1.0$. Further increase in M ($M=1.5$ and 2.0) results in jet penetration to the mainstream and reduces the effectiveness level. For the shaped holes, the film effectiveness increases with the increase in average blowing ratio. The hole exit area is enlarged for the shaped holes; consequently, the jet momentum reduces. The coolant jet is easier to stay close to the surface with low momentum jet. In addition, the jets from the shaped holes are more deflected than the cylindrical holes with the relatively low momentum. The wider coolant trace from the shaped holes also benefits from the enlarged hole breakout area.

The previous study [29] shows that a large area of the passage is left unprotected when the platform is only cooled by the upstream purge flow cooling. The addition of the discrete holes should help alleviate this problem. Figures 8–11 show the detailed film-cooling distributions for the cases of combined purge flow cooling with discrete-hole film cooling.

Figure 8 is film effectiveness contour for Configuration A. Combined with the two cooling schemes (slot purge flow cooling and discrete-hole film cooling), the film coverage on the platform is much improved. Due to the large turning angle of the blade (116.9 deg), the passage vortex is very strong. The flow field near the endwall region downstream of the separation line of the passage vortex is barely influenced by the purge flow ejection. Therefore, the downstream discrete-hole film cooling is almost unaffected by the upstream purge flow. In other words, the isolated effect from the purge flow and discrete-hole film cooling can be simply superimposed to achieve the film effectiveness for the combined film cooling. Similar to the case of discrete-hole film cooling alone, the best effectiveness for this configuration is obtained at $M=1.0$. Further increase in M will cause jet lift-off. The upstream coolant accumulation results in better film-cooling effectiveness on the downstream regions. Better film coverage may be

obtained if one more hole is added upstream of holes 1 and 2.

Figure 9 shows the film effectiveness contour for Configuration B. The film-cooling holes are widely distributed over the platform surface with this configuration. In terms of film coverage, Configuration B has slightly less coverage than Configuration A. Because the alternative holes are shifted toward the suction side, the jet deflection causes a slightly larger uncovered area near the pres-

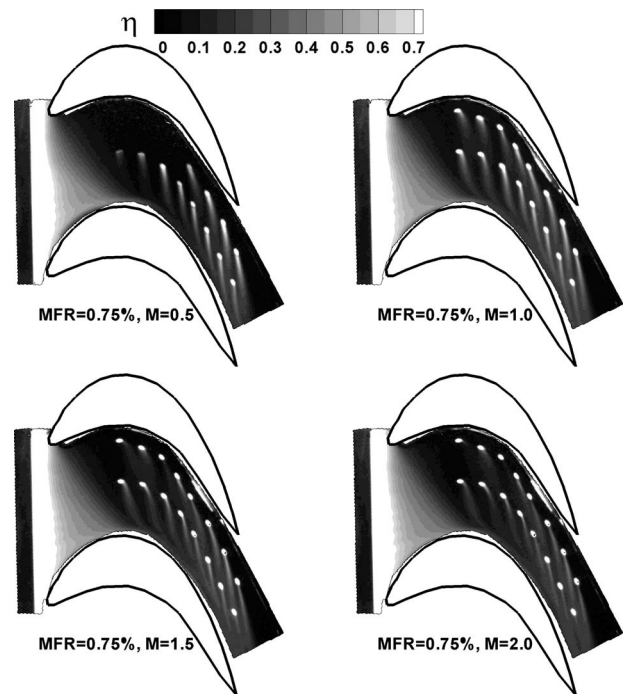


Fig. 8 Film-cooling effectiveness on platform with combined slot film cooling and discrete-hole film cooling (Configuration A)

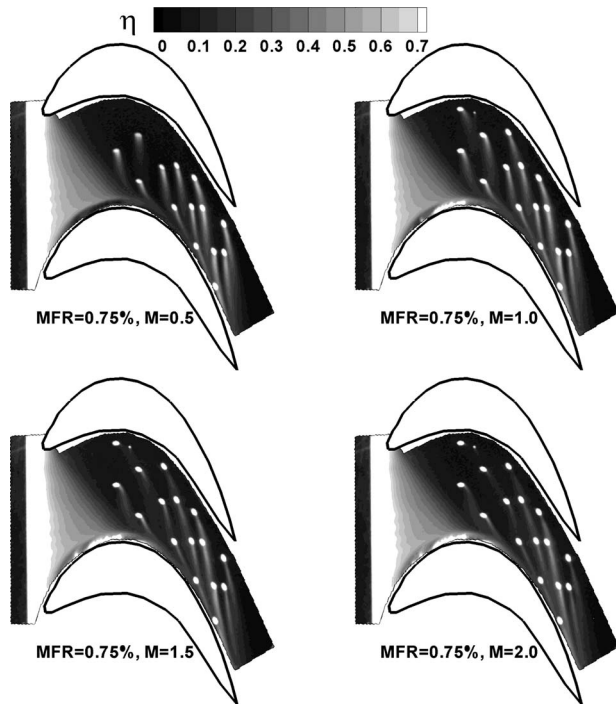


Fig. 9 Film-cooling effectiveness on platform with combined slot film cooling and discrete-hole film cooling (Configuration B)

sure side of the passage. Due to the rearrangement of the hole location, the local blowing ratio for each holes is changed a little bit. Consequently, the effectiveness for the individual hole is varied slightly. On the whole, the film-cooling effectiveness levels for the two configurations (A and B) are very comparable. The effect of blowing ratio on the film effectiveness is the same. It should be

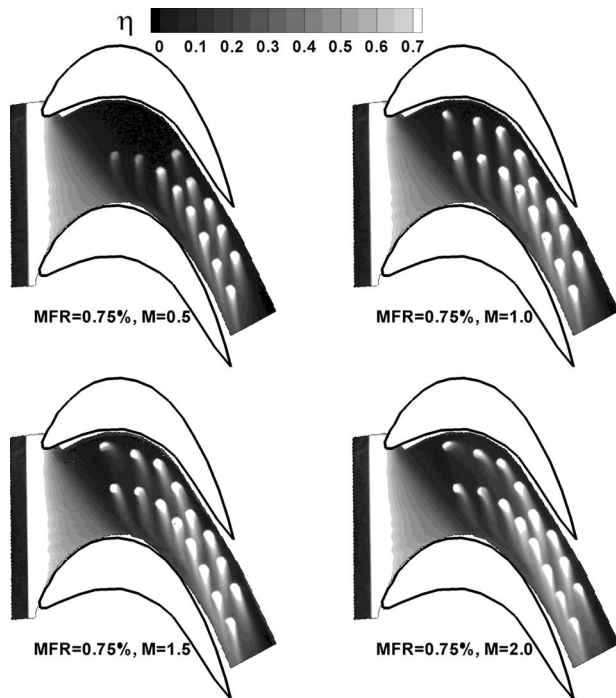


Fig. 10 Film-cooling effectiveness on platform with combined slot film cooling and discrete-hole film cooling (Configuration C)

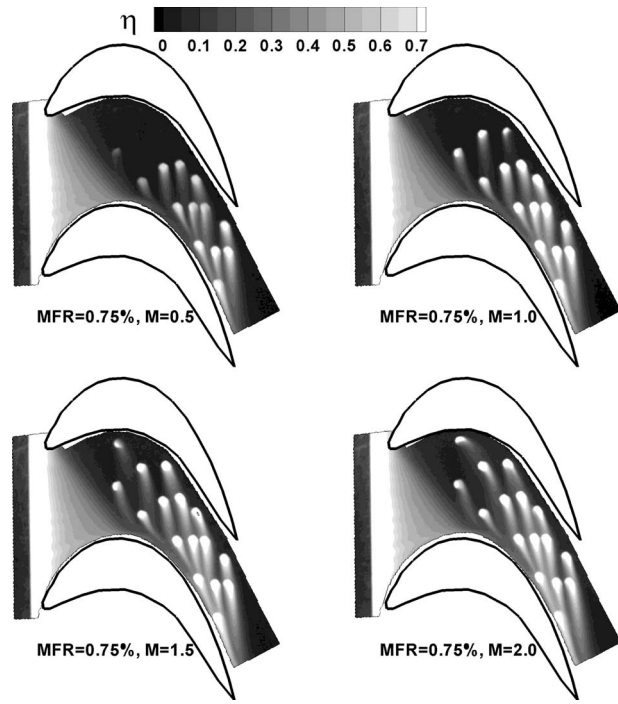


Fig. 11 Film-cooling effectiveness on platform with combined slot film cooling and discrete-hole film cooling (Configuration D)

mentioned that local high effectiveness close to the front part of the suction side is a measurement error resulting from the epoxy glue. The true effectiveness value at this location should be similar to that in Fig. 8.

Figure 10 shows the film-cooling effectiveness for Configuration C. The film coverage and film effectiveness level for Configuration C are much improved over Configuration A, particularly at higher average blowing ratios. Again, the film-cooling characteristics that appeared in Fig. 7(b) are also observed in this figure. The film-cooling effectiveness increases with increase in blowing ratio. Film coverage from offset PS row extends closer to the pressure side. Close to the suction side of the blade, there is a sharp decrease in effectiveness. This implicates the strong horse-shoe vortex (of suction side leg) and corner vortex entraining the coolant away from the platform surface.

Figure 11 shows the film effectiveness for Configuration D. The film coverage is reduced when compared with Configuration C. Close to the suction surface of the passage, the local effectiveness increases. The film effectiveness from the four rows of film holes are not as evenly distributed on the platform as from Configuration C. From the above effectiveness contours, it is perceived that the varying arrangement of the film holes may result in completely different effectiveness distribution. Due to the complex three dimensional nature of the platform secondary flow, it is of importance to strategically lay out the film-cooling holes on the platform.

Figure 12 shows the effect of blowing ratio on the laterally averaged film-cooling effectiveness. The laterally averaged film-cooling effectiveness for the case purge flow cooling only [29] is also presented (in black solid lines) as reference. The data repeatability is proven from the overlaps of the spanwise averaged effectiveness data resulted from the upstream purge flow. The film-cooling effectiveness on the downstream of the platform from the purge flow alone is negligible. With the discrete-hole film cooling, the film-cooling effectiveness in the downstream region increases significantly. For the cylindrical holes (Configurations A and B), the best film-cooling effectiveness is obtained at $M=1.0$. The effectiveness for $M=1.5$ and $M=2.0$, which is slightly lower than

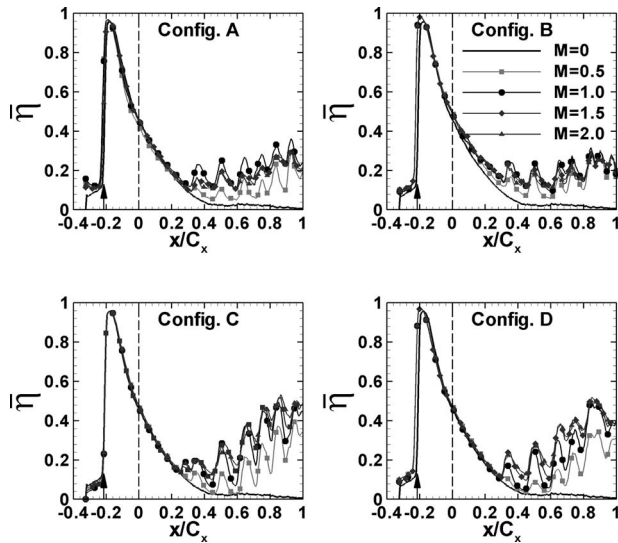


Fig. 12 Laterally averaged film-cooling effectiveness (effect of blowing ratio)

$M=1.0$, are comparable. For the shaped holes (Configurations C and D), the film-cooling effectiveness increases with the increase in averaged blowing ratio. From $M=1.5$ to $M=2.0$, the increment is not significant.

Figure 13 shows the effect of hole configurations on laterally averaged film-cooling effectiveness. At low blowing ratio $M=0.5$, the film-cooling effectiveness from the four hole configurations are comparable. The advantage of shaped holes becomes evident when the averaged blowing ratio increases. At $M=1.5$ and 2.0 , the spanwise averaged film-cooling effectiveness from the shaped hole is substantially higher than that from the cylindrical holes. The difference in spanwise averaged effectiveness resulting from the different layouts is subtle. The two-row layout presents slightly better averaged effectiveness than the four-row.

4.3 Total Pressure Loss Measurement. The total pressure loss was measured on an exit plane at an axial distance of $0.5C_x$ downstream of trailing edge. The location of the traversing plane was indicated in Fig. 1. An array of eight Pitot tubes, with a diameter of 2.38 mm (3/32 in.), was placed spanning 1.5 pitches.

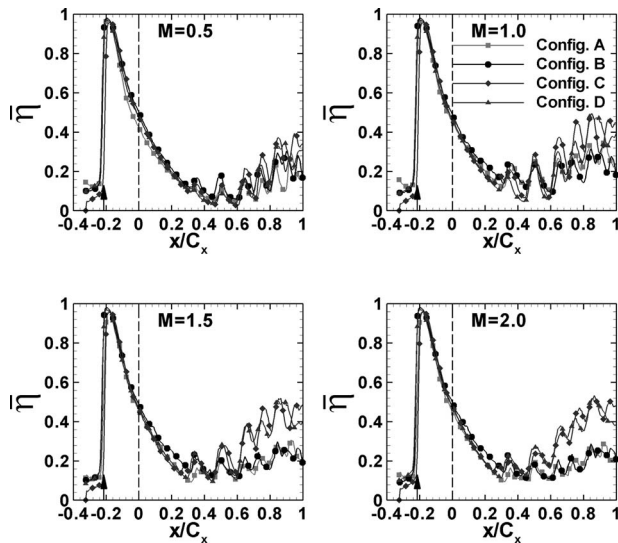


Fig. 13 Laterally averaged film-cooling effectiveness (effect of hole configuration)

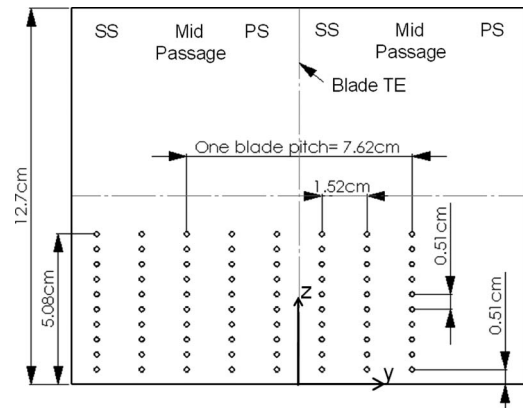


Fig. 14 Traversing plane for total pressure measurement

The film cooled platform is located in the passage with negative y values. The Pitot tubes traversed ten positions and crossed 40% of the span from the hub. The matrix of probe locations is shown in Fig. 14. The pressures were recorded with a 48-channel Scanivalve System coupled with LABVIEW software. The total pressure maps on the exit plane were measured for the cooled and uncooled platforms. The exit total pressure is normalized with the inlet total pressure ($\pi = P_{t,ex} / P_{t,in}$) to evaluate the aerodynamic losses. The inlet total pressure was measured upstream of the purge slot by means of a Pitot tube.

It can be seen from Fig. 15 that the dominant loss is generated by the passage vortex. The loss core is located at 30% of the span approximately for the uncooled platform. The loss core is slightly raised up and shifted away from the suction side with the purge flow ejection. The purge slot ejection ($MFR=0.75\%$) produces a wider wake with more losses.

Since the cooling hole layouts do not show a significant impact on the spanwise averaged film effectiveness and the hole shapes present substantial difference, it is deemed that the alteration of flow field from the hole layout is little. Therefore, only Configurations A (cylindrical holes) and C (shaped holes) are assessed for the total pressure loss with combined film-cooling scheme. Figure 16(a) shows the total pressure loss maps with the platforms cooled by both purge flow and discrete-hole ejection (Configuration A). Compared with Fig. 15(b), the wake from the passage vortex is further broadened with the additional coolant ejection from cylindrical holes. The total pressure loss is increased. After leaving the film holes, the coolant interacts with the mainstream. The interaction between the coolant jets and mainstream causes mixing loss. Figure 16(b) shows the total pressure maps for Configuration C. With this configuration, the wake from the passage vortex becomes smaller, comparable to that in Fig. 15(b) (purge flow ejection only) with much reduced loss from passage vortex. The loss associated with the boundary layer is also reduced. Due to de-

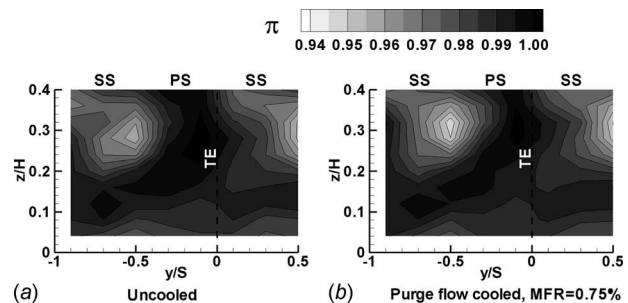


Fig. 15 Total pressure distribution at the cascade exit. (a) No coolant ejection. (b) Coolant ejection from purge slot.

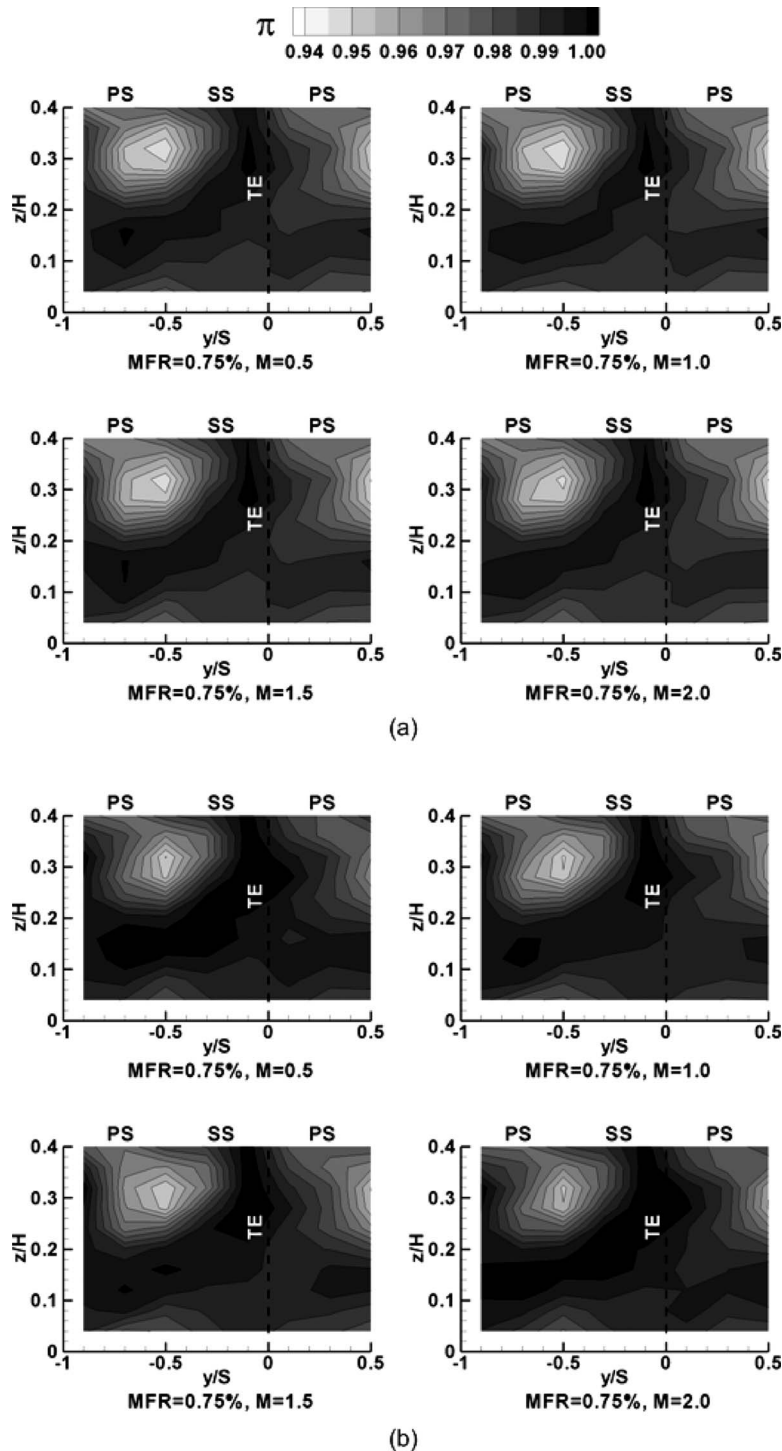


Fig. 16 Total pressure distribution at the cascade exit for coolant ejection with purge flow combined with discrete holes. (a) Configuration A and (b) Configuration C.

creased jet momentum, the coolant from the shaped holes tends to stay attached to the platform surface. This may reduce the boundary layer separation, which is a major contribution to the boundary layer loss. The losses associated with discrete-hole ejection seem insensitive to the blowing ratios.

5 Conclusions

An experimental study was undertaken to measure the film-cooling effectiveness and total pressure loss on a turbine blade

platform within a five-blade linear cascade. The platform is cooled by purge flow from a typical stator-rotor seal combined with discrete-hole film cooling. Pressure sensitive paint was used to measure the film-cooling effectiveness. The purge flow through the seal is fixed at $MFR=0.75\%$. Cylindrical holes and shaped holes are employed in the film-cooling design. The holes are laid out four rows or two rows on the platform. The average blowing ratios for the discrete holes are varied from 0.5 to 2.0. Results show that the platform can be effectively cooled with stator-rotor

purge flow combined with the downstream discrete-hole film cooling. The shaped holes provide wider film coverage and higher effectiveness than the cylindrical holes. The effectiveness of the shaped holes increases with increase in the average blowing ratio ($M=0.5-2.0$), whereas an optimal blowing ratio of 1.0 exists for the cylindrical holes. The two-row or four-row layout does not show much difference in spanwise averaged effectiveness. However, the local effectiveness distribution, which will determine the thermal stress, hotspots, etc., is definitely dependent on the layout. It is of importance to strategically arrange film holes on platform. The shaped holes also exhibit lower total pressure loss.

Acknowledgment

This publication was sponsored by Marcus Easterling Endowment Fund.

Nomenclature

C	= oxygen concentration
C_D	= discharge coefficient
C_x	= axial chord length of the rotor blade (8.13 cm)
d	= diameter of the film-cooling hole (mm)
H	= cascade height (12.7 cm)
I	= pixel intensity of an image
\dot{m}_c	= coolant mass flow rate for purge flow (kg/s)
MFR	= mass flow ratio of slot purge flow (percentage of mainstream mass flow rate)
M	= average blowing ratio for discrete film holes
P	= local static pressure (Pa)
PS	= abbreviation for "pressure side"
P_t	= total pressure (Pa)
P_{O_2}	= partial pressure of oxygen (Pa)
S	= blade pitch (cm)
SS	= abbreviation for "suction side"
T	= temperature ($^{\circ}\text{C}$)
x	= axial distance measured from the blade leading edge (cm)
y	= pitchwise distance measured from the suction side (cm)
z	= spanwise distance measure from the platform (cm)
V_c	= average coolant velocity (m/s)
V_m	= mainstream velocity (m/s)
η	= local film-cooling effectiveness
$\bar{\eta}$	= laterally averaged film-cooling effectiveness
π	= total pressure ratio ($=P_{t,ex}/P_{t,in}$)
ρ_c	= density of coolant (kg/m^3)
ρ_m	= density of mainstream air (kg/m^3)

Subscript

air	= mainstream air with air as coolant
blk	= image without illumination (black)
c	= coolant
ex	= exit of cascade
in	= inlet of cascade
m	= mainstream
mix	= mainstream air with nitrogen as coolant
ref	= reference image with no mainstream and coolant flow

References

[1] Han, J. C., Dutta, S., and Ekkad, S. V., 2000, *Gas Turbine Heat Transfer and Cooling Technology*, Taylor and Francis, New York.

[2] Langston, L. S., 2001, "Secondary Flows in Axial Turbines—A Review," *Ann. N.Y. Acad. Sci.*, **934**, pp. 11–26.

[3] Chyu, M. K., 2001, "Heat Transfer Near Turbine Nozzle Endwall," *Ann. N.Y. Acad. Sci.*, **934**, pp. 27–36.

[4] Simon, T. W., and Piggush, J. D., 2006, "Turbine Endwall Aerodynamics and Heat Transfer," *J. Propul. Power*, **22**(2), pp. 301–312.

[5] Langston, L. S., Nice, L. M., and Hooper, R. M., 1976, "Three-Dimensional Flow Within a Turbine Cascade Passage," ASME Paper No. 76-GT-50.

[6] Langston, L. S., 1980, "Crossflows in a Turbine Cascade Passage," *ASME J. Eng. Power*, **102**, pp. 866–874.

[7] Goldstein, R. J., and Spores, R. A., 1988, "Turbulent Transport on the Endwall in the Region Between Adjacent Turbine Blades," *ASME J. Heat Transfer*, **110**, pp. 862–869.

[8] Wang, H. P., Olson, S. J., and Goldstein, R. J., 1997, "Flow Visualization in a Linear Turbine Cascade of High Performance Turbine Blades," *ASME J. Turbomach.*, **119**, pp. 1–8.

[9] Takeishi, K., Matsuura, M., Aoki, S., and Sato, T., 1990, "An Experimental Study of Heat Transfer and Film Cooling on Low Aspect Ratio Turbine Nozzles," *ASME J. Turbomach.*, **112**, pp. 488–496.

[10] Haragama, S. P., and Burton, C. S., 1992, "Film Cooling Research on the Endwall of a Turbine Nozzle Guide Vane in a Short Duration Annular Cascade: Part I—Experimental Technique and Results," *ASME J. Turbomach.*, **114**, pp. 734–740.

[11] Jabbari, M. Y., Marston, K. C., Eckert, E. R. G., and Goldstein, R. J., 1996, "Film Cooling of the Gas Turbine Endwall by Discrete-Hole Injection," *ASME J. Turbomach.*, **118**, pp. 278–284.

[12] Friedrichs, S., Hodson, H. P., and Dawes, W. N., 1996, "Distribution of Film-Cooling Effectiveness on a Turbine Endwall Measured Using the Ammonia and Diazo Technique," *ASME J. Turbomach.*, **118**, pp. 613–621.

[13] Friedrichs, S., Hodson, H. P., and Dawes, W. N., 1997, "Aerodynamic Aspects of Endwall Film Cooling," *ASME J. Turbomach.*, **119**, pp. 786–793.

[14] Friedrichs, S., Hodson, H. P., and Dawes, W. N., 1998, "The Design of an Improved Endwall Film Cooling Configuration," ASME Paper No. 98-GT-483.

[15] Barigozzi, G., Benzoni, G., Franchini, G., and Derdichizzi, A., 2005, "Fan-Shaped Hole Effects on the Aero-Thermal Performance of a Film Cooled Endwall," ASME Paper No. GT2005-68544.

[16] Barigozzi, G., Franchini, G., and Perdicchizzi, A., 2007, "Endwall Film Cooling Through Fan-Shaped Holes With Different Area Ratios," *ASME J. Turbomach.*, **129**, pp. 212–220.

[17] Colban, W., Thole, K. A., and Haendler, M., 2006, "A Comparison of Cylindrical and Fan-Shaped Film-Cooling Holes on a Vane Endwall at Low and High Freestream Turbulence Level," ASME Paper No. GT2006-90021.

[18] Blair, M. F., 1974, "An Experimental Study of Heat Transfer and Film Cooling on Large-Scale Turbine Endwall," *ASME J. Heat Transfer*, **96**, pp. 524–529.

[19] Granser, D., and Schulenberg, T., 1990, "Prediction and Measurement of Film Cooling Effectiveness for a First-Stage Turbine Vane Shroud," ASME Paper No. 90-GT-95.

[20] Roy, R. P., Squires, K. D., Gerendas, M., Song, S., Howe, W. J., and Ansari, A., 2000, "Flow and Heat Transfer at the Hub Endwall of Inlet Vane Passages—Experiments and Simulations," ASME Paper No. 2000-GT-198.

[21] Burd, S. W., Satterness, C. J., and Simon, T. J., 2000, "Effects of Slot Bleed Injection Over a Contoured End Wall on Nozzle Guide Vane Cooling Performance: Part II—Thermal Measurements," ASME Paper No. 2000-GT-200.

[22] Oke, R., Simon, T., Shih, T., Zhu, B., Lin, Y. L., and Chyu, M., 2001, "Measurements Over a Film-Cooled Contoured Endwall With Various Coolant Injection Rates," ASME Paper No. 2001-GT-0140.

[23] Oke, R. A., and Simon, T. W., 2002, "Film Cooling Experiments With Flow Introduced Upstream of a First Stage Nozzle Guide Vane Through Slots of Various Geometries," ASME Paper No. GT-2002-30169.

[24] Zhang, L. J., and Jaiswal, R. S., 2001, "Turbine Nozzle Endwall Film Cooling Study Using Pressure-Sensitive Paint," *ASME J. Turbomach.*, **123**, pp. 730–735.

[25] Zhang, L. J., and Moon, H. K., 2003, "Turbine Nozzle Endwall Inlet Film Cooling—The Effect of a Backward Facing Step," ASME Paper No. GT2003-38319.

[26] Wright, L. M., Gao, Z., Yang, H., and Han, J. C., 2006, "Film Cooling Effectiveness Distribution on a Gas Turbine Blade Platform With Inclined Slot Leakage and Discrete Film Hole Flows," ASME Paper No. GT2006-90375.

[27] Wright, L. M., Blake, S., and Han, J. C., 2006, "Effectiveness Distributions on Turbine Blade Cascade Platforms Through Simulated Stator-Rotor Seals," AIAA Paper No. AIAA-2006-3402.

[28] Wright, L. M., Blake, S., Rhee, D. H., and Han, J. C., 2007, "Effect of Upstream Wake With Vortex on Turbine Blade Platform Film Cooling With Simulated Stator-Rotor Purge Flow," ASME Paper No. GT2007-27092.

[29] Gao, Z., Narzary, D., Mhetras, S., and Han, J. C., 2007, "Upstream Vortex Effect on Turbine Blade Platform Film Cooling With Typical Stator-Rotor Purge Flow," ASME Paper No. IMECE2007-41717.

[30] Suryanarayanan, A., Ozturk, B., Schobeiri, M. T., and Han, J. C., 2007, "Film Cooling Effectiveness on a Rotating Turbine Platform Using Pressure Sensitive Paint Technique," ASME Paper No. GT2007-27122.

[31] Nicklas, M., 2001, "Film-Cooled Turbine Endwall in a Transonic Flow Field: Part II—Heat Transfer and Film Cooling Effectiveness," *ASME J. Turbomach.*, **123**, pp. 720–729.

[32] Wright, L. M., Blake, S., and Han, J. C., 2006, "Film Cooling Effectiveness Distributions on a Turbine Blade Cascade Platform With Stator-Rotor Purge and Discrete Film Holes Flows," ASME Paper No. IMECE2006-15092.

[33] Suryanarayanan, A., Mhetras, S. P., Schobeiri, M. T., and Han, J. C., 2006, "Film Cooling Effectiveness on a Rotating Blade Platform," ASME Paper No. GT2006-90034.

[34] Coleman, H. W., and Steele, W. G., 1989, *Experimentation and Uncertainty Analysis for Engineers*, Wiley, New York.

Heat Transfer Coefficients of Film Cooling on a Rotating Turbine Blade Model—Part I: Effect of Blowing Ratio

Zhi Tao

Zhenming Zhao

Shuiting Ding

Guoqiang Xu

Bin Yang

Hongwei Wu

Department of Engineering Thermophysics,
and National Key Laboratory on Aero-Engines,
School of Jet Propulsion,
Beihang University,
Beijing 100083, P. R. China

Experimental investigations were performed to measure the local heat transfer coefficient (h_g) distributions of film cooling over a flat blade under both stationary and rotating conditions. Film cooling was via a straight circular hole of 4 mm in diameter located in the middle section of the blade angled 30 deg along the streamwise direction and 90 deg along the spanwise direction. The Reynolds (Re_D) number based on the mainstream velocity and the film hole diameter was fixed at 3191, and the rotating speed (ω) was either 0 rpm or 800 rpm; the film cooling blowing ratios ranged from 0.4 to 2.0, and two averaged density ratios of 1.02 and 1.53 were employed with air and carbon dioxide (CO_2) as the coolant, respectively. Thermochromic liquid crystal was used to measure the solid surface temperature distributions. Experimental results showed the following: (1) In the stationary case, the blowing ratio has a significant influence on the nondimensional heat transfer coefficient (h_g/h_0) especially in the near hole region. (2) The film trajectory in rotation had an obvious deflection in the spanwise direction, and the deflection angles on the suction surface are larger than those on the pressure surface. This was attributed to the combined action of the Coriolis force and centrifugal force. (3) In the rotating case, for CO_2 injection, the magnitude of heat transfer coefficient on the pressure surface is reduced compared with the stationary case, and the blowing ratio has smaller effects on h_g/h_0 distribution. However, on the suction surface, the heat transfer coefficient at $x/D < 1.0$ is enhanced and then rapidly reduced to be also below the stationary values. For air injection, rotation also depresses the h_g/h_0 for both the pressure and the suction surface. (4) The density ratio shows a considerable effect on the streamwise heat transfer coefficient distributions especially for the rotating cases. [DOI: 10.1115/1.3068329]

1 Introduction

For modern gas turbine engines, the turbine inlet temperatures may be much higher than the melting temperatures of the blade materials. Therefore, various cooling methods are used on the turbine blades to keep the working temperature within a safety limit. Among the cooling techniques, film cooling is widely used to protect the turbine blades from hot gas thermal deterioration. In the case of film cooling, the coolant is injected from the discrete holes into the mainstream boundary layer and generates a thin coolant film acting as a buffer to reduce the thermal loads. Film cooling performance is usually characterized by two parameters, the adiabatic film cooling effectiveness and the heat transfer coefficient. To better understand the physical mechanism and to optimize the design of film cooling, a considerable number of studies have been conducted during the past 4 decades. A comprehensive compilation of the available results was summarized by Han et al. [1]. A brief review of relevant experimental works is given below for easy reference.

In the earlier studies, Eriksen and Goldstein [2] indicated that the heat transfer coefficient with film cooling was lower than that without injection because the cooling air thickened the boundary layer. However, this conclusion seemed only to prevail in the cases of low blowing ratios. Later, Hay et al. [3] pointed out that there was an enhance trend of h_f/h_0 with the increase in blow-

ing ratio so that a maximum value of h_f/h_0 reached around $M = 1.35$ for the case with an inclination angle of 35 deg.

Lloyd and Brown [4] reported that the short injection holes could give rise to greater heat transfer coefficients than the longer ones, and this conclusion was confirmed by Andrews et al. [5]. Makki and Jakubowski [6] investigated the downstream heat transfer results for film holes, which had the trapezoidal cross sections diffused in the direction of the mainstream flow. Hyams and Leylek [7] reported that the heat transfer coefficients for a film hole with a laterally diffused exit, a hole with a forward diffused exit, and a standard cylindrical hole were slightly elevated for the cases of $M=1.25$ and $DR=1.6$ as compared with that without injection. The highest heat transfer coefficients were found downstream of the laterally expanded hole, and nearly the same distributions were found downstream of the cylindrical and forward expanded holes.

Among the film cooling researches in publication, the thermochromic liquid crystal (TLC) technique was widely used. Ekkad et al. [8] investigated the effect of mainstream turbulence on the detailed distributions of adiabatic effectiveness and heat transfer coefficient on a cylindrical leading edge model using a transient liquid crystal image method. They found that the heat transfer coefficients increased with the augmentation of blowing ratio, but the adiabatic effectiveness reached a peak value at $M=0.4$.

Ou and Rivir [9] employed a transient liquid crystal image technique to obtain the film cooling effectiveness and heat transfer coefficient distributions on a large scale symmetric circular leading edge with three rows of film holes. Yu et al. [10] conducted an experimental study focusing on the effects of diffusion hole geometry on overall film cooling performance with the blowing ra-

Contributed by the Turbomachinery Division of ASME for publication in the JOURNAL OF TURBOMACHINERY. Manuscript received August 18, 2008; final manuscript received August 29, 2008; published online July 1, 2009. Review conducted by David Wisler. Paper presented at the ASME Power 2008 (Power2008), Orlando, FL, July 22–24, 2008.

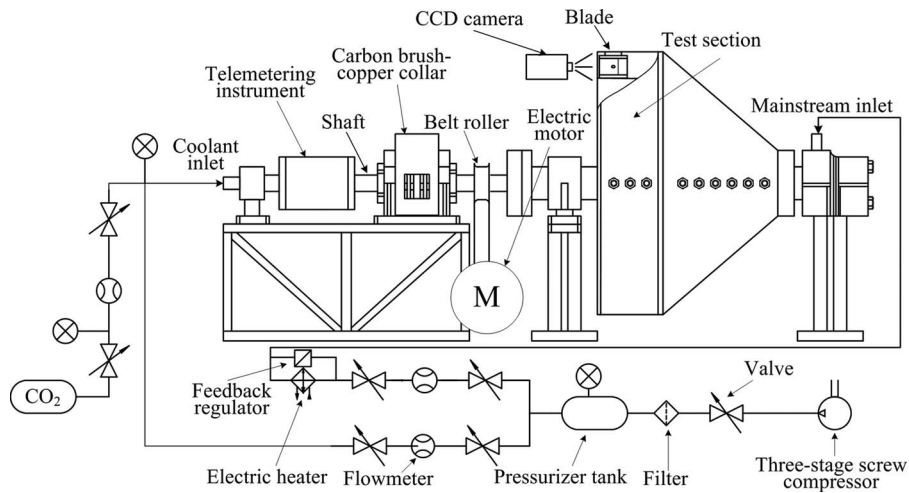


Fig. 1 Schematic view of the test rig

tios of 0.5 and 1.0. By using the transient liquid crystal technique, the local distributions of both adiabatic effectiveness (η) and heat transfer coefficient (h_f) were measured. They found that the film hole with combined forward and lateral diffusion produced a significant increase in η and decrease in h_f as compared with the straight circular hole with 30 deg inclination angle. Yuen and Martinez-Botas [11] performed an experimental study to measure the heat transfer coefficient (h_f) for single jets with streamwise angles of 30 deg, 60 deg, and 90 deg with a short but engine representative hole length ($L/D=4$). As a further study, Yuen and Martinez-Botas [12] reported the heat transfer characteristics for a row of round holes, which were measured on the same experimental equipment. In their experimental works, the TLC technique was also employed to obtain the heat transfer distributions.

Although extensive research has been carried out on various aspects of film cooling, little work was available in the open literature about the experimental study of the rotation effects, and this may be due to the great difficulties associated with the experiments. Abhari and Epstein [13] gave their effort to the studies of the time-resolved heat transfer for cooled and uncooled rotors by thin heat flux gauges. Their findings showed that the film cooling reduced the time-averaged heat transfer compared with the uncooled rotor on the blade suction surface by as much as 60% but had relatively little effect on the pressure surface.

The present research aims to experimentally investigate the effects of rotation to film cooling at different blowing ratios with a rotating heat transfer test rig, and to the best of the authors' knowledge, no similar work exists in the open literature. As the start of

a series of research work, a blade with a simple flat test surface with a cylindrical film hole was employed to eliminate the influences of film hole geometry, curvature, etc. The wideband thermochromic liquid crystal technique was used in the rotating experiment to measure the film-cooled surface temperature.

2 Experimental Apparatus and Procedure

2.1 Test Rig. Experiments were carried out in the rotating heat transfer test rig at the National Key Laboratory on Aero-Engines, Beihang University, China. A schematic of the test rig is shown in Fig. 1, and it consists of four parts: the air supply system, the telemetering data acquisition system, the rotating test section, and a 30 kW electric motor for power. For the air supply system, the air was delivered by a three-stage screw compressor and then led to a pressurized tank. The mainstream air and the coolant were extracted from the tank independently. The mass flux of the mainstream was controlled by valves and measured by a thermal flowmeter, and just before the mainstream inlet, a 30 kW electric heater with a feedback regulator was installed, enabling a maximum temperature of 333.15 K at the maximum mass flow rate of 0.2 kg/s. The cooling air from the pressurized tank was controlled by valves and measured by a suspended body flowmeter. In the experiment, the CO₂ was also used as the coolant to provide a different density ratio. On the test rig a telemetering instrument was installed to transfer measuring temperature signals between the rotating frame and the stationary. A carbon brush-copper collar was fixed to conduct the current from the

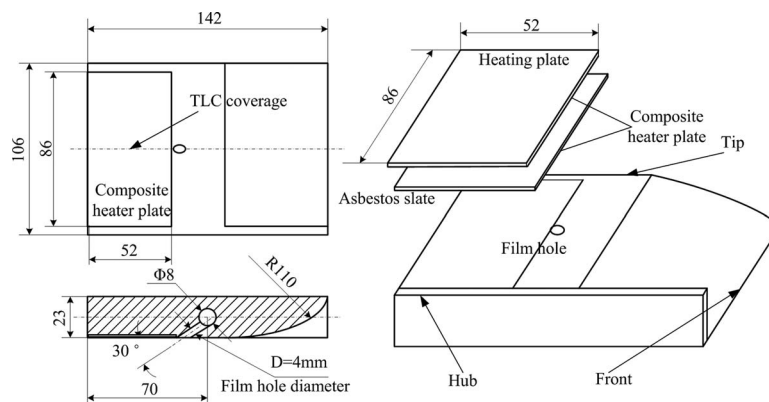


Fig. 2 Configuration of the flat blade

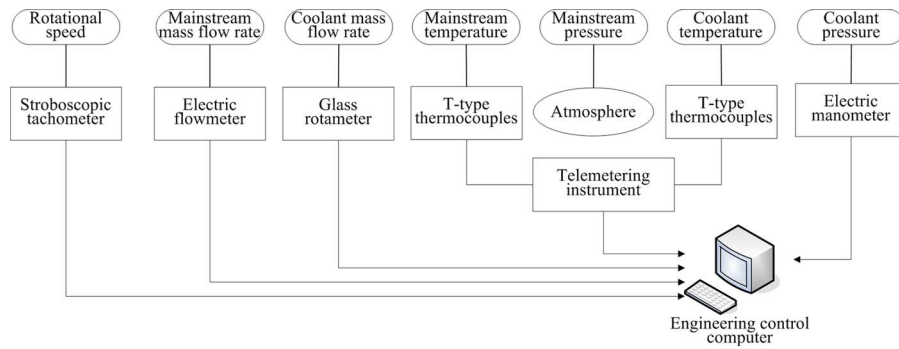


Fig. 3 Schematic of the data acquisition system

electric power into the heating plate. The test section was conical, and the flat blade was placed along the radial direction (see Fig. 1). The rotating section was driven by a 30 kW electric motor to reach the operating rotating speed.

2.2 Flat Blade. Figure 2 illustrates the configuration of the flat blade for the current study. The blade was made of Bakelite, which had better thermal resistance and insulation characteristics. The thermal conductivity was $k=0.28$ W/m K. The front section of the blade is a circular arc to simulate the flow over the blade tip. The test region on the blade was flat with a cylindrical film hole on it. The hole had a diameter of $D=4$ mm and a length-to-diameter ratio of $L/D=5.75$. It was located in the middle of the blade angled 30 deg along the streamwise direction and 90 deg along the spanwise direction. The rotational radius of the film hole was 450 mm. Since the test section was flat, which was different from the real turbine blade, the pressure surface and suction surface in this study were obtained by means of setting opposite rotating directions of the test rig. A two layer composite heating plate, which was 86 mm wide \times 52 mm long \times 3 mm thick, was adhered immediately downstream of the injection hole to facilitate the investigations of heat transfer coefficient. The upper layer of the plate was a heating sheet made of a special plastic. The carbonous slurry was sprayed homogeneously on the plastic to ensure a uniform heat flux distribution. Two sheets of conductive silver paste were brushed on both ends of the heating plate as the electrodes. The heating plate was powered by a direct current supply. An asbestine sheet with good insulation characteristic was underneath the heating sheet, and it had a thermal conductivity of $k=0.08$ W/m K. To measure the temperature distributions over the heating plate, the wideband thermochromic liquid crystal was sprayed onto the heating plate, and it had a color-changing temperature ranging from 30°C to 60°C.

2.3 Data Acquisition System. Figure 3 shows the data acquisition system for the present study. A stroboscopic tachometer was used to measure the rotating speed. The mass flow rates of mainstream and coolant were recorded, respectively, by means of an electric flowmeter and a suspended body flowmeter. Two T-type (copper-constantan) thermocouples were located upstream of the blade to measure the mainstream temperature. Prior to the experiment, the thermocouples were calibrated in a constant thermal bath with a precise platinum resistance thermometer. The coolant temperature was measured by a T-type thermocouple at the injection hole entrance of the blade chamber, and its pressure was obtained from an electric manometer. The mainstream and coolant temperatures measured by the thermocouples were transmitted through the telemetering instrument to the stationary receiver. All the signals measured by the thermocouples and the electric flowmeter were finally transferred to a computer for data acquisition. The temperature distributions on the test surface were obtained by using TLC. And a stationary charge coupled device (CCD) camera was used to capture the TLC images. The camera had a built-in

flash and was fixed in front of the test section without rotating, as shown in Fig. 1. In order to capture the images accurately, a synchronous control system was used to trigger the camera and the flash at the right moment.

2.4 Thermochromic Liquid Crystal Calibration. The steady-state hue capturing technique was adopted in the present study. To reveal the relationship between the hue values of the color image and the temperatures, a calibration experiment was performed on the actual test surface without the cooling film injection. Considering the working range of the TLC, the surface temperatures were maintained from 35°C to 60°C with a 1°C increase each step in the calibration experiment, and four calibrated K-type thermocouples with an accuracy of ± 0.33 °C were mounted on the test surface to measure the temperatures. During the calibration experiment, when the surface temperature and color were stabilized, the image of the TLC was captured by a CCD camera and the corresponding temperatures measured by the thermocouples were recorded by an Adam4018 module. After the calibration experiment, the images captured by the CCD camera were converted from RGB to HSI format, and the corresponding averaged temperatures were calculated from the four thermocouples. Figure 4 illustrates the fitted polynomial curve of the hue-temperature calibration, and a polynomial to the power of 10 was used.

2.5 Operating Conditions and Experimental Uncertainties. A complete set of the operating conditions in the present study is given in Table 1. The measured mass flow rates were varied from 300 kg/h to 700 kg/h for mainstream and from 0 m³/h to 1 m³/h for the coolant. A honeycombed section was installed in front of the test blade to straighten the flow and deliver an adequately uniform flow field. At the coolant inlet, the hole

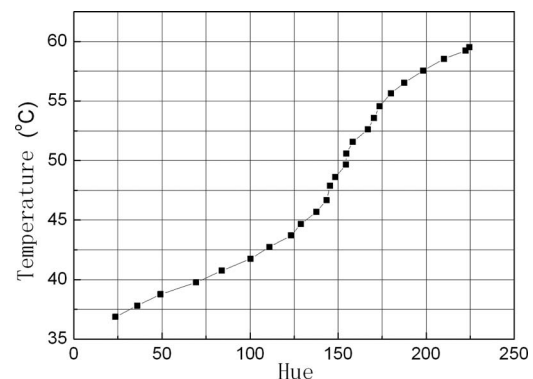


Fig. 4 Hue-temperature calibration curve for thermochromic liquid crystal

Table 1 Operating conditions

Mainstream temperature	313.15–315.15 K
Coolant temperature	306.15–307.15 K
Reynolds number Re_D	3191
Rotation number Rt	0, 0.0249 (800 rpm)
Blowing ratio M	0.4–2.0
Density ratio DR	1.01–1.03 (air), 1.52–1.54 (CO ₂)

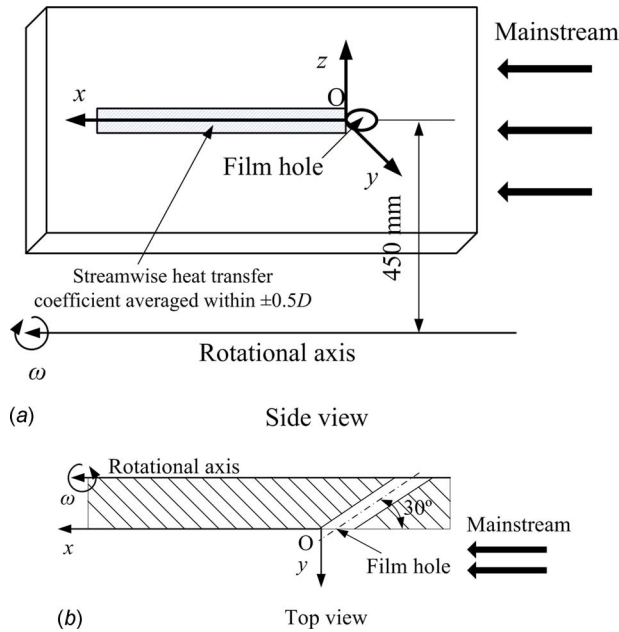


Fig. 5 Coordinate system

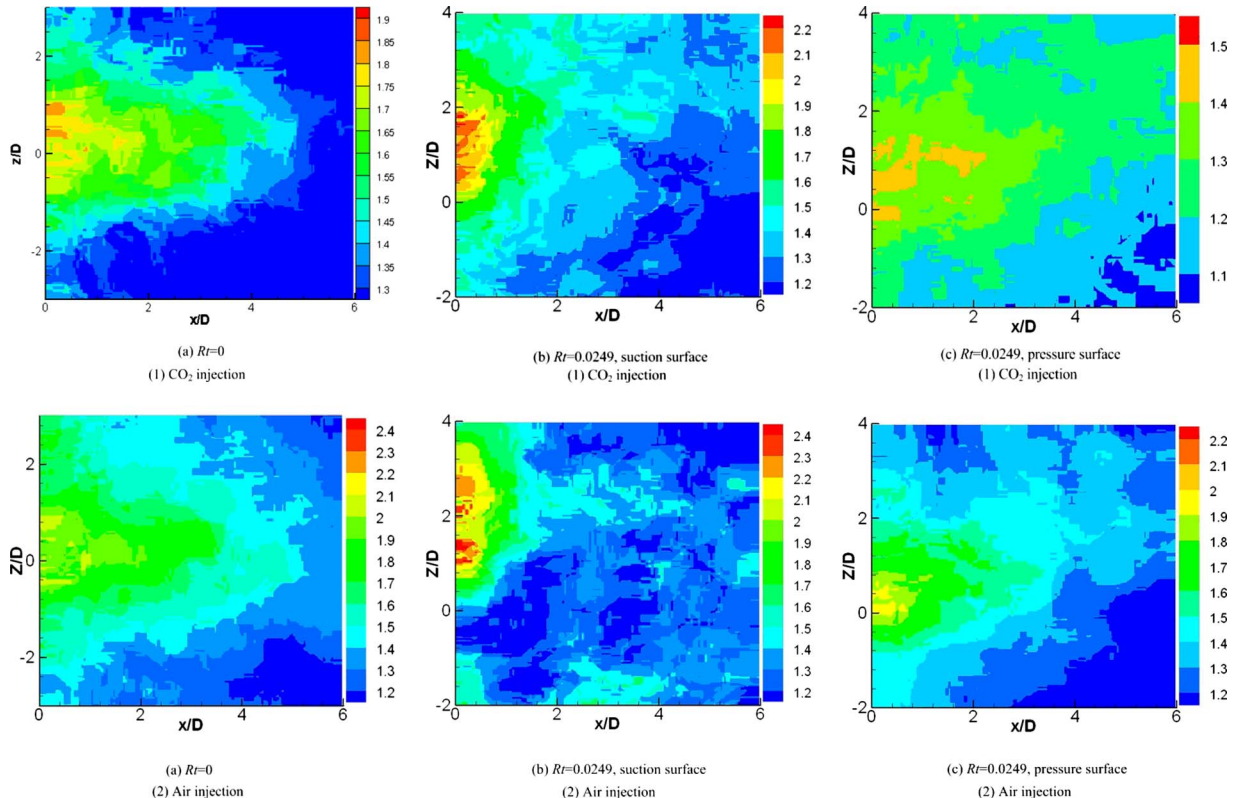


Fig. 6 Distributions of nondimensional heat transfer coefficient h_g/h_0 with rotating effect, $M=1.0$

length was $5.75D$, which would be long enough for the cooling air to be fully developed. In the experiment, the rotating speed is either 0 rpm or 800 rpm.

Following the method of Kline and McClintock [14], the maximum experimental uncertainty of the dimensionless heat transfer coefficient h_g/h_0 is $\pm 10.8\%$.

3 Results and Discussion

Figure 5 illustrates the coordinate system employed in the present study. The x -axis is along the mainstream direction, the y -axis is normal to the test surface, and the z -axis conforms to the right-hand law. The origin is located at the downstream tip of the film hole.

3.1 Contour Plots. Figures 6–9 show the contours of the nondimensional heat transfer coefficient h_g/h_0 with CO₂ and air injection. The particular cases shown here are $Rt=0$ and 0.0249 and $M=0.6, 1.0, \text{ and } 1.6$.

3.1.1 Rotating Effects. Figure 6 reveals the rotating effects on the distributions of the nondimensional heat transfer coefficient h_g/h_0 for both CO₂ and air injection with a constant blowing ratio of $M=1.0$. Figure 6(1) clearly shows the effects of rotation when we compare the stationary case of Fig. 6(1)(a) with the rotating cases of Fig. 6(1)(b) and Fig. 6(1)(c), and a significant deflection of coolant trajectory could be observed under rotation. Under rotating condition, the flow characteristic of coolant is governed by three additional forces, i.e., the centrifugal force, the Coriolis force, and the buoyancy force. The buoyancy force, however, can be neglected in the present study due to the small temperature difference between the mainstream and coolant. The main influencing factors are the centrifugal and the Coriolis forces, and they will push the coolant in the spanwise direction and lead to asymmetry of the flow downstream and cause the different characteristics of the heat transfer process.

In Fig. 6(1)(b) and Fig. 6(1)(c), it could be concluded that at the

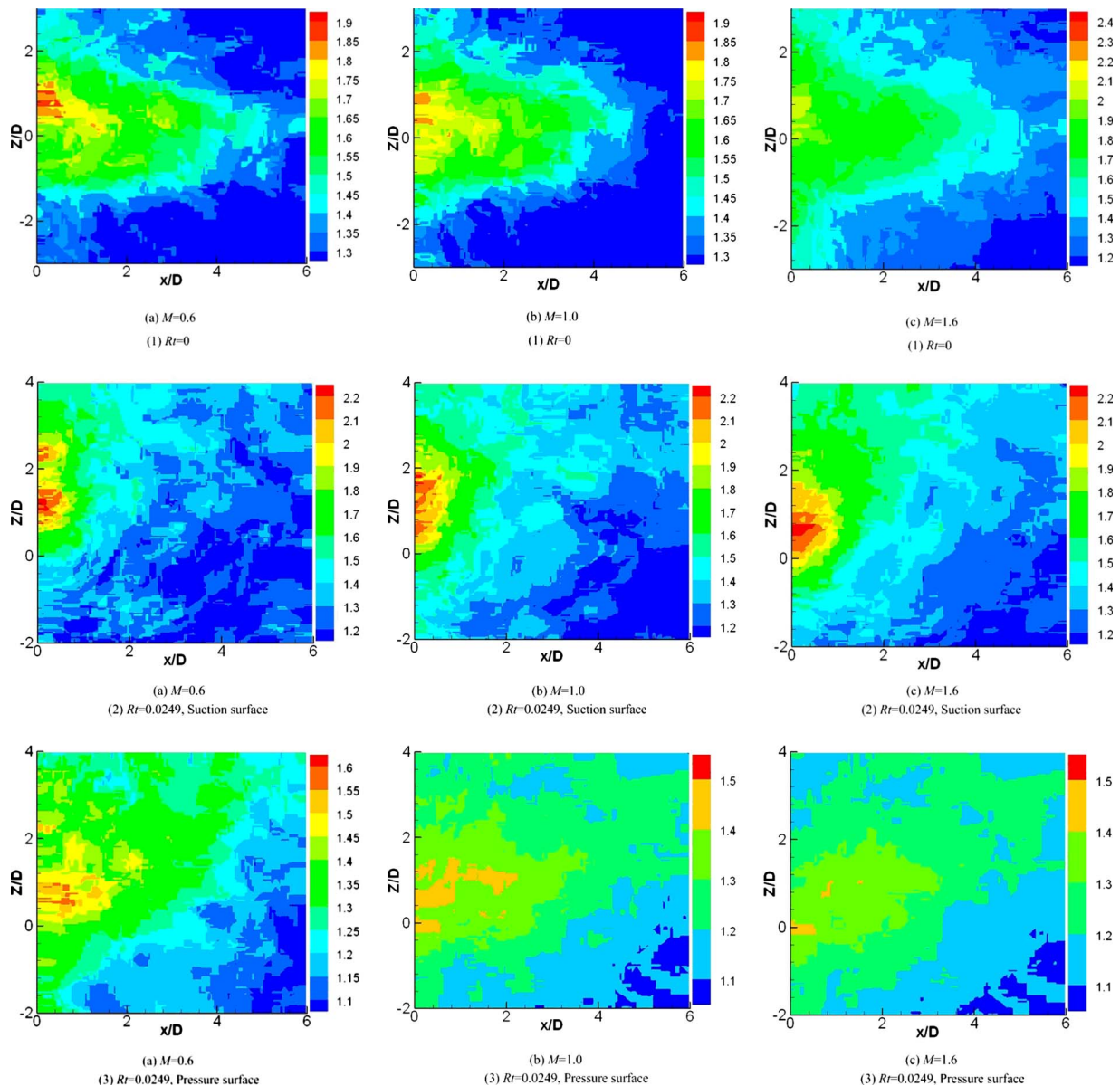


Fig. 7 Distributions of nondimensional heat transfer coefficient h_g/h_0 with blowing ratio effect for CO_2 injection

same blowing ratio the deflection on the suction surface is more evident than that on the pressure surface. This is mainly due to the action of the Coriolis force. It is well known that on the suction surface both the centrifugal force and the Coriolis force point to the high-radius location. However, on the pressure surface, the Coriolis force points to the low radius, which is opposite to the centrifugal force. Therefore, the Coriolis force tends to weaken the deflection of the film trajectory on the pressure surface but to strengthen it on the suction surface. Similar conclusions could also be found in Fig. 6(2), which shows the contours of h_g/h_0 with air injection at $Rt=0$ and 0.0249.

3.1.2 Blowing Ratio Effects. In the experiment, the effects of the coolant to mainstream flux ratio on film cooling performance were investigated, and the blowing ratios used are 0.6, 1.0, and 1.6. Figure 7 shows the h_g/h_0 contours with CO_2 as the coolant. From this figure it can be seen that in the stationary case (see Fig. 7(1)) the blowing ratio performs negligible influence on the distributions of h_g/h_0 . However, the obvious variations in h_g/h_0 only occurs near the hole region, that is, $x/D=0-2$, as the blowing

ratio varies. In the rotating case of $Rt=0.0249$, shown in Fig. 7(2) and Fig. 7(3), with the increase in blowing ratio the deflection angle of film trajectory on the suction surface has no obvious change. However, on the pressure surface, the deflection angle of coolant decreases a little. This might be because the Coriolis force is enhanced with the increase in blowing ratio, which could reduce the coolant deflection on the pressure surface.

Figure 8 shows the contours of the blowing ratio effect on h_g/h_0 with air injection, and they presented similar characteristics, as shown above for the CO_2 case.

3.1.3 Density Ratio Effects. Figure 9 shows the contours of h_g/h_0 with different coolants at $Rt=0$ and 0.0249. The blowing ratio is maintained at $M=1.0$. From the contours in Fig. 9 we could find that, in the stationary case, the influence of density ratio on heat transfer coefficient distributions is unobvious at the same blowing ratio. However, the h_g/h_0 values are changed with the variation in density ratio, especially on the pressure surface at $Rt=0.0249$ shown in Fig. 9(3)(a) and Fig. 9(3)(b). This indicates

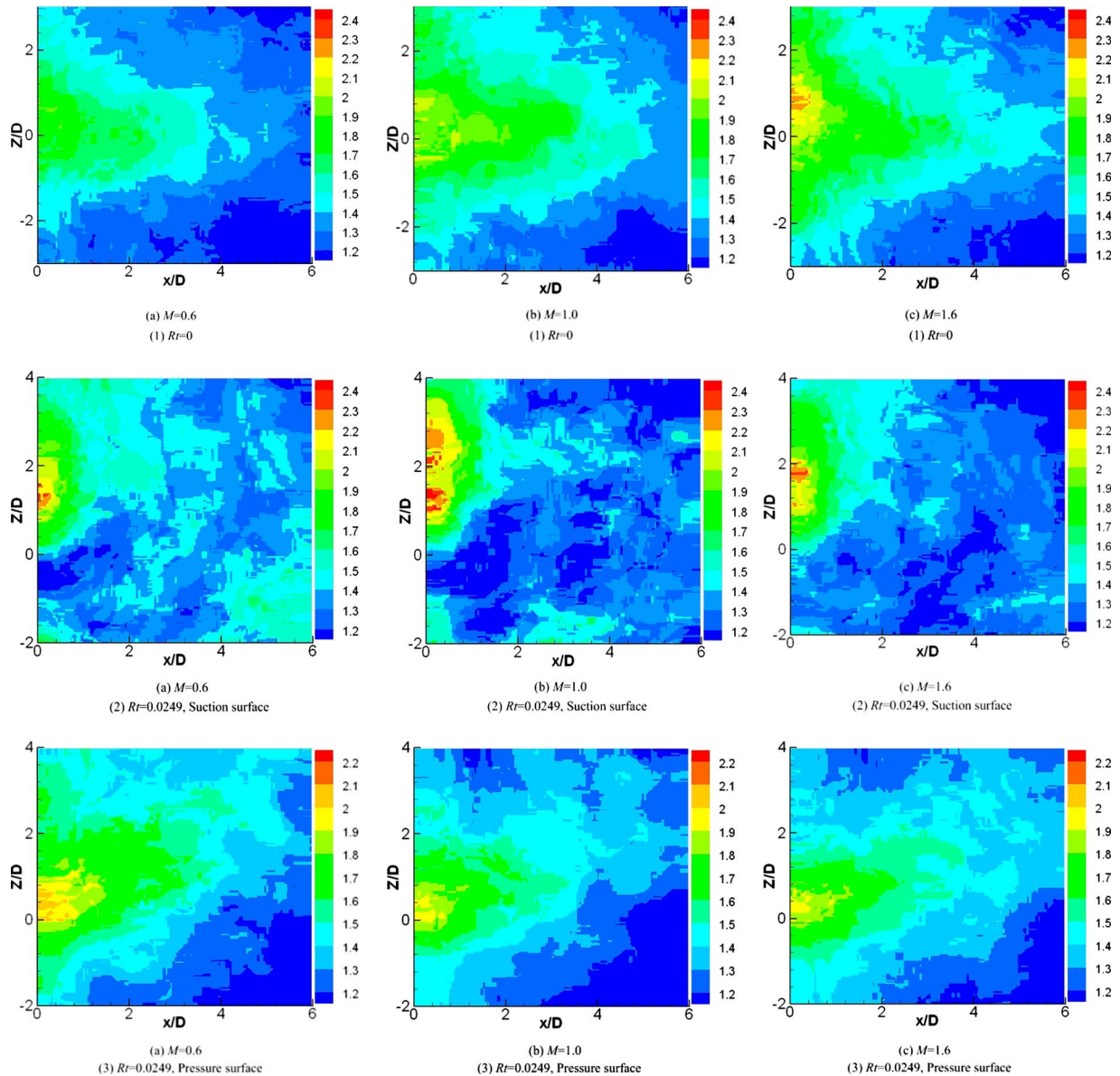


Fig. 8 Distributions of nondimensional heat transfer coefficient h_g/h_0 with blowing ratio effect for air injection

that the density ratio does not provide a significant influence on the film trajectory but performs an evident effect on the h_g/h_0 values.

3.2 Nondimensional Streamwise Heat Transfer Coefficient. Figure 10 presents the profiles of nondimensional streamwise heat transfer coefficients for the stationary cases. Local heat transfer coefficients are averaged over $\pm 0.5D$ in spanwise and plotted against the normalized axial distance x/D . The blowing ratio varies from 0.4 to 2.0, varying with a step of 0.2, and the cooling air used here are CO_2 and air. Figure 10(a) presents the results of h_g/h_0 with CO_2 injection.

In Fig. 10(a), it can be seen that the overall trend of h_g/h_0 versus x/D is that it decreases with increasing dimensionless axial distance from the jet hole, and this is mainly due to the gradual dissipation of the coolant jet along its path. The exceptions are for the low blowing ratio cases for $M \leq 0.8$ where the heat transfer coefficient experiences a region of increase right after the hole. This may be due to the cooling film flow transition from laminar to turbulent. For low blowing ratio cases, the cooling jet remains

attached to the surface, and the interaction with the mainstream rapidly leads the film into a state of transition. The region of heat transfer coefficient increase corresponds to the region of flow transition.

Figure 10(a) also shows that the heat transfer coefficient is enhanced by the blowing ratio because of the increase in turbulence caused by the coolant jet-mainstream interaction. This is typical and is in agreement with all earlier studies [3,8]. However, an interesting point is that h_g/h_0 does not increase monotonously with the blowing ratio, and there is a maximum at $M=1.4$ for our tests. Below this value, the heat transfer coefficient increases with the increase in blowing ratio, while, above this blow ratio, the heat transfer coefficient starts to decrease with blow ratio increase. We consider this phenomenon as the result of jet detachment from the wall, and the distribution curves indeed show that there are jet reattachments at around $x/D=1.5-2.0$.

Figure 10(b) is the case with air as the coolant. It is clear from this figure that the trends of h_g/h_0 versus x/D are quite similar to CO_2 , but the air has a higher heat transfer coefficient. This is due to the fact that air is lighter, and so it has a greater momentum

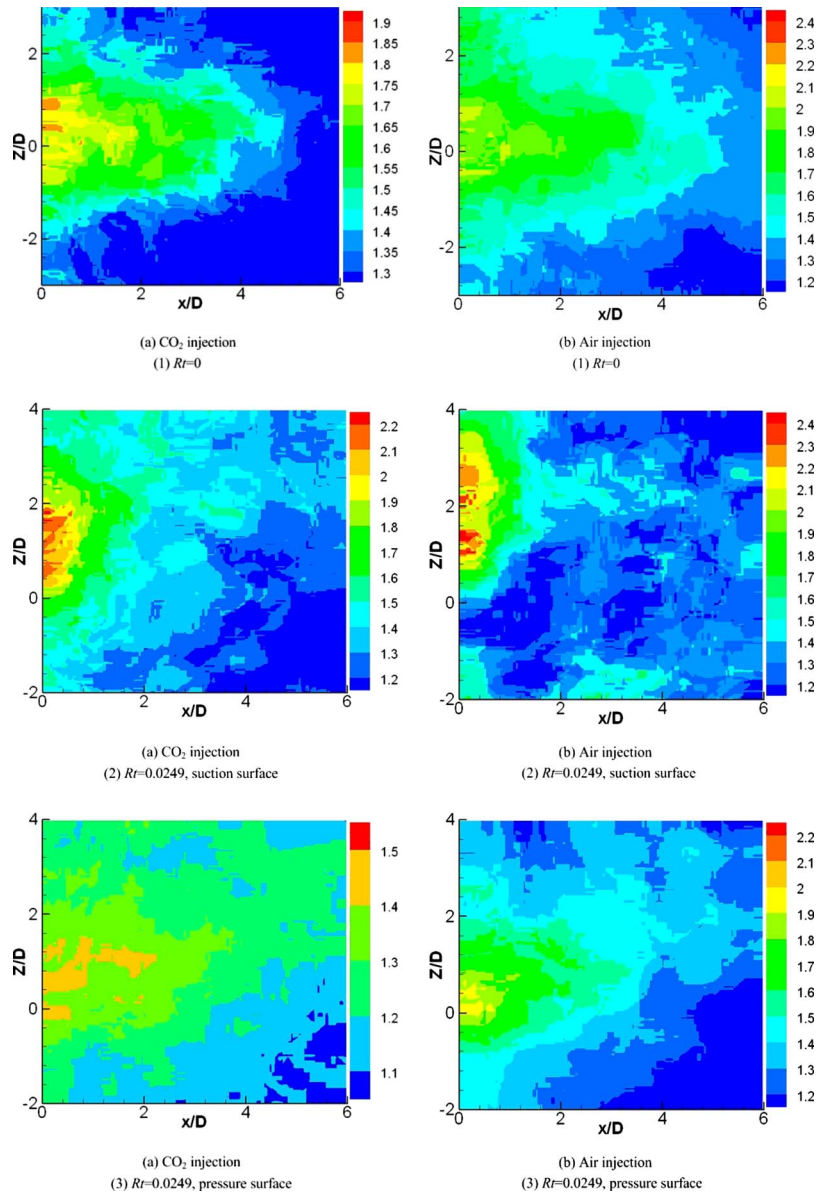


Fig. 9 Distributions of nondimensional heat transfer coefficient h_g/h_0 with density ratio effect, $M=1.0$

under the same blowing ratio and thus results in higher heat transfer coefficients [15]. Figure 10(b) also indicates that the heat transfer coefficient versus blowing ratio is much more complex for air than for CO₂.

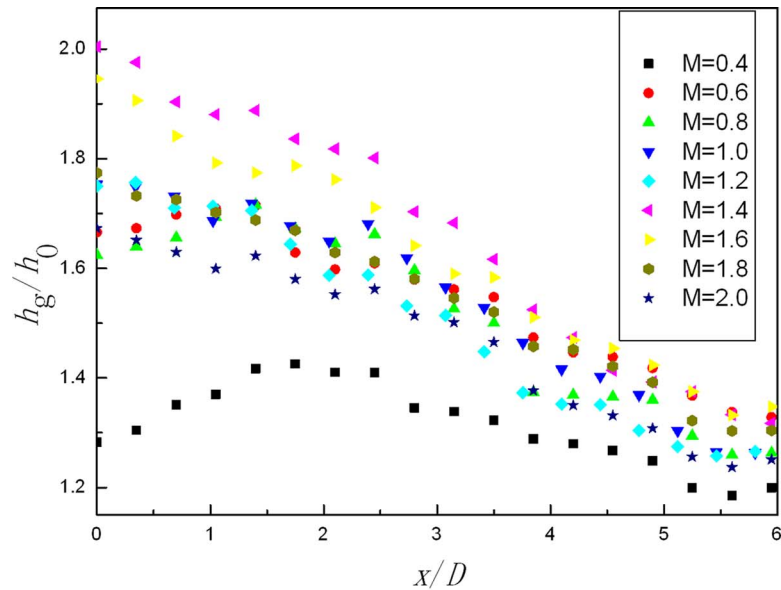
For CO₂, $M=1.4$ is the blowing ratio where heat transfer coefficient reaches its maximum. For air, the h_g/h_0 versus the blow ratio has several extrema instead of only one maximum for CO₂.

Figure 11 shows the profiles of nondimensional streamwise heat transfer coefficient versus x/D under rotation. Similarly, Fig. 11(a) is for CO₂ and Fig. 11(b) is for air, and the rotation number $Rt=0.0249$ for all the tests.

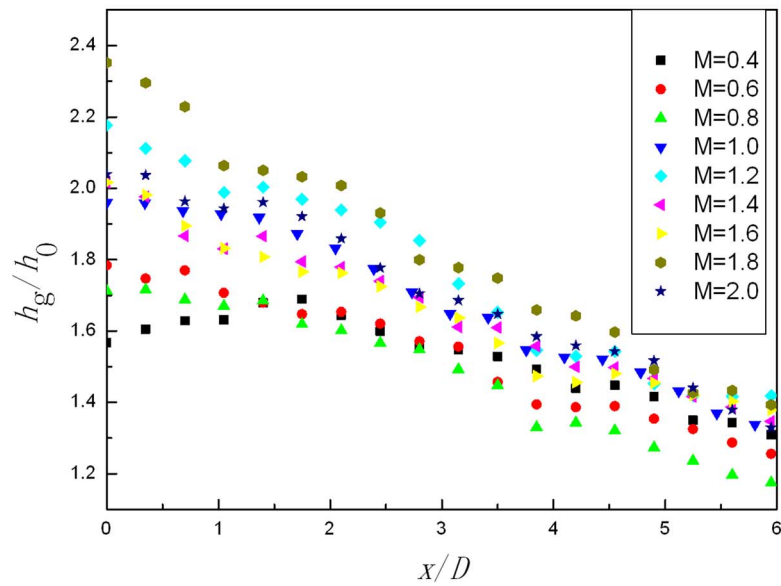
Compared with Fig. 10(a), Fig. 11(a) shows a significant change in heat transfer coefficient due to rotation, especially for the suction surface. On the pressure surface, we see that the magnitude of heat transfer coefficient is reduced compared with the stationary case. The dimensionless heat transfer coefficient varies from 1.1 to 1.4 for the pressure surface and its stationary counterpart from 1.2 to 2.0. Another change for pressure surface is that the blowing ratio has smaller effects on heat transfer coefficient,

and all the distribution curves tend to overlap.

The suction surface experiences a dramatic change, as we would have expected due to the combined action imposed by the centrifugal force and the Coriolis force. The heat transfer coefficient for the very near hole region at $x/D < 1.0$ is enhanced especially for high blowing ratios; for example, there is a 20% increase for blowing ratio $M=1.8$ at the hole edge. However, this enhancement is rapidly reduced, and the heat transfer coefficients are all below the stationary results for the rest of the surfaces for all blowing ratios. As mentioned above, both the Coriolis force and the centrifugal force on the suction surface are pointed to the high-radius direction, and this leads to a great deflection of coolant, and thus we would have expected higher heat transfer coefficient due to stronger interaction between mainstream and the cooling jet. Why only enhanced over the near hole region? Re-examining our data processing method, we speculate that this may be because we have chosen a too narrow region for data averaging. For each x/D location, we only chose $\pm 0.5D$ in spanwise for heat transfer coefficient averaging. This is reasonable for the sta-



(a) CO₂ injection



(b) Air injection

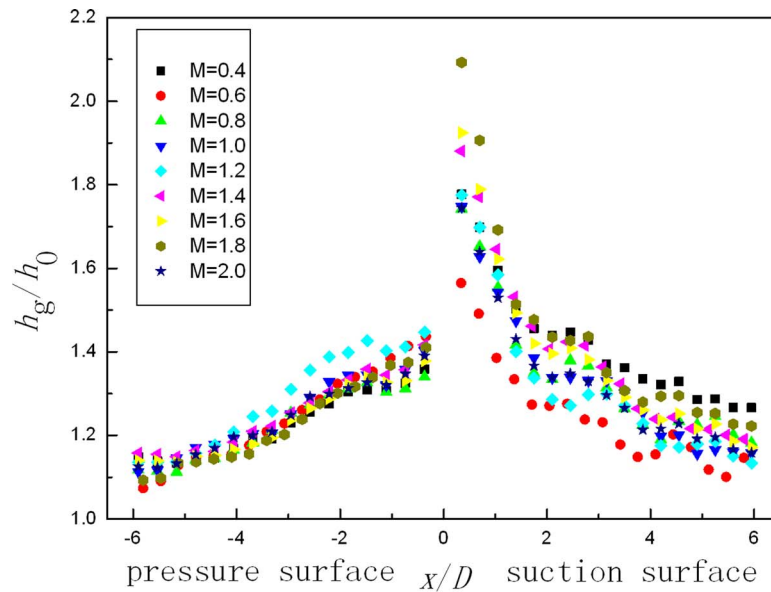
Fig. 10 Nondimensional streamwise heat transfer coefficient versus x/D for air and CO₂ injection at $Rt=0$ and different M

tionary analysis, but when it is under strong rotation, the film may be outside this averaging area and may leave much undervalued heat transfer ability. We may have to choose a much larger area for averaging for film cooling under rotation, and this area may have to be oblique to the mainstream.

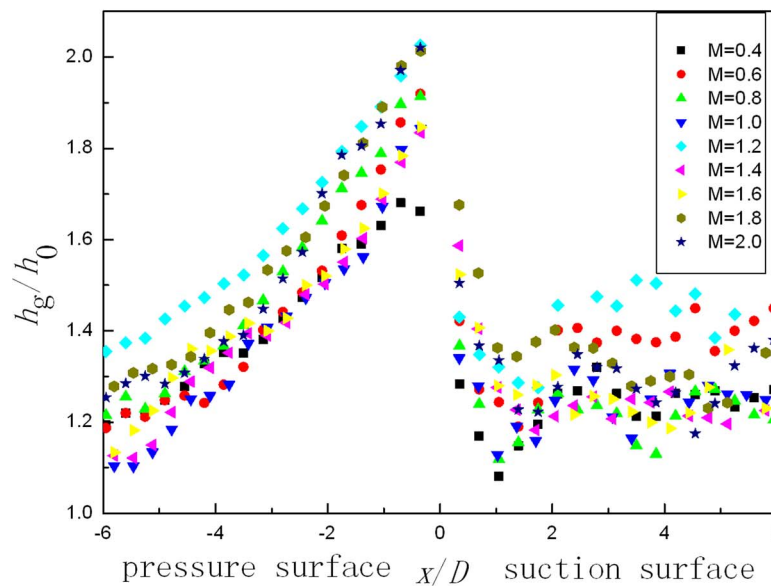
Figure 11(b) presents the measured values of h_g/h_0 with the air injection. On the pressure surface, as shown in this figure, the values of h_g/h_0 are again depressed than the stationary results, as we have seen for the CO₂. On the suction surface, the magnitudes of heat transfer coefficients are also reduced compared with their stationary counterparts. The h_g/h_0 decreases rapidly for the first 1D downstream from the film hole, then increases gradually in the region of $x/D=1-3$, and finally levels off at far downstream. This reduction may also be caused by the too narrow averaging area we chose for data processing, as mentioned above for the CO₂ case.

3.3 Blowing Ratio Effects at Different Streamwise Locations. Figures 12 and 13 present the distributions of nondimensional streamwise heat transfer coefficient versus blowing ratios at different streamwise locations for stationary and rotating cases, respectively. In these figures, six different streamwise locations ranging from $x/D=0-5$ were chosen.

Figure 12 shows the distributions of h_g/h_0 at $Rt=0$. In Fig. 12(a) we could find that the h_g/h_0 with CO₂ injection increases first and then decreases as the blowing ratio varies from 0.4 to 2.0. The maximum value of h_g/h_0 corresponds to $M=1.4$ for all six streamwise locations. However, the trend of h_g/h_0 with air injection is more complicated, and two evident peak values at $M=1.2$ and 1.8 can be found in Fig. 12(b). This might be because the decrease in density ratio with air injection enhances the turbulence mixing between the mainstream and coolant, which leads to



(a) CO_2 injection



(b) Air injection

Fig. 11 Nondimensional streamwise heat transfer coefficient versus x/D for air and CO_2 injection at $Rt=0.0249$ and different values of M

an earlier transition. From Fig. 12, it can also be concluded that the blowing ratios only give great influences on h_g/h_0 or a region not far from the hole with $x/D < 3$.

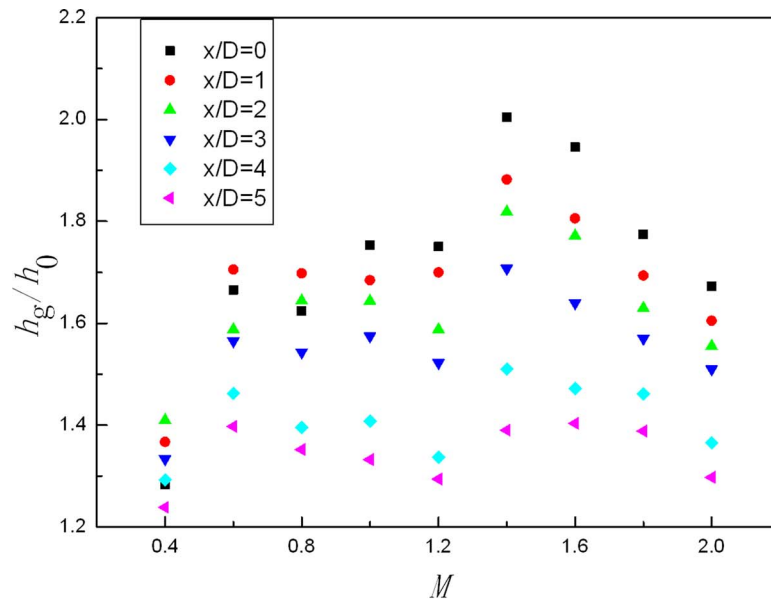
Figure 13 presents the profiles of h_g/h_0 versus blowing ratios at different streamwise locations for the rotating cases. The results show that for the CO_2 injection with the increase in blowing ratio, the values of h_g/h_0 increase continuously for the near hole region with $x/D \leq 1$ on the suction surface; however, on the pressure surface the blowing ratio has little influence, as shown in Fig. 13(a). Figure 13(b) shows the blowing ratio effects for air injection under rotation. On the pressure surface, the blowing ratio has evident influences on h_g/h_0 at all the six streamwise locations, and the values are fluctuant with the increase in blowing ratios. However, on the suction surface, the heat transfer coefficients increase slightly with the variation in M values from 0.4 to 2.0 for the first $2D$. However, we have to bear in mind that our data

processing method may have chosen a too narrow area for data averaging, and we may not have revealed the true picture of variation.

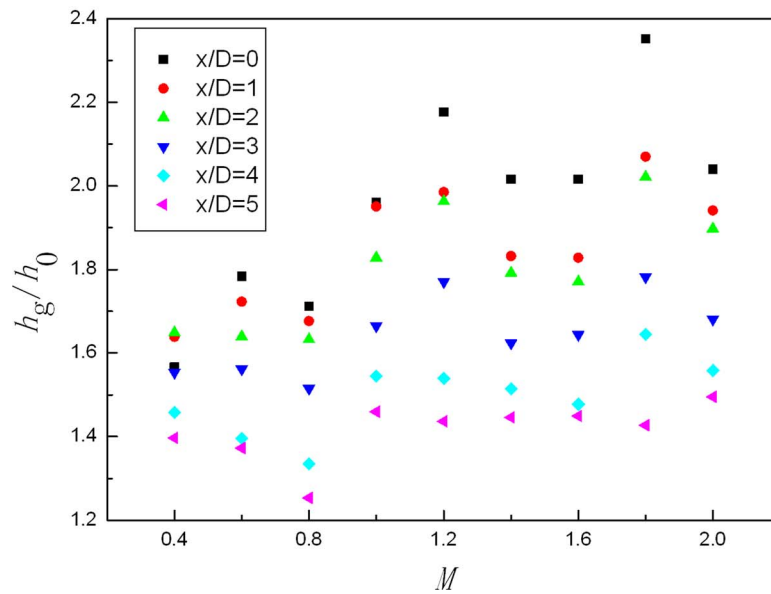
4 Conclusions

The present experimental study was conducted to investigate the distribution of heat transfer coefficient for a film-cooled blade under rotation. The test section is flat with a straight circular hole angled 30 deg along the streamwise direction. The TLC technique was used as it reveals a detailed temperature field. The blowing ratios vary from 0.4 to 2.0, and air and CO_2 were used as the coolant to investigate the effects of the density ratio. We may draw the following conclusions.

1. For the stationary cases, the blowing ratio has a significant influence on the convection heat transfer, especially in the



(a) CO₂ injection



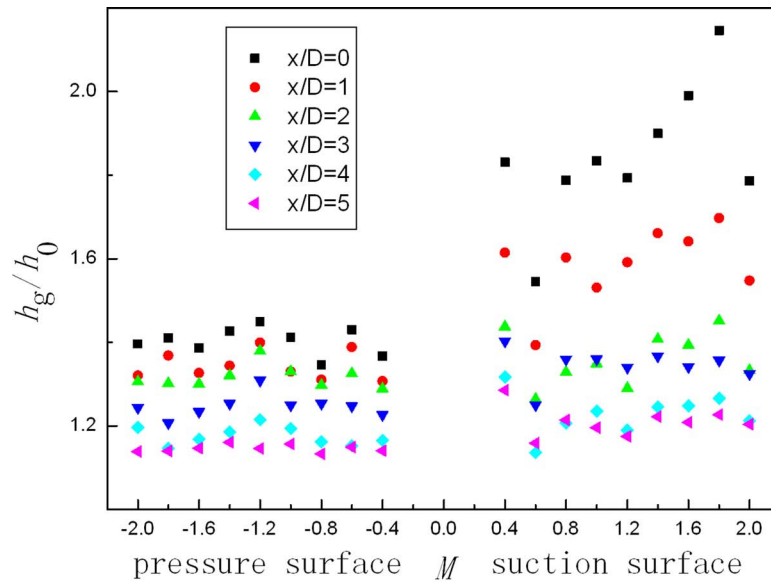
(b) Air injection

Fig. 12 Nondimensional streamwise heat transfer coefficient versus blowing ratios for air and CO₂ injection with different streamwise distance at $Rt=0$

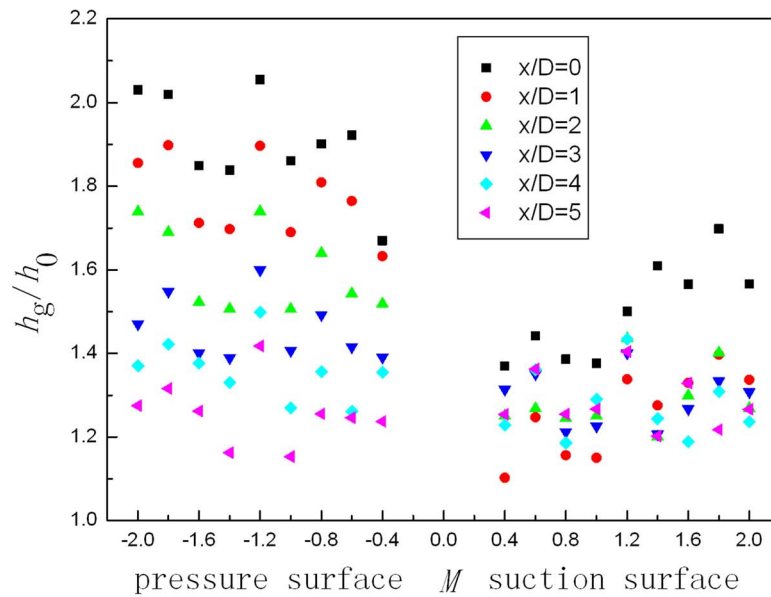
near hole region of $x/D=0-3$ in this study. With the increase in blowing ratio, the heat transfer coefficient with CO₂ injection is increased first and then decreased, and the maximum value of h_g/h_0 corresponds to $M=1.4$. However, for the air injection, there may be more than one peak value.

- For the rotating cases, the film trajectory has an obvious deflection in the spanwise direction. And the deflection angles on the suction surface are much more evident than those on the pressure surface. This phenomenon can be attributed to the combined action of the Coriolis force and centrifugal force. The variations in density ratio and blowing ratios have slight influences on the deflection.
- The influences of blowing ratio under rotation are more complicated. For CO₂ injection, the magnitude of heat transfer coefficient on the pressure surface is reduced compared

with the stationary case, and the blowing ratio has smaller effects on the h_g/h_0 distribution. However, on the suction surface, the heat transfer coefficient for the very near hole region at $x/D < 1.0$ is enhanced and then rapidly reduced to be also below the stationary values. For air injection, rotation also depresses the h_g/h_0 for both the pressure and the suction surface. However, on the suction surface, the h_g/h_0 decreases rapidly for the first $1D$ downstream from the film hole, then increases gradually in the region of $x/D=1-3$, and finally levels off at far downstream. These heat transfer coefficient reduction compared with their stationary counterparts may be due to the too narrow area we have chosen for data averaging, and the film may be deflected well outside this area.



(a) CO_2 injection



(b) Air injection

Fig. 13 Nondimensional streamwise heat transfer coefficient versus blowing ratios for air and CO_2 injection with different streamwise distance at $Rt=0.0249$

4. The density ratio shows a considerable effect on the streamwise heat transfer coefficient distributions especially for the rotating cases.

Acknowledgment

The authors gratefully acknowledge funding support from the Program for New Century Excellent Talents in University (Grant No. NCET-05-0189), the Research Fund for the Doctoral Program of Higher Education (Grant No. 200604114), and the Fanzhou Youth Science Foundation (Grant No. 20070401).

Nomenclature

D = film cooling hole diameter, mm
 DR = density ratio

h_{f0} = heat transfer coefficient in the presence of film cooling, $\text{W}/\text{m}^2 \text{K}$ ($h_f = q / (T_{aw} - T_w)$)

h_g = heat transfer coefficient in the presence of film cooling, $\text{W}/\text{m}^2 \text{K}$ ($h_g = q / (T_g - T_w)$)

h_0 = heat transfer coefficient in the absence of film cooling, $\text{W}/\text{m}^2 \text{K}$ ($h_0 = q / (T_{g0} - T_{w0})$)

k = thermal conductivity, $\text{W}/\text{m K}$

L = hole length, mm

M = blowing ratio ($M = (\rho_c U_c) / (\rho_g U_g)$)

Nc = critical jet momentum, kg m/s

P = hole pitch

q = wall heat flux, W/m^2

Re_D = Reynolds number ($\text{Re}_D = U_g D / \nu_g$)

Rt = rotation number ($Rt = \omega D / U_g$)

T = temperature, K
 U = velocity, m/s
 x, y, z = Cartesian coordinate system: x , streamwise direction; y , normal to the wall; z , spanwise direction, mm

Greek Symbols

ρ = density, kg/m³
 η = adiabatic film cooling effectiveness ($\eta = (T_g - T_{aw}) / (T_g - T_c)$)
 ν = kinetic viscosity
 ω = rotating speed, rpm

Subscripts

0 = in the absence of film cooling
 aw = adiabatic
 c = coolant
 g = mainstream
 w = wall

References

- [1] Han, J. C., Dutta, S., and Ekkad, S. V., 2000, *Gas Turbine Heat Transfer and Cooling Technology*, Taylor & Francis, New York.
- [2] Eriksen, V. L., and Goldstein, R. J., 1974, "Heat Transfer and Film Cooling Following Injection Through Inclined Tubes," *ASME J. Heat Transfer*, **96**, pp. 239–245.
- [3] Hay, N., Lampard, D., and Saluja, C. L., 1985, "Effects of Cooling Films on the Heat Transfer Coefficient on a Flat Plate With Zero Mainstream Pressure Gradient," *ASME J. Eng. Gas Turbines Power*, **107**, pp. 105–110.
- [4] Lloyd, S., and Brown, A., 1985, "Fluid Flow and Heat Transfer Characteristics in the Entrance Region of Circular Pipes," ASME Paper No. 85-GT-120.
- [5] Andrews, G. E., Alikhanizadeh, M., Asere, A. A., Hussain, C. I., Khoshkbar, M. S., Azari, M. S., and Mkpadi, M. C., 1986, "Small Diameter Film Cooling Holes: Wall Convective Heat Transfer," *ASME J. Turbomach.*, **108**, pp. 283–289.
- [6] Makki, Y. H., and Jakubowski, G. S., 1986, "An Experimental Study of Film Cooling From Diffused Trapezoidal Shaped Holes," AIAA Paper No. 86-1326.
- [7] Hyams, D. G., and Leylek, J. H., 1997, "A Detailed Analysis of Film Cooling Physics—Part III: Streamwise Injection With Shaped Holes," ASME Paper No. 97-GT-271.
- [8] Ekkad, S. V., Du, H., and Han, J. C., 1995, "Local Heat Transfer Coefficient and Film Effectiveness Distributions on a Cylindrical Leading Edge Model Using a Transient Liquid Crystal Image Method," ASME Winter Annual Meeting, San Francisco, CA.
- [9] Ou, S., and Rivir, R. B., 2001, "Leading Edge Film Cooling Heat Transfer With High Free Stream Turbulence Using a Transient Liquid Crystal Image Method," *Int. J. Heat Fluid Flow*, **22**, pp. 614–623.
- [10] Yu, Y., Yen, C.-H., Shih, T. I.-P., Chyu, M. K., and Gogineni, S., 2002, "Film Cooling Effectiveness and Heat Transfer Coefficient Distributions Around Diffusion Shaped Holes," *ASME J. Heat Transfer*, **124**, pp. 820–827.
- [11] Yuen, C. H. N., and Martinez-Botas, R. F., 2003, "Film Cooling Characteristics of a Single Round Hole at Various Streamwise Angles in a Crossflow—Part II: Heat Transfer Coefficients," *Int. J. Heat Mass Transfer*, **46**, pp. 237–249.
- [12] Yuen, C. H. N., and Martinez-Botas, R. F., 2005, "Film Cooling Characteristics of Rows of Round Holes at Various Streamwise Angles in a Crossflow—Part II: Heat Transfer Coefficients," *Int. J. Heat Mass Transfer*, **48**, pp. 5017–5035.
- [13] Abhari, R. S., and Epstein, A. H., 1994, "An Experimental Study of Film Cooling in a Rotating Transonic Turbine," *ASME J. Turbomach.*, **116**, pp. 63–70.
- [14] Kline, S. J., and McClintock, F. A., 1953, "Describing Uncertainties in Single-Sample Experiments," *Mech. Eng. (Am. Soc. Mech. Eng.)*, **75**, pp. 3–8.
- [15] Ammari, H. D., Hay, N., and Lampard, D., 1990, "The Effect of Density Ratio on the Heat Transfer Coefficient From a Film Cooled Flat Plate," *ASME J. Turbomach.*, **112**, pp. 444–450.

Film-Cooling Flowfields With Trenched Holes on an Endwall

N. Sundaram

Creative Power Solutions USA, Inc.,
11010 North Saguardo Boulevard,
Fountain Hills, AZ 85268
e-mail: sundar.narayan@cpsusainc.net

K. A. Thole

Department of Mechanical and Nuclear
Engineering,
Pennsylvania University,
University Park, PA 16802

The leading edge region along the endwall of a stator vane experiences high heat transfer rates resulting from the formation of horseshoe vortices. Typical gas turbine endwall designs include a leakage slot at the combustor-turbine interface as well as film-cooling holes. Past studies have documented the formation of a horseshoe vortex at the leading edge of a vane, but few studies have documented the flowfield in the presence of an interface slot and film-cooling jets. In this paper, a series of flowfield measurements is evaluated at the leading edge with configurations including a baseline with neither film-cooling holes nor an upstream slot, a row of film-cooling holes and an interface slot, and a row of film-cooling holes in a trench and an interface slot. The results indicated the formation of a second vortex present for the case with film-cooling holes and a slot relative to the baseline study. In addition, turbulence intensity levels as high as 50% were measured at the leading edge with film-cooling holes and a slot compared with the 30% measured for the baseline study. A trench was shown to provide improved overall cooling relative to the no trench configuration as more of the coolant stayed attached to the endwall surface with the trench. [DOI: 10.1115/1.3068316]

1 Introduction

An endwall near the leading edge of a first stage vane experiences high heat transfer coefficients and high fluid temperatures from the combustor as a result of the formation of a leading edge vortex. As the flow in the endwall boundary layer approaches the vane stagnation location it decelerates as it experiences an increase in the local static pressure. This deceleration is greater outside of the boundary layer, than in the near-wall region resulting in a pressure gradient in the radial direction along the vane. The pressure gradients result in the flow separating from the endwall and turning the flow toward the endwall. The motion of the horseshoe vortex is one in which the less dense, higher temperature fluid convects toward the endwall causing an increase in the local fluid temperature and convective heat transfer coefficient.

Past studies by Friedrichs et al. [1,2] showed that an endwall leading edge is the most difficult region to cool. This is primarily because the formation of horseshoe vortices lifts the coolant off the surface, making it a challenge to cool the endwall. To date a number of studies have been carried out that have measured the flowfield at the leading edge but very few in the presence of film-cooling holes and an upstream slot.

This study is unique as flowfield measurements with film-cooling holes and film-cooling holes placed in a two-dimensional transverse slot (trench) are presented. Recent studies by Bunker [3], Wayne and Bogard [4], and Sundaram and Thole [5] have shown that a trench enhances the adiabatic effectiveness levels when placed on a flat plate [3], a vane surface [4], or on an endwall [5]. Our study focuses on applying the trench geometry at the leading edge and measuring the resulting flowfield. These measurements illustrate the leading edge flowfields and the turbulence levels that are modified in the presence of film-cooling holes and a trench.

The work presented in this paper compares three different leading edge endwall configurations including an endwall with neither film-cooling holes nor an upstream slot, an endwall with film-cooling holes and an upstream slot, and an endwall with film-cooling holes placed in a trench and an upstream slot.

2 Relevant Past Studies

Due to the formation of horseshoe vortices, the endwall leading edge is a region of high heat transfer thus making it a challenge to cool with only film-cooling holes. To enhance film-cooling at the leading edge, few past studies focused on developing alternate methods in addition to placing film-cooling holes. These studies at the endwall leading edge focused on understanding the effects of coolant injection through continuous and discrete slots. Studies by Blair [6], Burd et al. [7], Oke et al. [8], and Zhang and Jaiswal [9] showed that coolant flow from an upstream slot at the endwall leading edge resulted in cooling only the suction side and not the pressure side.

Kost and Nicklas [10] and Nicklas [11] were the first to carry out an endwall study with coolant injection from an upstream slot in addition to film-cooling holes. They confirmed that the adiabatic effectiveness levels on the suction side were higher than the pressure side due to the slot coolant migration. They also showed that the slot flow intensified the horseshoe vortex as the ejection through the slot occurred at the saddle point where the boundary layer was already separated. Colban et al. [12,13] studied the effect of placing a backward facing slot at the combustor-turbine interface. They showed that the slot flow enhanced the adiabatic effectiveness levels on the suction side and eliminated the horseshoe vortex at the leading edge. Knost and Thole [14] studied the effect of leakage flow through a slot at the combustor-vane interface in the presence of film-cooling. They observed that the coolant exited the upstream slot in a nonuniform fashion. This non-uniformity was associated with the formation of a hot ring around the stagnation region even in the presence of coolant ejection from a row of film-cooling holes. A later study by Cardwell et al. [15] showed that the size of this hot ring can be reduced by decreasing the width of the upstream slot while maintaining a constant coolant flowrate. This resulted in uniformly spreading the coolant due to the higher momentum flux ratio associated with the jets.

Rehder and Dannhauer [16] studied the effect of tangential and perpendicular ejections of leakage flow through a backward facing slot placed upstream of a cascade. They observed that at a leakage mass flowrate of 2%, the tangential ejection removed the horseshoe vortex and weakened the passage vortex, whereas the perpendicular ejection had an opposite effect of strengthening the horseshoe and passage vortices. A recent study by Kost and Mullaert [17] showed that the horseshoe vortex is not intensified if the upstream slot is placed away from the saddle point of the up-

Contributed by the International Gas Turbine Institute of ASME for publication in the JOURNAL OF TURBOMACHINERY. Manuscript received August 19, 2008; final manuscript received August 27, 2008; published online July 1, 2009. Review conducted by David Wisler. Paper presented at the ASME Turbo Expo 2008: Land, Sea and Air (GT2008), Berlin, Germany, June 9–13, 2008.

stream endwall boundary layer. They reported that a slot placed further upstream from the vane leading edge results in better attachment of the coolant to the endwall surface. Lynch and Thole [18] showed that there is a uniform distribution of the coolant exiting the combustor interface slot when it is placed further upstream from the vane stagnation location. They observed that the adiabatic effectiveness levels downstream of the slot were higher when the slot was located at a distance of $0.32C$ from the vane stagnation location relative to when it was located at a distance of $0.13C$. These studies of coolant flow through a slot showed that effective cooling could be achieved by injecting a two-dimensional layer of film-cooling over the surface.

Even though leakage flows through upstream slots improved the effectiveness levels on the suction side, the leading edge especially along the pressure side was still devoid of coolant flow. As such, better cooling designs have to be implemented to enhance adiabatic effectiveness levels at the leading edge. A study carried out by Bunker [3] on a flat plate showed that discrete film-cooling holes placed within a trench gave improved film-cooling effectiveness levels. Bunker [3] showed that the narrowest possible trench width relative to the interior cooling hole diameter is most desirable. Lu et al. [19] investigated the effect of slot exit area and edge shape on film effectiveness measurements made on a flat plate. Their study showed that a straight edge exit performed the best at a blowing ratio of $M=1.0$, whereas a ramped exit enhanced the adiabatic effectiveness levels at lower blowing ratios.

As film-cooling holes in trenches modify the hole exit, there have been a few studies that have investigated this particular effect on actual turbine geometries. Waye and Bogard [4] applied the trench configuration on the suction side of a first stage vane with varying slot exit configurations. They tested a narrow trench where the trench wall was at the film-cooling hole exit, a wide trench where the trench wall was at a distance of one cooling hole diameter from the hole exit, and a trench with an angled exit. Similar to Bunker [3] they also found that the narrow trench performed the best relative to a wide and angled exit trench and the adiabatic effectiveness levels peaked for blowing ratios beyond $M=1.0$.

Trenches were also tested on a vane endwall where the flows are highly three dimensional with intense secondary flows. Sundaram and Thole [5] studied the effect of trench and trench depths for a row of film-cooling holes at the leading edge of a vane endwall. They measured the adiabatic effectiveness levels at different blowing ratios for trench depths corresponding to $0.4D$, $0.8D$, and $1.2D$ and found the adiabatic effectiveness levels to be highest at a depth of $0.8D$. Dorrington et al. [20] also observed that a trench on a vane surface performs the best at a critical depth of $0.75D$. In addition, film-cooling holes in a trench were found to reduce the heat transfer to a surface. Harrison et al. [21] measured the heat transfer coefficient augmentation on a film-cooled vane surface with and without a trench. They reported that the heat transfer coefficient augmentations on the vane surface were similar for the cases with and without a trench. However, as a trench resulted in higher adiabatic effectiveness levels, the net heat flux reduction with a trench was higher than the case without a trench thus indicating lower heat transfer to the surface.

This work focuses on measuring the flowfield at the leading edge of a vane endwall with a row of film-cooling holes with and without a trench. The purpose of these measurements is to gain a greater physical understanding of why the trench design results in superior cooling performance.

3 Experimental Design and Measurements

Figure 1 shows the experimental set up for this study that consists of a large-scale corner test section attached to a low-speed recirculating wind tunnel facility. Cardwell et al. [15] and Sundaram and Thole [5] previously documented the wind tunnel facility used in this study. The flow in the wind tunnel first passes

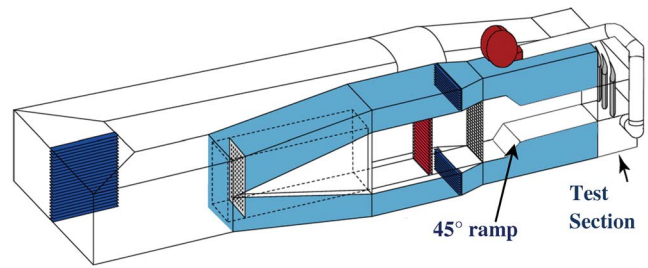


Fig. 1 Illustration of the wind tunnel facility

through a primary heat exchanger to cool the bulk flow. Downstream of the primary heat exchanger is a transition section that divides the flow into three passages including the primary mainstream flow and two secondary coolant flows located above and below the test section. Note that only the top secondary flow passage was used in this study. Two different temperature settings were maintained through the primary and secondary channels while measuring the adiabatic effectiveness levels and flowfield on the endwall. For the adiabatic effectiveness measurements, the core flow was heated to 60°C and the secondary flow was cooled to 20°C . However, for flowfield measurements, the mainstream and coolant flows were both maintained at 30°C .

The scaled-up test section was attached to a corner of the wind tunnel facility as shown in Fig. 1. The test section consisted of two full passages with one center vane and two half vanes. Descriptions of the turbine vane geometry, cooling hole geometry, and operating conditions are provided in Table 1. Kang et al. [22] and Radomsky and Thole [23] previously documented the details of the construction and development of the vane test section used in this study. Similar to the current investigation, these studies focused on measuring the endwall flowfield along a plane parallel to the flow and intersecting the vane stagnation location. Kang et al. [22] measured the flowfield at a freestream turbulence level of 0.6%, whereas Radomsky and Thole [23] measured the flowfield at a turbulence level of 19.5%. The primary difference between the current and the past studies (Refs. [22,23]) was the presence of film-cooling and upstream slot flows at the endwall leading edge. In addition, the boundary layer in the current study developed over a 45 deg ramp that contracted the flow channel (refer to Fig. 1). However, in the previous studies (Refs. [22,23]), the boundary layer development occurred along a straight channel with no contractions.

4 Endwall Geometry

The vane geometry in this study consists of top and bottom endwall surfaces. Figure 2 illustrates the bottom endwall geometry where the adiabatic effectiveness levels and the flowfields were measured. The bottom endwall was made of low thermal conductivity (0.033 W/mK) foam for measuring the adiabatic effectiveness levels and the top endwall was made of plexiglass to

Table 1 Geometric and flow conditions

Scaling factor	9
Scaled up chord length (C)	59.4 cm
Pitch/chord (P/C)	0.77
Span/chord (S/C)	0.93
Hole L/D	8.3
Hole P/D	3
R_{in}	2.1×10^5
Inlet and exit angles	0 deg and 72 deg
Inlet and exit Mach numbers	0.017 and 0.085
Inlet mainstream velocity	6.3 m/s
Upstream slot width	0.024C

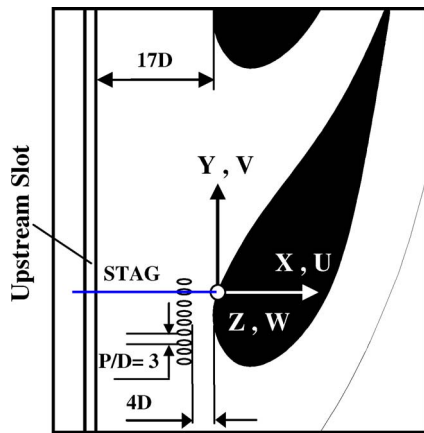


Fig. 2 Illustrates the endwall design studied at the leading edge

provide optical access to measure the flowfield. Similar to Sundaram and Thole [5], the bottom endwall consists of a row of nine axial film-cooling holes ($P/D=3$) placed four cooling hole diameters ($X/D=4D$) from the vane stagnation location. An upstream slot was also placed at a distance of $X/D=17$ from the vane stagnation location. Note that the vane stagnation is located at the origin of the coordinate system shown in Fig. 2. The film-cooling holes injected at an angle of 30 deg and the upstream slot injected at an angle of 45 deg with respect to the endwall surface.

Measurements were carried out on three different endwall configurations as shown in Figs. 3(a)–3(c). Figure 3(a) illustrates an endwall with no film-cooling holes or an upstream slot and this will be referred to as the baseline. This leading edge endwall configuration is similar to the study by Kang et al. [22]. Figure 3(b) illustrates an endwall with film-cooling holes and an upstream slot and Fig. 3(c) illustrates an endwall with a row of film-cooling holes in a trench and an upstream slot. The trench design adopted in this study is similar to the row trench design previously described in Ref. [5]. The trenches on a surface can be manufactured during the application of the thermal barrier coating (TBC). In most land based gas turbines the TBC thickness on the vanes and the blades are on the order of 300 μm . In this study, a thin piece of balsa wood (0.048 W/mK) was used to simulate a TBC of thickness 200 μm on the engine scale, corresponding to a trench depth of $h=0.4D$.

Two separate plenums were used to control the coolant flowrate through the upstream slot and the film-cooling holes. The flow through the upstream slot was set by assuming a discharge coefficient of 0.6 taken as the value for flow through a sharp-edged

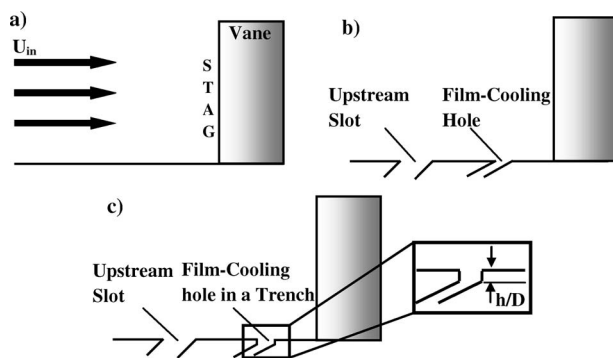


Fig. 3 Illustrates the three-endwall configurations: (a) baseline, (b) film-cooling without a trench, and (c) film-cooling with a trench studied at the leading edge

orifice. The flowrate through the film-cooling holes was controlled by setting an inviscid blowing ratio (M) that was based on the inlet mainstream velocity, U_{in} . To set the blowing ratio, an inviscid coolant jet velocity was calculated by measuring the difference between total pressure in the plenum and the stagnation pressure at the vane leading edge.

5 Endwall Adiabatic Effectiveness Measurements

The technique used in our study to measure the adiabatic effectiveness levels has been previously explained in detail by Sundaram and Thole [5]. A FLIR P20 infrared (IR) camera with a spatial integration of 0.16 hole diameters (0.073 cm) was used to spatially resolve the adiabatic temperatures on the endwall. Six images were taken at each viewing location for averaging purposes, and three viewing locations were required to completely map the leading edge region on the endwall. The camera was placed at a distance of 55 cm from the bottom endwall with each image covering an area of $24 \times 18 \text{ cm}^2$ (320×240 pixel resolution). The infrared images were calibrated using temperatures directly measured by thermocouples on the endwall. The calibrated images were then averaged and assembled using a MATLAB program to obtain the temperature distribution around the leading edge. To calculate the adiabatic effectiveness levels, freestream temperatures were measured at multiple locations along the pitch using a rake consisting of three thermocouples at span locations of $Z/S=0.25, 0.5,$ and 0.75 . The adiabatic temperature data were compiled after the system reached steady state, which typically took 3 h.

To account for conduction losses, a one-dimensional conduction correction described by Ethridge et al. [24] was applied to all adiabatic effectiveness measurements. At the entrance to the flow passage a correction of 0.16 was typical for a measured value of $\eta=0.9$, while along the pressure side a correction of 0.03 was applied for a measured value of $\eta=0.1$. The partial derivative method described by Moffat [25] was used to calculate the uncertainty associated with the adiabatic effectiveness measurements. As explained in Ref. [5], to determine the total uncertainty associated with the adiabatic effectiveness levels, individual uncertainties related to the IR images, the thermocouples, and the data acquisition system were calculated. For these measurements, the total uncertainties were calculated to be $\pm 1.02^\circ\text{C}$ for the images and $\pm 0.62^\circ\text{C}$ for the thermocouple measurements. Uncertainties in adiabatic effectiveness were then calculated to be $\partial\eta = \pm 0.032$ for a η value of 0.2 and $\partial\eta = \pm 0.033$ for a η value of 0.9.

6 Endwall Flowfield Measurements

Laser Doppler velocimetry (LDV) was used to measure the three velocity components associated with the flow. Kang et al. [22] and Radomsky and Thole [23] previously documented the LDV system used for this study. The LDV system consists of a 5 W laser and a TSI 9201 Colorburst beam separator. The measured velocity was processed using a digital burst correlator, which was controlled using the TSI FIND software. To measure the flowfield, the flow was seeded with 1 μm diameter olive oil particles. The three velocity components were measured using a 750 mm focusing lens with a beam expander. The length and diameter of the probe volume were 850 and 46 μm for the 750 mm lens. A total of 10,000 data points were measured at each location to compute the mean and turbulent components of the velocity.

The streamwise (U) and the spanwise (W) velocity components were measured from the side and the pitchwise (V) component was measured through the top endwall. To allow measurements to be made close to the stagnation location, the probe had to be turned by 18 deg. The probe was also tilted by 7 deg downwards to facilitate measurements close to the endwall. The tilting of the probe resulted in transforming the measured spanwise component by 7 deg in the W - V plane. As a result of turning and tilting the

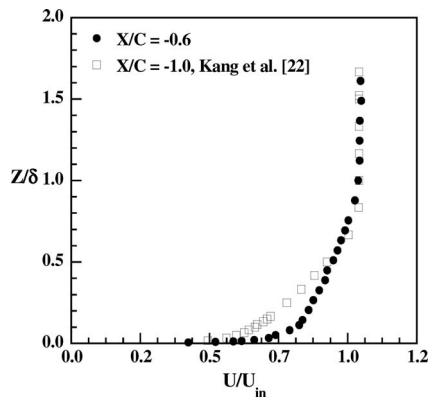


Fig. 4 Boundary layer profiles comparing the current study with Kang et al. [22]

probe, the measured velocity components were corrected to obtain the true velocities using the scheme previously described by Kang and Thole [26].

Similar to the adiabatic effectiveness measurements, an uncertainty analysis based on the partial derivative method described by Moffat [25] was applied to the measured velocities. A 95% confidence interval and 10,000 data points were used to calculate the uncertainties in the mean and fluctuating velocity components. The estimate of the bias and precision uncertainties for the mean streamwise velocity in the near-wall region were 1% and 0.44%, respectively. In the midspan region, the bias uncertainty was 1% and the precision uncertainty was estimated to be 0.06% for the mean streamwise velocity, and 1.0% for the mean pitchwise and spanwise velocities. In the measurements carried out at the near-wall region, the precision uncertainties of the fluctuating velocities were found to be 2% for u_{rms} , 1.9% for v_{rms} , and 4.4% for w_{rms} .

7 Inlet Flow Conditions

For every test condition, the vane static pressure distribution was verified to ensure a periodic flow through the vane passage. The inlet boundary layer was measured at an axial distance of $0.6C$ upstream from the vane stagnation location. At this location, measurements showed an incident turbulence level of 1.3% and a turbulence length scale of 4 cm ($0.07C$). Figure 4 compares the streamwise velocity profiles between the current study and the previous study by Kang et al. [22]. It is seen that in the current study, the near-wall velocities are higher than the measurements by Kang et al. [22]. Table 2 compares the inlet boundary layer characteristics between the current study and the study by Kang et al. [22]. The boundary layer measured at $X/C = -0.6$ was $\delta_{99}/S = 0.25$ and was thicker than $\delta_{99}/S = 0.10$ measured by Kang et al. [22] at location $X/C = -1$. A thicker boundary layer was a result of

Table 2 Inlet boundary layer characteristics

	Current study	Kang et al. ^a
Measurement location, X/C	-0.6	-1.0
Freestream turbulence level	1.3%	0.6%
Boundary layer thickness (δ/S)	0.29	0.11
Displacement thickness (δ^*/S)	0.033	0.017
Momentum thickness (θ/S)	0.027	0.011
Shape factor (δ^*/θ)	1.25	1.54
Momentum thickness	5318	2960
Reynolds number (Re_θ)		

^aReference [22].

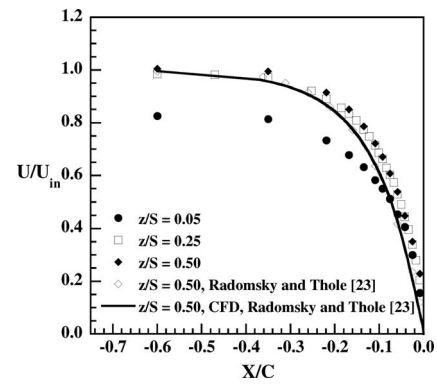


Fig. 5 Variation of the streamwise velocity approaching the vane stagnation location

the acceleration in the flow caused by the 45 deg ramp that was located two chords upstream from the vane stagnation location (refer to Fig. 1).

Figure 5 shows the variation of the mainstream velocity as the flow approaches the vane stagnation locations at different spanwise positions. These measurements were made for the case having neither film-cooling holes nor an upstream slot. It is observed that the flow decelerates at all span locations as it approaches the vane with the deceleration beginning at $X/C > -0.35C$. The deceleration at the midspan for the current study is compared with Radomsky and Thole [23] and it is seen that there is a good agreement between the two studies.

8 Adiabatic Effectiveness Measurements at the End-wall Leading Edge Junction

The adiabatic effectiveness measurements presented in this section were previously reported in Ref. [5]. The adiabatic effectiveness levels on the endwall leading edge were measured to compare the performance of film-cooling holes with and without a trench. These measurements were made at varying film-cooling blowing ratios while maintaining a constant coolant flowrate through the upstream slot.

Figure 6(a) compares the contours of adiabatic effectiveness levels for film-cooling holes without a trench at blowing ratios of $M = 1.0, 2.0,$ and 3.0 . From Fig. 6(a) it is seen that at a blowing ratio of $M = 1.0$, the adiabatic effectiveness levels are higher on

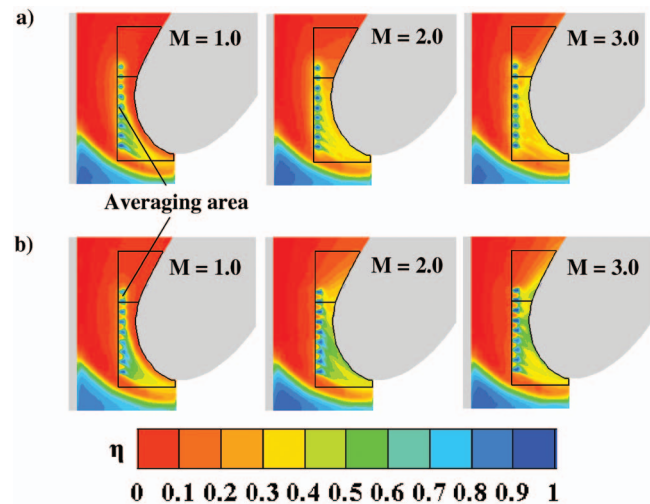


Fig. 6 Contours of adiabatic effectiveness levels comparing the effect of (a) film-cooling holes without a trench and (b) film-cooling holes with a trench

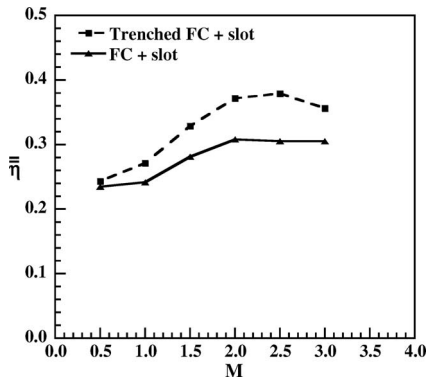


Fig. 7 Area-averaged effectiveness comparing the effect of a trench on leading edge film-cooling

the suction side of the endwall than on the pressure side. A lower static pressure on the suction side forces more coolant to exit the cooling holes near the suction side than on the pressure side. With an increase in blowing ratio to $M=2.0$, the adiabatic effectiveness levels gradually increase along the pressure and suction sides. A further increase to $M=3.0$ results in an increase in effectiveness levels on the pressure side with a subsequent decrease in the suction side when compared with $M \leq 2$. At high blowing ratios, high jet momentum results in coolant lift-off from the surface. This causes the temperature of the coolant to increase as the coolant mixes with the hot mainstream gases, thereby degrading the adiabatic effectiveness levels. However, at high blowing ratios, the adiabatic effectiveness levels increase near the vane-endwall junction. The enhancements in the effectiveness levels are due to the leading edge horseshoe vortex that pulls injected coolant back to the endwall surface. As a result, at high blowing ratios there is an

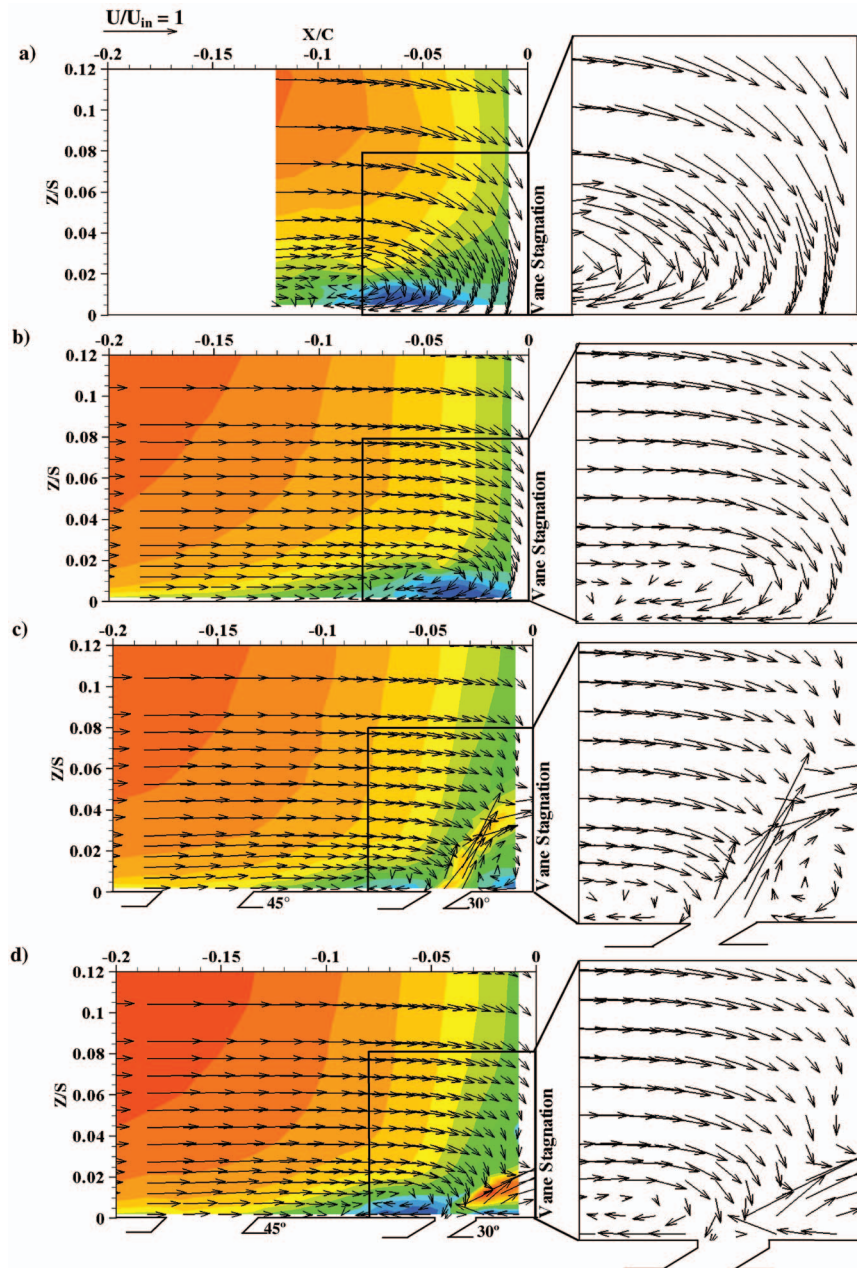


Fig. 8 Comparison of leading edge flowfield superimposed with the streamwise velocity for (a) Kang et al. [22], (b) baseline, (c) film-cooling holes without a trench at $M=2.5$, and (d) film-cooling with a trench at $M=2.5$

increase in the adiabatic effectiveness levels at the vane-endwall junction but a decrease in effectiveness levels downstream of the film-cooling holes when compared with low blowing ratios.

To enhance the adiabatic effectiveness levels with cylindrical film-cooling holes, new cooling hole exit designs have to be implemented. One such design is the placement of film-cooling holes in a trench (refer to Fig. 3(c)). From Fig. 6(b) it is seen that the adiabatic effectiveness levels are comparatively higher in the presence of a trench than without a trench. This is because the downstream edge of the trench forms a wall at the cooling hole exit, which forces the coolant to spread laterally within the trench before convecting over the endwall surface. It is observed that even at a high blowing ratio of $M=3.0$, adiabatic effectiveness levels downstream of the trenched holes are higher than the case without a trench.

Figure 7 compares the area-averaged effectiveness levels for film-cooling with and without a trench at different blowing ratios. An area-averaged effectiveness value was calculated for the end-wall leading edge (boxed region in Fig. 6) by averaging the adiabatic effectiveness levels extending from the suction side to the pressure side. It is seen that for cylindrical film-cooling holes without a trench, the adiabatic effectiveness levels plateau at high blowing ratios. However, in the presence of a trench, the adiabatic effectiveness levels steadily increase with the maximum enhancement occurring at a blowing ratio of $M=2.5$. At $M=3.0$ the effectiveness levels decrease due to possible jet lift-off associated with higher momentum coolant flow. Overall film-cooling holes in a trench outperform the case without a trench for a large range of blowing ratios.

The aim of the work that followed the adiabatic effectiveness measurements was to measure the leading edge flowfield and understand the flow physics behind the superior performance of trenched film-cooling holes. Flowfields were measured at a blowing ratio of $M=2.5$ as the trench showed the highest adiabatic effectiveness levels at this blowing ratio and also to understand the effect of jet lift-off that occurs in the absence of a trench.

9 Flowfield Measurements at the Endwall Leading Edge Junction

Flowfields were measured for each endwall configuration shown in Fig. 3. First, the streamwise velocity contours superimposed with the flow vectors are compared for each endwall configuration. Next, the variation in the turbulence intensities and the turbulence kinetic energy are compared at the leading edge and, finally, the effects of film-cooling with and without a trench on the leading edge vorticity are discussed.

9.1 Comparison of Mean Velocity Flowfield. The mean velocity flowfield was measured at the endwall leading edge along a plane parallel to the incoming flow and intersecting the vane stagnation location. Figures 8(a)–8(d) compare the contours of the normalized mean streamwise velocity (U/U_{in}) superimposed with the flow vectors for the three-endwall configurations with the measurements by Kang et al. [22].

From Figs. 8(a) and 8(b) it is observed that a horseshoe vortex is formed at the endwall leading edge as the flow approaches the vane stagnation location. In the study by Kang et al. [22], the core of the vortex is located at a spanwise location of $Z/S=0.025$ and at a streamwise distance of $X/C=-0.08$. However, for our baseline case (Fig. 8(b)), the vortex core is located closer to the end-wall and the vane surface relative to the study by Kang et al. [22]. In the baseline study, the vortex core is located at $Z/S=0.015$ and at $X/C=-0.05$. The shift in the vortex location is because the near-wall velocities in the baseline study are higher than the velocities measured by Kang et al. [22]. It is also observed that the vortex measured by Kang et al. [22] has a more complete roll up and is spread over a larger region. The contours in Figs. 8(a) and 8(b) show that for both studies, the velocity gradients near the vortex core are stronger than the gradients at locations upstream

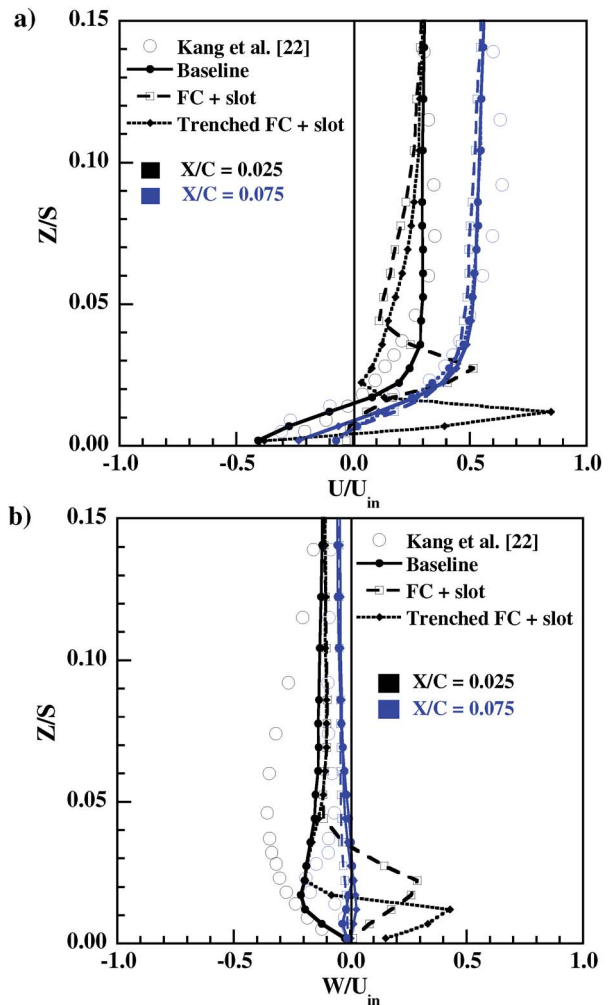


Fig. 9 Velocity profiles showing the spanwise variation of (a) U - and (b) W -velocity components

of the vortex. The contours also indicate that away from the wall, the U -velocity profiles flatten out as they approach the vane. Note that near the vane stagnation location there is a significant amount of turning in the pitchwise direction.

Figure 8(c) shows the flow vectors at the leading edge with coolant flows from the upstream slot and film-cooling holes. The blowing ratio through the film-cooling holes was set at $M=2.5$ and the blowing ratio through the upstream slot was set at $M=0.3$, which was based on the inlet mainstream velocity, U_{in} . At $M=2.5$, there is a greater separation of the coolant jets from the endwall surface when compared with $M \leq 2$. As a result, the effectiveness levels downstream of the film-cooling holes are lower at $M=2.5$ than when the cooling holes are operating at $M \leq 2$ (see Figs. 6(a)). The coolant injection results in the formation of dual vortices located upstream ($X/C=-0.07$) and downstream ($X/C=-0.02$) of the film-cooling holes. A vortex is formed downstream of the holes as the high momentum jets impede the mainstream flow creating a low-pressure region near the vane stagnation location. The low-pressure region pulls the injected coolant back to the surface, thus creating a vortex and increasing the effectiveness levels along the vane-endwall junction (see Fig. 6(a)). It is also seen that the downstream vortex is larger than the vortex formed upstream of the film-cooling holes. From the streamwise velocity contours it is observed that, in the presence of film-cooling, the velocity gradients near the vane stagnation location are relatively higher than the gradients in the baseline study.

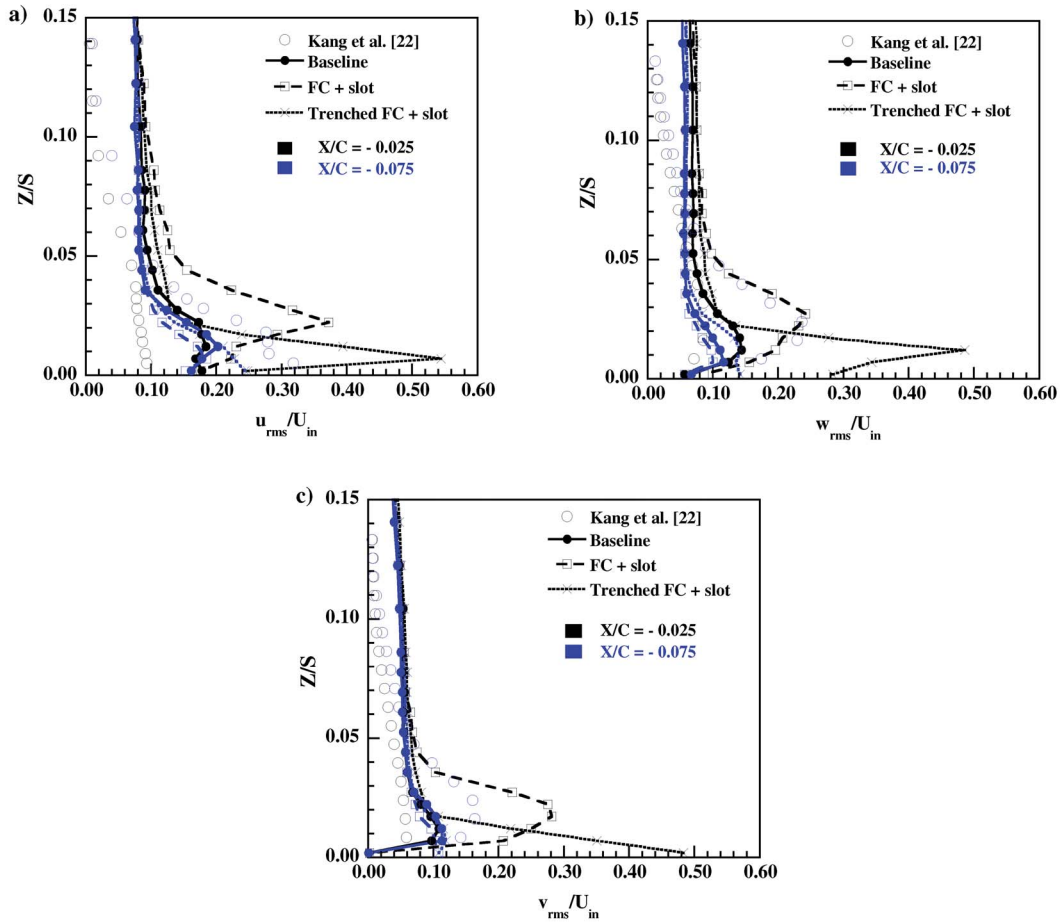


Fig. 10 Comparison of (a) streamwise, (b) spanwise, and (c) pitchwise turbulence levels at the endwall leading edge

Figure 8(d) shows the leading edge flow vectors superimposed with the streamwise velocity contours for film-cooling holes placed in a trench. The flow vectors indicate that a trench causes the coolant jets to stay attached to the surface compared with the jets in the absence of a trench. Better jet attachment results in higher adiabatic effectiveness levels, even at a blowing ratio of $M=2.5$ (see Fig. 6(b)). It should be noted that in the presence of a trench the downstream vortex disappears. As the coolant jets exiting a trench are better attached to the surface, they do not impede the mainstream flow as much as the jets without a trench and thus prevent the formation of a downstream vortex. However, because the boundary layer of the approaching flow separates before the location of the trenched holes, an upstream vortex still exists at $X/C=-0.06$.

Additionally, Figs. 8(c) and 8(d) show that the upstream slot flow does not affect the mainstream flow approaching the vane stagnation location. It was previously shown in Fig. 6 that the coolant from the upstream slot is swept from the pressure side to the suction side due to the secondary flow within the vane passage. At low blowing ratios, the coolant flow from the slot is mainly concentrated in the vane passage toward the suction side and not around the vane stagnation location. As there is minimal coolant exiting the slot from upstream of the vane stagnation location, the boundary layer stays undisturbed.

Figures 9(a) and 9(b) compare the spanwise variation of U - and W -velocity components measured at $X/C=-0.025$ and $X/C=-0.075$. $X/C=-0.025$ is located downstream of the cooling holes and $X/C=-0.075$ is located between the upstream slot and film-cooling holes. It is observed that the U -velocity profile for the

baseline study and the study by Kang et al. [22] resembles a flat plate turbulent boundary layer. This trend is seen for measurements at both the streamwise locations. In the presence of film-cooling, the approaching boundary layer is significantly different than the baseline. At $X/C=-0.025$, the profiles with film-cooling with and without a trench show inflection points. Near the leading edge the coolant jets inject at velocities higher than the mainstream flow velocities. This causes the near-wall U -velocities to be higher than the velocities at the midspan and thus the inflection points along the span. With trenched holes as the jets are better attached to the surface, the inflection points are closer to the endwall. Upstream of the cooling holes at $X/C=-0.075$, the velocity profiles for the three-endwall configurations are similar. This indicates that the coolant injection affects the stagnation plane flow-field only downstream of the cooling holes and the upstream slot flow has insignificant effects on the approaching mainstream flow.

Another important feature as the flow approaches the stagnation location is the spanwise variation of the W -velocities. Comparing the spanwise variation of the W -velocities at $X/C=-0.025$, it is seen from Fig. 9(b) that Kang et al. [22] measured higher negative velocities in the near-wall region than the baseline case. This explains the higher flow turning observed at the leading edge in the measurements by Kang et al. [22] relative to the baseline. Approaching the wall in the presence of film-cooling indicates low negative velocities followed by an inflection point with a tendency toward positive velocities. The negative velocities are a result of the mainstream flow being pulled toward the wall whereas the positive near-wall velocities are a result of coolant injection. At $X/C=-0.075$, the W -velocities are nearly zero for all current stud-

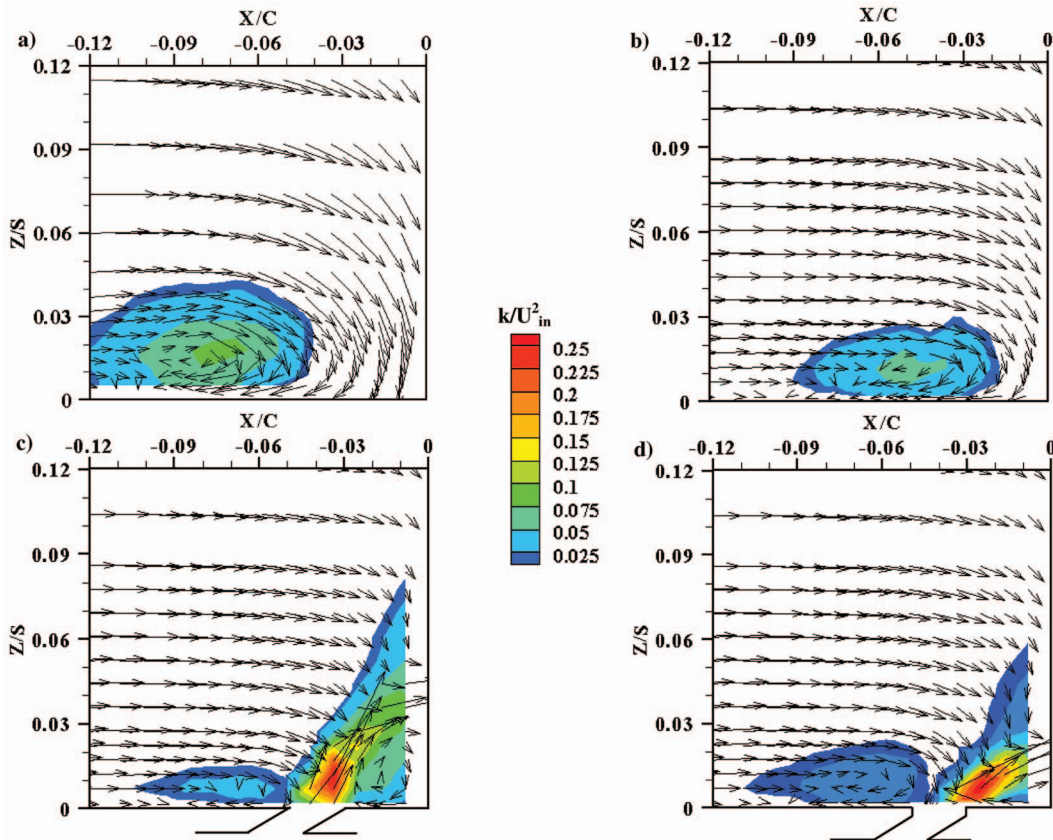


Fig. 11 Contours comparing the normalized turbulence kinetic energy for (a) Kang et al. [22], (b) baseline, (c) film-cooling holes without a trench at $M=2.5$, and (d) film-cooling holes with a trench at $M=2.5$

ies, which shows a weak downward motion of the mainstream flow. However, the measurements by Kang et al. [22] at $X/C = -0.075$ indicate slightly larger negative W -velocities than the baseline study as the horseshoe vortex in their study was formed further away from the leading edge at $X/C = -0.08$.

9.2 Comparison of Turbulence Components. The velocity profiles at the leading edge show that film-cooling modifies the near-wall flow characteristics. This in turn causes a variation in the mainstream turbulence levels at the leading edge. Figure 10 compares the normalized turbulence components measured at $X/C = -0.025$ and $X/C = -0.075$ for the different endwall configurations. The streamwise turbulence component at $X/C = -0.025$ (refer to Fig. 10(a)) shows that the turbulence levels in the baseline study are higher than the levels measured by Kang et al. [22] as the vortex in the baseline study is formed closer to the vane surface. In the presence of film-cooling, the peak turbulence levels occur downstream of the cooling holes along the coolant jet trajectory. This is observed for the endwall configurations with and without a trench. Coolant injection results in the formation of a shear layer along the interface line between the high velocity coolant jet and low velocity freestream flow. As such, large velocity gradients exist along this interface line causing the turbulence levels to be higher. In the presence of a trench as the coolant jets are more attached to the surface, the peak turbulence levels are closer to the near-wall region. The turbulence levels away from the leading edge at $X/C = -0.075$ are constant along the span for the three-endwall configurations compared with Kang et al. [22]. High turbulence levels at $X/C = -0.075$ were seen by Kang et al. [22] as they measured their vortex at $X/C = -0.08$.

For each endwall configuration, the turbulence components at the leading edge are largely isotropic. Figures 10(b) and 10(c) compare the spanwise and pitchwise turbulence levels measured

at two streamwise locations upstream from the vane leading edge. Similar to the streamwise turbulence levels shown in Fig. 10(a), the pitchwise and spanwise turbulence levels at $X/C = -0.025$ are higher for the baseline configuration than in the measurements by Kang et al. [22]. For the streamwise turbulence levels at $X/C = -0.075$, Kang et al. [22] measured higher spanwise and pitchwise turbulence levels than the levels measured in the current study.

Figures 10(a)–10(c), show that in the near-wall region a trench causes the highest velocity fluctuations relative to the other cases when measured at $X/C = -0.025$. This is because in the near-wall region, low velocities and hence low fluctuations exist for all the cases except for film-cooling holes in a trench. In the baseline study, low velocities exist as the flow decelerates when it approaches the vane stagnation location. In the case with film-cooling without a trench, as the coolant jets are detached from the surface high turbulence levels occur away from the wall and not in the near-wall region. As a trench results in better coolant jet attachment, high turbulence levels are observed in the near-wall region.

Fluctuations of the three velocity components were combined to calculate the turbulent kinetic energy (TKE). The results shown in Figs. 11(a)–11(d) were normalized by the inlet velocity and compared with the measurements of Kang et al. [22]. The contours show that Kang et al. [22] ($TKE_{\text{peak}} = 0.076$) measured peak TKE levels similar to our baseline case ($TKE_{\text{peak}} = 0.07$). However, the study by Kang et al. [22] indicates that the vortex in their study was larger than the baseline study. The contours in Figs. 11(c) and 11(d) show that the highest turbulent kinetic energy levels occur at the exit of the film-cooling hole. Kinetic energy levels along the jet-mainstream interface line are similar for studies with and without a trench. However, the turbulent kinetic en-

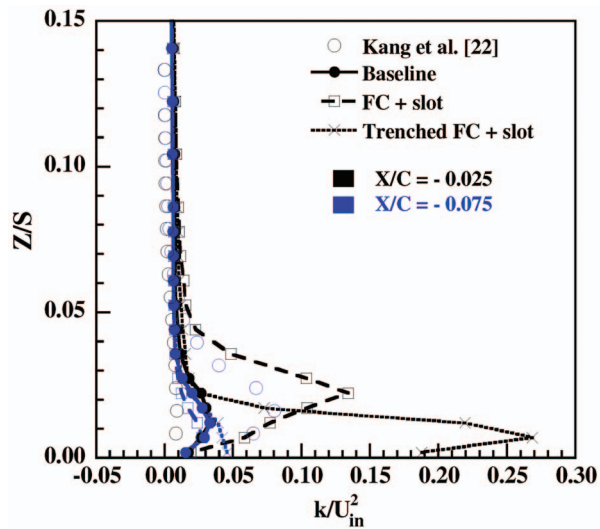


Fig. 12 Profiles comparing the normalized kinetic energy at the endwall leading edge

ergy levels decrease away from the endwall and the vane surface. The spanwise variation of TKE levels was calculated at the two streamwise locations and is shown in Fig. 12. The trends shown by the TKE levels at the two streamwise locations were similar to the trends shown by the turbulence components.

9.3 Comparison of Leading Edge Vorticity. The leading edge vortex in each endwall configuration is formed at a different location along the endwall. Calculating the vorticity aids in ascer-

taining the strength of the vortex at the leading edge. A second order central differencing scheme was used to calculate the vorticity component normal to the stagnation plane (ω_y). Figures 13(a)–13(d) show a comparison of the normalized vorticity component for the three-endwall configurations with the previous study by Kang et al. [22].

In comparing the baseline study with Kang et al. [22], it is seen that the peak values of vorticity are similar for both studies. However, from Figs. 13(a) and 13(b), it is observed that the vortex measured by Kang et al. [22] has a more complete roll up and is spread over a larger region. Figures 13(c) and 13(d) show that in the presence of endwall film-cooling, the vorticity levels near the endwall are higher than the baseline case. Figure 13(d) shows that the highest vorticity levels occur downstream of the trenched holes. These peak values with trenched holes occur in the near-wall region at the location of coolant flow reversal as shown by the secondary flow vectors. The flow reversals result in large velocity gradients thus increasing the vorticity levels downstream of the trench. The coolant flow exiting the trench reverses upon striking the vane leading edge and aids in enhancing the near-wall effectiveness levels.

10 Conclusions

This study was unique in showing the stagnation plane flow field with film-cooling injection in the presence of coolant flow from an upstream slot. Adiabatic effectiveness and flowfield measurements were presented to understand the performance of film-cooling holes in a trench. Film-cooling holes in a trench resulted in enhancing the adiabatic effectiveness levels at all blowing ratios compared with film-cooling holes without a trench. Even at a high blowing ratio of $M=2.5$, a trench was found to spread the coolant uniformly on both the suction and pressure sides, thereby increasing the overall endwall effectiveness levels.

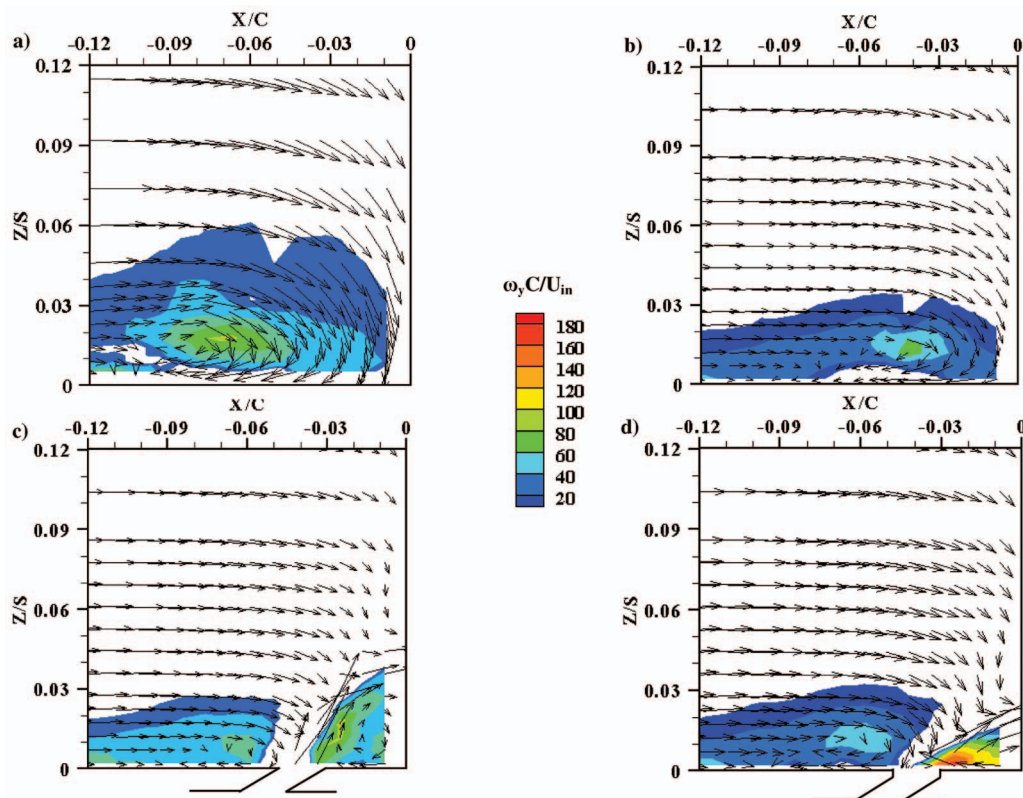


Fig. 13 Comparison of normalized vorticity at the stagnation plane for (a) Kang et al. [22], (b) baseline, (c) film-cooling holes without a trench at $M=2.5$, and (d) film-cooling holes with a trench at $M=2.5$

In order to explain the better performance of a trench, flow-fields were measured at a high blowing ratio of $M=2.5$ at the endwall leading edge. These measurements indicated some clear differences in the flowfield characteristics at the leading edge. In the presence of a trench, the coolant jets did not separate as severely from the endwall surface compared with the configuration without a trench. This explained the higher adiabatic effectiveness levels caused by the trench. At a high blowing ratio of $M=2.5$, it was found that without a trench the coolant penetrated further into the mainstream flow, thereby rendering much of the coolant ineffective. Also, in the absence of a trench, a low-pressure region is formed closer to the vane stagnation location that results in the formation of a downstream vortex in addition to a horseshoe vortex formed upstream of the cooling holes. However, placing a trench caused the downstream vortex to disappear leading to better adiabatic effectiveness levels.

These measurements also showed an important result that the leading edge turbulence levels were isotropic for all endwall configurations. In general, film-cooling resulted in increased turbulence levels compared with the baseline configuration. The near-wall turbulence levels with a trench were higher than without a trench as the jets were closer to the endwall. Away from the endwall, the turbulence levels were higher for film-cooling holes without a trench due to the higher coolant trajectory. A trench also resulted in flow reversals at the leading edge that resulted in high vorticity levels thereby enhancing the adiabatic effectiveness levels. Due to better coolant jet attachment, trenched holes resulted in higher adiabatic effectiveness levels even at low blowing ratios compared with nontrenched holes. As such it can be said that the use of trenched holes will improve the overall performance of a gas turbine engine.

Acknowledgment

This publication was prepared with the support of the U.S. Department of Energy-National Energy Technology Laboratory through a cooperative agreement with the South Carolina Institute for Energy Studies at Clemson University. The authors also thank Mike Blair (Pratt and Whitney) and Ron Bunker (GE) for their input.

Nomenclature

C	= true chord of the stator vane
D	= diameter of the film-cooling hole
FC	= film-cooling holes
M	= blowing ratio based on inlet mainstream velocity $M = \rho_j U_j / \rho_{in} U_{in}$
P	= vane pitch; hole pitch
Re_{in}	= Reynolds number defined as $Re_{in} = CU_{in} / \nu$
S	= span of the stator vane
stag	= stagnation plane/point
T	= temperature
TKE	= turbulent kinetic energy
U and u_{rms}	= local mean and rms velocities in the X -direction
V and v_{rms}	= local mean and rms velocities in the Y -direction
W and w_{rms}	= local mean and rms velocities in the W -direction
X, Y, Z	= fixed Cartesian coordinates

Greek

δ_{99}	= boundary layer thickness
η_{aw}	= adiabatic effectiveness, $\eta = (T_{\infty} - T_{aw}) / (T_{\infty} - T_c)$
$\bar{\eta}_{aw}$	= area-averaged effectiveness
ν	= kinematic viscosity

$$\omega_y = \text{pitchwise vorticity, } \partial U / \partial Z - \partial W / \partial X$$

Subscripts

aw	= adiabatic wall
in	= inlet conditions
j	= coolant flow through film-cooling holes
E	= enhancement

References

- [1] Friedrichs, S., Hodson, H. P., and Daws, W. N., 1996, "Distribution of Film-Cooling Effectiveness on a Turbine Endwall Measured Using Ammonia and Diazo Technique," *ASME J. Turbomach.*, **118**, pp. 613–621.
- [2] Friedrichs, S., Hodson, H. P., and Dawes, W. N., 1997, "Aerodynamic Aspects of Endwall Film-Cooling," *ASME J. Turbomach.*, **119**, pp. 786–793.
- [3] Bunker, R. S., 2002, "Film-Cooling Effectiveness Due to Discrete Holes Within a Transverse Surface Slot," *ASME Paper No. GT2002-30178*.
- [4] Waye, S. K., and Bogard, D. G., 2007, "High-Resolution Film Cooling Effectiveness Measurements of Axial Holes Embedded in a Transverse Trench With Various Trench Configurations," *ASME J. Turbomach.*, **129**, pp. 294–302.
- [5] Sundaram, N., and Thole, K. A., 2008, "Bump and Trench Modifications to Film-Cooling Holes at the Vane Endwall Junction," *ASME J. Turbomach.*, **130**(4), p. 041013.
- [6] Blair, M. F., 1974, "An Experimental Study of Heat Transfer and Film-Cooling on Large-Scale Turbine Endwalls," *ASME J. Heat Transfer*, **96**, pp. 524–529.
- [7] Burd, S. W., Satterness, C. J., and Simon, T. W., 2000, "Effects of Slot Bleed Injection Over a Contoured Endwall on Nozzle Guide Vane Performance: Part II-Thermal Measurements," *ASME Paper No. 2000-GT-0200*.
- [8] Oke, R., Simon, T. W., Shih, T., Zhu, B., Lin, Y. L., and Chyu, M., 2001, "Measurements Over a Film-Cooled Contoured Endwall With Various Coolant Injection Rates," *ASME Paper No. 2001-GT-0140*.
- [9] Zhang, L. J., and Jaiswal, R. S., 2001, "Turbine Nozzle Endwall Film-Cooling Study Using Pressure Sensitive Paint," *ASME J. Turbomach.*, **123**, pp. 730–738.
- [10] Kost, F., and Nicklas, M., 2001, "Film-Cooled Turbine Endwall in a Transonic Flow Field: Part I—Aerodynamic Measurements," *ASME Paper No. 2001-GT-0145*.
- [11] Nicklas, M., 2001, "Film-Cooled Turbine Endwall in a Transonic Flow Field: Part II—Heat Transfer and Film-Cooling Effectiveness," *ASME J. Turbomach.*, **123**, pp. 720–729.
- [12] Colban, W. F., Thole, K. A., and Zess, G., 2003, "Combustor Turbine Interface Studies-Part I: Endwall Effectiveness Measurements," *ASME J. Turbomach.*, **125**, pp. 193–202.
- [13] Colban, W. F., Lethander, A. T., Thole, K. A., and Zess, G., 2003, "Combustor Turbine Interface Studies-Part I: Flow and Thermal Field Measurements," *ASME J. Turbomach.*, **125**, pp. 203–209.
- [14] Knost, D. G., and Thole, K. A., 2005, "Adiabatic Effectiveness Measurements of Endwall Film-Cooling for a First Stage Vane," *ASME J. Turbomach.*, **127**, pp. 297–305.
- [15] Cardwell, N. D., Sundaram, N., and Thole, K. A., 2007, "The Effects of Varying the Combustor-Turbine Gap," *ASME J. Turbomach.*, **129**, pp. 756–764.
- [16] Rehder, H. J., and Dannhauer, A., 2007, "Experimental Investigation of Turbine Leakage Flows on the 3D Flowfield and Endwall Heat Transfer," *ASME J. Turbomach.*, **129**, pp. 608–618.
- [17] Kost, F., and Mullaert, A., 2006, "Migration of Film-Coolant From Slot and Hole Ejection at a Turbine Vane Endwall," *ASME Paper No. GT2006-90355*.
- [18] Lynch, S. P., and Thole, K. A., 2008, "The Effect of Combustor-Turbine Interface Gap Leakage on the Endwall Heat Transfer for a Nozzle Guide Vane," *ASME J. Turbomach.*, **130**(4), p. 041019.
- [19] Lu, Y., Nasir, H., and Ekkad, S. V., 2005, "Film-Cooling From a Row of Holes Embedded in Transverse Slots," *ASME Paper No. GT2005-68598*.
- [20] Dorrington, J. R., Bogard, D. G., and Bunker, R. S., 2007, "Film Effectiveness Performance for Coolant Holes Imbedded in Various Shallow Trench and Crater Depressions," *ASME Paper No. GT2007-27992*.
- [21] Harrison, K. L., Dorrington, J. R., Dees, J. E., Bogard, D. G., and Bunker, R. S., 2007, "Turbine Airfoil Net Heat Flux Reduction With Cylindrical Holes Embedded in a Transverse Trench," *ASME J. Turbomach.*, **131**(1), p. 011012.
- [22] Kang, M. B., Kohli, A., and Thole, K. A., 1999, "Heat Transfer and Flowfield Measurements in the Leading Edge Region of a Stator Vane Endwall," *ASME J. Turbomach.*, **121**, pp. 558–568.
- [23] Radomsky, R., and Thole, K. A., 2000, "Flowfield Measurements for a Highly Turbulent Flow in a Stator Vane Passage," *ASME J. Turbomach.*, **122**, pp. 255–262.
- [24] Ethridge, M. I., Cutbirth, J. M., and Bogard, D. G., 2001, "Scaling of Performance for Varying Density Ratio Coolants on an Airfoil With Strong Curvature and Pressure Gradient Effects," *ASME J. Turbomach.*, **123**, pp. 231–237.
- [25] Moffat, R. J., 1988, "Describing the Uncertainties in Experimental Results," *Exp. Therm. Fluid Sci.*, **1**, pp. 3–17.
- [26] Kang, M. B., and Thole, K. A., 2000, "Flowfield Measurements at the Endwall Region of a Stator Vane," *ASME J. Turbomach.*, **122**, pp. 458–466.

The Effects of Aerodynamic Asymmetric Perturbations on Forced Response of Bladed Disks

Tomokazu Miyakozawa

Mem. ASME
Postdoctoral Associate
Department of Mechanical Engineering and
Materials Science,
Duke University,
Durham, NC 27708-0300

Robert E. Kielb

Fellow ASME
Associate Chair
Department of Mechanical Engineering and
Materials Science,
Duke University,
Durham, NC 27708-0300

Kenneth C. Hall

Fellow ASME
Julian Francis Abele Professor
Department of Mechanical Engineering and
Materials Science,
Duke University,
Durham, NC 27708-0300

Most of the existing mistuning research assumes that the aerodynamic forces on each of the blades are identical except for an interblade phase angle shift. In reality, blades also undergo asymmetric steady and unsteady aerodynamic forces due to manufacturing variations, blending, mis-staggered, or in-service wear or damage, which cause aerodynamically asymmetric systems. This paper presents the results of sensitivity studies on forced response due to aerodynamic asymmetry perturbations. The focus is only on the asymmetries due to blade motions. Hence, no asymmetric forcing functions are considered. Aerodynamic coupling due to blade motions in the equation of motion is represented using the single family of modes approach. The unsteady aerodynamic forces are computed using computational fluid dynamics (CFD) methods assuming aerodynamic symmetry. Then, the aerodynamic asymmetry is applied by perturbing the influence coefficient matrix in the physical coordinates such that the matrix is no longer circulant. Therefore, the resulting aerodynamic modal forces in the traveling wave coordinates become a full matrix. These aerodynamic perturbations influence both stiffness and damping while traditional frequency mistuning analysis only perturbs the stiffness. It was found that maximum blade amplitudes are significantly influenced by the perturbation of the imaginary part (damping) of unsteady aerodynamic modal forces. This is contrary to blade frequency mistuning where the stiffness perturbation dominates.

[DOI: 10.1115/1.3068319]

1 Introduction

1.1 Mistuning Research With Aerodynamic Coupling. The vast majority of turbomachinery blade mistuning studies have been conducted using only the effect of structural coupling. However, aerodynamic coupling between blades also influences the stability and blade amplitudes. The significance of the aerodynamic coupling effect has been shown in recent literature. For example, Kielb et al. [1,2] investigated the effect of aerodynamic coupling on both flutter and forced response using the single family of modes approach. The results suggested that the mistuning effects on flutter and forced response are dependent on the structural coupling levels. Campobasso and Giles [3] conducted mathematical studies of flutter and forced response including the aerodynamic coupling effect assuming that the effect of the aerodynamic force is due to the blade motions of immediate neighbors. Sladojevic et al. [4] studied the correlation between the aerodynamic blade-to-blade coupling in mistuned bladed disk assemblies and the level of forced response. The analysis showed that the amplification factors were greatly increased due to aerodynamic coupling. He et al. [5] investigated the effects of aerodynamic coupling on both flutter and forced response problems using the tuned system modes to calculate the unsteady aerodynamic forces. For the case studied, aerodynamic coupling showed significant effects on the vibration amplitudes. The previous mistuning studies for both structural and aerodynamic coupling are reviewed by Castanier et al. [6] and Srinivasan [7]. All of these studies considered only blade frequency mistuning.

1.2 Aerodynamic Asymmetries Research. CFD analyses to compute the aerodynamic coupling terms almost always assume

that steady aerodynamic forces from blade to blade are identical. For unsteady cases, the forces are still identical but with a constant interblade phase angle. Therefore, the CFD calculation assumes aerodynamically “tuned” or symmetric systems. In reality, bladed disks experience different steady and unsteady aerodynamic forces from blade to blade. Similar to frequency mistuning, manufacturing tolerance and operational wears can cause perturbed unsteady forces from blade to blade. Intentional mistuning such as alternate frequency mistuning, which can be a flutter suppression tool, might cause different aerodynamic unsteady forces due to the changes in mode shape. Therefore, aerodynamic asymmetry is not considered in most blade design procedures.

However, stability studies due to aerodynamic asymmetry have received some attention in literature. Fleeter and Hoyniak [8] studied the effect of variation of circumferential blade spacing. It was found that alternating blade spacing stabilized a system that was unstable with equal spacing. Sladojevic et al. [9] investigated the effect of alternating stagger angle on stability. Small stagger angle deviations (0.5 deg) did not significantly affect the stability. However, larger variations (2.0 deg) significantly destabilize the system.

Kielb et al. [10] conducted a flutter sensitivity study using the single family of modes approach by perturbing the influence coefficient matrix. It was found that a system was stabilized when the unsteady aerodynamic forces for a single blade were reduced. The system was also stabilized when the unsteady forces were alternately perturbed for even and odd blades. However, a destabilizing effect was found when the unsteady aerodynamic forces for all blades were randomly perturbed. Ekici et al. [11] conducted stability analysis for cases with alternate blade spacing and stagger angles. Diagonal and off-diagonal terms in the modal force matrix in the traveling wave coordinate were computed using CFD techniques. Then, a flutter analysis was conducted using the single family of modes approach. The alternate blade-to-blade spacing case showed a stabilizing effect. However, the alternate blade stagger showed both stabilizing and destabilizing effects on

Contributed by the International Gas Turbine Institute of ASME for publication in the JOURNAL OF TURBOMACHINERY. Manuscript received August 20, 2008; final manuscript received September 3, 2008; published online July 2, 2009. Review conducted by David Wisler. Paper presented at the ASME Turbo Expo 2008: Land, Sea and Air (GT2008), Berlin, Germany, June 9–13, 2008.

the least stable mode depending on the direction of mistagging. Therefore, all of the previous studies of aerodynamic asymmetries focused on flutter analysis.

In terms of the perturbation of unsteady aerodynamics, forced response due to the perturbation of the forcing function (engine order excitation) was studied by Kielb et al. [12]. The assumption was that the forcing function may be perturbed in both amplitude and phase due to small deviations in blade geometry by manufacturing tolerance or field usage, such as erosion and blending. Then, the forced responses were computed by nonpure traveling wave excitation, which is also referred to as forcing function mistuning. This problem can be thought of adding low level noise to pure traveling wave excitations. The results show that the amplification factor became significant only when the structural coupling level is very small (i.e., relatively stiff disks). It was also found that the forcing function mistuning has a small effect on frequency mistuned blade responses. However, the study did not consider the effect of perturbation of the unsteady aerodynamic forces due to blade motions.

The motivation of this study is to investigate the forced response amplification factors from asymmetric perturbation of unsteady aerodynamic forces due to blade motion and compare the resulting behaviors with the effect of frequency mistuning. In previous research, it has been shown that for systems with frequency mistuning, the blade amplification factor can vary over a broad range depending on a variety of parameters such as blade mode shapes, structural and aerodynamic coupling, nodal diameter excitation, and number of blades. The typical maximum amplification factor is 1.6–1.8 (60–80% increase in amplitude) due to frequency mistuning. However, this value can become significantly higher due to strong mode localization, and maximum blade amplifications of larger than 3.0 have been observed. Forced responses due to aerodynamic asymmetries and frequency mistuning will be compared in the section on random force perturbation for all blades.

The structural reduced order model is based on the single family of modes approach developed by Feiner and Griffin [13,14]. The aerodynamic coupling model is determined using unsteady CFD simulations (3D RANS (Reynolds-averaged Navier-Stokes)). Since the structural coupling levels are known to greatly influence stability and blade response due to frequency mistuning, three types of structural coupling levels were also investigated. The aerodynamic asymmetric perturbation shown herein is limited to a sensitivity study. Thus, the perturbed unsteady forces used in this paper do not represent the actual unsteady forces calculated by bladed disks. However, the perturbations used herein are of the same order as those given by Ekici et al. [11].

2 Theory

2.1 Modal Equation of Motion for a Bladed Disk. This section explains the modal equation of motion for an aerodynamically asymmetric and structurally mistuned bladed disk. The equation of motion was initially derived for a structurally mistuned bladed disk to solve flutter and forced response including the aerodynamic coupling effect based on the “single family of modes” approach [1,2]. The single family of approach assumes that the frequencies of the modes are well separated from other families [13,14]. Also, it is assumed that the strain energy is primary stored in the blade, and blade mode shape does not significantly vary.

The reduced order modal equation of motion for forced response of a structurally mistuned bladed disk in the traveling wave coordinates is written as

$$[(\Lambda^0 + \Delta K) - \omega^2(I + \Delta M)]\{Y\} = \{F^m\} + \{W\} \quad (1)$$

where $[\Lambda^0]$ represents the modal stiffness matrix. The structural damping is added to the diagonal terms of the $[\Lambda^0]$ as a complex stiffness.

$$\Lambda_{r,r}^0 = \omega_r^2(1 + i2\zeta_r) \quad (2)$$

where r represents the traveling wave index, which is numbered from 0 to $N-1$. ω_r is the r th tuned system mode frequency due to structural coupling, which is computed using cyclic symmetry finite element methods. ζ_r is the structural damping expressed in terms of the critical damping ratio. $\zeta=0.1\%$ is used for the forced response analyses in this paper. $[I]$ represents the modal mass matrix, which is typically the identity matrix, and ω is the excitation frequency. $[\Delta K]$ and $[\Delta M]$ represent the perturbations in the modal stiffness and mass matrices due to structural mistuning. The effect of structural mistuning is compared with the effect of aerodynamic asymmetric perturbation in the section on random force perturbation for all blades.

The vector $\{Y\}$ is the complex modal displacements expressed in traveling wave coordinates. For a perfectly tuned and symmetric system both structurally and aerodynamically, the blades have the same amplitude by a constant interblade phase angle. The interblade phase angle is a function of traveling wave index and the number of blades and is expressed as

$$\beta_r = \frac{2\pi r}{N} \quad (3)$$

$\{F^m\}$ is the modal force vector due to blade motion, and $\{W\}$ is the modal force vector due to external excitation such as wake passing (engine order excitation). In general, the modal force due to the blade motion is assumed to have identical unsteady aerodynamic forces from blade to blade with a constant interblade phase angle shift. In traveling wave space, the modal force vector becomes

$$\{F^{m0}\} = [A^{m0}]\{Y\} \quad (4)$$

where

$$[A^{m0}] = \begin{bmatrix} a_0 & & & \\ & a_1 & & \\ & & \ddots & \\ & & & a_{N-1} \end{bmatrix} \quad (5)$$

The diagonal matrix $[A^{m0}]$ contains the traveling wave unsteady aerodynamic coefficients, which are usually determined by CFD analysis. a_r represents the complex unsteady force term for the r th interblade phase angle computed using the mode shape and frequency. The unsteady aerodynamic coefficient a_r is computed by integrating the dot product of the local mode shape with the unsteady pressure p_r times the incremental area in the direction of the local normal \mathbf{n} .

$$a_r = -\frac{1}{m_r} \int \phi \cdot (p_r \mathbf{n}) dA \quad (6)$$

The positive and negative values of the real part of the modal forces represent the softening and stiffening effects, respectively, at the corresponding traveling wave indices. Similarly, the positive and negative values of the imaginary parts represent destabilizing and stabilizing effects, respectively.

In reality, blades experience asymmetric unsteady forces referred to as an aerodynamic asymmetry [10]. Therefore, the modal force vector $\{F^m\}$ is expressed by summing the symmetric (tuned) and asymmetric (mistuned) aerodynamic matrices as

$$\{F^m\} = [A^m]\{Y\} = [[A^{m0}] + [\hat{A}^m]]\{Y\} \quad (7)$$

The $[A^m]$ matrix is a full matrix that represents modal coupling effects. Then, the equation of motion with both frequency mistuning and aerodynamic asymmetries becomes

$$[[\Lambda^0] + [\hat{A}] - [A^{m0}] - [\hat{A}^m] - \omega^2[I]]\{Y\} = \{W\} \quad (8)$$

The frequency mistuned matrix $[\hat{A}]$ can be expressed by the fre-

quency variation in each individual blade/disk sector [13].

The aeroelastic eigenvalues (frequency and damping) and their mode shapes can be computed by solving

$$[[\Lambda^0] + [\hat{A}] - [A^{m0}] - [\hat{A}^m] - \omega^2[I]]\{Y\} = \{0\} \quad (9)$$

The blade forced response due to engine order excitation can be computed as

$$\{Y\} = [[\Lambda^0] + [\hat{A}] - [A^{m0}] - [\hat{A}^m] - \omega^2[I]]^{-1}\{W\} \quad (10)$$

The blade responses are calculated as amplification factors, which are the ratio of mistuned to tuned blade amplitude. The tuned magnitude for a single pure traveling wave excitation is given as

$$|y_{r,\text{tuned}}| = \left| \frac{w_r}{2\zeta_r \omega_r^2 - \text{Im}(a_r)} \right| \quad (11)$$

where w_r is the modal forcing function for the nodal diameter of interest. Since the problem is linear and the goal is to find the ratio of mistuned to tuned, a magnitude of 1 can be used for w_r . In this paper, aerodynamic asymmetry is only applied to unsteady aerodynamics due to blade motions. Therefore, unsteady aerodynamic forcing functions are assumed to be symmetric, hence, pure nodal diameter excitations. The mistuned amplitudes are normalized by different tuned amplitudes as the nodal diameter excitation changes, since the tuned system frequency ω_r and unsteady aerodynamic coefficient a_r vary as nodal diameter excitation changes. ζ_r is assumed to be the same for all nodal diameters in this paper.

The physical blade displacements can be obtained by transferring the traveling wave displacement to physical coordinates as

$$\{X\} = [E]\{Y\}, \quad E_{s,r} = e^{-i\beta_s r} \quad (12)$$

where $[E]$ is the discrete Fourier transformation matrix [15].

2.2 Methods of Aerodynamic Asymmetric Perturbations.

This paper focuses on a sensitivity study due to a perturbed aerodynamic matrix. The aerodynamic matrix shown herein does not represent the actual physical aerodynamically asymmetric system. Forced responses analysis using the actual $[A^m]$ matrix computed by CFD given by Ekici et al. [11] is the subject of future research. For the sensitivity study, the unsteady aerodynamic forces due to blade motion will be perturbed in the physical coordinates rather than in the traveling wave coordinates. The representation of the unsteady aerodynamic forces in the physical coordinates can be understood physically since they represent the actual forces on blades.

The physical aerodynamic force matrix can be computed as

$$[A_x^{m0}] = \frac{1}{N} [E][A^{m0}][E^*] \quad (13)$$

The resulting matrix $[A_x^{m0}]$ is known as the influence coefficient matrix.

$$[A_x^{m0}] = \begin{bmatrix} a_{0,0}^0 & a_{0,1}^1 & a_{0,2}^2 & \cdots & a_{0,N-1}^{N-1} \\ a_{1,0}^{N-1} & a_{1,1}^0 & a_{1,2}^1 & \cdots & a_{1,N-1}^{N-2} \\ a_{2,0}^{N-2} & a_{2,1}^{N-1} & a_{2,2}^0 & \cdots & a_{2,N-1}^{N-3} \\ \vdots & \ddots & \ddots & \ddots & \vdots \\ a_{N-1,0}^1 & a_{N-1,1}^2 & a_{N-1,2}^3 & \cdots & a_{N-1,N-1}^0 \end{bmatrix} \quad (14)$$

The diagonal terms represent the unsteady aerodynamic force due to the motion of the blade itself (blade 0 to $N-1$). The blade $N-1$ is identical to the blade -1 . For example, the first row represents the unsteady forces on the zeroth (reference) blade. The entry (0,0) represents the force due to its own motion. (0,1) is the force on the zeroth blade due to motion of blade 1. This contribution of unsteady force on blades is known to be dominated by the reference blade and its adjacent blades [16]. Thus, the tridiagonal terms generally dominate. The real and imaginary parts of each entry represent the frequency and damping due to blade motions. For turbomachinery blades, the imaginary part of the diag-

onal terms is generally negative. Thus, the motion of the blade itself has self-stabilizing effects. If aerodynamically symmetric, the matrix is circulant.

In this paper, the influence coefficient matrix was perturbed similarly to the previous sensitivity study on flutter [10]. The three perturbation types are force perturbation on a single blade, symmetric group force perturbation for even and odd blades, and random force perturbation for all blades.

The first type is when the force on a single blade (reference blade or blade 0) is perturbed. The forces on the reference blade and forces due to other blades on the reference blades are shown in the first row and first column of the influence coefficient matrix. The rest of the entries are unperturbed.

The second type is when the forces for even and odd blades are perturbed as shown in

$$[A_x^m] = \begin{bmatrix} a_{e,e}^0 & a_{e,o}^1 & a_{e,e}^2 & \cdots & a_{e,o}^{N-1} \\ a_{o,e}^{N-1} & a_{o,o}^0 & a_{o,e}^1 & \cdots & a_{o,o}^{N-2} \\ a_{e,e}^{N-2} & a_{e,o}^{N-1} & a_{e,e}^0 & \cdots & a_{e,o}^{N-3} \\ \vdots & \ddots & \ddots & \ddots & \vdots \\ a_{o,e}^1 & a_{o,o}^2 & a_{o,e}^3 & \cdots & a_{o,o}^0 \end{bmatrix} \quad (15)$$

The forces on the blade with the subscripts (e,e) and (o,o) are perturbed. In this case, the resulting influence coefficient matrix becomes a block circulant matrix.

The third type is when the forces for all blades are perturbed randomly. The force perturbation of each entry is applied to all entries for both real and imaginary parts based on their magnitudes. Random perturbations are assumed to be normally distributed and uncorrelated. Monte Carlo simulations were conducted for this case.

This paper focuses on performing sensitivity study without actually calculating the perturbed matrix by CFD. Ekici et al. [11] computed the actual perturbed influence coefficient matrix due to alternately spaced blades. When the influence coefficient is normalized by the magnitude symmetric influence coefficient, the differences between symmetric and perturbed cases were $\pm 4\%$ for the blade itself, 50% for force due to the motion of +1 blade, and 103% for the force due to the motion of +2 blade. Therefore, the amount of perturbation of influence coefficients becomes larger as one goes away from the reference blade. In this paper, for the single blade perturbation, forces related to the reference blade will be reduced by 50%. For the even and odd blades' perturbation, their forces will be perturbed by $\pm 25\%$. For the random perturbation for all blades, three levels of standard deviation of 5%, 10%, and 15% will be applied. Therefore, the perturbation amounts used herein for sensitivity studies are larger for the diagonal terms and of the same order of those for the real CFD results for off-diagonal terms.

Finally, unsteady aerodynamic modal forces in traveling wave space can be recovered as

$$[A^m] = \frac{1}{N} [E^*][A_x^m][E] = \frac{1}{N} [E^*][A_x^{m0} + \hat{A}_x^m][E] \quad (16)$$

The resulting modal force matrix in traveling wave coordinates is no longer diagonal. The flutter and forced response due to the aerodynamic asymmetric perturbation are then calculated using the full modal force matrix using Eqs. (9) and (10).

3 Case Studies

The representative rotor consists of 34 blades, and the blade alone frequency is 977 Hz. Figure 1 shows the tuned system mode frequencies as a function of nodal diameter for the first flex mode. The level of structural coupling is expressed by the frequency separation parameter, Δf , which is computed as the frequency separation between the maximum and minimum and normalized by the average frequency. The frequency separation parameters are 1.95% for a stiff disk and 4.9% for a flexible disk. The mode shapes are

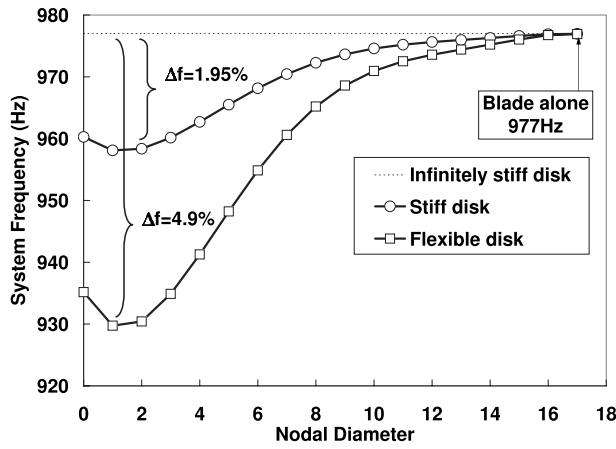


Fig. 1 Tuned system mode frequencies for stiff and flexible rotors versus nodal diameter

blade dominated modes, and hence, the strain energy is primary in the blades at all nodal diameters. These families of modes are assumed to be isolated from neighboring families. Therefore, the modal coupling effect from other families due to structural mistuning is negligible. If the disk is infinitely stiff (aerodynamic coupling only), the tuned system frequency at all nodal diameters becomes the blade alone frequency of 977 Hz. The effect of structural coupling levels will be investigated in the later sections by considering the infinitely stiff, stiff, and flexible disks.

Figure 2 shows the unsteady aerodynamic traveling wave modal forces for the stiff and flexible rotors, which were computed using the first flex mode shape and blade alone frequency of 977 Hz. The modal forces are assumed to be the same for the stiff and flexible rotors. The positive nodal diameter indicates a forward traveling wave (FTW), and the negative indicates a backward traveling wave (BTW). Since the imaginary parts of the modal forces are all negative, these two rotors are stable without structural damping at all nodal diameters.

Figure 3 shows the aeroelastic eigenvalues for the stiff disk by assuming that no structural damping exists in the system. The corresponding nodal diameters are labeled. Stiffening effects are observed at higher nodal diameter modes. All nodal diameter modes are stable because the aeroelastic damping values are positive. The damping becomes larger as the nodal diameter increases.

Figure 4 shows the tuned blade amplitudes for all nodal diameters for the three types of structural coupling, which were computed by Eq. (11). All of the later forced response results will be normalized by the corresponding tuned amplitudes. For the per-

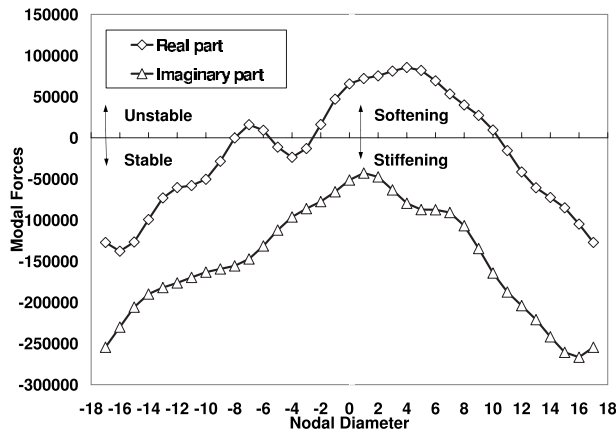


Fig. 2 Unsteady aerodynamic modal forces due to blade motion for first flex mode versus nodal diameter

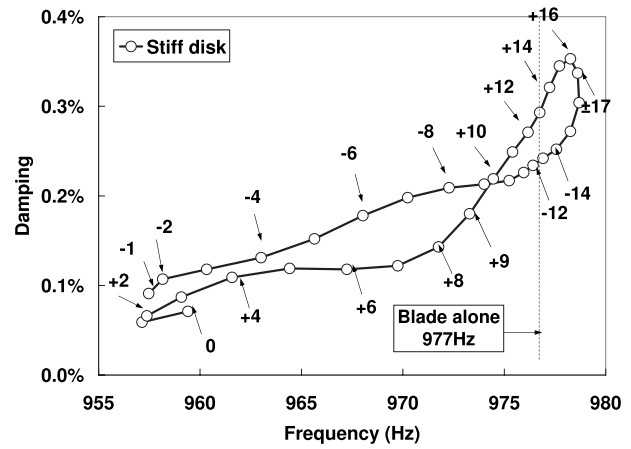


Fig. 3 Aeroelastic eigenvalues for stiff disk without structural damping for all nodal diameters

fectedly structurally and aerodynamically symmetric system, the maximum tuned response is produced by a 1ND excitation using a flexible disk. The tuned amplitudes decrease as nodal diameter increases due to higher aerodynamic damping that can be observed in Fig. 2, where the imaginary part of modal force is maximum at 1ND. It can be seen that the addition of structural coupling shows only a small effect at small nodal diameters.

4 Forced Response Results

4.1.1 Single Blade Perturbation. The unsteady aerodynamic forces for the reference blade (zeroth blade) were reduced by 50%. Therefore, the real and imaginary parts in the first row and first column of the influence coefficient matrix shown in Eq. (14) were reduced by 50% from the symmetric values.

Figure 5 shows the frequency response function (FRF) for the stiff disk that was subjected to a 12ND FTW excitation. The maximum blade amplification of 1.3 was produced by the reference blade at an excitation frequency of 975.9 Hz. Amplifications of the adjacent ± 1 blades became the next greatest at 975.7 Hz for +1 and 976.5 Hz for -1 blade. No secondary resonant peak was observed.

Figure 6 shows amplification factors for all blades at the excitation frequency of 975.9 Hz. (± 17 blade is the same blade.) The amplification factor of the reference blade increased as well as adjacent ± 1 blades. The influence of amplification factors is clear within ± 3 blades. The rest of the blade amplification factors be-

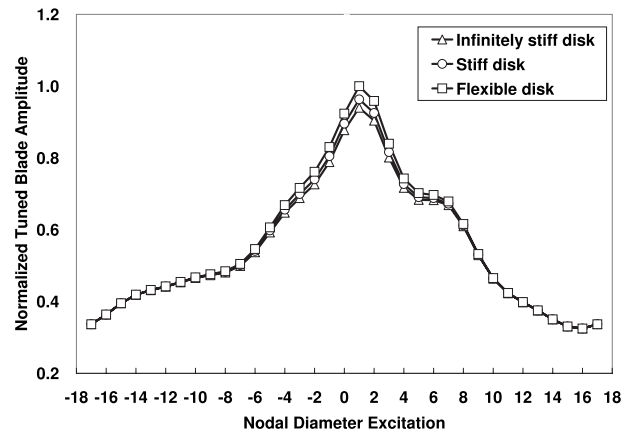


Fig. 4 Normalized tuned blade amplitude versus nodal diameter excitations

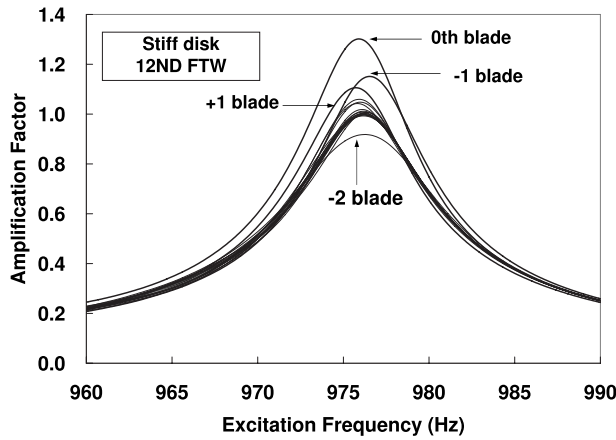


Fig. 5 FRF for all blades due to single blade force perturbation reduced by 50% that is subjected to a 12ND FTW excitation

come almost the same as the symmetric amplification factor of 1. Figure 7 shows the maximum blade amplifications using three structural coupling levels as a function of all nodal diameter excitations. For stiff and flexible disks, the amplification factors between ± 6 nodal diameter excitations are almost the same as the tuned case. In these cases, the maximum amplifications were not produced by the reference blade. The blade amplifications become higher when the system was subjected to higher nodal diameter

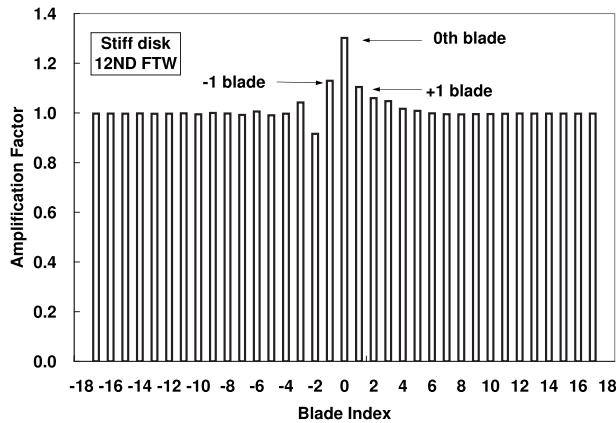


Fig. 6 All blade amplifications at resonant frequency due to single blade force perturbation reduced by 50% that is subjected to a 12ND FTW excitation

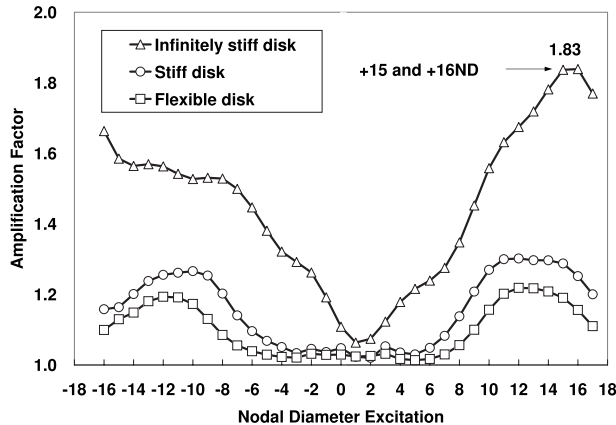


Fig. 7 Maximum blade amplifications due to single blade force perturbation reduced by 50% versus nodal diameter excitations

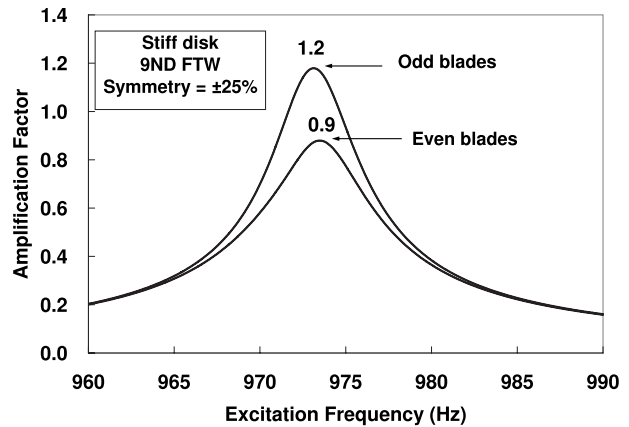


Fig. 8 FRF for all blades due to symmetric group force perturbation by $\pm 25\%$ that is subjected to a 9ND FTW excitation

FTW and BTW excitations. In these cases, the reference blade became the maximum response. When no structural coupling exists in the system (aerodynamic coupling only), the blade amplification increases as nodal diameter increases. The maximum amplification became 1.84 at a 16ND FTW excitation.

Reduction in the aerodynamic damping by 50% on the reference blade does not double the amplification as a single degree freedom system because the amplification factors are still suppressed due to the aerodynamic damping effects from the motions of the neighboring blades. However, for the infinitely stiff disk, the behavior becomes similar to the single degree freedom system as nodal diameter increases. In fact, the trend of amplifications as a function of nodal diameter for the aerodynamic coupling only case matches the trend of the imaginary parts of the modal forces shown in Fig. 2 when they are inverted. Therefore, the larger the aerodynamic damping in the symmetric case, the higher the blade amplification due to the single blade force perturbation. The amplification factors are much more suppressed when structural coupling exists. It should be noted that each amplification factor is normalized by different tuned amplitudes as shown in Fig. 4 because the tuned amplitude varies as nodal diameter excitation changes.

4.1.2 Symmetric Group Force Perturbation. The amplification factors of the blade responses were computed to investigate the effect of symmetric group force perturbation. The unsteady aerodynamic forces were perturbed by increasing even blades by 25% and reducing odd blades by 25%. When the block circulant matrix as shown in Eq. (15) is transferred to the traveling wave coordinate using Eq. (16), the resulting modal force matrix can be considered as 2×2 matrices as shown in Eq. (17). It can be noticed that mode i will only be coupled with the mode $i+N/2$.

$$[A^m] = \begin{bmatrix} a^{i,i} & a^{i,i+N/2} \\ a^{i+N/2,i} & a^{i+N/2,i+N/2} \end{bmatrix} \quad (17)$$

Figure 8 shows the FRF for a stiff disk when subjected to 9ND FTW excitation. The amplifications for even and odd blades were clearly split into two different amplitudes. Their resonant amplitudes and frequency were 1.18 at 973.1 Hz for odd blades and 0.88 at 973.5 Hz for even blades. Thus, the blades with reduced unsteady forces produced higher amplification factors, and for increased unsteady forces produced less amplification factor.

Figure 9 shows the maximum blade amplifications as a function of all nodal diameters. When structural coupling exists in the system, the amplifications are strongly influenced by nodal diameter excitations. For stiff and flexible disks, the amplification becomes highest at -8 and $+9$ nodal diameter excitations and their immediate neighbors. For the rest of nodal diameters, the amplification factors did not increase. According to Eq. (17), $+9$ and -8 are the

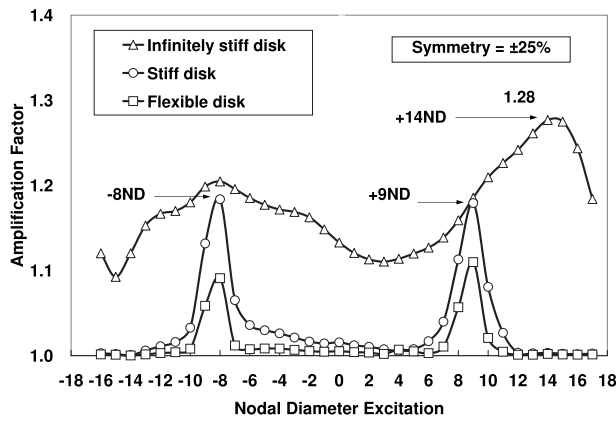


Fig. 9 Maximum blade amplifications due to symmetric group force perturbation by $\pm 25\%$ versus nodal diameter excitations

coupled nodal diameters. In fact, the modal coupling pairs of (8, -9), (9, -8), and (10, -7) nodal diameters have less frequency separations between the two modes, which can be confirmed in Fig. 3. Figure 9 shows that only those combinations of nodal diameters show an increase in amplification factor. Other combinations of modal coupling are not close enough in frequency to increase in amplitude. When no structural coupling exists in the system (aerodynamic coupling only), the amplification factors increase at all nodal diameter excitations. The highest amplification factor was observed as 1.28 when subjected to 14 and 15 nodal diameter FTW excitations. For the 14 nodal diameter excitation, the blade amplification became 0.77 for even and 1.28 for odd blades.

4.1.3 Random Force Perturbation for All Blades. Amplifications of blade responses were calculated to investigate the effect of randomly perturbed aerodynamic asymmetries. The standard deviations applied at all entries of the real and imaginary parts of Eq. (14) were based on their magnitudes of the complex value, and it is assumed to be normally distributed. 1000 Monte Carlo simulations were conducted. At each simulation, the maximum blade amplifications were selected, and the order of the 1000 maximum amplifications were sorted to find the 95 percentile amplifications.

Figure 10 shows the FRF for a stiff disk, which is subjected to a 3ND BTW excitation by applying a standard deviation of 15% by aerodynamic asymmetries. The results were compared with the effect of frequency random mistuning of a standard deviation of

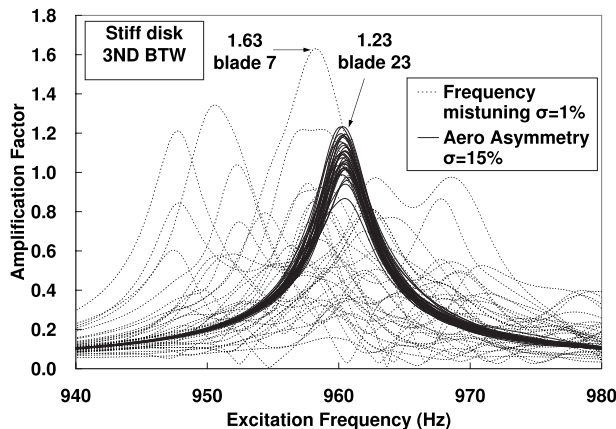


Fig. 10 FRF for all blades due to random aerodynamic asymmetric force perturbation and frequency mistuning that are subjected to a 3ND BTW

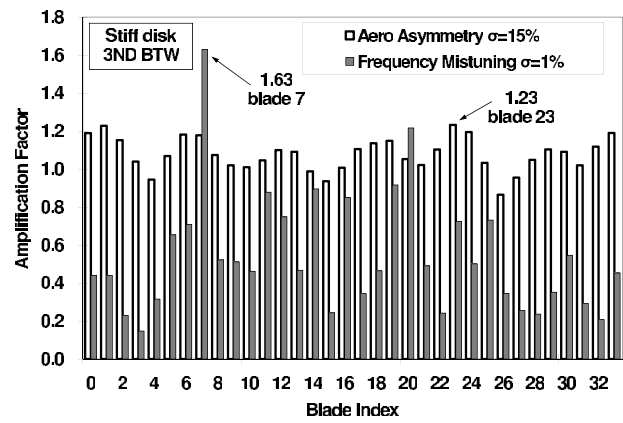


Fig. 11 All blade amplifications at resonant frequency due to random aerodynamic asymmetric force perturbation and frequency mistuning that are subjected to a 3ND BTW

1%, which would be considered the variation in manufacturing tolerance. Both results represent the 95 percentile amplification factors of 1000 Monte Carlo simulations. For the aerodynamic asymmetries, the maximum amplification of 1.23 was experienced by blade 23 at an excitation frequency of 960.3 Hz. No secondary resonant peaks were observed. On the other hand, the results of frequency mistuning showed that multiple peaks were observed over a broad range of excitation frequencies. The maximum amplification factor of 1.63 was produced by blade 7 at the excitation frequency of 958.3 Hz.

Figure 11 shows the blade amplifications due to aerodynamic asymmetries and frequency mistuning for a stiff disk at each resonant frequency. For aerodynamic asymmetries, the blade amplification factors show global responses whose blade amplifications are nearly the same. Thus, the maximum blade amplification factor at blade 23 is not a localized response. However, for frequency mistuning, significant mode localizations were observed at blade 7, and most of the blades became less than the tuned amplification factor.

Figures 12 and 13 show the amount of the perturbed imaginary parts of the influence coefficient matrix, \hat{A}_x^m for top and bottom views, respectively. The top view shows how much imaginary parts are added, and the bottom view shows how much imaginary parts are reduced. Diagonal terms represent the differences of self-

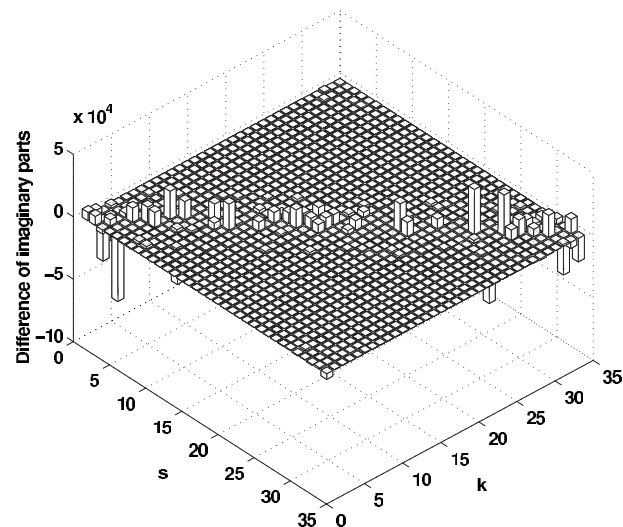


Fig. 12 Top view of perturbed forces of imaginary parts of influence coefficient matrix

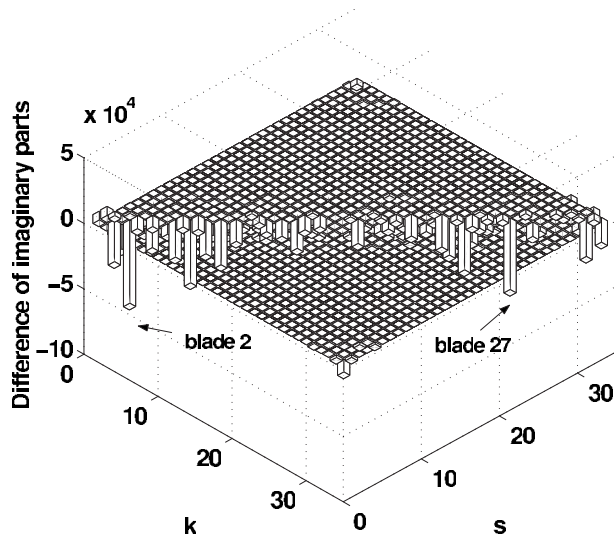


Fig. 13 Bottom view of perturbed forces of imaginary parts of influence coefficient matrix

damping. The maximum blade amplification factor for a stiff disk due to aerodynamic asymmetric perturbation was found to be 1.23 at blade 23 as shown in Fig. 11. It can be seen that the self-damping at blades 2 and 27 is significantly reduced as shown in Fig. 13. However, their amplification factors did not become significantly high due to the coupling effect from neighboring blades. In fact, the imaginary part for blade 23 was reduced drastically, but the self-damping of blade 24 also was reduced. Therefore, blades 23 and 24 both became high amplification factors as shown in Fig. 11.

Figure 14 shows the cumulative distribution function of the 1000 maximum blade amplifications for a stiff disk subjected to a 3ND BTW excitation for aerodynamic asymmetries and frequency mistuning. Each line represents the 1000 maximum blade amplification factors computed using a standard deviations of 5%, 10%, and 15% for aerodynamic asymmetries and 1% for frequency mistuning. For frequency mistuning, the amplification factors increase significantly and the 95 percentile response becomes 1.63. For aerodynamic asymmetries, for the standard deviation of 5%, the maximum blade amplifications increase, and the 95 percentile response becomes only 1.07. For the larger standard deviations of 10% and 15%, the maximum blade amplifications became larger, especially at higher cumulative probabilities. Thus, the maximum blade amplification increased as random aerodynamic asymmetric

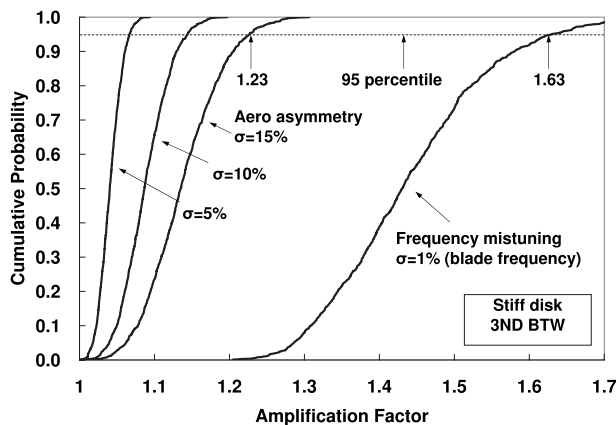


Fig. 14 CFD of maximum blade amplifications due to random aerodynamic asymmetric force perturbation and frequency mistuning that are subjected to a 3ND BTW

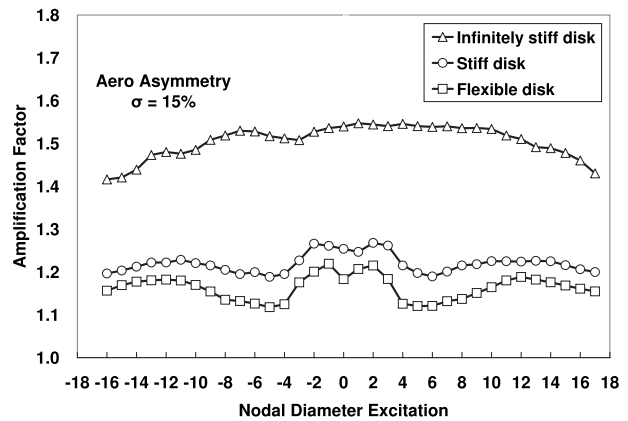


Fig. 15 95 percentile of maximum blade amplification factors due to random aerodynamic asymmetric force perturbation versus nodal diameter excitations.

perturbation level increased. However, the system showed much more sensitivity of amplification factors to frequency mistuning than aerodynamic asymmetric perturbations.

Figure 15 shows the 95 percentile maximum blade amplification factors for three structural coupling levels as a function of nodal diameter excitations by applying a standard deviation of 15% due to aerodynamic asymmetries. For stiff and flexible disks, no significant amplifications were observed. The amplifications became higher within ± 3 or higher nodal diameters. For an infinitely stiff disk, the amplifications at all nodal diameter excitations increased significantly. For all structural coupling cases, the amplification factors were nearly the same at all nodal diameters.

Figure 16 shows the effect of aerodynamic asymmetries on a structurally mistuned system. The results show the 95 percentile maximum blade amplification factors for a stiff disk as a function of nodal diameter excitation by applying frequency mistuning only or both frequency mistuning and aerodynamic asymmetry perturbation. The case of only frequency mistuning significantly increases the amplification factor at all nodal diameters compared with those by only aerodynamic asymmetries as shown in Fig. 15. High amplification factors are observed such as 1.76 at +16ND and 1.68 at -2ND. When aerodynamic asymmetries due to a standard deviation of 15% are added, the 95 percentile amplification factors increased at all nodal diameters. However, the behavior is still predominantly determined by frequency mistuning rather than aerodynamic asymmetric perturbations.

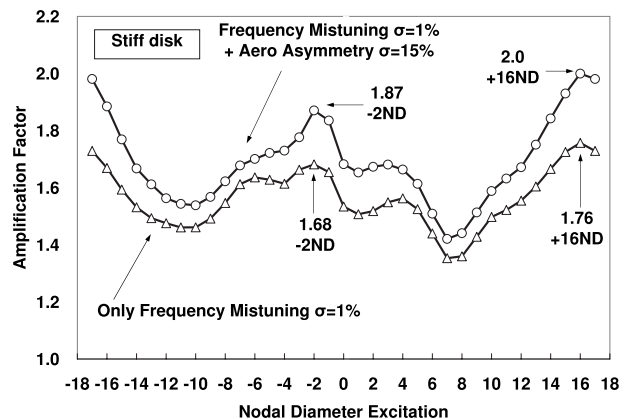


Fig. 16 95 percentile of maximum blade amplification factors due to random aerodynamic asymmetric force perturbation and frequency mistuning versus nodal diameter excitations

5 Summary and Conclusions

This paper presents the results of the effects of aerodynamic asymmetric perturbations on forced response for bladed disks and blisks. The high fidelity model includes both structural and aerodynamic coupling based on the single family of modes approach. The aerodynamic asymmetry perturbations were applied in the influence coefficient matrix. The resulting unsteady aerodynamic matrix is generally full.

For the case of force perturbation for a single blade, amplifications of the reference blade and its adjacent blades increased when the unsteady forces were reduced by 50% for the reference blade. However, inclusion of structural coupling greatly suppressed the amplification. No significant modal coupling effect was observed.

For the case of symmetry group force perturbation, the behavior was found to be monotonic such that the blade amplifications increased because their unsteady forces were reduced for odd blades, and amplifications decreased when their unsteady forces were increased for even blades. A modal coupling effect was observed only when the two tuned system modes are close in frequency.

For the case of random force perturbation for all blades, the blade amplifications increased as the random perturbation level increased. Therefore, the behavior was similar to that of frequency mistuning. However, even 15% of random perturbation level did not produce significant blade amplification factors. No significant localized responses were observed. The amplification factors were dominated by frequency mistuning when the system was perturbed both structurally and aerodynamically.

For all the cases, increased structural coupling showed beneficial effects to suppress the maximum blade amplifications. For most of the cases, the maximum blade amplifications were observed when the aerodynamic damping on the blade itself was reduced. Thus, the maximum blade amplifications were predominantly determined by perturbation of the imaginary part of the unsteady aerodynamic forces. No significant mode localization effects were found.

Nomenclature

a_r	= unsteady aerodynamic coefficients, traveling wave space
$a^{i,i}$	= unsteady aerodynamic block matrix, traveling wave space
$a_{s,k}^n$	= force on blade s due to motion of blade k
\hat{A}	= frequency mistuning matrix
A^m	= aerodynamic force matrix in traveling wave space
\hat{A}^m	= mistuned aerodynamic matrix in traveling wave space
A_x^m	= aerodynamic force matrix in physical blade space
\hat{A}_x^m	= mistuned aerodynamic matrix in physical blade space
E	= discrete Fourier transformation matrix
F^m	= aerodynamic modal forces due to blade motion
i	= imaginary unit
I	= identity matrix (tuned mass matrix)
Δf	= frequency separation parameter
ΔK	= stiffness matrix perturbation due to mistuning
ΔM	= mass matrix perturbation due to mistuning
m_r	= modal mass

N	= number of blades
p_r	= unsteady pressure
r	= traveling wave index
W	= modal force vector due to external excitation
X	= blade displacement, physical blade coordinates
Y	= modal blade displacement, traveling wave coordinates
ω	= complex frequency
Λ^0	= tuned stiffness matrix
β_r	= interblade phase angle
ϕ	= mode shape
ζ	= critical damping ratio
0	= tuned or symmetric
$*$	= complex conjugate

Acknowledgment

This work was partially sponsored by an STTR grant from the Blade Diagnostics Corporation (BDC) and the U.S. NAVY with technical oversight provided by Dr. Jerry Griffin and Mr. Mark Klein.

References

- [1] Kielb, R. E., Feiner, D. M., Griffin, J. H., and Miyakozawa, T., 2004, "Flutter of Mistuned Bladed Disks and Blisks With Aerodynamic and FMM Structural Coupling," *Proceedings of the ASME Turbo Expo*, Vol. 6, pp. 573–579.
- [2] Kielb, R. E., Feiner, D. M., Griffin, J. H., and Miyakozawa, T., 2005, "Probabilistic Analysis of Mistuned Bladed Disks and Blisks With Aerodynamic and FMM Structural Coupling," Ninth National Turbine Engine HCF Conference, Mar.
- [3] Campobasso, M., and Giles, M., 2000, "Flutter and Forced Response of Mistuned Turbomachinery," Oxford University Computing Laboratory, Report No. NA 00/20.
- [4] Sladojevic, J., Petrov, E., Sayma, A., Imregun, M., and Green, J., 2005, "Investigation of the Influence of Aerodynamic Coupling on Response Levels of Mistuned Bladed Disks With Weak Structural Coupling," *Proceedings of the ASME Turbo Expo*, Vol. 4, pp. 543–551.
- [5] He, Z., Epureanu, B., and Pierre, C., 2007, "Fluid-Structural Coupling Effects on the Dynamics of Mistuned Bladed Disks," *AIAA J.*, **45**(3), pp. 552–561.
- [6] Castanier, M. P., and Pierre, C., 2006, "Modeling Analysis of Mistuned Bladed Disk Vibration: Status and Emerging Directions," *J. Propul. Power*, **22**(2), pp. 384–396.
- [7] Srinivasan, A. V., 1997, "Flutter and Resonant Vibration Characteristics of Engine Blades," *ASME J. Eng. Gas Turbines Power*, **119**(4), pp. 742–775.
- [8] Fleeter, S., and Hoyniak, D., 1989, "Aeroelastic Detuning for Stability Enhancement of Uninstalled Supersonic Flutter," *Int. J. Turbo Jet Engines*, **6**, pp. 17–26.
- [9] Sladojevic, J., Sayma, A., and Imregun, M., 2007, "Influence of Stagger Angle Variation on Aerodynamic Damping and Frequency Shifts," *Proceedings of the ASME Turbo Expo*, Vol. 5, pp. 683–700.
- [10] Kielb, R. E., Hall, K. C., and Miyakozawa, T., 2007, "The Effect of Unsteady Aerodynamic Asymmetric Perturbations on Flutter," *Proceedings of the ASME Turbo Expo*, Vol. 5, pp. 649–654.
- [11] Ekici, K., Kielb, R. E., and Hall, K. C., 2008, "Aerodynamic Asymmetry Analysis of Unsteady Flows in Turbomachinery," *Proceedings of the ASME Turbo Expo 2008*.
- [12] Kielb, R. E., Hall, K., Miyakozawa, T., and Hong, E., 2006, "Mistuning Pattern Effects on Probabilistic Flutter and Forced Response," 11th International Symposium on Unsteady Aerodynamics, Aeroacoustics and Aeroelasticity of Turbomachines, ISUAAAT-2006.
- [13] Feiner, D., and Griffin, J., 2003, "Mistuning Identification of Bladed Disks Using a Fundamental Mistuning Model—Part 1: Theory," *Proceedings of the ASME Turbo Expo*, Vol. 4, pp. 267–277.
- [14] Feiner, D., and Griffin, J., 2003, "Mistuning Identification of Bladed Disks Using a Fundamental Mistuning Model—Part 2: Application," *Proceedings of the ASME Turbo Expo*, Vol. 4, pp. 279–286.
- [15] Whitehead, D. S., 1966, "Effect of Mistuning on the Vibration of Turbomachine Blades Induced By Wakes," *J. Mech. Eng. Sci.*, **8**, pp. 15–21.
- [16] Panovsky, J., and Kielb, R. E., 2000, "A Design Method to Prevent Low Pressure Turbine Blade Flutter," *ASME J. Eng. Gas Turbines Power*, **122**, pp. 89–98.

Investigations on the Discharge and Total Temperature Increase Characteristics of the Labyrinth Seals With Honeycomb and Smooth Lands

Xin Yan

Jun Li

e-mail: junli@mail.xjtu.edu.cn

Liming Song

Zhenping Feng

Institute of Turbomachinery,
School of Energy and Power Engineering,
Xi'an Jiaotong University,
Xi'an 710049, P. R. China

The viscous work generated by the rotating components of a seal not only represents a direct loss of power but also causes an increase in the total temperature of fluid (windage effect). In order to study the discharge and total temperature increase characteristics of the stepped labyrinth seals with smooth and honeycomb lands, 3D Reynolds-averaged Navier–Stokes solutions from CFX is used in this work. At first, the influences of the inlet preswirl, leakage flow rate, and rotational speed on the total temperature increase in the convergent and divergent stepped labyrinth seals with smooth and honeycomb lands are conducted. The obtained 3D numerical results are well in agreement with the referenced experimental data. It shows that the utilized numerical approach has sufficient precision to predict the total temperature increase in seals. Then, a range of pressure ratios and four sizes of sealing clearance are performed to investigate the effects of sealing clearances and pressure ratio impact on the discharge and total temperature increase of the stepped labyrinth seals with honeycomb and smooth liners. [DOI: 10.1115/1.3068320]

1 Introduction

Nowadays, the increasing demands of performance and fuel efficiencies for the gas turbine engine lead to an increase in core flow temperature. In order to protect the turbine airfoil from thermal stress fields created by exposure to the combustion gases, more and more advanced cooling technologies are introduced by the researchers. However, achievements of enhancing cooling for the gas turbine engine will encounter the windage heating effect in seals. In the internal cooling air system, seals serve the purpose of metering the cooling air to prevent hot air ingress. The viscous work generated by the rotating components, the so-called windage heating effect, will induce an increase in the total temperature of the fluid. It degrades the cooling quality and in turn necessitates increasing the quantities of cooling flow extracted from the main gas path. Neglect of such effect will decrease the lifetime of blades working in a high temperature environment. Second, the cooling air is contaminated by the labyrinth seal leakage flow and then passes into the blades or interstage cavities for the purpose of cooling. The heat transfer characteristics in the next gas path are directly affected by the former outlet temperature and exit swirl. As a result, cooling air temperature is the most important information for a gas turbine designer or researcher to evaluate the cooling quality of the components and quantity of the cooling flow. Hence it is crucial to study the total temperature increase characteristic in the seal.

There are many factors that can affect windage effect. One of these factors is the inlet preswirl. The positive preswirl will decrease the total temperature difference between seal inlet and outlet [1–3]. Another factor is the swirl development in the seal chamber. Moreover, for interstage seals, the exit swirl can change the incidence angle of the main flow into the downstream blades,

thereby generating stage loss [4]. Empirical results as well as theoretical analysis have shown that other factors, such as pressure ratio, seal geometry, rotational speed, and thermodynamic parameters, may impact the discharge characteristics [5–7] and temperature distributions [8] of a seal. Many simple correlation equations based on the experimental data were derived and used to predict the performance of the seal. However, these equations require empirical corrections to have the prediction match the experimental results. And different researchers may choose different correction factors for different seals [1]. Therefore, it is hard to decide the factors for every new design. Recently, the progress of computer and computational fluid dynamics (CFD) technologies makes it possible to utilize a numerical simulation to predict the performance of rotating seals. And it is also convenient to obtain the correction factors directly if the validity of the numerical method has been demonstrated.

In the present paper, in order to investigate how these factors, such as pressure ratio and sealing clearance, affect the windage heating and discharge behavior, numerical investigations are performed to calculate the total temperature increase and leakage rate in the stepped labyrinth seals configured with smooth and honeycomb lands. First of all, the computed windage heating numbers and detailed velocity profiles within the seal chambers are compared with the obtained experimental data. After the accuracy and reliability of the utilized numerical method have been demonstrated, the influence of pressure ratios and sealing clearance sizes on the leakage flow and windage heating is investigated in detail.

2 Literature Review

The research on windage heating effect was initially performed by using the experimental methods. Based on the experimental data, simple correlations were derived and used to predict the windage loss for other seals. The first experimental data for the windage heating was reported by Stocker et al. [9]. They measured the power losses of the straight-through and stepped labyrinth seals. The experiment conducted by Tipton et al. [10] in the

Contributed by the International Gas Turbine Institute of ASME for publication in the JOURNAL OF TURBOMACHINERY. Manuscript received August 21, 2008; final manuscript received September 1, 2008; published online July 2, 2009. Review conducted by David Wisler. Paper presented at the ASME Turbo Expo 2008 Land, Sea and Air (GT2008), Berlin, Germany, June 9–13, 2008.

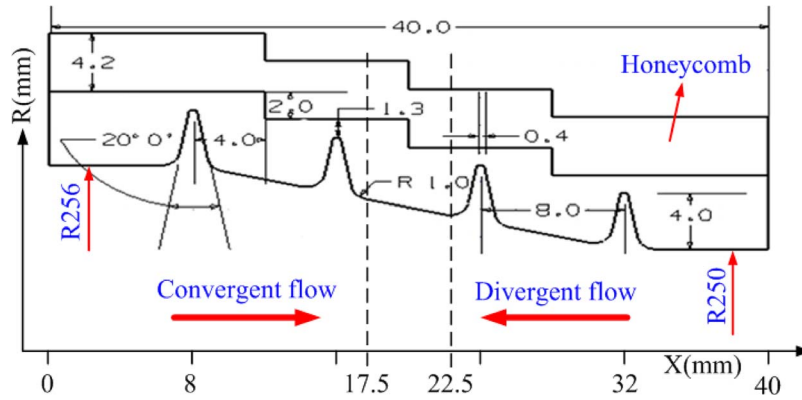


Fig. 1 Stepped labyrinth seal geometry

test seal rig shows that the temperature increase can reach up to 19.4 K and is influenced by the pressure ratio, rotor speed, and sealing clearance.

McGreehan and Ko [3] presented a correlation based on the energy conservation law and wall shear stress expressions to predict the total temperature increase with different inlet preswirl ratio, mass flow rate, and rotational speed. But it requires empirical correction to have the predictions match the experimental results.

Millward and Edwards [11] measured the windage heating power in various seals with a plain liner and derived a simple correlation (Eq. (1)) for windage power prediction in labyrinth seals with smooth and honeycomb lands. However, the credibility of the predictions for plain liner seals in their experiments was within $\pm 25\%$, and the worst value can reach up to $+40\%$. Moreover, this correlation was not suitable for the seal with inlet preswirl,

$$H = Cms \cdot \pi X \rho \omega^3 R_m^4$$

$$Cms = 6 \times 10^{-5} \left[\frac{C_w}{Re} \right]^{0.55} \cdot n^{-0.65}$$

$$H_{HC} = 1.15H \quad (1)$$

Denecke et al. [4] reported that the discharge behavior, windage heating, and exit swirl velocity can be uniquely defined by several dimensionless numbers in Eq. (2) from dimensional analysis and scaling methods. They utilized experiments [1] to measure the windage heating in the labyrinth seals with smooth and honeycomb stators. They also measured the tangential velocity at two special positions in the seal chamber using the laser Doppler velocimeter (LDV) method. Besides these investigations, they calculated the windage heating number for a labyrinth seal with a smooth stator by using the CFD commercial software FLUENT. They used a 2D axis-symmetric geometry model to investigate the total temperature difference in the smooth configuration. Their numerical results did not show good agreement with the experiment data in most cases, and they did not calculate the windage heating number of the honeycomb configuration. So, the main objective of the present work is to utilize a 3D numerical method to investigate the windage heating effect and discharge behavior in the labyrinth seals with smooth and honeycomb lands based on the experimental work [1],

$$\left. \begin{matrix} C_D \\ \sigma \\ K_{out} \end{matrix} \right\} = f(\Pi, Re_x, M_U, K_{in}, \text{geometry}, \kappa, Pr)$$

$$C_D = \frac{\dot{m}}{\dot{m}_{id}} = \frac{\dot{m} \sqrt{T_{total,in}}}{\dot{Q}_{id} \cdot P_{in} \cdot A}$$

$$\dot{Q}_{id} = \sqrt{\frac{2\kappa}{R(\kappa-1)} \cdot \left[\left(\frac{1}{\Pi} \right)^{2/\kappa} - \left(\frac{1}{\Pi} \right)^{(\kappa+1)/\kappa} \right]}$$

$$\Pi = \frac{P_{in}}{P_{out}} \cdot \left(1 + \frac{\kappa-1}{2} K_{in}^2 M_U^2 \right)^{-\kappa/(\kappa-1)} \quad (2)$$

3 Numerical Approach

3.1 Computational Model. In this work, the computational geometrical parameters of the convergent and divergent stepped labyrinth seals with smooth and honeycomb lands are obtained from Ref. [1]. The stepped labyrinth seal geometry with smooth and honeycomb configurations is defined in Fig. 1. It features four straight knives for convergent or divergent steps (depending on the flow direction) on the rotor. The cell width of the honeycomb configuration is 1.59 mm (1/16 in.), and the cell depth is 4.2 mm. Also, each seal has a tip thickness of 0.4 mm.

3.2 Numerical Method. Since the flow in stepped labyrinth seals with smooth and honeycomb lands is typically three-dimensional turbulence due to their structures and flow conditions and since there exists high relative rotating speed, it is necessary to solve 3D Reynolds-averaged Navier–Stokes (RANS) equations to analyze their flow patterns and predict their total temperature increase.

A multiblock structured grid is generated for the computational case. Figure 2 gives the impression of the computational grids for two seals and corresponding boundary condition definitions. In Fig. 2(a), the mesh generation of the honeycomb labyrinth seal is shown. In the honeycomb land case, two honeycomb cells are used in the circumferential direction and periodic boundary definition. Figure 2(b) shows the mesh and boundary definitions for the smooth labyrinth seal.

In order to study the flow and heat transfer characteristics for the convergent and divergent stepped labyrinth seals with smooth and honeycomb lands, the commercial finite volume code CFX [12] is used. This software solves the compressible time-averaged RANS equations. And a second order high resolution discretization scheme is used. The turbulence characteristics of the flow are modeled by the standard $k-\epsilon$ equations. The scalable logarithmic wall function is used to describe the near wall velocity. The y^+ criterion is met over almost the entire wall region. The boundary conditions and numerical methods are listed in Table 1. The total temperature (300 K) and mass flow rate or the total temperature and total pressure are given at the inlet. The outlet static pressure

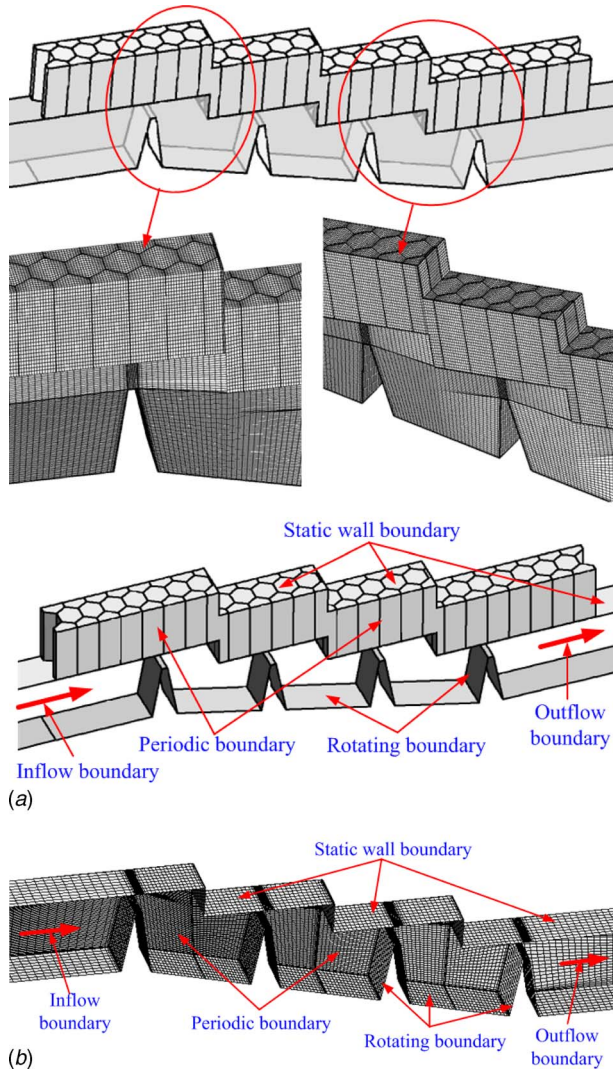


Fig. 2 Calculated seal mesh and boundary condition definition

is 200,000 Pa. The desired convergent target of each simulation is that the root mean square (rms) residuals of the momentum and mass equations, energy equation, and turbulence equations reach (or even lower than) 10^{-6} .

3.3 Windage Heating. In the adiabatic flow condition, the total temperature increase due to the internal losses in labyrinth seals is described as windage heating H using

$$H = \dot{m} \cdot C_p \cdot \Delta T_{\text{total}} \quad (3)$$

The windage heating number σ is defined as

$$\sigma = 2C_p \Delta T_{\text{total}} / U^2 \quad (4)$$

Table 1 Conditions and numerical methods

Average rotor radius	0.253 m
Inlet total temperature	300 K
Outlet static pressure	200,000 Pa
Discretization scheme	High resolution
Computational method	Time marching method
Turbulence model	$k-\epsilon$, scalable log wall function
Fluid	Air (ideal gas)
Wall properties	Adiabatic smooth surface

Table 2 Windage heating numbers σ of the labyrinth seal with smooth land

Grid number	CFD	Expt.
94,000	0.38	
142,000	0.39	0.38
250,000	0.39	

The discharge behavior can affect the windage heating and swirl within the seal, as Scherer [13] found from numerical simulations. In that study, an effective pressure ratio Π is used instead of π to account for the influence of the inlet preswirl on the leakage [14].

3.4 Grid Independence Analysis. Before comparisons are made to the experiment, a mesh independence study is performed to determine how fine a mesh density is necessary to capture the flow physics.

The axial Reynolds number Re_x was kept at 10,000, and a circumferential Mach number Mu was 0.31. Then the windage heating number of the stepped labyrinth seal with smooth land was derived with 94,000, 142,000, and 250,000 nodes separately, as shown in Table 2. The differences between the CFD value and experimental data are about 0%, 2.6%, and 2.6%. In order to balance the calculation accuracy and simulation time, a 142,000 node mesh is employed in the present numerical study for the smooth labyrinth seal, while for the labyrinth seal with the honeycomb land case, the node number in the chamber part is increased to 289,000 because the flow field becomes more complex than that of smooth configuration. And 244,000 nodes are generated in the honeycomb part.

4 Results and Discussions

To demonstrate the accuracy and reliability of the present numerical approach, the effects of different rotational speeds, leakage flow rates, and two kinds of inlet swirl on the total temperature increase in convergent and divergent stepped labyrinth seals are calculated and compared with the experimental data. Then, the influence of the pressure ratio and sealing clearance on the discharge and total temperature increase in convergent stepped labyrinth seals with smooth and honeycomb lands is investigated and discussed in detail.

4.1 Windage Heating and Numerical Method

Demonstration. The uncertainties for the windage heating varied from 2% to 30% in extreme cases, e.g., $Re=20,000$ and $Mu=0.3$, and yielded 10.2% as an average value, mentioned in Ref. [1]. Figure 3 shows the relation between the windage heating number and the circumferential Mach number in the convergent stepped labyrinth seal with smooth land. Different circumferential Mach numbers mean different rotational speeds. The present 3D model is more agreeable with the experimental data at $Re_x=10,000$ than the 2D axis-symmetric model, which was adopted by Denecke et al. [1]. Additionally, the windage heating number increases as the circumferential Mach number (which indicates the rotational speed) increases. This can be explained by the wall shear stress increasing as the rotational speed increases.

Figure 4 shows the relation between the windage heating number and the circumferential Mach number in the divergent stepped labyrinth seal with smooth land at two kinds of inlet swirl conditions. The present numerical results are well in agreement with experimental data at $Re_x=10,000$. And the windage heating number decreases by about 25% in the case of $K_{in}=0.3$ compared with the no preswirl case. The obtained numerical results with the 3D model show that the present method is able to analyze the windage heating effect in the convergent and divergent labyrinth seals at different inlet swirls.

Figure 5 shows the relations between σ and Mu for the conver-

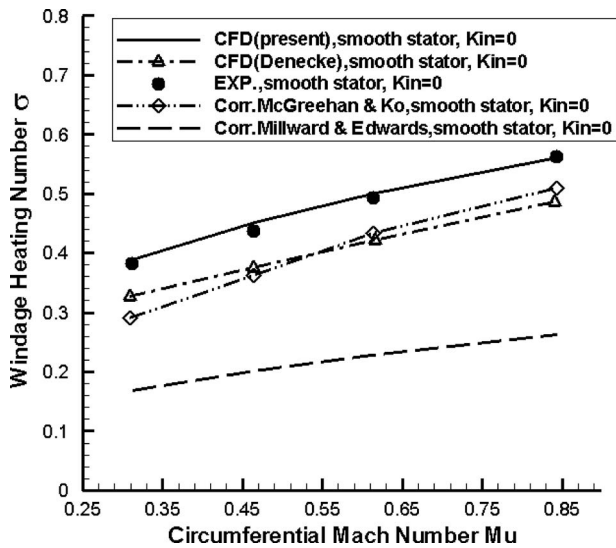


Fig. 3 σ versus Mu in the convergent labyrinth seal ($Re_x = 10,000$)

gent stepped labyrinth seal with 1/16 in. honeycomb cell land. It gives the comparison between numerical data and experimental data. The present CFD results are lower than that of the experiment data by about 8% at $Re_x = 10,000$, and two lines are almost parallel, indicating the reasonability of simulations. The CFD results show excellent agreement with the experimental one at $Re_x = 20,000$.

The above discussion shows that the numerical method has sufficient accuracy to simulate the total temperature difference in the labyrinth seal. However, we do not know whether the simulated flow field in the chamber is right or not. Therefore, two special positions in the chamber were selected for the divergent flow in the smooth configuration, as shown in Figs. 6 and 7. The swirl velocity is plotted and compared with the LDV measurement [1]. The results show that the calculated swirl velocity presented is in agreement with the experimental data and better than the 2D axis-symmetry one performed by Denecke et al. [1]. It can also be deduced that the swirl velocity decreases along the axial direction, and the difference in tangential velocity between $K_{in}=0.3$ and $K_{in}=0$ increases along the axial direction.

4.2 Pressure Ratio and Sealing Clearance Effects. On the basis of the demonstration of the present numerical approach, the

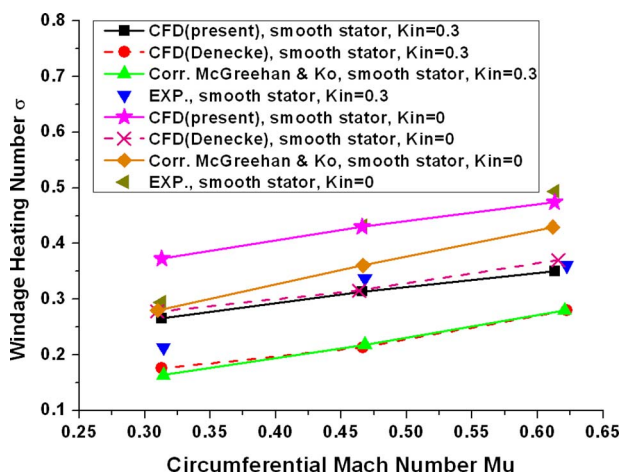


Fig. 4 σ versus Mu in the divergent labyrinth seal ($Re_x = 10,000$)

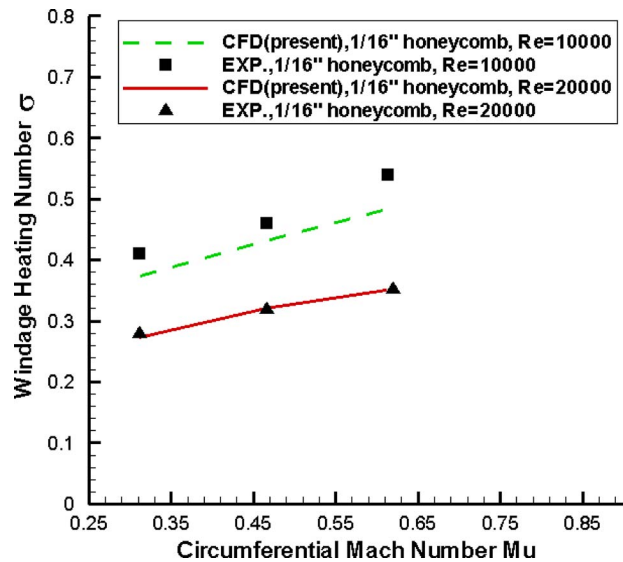


Fig. 5 σ versus Mu in the 1/16 in. honeycomb cell seal

effects of the pressure ratios and sealing clearances on the discharge and total temperature increase in the convergent stepped labyrinth seals with smooth and 1/16 in. honeycomb cell lands are conducted. Four sizes of sealing clearance for these two seal configurations are set to be 1.3 mm, 1.5 mm, 1.7 mm, and 1.9 mm. Five different pressure ratios ranging from 1.1 to 1.9 are calculated in this study. And no inlet preswirl is considered in these cases.

Figures 8 and 9 show the dependence of the leakage flow rate on radial clearance and pressure ratio. For these two configurations, the increase in leakage rate is almost linearly proportional to the clearance and pressure ratio, which corresponds to the study of Schramm et al. [5]. The similarity between the two figures means that radial clearance and pressure ratio have the same effect on the leakage rate of two different configurations. However, the leakage flow rate of the honeycomb configuration is a little larger ($\approx 10\%$) than that of the smooth configuration at the same radial clearance and pressure ratio.

Figures 10 and 11 illustrate the relations between the windage power and leakage flow of honeycomb and smooth configurations. The windage power increases as the leakage rate and clearance

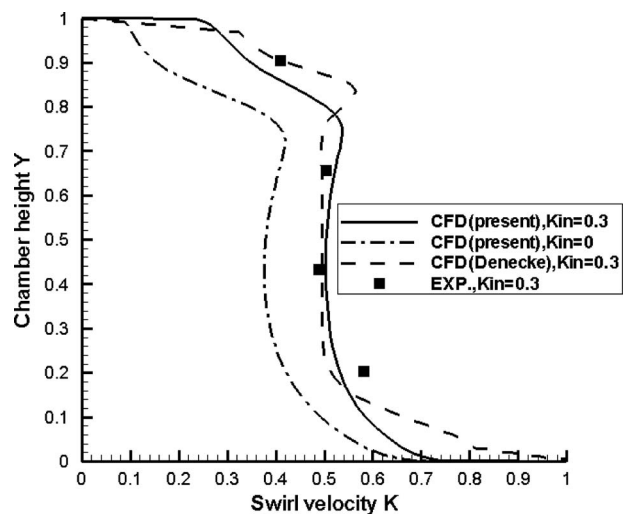


Fig. 6 Swirl velocity at $x=17.5$ mm, divergent flow, smooth configuration ($Mu \approx 0.46$, $Re_x = 10,000$)

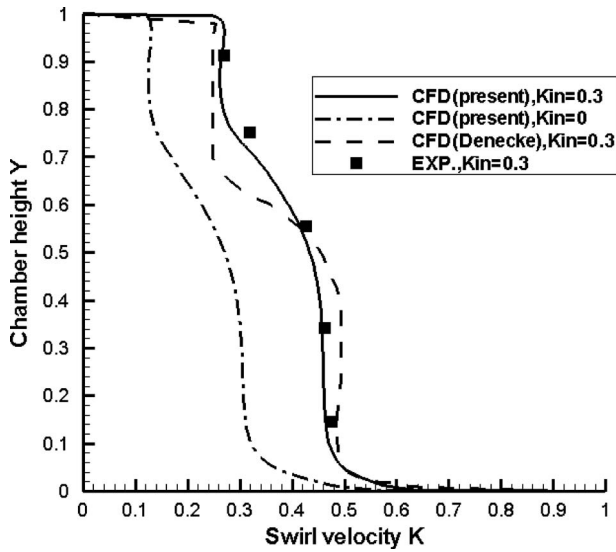


Fig. 7 Swirl velocity at $x=22.5$ mm, divergent flow, smooth configuration ($Mu \approx 0.46$, $Re_x = 10,000$)

increase, which corresponds to the research reported by Millward and Edwards [11]. As to the smooth configuration, the relations of the windage power and leakage rate at $C=1.7$ mm and $C=1.9$ mm nearly coincide with each other, which are different from the honeycomb configuration. The calculated windage power of the honeycomb configuration is a little higher than that of the smooth one due to the damping effect of the honeycomb, but it does not correspond to the +15% magnitude reported by Millward and Edwards [11].

The windage heating number of the honeycomb configuration in Fig. 12 was found to be 1–10% lower than that of the smooth case (Fig. 13 and Table 3). It can be explained by comparing the leakage flow and windage power between them. The leakage rate of the honeycomb is about 10% higher than that of the smooth case, as shown in Figs. 8 and 9. And the windage power of these two configurations is nearly the same. In addition, for both smooth and honeycomb configurations, the windage heating number decreases as the pressure ratio and clearance increase, which is opposite to the windage heating power.

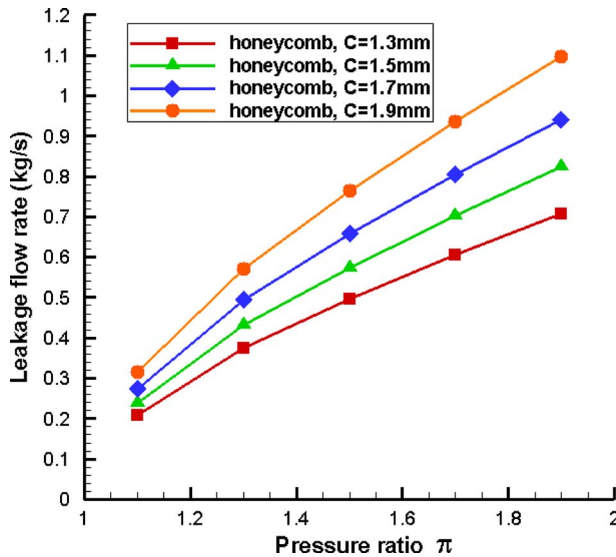


Fig. 8 Leakage flow versus π of the honeycomb configuration

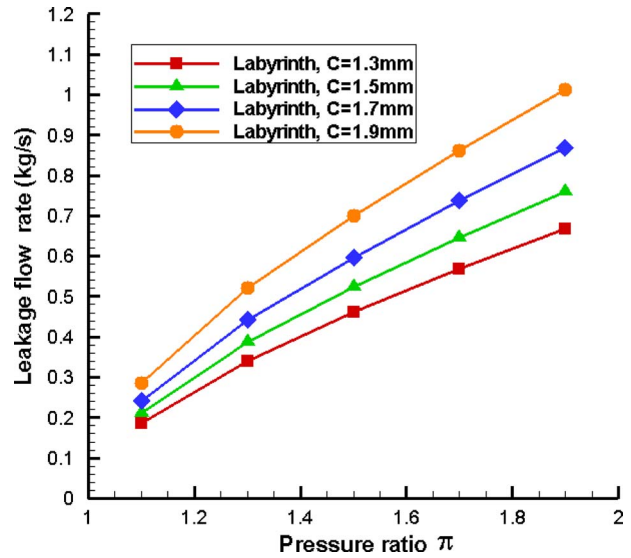


Fig. 9 Leakage flow versus π of the smooth configuration

4.3 Comparison Between Different Configurations. Selecting the convergent flow arrangement, smooth configuration $C=1.3$ mm, $n=10,000$ rpm, and $\pi=1.1$ case as a reference point, the difference between the other case and the reference case can be defined as

$$\Delta_1 = \frac{\sigma - \sigma_{\text{smooth,convergent}}}{\sigma_{\text{smooth,convergent}}} \times 100\%$$

$$\Delta_2 = \frac{H - H_{\text{smooth,convergent}}}{H_{\text{smooth,convergent}}} \times 100\%$$

$$\Delta_3 = \frac{\dot{m} - \dot{m}_{\text{smooth,convergent}}}{\dot{m}_{\text{smooth,convergent}}} \times 100\% \quad (5)$$

The percentage differences in windage heating number, windage heating power, and leakage rate for both convergent and divergent configurations with smooth land and honeycomb land at five different pressure ratios are listed in Table 3. Several conclusions can

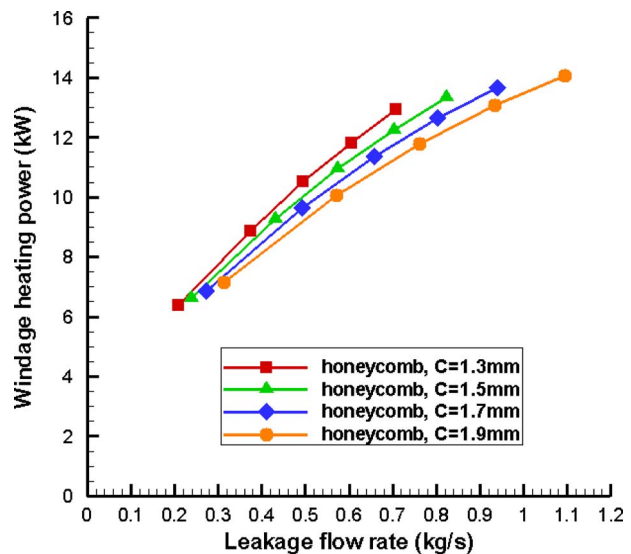


Fig. 10 Windage power versus leakage flow of the honeycomb configuration

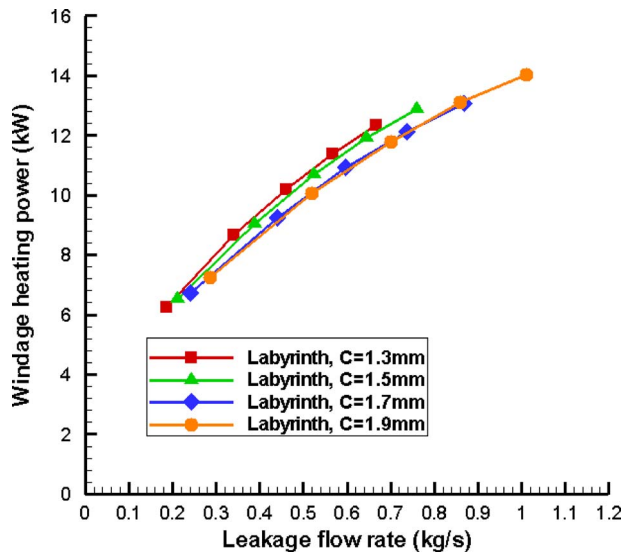


Fig. 11 Windage power versus leakage flow of the smooth configuration

be deduced from this table.

At the same clearance and rotor speed, the windage heating number decreases as the pressure ratio increases. But the windage heating power and leakage rate increase as the pressure ratio increases.

As to the same configuration (smooth land or honeycomb land), the windage heating number of the convergent arrangement is larger than that of the divergent arrangement. It means that the total temperature difference is smaller in the divergent arrangement. For the smooth configuration, the windage power of the convergent arrangement is smaller than that of the divergent arrangement, but it is the opposite for the honeycomb configuration. For both smooth and honeycomb configurations, the leakage rate of the convergent flow is smaller than that of the divergent flow.

As to the same flow arrangement (divergent or convergent), the windage heating number of the smooth land is larger than that of the honeycomb land. And the leakage rate of the smooth land is smaller than that of the honeycomb land. For the convergent arrangement, the windage heating power of the smooth land is smaller than that of the honeycomb land by about 2–10%. But the

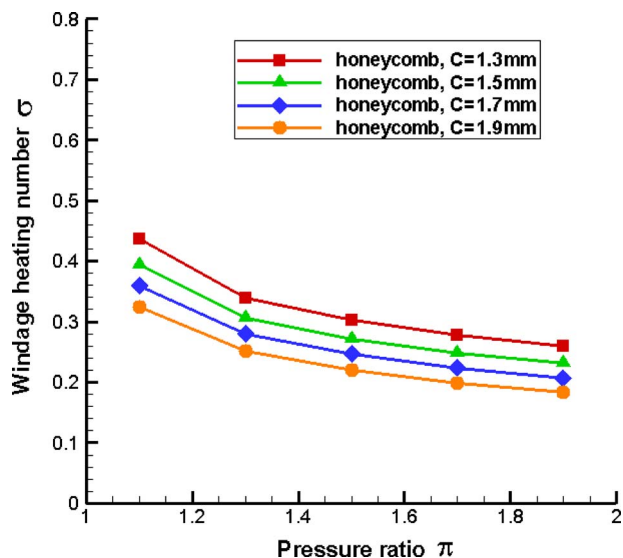


Fig. 12 σ versus π in the honeycomb configuration

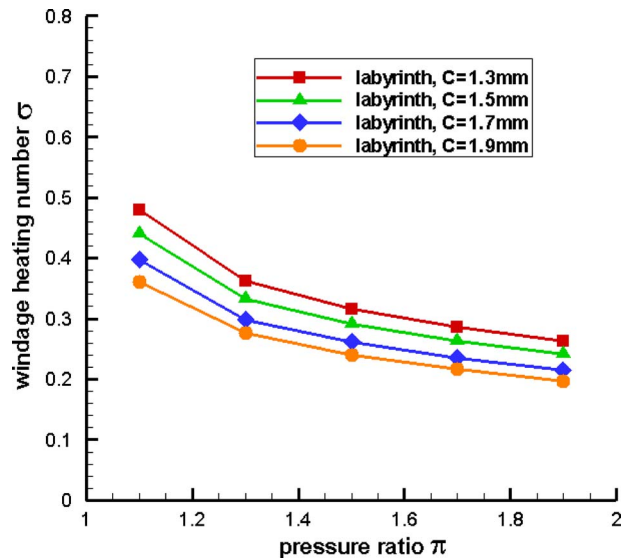


Fig. 13 σ versus π in the smooth configuration

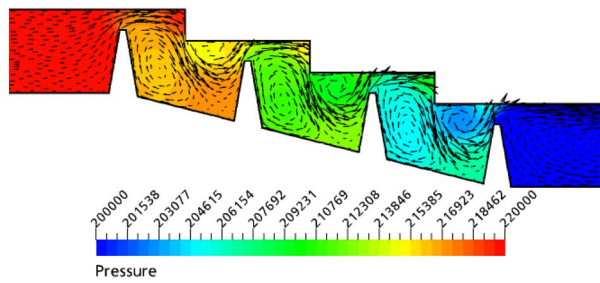
windage heating power of the smooth land is a little larger than that of the honeycomb land for the divergent arrangement.

4.4 Flow Fields. Figure 14 shows the velocity vectors and static pressure contour distribution in the smooth configuration with two sealing clearances at $\pi=1.1$. According to Figs. 14(a) and 14(b), the flow patterns are nearly similar. The fluid flows into the seal and is accelerated through the gap. Then, it impinges toward the step and causes the pressure to increase near the step wall. In each chamber, the jet separates the flow into two counter-rotating vortices, one is behind the knife with higher pressure, and the other is behind the step with lower pressure. The size of the former becomes larger as the clearance increases. And the shape of the latter decides the incidence angle into the gap, which has a lot of influence on the leakage.

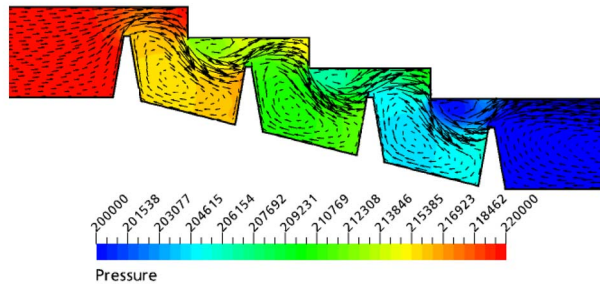
The computed flow fields of the honeycomb configuration are shown in Fig. 15. The pressure decreases along the chamber, while the pressure along the axial direction does not always de-

Table 3 σ , H , and \dot{m} differences at $C=1.3$ mm, $n=10,000$ rpm

Configuration	Flow arrangement	π	Δ_1 (%)	Δ_2 (%)	Δ_3 (%)
Smooth land	Convergent	1.1	0.0	0.0	0.0
		1.3	-24.4	38.7	83.5
		1.5	-34.2	63.3	148.2
		1.7	-40.3	82.6	205.9
		1.9	-45.0	97.8	259.6
	Divergent	1.1	-12.8	3.7	19.0
		1.3	-33.5	44.0	116.5
		1.5	-42.4	67.9	191.4
		1.7	-47.9	86.5	258.2
Honeycomb land	Convergent	1.1	-8.7	2.3	12.0
		1.3	-29.3	42.2	101.2
		1.5	-36.8	68.6	166.9
		1.7	-41.9	89.1	225.6
		1.9	-45.6	107.4	281.3
	Divergent	1.1	-17.5	0.16	21.4
		1.3	-39.1	37.9	126.5
		1.5	-45.7	66.0	206.0
		1.7	-50.7	85.0	275.3
		1.9	-54.7	99.0	339.0



(a) $c=1.3\text{mm}$, $\pi = 1.1$



(b) $c=1.9\text{mm}$, $\pi = 1.1$

Fig. 14 Static pressure contours and velocity vector distribution of the stepped labyrinth seal with smooth land, convergent flow

crease in the cells, and the pressure in the cell above the knife is higher than that of the neighbors. Compared with the smooth case, the vortices behind the step disappeared, and the one in the chamber almost occupies the whole chamber volume. Low speed fluid is filled within the honeycomb cells in the form of vortices, which push the chamber flow to the seal bottom, or it is pushed back into the cells.

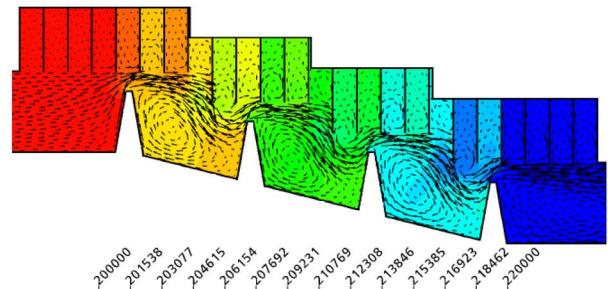
5 Conclusions

Based on the experimental data of Denecke et al. [1], three-dimensional RANS solution with the commercial CFD software CFX is utilized to analyze the influence of the pressure ratios and sealing clearances on the discharge and total temperature increase in the convergent and divergent labyrinth seals with smooth and honeycomb lands.

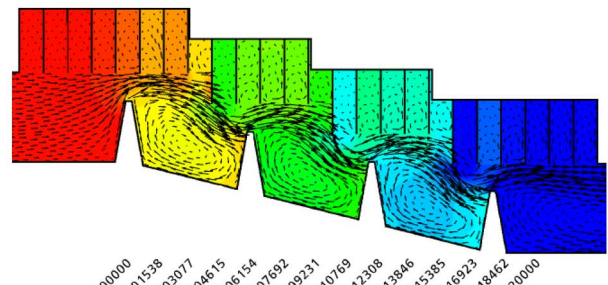
As to both smooth and honeycomb configurations with convergent arrangement, the computed windage heating number decreases with increasing pressure ratio and sealing clearance. But the leakage flow rate and windage heating power follow the opposite trend with these two factors. The influence of the pressure ratio on the leakage flow pattern is nearly negligible.

As to the same configuration (smooth land or honeycomb land), the windage heating number of the convergent configuration is larger than that of the divergent configuration, and the leakage rate of the convergent flow is smaller than the divergent flow arrangement. For the smooth configuration, the windage power of the convergent arrangement is smaller than the divergent arrangement, but it is opposite for the honeycomb configuration.

As to the same flow arrangement (divergent or convergent), the windage heating number of the smooth land is larger than that of the honeycomb land at the same sealing clearance and pressure ratio. And the leakage flow rate of the honeycomb configuration is higher than that of the smooth one due to the larger effective sealing gap of the honeycomb. For the convergent arrangement, the windage heating power of the seal with smooth land is smaller than that of honeycomb land by about 2–10%, but it is opposite for the divergent flow.



(a) $c=1.3\text{mm}$, $\pi = 1.1$



(b) $c=1.9\text{mm}$, $\pi = 1.1$

Fig. 15 Static pressure contours and velocity vector distribution of the stepped labyrinth seal with honeycomb land, convergent flow

Acknowledgment

The authors are grateful for Project No. 50506023 supported by the National Natural Science Foundation and Program for New Century Excellent Talents in University of China (Project No. NCET-07-0669). Additionally, the authors thank Dr. Denecke for his kind help to provide us a lot of information, which was helpful for the present numerical study.

Nomenclature

$a = \sqrt{\kappa \mathfrak{R} T_{\text{static, in}}}$	= speed of sound (m/s)
C	= sealing clearance (mm)
$C_D = \dot{m} / m_{id}$	= discharge coefficient
C_p	= specific heat capacity (J/kg K)
$H = C_p \cdot \dot{m} \cdot \Delta T$	= windage heating power (kW)
$K = V_i / U$	= swirl ratio
\dot{m}	= mass flow rate (kg/s)
$Mu = U / a$	= circumferential Mach number
n	= rotor speed (rpm)
p	= static pressure (Pa)
P	= total pressure (Pa)
R	= radial distance (m)
$\mathfrak{R} = 287.2$	= specific gas constant (J/kg K)
R_m	= average rotor radius (m)
$Re_x = \dot{m} / \mu_m \pi R_m$	= axial Reynolds number
T	= temperature (K)
$U = \omega \cdot R_m$	= rotor circumferential velocity (m/s)
X	= axial discharge along seal (m)

Greek Letters

Δ	= difference
κ	= ratio of specific heats

μ = dynamic viscosity (N s/m²)
 $\pi = P_{in}/P_{out}$ = pressure ratio
 Π = effective pressure ratio
 ρ = density (kg/m³)
 $\sigma = 2C_p\Delta T_{total}/U^2$ = windage heating number
 ω = rotor angular velocity (rad/s)

Subscripts

HC = honeycomb
 id = ideal
 in/out = inlet/outlet condition
 m = arithmetic average of the inlet and outlet
 r/t/x = radial/tangential/axial direction
 static/total = static/total value

References

- [1] Denecke, J., Dullenkopf, K., Wittig, S., and Bauer, H.-J., 2005, "Experimental Investigation of the Total Temperature Increase and Swirl Development in Rotating Labyrinth Seals," ASME Paper No. GT2005-68677.
- [2] Peitsch, D., Friedl, W.-H., Dittmann, M., and Denecke, J., 2003, "Detailed Investigation of the Flow Within the Secondary Air System in High Pressure Turbines of Aero Engines," ISABE Paper No. 2003-1038.
- [3] McGreehan, W., and Ko, S., 1989, "Power Dissipation in Smooth and Honeycomb Labyrinth Seals," ASME Paper No. 89-GT-220.
- [4] Denecke, J., Färber, J., Dullenkopf, K., and Bauer, H.-J., 2005, "Dimensional Analysis and Scaling of Rotating Seals," ASME Paper No. GT2005-68676.
- [5] Schramm, V., Willenborg, K., Kim, S., and Wittig, S., 2002, "Influence of a Honeycomb Facing on the Flow Through a Stepped Labyrinth Seal," ASME J. Eng. Gas Turbines Power, **124**, pp. 140–146.
- [6] Paolillo, R., Moore, S., Cloud, D., and Glahn, J. A., 2007, "Impact of Rotational Speed on the Discharge Characteristic of Stepped Labyrinth Seals," ASME Paper No. GT2007-28248.
- [7] Morrison, G. L., and Al-Ghasem, A., 2007, "Experimental and Computational Analysis of a Gas Compressor Windback Seal," ASME Paper No. GT2007-27986.
- [8] Willenborg, K., Schramm, V., Kim, S., and Wittig, S., 2002, "Influence of a Honeycomb Facing on the Heat Transfer in a Stepped Labyrinth Seal," ASME J. Eng. Gas Turbines Power, **124**, pp. 133–139.
- [9] Stocker, H., Cox, D., and Holle, G., 1977, "Aerodynamic Performance of Conventional and Advanced Design Labyrinth Seals With Solid-Smooth, Abradable and Honeycomb Lands," NASA Report No. CR-135307.
- [10] Tipton, D., Scott, T., and Vogel, R., 1986, "Labyrinth Seal Analysis: Volume III—Analytical and Experimental Development of Design Model for Labyrinth Seals," Allison Gas Turbine Division, General Motors Corporation, Technical Report No. AFWAL-TR-85-2103.
- [11] Millward, J., and Edwards, M., 1996, "Windage Heating of Air Passing Through Labyrinth Seals," ASME J. Turbomach., **118**, pp. 414–419.
- [12] AEA Technology GmbH, 2004, CFX-TASCFLOW User Documentation, AEA Technology, Software Ltd., Waterloo.
- [13] Scherer, T., Waschka, W., and Wittig, S., 1992, "Numerical Predictions of High-Speed Rotating Labyrinth Seal Performance: Influence of Rotating on Power Dissipation and Temperature Rise," ICHMT 1992 International Symposium on Heat Transfer in Turbomachinery, Athens, Greece, Vol. 26, pp. 1514–1522.
- [14] Denecke, J., Dullenkopf, K., and Wittig, S., 2004, "Influence of Preswirl and Rotation on Labyrinth Seal Leakage," *Proceedings of the Tenth International Symposium on Transport Phenomena and Dynamics of Rotating Machinery ISROMAC*, HI, Paper No. ISROMAC10-2004-105.

Sensitization of the SST Turbulence Model to Rotation and Curvature by Applying the Spalart–Shur Correction Term

Pavel E. Smirnov
New Technologies and Services,
Dobrolyubov Avenue 14,
197198 St.-Petersburg, Russia
e-mail: pavel.smirnov@nts-int.spb.ru

Florian R. Menter
ANSYS/CFX Germany,
Staudenfeldweg 12,
83624 Otterfing, Germany
e-mail: florian.menter@ansys.com

*A rotation-curvature correction suggested earlier by Spalart and Shur (1997, "On the Sensitization of Turbulence Models to Rotation and Curvature," *Aerosp. Sci. Technol.*, 1(5), pp. 297–302) for the one-equation Spalart–Allmaras turbulence model is adapted to the shear stress transport model. This new version of the model (SST-CC) has been extensively tested on a wide range of both wall-bounded and free shear turbulent flows with system rotation and/or streamline curvature. Predictions of the SST-CC model are compared with available experimental and direct numerical simulations (DNS) data, on the one hand, and with the corresponding results of the original SST model and advanced Reynolds stress transport model (RSM), on the other hand. It is found that in terms of accuracy the proposed model significantly improves the original SST model and is quite competitive with the RSM, whereas its computational cost is significantly less than that of the RSM.*

[DOI: 10.1115/1.3070573]

1 Introduction

Despite a fast growth of computing power and more and more intensive use, the turbulence-resolving approaches (LES, DES, SAS, etc.), the Reynolds-averaged Navier–Stokes (RANS) equations still remain the most widely used approach in industrial computational fluid dynamics (CFD). Further progress in this area is often associated with Reynolds stress models (RSMs). However, potential advantages of these models over the conventional eddy-viscosity models (EVMs) in terms of accuracy have not been systematic, whereas in terms of the robustness and computational cost the RSM are noticeably inferior to EVM. Thus, along with further improvements of RSM, enhancement of existing EVM presents an important practical alternative.

One of the most serious weaknesses of EVMs is that they are not capable of capturing the effects of streamline curvature and system rotation, which play a significant role in many turbulent flows of practical interest. An efficient approach for resolving this issue is proposed by Spalart and Shur [1]. It is close to that of Knight and Saffman [2] but differs from the latter in many details and, in particular, avoids computing and differentiating the principal directions of the strain tensor. In addition, it is much easier to apply to 3D flows due to an explicit formula produced in Ref. [1]. When applied to the one-equation Spalart–Allmaras (SA) turbulence model, the approach resulted in a simple rotation-curvature correction to the SA model. The corrected model, denoted as the SARC model, is shown to be much more accurate than the SA for a wide range of rotating and curved channel flows [3,4]. This motivates the approach of applying the modification to two-equation EVMs and, in particular, to the k - ω shear stress model (SST) of Menter [5] as described in the present work.

In the first section of this paper, we outline a formulation of the SST model modified with the rotation-curvature correction (CC) term and then present the results of this model (SST-CC) for a wide range of flows varying from one-dimensional rotating and

curved channel flows up to 3D flows with rather complex geometry. Note that due to space limitations, the results are demonstrated only for some of the considered flows (more than 15 in total), which seem to provide a sufficient basis for the validation of the proposed model hereafter referred to as SST-CC. These flows are fully developed 1D turbulent flow in a plane rotating channel [6,7], 1D developed flow in a curved channel [8], 2D flow in a channel with U -turn [9], 3D flow in a hydro cyclone [10], 3D flow in a centrifugal compressor [11], and, finally, 3D free shear flow past NACA 0012 airfoil with a round tip [12].

All the computations have been carried out with the commercial CFD solver ANSYS CFX 11. The results obtained with the use of the SST-CC model are compared with available experimental data and direct numerical simulations (DNS) predictions, as well as with the similar results obtained with the original SST model. In addition, some of the cases were computed with a version of the RSM in combination with the baseline ω -equation (BSL) [5]. The hydro cyclone flow was simulated using another version of the RSM developed by Speziale–Sarkar–Gatski (SSG) [13]. The SSG model is combined with the ε -equation and uses quadratic relation for the pressure-strain correlation. All obtained numerical solutions are compared and discussed.

2 SST-CC Model Formulation

The empirical function suggested in Ref. [1] for sensitization of the SA model to the effects of streamline curvature and system rotation is defined by

$$f_{\text{rotation}} = (1 + c_{r1}) \frac{2r^*}{1 + r^*} [1 - c_{r3} \tan^{-1}(c_{r2}\bar{r})] - c_{r1} \quad (1)$$

and is used as a multiplier of the production term in the SA eddy viscosity transport equation.

In the present work, based on the tests discussed below, this function is slightly modified (replaced with the function f_{r1}) and is used to control the production terms of the original SST model as follows:

$$\frac{\partial(\rho k)}{\partial t} + \frac{\partial(\rho u_j k)}{\partial x_j} = P_k f_{r1} - \beta^* \rho k \omega + \frac{\partial}{\partial x_j} \left[\mu_{\text{eff}} \frac{\partial k}{\partial x_j} \right] \quad (2)$$

Contributed by the International Gas Turbine Institute of ASME for publication in the *JOURNAL OF TURBOMACHINERY*. Manuscript received August 21, 2008; final manuscript received October 7, 2008; published online July 2, 2009. Review conducted by David Wisler. Paper presented at the ASME Turbo Expo 2008: Land, Sea and Air (GT2008), Berlin, Germany, June 9–13, 2008.

$$\frac{\partial(\rho\omega)}{\partial t} + \frac{\partial(\rho u_j \omega)}{\partial x_j} = \alpha \frac{\rho P_k}{\mu_i} f_{r1} - D_\omega + C d_\omega + \frac{\partial}{\partial x_j} \left[\mu_{\text{ef}} \frac{\partial \omega}{\partial x_j} \right] \quad (3)$$

where the modified function f_{r1} reads as

$$f_{r1} = \max\{\min(f_{\text{rotation}}, 1.25), 0.0\} \quad (4)$$

The definition (4) differs from Eq. (1) by limiting the function in the range from 0 corresponding, e.g., to a strong convex curvature (stabilized flow, no turbulence production) up to 1.25 (e.g., strong concave curvature, enhanced turbulence production). The lower limit is introduced for numerical stability reasons, whereas the upper one turns out to be needed since, unlike the production term of the SA model, which includes the vorticity tensor Ω , the SST production terms are based on the strain rate tensor, S . It is known that the S-based turbulence production is typically higher than the Ω -based one, which justifies the use of the limiter in order to avoid overgeneration of the eddy viscosity in flows with a destabilizing curvature/rotation. The specific limiter value of 1.25 provided the best compromise for all the cases considered in the present study.

Assuming that all the variables and their derivatives are defined with respect to the reference frame of the calculation, which is rotating with a rate Ω^{rot} , the arguments of the function (1), r^* and \tilde{r} , are defined as follows:

$$r^* = \frac{S}{\Omega} \quad (5)$$

$$\tilde{r} = 2\Omega_{ik} S_{jk} \left[\frac{DS_{ij}}{Dt} + (\varepsilon_{imn} S_{jn} + \varepsilon_{jmn} S_{in}) \Omega_m^{\text{rot}} \right] \frac{1}{\Omega D^3} \quad (6)$$

Here

$$S_{ij} = \frac{1}{2} \left(\frac{\partial u_i}{\partial x_j} + \frac{\partial u_j}{\partial x_i} \right) \quad (7)$$

$$\Omega_{ij} = \frac{1}{2} \left(\left(\frac{\partial u_i}{\partial x_j} - \frac{\partial u_j}{\partial x_i} \right) + 2\varepsilon_{mji} \Omega_m^{\text{rot}} \right) \quad (8)$$

$$S^2 = 2S_{ij} S_{ij} \quad (9)$$

$$\Omega^2 = 2\Omega_{ij} \Omega_{ij} \quad (10)$$

$$D^2 = \max(S^2, 0.09\omega^2) \quad (11)$$

and DS_{ij}/Dt are the components of the Lagrangian derivative of the strain tensor. The Einstein summation convention is used.

Note that in the present work the term D^2 (11) is introduced somewhat differently in Refs. [1,3]. In particular, in order to avoid zero values in the freestream, it is defined as the maximum of the strain rate squared and the turbulence eddy frequency, ω , squared, rather than as $0.5(S^2 + \Omega^2)$. In shear flows, the two definitions are equivalent, while in the freestream, the shear strain goes to zero and the turbulence eddy frequency has a nonzero value. For consistency, the denominator of Eq. (6) is also changed from D^4 used in Refs. [1,3] to ΩD^3 in order to account for Ω value in the new denominator.

Finally, based on the performed tests, the empirical constants c_{r1} , c_{r2} , and c_{r3} involved in Eq. (1) are set equal to 1.0, 2.0, and 1.0, respectively.

3 Example of the DS_{ij}/Dt Term Implementation

This section describes a possible technique of calculation of the DS_{ij}/Dt term (formula (6)) in a three-dimensional Navier–Stokes CFD solver, which is based on the control volume method.

As it was already mentioned in Sec. 2, DS_{ij}/Dt are the components of the total (Lagrangian) derivative of the strain tensor. For further application of the control volume method, it is more convenient to represent the DS_{ij}/Dt term using the integral (Eulerian)

flow formulation. With that formulation, the total derivative of each component of the strain tensor in an arbitrary volume τ can be written as

$$\int_\tau \frac{DS_{ij}}{Dt} d\tau = \frac{D}{Dt} \int_\tau S_{ij} d\tau = \frac{\partial}{\partial t} \int_\tau S_{ij} d\tau + \int_\sigma S_{ij} V_n d\sigma \quad (12)$$

The first term on the right-hand side of the above equation is the local derivative over the physical time. The second term, $\int_\sigma S_{ij} V_n d\sigma$, is the convective derivative. Here σ is the surface of the volume τ , $V_n = \mathbf{V} \cdot \mathbf{n}$, \mathbf{V} and \mathbf{n} are the velocity and normal vectors at a local integration point.

For the steady-state flows, there is no need to compute $\partial/\partial t \int_\tau S_{ij} d\tau$ during iterations, since it is zero in converged solution. Therefore, Eq. (12) becomes as follows:

$$\frac{D}{Dt} \int_\tau S_{ij} d\tau = \int_\sigma S_{ij} V_n d\sigma \quad (13)$$

Application of the control volume approach for the discretization of the right-hand side of Eq. (13) results in

$$\int_\sigma S_{ij} V_n d\sigma \rightarrow \sum_{k=1}^N S_{ij}^{(k)} V_n^{(k)} \sigma^{(k)} \quad (14)$$

where the summing is done over N surfaces of the control volume (computational cell). Superscript index (k) refers to centers of faces, which surround the control volume. The variable $\sigma^{(k)}$ is just the area of the face with the index k , while $S_{ij}^{(k)}$ and $V_n^{(k)}$ have to be computed on the face center, and that depends on the employed control volume scheme. For example, if the cell-centered variables arrangement is used, then $S_{ij}^{(k)}$ and velocity vector on the face center can be obtained using the linear interpolation from two neighboring cells. Then $V_n^{(k)}$ is computed as the dot product of the interpolated velocity vector and face normal vector. Other than that, one can compute $V_n^{(k)}$ as the mass flux through the k th face divided by $\sigma^{(k)} \rho^{(k)}$, where $\rho^{(k)}$ is the density on the face center; it also can be restored from the linear interpolation procedure.

The technique described above provides the second order accuracy in space for the DS_{ij}/Dt term. However, the first order scheme was found to be acceptable as well. In that case, for the cell-centered scheme, variables at the face center can be directly taken from the adjacent cell.

The final discrete formula for the DS_{ij}/Dt components is obtained from Eq. (14) by dividing through the cell volume:

$$\frac{DS_{ij}}{Dt} \rightarrow \left[\sum_{k=1}^N S_{ij}^{(k)} V_n^{(k)} \sigma^{(k)} \right] / \tau \quad (15)$$

where τ is the volume of the computational cell. However, formula (14) is valid for the steady-state simulations only. For the unsteady flows, it is necessary to account for the contribution from the $\partial/\partial t \int_\tau S_{ij} d\tau$ term. To do that numerically, one has to compute time derivatives of S_{ij} in centers of control volumes, and divide by cell volumes. This standard procedure should be available in all CFD solvers, which allow for unsteady simulations.

4 Results and Discussions

4.1 Developed Flow in Plane Rotating Channels. Although very simple in terms of geometry, this flow is quite representative in terms of evaluation of the capability of turbulence models to capture the effects of rotation. Computations were performed for the conditions considered in DNS of Kristoffersen and Andersson [6], and Lamballais et al. [7]. In Ref. [6], the DNS simulations were carried out at a Reynolds number based on the mean flow velocity, U_m , and channel width, H , of $\text{Re}=5800$ and for different values of the Rossby number, Ro , up to 0.5. The DNS simulations in Ref [7] were performed at somewhat lower $\text{Re}=5000$ but at

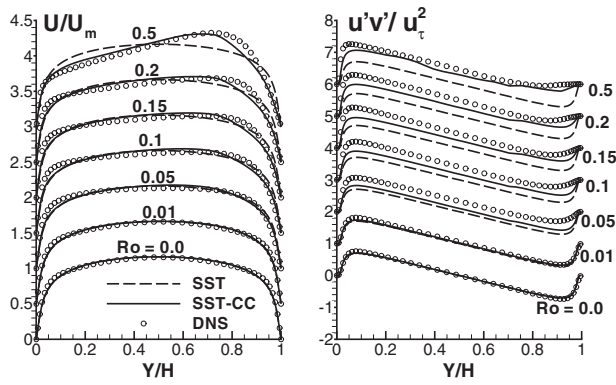


Fig. 1 Developed channel flow at $Re=5800$; comparison with DNS of Kristoffersen and Andersson [6]

extremely intensive rotation rates ($Ro=1.5$), which results in a strong suppression of turbulence. It should be mentioned here that along with the DNS, at least two experimental studies of the considered type of flow, namely, those of Halleen and Johnston [14] and of Johnston et al. [15], are available. These experiments are carried out at Reynolds numbers much higher than those in the DNS. However, as has been discussed in previous publications (see, for example, Ref. [3]), they suffer from a lack of full flow development and side-wall effects. Therefore, the evaluation of the SST-CC model was solely based on the comparison with the DNS predictions.

The generated grids have y^+ values smaller than unity and provide grid-independent solutions. This was checked through the comparison of numerical solutions computed on a sequence of grids with gradually increasing number of nodes across the channel.

A comparison of the velocity and shear stress profiles computed with the use of the SST-CC model with the DNS data [6] is presented in Fig. 1. Shear stress profiles for the RANS solutions were computed from the product of eddy viscosity and proper component of the strain tensor. One can see that the model provides a good agreement with the DNS at all the considered Rossby numbers, especially for the velocity profiles. In contrast to this, the original SST model, which does not include any mechanism for representation of the effect of rotation, gives identical solutions at all the Rossby numbers.

Figure 2 presents a comparison of the SST-CC model with the DNS data [7] obtained for a channel flow with very intensive rotation ($Ro=1.5$). It suggests that even at that high Ro , the model predicts both the velocity and the radial distribution of the parameter $2Ro/S$ (S is the strain magnitude) very well.

It should be noted also that for both considered flows, the SST-CC predictions are quite competitive with those (not shown) obtained by Andersson [16] and Jongen et al. [17] with the use of rather complex algebraic Reynolds Stress models.

4.2 Developed Flow in a Curved Channel. This flow has been computed at the conditions corresponding to the experimen-

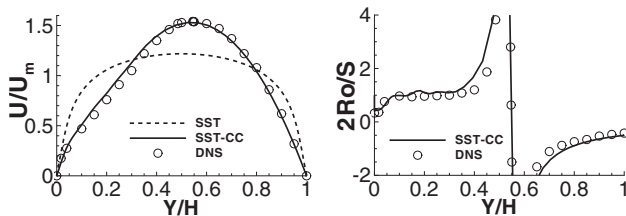


Fig. 2 Developed channel flow at $Re=5000$, $Ro=1.5$; comparison with DNS of Lamballais et al. [7]

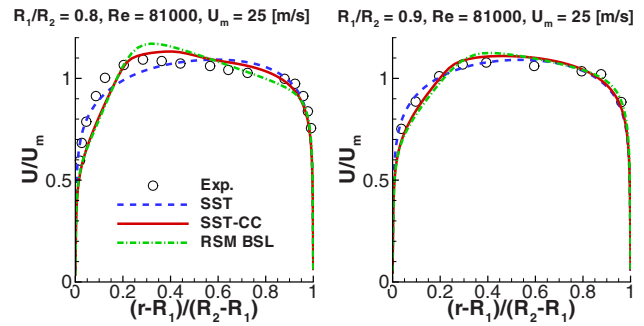


Fig. 3 Developed flow in the curved channel; comparison with experiment of Wattendorf [8]

tal studies of Wattendorf [8]. In particular, the ratio of the internal (convex) and external (concave) channel wall radii, R_1/R_2 , varied in the range 0.8–0.9, and the Reynolds numbers based on the channel width, R_2-R_1 , and the bulk flow velocity U_m , were 47,000 and 81,000.

Similar to the plane channel flow, the computational grid was fine enough to provide grid-independent solution and had y^+ values smaller than unity.

In Fig. 3, the velocity profiles computed with the use of three turbulence models (original SST, SST-CC, and the baseline version of RSM) are compared with each other and with the experimental data. One can see that the SST-CC model provides a much better agreement with the data than the original SST model and is quite competitive with the RSM.

4.3 Two-Dimensional Flow in a Duct With U -Turn. This flow is characterized by a strong streamline curvature and by the formation of a separation bubble on the inner (convex) wall of the duct. It is well known that such flow features are challenging for any RANS model, thus providing a severe test of the SST-CC model. In addition, the experiment is known to not be fully 2D, making a one-to-one comparison more difficult than for the 1D cases.

Figure 4 illustrates a computational domain used in the present work. This domain and also the grid with 231×111 nodes used in the present work are identical to those used in Ref. [3]. The grid provides good near-wall resolution with y^+ values less than 0.5. A grid-refinement study was done on a grid with doubled number of nodes in each direction, which resulted in a negligible difference for all of the meaningful quantities (less than 1%). The Reynolds number of the flow based on the channel width, H , and mean flow velocity, U_m , is equal to $Re=10^6$.

Boundary conditions in the computations are as follows. At the inlet section ($s/H=-10.0$), in accordance with the experiment [9], the flow was assumed to be fully developed. So, for each turbulence model, the corresponding inlet profiles of velocity and turbulent flow quantities were obtained from preliminary computations of the fully developed turbulent flow in a plane channel. At the outlet of the domain, zero gauge static pressure was specified,

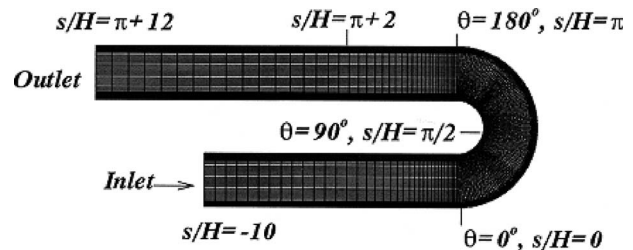


Fig. 4 Schematic of the flow geometry and grid for the U -turn flow of Monson et al. [9]

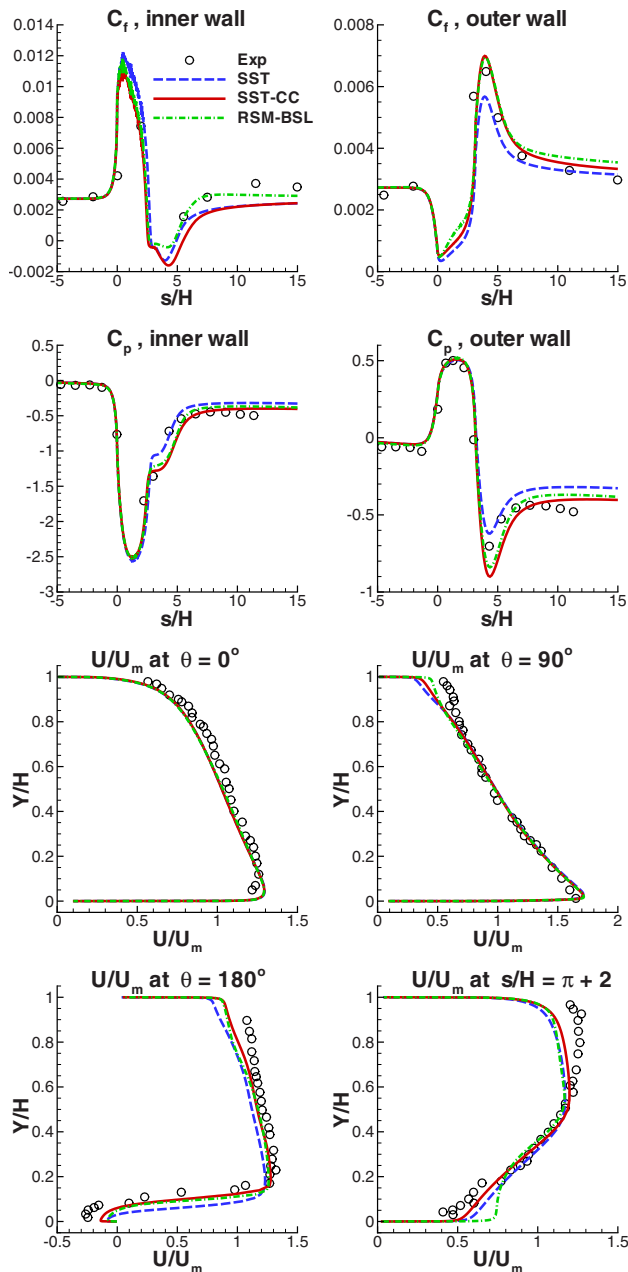


Fig. 5 Turbulent flow in a duct with U -turn; comparison with experiment of Monson et al. [9]

and on the solid walls the no-slip condition was used.

Along with the SST-CC and the original SST models, the flow was also computed with the use of the baseline RSM. The results of the computations are summarized in Fig. 5, which clearly demonstrates a positive effect of the correction on the performance of the SST model in the curved part of the duct. For this flow, the SST-CC turns out to be not only competitive with the RSM but even somewhat surpasses it, especially with regard to the velocity profile at the section $s/H = \pi + 2$, where the RSM prediction is qualitatively wrong. On the other hand, the SST-CC model still predicts a slow flow recovery after reattachment downstream of the separation bubble. This deficiency is most probably caused by the SST model itself rather than by the inefficiency of the curvature correction.

4.4 Flow in a Hydro Cyclone. This test case (see Fig. 6) represents a wall-bounded 3D flow with a complex geometry. Its

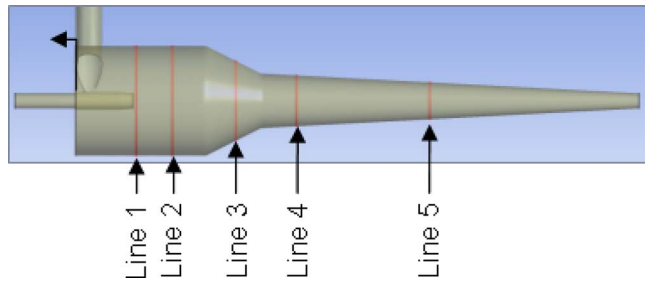


Fig. 6 Schematic of the hydro cyclone, computational domain, and positions of measurement planes (experiments of Hartley [10])

peculiar features are a high-gradient vortex core in the central region of the hydro cyclone with strong swirl and streamline curvature, which are all difficult to represent adequately with RANS turbulence models. The computations are carried out for the conditions studied experimentally by Hartley [10]. Experimental data are available for the axial and tangential velocity components at five vertical sections shown in Fig. 6.

It should be noted that for this flow no physically meaningful steady solutions were obtained. This is not surprising, since it is well known that the vortex core in hydro cyclone is unstable (meandering around its axis). So, time-accurate computations with the use of the SST-CC model were performed, and the time average of the obtained unsteady solution was compared with the experimental data. Other than that, the results of the computations obtained in the present study are compared with similar results obtained by ESSS¹ with the use of the original SST model and nonlinear (quadratic) SSG version of the Reynolds stress transport model.

A computational grid was based on hexahedral control volumes with 463,370 nodes. It provides the y^+ values for the near-wall nodes of about 20. Some additional simulations were carried out on a coarser mesh with 158,122 nodes utilizing the SSG RSM. Although some distinctions were observed in velocity profiles computed on the two meshes, the results did not differ qualitatively. Unfortunately, simulations on a finer grid have not been performed, due to computer resource limitations.

The time-averaged tangential velocity profiles, compared with the experimental data at various z -sections, are shown in Fig. 7. As expected, the standard SST model fails in capturing the correct vortex profile, while the SST-CC model is in good agreement with the data. More specifically, the SST model fails to represent the Rankine vortex with the potential vortex at the peripheral part of the cyclone and the solid body rotation close to its axis. As all noncorrected eddy viscosity models, it has a trend of predicting a solid-body rotation across the hydro cyclone, being most pronounced at lines 4 and 5.

The SST-CC model does capture the real flow structure well and performs only slightly worse than the SSG model (by overestimating the peak values of the velocity). This plausible behavior of the model is explained by a crucial reduction in eddy viscosity provided by the curvature correction in the near-axis area of the "solid-body" rotation.

Note that the CPU requirements for the computations with the SSG model are much higher than those for the SST-CC model. The former not only involves more equations but, what is more important, demands a considerably smaller (up to ten times) time step for convergence.

4.5 Flow in a Centrifugal Compressor. The last wall-bounded flow considered in the present study originates from the turbomachinery area. The SST-CC model has been applied to predict the total pressure rise of a centrifugal compressor at different

¹<http://www.esss.com.br/>.

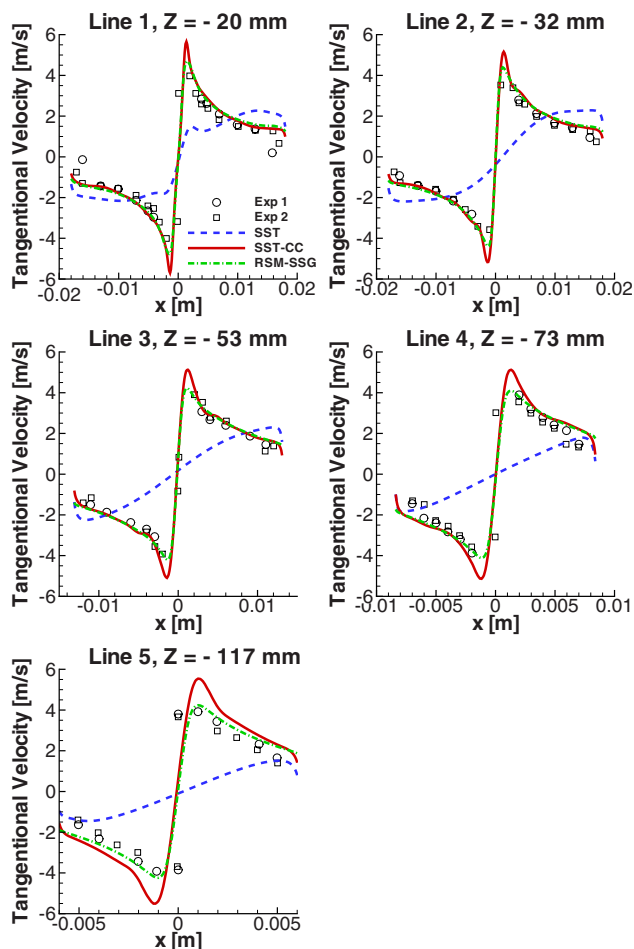


Fig. 7 Time-averaged profiles of the tangential velocity in the hydrocyclone; comparison with experiments of Hartley [10].

operating points. The compressor selected for the present simulations (see Fig. 8) was investigated experimentally in much detail at the Institute of Jet Propulsion and Turbomachinery of the RWTH Aachen [11] (open CFD test case “Radiver”). Also, a numerical study for this test case has been carried out recently with the use of different turbulence models [18]. The results shown in Ref. [18] indicate that the SST model is superior over the standard $k-\epsilon$ and Wilcox $k-\omega$ models in terms of predictions of the flow



Fig. 8 General view of the compressor stage, reproduced from Ref. [11]

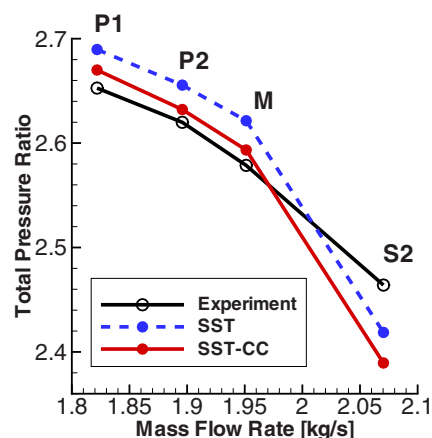


Fig. 9 Total pressure ratio for the centrifugal compressor; comparison with the experiment of Ziegler [11]

field and compressor characteristics, but it still somewhat overpredicts the total pressure rise of the compressor. Therefore, there is a practical interest to check performance of the SST-CC model for this test case, since the flow in centrifugal compressor is characterized by strong channel curvature and intensive rotation.

In the present work, the steady-state computations were performed for the vaned compressor geometry defined by the radius ratio $r_4/r_2=1.14$ and vane suction side angle 16.5 deg. Here r_2 and r_4 are the radii of the impeller blade trailing edge and diffuser vane leading edge, respectively. The computational domain and boundary conditions were identical to those adopted in Ref. [18]. A single blade passage was modeled in both impeller and diffuser, employing a mixing plane approach to connect rotating and stationary frames of reference. The simulations were done on a fully hexahedral mesh comprising 762,695 elements. The mesh was clustered to the walls so as to always maintain values of y^+ for the wall neighboring nodes smaller than 2. In Ref. [18], this mesh was found to be sufficient to provide a mesh-independent solution.

Figure 9 shows the computed and measured total pressure ratio of the compressor versus the mass flow rate. The nomenclature of the operating points coincides with that assumed in Ref. [11]. One dimensional average values of total pressure are obtained by mass flow averaging over inlet and outlet sections.

Comparing computational results, one can see that the SST-CC model results in a considerably better agreement with the experiment than the original SST for most of the operating points. An exception is the point S2, but the problem is apparently related to the poor adequacy of the RANS approach for predicting compressor flows near the choke limit rather than to the weakness of the rotation-curvature correction. Remarkably, the difference between the two models does not vary significantly from one operating point to another. This implies that the correction affects the flow in a similar way at all the mass flow rates considered, which excludes occasional “improvement” at a certain point.

It is important to note also that the convergence rate of the SST-CC model and the total CPU time needed to get a fully converged solution were almost the same as for the original SST model at all operating points.

5 NACA 0012 Wing Tip Vortex

This flow, studied experimentally by Chow et al. [12], presents a complex fully 3D test of the proposed model. It differs from the wall-bounded flows considered in the previous sections and was used for validation of turbulence models in many studies including those carried out in Flomania European project [19].

The wing has a rounded tip and is placed in the wind tunnel at an angle of attack $\alpha=10$ deg. The chord-based Reynolds number is 4.6×10^6 and the Mach number is around 0.1. In the experi-

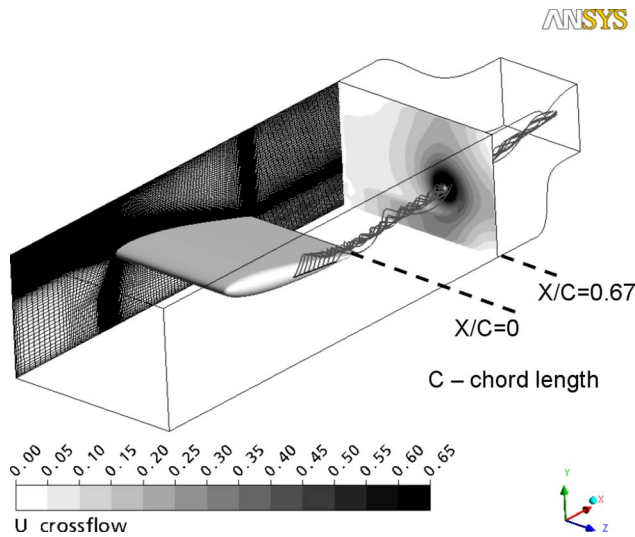


Fig. 10 Computational domain and grid used for NACA 0012 wing with rounded tip (experiments of Chow et al. [12])

ment, the flow is tripped at the leading edge of the wing so that in the computations it can be considered as a fully turbulent flow.

Computational domain and grid on the tunnel wall used in the computations are shown in Fig. 10. The figure also shows the vortex streamlines and contours of the nondimensional cross flow velocity $U_{\text{crossflow}} = \sqrt{v^2 + w^2} / U_{\text{inlet}}$ in the wake of the wing, which illustrate the size of the core of the wing-tip vortex. The 3D grid has 5.6×10^6 nodes and consists of hexahedral elements only. It is clustered near the airfoil surface so that the values of y^+ in the wall neighboring nodes are smaller than 2 (note that a y^+ -insensitive wall treatment was used). Other than that, it has over 40×40 nodes across the vortex core, which was found to be sufficient for obtaining grid-independent results in the downstream vortex.

The boundary conditions used in the computations are as follows.

At the inlet section, the total pressure was specified 1760 Pa higher than the atmospheric pressure. Turbulent characteristics at the inlet were estimated based on the known turbulence intensity of 0.15% and the eddy-to-molecular viscosity ratio equal to 5. At the outflow of the domain, a mass flow rate of 67.25 kg/s was imposed, which results in the experimental value of the area-averaged inlet velocity, U_{inlet} , equal to 51.81 m/s. Finally, at the solid walls the no-slip condition was imposed.

Some results of the computations are presented in Fig. 11–13.

Figure 11 compares the computed and experimental profiles of the nondimensional cross flow and axial ($=u$) velocity components at three planes located downstream of the trailing edge of the wing. The comparison visibly reveals a superiority of the SST-CC model, which predicts the vortex strength measured by the maximum cross-flow velocity much better than the original SST model. The latter results in an overly rapid vortex decay, which is typical of EVM. This deficiency of the SST model is seen also in the axial velocity profiles: At the most distant plane ($X/C=0.67$), the model predicts axial velocity values in the vortex core being less than even the freestream velocity. A reason of the failure of the SST model becomes clear from analysis of the flow characteristics presented in Figs. 12 and 13. In particular, Fig. 12, which compares the axial velocity contours in the plane passing through the vortex core computed with the use of the original SST and SST-CC models, suggests that the former tangibly overestimates the rate of decay of the axial velocity, whereas the latter results in a farther penetration of the vortex and better agrees with the experimental observations. Unfortunately, even the SST-CC

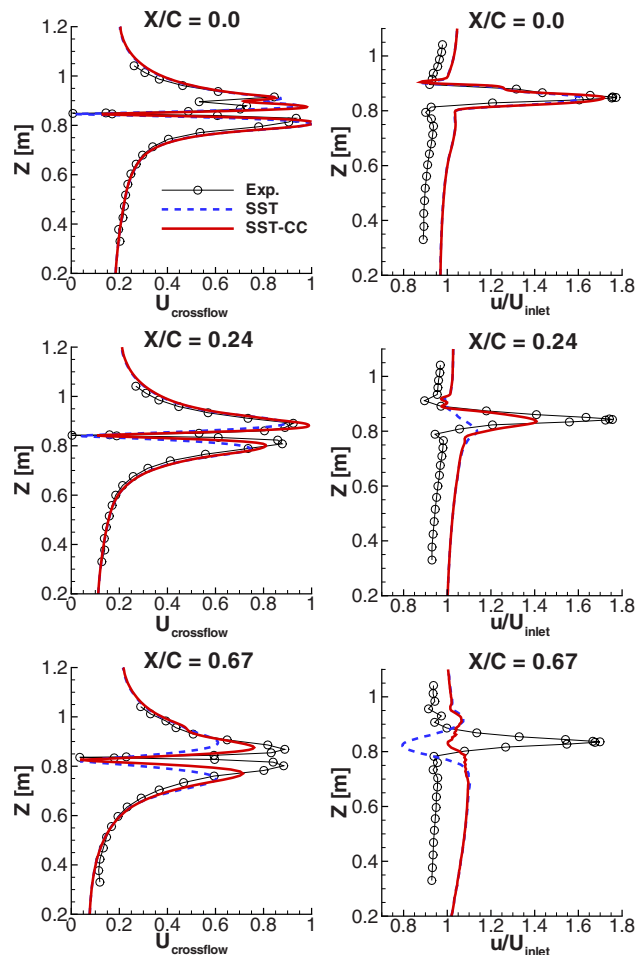


Fig. 11 NACA 0012 wing with rounded tip: profiles of nondimensional cross flow and axial velocity components at three planes located downstream of the trailing edge; comparison with experiments of Chow et al. [12]

model does not accurately represent the axial velocity at the two downstream measurement locations. The reasons for the differences with the experiments in this variable are not entirely clear. It should be noted, however, that even for the first station, the freestream velocity is already different between the simulations and the experiments, indicating a different freestream pressure gradient, which in turn can affect the development of the vortex. For this flow, no solution could be obtained with the RSM.

A mechanism of the positive effect of the curvature correction is displayed in Fig. 13, where the turbulent viscosity fields are compared for the two models. One can see that in accordance with the physics, the SST-CC model predicts a suppression of turbulence in the vortex core, whereas the original SST model results in an increase in the eddy viscosity inside the vortex. Exactly, this (a crucial overestimation of the eddy viscosity in the vortex) causes the overly fast decay of the core axial velocity discussed above.

6 Conclusions

A modification of the shear stress transport turbulence model is suggested based on adaptation of the rotation-curvature correction of Spalart and Shur. The modified model (SST-CC) was tested for a wide range of both wall-bounded and free shear flows with system rotation and/or streamlines curvature. A comparison of the model predictions with experimental data and DNS, on the one hand, and with the results obtained with the use of the original

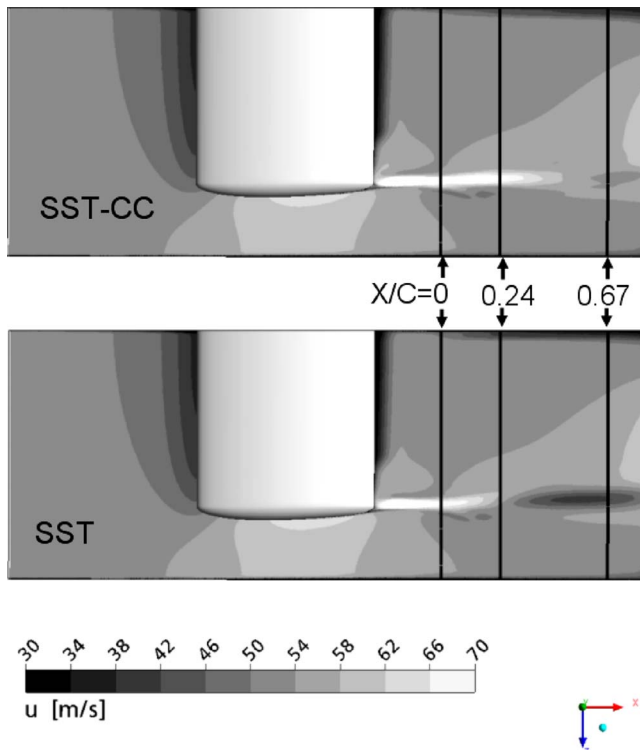


Fig. 12 NACA 0012 wing with rounded tip [12]: computed distributions of the axial velocity at the plane passing through the vortex core

SST model and the baseline version of Reynolds stress transport model, on the other hand, permits to draw the following conclusions.

For the 1D flows with system rotation, the correction is essential for a proper representation of the velocity and turbulent stresses. For a wide range of Rossby numbers, the SST-CC model captures the effect of rotation very well and provides for a good agreement with the DNS data.

For the 1D curved channels, the correction permits to reproduce the deformation of the velocity profile caused by the curvature. It significantly improves the performance of the original SST model and makes it quite competitive with the BSL RSM.

The same conclusions are true also with regard to a more complex 2D flow in a channel with U-turn. Although for this flow the model still predicts a slow flow recovery after reattachment down-

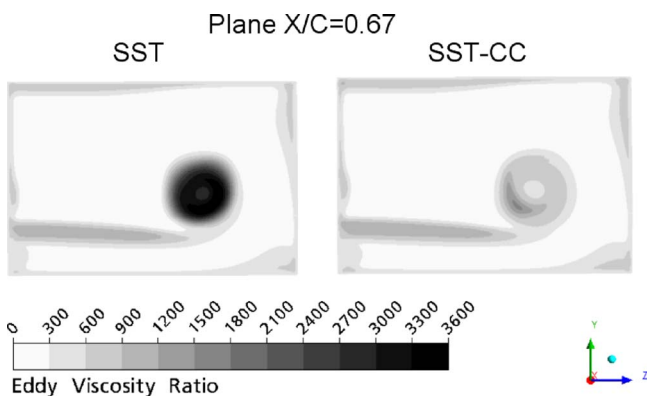


Fig. 13 NACA 0012 wing with rounded tip [12]: eddy viscosity ratio computed with the use of SST and SST-CC turbulence models

stream of the separation bubble, this deficiency is most probably caused by the SST model itself rather than by the inefficiency of the curvature correction. This behavior is well known and shared by all RANS models.

Finally, the SST-CC model results in a significant improvement of predictions of the complex 3D flows, namely, the flows in a centrifugal compressor, in a hydrocyclone, and over a NACA 0012 wing with a rounded tip. In the two latter cases, the model does capture the stabilizing effect of rotation near the vortex axis, which results in a strong suppression of the eddy viscosity in this region. This capability is essential for a proper prediction of such flows.

The SST-CC model is found to be not only rather accurate but also computationally efficient and robust. Activation of the CC-term results in an increase in the CPU time per iteration by less than 1%, and the number of iterations needed for convergence remains almost the same as without the correction. This contrasts with the RSM, which provides a comparable improvement in terms of accuracy, but with a significant “penalty” in terms of the computational cost. For instance, for the hydro cyclone flow, predictions of the SST-CC model are close to those of the quadratic version of the Reynolds stress transport model (SSG RSM), whereas the CPU time required by the SST-CC is about one order of magnitude less.

In terms of the implementation, the most difficult part of the correction in a CFD code is the DS_{ij}/dt term in Eq. (4). However, it can be computed with first order of accuracy without any loss of the model accuracy.

Note, finally, that the correction, originally developed for the one-equation Spalart–Allmaras model, was adapted to the SST model with only minor modifications. This implies that the approach can be easily extended to other eddy viscosity models as well.

Acknowledgment

The authors highly appreciate advices and fruitful discussions with Dr. M. Shur, Dr. E. Smirnov, and Dr. M. Strelets and acknowledge the use of the data provided by the ESSS Co. (<http://www.esss.com.br>).

Nomenclature

- C_f, C_p = friction and pressure coefficients
- c_{r1}, c_{r2}, c_{r3} = additional empirical constants of the SST-CC model
- Cd_ω = cross-diffusion term in the SST model [5]
- D_ω = dissipation term in ω -equation [5]
- H = channel height
- K = turbulence kinetic energy
- P_k = production of turbulence kinetic energy
- Ro = Rossby number = $|\Omega^{rot}|H/U_m$
- R = radius
- s = streamwise distance
- S = strain tensor magnitude
- S_{ij} = components of the mean strain tensor
- u, v, w = Cartesian velocity components
- u_i = components of the mean velocity vector
- U = streamwise velocity
- $U_{crossflow}$ = cross flow velocity = $\sqrt{v^2 + w^2}/U_{inlet}$
- U_{inlet} = freestream velocity at inlet section
- U_m = bulk velocity
- $u'v'$ = mean shear stresses
- u_τ = friction velocity = $\sqrt{\tau_w/\rho}$
- x, y, z = Cartesian coordinates
- X/C = axial distance over axial chord
- x_i = coordinates
- Y = coordinate normal to wall
- y^+ = dimensionless wall distance = $\rho Y u_\tau / \mu$

α, β^* = empirical constants of the SST model [5]
 ε = dissipation rate of turbulent kinetic energy
 ε_{jmn} = tensor of Levi-Civita
 μ = molecular viscosity
 μ_{eff} = effective viscosity = $\mu + \mu_t$
 μ_t = turbulent viscosity
 θ = U -turn angle (see Fig. 4)
 ρ = density
 τ_w = wall friction
 Ω_{ij} = components of the vorticity tensor
 Ω_m^{rot} = components of the system rotation vector
 $|\Omega_m^{\text{rot}}|$ = magnitude of the system rotation vector
 ω = turbulence eddy frequency

References

- [1] Spalart, P. R., and Shur, M. L., 1997, "On the Sensitization of Turbulence Models to Rotation and Curvature," *Aerosp. Sci. Technol.*, **1**(5), pp. 297–302.
- [2] Knight, D. D., and Saffman, P. C., 1978, "Turbulence Models Predictions for Flows With Significant Mean Streamline Curvature," AIAA Paper No. 78-258.
- [3] Shur, M., Strelets, M., Travin, A., and Spalart, P. R., 2000, "Turbulence Modelling in Rotating and Curved Channels: Assessment of the Spalart–Shur Correction Term," *AIAA J.*, **38**(5), pp. 784–792.
- [4] Shur, M., Strelets, M., Travin, A., and Spalart, P. R., 1998, "Two Numerical Studies of Trailing Vortices," AIAA Paper No. 98-0595.
- [5] Menter, F. R., Kuntz, M., and Langtry, R., 2003, "Ten Years of Experience With the SST Turbulence Model," *Turbulence, Heat and Mass Transfer 4*, K. Hanjalic, Y. Nagano, and M. Tummers, eds., Begell House Inc., Redding, CT, pp. 625–632.
- [6] Kristoffersen, R., and Andersson, H. I., 1993, "Direct Simulation of Low-Reynolds-Number Turbulent Flow in a Rotating Channel," *J. Fluid Mech.*, **256**, pp. 163–197.
- [7] Lamballais, E., Lesieur, M., and Metais, O., 1996, "Effects of Spanwise Rotation on the Stretching in Transitional and Turbulent Channel Flow," *Int. J. Heat Fluid Flow*, **17**(3), pp. 324–332.
- [8] Wattendorf, F. L., 1935, "Study of the Effect of Curvature on Fully Developed Turbulent Flow," *Proc. R. Soc. London, Ser. A*, **148**, pp. 1299–1310.
- [9] Monson, D. J., Seegmiller, H. L., Mc Connaughey, P. K., and Chen, Y. S., 1990, "Comparison of Experiment With Calculations Using Curvature-Corrected Zero and Two Equation Turbulence Models for a Two-Dimensional U-Duct," AIAA Paper No. 90-1484.
- [10] Hartley, C. D., 1994, "Measurement of Flow Velocities Within a Hydrocyclone Using Laser Doppler Anemometry," AEA, Power Fluidics, BNFL, Technical Report No. FTN/X/82.
- [11] Ziegler, K. U., 2003, "Experimentelle Untersuchung der Laufrad-Diffuser-Interaktion in einem Radialverdichter variabler Geometrie," thesis, RWTH Aachen, Aachen.
- [12] Chow, J. S., Zilliac, G. G., and Bradshaw, P., 1997, "Mean and Turbulence Measurements in the Near Field of a Wingtip Vortex," *AIAA J.*, **35**(10), pp. 1561–1567.
- [13] Speziale, C. G., Sarkar, S., and Gatski, T. B., 1991, "Modelling the Pressure-Strain Correlation of Turbulence: An Invariant Dynamical Systems Approach," *J. Fluid Mech.*, **227**, pp. 245–272.
- [14] Halleen, R. M., and Johnston, J. P., 1967, "The Influence of Rotation on Flow in a Long Rectangular Channel—An Experimental Study," Department of Mechanical Engineering, Stanford University, Report No. MD-18.
- [15] Johnston, J. P., Halleen, R. M., and Lezius, K., 1972, "Effects of Spanwise Rotation on the Structure of Two-Dimensional Fully Developed Turbulent Channel Flow," *J. Fluid Mech.*, **56**(Pt. 3), pp. 533–557.
- [16] Andersson, H. I., 1997, "Turbulent Shear Flows Affected by Coriolis Forces," *ERCOFTAC Bulletin*, **32**, pp. 25–28.
- [17] Jongen, T., Machiels, L., and Gatski, T. B., 1997, "Predicting Non-Inertial Effects With Algebraic Stress Models Which Account for Dissipation Rate Anisotropies," *Proceedings of the 11th Symposium on Turbulent Shear Flows*, Grenoble, Vol. 2, pp. 13.7–13.12.
- [18] Smirnov, P. E., Hansen, T., and Menter, F. R., 2007, "Numerical Simulation of Turbulent Flows in Centrifugal Compressor Stages With Different Radial Gaps," ASME Paper No. GT 2007-27376.
- [19] 2006, *FLOMANIA: A European Initiative on Flow Physics Modelling*, W. Haase, ed., Springer, New York.

Effect of Unsteadiness on the Performance of a Transonic Centrifugal Compressor Stage

Isabelle Trébinjac

Pascale Kulisa

Nicolas Bulot

Laboratoire de Mécanique des Fluides et
d'Acoustique,
UMR CNRS 5509,
Ecole Centrale de Lyon,
UCBLyon I, INSA 36 Avenue Guy de Collongue,
69134 Ecully Cedex, France

Nicolas Rochuon

TURBOMECA,
Groupe SAFRAN,
64511 Bordès, France

Numerical and experimental investigations were conducted in a transonic centrifugal compressor stage composed of a backswept splintered unshrouded impeller and a vaned diffuser. The characteristic curves of the compressor stage resulting from the unsteady simulations and the experiments show a good agreement over the whole operating range. On the contrary, the total pressure ratio resulting from the steady simulations is clearly overestimated. A detailed analysis of the flow field at design operating point led to identify the physical mechanisms involved in the blade row interaction that underlie the observed shift in performance. Attention was focused on the deformation in shape of the vane bow shock wave due its interaction with the jet and wake flow structure emerging from the impeller. An analytical model is proposed to quantify the time-averaged effects of the associated entropy increase. The model is based on the calculation of the losses across a shock wave at various inlet Mach numbers corresponding to the moving of the jet and wake flow in front of the shock wave. The model was applied to the compressor stage performance calculated with the steady simulations. The resulting curve of the overall pressure ratio as a function of the mass flow is clearly shifted toward the unsteady results. The model, in particular, enhances the prediction of the choked mass flow.

[DOI: 10.1115/1.3070575]

1 Introduction

The unsteady interaction between impeller and diffuser plays an important role in the compression process, especially in high loaded compressors. Actually, the vaned diffuser has to tolerate the distorted upstream flow due to the jet-wake structure coming from the impeller, whereas the impeller is submitted to the potential effect of the vaned diffuser.

Many studies dedicated to impeller-diffuser interaction are focused on the diffuser performances. Krain [1], Inoue and Cumpsty [2], and Ziegler et al. [3,4] tested different diffuser configurations with subsonic inlet conditions. They concluded that the axisymmetric time-averaged inlet flow angle governed the diffuser pressure recovery. Deniz et al. [5] realized experimental studies of two vaned diffusers with variable upstream flow conditions. They confirmed that the diffuser performances are essentially correlated with the inlet flow angle (by means of linear relation), even at supersonic upstream conditions. Nevertheless, the generated upstream flow was axisymmetric, and therefore unable to model the impeller outlet flow distortion due to the jet-wake.

In the works that are mentioned above, unsteadiness had no significant effect on the performances, due to the fact that the compressors were low loaded. However, for the industrial centrifugal compressors, especially in aeronautical domain, the technical constraints (low weight, small size, high performances, etc.) lead to increase the compressor loading and specific speed. Therefore, the blade passage frequency increases and the flow emerging from the impeller is even more distorted because of the loading increase. Consequently the unsteady flow structures may play an important role from an energetic point of view. Shum et al. [6] provided a detailed numerical analysis of the unsteady potential effect (due to the vaned diffuser) on the impeller tip leakage flow, within a high loaded centrifugal compressor. They showed that an

optimum size of radial gap exists, which provides an optimum pressure ratio. Krain [7] and Krain and Hah [8] investigated the unsteady flow field in a high-pressure ratio centrifugal compressor. Both the experimental and numerical results have shown a high level of unsteadiness in the inter-row gap, and a quasisteady behavior of the flow through the vaned diffuser passage. Actually, the relatively large radial gap allowed an efficient mixing process, which minimizes the interaction phenomena. Moreover, the vaned diffuser was fully shocked and the shock did not go upstream the vaneless diffuser.

In the present work, on one hand, the diffuser is fully shocked and, on the other hand, the radial gap is too small to allow a good mixing. Therefore the unsteady processes significantly impact the stage pressure rise.

The aim of this paper is to identify the physical mechanisms involved in the blade row interaction that underlie the change in performance and to propose a corrective model.

In the first part of the paper, the test case is briefly presented. Then the numerical simulations (steady/unsteady) are described. The good agreement between unsteady numerical results and available experiments allowed the use of the computational fluid dynamics (CFD) results for investigating the mechanisms involved in the interaction. Finally, an analytical model is proposed in order to correct part of the change in performance, from only steady data.

2 Test Case

The centrifugal compressor stage designed and built by TURBOMECA is composed of a backswept splintered unshrouded impeller (composed of $2N_R$ blades) and a vaned diffuser (composed of N_S vanes). A 3D sketch of the stage is given in Fig. 1.

Figure 2 shows a meridional view of the compressor stage and the two sections where LDA measurements are shown in this paper. Results of LDA measurements at cross sections from the impeller inlet up to the diffuser throat can be found in Ref. [9].

The measurements and calculations were performed at a rotation speed $\Omega_R = 0.927 \cdot \Omega_{nom}$. At that speed, the rotor runs with

Contributed by the International Gas Turbine Institute of ASME for publication in the JOURNAL OF TURBOMACHINERY. Manuscript received August 21, 2008; final manuscript received September 10, 2008; published online July 2, 2009. Review conducted by David Wisler. Paper presented at the ASME Turbo Expo 2008: Land, Sea and Air (GT2008), Berlin, Germany, June 9–13, 2008.

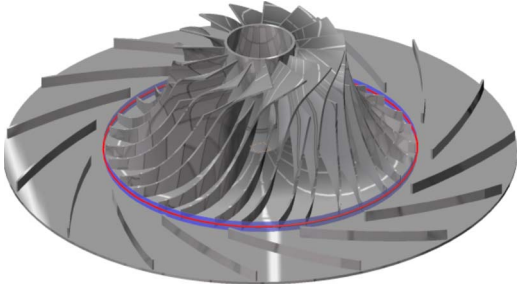


Fig. 1 3D sketch of the centrifugal compressor stage

subsonic inlet conditions all over the span whereas the absolute Mach number at the vaned diffuser inlet is supersonic.

3 Numerical Procedure

3.1 Physical Model and Turbulence Modeling. The physical model of the flow is based on the compressible three-dimensional Reynolds-averaged Navier–Stokes (RANS) equations written in the rotating frame of reference of each row

$$\frac{\partial \rho}{\partial t} + \nabla[\rho \mathbf{W}] = 0 \quad (1)$$

$$\frac{\partial \rho \mathbf{W}}{\partial t} + \nabla[\rho \mathbf{W} \otimes \mathbf{W} + \bar{\sigma} - \bar{\tau}_t] = \rho(\Omega^2 \mathbf{r} - 2\Omega \times \mathbf{W}) \quad (2)$$

$$\frac{\partial \rho E}{\partial t} + \nabla[\rho E \mathbf{W} + (\bar{\sigma} - \bar{\tau}_t) \cdot \mathbf{W} + \mathbf{q} + \mathbf{q}_t] = \rho \Omega^2 \mathbf{r} \cdot \mathbf{W} \quad (3)$$

where $\sigma = \rho \bar{l} - \bar{\tau}$. The closure of the previous system requires the specification of the Reynolds tensor $\bar{\tau}_t$ and the turbulent heat flux \mathbf{q}_t . By analogy with the Newtonian description of viscous stresses in a laminar flow, the Reynolds stress tensor is assumed to be proportional to the rate-of-strain tensor

$$\bar{\tau}_t = 2\mu_t \bar{D} - \frac{2}{3}\mu_t \nabla \cdot \mathbf{W} \bar{I} - \frac{2}{3}\rho k \bar{I} \quad (4)$$

According to the Boussinesq hypothesis μ_t is the turbulent eddy viscosity, which has to be modeled. The two last terms provide the proper trace of the Reynolds stress tensor. This relation leads to determine two turbulent scales. The first scale is the turbulent kinetic energy and the second one is often ε , the dissipation rate of k . Smith [10] proposed a linear model, which is directly based on a length scale l , defined by $k^{3/2}/\varepsilon$. Two supplementary transport equations for k and l are solved:

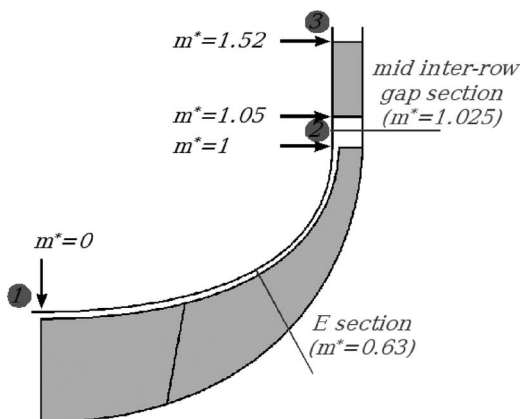


Fig. 2 Meridional view of the compressor stage

$$\begin{aligned} \frac{\partial \rho k}{\partial t} + \nabla \cdot (\rho k \mathbf{W}) - \nabla \cdot \left[\left(\mu + \frac{\mu_t}{\sigma_k} \right) \nabla k \right] \\ = \bar{\tau}_t : \overline{\text{grad}} \mathbf{W} - \frac{\rho}{B_1} \frac{(2k)^{3/2}}{l} - 2\mu_t \|\overline{\text{grad}} \sqrt{k}\|^2 \end{aligned} \quad (5)$$

$$\begin{aligned} \frac{\partial \rho l}{\partial t} + \nabla \cdot (\rho l \mathbf{W}) - \nabla \cdot \left[\left(\mu + \frac{\mu_t}{\sigma_l} \right) \nabla l \right] \\ = \frac{(2 - E_2) \rho \sqrt{2k}}{B_1 l} + \frac{2\mu_t}{\sigma_k k} \overline{\text{grad}} l \cdot \overline{\text{grad}} k \\ + \rho l \operatorname{div} \mathbf{W} - \frac{\mu_t}{\sigma_l l} \|\overline{\text{grad}} l\| \left(\frac{l}{kd} \right)^2 \end{aligned} \quad (6)$$

The turbulent viscosity is evaluated using the following relation:

$$\mu_t = \mu \chi f_\mu \quad (7)$$

with

$$\chi = \frac{\rho \sqrt{2kl}}{\mu B_1^{1/3}} \quad (8)$$

and

$$f_\mu = \left(\frac{c_1^4 f_1 + c_2^2 \chi^2 + \chi^4}{c_1^4 + c_2^2 \chi^2 + \chi^4} \right)^{1/4} \quad (9)$$

The damping function f_1 and constants are defined as

$$f_1 = \exp\left(-50 \left(\frac{l}{kd}\right)^2\right) \quad (10)$$

and

$$c_1 = 25.5, \quad c_2 = 2, \quad \kappa = 0.41, \quad \sigma_l = \sigma_k = 1.43,$$

$$B_1 = 18, \quad E_2 = 1.2$$

The specification of each mesh node distance to wall, d , is needed and computed at the beginning of the simulation. This model was previously evaluated for different turbomachinery configurations [11] and is suitable for such applications.

By analogy with the laminar heat flux, the turbulent heat flux is expressed by $\mathbf{q}_t = -K_t \nabla T$. K_t is a turbulent thermal diffusivity defined by $K_t = C_p \mu_t / \operatorname{Pr}_t$ and related to the eddy viscosity using a constant turbulent Prandtl number Pr_t . With the assumption of a constant Prandtl number, the closure of the system is reduced to the determination of μ_t and k .

3.2 Boundary Conditions. According to a subsonic flow, total pressure, total temperature, and flow angles are prescribed at the inlet of the domain. The turbulent inlet conditions are determined from a freestream turbulence rate (T_{u_∞}) equal to 5% and a characteristic length scale set to 1% of the blade pitch at the leading edge. The turbulent kinetic energy is then deduced using Bradshaw's relation $k_\infty = 1.5(T_{u_\infty} U_\infty)^2$. At the blade wall, nonslip and adiabatic conditions are prescribed. A uniform value of the static pressure is given at the outlet section. These conditions are implemented according to a technique based on characteristic relations.

In the steady approach, the flow communication between the two blade rows used a mixing plane method. In this interblade plane, a circumferential average is applied to the conservative flow quantities but preserving radial variations.

In the unsteady calculations, the phase lagged approach is used. In this approach, the computation domain is limited to a single blade passage for each row. At a stable operating point and assuming uniform inlet conditions, the unsteady effects are only due to the impeller-diffuser interaction. Then, the flow is time-periodic in the frame of reference of the rows, $T_S = 2\pi / \Omega_R N_R$ being the period in the diffuser frame and $T_R = 2\pi / \Omega_R N_S$ being the period in

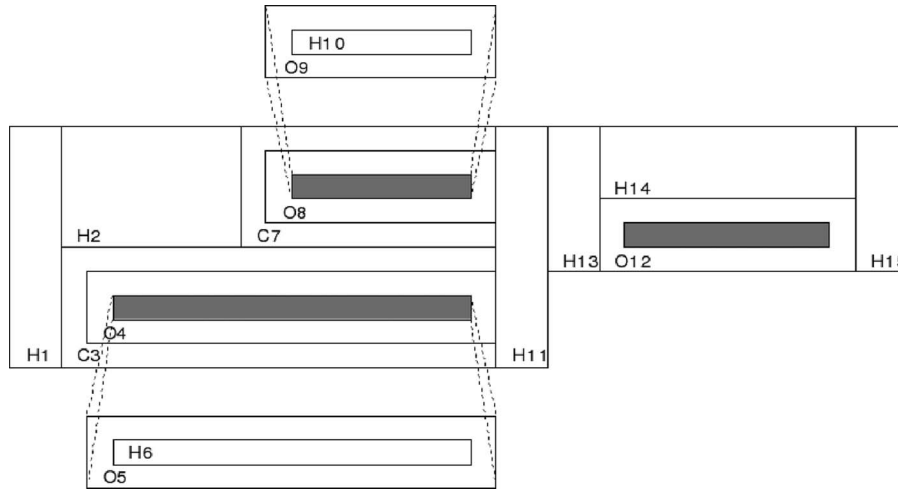


Fig. 3 H-C-O topology of the mesh

the impeller frame (N_S and N_R are, respectively, the number of stator and rotor blades). As a consequence of the time-periodicity in each frame, a phase-lag exists between two adjacent blade passages. For each row, this phase-lag is the time taken by a blade of the next row to cover the pitch of the row, modulo the time-period of the row. Basically, the phase-lagged technique consists in storing the flow values on the periodic boundaries and on the impeller-diffuser interface boundaries in order to deal with the phase-lag existing between adjacent blade passages. In order to manage the stored data, the constant time-step used by the solver, Δt , is conveniently defined such as $T_S = N_S N_q \Delta t$ and $T_R = N_R N_q \Delta t$, with N_q an integer intended to satisfy the Courant-Friedrichs-Lewy (CFL) stability criterion. When N_S and N_R are prime numbers, the number of iterations to describe a thorough revolution of the impeller is then equal to $N_S N_R N_q$.

3.3 Numerical Scheme. The numerical code used for this study was the elsA solver developed by Cambier and Gazaix [12] and validated for external aerodynamic and steady or unsteady turbomachinery configurations. This code solves the previous presented equations (the compressible Reynolds-averaged Navier-Stokes equations, associated with the two-equation turbulence model $k-l$) in the rotating frame of reference.

A cell-centered finite volume technique is used on structured meshes.

The time integration is a backward Euler scheme with implicit operators. In this work, the implicit operators were approximated with scalar linearizations and inverted by a lower-upper (LU) relaxation method.

The space discretization used a centered Jameson scheme. Second and fourth order dissipative terms were added to capture the discontinuities and ensure numerical stability. Martinelli's correction [13] was also applied. For the turbulent transport equation system, only the viscous part is discretized using the previous space centered scheme.

In order to accelerate the convergence to the steady state the classical multigrid method proposed by Jameson [14] was used.

3.4 Mesh. A multidomain approach on structured meshes is used with classical H, O, and C topologies (Fig. 3). The near-wall regions around the blades are described by an O-block to allow a precise description of the viscous effects. C-blocks are used to connect O-blocks of the main blade and the splitter. Upstream, downstream, and interface regions are defined with classical H-blocks.

4 Overall Performances

The pressure ratio curves coming from the steady calculations, the unsteady calculations, and the experiments are plotted in Fig. 4 as a function of the specific mass flow, at rotor speed $\Omega_R = 0.927 \cdot \Omega_{nom}$. The pressure ratio is defined as $\pi = p_3 / p_{01}$, and the specific mass flow as

$$\dot{m}_{sp} = \frac{\dot{m} \sqrt{\gamma r T_{01}}}{D_{1S}^2 p_{01}} \quad (11)$$

The experimental value of p_3 is the mean value of the static pressures measured on the shroud and hub wall surfaces at the stage outlet (Fig. 2). The health of the facility during the test was continuously monitored via the measured pressures, temperatures, and flow rate, which are given at $\pm 0.4\%$, ± 1 K, and $\pm 0.2\%$, respectively.

The numerical values come from data extracted in the same sections. The mean outlet static pressures from steady and unsteady calculations come from area-averaged and time and area-averaged values, respectively. For the mean mass flow calculation, the data were mass-averaged and time and mass-averaged.

An excellent agreement between the unsteady numerical data and the experiments is found for the four calculated points. It is

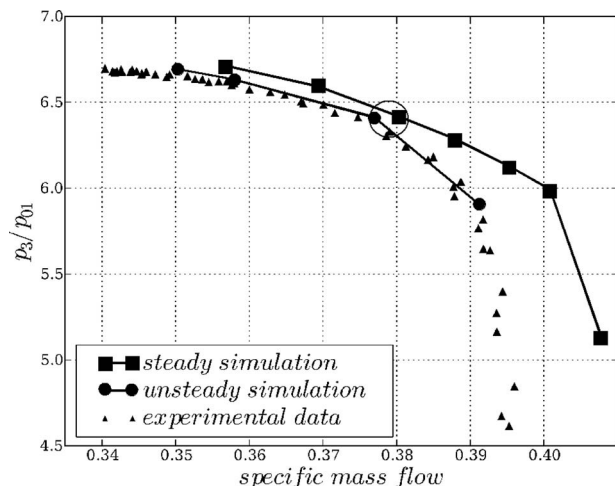


Fig. 4 Pressure ratio of the compressor stage

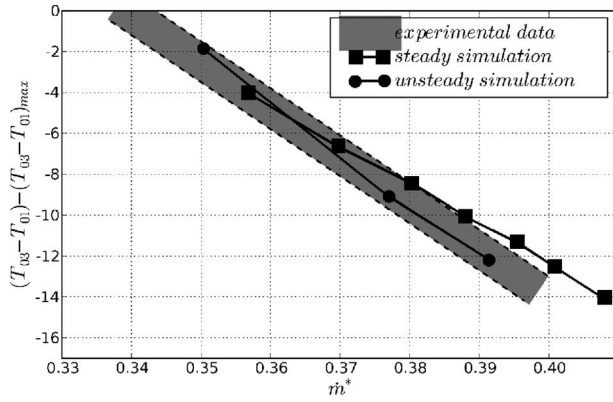


Fig. 5 Reduced temperature rise

important to note that neither operating points close to the compressor stall nor close to choke were calculated in the present study.

The pressure ratio–mass flow curve resulting from the steady simulations is clearly shifted, which leads to overestimate the pressure ratio whatever the mass flow. The calculated choking mass flow is overestimated by 3.3%.

Figure 5 gives the stagnation temperature rise coming from the steady calculations, the unsteady calculations, and the experiments as a function of the specific mass flow. The experimental data are represented with a gray band, which takes into account the measurement uncertainty. The temperature rise $(T_{03}-T_{01})$ was reduced by the maximum value of the experimental temperature rise: $(T_{03}-T_{01}) - \max(T_{03}-T_{01})_{\text{exp}}$ is thus plotted versus \dot{m}_{sp} . The three sets of temperature rise are very similar so that the shift in pressure ratio between the unsteady and steady results is thought to be pressure loss related.

In order to understand the detrimental effect of the unsteadiness on the pressure ratio, attention is now focused on the origin of the unsteady processes, at a given operating point, which is circled in Fig. 4. This point was chosen because at this point, experimental internal flow data were available and the unsteady calculation exhibited an excellent convergence rate.

5 Flow Unsteadiness in The Compressor Stage

By solving an unsteady RANS equation system, it is possible to calculate the deterministic unsteady flow field $f(r, \theta_{R/S}, z, t)$. The subscript R/S means that the data may be expressed either in the relative frame of reference or in the absolute frame of reference. The time-dependent flow $f(r, \theta_{R/S}, z, t)$ may be decomposed into a time-averaged component $\overline{f(r, \theta_{R/S}, z, t)}$ and a fluctuating component $f'(r, \theta_{R/S}, z, t)$ as follows:

$$f(r, \theta_{R/S}, z, t) = \overline{f(r, \theta_{R/S}, z, t)} + f'(r, \theta_{R/S}, z, t) \quad (12)$$

The level of unsteadiness ($\overline{f'^2}$) was first quantified by calculating the time-averaged value of the fluctuating component absolute value

$$\overline{f'^2} = \overline{|f'(r, \theta_{R/S}, z, t)|} \quad (13)$$

Figure 6 shows the meridional evolution of the unsteadiness level, as defined in Eq. (13), based on the pressure ($\overline{p'^2}$) reduced by the axisymmetric value of the static pressure at the mid inter-row gap. The evolution is given through the impeller (calculated in the relative frame) and through the diffuser (calculated in the absolute frame), at the operating point circled in Fig. 4. The abscissa is the reduced meridional distance, with $m^*=0$ located at the impeller leading edge, $m^*=1$ at the impeller trailing edge, $m^*=1.05$ at the vane leading edge, and $m^*=1.52$ at the vane trailing edge (cf. Fig.

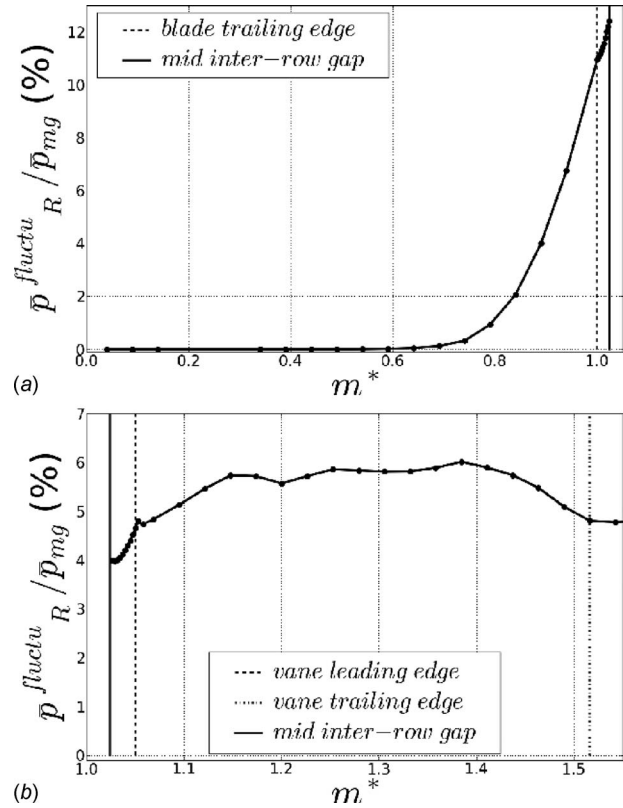


Fig. 6 Level of unsteadiness through the impeller (a) and through the vaned diffuser (b)

2). The scales of the ordinates are different because of the change in frame.

The flow behavior predicted by the unsteady simulation is completely steady up to around $m^* \approx 0.65$ (Fig. 6(a)). Moreover, up to this abscissa, a very good agreement is found regarding the internal flow field, which is measured or calculated with both the steady and unsteady codes. Figures 7 and 8 show the reduced meridional and tangential velocity components (V_m/U_2 and V_t/U_2) at a cross section located in the highest meridional curvature of the impeller ($m^*=0.63$). Maps (a), (b), and (c) are plotted with data coming from the experiments, unsteady calculation (time-averaged data), and steady calculation, respectively.

In the experimental maps, the grid within the black frame shows the points where the accuracy of the data is better than $\pm 1\%$. In the outer parts, data were erased because accuracy is poor due to the decrease in signal-to-noise ratio resulting from a decrease in seeding and an increase in the light reflections from the blade surfaces.

The frame superimposed over the numerical data shows the domain where the reliable LDA data are available. Both experimental and numerical maps are drawn with the same scale. Within the comparable domains, a reasonable agreement is obtained, which notably justifies the use of the CFD results for a deeper analysis.

From $m/m_s \approx 0.65$ the level of unsteadiness is significant, both in the rear part of the impeller, in the vaneless space, and in the vaned diffuser (Figs. 6(a) and 6(b)). At mid inter-row gap ($m^* = 1.025$) the absolute value of the fluctuating static pressure reaches 12% of the mean static pressure, which is not negligible.

If expressed in the absolute frame of reference, the fluctuating component f' actually contains the spatial fluctuations of the time-averaged field in the rotating frame of reference and the purely unsteady part of the field

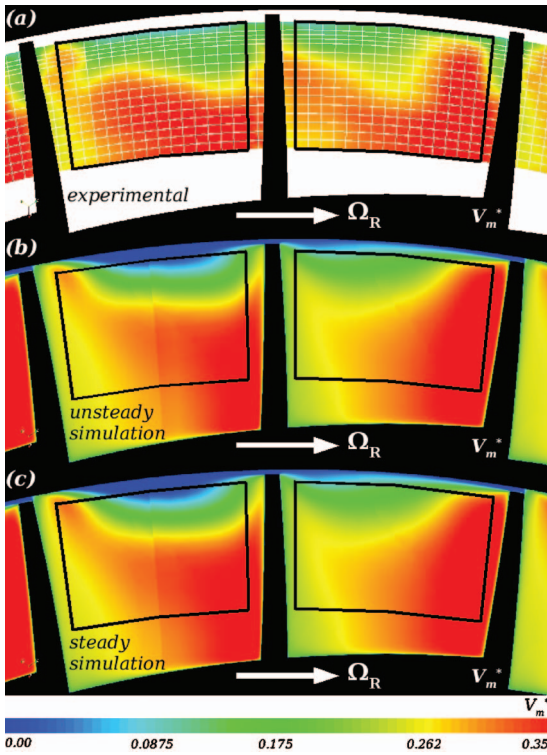


Fig. 7 Reduced meridional velocity at section E ($m^*=0.63$)

$$f'(r, \theta_S, z, t) = f^R(r, \theta_R, z) + f''(r, \theta_S, z, t) \quad (14)$$

The purely unsteady effects of the impeller-diffuser interaction are included in that term f'' , which is obviously absent in a steady simulation.

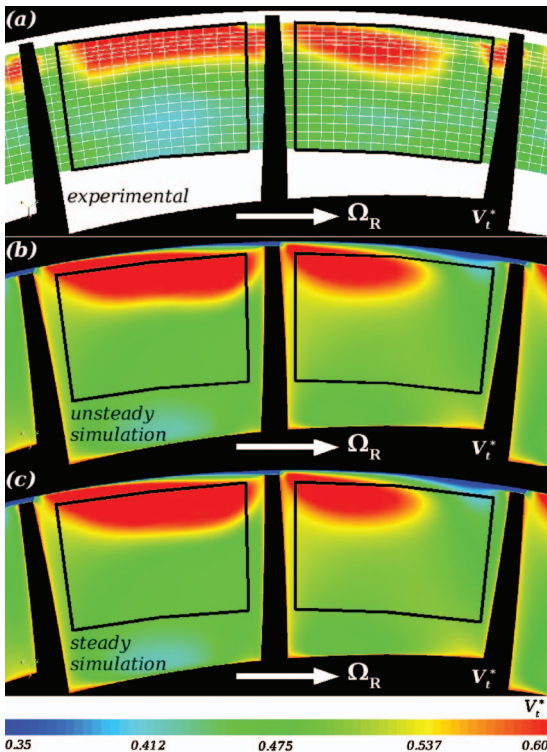


Fig. 8 Reduced tangential velocity at section E ($m^*=0.63$)

Figure 9 shows the purely unsteady part of the relative velocity plotted in a time/space plot, over a stator pitch (abscissa) and a rotor time-period (ordinate), at mid inter-row gap ($m^*=1.025$) and at 70% of blade height. The inclined lines represent the blade wake locations. Maps (a) and (b) are plotted with data coming from the experiments and the unsteady calculation, respectively, with the same scale. According to Eqs. (12) and (14), the purely unsteady part of the relative velocity was calculated as

$$\underbrace{W''(r, \theta_S, z, t)}_{(5)} = \underbrace{W(r, \theta_S, z, t)}_{(1)} - \left[\underbrace{W^{\text{axi}}}_{(2)} + \underbrace{W^S(r, \theta_S, z)}_{(3)} + \underbrace{W^R(r, \theta_R, z)}_{(4)} \right] \quad (15)$$

It was obtained by subtracting the axisymmetric field (term (2)) and the time-averaged fields calculated in the frame of reference of the vaned diffuser (term (3)) and impeller (term (4)) from the time-dependent flow field (term (1)). It is important to note that in both the experiments and the calculation, the random time scales of the turbulent flow are filtered. Thus, the unsteadiness captured in the periodic evolution of the flow field only relates to the phenomena clocked with the rotor main blade passing frequency.

Despite the lower amount of grid points described in the experiments compared with the calculation, the agreement is rather satisfying in terms of both flow pattern and unsteadiness level. Spots of high level of unsteadiness are observed near the coincidence between a blade trailing edge and a vane leading edge (marked out by the vertical lines). This may be further explained; thanks to the temporal maps of the flow field (given in Fig. 11). Concerning the experiments (Fig. 9(a)), the energetic contribution of the purely unsteady velocity W'' reaches 20% of the energy contained in the fluctuating component W' . Regarding the numerical results (Fig. 9(b)), this value is equal to 21%. These values are very similar and show that the purely unsteady component has a significant contribution to the total fluctuating component.

6 The Origin of Performance Changes

The unsteadiness may be source of additional entropy increase. Figure 10 gives the meridional evolution of entropy from the impeller leading edge ($m^*=0$) up to the diffuser vane trailing edge ($m^*=1.52$), resulting from the steady and unsteady calculations at the operating point circled in Fig. 4.

The entropy from steady and unsteady calculations was mass-averaged and mass and time-averaged, respectively. The mid inter-row gap ($m^*=1.025$) is marked with a continuous line; the leading and trailing edges of the impeller and vane are marked with dotted lines. The difference in entropy between the steady and unsteady calculations is situated in a region between $m^* \approx 0.90$ and $m^* \approx 1.15$, around the vaneless space. Upstream $m^* = 0.90$ the two entropy evolution curves are superimposed: The unsteadiness observed between $m^* \approx 0.65$ and $m^* \approx 0.90$ (Fig. 6(a)) is not a source of entropy. Downstream $m^* = 1.15$, the two curves are parallel: Nor does the unsteadiness within the diffuser has a significant effect in terms of entropy (keeping in mind that the turbulence model is based on the Reynolds-averaged flow, i.e., the turbulence model is a quasisteady model), even if it has been shown [15] that it led to a pulsating behavior of separated bubbles on the vane pressure side, which may be an onset of strength instabilities.

It is thus found that the discrepancy in performances predicted by the unsteady and steady simulations comes from the inter-row gap region ($0.90 < m^* < 1.15$). The physical mechanisms responsible for this change in entropy are highlighted in Fig. 11, which shows the time-dependent absolute Mach number in the interaction region, at 50% section height for 12 time steps over the rotor blade passing period. The white lines, which are superimposed in each frame, localize $m^*=0.90$, $m^*=1.025$, and $m^*=1.15$. The sonic lines (SLs) are marked out with black curves.

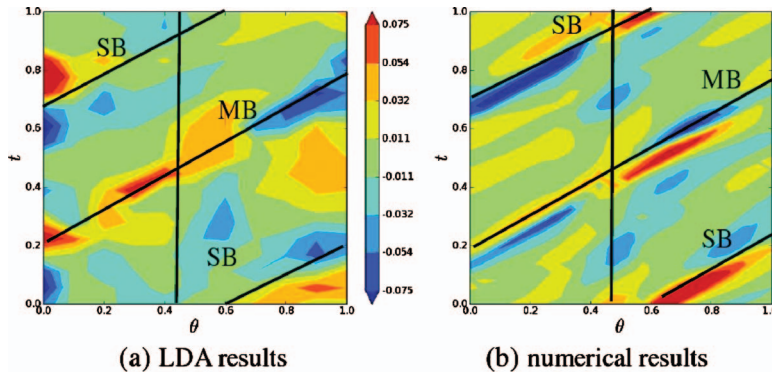


Fig. 9 Purely unsteady relative velocity at mid inter-row gap and 70% section height, over a stator pitch and a rotor time-period

As a blade moves close to a vane leading edge, it interacts with the vane bow shock, which shape is thus very deformed. At these “metal coincidence” time steps, high fluctuations are generated, as it was observed in Fig. 9. Subsonic pockets move upstream along

the pressure side of both the main blade (Figs. 11(c) and 11(d)) and the splitter blade (Figs. 11(i) and 11(j)). They lead to an area of low Mach number visible even upstream $m^*=0.9$, which explains unsteadiness between $m^*=0.65$ and $m^*=0.9$ (cf. Fig. 6(a)) without any entropy generation.

Other subsonic pockets are torn out from the vane leading edge bow shock and swept along the vane suction side (Figs. 11(g), 11(h), and 11(l)). This is very similar to the observations of Gorrell et al. [16] from a study of the interaction of an inlet guide vane and a transonic rotor.

Moreover, the flow emerging from the impeller is distorted because of combined effects of curvatures, rotation, and tip leakage flow. This distortion leads to the classical “jet and wake” structure, which, as it moves, is responsible of a periodic increase in Mach number ahead of the bow shock wave. Therefore the shock wave periodically steepens and flattens upstream of the vane channels and the entropy increase in passing through the shock periodically fluctuates.

The time-averaged effect of the moving of the jet-wake structure ahead of the vaned diffuser and the associated deformation of the bow shock are summarized in Fig. 12, which gives the abso-

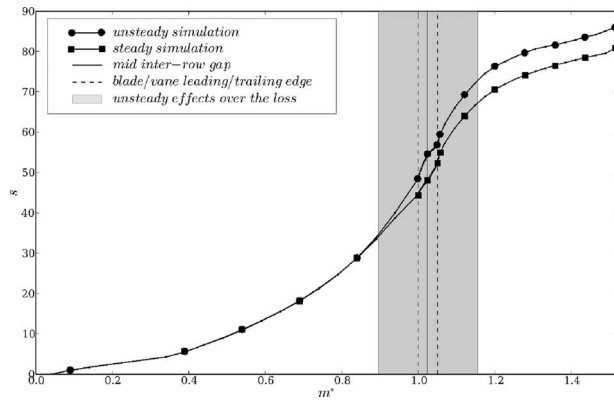


Fig. 10 Meridional evolution of entropy

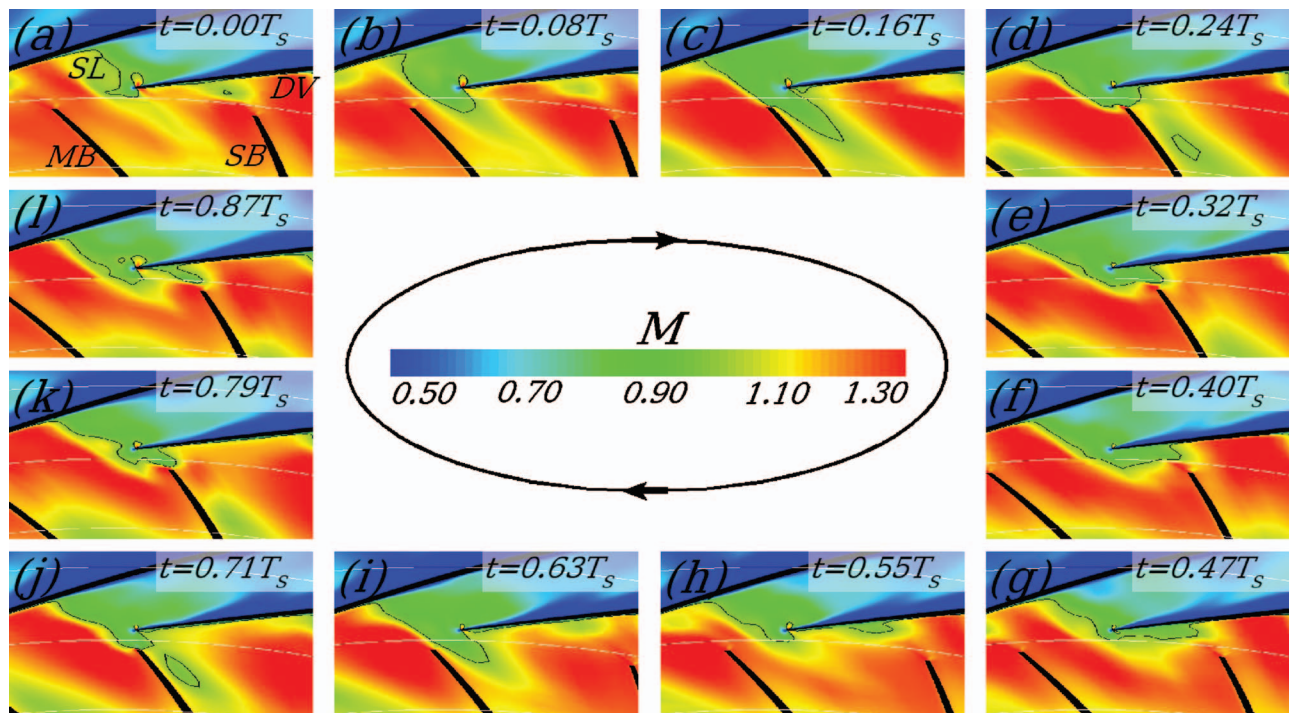


Fig. 11 Absolute Mach number contours, at 50% section height

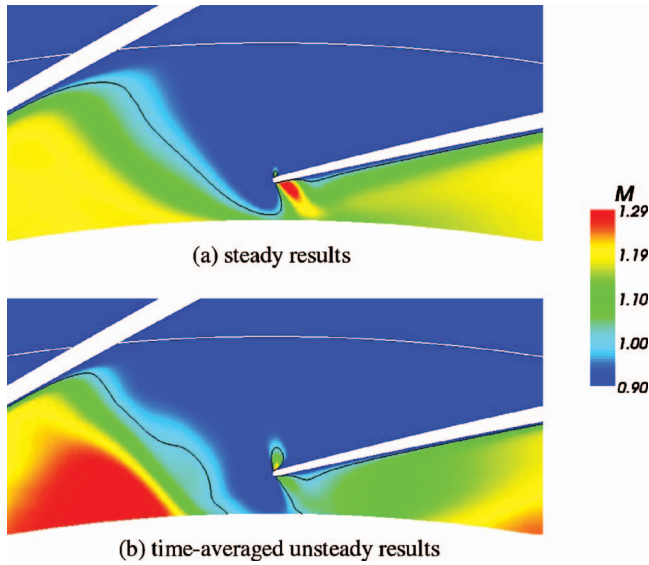


Fig. 12 Absolute Mach number, at 50% height

lute Mach number contours in the diffuser entry zone, from the rotor/stator meshes' interface where the mixing plane method is applied in the steady simulation ($m^*=1.025$) up to $m^*=1.15$.

Figure 12(a) shows the results obtained from the steady simulation: The bow shock obviously cannot extend upstream of the mixing plane. Therefore, even if the circumferentially averaged Mach number at $m^*=1.025$ has the same value as the time and circumferentially averaged Mach number resulting from the unsteady simulation (Fig. 12(b)), the Mach number in front of the shock is far lower in the steady case than in the time-averaged unsteady case. Consequently, the losses associated with the shock are lower in the steady case than in the unsteady one.

As the moving of the jet and wake flow structure in front of the bow shock was supposed to account for the majority of the performance change, a model is hereafter proposed in order to integrate the associated additional loss in the steady performances.

7 A Corrective Model

The model aims to introduce the effects of the moving of the jet-wake structure in front of the vane bow shock in the pressure ratio coming from the steady calculations. The pressure ratio is expressed as

$$\pi = \frac{p_3}{p_01} = \frac{p_{02} p_{02'}}{p_{01} p_{02} p_{02'}} \quad (16)$$

which means that the overall pressure ratio is written as the product of the ratios (p_{02}/p_{01}) in the impeller, ($p_{02'}/p_{02}$) across the shock, and ($p_3/p_{02'}$) in the subsonic part of the diffuser. This decomposition supposes that the loss across the shock is dissociated from other losses. This assumption is acceptable as long as the shock/vane suction side boundary layer interaction does not lead to any boundary layer separation, which is the case if the incident Mach number is lower than around 1.35.

Supposing that the pressure ratios within the impeller (p_{02}/p_{01}) and in the subsonic part of the diffuser ($p_3/p_{02'}$) are unchanged, the corrected overall pressure ratio is thus calculated as

$$\pi|_{\text{corr}} = \pi \frac{\left. \frac{p_{02'}}{p_{02}} \right|_{\text{corr}}}{\left. \frac{p_{02'}}{p_{02}} \right|_{\text{steady}}} \quad (17)$$

The stagnation pressure ratio across a shock, $p_{02'}/p_{02}$, is given by

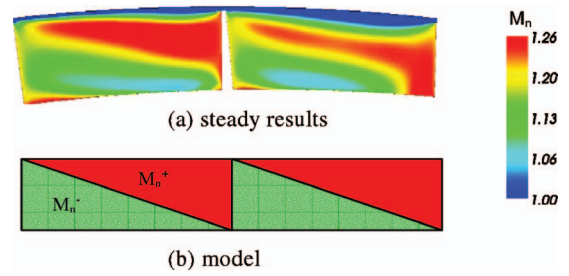


Fig. 13 Absolute normal Mach number, close to impeller exit

$$\frac{p_{02'}}{p_{02}} = \left(1 + \frac{2\gamma}{\gamma+1} (M_{n2}^2 - 1) \right)^{-1/(\gamma-1)} \left(1 - \frac{2\gamma}{\gamma+1} \left(1 - \frac{1}{M_{n2}^2} \right) \right)^{-\gamma/(\gamma-1)} \quad (18)$$

or for short

$$\frac{p_{02'}}{p_{02}} = \frac{p_{02'}}{p_{02}} (M_{n2}) \quad (19)$$

The difference between $p_{02'}/p_{02}|_{\text{steady}}$ and $p_{02'}/p_{02}|_{\text{corr}}$ in Eq. (17) comes from the normal Mach number, which is introduced into Eq. (18).

- (1) For the calculation of $p_{02'}/p_{02}|_{\text{steady}}$, the considered normal Mach number is the mass-averaged normal Mach number in front of the shock, $\overline{M_n}|_{\text{inlet-shock}}$, extracted from the steady calculation.
- (2) For the calculation of $p_{02'}/p_{02}|_{\text{corr}}$, the time-averaged effect of the moving of the jet-wake structure ahead of the shock is taken into account through the induced fluctuations of the normal Mach number. Figure 13(a) gives the absolute normal Mach number close to the impeller exit, coming from the steady calculation. The jet and wake structure is identifiable by a high Mach number zone in the shroud-suction side corner. Ignoring the tip leakage flow, the flow pattern may be modeled as shown in Fig. 13(b), which derives from the jet-wake model proposed by Rohne and Banzhaf [17]. At any section height, a high Mach number M_n^+ occurs in a portion of the blade passage and a low Mach number M_n^- occurs in the rest of the passage. Therefore the loss across the shock is calculated as

$$\left. \frac{p_{02'}}{p_{02}} \right|_{\text{corr}} = \xi \frac{p_{02'}}{p_{02}} (M_n^+) + (1 - \xi) \frac{p_{02'}}{p_{02}} (M_n^-) \quad (20)$$

with $\xi=0.5$, at 50% section height.

As shown in Fig. 13(b), ξ linearly varies from 1 at shroud to 0 at the hub.

Due to the fact that the loss increase across a shock is not a linear function of the inlet Mach number (Eq. (18)), the loss calculated with Eq. (20) differs from the loss based on the mean value of M_n^+ and M_n^- .

The flow diffusion from the impeller exit up to the shock is taken into account through the mass-averaged normal Mach number. Therefore, the values of M_n^+ and M_n^- , which are injected in Eq. (20), are calculated as

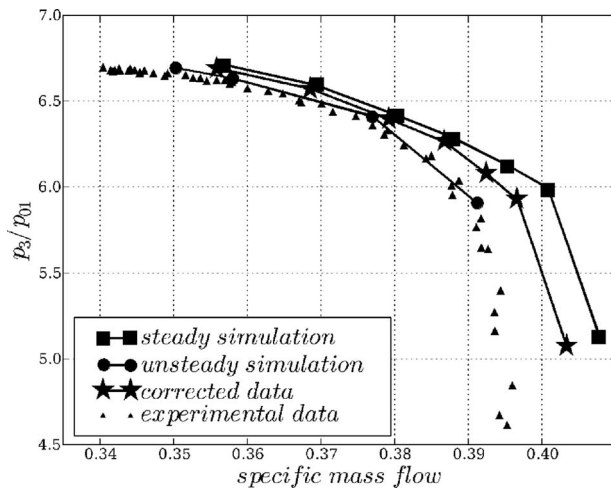


Fig. 14 Corrected pressure ratio of the compressor stage

$$M_n^+ = \overline{M}_n|_{\text{inlet-shock}} + (M_n^+|_{\text{impeller_exit}} - \overline{M}_n|_{\text{impeller_exit}})$$

$$M_n^- = \overline{M}_n|_{\text{inlet-shock}} - (M_n^-|_{\text{impeller_exit}} - \overline{M}_n|_{\text{impeller_exit}}) \quad (21)$$

7.1 Application. This model was applied to the pressure ratio–mass flow curve obtained with the steady calculations. Each operating point was corrected both in pressure ratio and in mass flow rate according the relation $\pi/\dot{m} = C$ (C being a constant). Assuming a prescribed static outlet temperature T_3 , such a relation imposes the Mach number and the flow angle at the stage outlet (M_3 and α_3).

At any given operating point the pressure ratio was corrected accordingly the corrective model. Knowing the constant C , the corrected mass flow was thus calculated as

$$\dot{m}_{sd|corr} = C^{-1} \cdot \pi|_{corr} \quad (22)$$

Figure 14 shows the pressure ratio–mass flow rate curves coming from the experiments, the unsteady calculations, the steady calculations, and the corrective model applied to the steady results.

The model leads to a significant shift of the steady prediction toward the unsteady (experimental and numerical) results. Due to the fact that only a part of the identified mechanisms responsible for the additional losses were taken into account, the correction is not perfect. Nevertheless, around half of the difference was corrected. That is particularly noticeable regarding the choking mass flow prediction, which overestimation is reduced from 3.3% to 2%.

8 Conclusion

The pressure ratio achieved in a high-pressure transonic centrifugal compressor showed to be overestimated by steady computations in comparison with unsteady numerical results and experiments. A detailed analysis of the internal flow field led to identify the physical mechanisms responsible for the additional losses associated with unsteadiness. The origin of these additional losses was mainly located in the inter-row gap region.

A simple analytical model was proposed in order to correct the steady predictions from the losses associated with the moving of the jet and wake flow structure emanating from the impeller in front of the vane leading bow shock. The model requires only data extracted from the steady calculations. In the present case, the model enhances the performances prediction, notably regarding the choking flow. Nevertheless, it should be interesting to test it in other transonic compressors for validation.

In the present work, major effort was focused on the impeller-diffuser interaction losses generated in the inter-row gap. There are clearly other additional losses of which mixing losses, tip-gap

losses, and those due to shock-vane boundary layer interaction. This last phenomenon is all the more important as the operating point moves toward the choke. Current analysis of unsteady simulations shows that the periodic change in strength of the shock leads to a severe vane boundary layer separation, which may be source of a choking mass flow decrease and additional unsteady losses. This has to be deeper investigated in order to enhance the proposed corrective model.

Acknowledgment

We would like to thank TURBOMECA, which supported this research. G. Halter, P. Krikorian, and B. Paoletti are acknowledged for experimental support. The numerical simulations were performed on NEC SX6 computer of the CNRS-IDRIS Center.

Nomenclature

Latin Letters

- D = diameter
- f = arbitrary flow variable
- k, l = kinetic turbulent energy, length scale of turbulence
- LDA = Laser Doppler anemometry
- m = meridional coordinate
- \dot{m} = mass flow
- M = Mach number
- MB, SB = main blade, splitter blade
- N = number of blades
- PS, SS = pressure side, suction side
- p = pressure
- r, θ, z = cylindrical coordinates
- T = time-period, temperature
- t = time
- U = impeller speed
- V = absolute velocity
- W = relative velocity

Greek Letters

- γ = specific heat ratio
- π = pressure ratio
- ρ = density
- Ω = rotation speed

Superscripts and Subscripts

- $*$ = reduced variable
- \bar{f} = mass-averaged value of f
- axi = axisymmetric variable
- 0 = total variable
- 1 = at impeller inlet
- 2 = at impeller exit
- 3 = at diffuser exit
- m, r, t = meridional, radial, tangential
- n = normal
- nom = nominal
- R/S = relative to rotor/stator (impeller/diffuser)

References

- [1] Krain, H., 1981, "A Study on Centrifugal Impeller and Diffuser Flow," ASME J. Eng. Power, **103**, pp. 688–697.
- [2] Inoue, M., and Cumpsty, N. A., 1984, "Experimental Study of Centrifugal Impeller Discharge Flow in Vaneless and Vaned Diffusers," ASME J. Eng. Gas Turbines Power, **106**, pp. 455–467.
- [3] Ziegler, K. U., Gallus, H. E., and Niehuis, R. A., 2003, "A Study on Impeller-Diffuser Interaction—Part I: Influence on the Performance," ASME J. Turbomach., **125**, pp. 173–182.
- [4] Ziegler, K. U., Gallus, H. E., and Niehuis, R. A., 2003, "A Study on Impeller-Diffuser Interaction—Part II: Detailed Flow Analysis," ASME J. Turbomach., **125**, pp. 183–192.
- [5] Deniz, S., Greitzer, E. M., and Cumpsty, N. A., 2000, "Effects of Inlet Flow Field Conditions on the Performance of Centrifugal Compressor Diffusers—Part II: Straight-Channel Diffuser," ASME J. Turbomach., **122**, pp. 11–21.

- [6] Shum, Y. K. P., Tan, C. S., and Cumpsty, N. A., 2000, "Impeller-Diffuser Interaction in a Centrifugal Compressor," *ASME J. Turbomach.*, **122**, pp. 777–786.
- [7] Krain, H., 2002, "Unsteady Diffuser Flow in a Transonic Centrifugal Compressor," *Int. J. Rotating Mach.*, **8**, pp. 223–231.
- [8] Krain, H., and Hah, C., 2003, "Numerical and Experimental Investigation of the Unsteady Flow Field in a Transonic Centrifugal Compressor," *Proceedings of the International Gas Turbine Congress, IGTC2003*, Tokyo, Japan.
- [9] Rochuon, N., 2007, "Analyse de l'écoulement tridimensionnel instationnaire dans un compresseur centrifuge à fort taux de pression," Ph.D. thesis, Ecole Centrale de Lyon, Cedex, France.
- [10] Smith, B. R., 1994, "Prediction of Hypersonic Shock Wave Turbulent Boundary Layer Interactions With the k-1 Two-Equation Turbulence Model," AIAA Paper No. 95-02232.
- [11] Kulisa, P., and Dano, C., 2006, "Assessment of Linear and Non-Linear Two-Equation Turbulence Models for Aerothermal Turbomachinery Flows," *J. Therm. Sci.*, **15**(1), pp. 14–26.
- [12] Cambier, L., and Gazaix, M., 2002, "elsA: An Efficient Object-Oriented Solution to CFD Complexity," 40th AIAA Aerospace Science Meeting and Exhibit, Reno, NV.
- [13] Martinelli, L., 1987, "Calculation of Viscous Flows With a Multigrid Method," Ph.D. thesis, Princeton University, Princeton, NJ.
- [14] Jameson, A., 1985, "Multigrid Algorithms for Compressible Flow Calculations," *Lecture Notes in Mathematics*, Vol. 1228, Springer-Verlag, Berlin.
- [15] Bulot, N., and Trébinjac, I., 2007, "Impeller-Diffuser Interaction: Analysis of the Unsteady Flow Structures Based on Their Direction of Propagation," *J. Therm. Sci.*, **16**(3), pp. 193–202.
- [16] Gorrell, S. E., Okiishi, T. H., and Copenhaver, W. W., 2002, "Stator-Rotor Interactions in a Transonic Compressor: Part 2—Description of a Loss Producing Mechanism," ASME Paper No. GT-2002-30495.
- [17] Rohne, K. H., and Banzhaf, M., 1991, "Investigation of the Flow at the Exit of an Unshrouded Centrifugal Impeller and Comparison With the Classical Jet-Wake Theory," *ASME J. Turbomach.*, **113**, pp. 654–659.

Effect of Wakes and Secondary Flow on Re-attachment of Turbine Exit Annular Diffuser Flow

David Kluß

e-mail: david.kluss@rub.de

Horst Stoff

Department for Fluid Energy Machines,
Ruhr-Universität Bochum,
44801 Bochum, Germany

Alexander Wiedermann

Mem. ASME
MAN Turbo AG,
46145 Oberhausen, Germany

In this paper numerical results of wake and secondary flow interaction in diffuser flow fields are discussed. The wake and secondary flow are generated by a rotating wheel equipped with 30 cylindrical spokes with a diameter of 10 mm as a first approach to the turbine exit flow environment. The apex angle of the diffuser is chosen such that the flow is strongly separated according to the well-known performance charts of Sovran and Klomp (1967, "Experimentally Determined Optimum Geometries for Rectilinear Diffusers With Rectangular, Conical or Annular Cross-Section," in Fluid Mechanics of Internal Flow, Elsevier, New York, pp. 272–319). This configuration has been tested in an experimental test rig at the Leibniz University Hannover (Sieker and Seume 2007, "Influence of Rotating Wakes on Separation in Turbine Exhaust Diffusers," Paper No. ISAI8-54). According to these experiments, the flow in the diffuser separates as free jet for low rotational speeds of the spoke-wheel, as expected by theory. However, if the 30 spokes of the upstream wheel rotate beyond the value of 500 rpm the measurements indicate that the flow remains attached to the outer diffuser wall. It will be shown by the present numerical analysis with the commercial solver ANSYS CFX-10.0 that only an unsteady approach using the elaborate scale adaptive simulation with the shear stress transport turbulence model is capable of predicting the stabilizing effect of the rotating wheel to the diffuser flow at larger rotational speeds. The favorable comparison with the experimental data suggests that the mixing effect of wakes and secondary flow pattern is responsible for the reattachment. As a result of our studies, it can be stated that the considerably higher numerical costs associated with unsteady calculations must be accepted in order to increase the understanding of the physical flow phenomena in turbine exit flow and its interaction with the downstream diffuser. [DOI: 10.1115/1.3070577]

1 Introduction

It is well known that a proper exit diffuser design can raise the gas or steam turbine power output considerably due to the better conversion of kinetic energy behind the last turbine stage into a high static pressure recovery of diffuser exhaust system. Therefore, turbine exit diffusers have a significant impact on the overall engine size and efficiency of steam and gas turbines.

Furthermore, it is generally accepted that the turbine outlet flow pattern has to be taken into account in the diffuser design process to reduce the size of diffusers for more compact designs of exhaust systems in turbomachines. Currently, annular diffuser design systems are based on the well-known performance maps developed by Sovran and Klomp [1] or the more advanced maps by ESDU [2]. These performance charts are important for the pre-design, but essential features of the turbine exit flow such as swirl, total pressure profiles, and tip-clearance flows are not considered. Concerning swirl and tip-clearance effects, experiments have shown a positive effect of moderate inlet swirl on the performance of diffusers, which are operated close to stall, see, for example, Ref. [3] for conical and Ref. [4] for annular diffusers. Back and Cuffel [5] and Nicoll and Ramaprian [6] investigated the strong effect of tip-clearance represented by a near-wall-jet injection by which the separation zone at the diffuser outlet could be reduced. A large number of experiments for isolated diffuser flow studies

are available in the open literature and a comprehensive overview on the current state-of-the-art of diffuser design correlations has been published by Japikse [7].

In addition to these isolated diffuser investigations, extensive experimental studies of interaction effects of an axial cold air turbine with annular diffuser flow fields were carried out by Quest and Kruse [8]. The favorable effect of inlet swirl on diffuser performance was confirmed in these investigations but unlike the isolated diffuser flow field investigations, the orientation of the absolute swirl with respect to the rotation of the turbine was shown to have a dominant effect on diffuser performance. An important result of these studies was that the optimum of static pressure recovery for constant area ratio diffusers could be moved toward shorter normalized diffuser sizes of L/h_1 than given by the performance charts of Sovran and Klomp [1].

The observations of all these experimental investigations indicate that for more accurate and compact design the entire system of last turbine stage, diffuser, and duct have to be taken into account during the design process.

In order to overcome these shortcomings, computational fluid dynamics (CFD) have become important to gain more insight in the interaction effects inherent with turbine and diffuser flows. Willinger and Hasselbacher [9] studied the effect of rotor tip-clearance flow on diffuser performance with a Navier–Stokes solver, where the turbulent flow was simulated using a $k-\varepsilon$ turbulence model. Vassiliev et al. [10] applied various turbulence models based on the eddy-viscosity hypothesis. A comparison of the computed diffuser pressure loss coefficients of coupled and uncoupled turbine-diffuser configurations showed that all flow field features, for example, turbulent kinetic energy and secondary flow, have to be captured in order to estimate realistic inlet boundary conditions for isolated diffuser flow field computations.

If applying CFD for design, cost and speed of the analysis are

Contributed by the International Gas Turbine Institute of ASME for publication in the JOURNAL OF TURBOMACHINERY. Manuscript received August 22, 2008; final manuscript received October 16, 2008; published online July 6, 2009. Review conducted by David Wisler. Paper presented at the ASME Turbo Expo 2008: Land, Sea and Air (GT2008), Berlin, Germany, June 9–13, 2008.

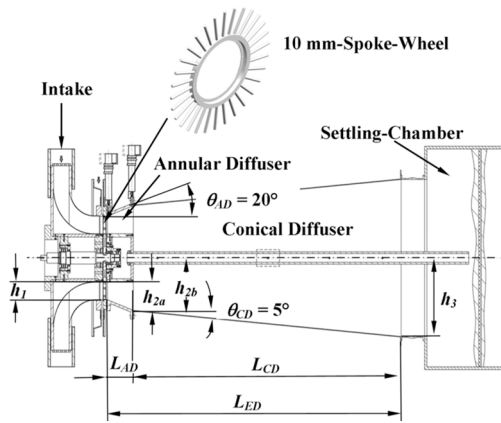


Fig. 1 Diffuser test rig facility

of crucial importance. In state-of-the-art applications steady-state analysis with mixing plane or frozen-rotor approaches are preferred. By using the frozen-rotor approach numerical investigations by Kluß et al. [11] have shown that circumferentially non-uniform flow at the diffuser entrance has a strong effect on the diffuser performance, which could not be obtained with the classical mixing plane approach.

The goal of the current paper is to understand the impact of secondary flows on the separated diffuser performance, which has been observed in a test rig at the Leibniz University Hannover [12], where the last stage of a turbine has been simulated using a wheel with 30 spokes. In order to estimate the effort to cover all essential features of the real flow in the numerical analysis, the experimental test rig facility, the numerical approach, selection of turbulence models, and their validation with steady and unsteady calculations are considered first. Finally, the effects of wakes and secondary flow, which vary with the rotational speed of the spoke-wheel, on the diffuser flow are studied with the validated numerical procedure.

2 Experimental Test Rig

The test rig is a model of a gas turbine exhaust diffuser in 1/10 scaling and was originally set up at the Leibniz University Hannover by Fleige et al. [13], which has been extended for the current investigations. Figure 1 shows the test facility and the main diffuser components. The geometrical parameters are given in Table 1.

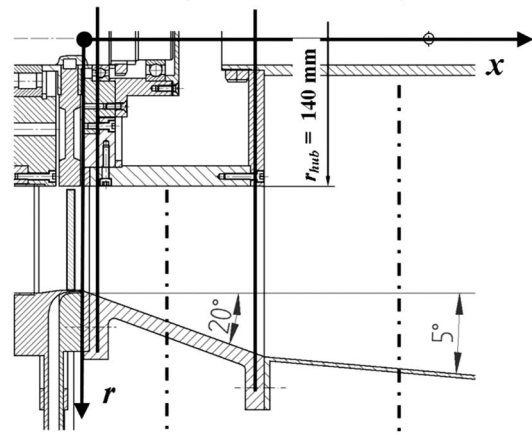
The mass-flow rate is controlled by a 37 kW axial fan, which pulls air at ambient condition through the test facility. The annular diffuser inlet Mach number is about 0.1 and the Reynolds number is in the range of 4.5×10^5 based on the inlet height h_1 and the axial mean velocity at the inlet.

In order to achieve a jetlike separation pattern of the isolated diffuser, the original configuration was replaced by a new annular diffuser with a half aperture angle of $\theta_{AD}=20$ deg. The area ratios for both the annular and conical diffusers, are kept the same.

Table 1 Geometrical parameters

Annular	Conical	Entire diffuser
$A_{2a}/A_1=1.93$	$A_3/A_{2b}=2.25$	$A_3/A_1=5.35$
$L_{AD}/h_1=1.78$	$L_{CD}/h_{2b}=5.78$	$L_{ED}/h_1=19.64$
$\nu=0.59$	-	-
$h_1=97$ mm	$h_{2b}=300$ mm, $h_3=450$ mm	-
$\theta_{AD}=20$ deg	$\theta_{CD}=5$ deg	-
Spoke-wheel diameter $d=10$ mm		
$h_1/d=9.7$	$s_m/d=3.95$	$L_{AD}/d=17.3$

Pneumatic probe position (At annular diffuser inlet) Pneumatic probe position (At annular diffuser outlet)



LDV-Position $x/h_1=0.89$ (50% of the annular diffuser length) LDV-Position $x/h_1=3.57$ (10% of the conical diffuser length)

Fig. 2 Measurement positions of pneumatic probes and LDV for the comparison of experiments with numerical data

In order to investigate the influence of perturbations caused by the last rotor of a real turbine, a rotating wheel equipped with 30 cylindrical spokes with a diameter of $d=10$ mm was added to the test rig in front of the annular diffuser as a simple way to generate rotating wakes [12]. The spoke-wheel is driven by a 4 kW electric motor with a frequency converter, and the rotational speed can be varied in the range of $n=0-3000$ rpm. Detailed overviews about the instrumentation, the measurement program and the test results are given in Ref. [12].

For the comparison of experimental and numerical results, the measured data of radial total and static pressure distributions at inlet and outlet of the annular diffuser and the radial distributions of axial and tangential velocity components at 50% annular diffuser length ($x/h_1=0.89$), as well as for 10% length of the conical diffuser ($x/h_1=3.57$), were used. The radial pressure distributions were measured by using miniaturized three-hole pneumatic probes and the radial velocity distributions by using a backward scattering two-dimensional laser Doppler velocimeter (2D-LDV). According to 2D-LDV measurements corresponding turbulence rms-velocity values are available for the comparison between the measured and computed turbulence characteristics. The positions of the pneumatic probes, as well as of the LDV system, can be seen in Fig. 2.

3 Numerical Approach

The numerical investigations were performed with the commercial solver ANSYS CFX-10.0. It is based on a combined finite-volume/finite-element algorithm, which uses a coupled solver for mass and momentum equations and an algebraic multigrid scheme for convergence acceleration. The numerical scheme is a collocated (nonstaggered) pressure-based method and a selective interpolation is applied in order to avoid the uncoupling of pressure and flow field.

For the transient flow simulation, an implicit second-order accurate time differencing scheme was used and the advection fluxes are evaluated using a blended second-order space discretization technique for transient and for steady-flow simulation.

A detailed description of the solver is given in the ANSYS CFX Manual [14].

3.1 Turbulence Models. ANSYS CFX-10.0 offers a wide range of turbulence models at different levels of complexity. Up to the present, the main problem has been that there exists no single universal turbulence model, which can describe different flow

types with the same accuracy. In order to identify a suitable turbulence model for the complex separated flows in diffusers, evaluation of the following turbulence models were carried out using measured test rig data published in the open literature:

- standard $k-\varepsilon$ turbulence model
- shear stress transport (SST) turbulence model
- scale adaptive simulation with the shear stress transport (SAS-SST) turbulence model

The standard $k-\varepsilon$ and the SST turbulence models are both based on the Reynolds-averaged Navier–Stokes (RANS) equations and belong to the group of statistical turbulence models based on the eddy-viscosity hypothesis. For the $k-\varepsilon$ turbulence model the scalable wall function was applied to ensure a consistent mesh refinement independent of the Reynolds number. SST combines the advantages of $k-\varepsilon$ and $k-\omega$ models and was first introduced by Menter [15]. By applying the $k-\varepsilon$ model in the outer turbulence wall region, the strong sensitivity to freestream condition inherent with the turbulent frequency rate ω can be avoided. The $k-\omega$ model is applied in the near-wall region in order to capture a realistic boundary layer flow without using wall functions. Moreover, for flow types with adverse pressure gradients, for example, diffuser flows, standard two-equation turbulence models do not properly account for principle shear stress transport in flow regions with separation. By using the Bradshaw [16] relation between shear stress and turbulent kinetic energy ($c_{ax}'c_{tg}' \sim 0.3 \cdot k$) a limiter in the SST model reduces the eddy viscosity in separated zones and leads to a better prediction of the separation line.

In case of unsteady Reynolds-averaged Navier–Stokes (URANS) calculations, recent investigations have shown that standard turbulence models are not able to resolve the time-dependent nature of the flow properly for all cases where unsteadiness dominates the large-scale eddies, for example, the detached eddies [17]. In order to resolve at least the large vortex structures, more sophisticated turbulence models must be applied such as large eddy simulation (LES). Unfortunately, the computational costs are still prohibitively expensive for high Reynolds number flows and the application of LES is not practicable for many industrial flow simulations. On the other hand, hybrid models, such as detached eddy simulation (DES) developed by Spalart et al. [18] or the recently developed SAS model by Menter et al. [19–21], allow to resolve various scales of detached eddies, while wall-bounded flow eddies are modeled by a RANS model. In the DES approach the wall-bounded RANS mode is switched to a LES mode in detached regions. Complex flows at high Reynolds number can be simulated in this manner. However, this model demands for a detailed understanding and a high accuracy of grid generation that hindered systematic grid refinement studies [17].

In the present work, the SAS-SST turbulence model for unsteady simulation with features comparable to LES was applied. In contrast with the DES approach exact grid information is not demanded and results of similar quality were obtained [22]. The SAS model is an improved URANS-type model and originally derived from the exact transport equation for the integral length scale by Rotta [23]. Menter et al. [19–21] reformulated this transport equation by using the second derivative of the velocity and incorporated the eddy-viscosity assumption for the shear stress to maintain the features of the SST model in RANS regions and to activate the SAS capability in URANS regions by using the von Kármán length scale, L_{VK} , as an appropriate indicator to detect the level of unsteadiness.

In this approach the SAS term increases the value of ω in unsteady regions resulting in a reduction in turbulent kinetic energy k , as well as the eddy viscosity, such that the overprediction of the diffusion, which is a common weakness of standard URANS computations, can be avoided.

3.2 Computational Domain. The computational model of the diffuser test rig is shown in Fig. 3. It consists of the intake, the

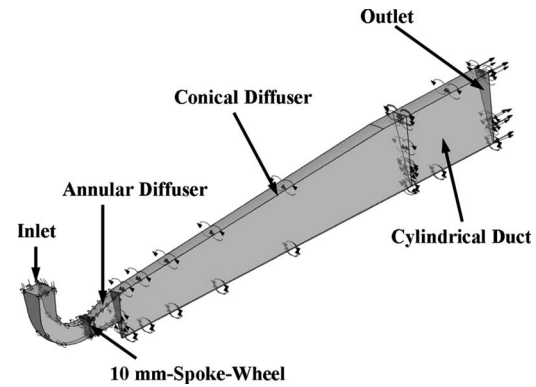


Fig. 3 Computational domain

spoke-wheel, the annular diffuser and the conical diffuser, which is extended by a constant cylindrical duct at the outlet instead of the settling chamber. Only one pitch in circumferential direction is used for the numerical analysis and periodicity conditions, marked by the circles with arrow, are applied at the circumferential boundaries.

Figure 4 shows the structured meshes for the computational domain generated by ANSYS ICEM CFD. About half a million grid points are used with the spoke-wheel and the annular diffuser covering about 50% of the total number.

In order to investigate mesh independency effects, steady-state 2D studies with different mesh settings were carried out previous to the 3D calculations. According to these studies, the normalized size of the first near-wall cell in the spoke-wheel and the annular diffuser regime amounts $y^+ < 2$, and more than 20 nodes in the boundary layer of the annular diffuser were necessary to ensure an appropriate near-wall resolution.

For all computations, boundary conditions were reduced to ISO-standard values (total pressure and total temperature). At the exit of the constant area duct downstream of the conical diffuser the static pressure was specified to match the measured mass-flow rate.

3.3 Influence of the Interface Position. At the interface of the rotating and stationary reference frames the following three options are available in ANSYS CFX:

- Steady calculation: (1) stage or (2) frozen-rotor interface model
- Unsteady calculation: (3) Transient interface model

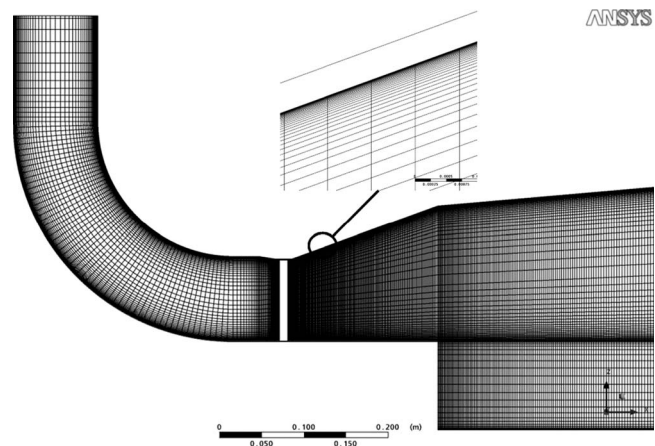


Fig. 4 Structured mesh topology at the meridional plane with ANSYS ICEM CFD

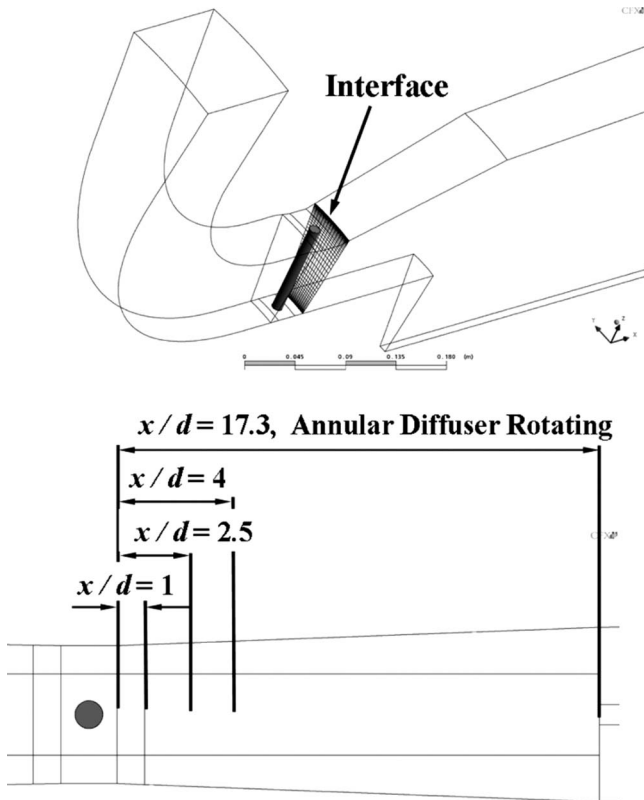


Fig. 5 Variation of interface distances downstream of the spoke-wheel

In our investigation the so-called stage interface (1) between rotor and stator is not appropriate because it causes a laterally uniform flow at the diffuser inlet.

The authors showed in an earlier paper that the circumferentially nonuniform flow, by using the frozen-rotor approach at the diffuser entrance, has a strong effect on the diffuser performance. In this numerical approach, the flow variables were directly transferred across the interface plane between rotor exit and diffuser inlet so that the influence of the computed stationary secondary flow pattern on the diffuser performance could be taken into account and therefore the frozen-rotor approach seems to be better suited [11].

For the present investigation, another important aspect was the position of the interface plane between the spoke-wheel and the annular diffuser regions. In the version of ANSYS CFX currently used, the steady-state approach does not support nonreflecting boundary conditions and this led to considerable numerical errors in our steady-state calculations if the interface was located in a region dominated by the wakes of the spoke. Numerical studies with varied interface positions between spoke-wheel and the inlet region of the annular diffuser have suggested that the distance of the interface plane must be located at least more than three spoke diameters downstream of the spoke-wheel in order to avoid numerical errors, Fig. 5.

As diffuser struts are not considered in the present analysis, interface planes can be avoided completely by the annular diffuser analysis in the rotating reference plane. The location of the interface plane is chosen at the inlet into the conical diffuser, which is equivalent to a normalized position of $x/d=17.3$. It must be mentioned here that although the conical diffuser could be considered in the rotating reference frame as well, it is more appropriate to leave it in the stationary frame because the relative flow angle at the exit of the entire computational domain would become too strongly skewed with regard to the mesh lines. Figure 6 shows the comparison of the computed absolute velocity flow field in the

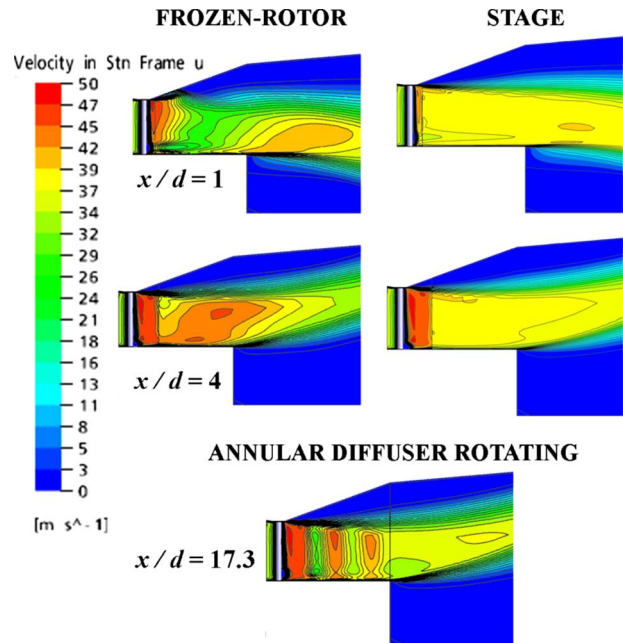


Fig. 6 Absolute velocity field in the meridional plane

meridional plane with two different interface positions for the frozen-rotor approach and for the stage approach in the upper half and with rotating annular diffuser in the lower half, respectively.

Concerning the direction of the core flow and the topology of the separated region trends are predicted with opposing flow characteristics for the interface distance of $x/d=1$. For the simultaneous computation with spoke-wheel and annular diffuser the computed flow field in front of the interface plane corresponds well with the flow pattern obtained with the frozen interface and the larger distance of $x/d=4$. For the cases considered in this section, the computed static pressure recovery factors (defined in Sec. 4.1) for varied normalized interface positions are shown in Fig. 7. It can be seen that they are very sensitive with the interface plane locations but approach a common value if the distance is sufficiently large.

Following these results, all steady and unsteady numerical studies discussed in the following chapters were done with a rotating domain covering both spoke-wheel and annular diffuser. In order to match the no-slip boundary conditions in the stationary reference frame, so-called “counter-rotating walls,” as offered by ANSYS CFX, were specified. The definitions of interface treatment for steady and unsteady computations are summarized in Table 2.

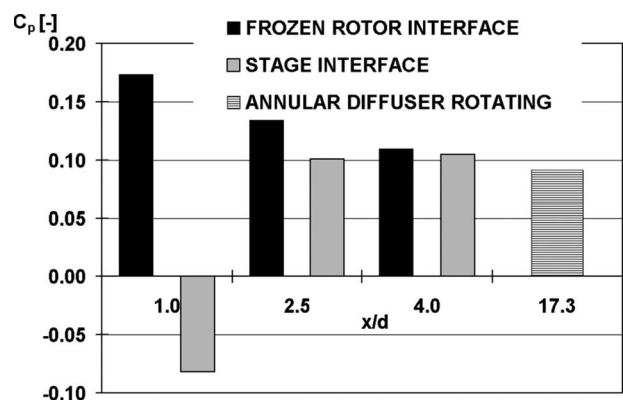


Fig. 7 Static pressure recovery versus normalized interface position

Table 2 Interface approach definition

	Interface (1)	Interface (2)
Steady	Frozen-rotor	Frozen-rotor
Unsteady	Transient	Transient

Figure 8 shows the positions of the interface planes and the locations of the counter-rotating walls.

4 Selection of the Numerical Approach for Steady and Unsteady Calculation

Before applying the numerical scheme to our problem the validation of the numerical method was accomplished by using the experimental data from the diffuser test rig at the Leibniz University Hannover [12]. At first, the test rig configuration without spoke-wheel and no swirl at annular diffuser inlet will be considered (Sec. 4.2). For the configuration with standing spoke-wheel condition, the comparison of steady and unsteady calculation will be presented. The investigation with steady calculations for the rotational speed of $n=1500$ rpm and the unsteady results between the SST and SAS-SST turbulence model will be discussed in Secs. 4.4 and 4.5, respectively.

4.1 Diffuser Performance Evaluation and Averaging Procedures. In order to evaluate the diffuser performance, the well-known static pressure recovery coefficient is used and defined by

$$C_p = \frac{\bar{p}_{s,outlet} - \bar{p}_{s,inlet}}{\bar{p}_{t,inlet} - \bar{p}_{s,inlet}} \quad (1)$$

Corresponding to the processing of experimental data the pressure difference between diffuser inlet and outlet is estimated with area-averaged data of the radial static pressure (p_s) distributions. To take into account the shape of the velocity distributions at the diffuser inlet, the mass-flow averaging procedure for the total pressure distributions (p_t) and the area-averaging method for the static pressure are applied. The adverse effect on the estimation of the static pressure recovery by the static pressure drop at the dif-

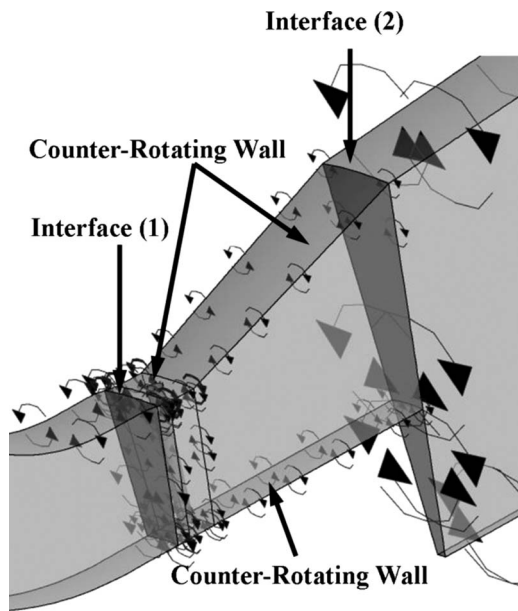


Fig. 8 Interface plane position and definition of counter-rotating wall for the entire rotating domain covering spoke-wheel and annular diffuser

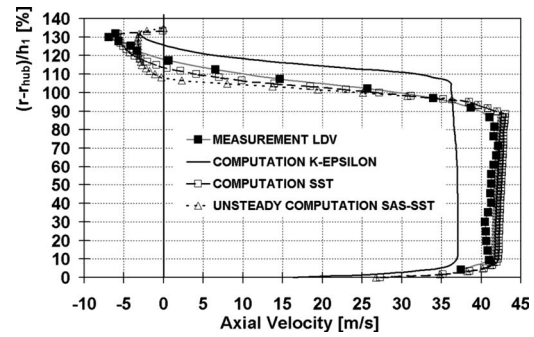


Fig. 9 Axial velocity distributions at 50% of the annular diffuser length ($x/h_1=0.89$)

fuser kink is avoided by shifting the normalized measuring position $x/h_1=0.155$ downstream from the diffuser inlet.

For unsteady calculations a time-averaging procedure for the flow field variables must be applied. This is done by using an automatic ANSYS CFX averaging procedure

$$\bar{\phi}(x_i)_{time} = \frac{\sum_{j=1}^N \phi(x_i, t)_j}{N} \quad (2)$$

N is the number of time steps used for the averaging procedure with a constant time step size and ϕ is a flow field variable for the corresponding time step. The choice of an adequate averaging-time scale will be discussed in Sec. 4.5. For the comparison between the measured and predicted unsteady static pressure recoveries, the area averaging for static pressure and mass-flow averaging for the total pressure were applied.

4.2 2D Calculation Without Spoke-Wheel. At first, we consider the test rig configuration without spoke-wheel. The measurements with different swirl (0 deg, 15 deg, 25 deg, and 30 deg) configurations at diffuser inlet were carried out at the Leibniz University Hannover [12]. In all experimental cases, strongly separated flow was observed at the casing. With the current geometry the early onset of jetlike stall is caused by the large half aperture angle of $\theta_{AD}=20$ deg. In this case the well-known positive effect of the inlet swirl is not able to stabilize the separated diffuser flow [3,4]. For a more comprehensive comparison of measured and predicted data, the test case without inlet swirl was chosen. Here, a quasi-2D analysis with only one mesh element in the circumferential direction is chosen.

In Fig. 9, the predicted radial-axial velocity distributions are compared with the experimental LDV-values in the middle of the annular diffuser. The steady-state calculation with SST turbulence model, as well as the unsteady calculation with SAS-SST model, show good agreement with the measured data while the results of the standard $k-\epsilon$ turbulence model are quite different from the measurement.

In Fig. 10, the radial distributions of computed and measured turbulent kinetic energy k are shown. The k value of the experiments is calculated with the rms values and normalized by the area-averaged axial velocity at the annular diffuser inlet:

$$\left(\frac{k}{(\bar{c}_{ax,1})^2} \right)_{measured} = \frac{\frac{1}{2} [c_{ax,1}^{\prime 2} + c_{tg}^{\prime 2}]}{(\bar{c}_{ax,1})^2} \quad (3)$$

The measured and normalized k distribution becomes very high near the casing due to the strong separation in this region, and the steady-state calculation with the SST turbulence model shows the best agreement. The SAS-SST and standard $k-\epsilon$ turbulence models deviate from the experiments to about the same extent but give different locations of the maxima. The standard $k-\epsilon$ turbulence

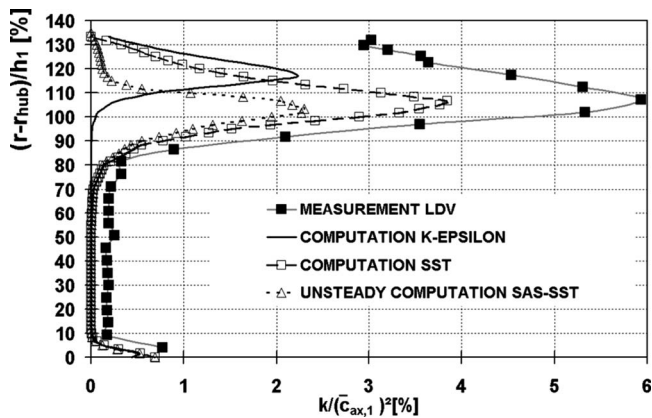


Fig. 10 Normalized turbulent kinetic energy distributions at 50% of the annular diffuser length ($x/h_1=0.89$)

model is known to overpredict the production of turbulent kinetic energy in adverse pressure gradient regions with no separated flow, which finally results in poor prediction of separated diffuser flows.

This property is confirmed in our results and is indicated by the reduced separation zone (Fig. 9) and the parallel offset of the maximum location of normalized k value with simultaneous reduced production of turbulent kinetic energy (Fig. 10). In contrast to the $k-\epsilon$ turbulence model the differences with the unsteady SAS-SST model can be explained by the reduced turbulent viscosity caused by the SAS term in the ω -equation.

A similar behavior for a separated asymmetric diffuser flow has also been obtained by Davidson [24]. In the present free jet configuration, the prediction of diffuser flow is adversely affected by the occurrence of the SAS term and does not provide more insight in the diffuser flow than the more cost-effective steady-state calculation with the SST model.

In summary, all models considered predict a strong jetlike separation for the isolated diffuser configuration, as we expected.

4.3 Calculation With Nonrotating Spoke. In this section the evaluation of computed results of a test case configuration with the standing spoke-wheel condition will be presented. Boundary conditions and the computational domain are defined, as shown in Sec. 3.2. For unsteady calculations with the SAS-SST model a physical time step of $\Delta t=10^{-5}$ s and three inner loop iterations were chosen in order to achieve an acceptable convergence rate. The unsteady simulation is very time extensive, and for the current case approximately 2 days for $N=1000$ physical time steps were necessary with five CPUs in a parallel environment (parallel virtual machine (PVM)). Unsteady flow field variables have been time-averaged.

The spanwise distributions of measured axial velocity components and the predicted circumferentially-averaged axial velocity components at 50% annular diffuser position, as well as at 10% conical diffuser position, are presented in Figs. 11 and 12, respectively.

The measured axial velocity distribution shows a strong separation at the casing and has been reproduced by both the steady and unsteady computations, Fig. 11.

In contrast to the case without spoke-wheel, the core flow and the flow pattern near the casing are affected by the wakes of the spoke-wheel near the downstream region between annular and conical diffusers. The steady-state calculation with standard $k-\epsilon$ and the SST turbulence model are not able to predict the reattachment at the casing at about 10% of the conical diffuser length, Fig. 12. In particular with regard to the reattachment and core flow the application of the unsteady analysis with the elaborate SAS-SST model gives the most reasonable agreement.

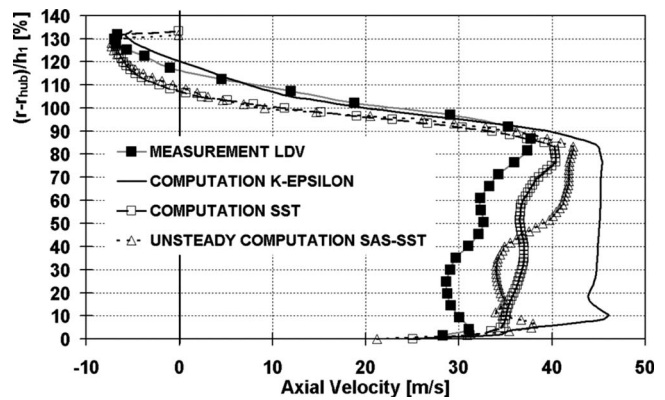


Fig. 11 Axial velocity distributions at 50% of the annular diffuser length ($x/h_1=0.89$) with nonrotating wheel

4.4 Steady Calculation for Rotating Wheel at 1500 rpm.

This section deals with the investigation of steady calculations for the rotational speed of $n=1500$ rpm. The experimental data for this rotational speed suggest a stable operating point with reattachment of the flow at both the annular and the conical diffuser casing walls. At a first numerical approach, steady-state analyses with the standard $k-\epsilon$ and SST turbulence models were done. The comparison between measured LDV-data and the computed circumferentially-averaged spanwise distributions of axial and tangential velocity components are shown in Figs. 13 and 14 at 50% of the annular and 10% of the conical diffuser length, respectively.

The measured axial velocity distribution indicates reattached flow at the casing wall for both the annular and the conical diffusers. Neither of the steady-state computations was able to predict the observed phenomena.

The comparison of static pressure recovery coefficients is shown in Table 3 and underlines the poor predictability of this test case with a steady-state approach.

4.5 Unsteady Calculation for Rotating Wheel at 1500 rpm.

The real diffuser flow pattern is obviously strongly affected by both three-dimensional and unsteady effects in the inlet region caused by the presence of the rotating spoke-wheel. These effects cannot be taken into account using steady-state analyses.

As a consequence of the disappointing results of steady-state codes, we carried out extensive unsteady computations with the SST and the SAS-SST turbulence models. The physical time step size was set $\Delta t=10^{-5}$ s for the SAS-SST model and for the unsteady computation with the SST model, and three inner loop

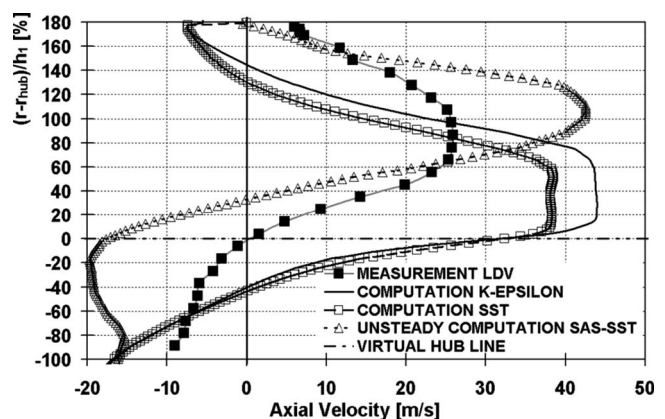


Fig. 12 Axial velocity distributions at 10% of the conical diffuser length ($x/h_1=3.57$) with nonrotating wheel

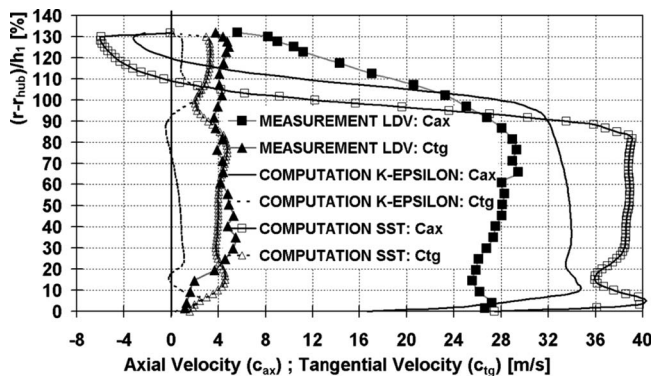


Fig. 13 Axial and tangential velocity distributions at 50% of the annular diffuser length ($x/h_1=0.89$); rotational speed $n=1500$ rpm

iterations were applied in order to achieve an acceptable convergence rate. The total CPU time for the unsteady computation with the SAS-SST turbulence model was approximately 2 days for $N=1000$ physical time steps if five CPUs in a parallel environment (PVM) were available. The unsteady flow field variables have to be time-averaged in order to be compared with the numerical results with the steady-state measurement data. It should be mentioned that LDV were sampled at 5 kHz. In order to give an example for the extensive effort of the analyses, we required $N=100,000$ time steps to simulate a real time of 1 s with our simulations. Based on the computer hardware available, the computation would last about 200 days. This would go far beyond the scope of this investigation and has to be taken into account for the time-averaging procedure. For the evaluation of its time scale, we used the distance of 0.4 m for one of our control stations of interest and the averaged axial velocity in the core flow was approximately 30 m/s.

Based on the time step size used, it can be expected that the convective transport of unsteady wakes requires about 1300 time steps, which we used for time-averaging. As an example for transient data monitoring, Fig. 15 shows time dependent values of the ratio of eddy viscosity/molecular viscosity closely behind the ro-

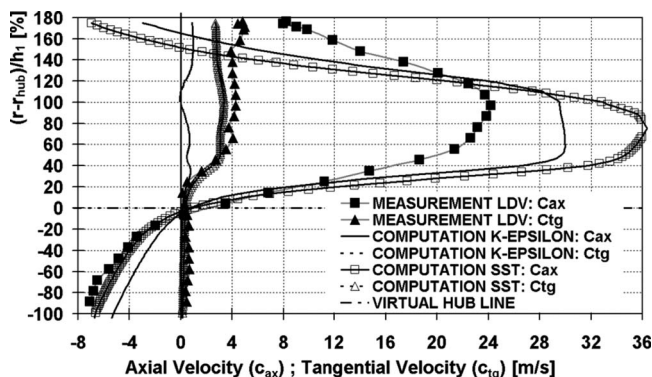


Fig. 14 Axial and tangential velocity distributions at 10% of the conical diffuser length ($x/h_1=3.57$); rotational speed $n=1500$ rpm

Table 3 Measured and stationary computed static pressure recovery coefficients for the annular diffuser; rotational speed $n=1500$ rpm

	SST	$k-\epsilon$	Measured
C_p	0.14	0.14	0.61

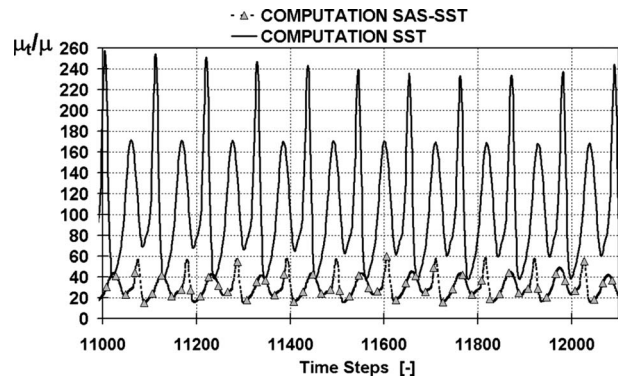


Fig. 15 Unsteady eddy-viscosity/molecular viscosity ratio versus time steps; rotational speed $n=1500$ rpm

tating spoke-wheel at midspan.

As mentioned in Sec. 3.1, the SAS model is switched on in regions where standard turbulence models normally produce the large-scale URANS regime, for example, in the wake region behind the spoke-wheel. In summary, the SAS term leads to reduction in eddy viscosity so that in comparison with the SST-URANS calculation, an impressively low level of eddy-viscosity ratio is obtained with the SAS-SST solution, Fig. 15. The different turbulence structures can be obtained by the turbulent length scale ratio on the isosurface of constant Mach numbers in Fig. 16. The turbulent length scale changes by almost a factor of 5 between the SST-URANS and SAS-SST solution due to resolved turbulence structures in the detached regions by using the SAS mode. The adaptive length scale in the SAS mode enables therefore features that can only be found with LES or DES.

It can be expected that the large vortex structures given by the SAS-SST scheme have a strong effect on the diffuser flow performance. A measure for the vortex structure is the vorticity, and in the contour plots in Fig. 17 the time-averaged secondary flow structures are shown behind the spoke with pronounced vorticity distributions in the axial and radial directions near the casing around the diffuser kink region. Additionally, back-flow regions are shown and demonstrate, by using the SAS-SST model, a considerably reduced separation zone at the casing, whereas the flow predicted by the SST-URANS scheme is still strongly separated.

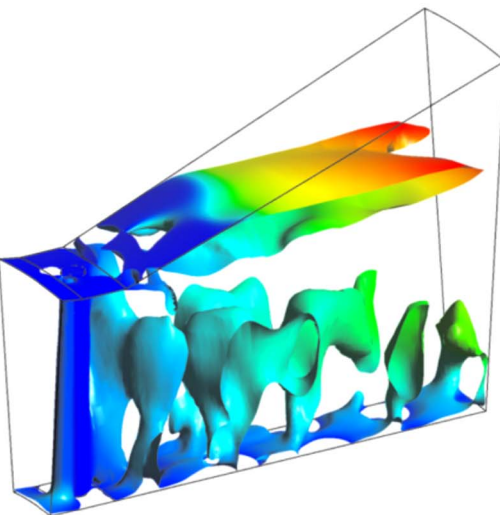
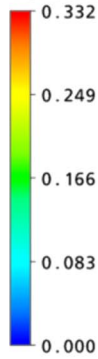
In general the axial (1) and radial vorticity patterns (2) around the diffuser kink at diffuser inlet show similar structures for both unsteady computations. With the SAS-SST computation the intensity of the pair of counter-rotating vortices (1) is considerably greater than that computed with the SST approach near the casing. Moreover, only the SAS-SST model sufficiently predicts the transport of the high-energy vortex structures into the separation region in the radial, as well as passing through the axial direction (3) near the diffuser outer wall.

Coming back to the evaluation of the adequate choice of the time-averaging period and the influence of unsteady perturbations on the diffuser performance, monitoring results of the axial velocity component at 50% of the diffuser length near casing for both unsteady computations are presented in Fig. 18.

Based on the studies presented above, strong fluctuations in the axial velocity near the diffuser outer wall can only be obtained when the SAS-SST model is applied, and these unsteady perturbations are obviously responsible for the flow reattachment in this region. In contrast the time dependent axial velocity of the SST suggests a more or less steady-state core flow condition with backflow near the casing. Comparisons of computed axial velocities, which are evaluated statistically, and measured ones with its radial distribution in the middle of the annular diffuser are plotted in Fig. 19. Time-averaged mean values for the averaging-time step numbers of $N=600$ and $N=1200$ show minor differences in the

SST-URANS

TURBULENT LENGTH SCALE / SPOKE WHEEL DIAMETER



SAS-SST

TURBULENT LENGTH SCALE / SPOKE WHEEL DIAMETER

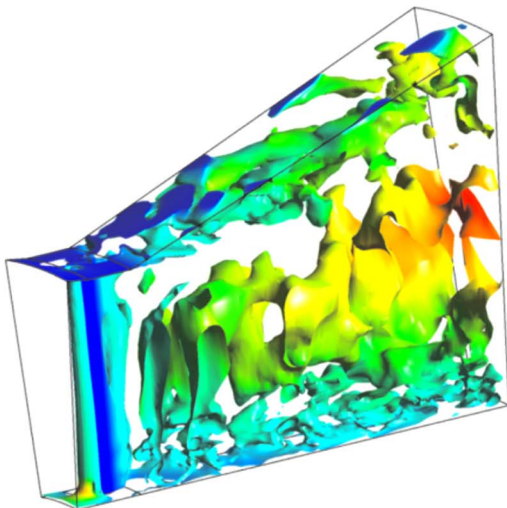
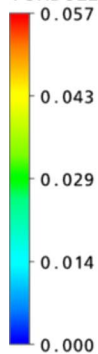


Fig. 16 Instantaneous isosurface of Mach number colored by the turbulent length scale/spoke-wheel diameter; top: SST-URANS, bottom: SAS-SST

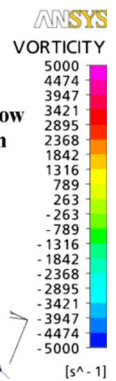
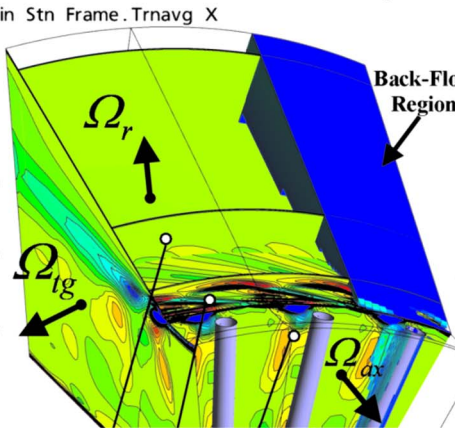
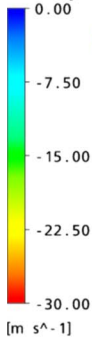
velocity fields near the casing, Fig. 19. Moreover, the good agreement with experimental data indicates that for the time-averaging of transient flow field values of 1200 time steps are appropriate.

Furthermore, a measure for velocity fluctuations during the time-averaging process are the locations of maxima and minima of the velocity distributions along the channel height, which are calculated always at the same position and confirm for the SAS-SST model the unsteady flow field behavior. In contrast the results with the SST-URANS approach show unsteady effects due to the spoke-wheel wakes in the core flow region, whereas the predicted diffuser flow is still separated without any unsteady interactions with the core flow.

Finally, the comparison of static pressure recovery coefficients given in Table 4 demonstrates a considerably better agreement with experiments due to a better prediction of the flow pattern in the annular diffuser flow by using the more elaborate SAS-SST model.

SST-URANS: $n = 1500$ rpm

Velocity in Stn Frame.Trnavig X



SAS-SST: $n = 1500$ rpm

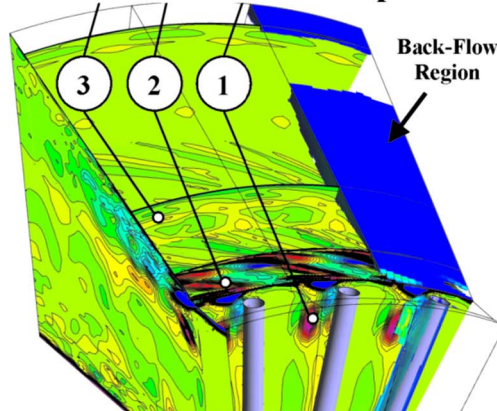


Fig. 17 Time-averaged axial and radial components of vorticity distributions and back-flow regions at casing; rotational speed $n=1500$ rpm

5 Effects of Secondary Flow on Diffuser Performance

The evaluation of numerical results discussed above indicates that, obviously, diffuser performance and pressure recovery are strongly influenced by heavily distorted and secondary flow patterns caused by spoke-wheel wakes, which can even lead to a stabilization of the diffuser flow. In order to study details of the physical mechanism, more comprehensively unsteady computations using the elaborate SAS-SST turbulence model were carried

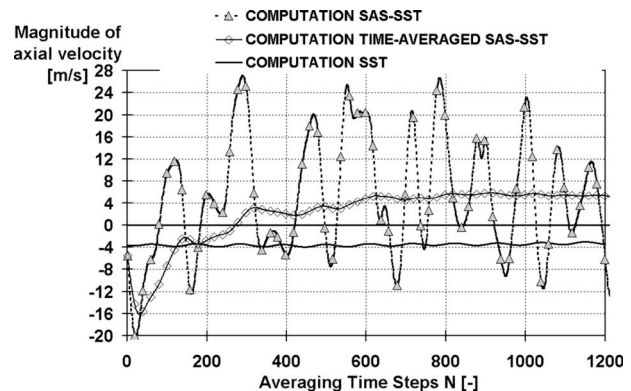


Fig. 18 Axial velocity fluctuations and time averaging at 50% of the annular diffuser length ($x/h_1=0.89$) near casing versus time steps used for averaging; rotational speed $n=1500$ rpm

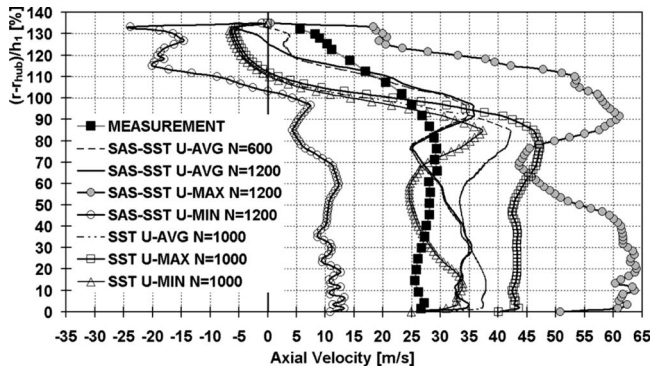


Fig. 19 Measured and computed axial velocity distributions at 50% of the annular diffuser length ($x/h_1=0.89$); rotational speed $n=1500$ rpm

out with varied rotational speeds (0 rpm, 500 rpm, 1500 rpm, and 2500 rpm). The numerical parameters for the computations are specified as described in Sec. 4.5.

At first, measured and computed spanwise distributions of normalized axial velocity components are shown in Figs. 20 and 21, which are calculated at the annular diffuser outlet and at 10% conical diffuser length. The computed results are averaged in time and circumference.

In Fig. 20 the measurements show the dependency of the diffuser flow pattern on separated and stabilized annular diffuser flow near the outlet casing wall. The predictions give a similar trend. The flow pattern near the junction of the annular and conical diffusers is shown in Fig. 21 and demonstrates a good agreement of experiments and theory above the virtual hub line. The recirculation zone in the core flow region is only predicted with sufficient accuracy for the operating point with $n=2500$ rpm.

In comparison with the annular diffuser flow pattern shown in Fig. 20, the effect of secondary flow on the diffuser performance is more pronounced in the graph containing static pressure recoveries versus the flow coefficient, Fig. 22.

For a more general evaluation of all the flow results a flow coefficient was defined as

$$\Phi = \frac{\bar{c}_{ax}}{u_m} \quad (4)$$

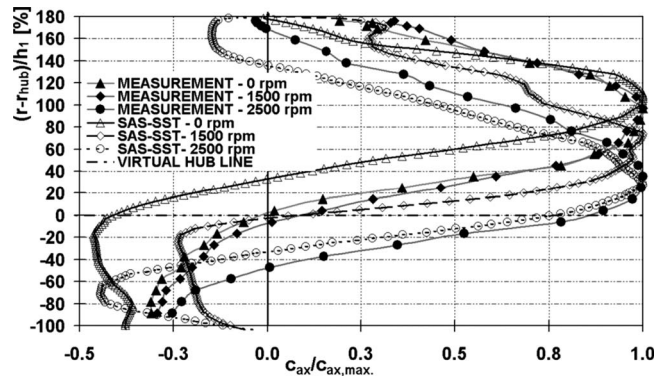


Fig. 21 Measured and computed axial velocity distributions at 10% of the conical diffuser length ($x/h_1=3.57$); rotational speed with $n=0, 1500, 2500$ rpm

with a mass-averaged axial velocity component c_{ax} at the entrance plane of the spoke-wheel and u_m the circumferential velocity at midspan. The optimum value of measured pressure recovery for the measured data is around $\Phi=2.0$, which is also given by the numerical results. However, the magnitude of computed pressure recoveries is considerably underpredicted and a better agreement is found for the kinetic energy (p_r, p_s) at the diffuser inlet. The wake area behind the spoke-wheel and the diffuser kink additionally influence the static pressure drop in this region. Additionally, the value of ideal static pressure recovery for the annular diffuser is shown in Fig. 22 and can be derived using Bernoulli's equation. This value is strictly valid only for one-dimensional inviscid flow, zero blockage, and no flow swirl at diffuser inlet. The comparison of measured and theoretical pressure recovery suggests a diffuser efficiency of 95%. This is an uncommonly high value so that the amount of pressure recovery coefficients obtained with the measured data should be watched critically.

Nevertheless, the effect of rotational speed on annular diffuser performance could be confirmed by the unsteady computations and this fact enables us to investigate the effect of the rotor wakes and secondary flow on the annular diffuser performance in greater detail. Currently, unsteady measurement techniques, such as hot-wire probes, and measurement techniques for the whole flow field, such as particle image velocimetry (PIV), have not been applied at

Table 4 Measured and unsteadily computed static pressure recovery coefficients for the annular diffuser; rotational speed $n=1500$ rpm

	SST-URANS	SAS-SST	Measured
C_p	0.13	0.40	0.61

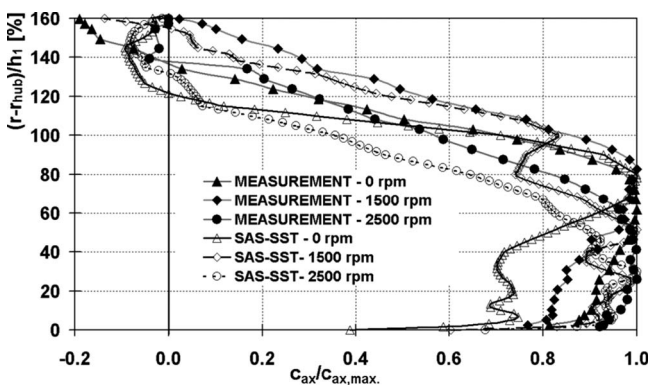


Fig. 20 Measured and computed axial velocity distributions at the outlet of the annular diffuser ($x/h_1=1.69$); rotational speeds $n=0, 1500, 2500$ rpm

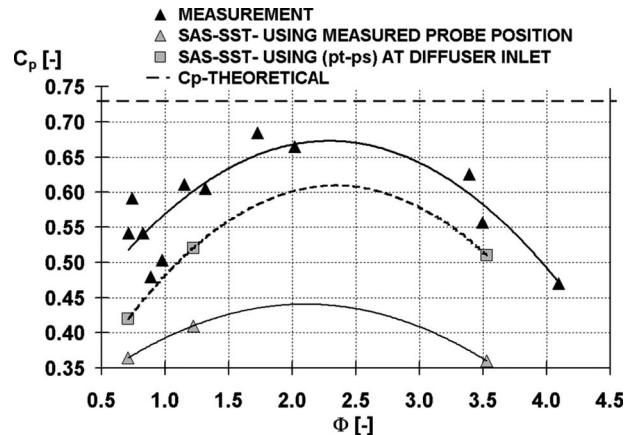


Fig. 22 Static pressure recovery coefficients versus flow coefficient

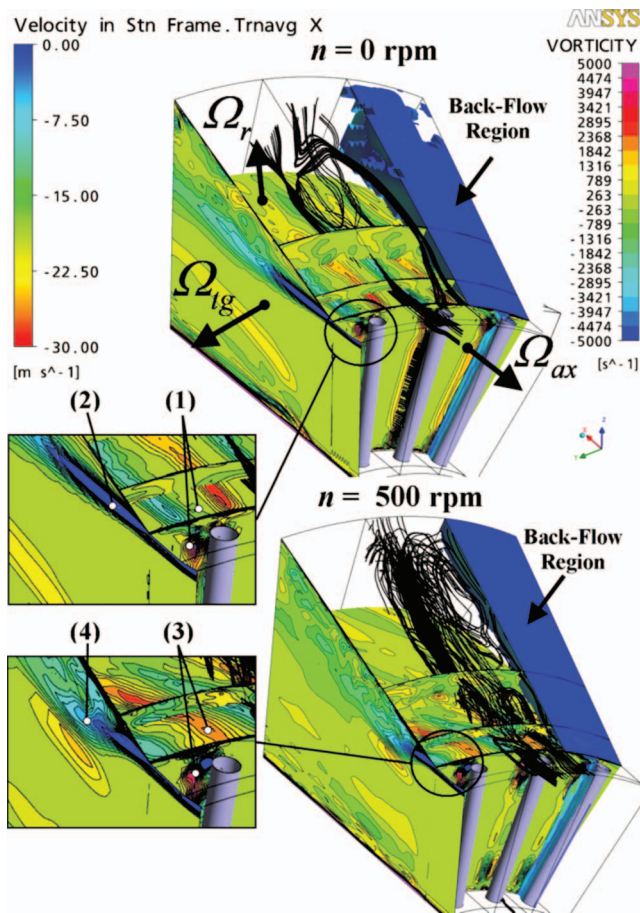


Fig. 23 Contour plots of time-averaged axial, radial, and tangential components of vorticity in stationary frame of reference and back-flow regions for rotational speeds $n=0$ rpm and $n=500$ rpm, respectively

the diffuser test rig of Leibniz University Hannover. These techniques would be required to do more validation of the results of the CFD code applied.

In Figs. 23 and 24, the absolute and time-averaged local axial, radial, and tangential components of the vorticity are displayed for the rotational speeds $n=0$, 500, 1500, and 2500 rpm. In order to show the affected flow pattern in the flow duct downstream of the diffuser kink, the time-averaged absolute streamlines and back-flow regions are additionally drawn in Figs. 23 and 24.

For the condition of nonrotating wheel ($n=0$ rpm) a pair of counter-rotating vortex cores (1) in the axial and radial directions near the casing at diffuser inlet can be obtained. The high concentration of vorticity in circumferential direction (2) near the casing wall is caused by the strong production rate of the boundary layer flow and by the separated shear layer due to the diffuser kink, Fig. 23. The impact of circumferentially nonuniform flow behind the spoke-wheel on the diffuser regime is already obtained for the low rotational speed of $n=500$ rpm. In particular, the intensity and the distribution of vorticities in axial and radial directions (3) indicate a pronounced secondary flow pattern at the diffuser inlet, whereas the local maxima of vorticities are displaced toward the casing wall and the diffuser kink, respectively. It should be pointed out here that this kind of secondary flow pattern is similar with the flow behind a turbine rotor, but transferability to the real turbine outflow is not trivial.

Due to the magnitude and the extension of the vortices the separated diffuser flow just behind the diffuser kink is more stabilized in the first half of the annular diffuser channel. For the rotational speed of $n=500$ rpm, this is indicated by the reduced

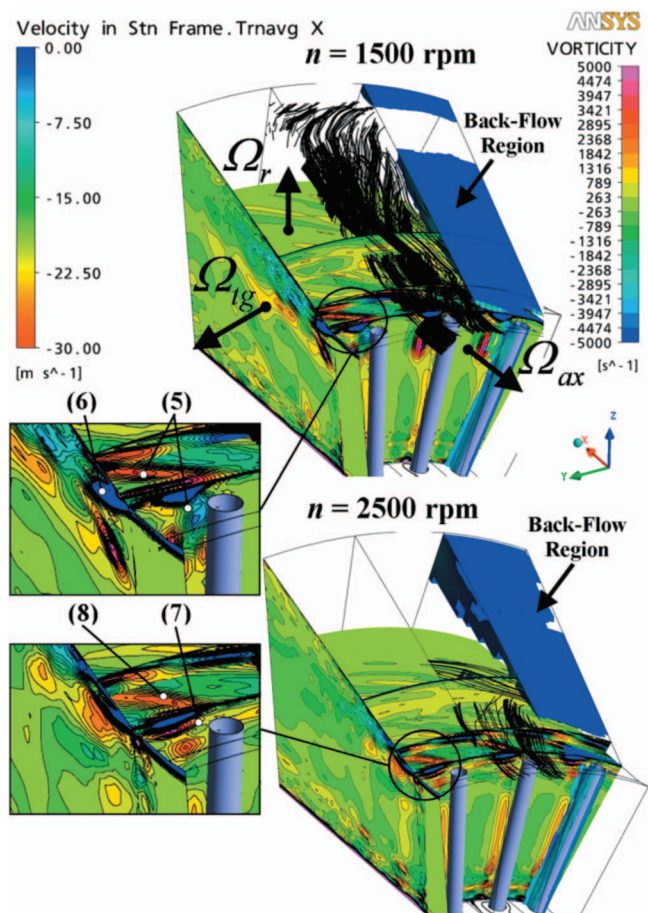


Fig. 24 Contour plots of time-averaged axial, radial, and tangential components of vorticity in stationary frame of reference and back-flow regions for rotational speeds $n=1500$ rpm and $n=2500$ rpm, respectively

vorticity component in circumferential direction (4) near the shear layer behind the diffuser kink and by the pattern of the absolute stream lines, Fig. 23.

By increasing the rotational speed ($n > 1000$ rpm, $\Phi \approx 2.0$) the vorticity components in the radial and axial directions (5) are strong enough to stabilize the detached diffuser flow, which is visible in the comparison of the tangential vorticity component (6) and the more regular absolute streamline pattern for the computed results of $n=1500$ rpm, Fig. 24. Beyond a rotational speed of $n=2000$ rpm ($\Phi < 1.5$) the measured static pressure recovery factors are considerably decreased and the stabilization effect on the diffuser flow separation is weaker, as shown in Fig. 22. This observation can be explained by considering the computed vorticity distributions for the rotational speed of $n=2500$ rpm in Fig. 24. Near the casing wall at diffuser inlet the intensity of the vorticity in axial direction (7) is also increased but the local extension of the pair of counter-rotating vortex cores is more strongly concentrated near the diffuser kink (7) while the radial component (8) is significantly reduced.

This coupled effect of vortex mixing causes a deficit of energy around the zone behind the diffuser kink so that the transport of energy along the diffuser outer wall into the flow separation zone is not strong enough to produce a re-attachment of the annular diffuser flow.

Additionally, a path at a fixed radial position was defined starting from the joint position of the diffusers and stretching up to the annular diffuser in the ANSYS CFX-POST environment in order to evaluate the local time and absolute circumferentially-averaged vorticity components in streamwise position. Computed absolute

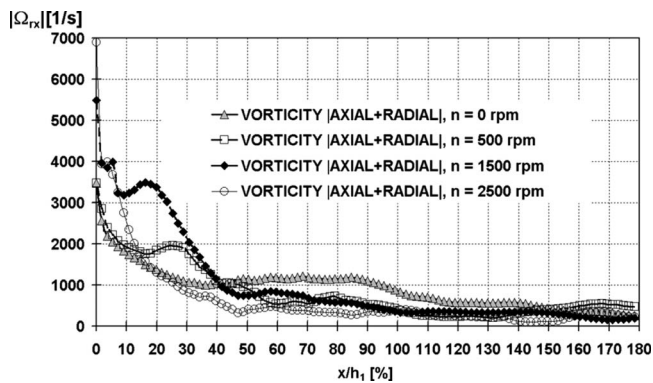


Fig. 25 Time-averaged absolute values of axial and radial vorticity at constant channel height versus normalized annular diffuser length

values of the axial and radial components of the vorticity are shown in Fig. 25, and their absolute components in Fig. 26 for the range of rotational speeds considered.

The distributions of absolute values shown in Fig. 25 confirm the discussed influence of the vortex interaction on the diffuser performance. The maximum vorticity is obtained for a rotational speed of $n=2500$ rpm, but it collapses directly behind the diffuser kink. The vorticity distribution for a rotational speed of $n=1500$ rpm shows comparatively high values over a wide space, which seems to be responsible for the improved diffuser performance.

The comparison of the absolute radial and axial components of the vorticity distributions in Fig. 26 shows for the radial component the highest values for a rotational speed of $n=1500$ rpm and for the axial component with a high value over a wider range, as it was obtained for the absolute values in Fig. 25.

Finally, it should be kept in mind that the high level of turbulence at the diffuser inlet favors the reduction in the separation zone with an improvement of the stability of the outlet flow [25]. The streamwise distributions of computed and normalized time-averaged turbulent kinetic energy along the annular diffuser path line for the entire rotational-speed range are shown in Fig. 27. The turbulent kinetic energy is calculated with the computed statistical normal stress components of Reynolds stress tensor, which are automatically generated using running statistic of the instantaneous transient velocity flow field, and normalized by the area and time-averaged absolute velocity at annular diffuser inlet. In all cases, the turbulence intensity downstream of the diffuser kink increases with larger rotational speeds. The largest amount of turbulent kinetic energy is produced at the rotational speed of n

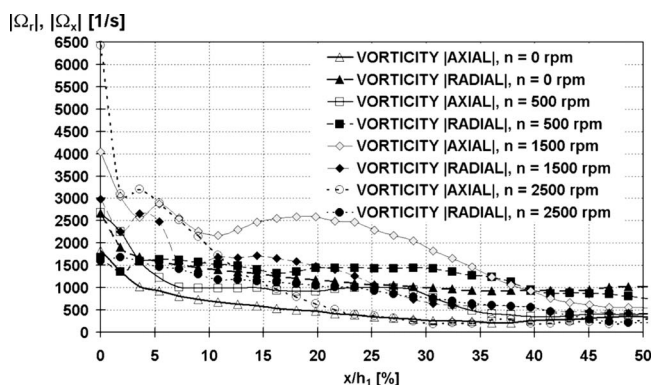


Fig. 26 Time-averaged axial and radial components of vorticity along a monitoring path at constant channel height versus normalized annular diffuser length

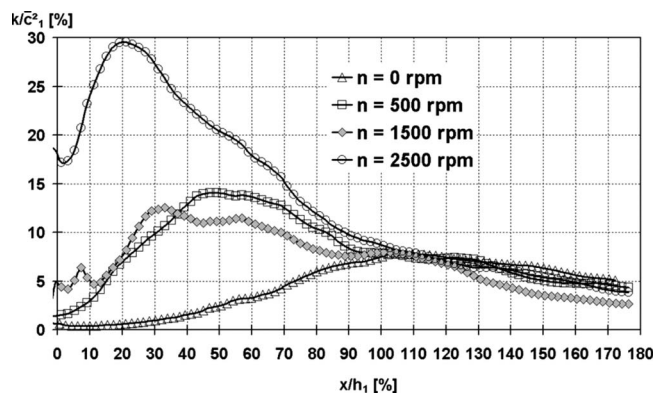


Fig. 27 Computed time-averaged turbulent kinetic energy distributions at constant channel height versus annular diffuser length

$=2500$ rpm over a wide extension of the annular diffuser length. In summary, the radial turbulent kinetic transport may support the stabilizing effect of the secondary flow on the diffuser performance, but a clear relation with stabilized diffuser flow could not be obtained in our numerical investigations.

6 Conclusions

In this paper numerical investigations using the commercial solver ANSYS CFX-10.0 have been applied to demonstrate the effect of wake and secondary flow interactions for a widely open diffuser, which was tested at the test rig facility of Leibniz University Hannover [12]. The wakes were generated by a rotating wheel equipped with 30 cylindrical 10 mm spokes.

The favorable comparison of unsteady calculations with a SAS-SST turbulence model using experimental data indicates that obviously the mixing effect of wakes and secondary flow pattern is responsible for the reattachment in the annular diffuser flow. These phenomena could only be predicted by such an elaborate unsteady analysis.

As a result of these studies it can be stated that diffuser design based on well-established simplified schemes using standard correlations and on steady-state multistage analysis is too conservative in many cases. Therefore, considerably higher numerical costs associated with unsteady calculations must be accepted in order to increase the understanding of the physical phenomena in turbine exit flow and its interaction with the subsequent exit diffuser in order to design more compact geometries.

Acknowledgment

The numerical investigation in the present paper is sponsored by German Ministry of Economics and Technology (Grant No. 0327720D) under AG Turbo's COOREFF-T program in association with MAN Turbo AG whose support is gratefully acknowledged.

Furthermore, we would like to thank Dr. F.R. Menter from ANSYS CFX who has provided the SAS-SST turbulence model so that the work could be successful carried out at the Department for Fluid Energy Machines at Ruhr-University Bochum/Germany.

We also like to thank the management board of MAN Turbo AG for the permission to publish this paper.

Nomenclature

- A = area
- c = absolute velocity
- C_p = static pressure recovery coefficient
- d = spoke-wheel diameter
- h = channel height
- k = turbulent kinetic energy

L = diffuser length
 N = time step number
 n = rotational speed
 p = pressure
 r = radial coordinate
 s = spoke-wheel spacing
 u = circumferential velocity
 x = axial coordinate
 θ = diffuser apex angle
 Ω = vorticity
 Φ = flow coefficient
 ω = turbulent frequency
 ε = dissipation rate
 ν = hub to tip ratio
 μ = dynamic viscosity
 ϕ = flow field variable

Subscripts

AD = annular diffuser
 ax = axial direction
 CD = conical diffuser
 ED = entire diffuser
 i, j = index number
 m = midspan
 r = radial direction
 s = static quantity
 tg = tangential direction
 t = total quantity, turbulent
 1 = annular diffuser inlet
 2a = annular diffuser exit
 2b = conical diffuser inlet
 3 = conical diffuser exit

Superscripts

$\bar{\phi}$ = averaged data
 ϕ' = rms velocity

References

- [1] Sovran, G., and Klomp, E. D., 1967, "Experimentally Determined Optimum Geometries for Rectilinear Diffusers With Rectangular, Conical or Annular Cross-Section," *Fluid Mechanics of Internal Flow*, G. Sovran, ed., Elsevier, New York, pp. 272–319.
- [2] 1990, "Introduction to Design and Performance Data for Diffusers," ESDU 76027, Engineering Science Data Unit, London, www.esdu.com.
- [3] Fox, R. W., McDonald, A. T., and van Dewoestine, R. V., 1971, "Effects of Swirling Flow on Pressure Recovery in Conical Diffusers," *AIAA J.*, **9**(10), pp. 2014–2018.
- [4] Kumar, D. S., and Kumar, K. L., 1980, "Effect of Swirl on Pressure Recovery in Annular Diffusers," *J. Mech. Eng. Sci.*, **22**(6), pp. 305–313.
- [5] Back, L., and Cuffel, R., 1982, "Experimental Investigation of Turbulent Wall-Jets in the Presence of Adverse Pressure Gradients in a Rectangular Diffuser," *Int. J. Heat Mass Transfer*, **25**(6), pp. 871–887.
- [6] Nicoll, W. B. and Ramaprian, B. R., 1970, "Performance of Conical Diffusers With Annular Injection at Inlet," *ASME J. Basic Eng.*, **92**, pp. 827–835.
- [7] Japikse, D., 2000, "Correlation of Annular Diffusers Performance With Geometry, Swirl and Blockage," Thermal and Fluids Analysis Workshop.
- [8] Quest, J., and Kruse, H., 1983, "Experimentelle Untersuchungen von Nabendiffusoren Hinter Turbinenstufen," *Motortech. Z.*, **44**, pp. 13–17.
- [9] Willinger, R., and Hasselbacher, H., 1998, "The Role of Tip Clearance on the Aerodynamic Interaction of a Last Gas Turbine Stage and an Exhaust Diffuser," ASME Paper No. 98-GT-94.
- [10] Vassiliev, V., Irmisch, S., and Florjancic, S., 2002, "CFD of Industrial Gas Turbines Exhaust Diffusers," ASME Paper No. 2002-GT-30597.
- [11] KluB, D., Wiedermann, A., and Volgmann, W., 2004, "Impact of Gas Turbine Outflow on Diffuser Performance—A Numerical Study," ASME Paper No. GT2004-53043.
- [12] Sieker, O., and Seume, J. R., 2007, "Influence of Rotating Wakes on Separation in Turbine Exhaust Diffusers," Paper No. ISAI8-54.
- [13] Fleige, H.-U., Riess, W., and Seume, J., 2002, "Swirl and Tip Leakage Flow Interaction With Struts in Axial Diffusers," ASME Paper No. GT-2002-30491.
- [14] ANSYS, 2005, "CFX User Document," Version 10.0, ANSYS, Europe.
- [15] Menter, F. R., 1994, "Two-Equation Eddy-Viscosity Turbulence Models for Engineering Applications," *AIAA J.*, **32**(8), pp. 1598–1605.
- [16] Bradshaw, P., Ferris, D. H., and Atwell, N. P., 1967, "Calculation of Boundary Layer Development Using the Turbulence Kinetic Energy Equation," *J. Fluid Mech.*, **28**(3), pp. 593–616.
- [17] Menter, F. R., and Egorov, Y., 2007, "Turbulence Modelling of Aerodynamic Flows," International Aerospace CFD Conference, Paris.
- [18] Spalart, P., Jou, W.-H., Strelets, M., and Allmaras, S. R., 1997, "Comments on the Feasibility of LES for Wings, and on a Hybrid RANS/LES Approach," *Advances in DNS/LES*, First AFOSR International Conference on DNS/LES, Greiden.
- [19] Menter, F. R., Kuntz, M., and Bender, R., 2003, "A Scale-Adaptive Simulation Model for Turbulent Flow Prediction," Paper No. AIAA-2003-0767.
- [20] Menter, F. R., and Egorov, Y., 2004, "Revisiting the Turbulent Length Scale Equation," IUTAM Symposium: One Hundred Years of Boundary Layer Research, Göttingen, Germany.
- [21] Menter, F. R., and Egorov, Y., 2005, "A Scale-Adaptive Simulation Model Using Two-Equation Models," Paper No. AIAA-2005-1095.
- [22] Menter, F. R., and Egorov, Y., 2005, "Turbulence Models Based on the Length-Scale Equation," Fourth International Symposium on Turbulent Shear Flow Phenomena, Williamsburg, VA, Paper No. TSFP4-268.
- [23] Rotta, J. C., 1972, *Turbulente Strömungen*, Teubner, Stuttgart.
- [24] Davidson, L., 2006, "Evaluation of SST-SAS Model: Channel Flow, Asymmetric Diffuser and Axi-Symmetric Hill," European Conference on Computational Dynamics, ECCOMAS CFD.
- [25] Stevens, S. J., and Williams, G. J., 1980, "The Influence of Inlet Conditions on the Performance of Annular Diffusers," *ASME J. Fluids Eng.*, **102**, pp. 357–363.

The Effect of Leading-Edge Geometry on Wake Interactions in Compressors¹

Andrew P. S. Wheeler²

e-mail: a.wheeler@qmul.ac.uk

Alessandro Sofia³

Robert J. Miller

Whittle Laboratory,
University of Cambridge,
Cambridge CB3 0DY, United Kingdom

The effect of leading-edge geometry on the wake/boundary-layer interaction was studied in a low-speed single-stage HP compressor. Both a 3:1 elliptic and a circular leading edge were tested on a controlled diffusion aerofoil stator blade. Experiments were undertaken on the stator suction surface; these included hotwire boundary-layer traverses, surface hotfilm measurements, and high resolution leading-edge pressure measurements. Steady computational fluid dynamics (CFD) predictions were also performed to aid the interpretation of the results. The two leading-edge shapes gave rise to significantly different flows. For a blade with an elliptic leading edge (Blade A), the leading-edge boundary layer remained attached and laminar in the absence of wakes. The wake presence led to the formation of a thickened laminar boundary layer in which turbulent disturbances were observed to form. Measurements of the trailing-edge boundary layer indicated that the wake/leading-edge interaction for Blade A raised the suction-surface loss by 20%. For a blade with a circular leading edge (Blade B), the leading-edge boundary-layer exhibited a separation bubble, which was observed to reattach laminar in the absence of wakes. The presence of the wake moved the separation position forward while inducing a turbulent reattachment upstream of the leading-edge time-average reattachment position. This produced a region of very high momentum thickness at the leading edge. The suction-surface loss was found to be 38% higher for Blade B than for Blade A. Wake traverses downstream of the blades were used to determine the total profile loss of each blade. The profile loss of Blade B was measured to be 32% higher than that of Blade A. [DOI: 10.1115/1.3104617]

1 Introduction

The leading-edge region is particularly important in compressor blade rows since the initial development of the boundary layer at the leading edge influences the boundary layer over the rest of the blade surface. Furthermore, the leading-edge radius of a core compressor blade can be as small as 0.2 mm. Therefore, manufacturing processes and in-service erosion can give rise to leading-edge shapes that vary significantly from the design intent. Despite this, it is not well understood how compressor performance is affected by variations in leading-edge geometry.

Walraevens and Cumpsty [1] studied both elliptic and circular shaped leading edges on a flat plate. They found that the circular geometry gave rise to a leading-edge separation bubble at zero incidence, while the elliptic geometry only exhibited a bubble at moderate incidences. The separation bubbles led to a transition of the boundary layer and turbulent reattachment. Between zero and two degrees of positive incidence, the momentum thickness downstream of the circular leading edge was found to be two to three times higher than that downstream of the elliptic leading edge. The reason for this was that, even when present, the bubbles on the elliptic leading edge were smaller than those on the circular leading edge at the same incidence.

Wheeler et al. [2] showed that the interaction of the incoming wake with the leading-edge region has a significant effect on the performance of compressor blades. They showed that immediately

downstream of the leading edge the wake caused the instantaneous momentum thickness of the laminar boundary layer to be raised by 18%. These regions of thickened boundary layer were found to provide favorable environments for the production of turbulent spots and thus led to an early transition. The leading and trailing edges of these regions of thickened turbulent boundary layer were observed to propagate at 70% and 60% of the freestream velocity. The interaction of the wake with the leading edge, therefore, caused an increase in the turbulent wetted area on the blade surface, and this was found to raise the suction-surface profile loss by 13%. Henderson et al. [3] also highlighted the importance of wakes at the leading-edge region by showing that it was a key receptivity site for turbulent spot formation.

In the present paper, the effects of leading-edge geometry were tested on a compressor blade with incoming wakes. Two geometries of leading edge were chosen. These were a 3:1 elliptic leading edge (Blade A) and a circular leading edge (Blade B). Both blades had an included wedge angle typical of those found in the compressors of modern aeroengines. Blade A was typical of the geometry of well designed leading edges used in modern aeroengines, and Blade B was typical of those found in many older designs of in-service aeroengines. The blades were tested in the stator-blade row of a large-scale single-stage HP compressor. The flow field in the leading-edge region was investigated with arrays of surface-mounted hotfilm sensors, microtraverses of the blade boundary layer using hotwires, and micropressure tappings. The effects of the leading-edge flow on both the stator-blade suction-surface boundary-layer and the profile loss were measured using hotwire boundary-layer traverses and exit pneumatic-probe traverses. A series of computational fluid dynamics (CFD) calculations was also used to aid in the analysis of the results.

2 Experimental Methods

2.1 Experimental Rig Details. The measurements were performed in the stator-blade row of the Deverson single-stage re-

¹2007 IGTI Best Technical Paper

²Corresponding author. Present address: School of Engineering and Materials Science, Queen Mary, University of London, UK.

³Present address: ETH Zürich. This author performed his portion of this work at the Whittle Laboratory while he was an MS exchange student from ETH Zürich.

Contributed by the International Gas Turbine Institute of ASME for publication in the JOURNAL OF TURBOMACHINERY. Manuscript received October 13, 2008; final manuscript received October 21, 2008; published online July 6, 2009. Review conducted by David Wisler. Paper presented at the ASME Turbo Expo 2007: Land, Sea and Air (GT2007), Montreal, QC, Canada, May 14–17, 2007.

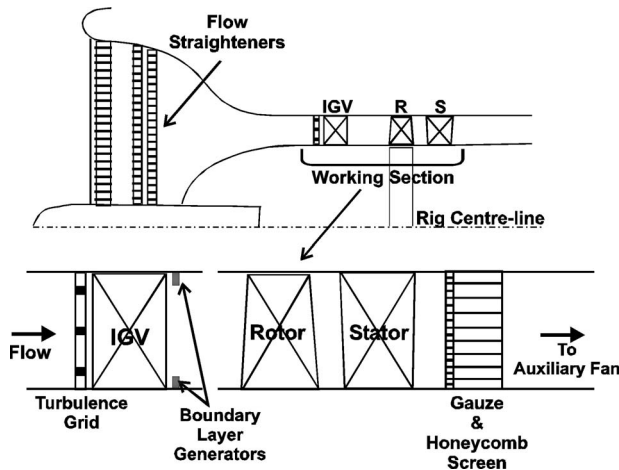


Fig. 1 The Deverson rig and working section

search compressor at the Whittle Laboratory, Cambridge. The rig is a large-scale model of an embedded high-pressure compressor. A schematic of the rig and the working section is shown in Fig. 1. After a 9.3:1 area contraction, air passes into a parallel annulus with hub and casing radii of 609.6 mm and 762.0 mm, respectively. A series of hub and casing boundary-layer blockage generators and a turbulence grid situated upstream of the stage simulate the flow conditions of an embedded stage. The air meets a row of inlet guide vanes (IGVs), which produce the swirl required for the following rotor blades. A pressure-loss screen and a honeycomb are situated approximately 0.4 stator axial chords downstream of the stator trailing edge. These are to simulate the steady potential-field effects of a downstream stage with a fixed characteristic slope. An auxiliary fan and a throttle situated far downstream of the pressure-loss screen allow for the mass flow through the rig to be controlled independently of the rotational speed.

The stage has 51 rotor blades, 49 stator blades, a design rotational speed of 500 rpm, and a design flow coefficient of $\phi = 0.51$. The stator-blade inlet and exit Reynolds numbers at midspan based on the chord are $Re = 2.8 \times 10^5$ and 1.9×10^5 , respectively. The stator inlet and exit flow angles at midspan are $\alpha_1 = 52.7$ deg and $\alpha_2 = 29.5$ deg, respectively [4]. The stage inlet turbulence level is 3.7% [5]. At the stator leading-edge plane, the freestream turbulence level was measured to be 2.5%, and the peak wake turbulence was 7%. The rotor/stator axial gap is a 30% span.

Two new stator-blade designs were used for the current investigation (see Fig. 2). The new designs were a modification of the existing stator blades, which had a circular leading edge of radius $r = 1.1$ mm. For the new blades, the front portion of the blade was altered to have a wedge angle, which was representative of blade leading edges in modern aeroengines [6]. Blade A had a 3:1 ellip-

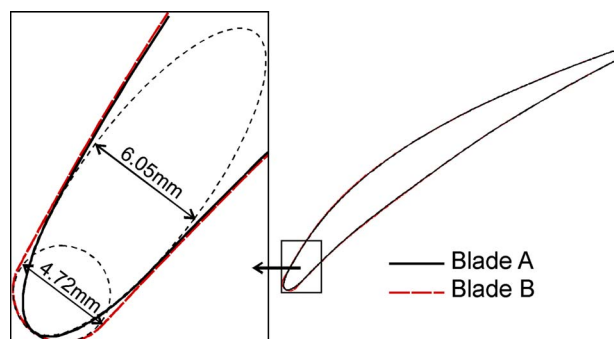


Fig. 2 Leading-edge geometries for Blades A and B

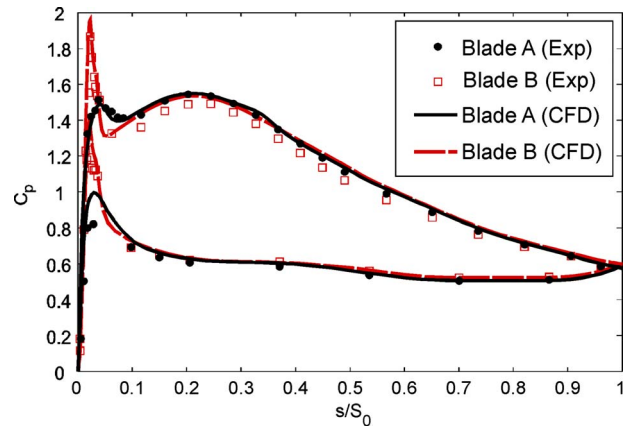


Fig. 3 The stator-blade pressure distribution for Blades A and B at midspan

tic shaped leading edge, while Blade B had a circular shaped leading edge. The leading edges were designed to have the same included wedge edge angle of 15 deg. The blades were identical downstream of the leading-edge region and had a chord of $c = 126$ mm. The leading-edge Reynolds number (based on r) for Blade B was $Re_r = 5.0 \times 10^3$. This is representative of engine compressor blades operating at a cruise for which typically $Re_r = 3 \times 10^3 - 9 \times 10^3$.

The blades were tested by replacing one stator blade from the existing blade row with the modified blades. The validity of this approach was verified using a 2D CFD prediction of the three stator-blade passages with a single central blade replaced with the modified geometry. During the experimental testing, a hub gap of 0.5% chord was introduced to ensure two-dimensional flow at the midheight plane for the tested blades. This was determined from the work of Gbadebo [7] and was confirmed with surface-oil flow visualizations.

Figure 3 shows the experimentally measured and computationally predicted time-average pressure distribution at midspan for Blades A and B. The stator blades are a controlled diffusion aerofoil (CDA) design, where the adverse pressure gradient on the suction surface is initially comparatively steep and then decreases in strength toward the trailing edge. The experimentally measured pressure distributions for the two blades are similar for $s/S_0 > 0.2$ but differ significantly in the leading-edge region. These differences will be discussed in detail later.

2.2 Experimental Methods. Measurements of the boundary layer were made with a hotwire probe, which was microtraversed across the suction-surface boundary layer at several positions along the blade surface. Boundary-layer traverses were performed close to the leading edge ($s/S_0 = 0.029 - 0.087$) and over the late suction surface at $s/S_0 = 0.63 - 0.97$. The hotwire was calibrated for velocity using the King's law method, and the Bearman and Cox correction methods were implemented to correct for ambient temperature variations and wall proximity effects. For the measurements close to the leading edge, the thinness of the boundary layer required that the distance of the first traverse point from the surface be estimated by comparing the time-average measured profile to that predicted by CFD calculations. For each traverse 15–20 points were measured through the time-average boundary layer (see Fig. 4).

A microtapping technique similar to that used by Bindon [8] was used to obtain high resolution measurements of the time-average pressure in the leading-edge region. An array of hotfilm sensors mounted around the leading-edge region was used to make quasi-shear-stress measurements over the leading edge and early suction surface of Blades A and B. These films were mounted on blades with recessed leading-edge sections to com-

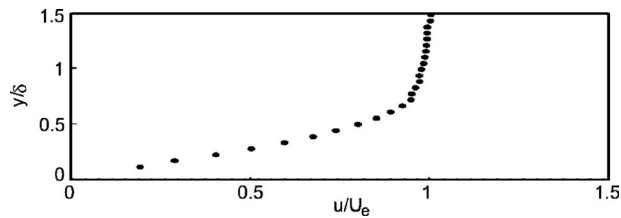


Fig. 4 Time-average boundary-layer profile at 8.68% S_0 for Blade A ($\delta/c=0.004$)

pensate for the film thickness and thickness of the adhesive layer. This ensured that the shape and thickness of the leading edges were not altered by the presence of the film. The quasi-wall-shear-stress was related to the measured output voltage by the relation [9]

$$\tau_w = \left(\frac{E^2 - E_0^2}{E_0^2} \right)^3, \quad (1)$$

where E_0 is the output voltage under zero flow conditions.

The data logging during all the unsteady measurements was triggered using a once-per-revolution signal from the rotor. The ensemble statistics were then obtained from a number of “phase-locked” time series. During the hotfilm and hotwire measurements, 256 and 128 phase-locked time series were logged, respectively.

2.3 CFD Details. The MISES Version 2.56 [10] program was used to aid the interpretation of the experimental results. MISES is a steady 2D/quasi-3D Euler code with a coupled boundary-layer solver. The transition location is determined from a modified version of the Abu-Ghannam and Shaw correlations [11] with an inlet turbulence level specified. For the current work, 2D calculations were performed on Blades A and B, where the boundary conditions were set according to measurements of the time-average conditions. These included the inlet flow angle, inlet Reynolds number, inlet and exit Mach numbers, and inlet turbulence level.

Figure 3 compares the computationally predicted and experimentally measured C_p distributions for Blades A and B. For Blade A, the CFD predicted and the measured C_p are in agreement over most of the blade surfaces, with some differences on the pressure surface close to the leading edge. For Blade A, the CFD predicts boundary-layer transition at $s/S_0=0.35$ on the suction surface and transition at $s/S_0=0.10$ on the pressure surface. For Blade B, the values of C_p close to the peak suction on the suction surface are approximately 3% lower than the CFD. For Blade B, the CFD predicts a separated-flow transition at approximately $s/S_0=0.04$ on both surfaces. Downstream of the leading edge, the predicted pressure distributions for the two blades are very similar. The differences in the leading-edge flow field will be discussed next.

3 Time-Average Leading-Edge Flow Field

The time-average pressure distribution in the leading-edge region of Blades A and B was investigated using microtapping pressure measurements. The results from these are shown in Fig. 5, which is a plot of the measured leading-edge C_p distribution for Blades A and B. For Blade A the experimental results show that on the suction surface there is a smooth acceleration up to $s/S_0=0.04$ followed by a gradual deceleration. On the pressure surface, there is also a moderate peak in C_p at $s/S_0=0.03$. For Blade B on the suction surface, the experimental results show a steep acceleration up to $s/S_0=0.023$ followed by a deceleration up to $s/S_0=0.03$. Downstream of $s/S_0=0.03$, there is a change in the gradient of the C_p distribution, which is indicative of a boundary-layer separation. On the pressure surface, there is a steep accel-

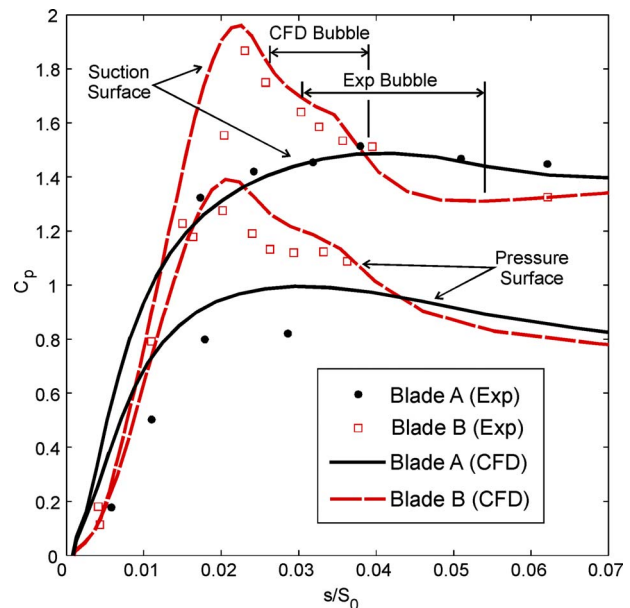


Fig. 5 The time-average leading-edge pressure distributions for Blades A and B at midspan

eration up to $s/S_0=0.020$ followed by a deceleration and a plateau in the C_p between $s/S_0=0.026$ and 0.035 , indicating boundary-layer separation in this region.

The CFD predictions of the C_p distributions in the leading-edge region are also shown in Fig. 5. For Blade A on the suction surface, the CFD results match the measured height and width of the peak in C_p . On the pressure surface, the CFD predicts a peak C_p , which is approximately 20% higher than the measurement. For Blade B on the suction surface, the CFD predicts a peak C_p , which is 5% higher than the measurement. Downstream of this peak, the CFD exhibits a “knee” in the C_p distribution typical of laminar separation and turbulent reattachment. This is followed by an accelerating pressure gradient. On the pressure surface the predicted peak in C_p is 9% higher than the measured peak. Again, this peak is followed by a knee in the C_p , indicating laminar separation and turbulent reattachment.

The peaks (or “spikes”) in the leading-edge C_p distributions are due to the overacceleration and then subsequent deceleration of the flow around the leading edge. At design incidence a blade with a leading edge that has been both well designed and manufactured will have either no or only a small leading-edge spike. However, in practice large leading-edge spikes occur either when well designed and manufactured leading edges are operated at incidence or when due to poor manufacture or in-service erosion the design intent does not occur.

The deceleration in the spike can lead to a separation of the boundary layer closely downstream of the blend point where the leading edge meets the blade. In Fig. 5 the location of the separation on the suction surface of Blade B is indicated. This was determined from hotwire and hotfilm data presented later in this paper. These showed that the boundary layer separated at approximately $s/S_0=0.03$ and reattached at $s/S_0=0.054$. The CFD predicted separation at $s/S_0=0.026$ and reattachment at $s/S_0=0.039$ (determined from the calculated wall shear stress). In the CFD, the separation bubble is closed through a turbulent reattachment. The measured bubble is significantly longer than predicted (by up to 50% depending on the time in the wake-passing period, as discussed later), and this indicates that the nature of the leading-edge separation bubble is not well predicted by the CFD.

In order to investigate the state of the boundary layers on Blades A and B, a series of boundary-layer traverses was performed close to the leading edge on the suction surfaces of both

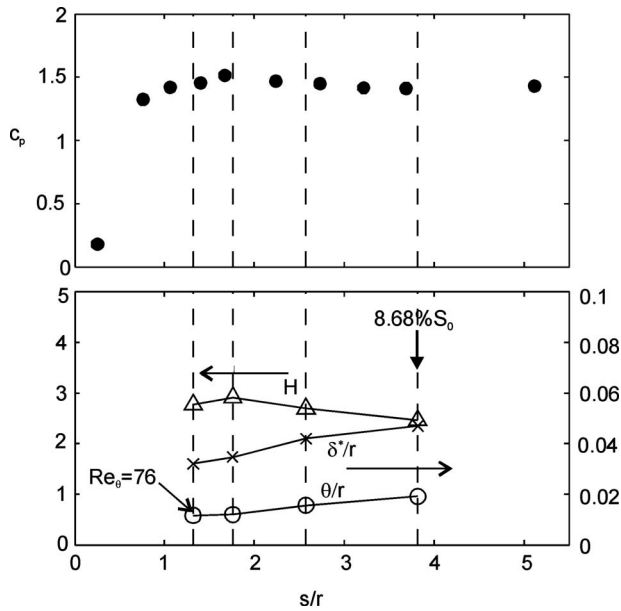


Fig. 6 The leading-edge time-average boundary-layer integral parameters for Blade A suction surface ($s/r=44s/S_0$)

blades. The results from these measurements for each blade are shown in Figs. 6 and 7. These figures show the variations in measured time-average boundary-layer shape factor (H), momentum thickness (θ), and displacement thickness (δ^*) normalized by r and plotted against s/r (for comparison with Ref. [1]). For the ellipse, r was defined as half the minor axis. For Blade A, $s/r=44s/S_0$, and for Blade B, $s/r=56s/S_0$. The leading-edge pressure distributions are also repeated in the figures for reference.

For Blade A, Fig. 6 shows that between s/r of 1.3 and 3.8 the boundary layer is attached and laminar with a shape factor (H) between 2.5 and 2.9. Further evidence of this is seen in the boundary-layer profile shown in Fig. 4. The measured displacement thickness (δ^*) shows that the time-average boundary layer is thin close to the peak in C_p ($\delta^*/r=0.034$). At this point the bound-

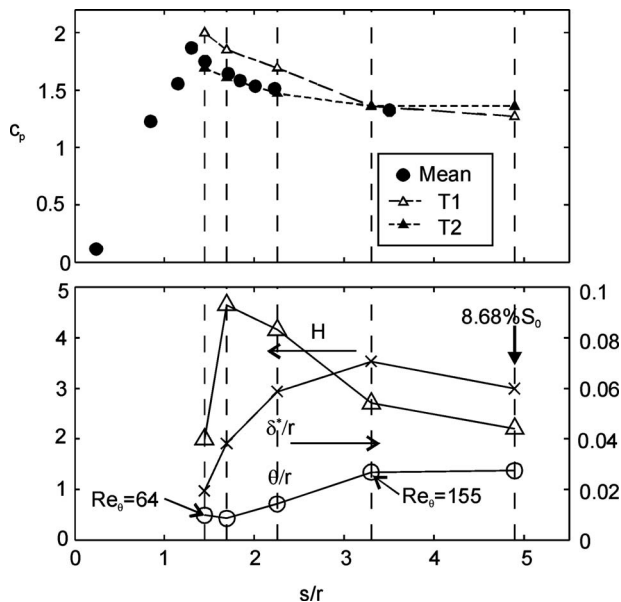


Fig. 7 The leading-edge time-average boundary-layer integral parameters for Blade B suction surface ($s/r=56s/S_0$)

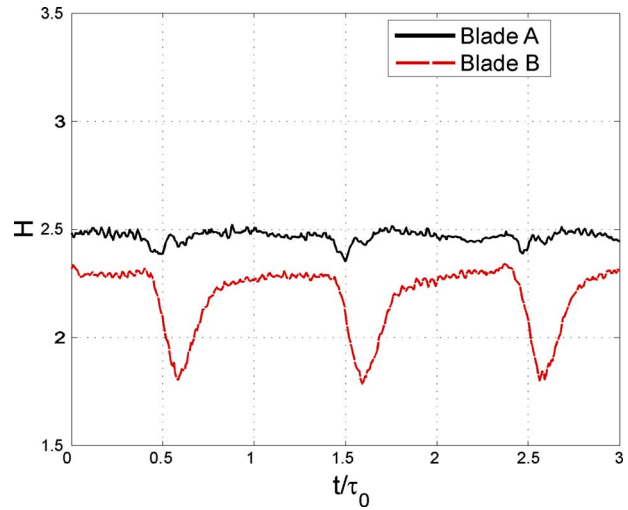


Fig. 8 Variation in shape factor (H) with time at 8.68% S_0 for Blades A and B

ary layer has had little distance to develop while also experiencing an accelerating pressure gradient that reduces the rate of boundary-layer growth. Downstream of the peak in C_p , the rates of increase in δ^* and momentum thickness (θ) are observed to increase due to the effect of the adverse pressure gradient.

For Blade B, Fig. 7 indicates that at $s/r=1.44$, the boundary is laminar with $H=2.0$. Downstream of the blend point ($s/r=1.46$) at $s/r=1.69$, there is a rise in H to 4.65. This indicates that laminar separation has occurred. By $s/r=3.3$, H has dropped to 2.7, indicating that a reattachment of the boundary layer occurs. A separation bubble is also indicated by the variation in δ^* , which rises from $\delta^*/r=0.02$ at $s/r=1.44$ to $\delta^*/r=0.07$ at $s/r=3.3$ and reduces to $\delta^*/r=0.06$ at $s/r=4.9$. Across the separation bubble, θ rises from $\theta/r=0.01$ to 0.027.

It is interesting to note that downstream of the reattachment at $s/r=4.9$, $H=2.2$, which is within the range where laminar flow might be expected. It is also interesting to note that the time-average Reynolds number based on momentum thickness at separation is low ($Re_{\theta_s}=64$), and this may reduce the chance of turbulent transition in the free shear layer on the edge of the bubble. Furthermore, after reattachment $Re_{\theta_r}=155$, which is below the stability limit for laminar boundary layers in zero pressure gradients. Downstream of the reattachment, there is an accelerating pressure gradient (see Fig. 3), which may also aid in a laminar reattachment.

4 Unsteady Leading-Edge Flow Field

The temporal variations in shape factor (H) and momentum thickness (θ) at 8.68% S_0 for both blades are plotted in Figs. 8 and 9, respectively. This position is downstream of the separation bubble of Blade B (see Fig. 7). Hotfilm measurements around the leading edges of Blades A and B are presented in Figs. 10–12. These results are discussed next.

4.1 Blade A: The Elliptic Leading Edge. For Blade A, Fig. 8 shows that the shape factor does not vary significantly with time but fluctuates by $\pm 2.4\%$ about a mean of $H=2.46$. This implies that the boundary layer remains laminar over the wake-passing cycle. Figure 9 shows that there is a rise in θ of approximately 16% due to the wake interaction. It was shown in Ref. [2] that an 18% rise in the instantaneous θ at the leading edge due to the wake interaction led to the formation of turbulent spots close to the leading edge. The turbulent spot formation was due to a combination of the destabilizing effects of regions of high θ as well as the increased turbulence level due to the wake presence at the

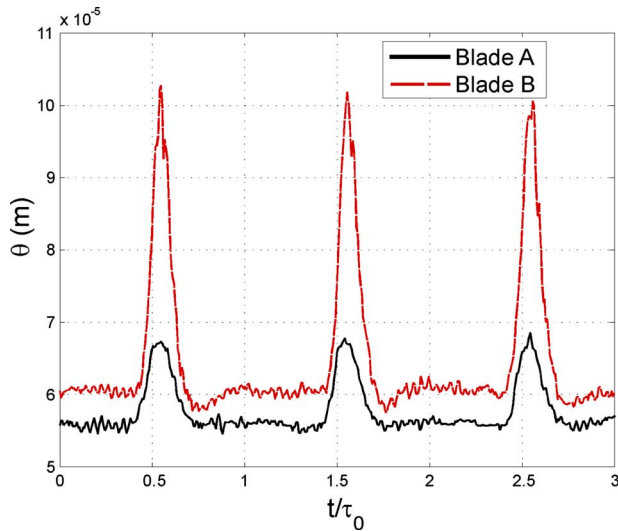


Fig. 9 Variation in momentum thickness (θ) with time at 8.68% S_0 for Blades A and B

leading edge.

To investigate whether turbulent spots formed on the early suction surface of Blade A, quasi-surface-shear-stress (τ_w) measurements were performed with an array of surface-mounted hotfilm sensors. The sensor array was mounted around the leading edge of the blade. Figure 10 shows the raw time traces measured by each sensor. For each trace, the time mean has been subtracted, and the traces are plotted at each sensor location. The traces were logged simultaneously so that the propagation of individual events could be tracked. Celerity lines at the freestream velocity V , $0.5V$ and $0.3V$, are plotted where these were determined from the measured pressure distribution. The celerity lines are plotted so that they meet at the location where the ensemble-averaged shear stress (not shown here) indicated the first appearance of turbulent disturbances ($s/S_0=0.07$). The variation in θ at 8.68% S_0 is also replotted for comparison. As expected, the figure shows that turbulent disturbances identified as locally raised τ_w (e.g., marked A)

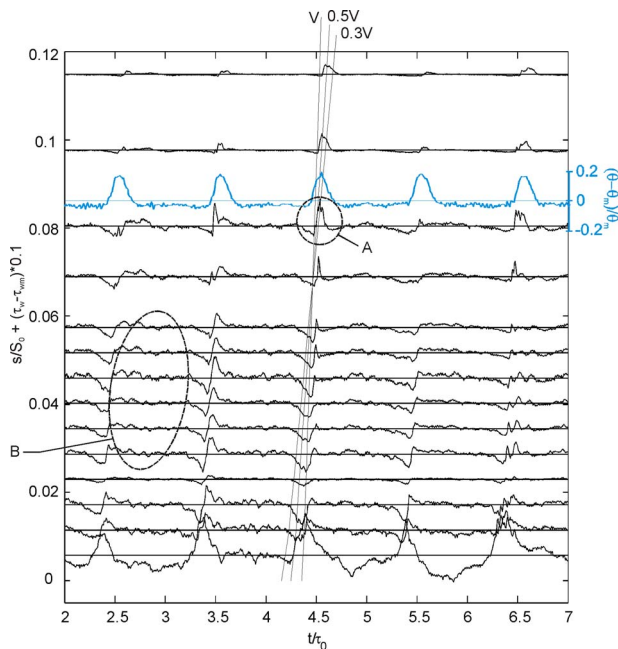


Fig. 10 Raw traces of quasi-shear-stress (τ_w) close to the leading edge for Blade A

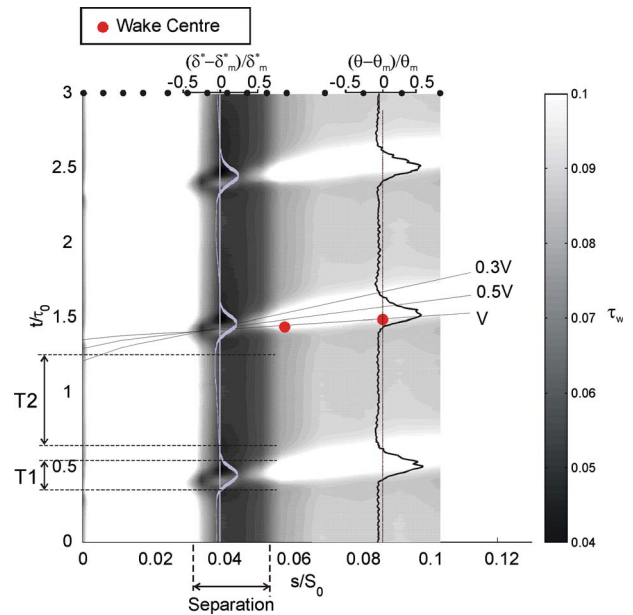


Fig. 11 Ensemble-averaged quasi-shear-stress (τ_w) close to the leading edge for Blade B

start in the region of high θ . Figure 10 shows that the front of the turbulent disturbance, marked A, moves at a speed between $0.5V$ and V . Figure 10 also shows significant fluctuations in between the wake-passing events, (e.g., marked B). The size of these fluctuations diminishes downstream of $s/S_0=0.06$ corresponding to the start of the accelerating pressure gradient (see Fig. 3). The fluctuations also appear to be of a relatively low frequency compared with the T-S type disturbances reported in Ref. [3].

4.2 Blade B: The Circular Leading Edge. For Blade B, Fig. 8 shows that the value of H for Blade B varies from $H=2.3$ to $H=1.8$ due to the wake interaction. Figure 9 shows that in the absence of the wake, the momentum thickness for Blade B is 5%

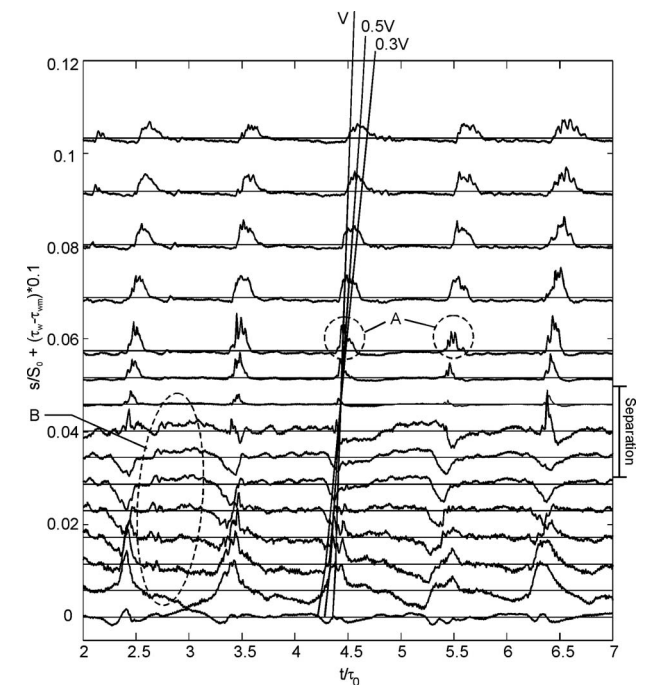


Fig. 12 Raw traces of quasi-shear-stress (τ_w) close to the leading edge for Blade B

higher than the laminar boundary layer of Blade A. The figure also shows that the momentum thickness rises by 53% in the region of low H . These results indicate that there is a change in the boundary-layer state from laminar to turbulent due to the presence of the wake. This implies that in between wake events the separated boundary layer remains laminar downstream of the reattachment location, whereas when the wake is present at the leading edge the separation bubble reattaches through turbulent transition.

To investigate the unsteady boundary-layer state further, surface-shear stress measurements were performed with a hotfilm sensor array mounted around the leading edge of Blade B. Figure 11 is a space-time diagram of the ensemble-averaged quasi-shear-stress (τ_w) from these measurements. Very high levels of shear stress occur at $s/S_0 < 0.03$ and are outside the contour range of the plot. These high levels are due to the thinness of the boundary layer combined with the high velocities in this region (see Fig. 5). As before, celerity lines at the freestream velocity V , $0.5V$ and $0.3V$, are plotted. In this case, the celerity lines meet at $s/S_0 = 0.04$ where the first appearance of turbulent disturbances is observed. The positions of the wake center, indicated by the larger dots, were determined from the peak freestream turbulence level measured from the boundary-layer traverses discussed previously. As expected, the wake is observed to move close to the freestream velocity.

In Fig. 11 a region of low shear stress exists between $s/S_0 = 0.035$ and $s/S_0 = 0.054$, which corresponds to the position of the separation bubble. The effect of the wake interaction with the separation bubble moves the separation point forward from approximately $s/S_0 = 0.035$ to $s/S_0 = 0.030$. At approximately $0.06t/\tau_0$ later, a turbulent reattachment occurs, which results in a forward movement of the reattachment location from $s/S_0 = 0.054$ to approximately $s/S_0 = 0.042$. This is shown by raised shear-stress levels within the previously separated region, indicating the formation of turbulent disturbances. The shortening of the bubble through turbulent transition is likely to be caused by the increased turbulence level within the wake. The turbulent regions of high shear stress are observed to propagate downstream of the reattachment. The measured variation in θ at $8.68\% S_0$ is repeated in the figure for comparison. It can be seen that the turbulent regions are also regions of raised θ , as was observed previously in Figs. 8 and 9.

Indicated in Fig. 11 are two fractions of the wake-passing period, T1 and T2. These represent the times when the separation bubble is affected by the wake (T1) and when the wake no longer affects the bubble (T2). In the C_p distribution shown in Fig. 7, two lines are plotted, which represent the average C_p distribution over the fractions T1 and T2. These were determined from the unsteady boundary-layer edge velocity measured from the hotwire traverses discussed previously. The results show that the increased local incidence caused by the presence of the wake at the leading edge (T1) results in a 20% rise in the height of the leading-edge C_p spike. The variation in separation bubble height (δ^*) at $4.0\% S_0$ is shown in Fig. 11. The plot shows that the presence of the wake causes a 30% rise in bubble height.

Figure 12 plots the raw quasi-shear-stress from the hotfilm measurements described above. As before, the traces are plotted at each sensor location, with the time-average shear-stress level subtracted. Close to the stagnation point at $s/S_0 = 0.006$, the fluctuations in τ_w are similar to those observed on Blade A. Further downstream, at $s/S_0 \approx 0.04$, turbulent disturbances (e.g., marked A) start to form within the separated region. The spots contain high frequency fluctuations, which typically occur prior to separated-flow transition [12]. The front of the turbulent spots moves close to the freestream velocity V . The trailing edge of the turbulent spots moves at approximately $0.5V$, which is then followed by a relatively slow drop in shear stress, typical of the calmed region that follows a turbulent spot. This is consistent with previous findings on the propagation of turbulent spots [12]. Disturbances between wake-passing events (e.g., marked B) propa-

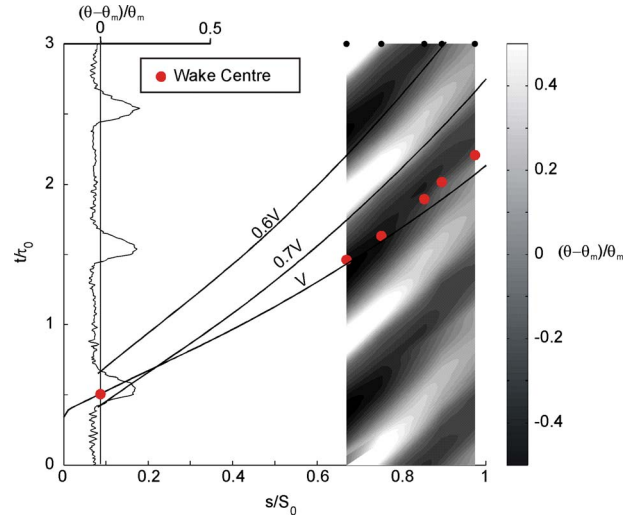


Fig. 13 S-t plot of normalized momentum thickness ($(\theta - \theta_m)/\theta_m$) for Blade A

gate from very close to the leading edge ($s/S_0 > 0.01$). Similar disturbances were also observed previously on Blade A. On Blade B, the magnitude of these disturbances is observed to reduce downstream of $s/S_0 = 0.04$. In between wake events, the fluctuations in τ_w are small in this region, indicating a laminar reattachment of the separation bubble.

5 Propagation of the Thickened Boundary Layer

The previous work of Ref. [2] showed that regions of high θ at the leading edge propagated over the blade surface as a thickened boundary-layer structure, the front of which moved at $0.7V$ and the back at $0.6V$. This structure was shown to be responsible for turbulent transition. To investigate the propagation of these structures, measurement of the late suction-surface boundary layer on both Blades A and B was performed. The measurements involved a series of hotwire boundary-layer traverses at $s/S_0 = 0.63-0.97$. The results from these measurements are plotted in Figs. 13 and 14. These figures are space-time diagrams of the normalized momentum thickness. The variations in θ at $8.68\% S_0$ are also plotted. Celerity lines at the freestream velocity V , $0.7V$ and $0.6V$, are plotted. The $0.7V$ and $0.6V$ lines start at the front and back of the

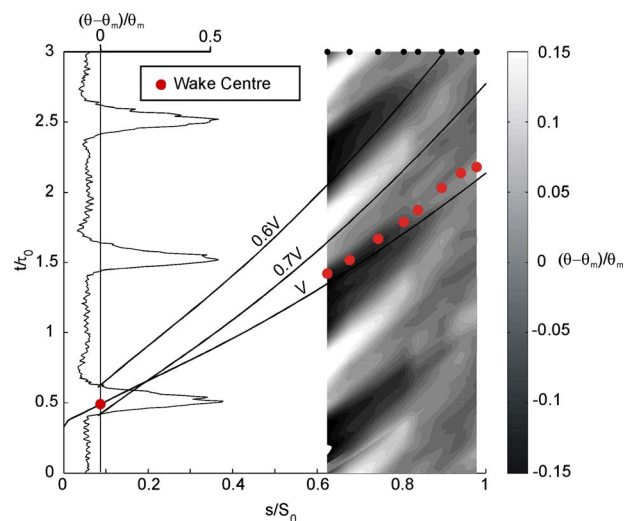


Fig. 14 S-t plot of normalized momentum thickness ($(\theta - \theta_m)/\theta_m$) for Blade B

region of high θ at 8.68% S_0 . As before, the positions of the center of the wake are indicated by the larger dots in the figures.

For Blade A, Fig. 13 shows that there is a region of high θ that propagates over the blade surface. The front of this structure travels at a speed close to 0.7 V, whereas the rear moves at approximately 0.6 V. This structure creates very large fluctuations in θ , which reduce from 86% θ_m at $s/S_0=0.67$ to 20% θ_m at $s/S_0=0.97$. For Blade B, Fig. 14 also shows that the region of high θ moves between the 0.7V and 0.6V lines. The size of the fluctuation in θ associated with this structure reduces as it propagates down the late suction surface from 20% θ_m at $s/S_0=0.62$ to less than 6% at the trailing edge. The propagation speeds observed on both blades are in agreement with the previous findings for the propagation rates of these structures reported in Ref. [2].

It is surprising that for Blade B the fluctuation in θ at 8.68% S_0 is 53% of the mean while at 97% S_0 it is only 6%. Evidence for the cause of reduction in size is shown in Fig. 14. Between the wake center and the region of peak θ , a region of higher θ is observed. This is a region of thickened turbulent boundary layer, which has formed behind the wake on the early suction surface. Thus the thickened boundary-layer structure emanating from the leading edge will propagate within a mainly turbulent boundary layer over the early suction surface. The turbulence in the boundary layer will cause an increased mixing of the thickened boundary-layer structure, thus reducing the fluctuation in θ . In contrast, the thickened boundary-layer structure on Blade A propagates through a mainly laminar boundary layer over the early suction surface and will therefore be less mixed out, thus giving rise to a larger fluctuation in θ over the late suction surface.

The cause of the thickened turbulent boundary layer on the rear of Blade B is caused by early boundary-layer transition. At 8.68% S_0 Fig. 8 shows that the boundary layer on both blades is laminar; however, the shape factor on Blade B is higher than that on Blade A. In addition the hotwire measurements showed that the reattaching boundary layer on Blade B exhibited higher levels of random unsteadiness and thus will be more susceptible to transition closer to the leading edge than the laminar boundary layer on Blade A.

6 Effect on Loss

The energy thickness (ε) at the trailing edge of the blade represents the loss created in the boundary layer up to that point. The momentum thickness (θ) at the trailing edge is directly proportional to the mixed-out loss for blades with thin trailing edges [13]. Both quantities are useful for determining the loss and can be calculated from the trailing-edge boundary-layer profile. For this reason a hotwire traverse was performed across the suction-surface boundary layer close to the trailing edge (at 97% S_0) for Blades A and B. The measured variations in the trailing-edge ε and θ for the two blades from these traverses are shown in Fig. 15. The predicted values of ε and θ for the two blades at 97% S_0 from the CFD calculations are also plotted.

For Blade A, Fig. 15 shows that there are significant fluctuations in both ε and θ of approximately $\pm 20\%$ of the mean levels. These are caused by the arrival of the thickened boundary-layer structure at the trailing edge discussed above (see Fig. 13). The CFD prediction for Blade A, which predicts laminar flow over the early suction surface with transition at $s/S_0=0.35$, gives values for ε and θ , which are close to the minimum measured values. This would suggest that these levels represent the levels in the absence of wakes. Assuming that the CFD prediction represents the loss level in the absence of wakes, then the effect of wakes on Blade A appears to raise the time-average ε and θ by 22% and 20%, respectively. The increase in loss is due to the formation of turbulent spots within the thickened boundary-layer structure close to the leading edge (see Fig. 10). This increases the turbulent wetted area over the suction surface as the thickened boundary-layer structure propagates over the blade surface, as seen in Fig. 13. This was also observed in Ref. [2].

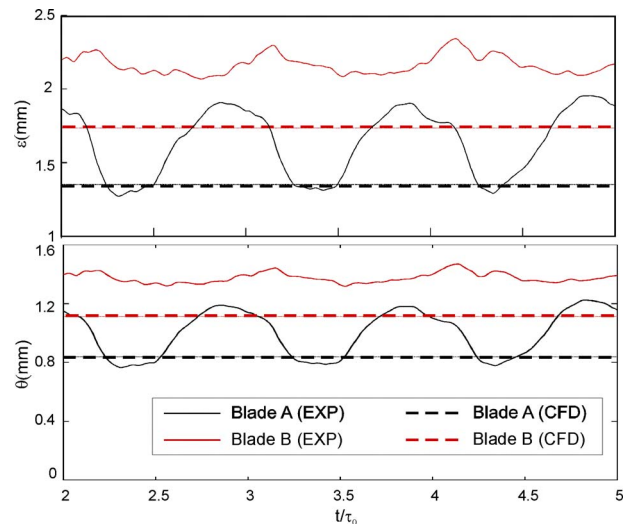


Fig. 15 Variation in energy thickness (ε) and momentum thickness (θ) at 97% S_0 for Blades A and B

For Blade B, Fig. 15 shows that the fluctuations in trailing-edge ε and θ are approximately $\pm 6.5\%$ of the mean levels. For Blade B, the time-average levels of ε and θ are 32% and 38% higher, respectively, than those for Blade A. The increased suction-surface loss for Blade B is likely to be due to two main factors. First is the interaction of the wake with the leading-edge bubble. The increased incidence caused by the wake increases the bubble height, while the increased turbulence in the wake causes a turbulent reattachment. Both the turbulent mixing in the reattachment region and the increase in bubble height will increase losses. Second is the increase in turbulent wetted area caused by earlier transition of the reattaching laminar boundary layer.

The CFD for Blade B predicted a turbulent reattachment of the leading-edge separation bubble and hence turbulent flow over the most part of the blade. Despite this, the CFD gives values of trailing-edge ε and θ , which are approximately 20% less than the measured time-average values. This is a surprising result since the measurements showed that the leading-edge separation bubble in the absence of wakes had a laminar reattachment and hence initially laminar flow downstream of the leading edge. This is an indication that the CFD fails to model correctly the sources of loss for Blade B.

In order to verify the observed increase in loss on Blade B, a pneumatic-probe traverse of the wakes from Blades A and B was performed in the presence of the upstream rotor wakes. The measured time-average total-pressure wake profiles are shown in Fig. 16. The wake for Blade B is 7% wider and 20% deeper than the wake of Blade A. The shift in the wake center is due to a 0.9 deg increase in the deviation of Blade B. The values for the profile

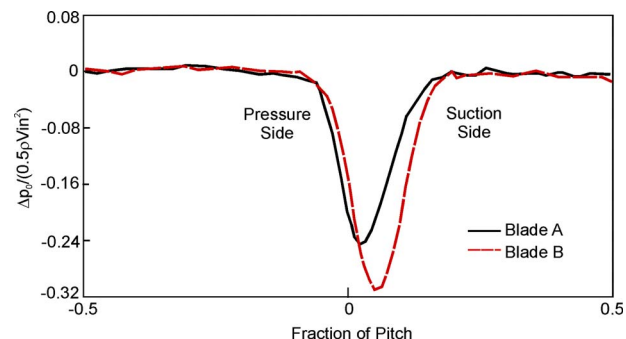


Fig. 16 Total-pressure wake profiles for Blades A and B at 0.3 axial chord downstream of the trailing edge

loss coefficient (mixed out) for Blades A and B are $Y_p=2.5\%$ and $Y_p=3.3\%$, respectively. This amounts to a 32% increase in the total profile loss for Blade B.

7 Conclusion and Discussion

In this paper, two leading-edge geometries were tested in the presence of wakes. The leading-edge geometries were a 3:1 ellipse and a circular leading edge. Both shapes were representative of typical engine leading edges. Furthermore, the leading-edge Reynolds numbers ($Re_r=5.0 \times 10^3$) were typical of engine compressor blades operating at cruise, and the tests were run at stator inlet freestream turbulence levels of 2.5%. The elliptic leading edge maintained attached laminar flow over the early suction surface. The effect of the wake/leading-edge interaction was found to create a thickened boundary-layer structure, which raised the suction-surface profile loss by 20% due to an increase in the turbulent wetted area. This was similar to the wake/leading-edge interaction reported by Wheeler et al. [2]. In contrast, the tests on the circular leading-edge blade showed a very different interaction mechanism. The boundary layer on the circular leading-edge blade separated close to the blend point and reattached laminar in the absence of wakes. This unexpected result differed from the previous flat plate tests of Walraevens and Cumpsty [1] who observed turbulent reattachment of the leading-edge separation bubble. The laminar reattachment was also not captured by the CFD. The laminar reattachment was thought to be aided by the accelerating pressure gradient downstream of the leading-edge spike and the low Re_θ at separation ($Re_{\theta_s}=64$). The effect of the wake on the circular leading edge was found to bring the separation point forward while also bringing forward the reattachment position through turbulent transition. The effect of the wake also increased the instantaneous height of the bubble by 30%. The boundary layer downstream of the leading edge was thus found to change from laminar to turbulent with a 53% higher momentum thickness when a wake was present at the leading edge. The suction-surface profile loss was found to be 38% higher for Blade B than for Blade A, and the total loss (suction surface and pressure surface) for Blade B was measured to be 32% higher than that for Blade A.

The results can be used to estimate the effect of leading-edge geometry on multistage compressor performance. This has been done here by applying the measured changes in profile loss to both rotor and stator-blade rows of the compressor stage discussed in this paper while assuming constant end wall losses. Thus the changes in stage efficiency can be calculated. With the elliptic leading edges, the results show that the wake/leading-edge interaction may contribute up to a 0.5% efficiency reduction. Replacing elliptical leading edges with circular leading edges would result in a 1.5% efficiency drop. These values are for a rotor/stator axial gap of 50% rotor axial chord but are likely to increase in engine compressors where the rotor/stator gaps are typically 30% axial chord.

It is useful to compare the size of the changes in efficiency reported in this paper to those reported for wake recovery by Smith [14]. Smith [14] reported that by reducing the gap from 37% to 7% axial chord the potential efficiency gain due to wake recovery would be 0.3%. The optimum rotor/stator axial gap is dependent, therefore, on the leading-edge shape. For a low loss leading edge, the detrimental effect of the wake/leading-edge interaction is comparable to the potential benefit due to wake recovery effects. Thus, the machine efficiency is likely to be less sensitive to the choice of axial gap. For higher loss leading-edge shapes caused by poor design, manufacturing errors, or in-service erosion, reducing the rotor/stator gap may cause significant reductions in compressor efficiency.

Acknowledgment

The authors would like to thank Rolls-Royce plc and the EPSRC-GB for their support. The authors also gratefully ac-

knowledge the fruitful discussion of the results with Nick Cumpsty, Martin Rose, Mike Howard, Neil Harvey, Hang Lung, and Howard Hodson.

Nomenclature

C_p	= pressure coefficient $(p_{0inlet}-p)/(p_{0inlet}-p_{inlet})$
c	= chord
E	= hot film bridge voltage
E_0	= zero flow hot film bridge voltage
H	= shape factor (δ^*/θ)
P	= blade pitch
p	= pressure
r	= circular leading-edge radius, elliptical leading-edge half-thickness
Re_θ	= Reynolds number based on momentum thickness
s	= surface distance from the leading edge
S_0	= total surface length
t	= time
u	= velocity
U	= midheight rotor-blade speed
U_e	= boundary-layer edge velocity
V	= freestream velocity
y	= normal distance from the blade surface

Greek Symbols

δ	= boundary-layer thickness
δ^*	= boundary-layer displacement thickness
ε	= boundary-layer energy thickness
ϕ	= flow coefficient V_x/U
ν	= kinematic viscosity
θ	= boundary-layer momentum thickness
τ_0	= wake period
τ_w	= quasi-shear-stress

Subscripts

exit	= stator exit
inlet	= stator inlet
m	= time average

References

- [1] Walraevens, R. E., and Cumpsty, N. A., 1995, "Leading Edge Separation Bubbles on Turbomachinery Blades," *ASME J. Turbomach.*, **117**, pp. 115–125.
- [2] Wheeler, A. P. S., Miller, R. J., and Hodson, H. P., 2006, "The Effect of Wake Induced Structures on Compressor Boundary-Layers," *ASME Paper No. GT2006-90892*.
- [3] Henderson, A., Walker, G. J., and Hughes, J., 2006, "Unsteady Transition Phenomena at a Compressor Leading-Edge," *ASME Paper No. GT2006-90641*.
- [4] Bolger, J. J., 1999, "Three-Dimensional Design of Compressor Blades," Ph.D. thesis, University of Cambridge.
- [5] Place, J. M. M., 1997, "Three-Dimensional Flow in Axial Compressors," Ph.D. thesis, University of Cambridge.
- [6] Sofia, A., 2006, "The Effect of Wakes on Leading Edge Loss," MS thesis, ETH Zürich.
- [7] Gbadebo, S. A., 2003, "Three-Dimensional Separations in Compressors," Ph.D. thesis, University of Cambridge.
- [8] Bindon, J. P., 1987, "Pressure Distributions in the Tip Clearance Region of an Unshrouded Axial Turbine as Affecting the Problem of Tip Burnout," *ASME Paper No. 87-GT-230*.
- [9] Hodson, H. P., Huntsman, I., and Steele, A. B., 1994, "An Investigation of Boundary-Layer Development in a Multistage LP Turbine," *ASME J. Turbomach.*, **116**, pp. 375–383.
- [10] Drela, M., and Youngren, H., A user's guide to MISES 2.56.
- [11] Abu-Ghannam, B. J., and Shaw, R., 1980, "Natural Transition of Boundary-Layers—The Effects of Turbulence, Pressure Gradient and Flow History," *J. Mech. Eng. Sci.*, **22**(5), pp. 213–228.
- [12] Cumpsty, N. A., Dong, Y., and Li, Y. S., 1995, "Compressor Blade Boundary Layers in the Presence of Wakes," *ASME Paper No. 95-GT-443*.
- [13] Denton, J. D., 1993, "Loss Mechanisms in Turbomachines," *ASME J. Turbomach.*, **115**, pp. 621–656.
- [14] Smith, L. H., 1996, "Wake Mixing in Axial Flow Compressors," *ASME Paper No. 96-GT-029*.

Shorten the Intermediate Turbine Duct Length by Applying an Integrated Concept

A. Marn

e-mail: andreas.marn@tugraz.at

E. Göttlich

Institute for Thermal Turbomachinery and
Machine Dynamics,
Graz University of Technology,
Graz 8010, Austria

D. Cadrecha¹

Aerothermal Department,
Industria de Turbopropulsores S.A.,
Madrid, Spain

H. P. Pirker

Institute for Thermal Turbomachinery and
Machine Dynamics,
Graz University of Technology,
Graz 8010, Austria

The demand of further increased bypass ratio of aero engines will lead to low pressure turbines with larger diameters, which rotate at lower speed. Therefore, it is necessary to guide the flow leaving the high pressure turbine to the low pressure turbine at larger diameters minimizing the losses and providing an adequate flow at the low pressure (LP)-turbine inlet. Due to costs and weight, this intermediate turbine duct has to be as short as possible. This would lead to an aggressive (high diffusion) s-shaped duct geometry. It is possible to shorten the duct simply by reducing the length but the risk of separation is rising and losses increase. Another approach to shorten the duct and thus the engine length is to apply a so called integrated concept. These are novel concepts where the struts, mounted in the transition duct, replace the usually following LP-vane row. This configuration should replace the first LP-vane row from a front bearing engine architecture where the vane needs a big area to hold bearing services. That means the rotor is located directly downstream of the strut. This means that the struts have to provide the downstream blade row with undisturbed inflow with suitable flow angle and Mach number. Therefore, the (lifting) strut has a distinct three-dimensional design in the more downstream part, while in the more upstream part, it has to be cylindrical to be able to lead through supply lines. In spite of the longer chord compared with the base design, this struts have a thickness to chord ratio of 18%. To apply this concept, a compromise must be found between the number of struts (weight), vibration, noise, and occurring flow disturbances due to the secondary flows and losses. The struts and the outer duct wall have been designed by Industria de Turbopropulsores. The inner duct was kept the same as for the base line configuration (designed by Motoren und Turbinen Union). The aim of the design was to have similar duct outflow conditions (exit flow angle and radial mass flow distribution) as the base design with which it is compared in this paper. This base design consists of a single transonic high pressure (HP)-turbine stage, an aggressive s-shaped intermediate turbine duct, and a LP-vane row. Both designs used the same HP-turbine and were run in the continuously operating Transonic Test Turbine Facility at Graz University of Technology under the same engine representative inlet conditions. The flow field upstream and downstream the LP-vane and the strut, respectively, has been investigated by means of five hole probes. A rough estimation of the overall duct loss is given as well as the upper and lower weight reduction limit for the integrated concept. [DOI: 10.1115/1.3070578]

1 Introduction

To shorten the intermediate turbine duct length and thus the engine length, a so called integrated concept (IC) has been investigated and compared with a base design. The results of the experimental investigation of this base design are well described in Refs. [1,2]. This new concept combines the function of a strut with that of a LP-vane. This means in our case that the upstream part of this strut has a cylindrical design and a large area to lead through supply lines (cooling air for the HP-turbine and lubrication for the bearings) and to support the bearings. Further downstream the strut has a distinct three-dimensional design where the turning of the flow takes place. The intention of the design of this strut was to have similar outflow conditions as it has been achieved with the base design. Moreover, both designs use the same inner duct. The outer duct contour has been modified to consider the blockage of the struts to avoid too high accelerations.

¹Also at Aerothermal Department, Industria de Turbopropulsores S.A., Madrid, Spain.

Contributed by the International Gas Turbine Institute of ASME for publication in the JOURNAL OF TURBOMACHINERY. Manuscript received August 22, 2008; final manuscript received October 1, 2008; published online July 6, 2009. Review conducted by David Wisler. Paper presented at the ASME Turbo Expo 2008: Land, Sea and Air (GT2008), Berlin, Germany, June 9–13, 2008.

The flow through an intermediate turbine duct (ITD) is mainly influenced by the radial pressure gradients imposed by both the meridional curvature of the duct and the swirl. This pressure gradient is changed by the altered swirl due to the turning in the strut. Additionally, a change in static pressure occurs due to the acceleration of the flow within the strut and counteracts the pressure rise due to the diffusion of the ITD. Furthermore, it must be considered that the radial pressure gradient significantly influences the radial motion of the low energy fluid, e.g., the boundary layer on the suction surface of the strut.

Norris et al. [3,4] illustrated the performance and the stability of interturbine diffusers with nonturning symmetrical airfoil struts fitted inside the duct compared with a duct configuration without struts. Pullan et al. [5] investigated the flow field, especially the formation of a streamwise shed vortex of two different designs of low aspect ratio vanes. Furthermore, Pullan et al. [6] studied the performance improvement of a NGV by aft-loading and compared it with the results in Ref. [5].

Less research work has been published describing the development of the exit flow from a transonic turbine stage within an interstage diffuser, e.g., Refs. [7–10,1,2].

This paper presents the results (contour plots and mass averaged radial profiles) of the five-hole-probe (5HP) measurements.

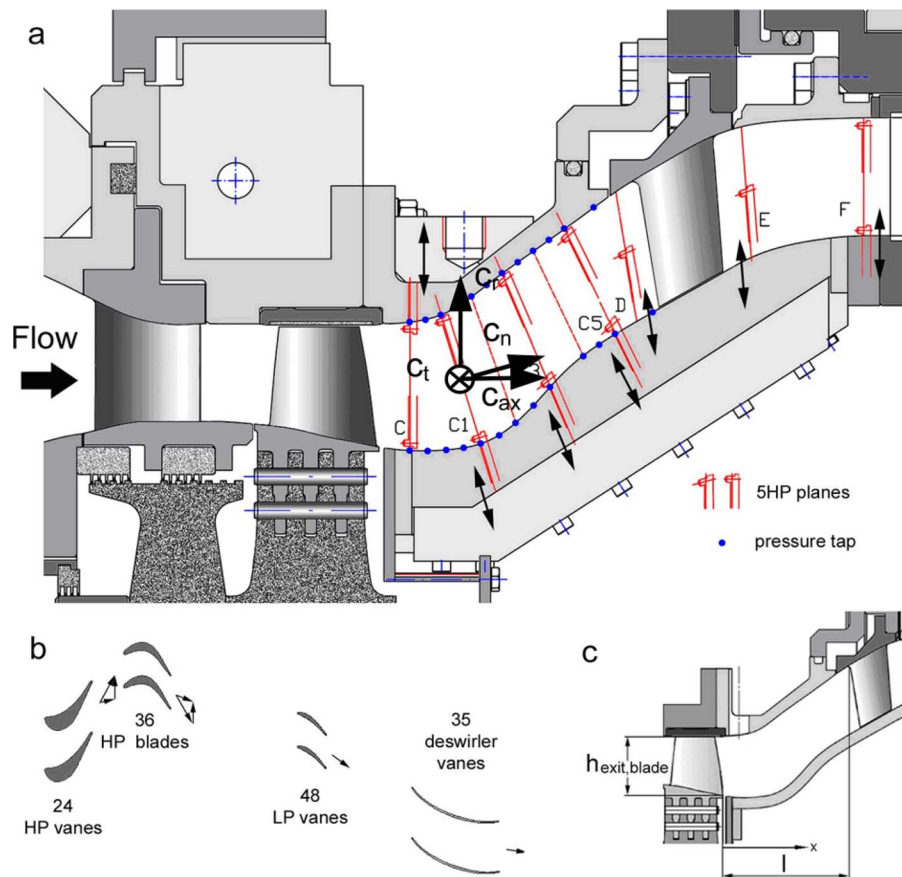


Fig. 1 Meridional section with probe measurement planes (a), blade counts and profiles (b), and definition of nondimensional duct length $l // h_{exit,blade}=2$ (c) for the base design

Additionally, oil flow visualization was done to obtain information about the surface flow at the outer and inner walls of the duct and the suction and pressure surface of the strut.

2 Experimental Facility and Instrumentation

To investigate the flow physics in high diffusion ITDs and the interaction between the neighboring components, a detailed test arrangement, which allows to perform tests under engine representative inlet conditions, is necessary. Therefore, the continuously operating Transonic Test Turbine Facility (TTTF) at Graz University of Technology has been adapted. Details can be seen in Ref. [11].

2.1 Test Facility. The TTTF is a continuously operating cold-flow open-circuit plant, which allows the testing of rig inserts with a diameter up to 800 mm in full flow similarity. All casing parts are split horizontally for easy maintenance and fast modifications of the test setups. An overhung-type turbine shaft allows the disk assembly without dismantling the bearings. The facility is also equipped with cooling air flow supply for vanes, blades, and cavities.

The facility is driven by pressurized air delivered by a separate 3 MW compressor station in the second basement of the institute. The shaft power of the test stage drives a three-stage radial brake compressor. This brake compressor delivers additional air to the flow from the compressor station and increases the overall mass flow. The air temperature at stage inlet can be adjusted by coolers between 40°C and 185°C. The maximum shaft speed of the test rig is limited to 11,550 rpm. Depending on the stage characteristic, a maximum coupling power of 2.8 MW at a total mass flow of

22 kg/s can be reached. Detailed information on the design and construction of the facility can be found in Ref. [12] and on the operation in Ref. [13].

2.2 AIDA Test Rig. Figure 1(a) shows a meridional section of the TTTF together with the Aggressive Intermediate Duct Aerodynamics (AIDA) test rig. The aerodynamic design of the HP-vane, the HP-turbine, the LP-vane, and the duct was done by Motoren und Turbinen Union (MTU) Aero Engines.

The struts and the outer duct for the integrated concept were designed by Industria de Turbopropulsores (ITP). The idea was to design a lifting strut, whose objective is to produce the same turning (same exit flow angle in plane E) and the same uniform radial mass flow distribution with the same loss as the conventional vane. In spite of the longer chord compared with the base design, this struts have a thickness to chord ratio of 18%. The outer duct has been redesigned to consider the blockage effect of the struts to avoid too high accelerations. The integrated concept uses the same inner duct as the base design. Additionally, the blade counts and the profiles (Figs. 1(b) and 2(b)) are given below. The incoming air is accelerated by the HP-vanes in circumferential direction and impinges on the HP-rotor with a cylindrical outer contour. The outer liner rings in the casing can be changed to investigate different rotor tip gaps. Then the flow is guided by the intermediate turbine duct to the vanes of a counter-rotating LP-turbine assembled at a larger radius. There it is accelerated again and turned in the opposite circumferential direction. A downstream deswirler turns the flow back and recovers some pressure. The air leaves the facility through a diffuser and the exhaust casing.

The HP- and LP-vanes (struts) are fitted into fully rotatable

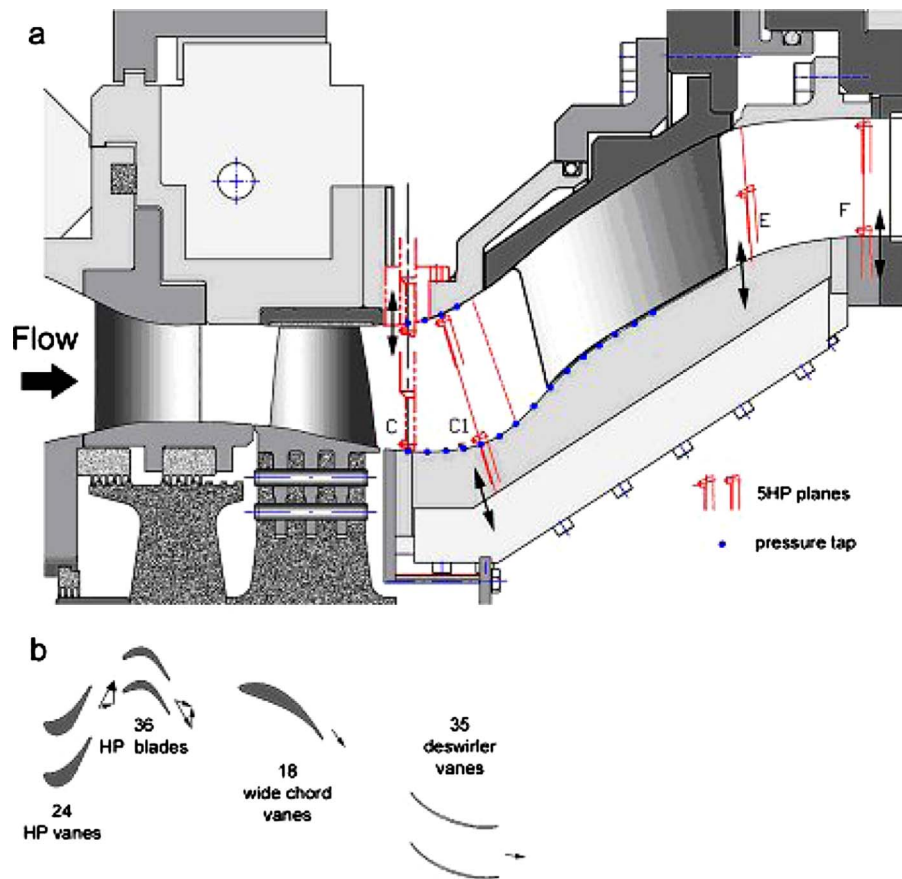


Fig. 2 Meridional section with probe measurement planes (a), and blade counts and profiles (b) for the integrated concept

casings to change the relative position between vanes and the applied measurement system, which can be kept fixed in space during measurement. The deswirler is not rotatable and is always in the same position relative to the 5HP. For probe measurements only one linear and one rotational axis are necessary to adjust the radial position and to turn the probe into the flow. The test rig allows probe measurements in seven (four) different planes downstream the HP-turbine, within the duct as well as upstream and downstream the LP-vane and the strut, respectively (see Figs. 1(a) and 2(a)).

The target is to provide enginelike intermediate turbine duct flow conditions and to perform high quality measurements to get a detailed understanding of the duct flow phenomena. Therefore, the main component of the test setup is a high diffusion intermediate turbine duct assembled downstream of the transonic turbine stage. The inlet flow of the ITD can be described as strongly transient with periodically impinging wake structures from the passing rotor blades, three-dimensional, and highly turbulent together with shocks extending from the blade trailing edges.

Table 1 explains the blading main parameters; there are 24 HP vanes and 36 rotor blades. The vanes of the following counter-rotating low pressure turbine are mounted at the end of the ITD to provide an enginelike radial mass flow distribution, which would be unrealistic without the blockage effect of them. The blade count of 48 was chosen to realize a blade count ratio of 2-3-4, which eases computational fluid dynamics (CFD) modeling of this test arrangement. For the integrated concept, 18 struts were chosen. The trailing edge of the strut is at the same axial position as the trailing edge of the LP-vane and has the same inclination.

The duct area ratio of the base design is approximately 1.5 and a nondimensional duct length $l/h_{\text{exit,blade}}$ of 2 (see Fig. 1(c)) is used. This means that the designed duct geometry is well above

Table 1 Operating condition and blading design parameters

Operating Point HP-turbine				
Mass flow	kg/s	15.9		
Total temp. inlet	K	432		
Total temp. exit	K	332		
Total pressure inlet	bar	3.4		
$Ma_{\text{exit,absolute}}$		0.6		
α_{exit}	deg	-15		
Stage pressure ratio		3.1		
Power	kW	1,590		
Speed	rpm	11,000		
$\Delta H/u^2$		1.6		
c_{ax}/u		0.64		
Tip clearance	% span (mm)	0.8		
Tip geometry		Plenum type seals		
Parameter	HP-vane	HP-blade	Strut	LP-vane
Blade No.	24	36	18	48
t/C	0.89	0.76		0.88
b (mm)	67.9	51		44.3
d_{TE} (mm)	1	1	1	1
h_{exit} (mm)	47	58	63	63
h/C_{ax}	1.1	1.2	0.7	2.0
Re_C	2×10^6	1×10^6	1.03×10^6	0.5×10^6
Ma_{inlet}	0.1	0.48		
Ma_{exit}	1.05	1.07	0.55	
α_{inlet}	0	34.4	-15	-14
α_{exit}	67.6	-57.2	-44	-44.7

the classical limit by Sovran and Klomp [14]. This paper describes the investigation of the basic design compared with an integrated concept.

2.3 Operating Conditions. At the design point of the applied HP-turbine, the stage pressure ratio is about 3.1 and the stage reaction based on the enthalpy is 0.46. The stage pressure ratio, the total temperature at stage inlet, and the speed, thus the corrected speed, were kept the same for both configurations: The blading has transonic conditions on the suction surface of the airfoils and at the exit of the blade rows. The turbine is choked for the whole operating area to be investigated. The mass averaged ITD inlet Mach number is adjusted to 0.6 and represents realistic duct inlet conditions of modern jet engines with a single stage HP-turbine. The mass averaged inlet swirl angle is about -15 deg (counterswirl) measured from the engine axis. The Reynolds number level based on the chord length is typically high and correlates with the HP-turbine inlet pressure level and will be in a similar range like for aero engines at take off condition.

2.4 Instrumentation and Measurement Locations. Figures 1(a) and 2(a) also show the measurement locations in the AIDA test rig. Full area traversing was performed in seven (base design) and four (IC) different planes: downstream the HP-turbine (plane C), within the duct (planes C1, C3, and C5), and upstream (plane D) and downstream (planes E and F) the LP-vane (strut). In planes C1 to F, the probes and the traverse gears were mounted on the inner liner of the ITD to protect the sensitive flow at the outer wall from disturbances by the probe fixation. Due to the uncommon flow direction relative to the measurement location in some planes, especially developed five-hole-probes (IST, RWTH Aachen) with an inclined probe head of 2.5 mm diameter were applied to extend the measurement range toward the probe shaft.

The probes are calibrated for Mach numbers between 0.1 and 0.8, yaw angles between -20 deg and $+20$ deg, and pitch angles between -16 deg and $+20$ deg. The negative values of the yaw angle indicate a counter-rotating flow and the negative values of the pitch angle indicate the flow direction toward the hub. The correlation between the calibration characteristic and the value to be measured is given by a multiparameter approximation.

Only small holes in the flow channel were necessary to traverse the probes inward and outward. The circumferential measurement position was changed by turning the stationary vane rows during operation of the facility. The measurement grid in each plane consists of 15 points in the radial direction and 21 (29) points in the circumferential direction. The grid covers two (one) LP-vane (strut) pitches and about 95% passage height. Traversing was done along the radial lines. In each measurement point, the probe was turned into the flow to reach the highest accuracy and to ensure to be always within the calibration range of the probe. Furthermore, the rig is equipped with static pressure taps around the circumference of the inner and outer casing parts at the indicated measurement positions (see Figs. 1(a) and 2(a)) to get the pressure distribution along the flow path. In planes C1–C5, the boundary layer rakes at the inner and outer surface of the ITD were used to record the total pressure profile near the walls.

2.5 Measurement Uncertainties. Instrumentation for the determination of duct flow characteristics has to meet not only high demands on accuracy and repeatability but requires higher numbers of channels, too. Therefore, the measurement system is made up by 11 multichannel pressure transducers PSI 9016 with a total amount of 176 channels and an accuracy of 0.05% full scale and four National Instruments Field Point FP-TC-120 eight-channel thermocouple input modules and one FP-RTD-122 resistance thermometer input module.

Table 2 shows the measurement uncertainties of the five-hole-probe measurements. These values contain the error due to the approximation and the systematic error of the PSI Modules.

The comparison of the yaw angle obtained by means of 5HP

Table 2 Measurement uncertainties of the 5HP

Ma	+0.006	−0.003	
α	+0.5	−0.08	deg
γ	+0.6	−0.3	deg
p_i	+3.3	−3.0	mbar
p	+5.3	−5.2	mbar

with the unsteady yaw angle measured by laser Doppler velocimeter (LDV) showed that the excursions of the flow were always within the calibration range of the probe.

The measurement uncertainties of the static pressure and the total pressure at stage inlet are ± 1 mbar. The variation in speed is below 10 rpm and the measurement uncertainty of the temperature measurement is about ± 0.5 K.

3 Results and Discussion

3.1 Five Hole Probe Measurements and Boundary Layer Rakes. The flow parameters $\Delta H/u^2=1.5$ and $c_{ax}/u=0.8$, the corrected speed of 529.5, and the pressure ratio of 3.1 over the stage have been kept the same for both the base design and the IC. The flow parameters differ a little bit from the design parameters.

3.1.1 Duct Inflow. Figures 3–10 present the measurement results obtained by means of five-hole-probes. Figure 3 shows the mass averaged Mach number distribution, Fig. 4 shows the total pressure distribution, and in Fig. 6 the mass averaged yaw angle distribution is depicted. Figure 5 shows the area averaged static

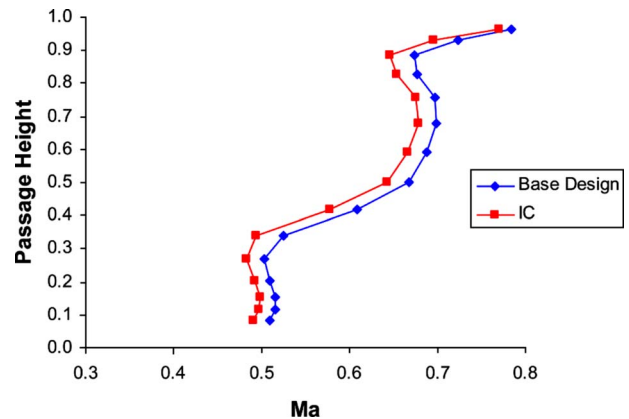


Fig. 3 Mass averaged Mach number distribution in plane C

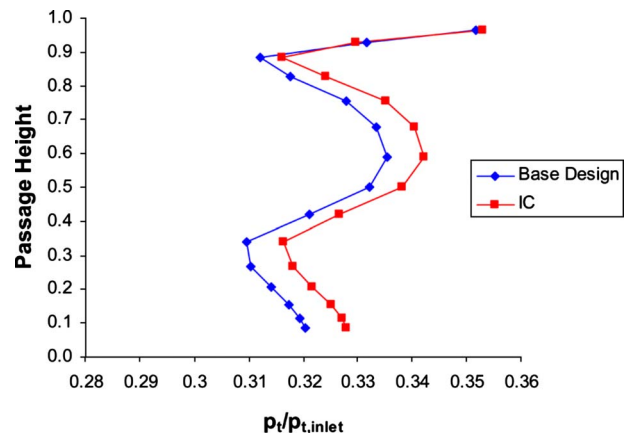


Fig. 4 Mass averaged total pressure distribution in plane C

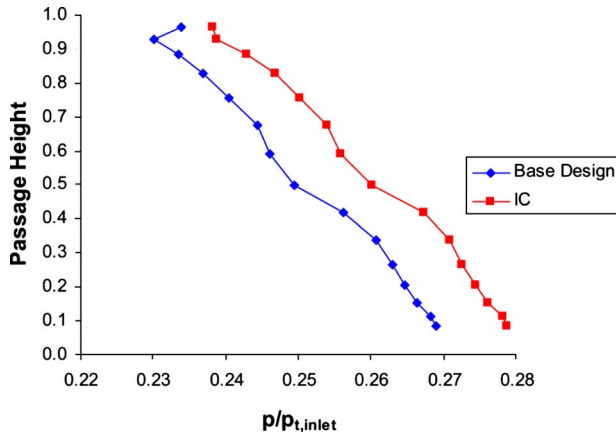


Fig. 5 Area averaged static pressure distribution in plane C

pressure distribution. Figures 7–10 are contour plots (two HP-vane pitches are plotted) where on the left side results of the base design and on the right side results of the IC are shown.

It can be seen that the strut does not affect the flow directly downstream the rotor (plane C). A marginal difference in the Mach number distribution can be observed. This can be seen in the Mach number contour plots (Figs. 7 and 9), as well. For both cases, a low Mach number region at the hub is visible. This is due

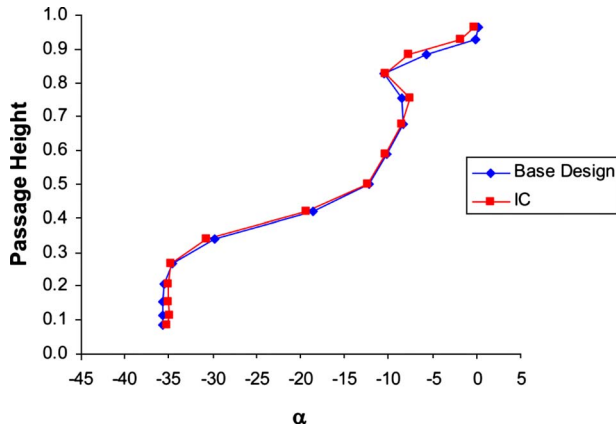


Fig. 6 Mass averaged yaw angle distribution in plane C

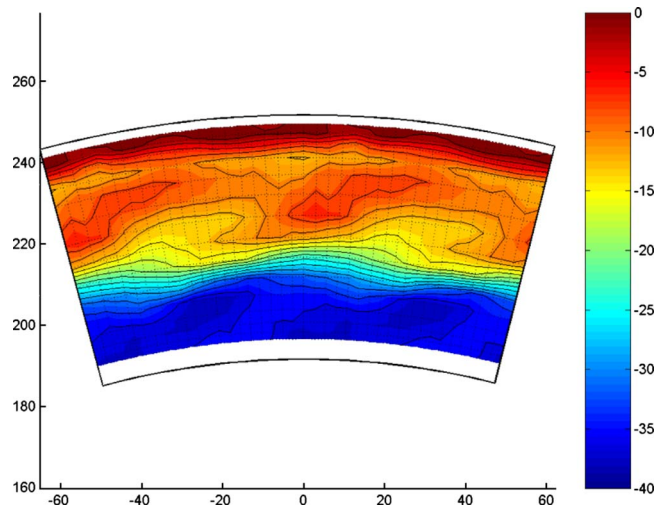


Fig. 8 Yaw angle distribution in plane C, base design

to the lower passage vortex, which extends up to approximately 40% passage height. The total pressure (see Fig. 4) is marginally larger for the IC. The above mentioned larger area increases the

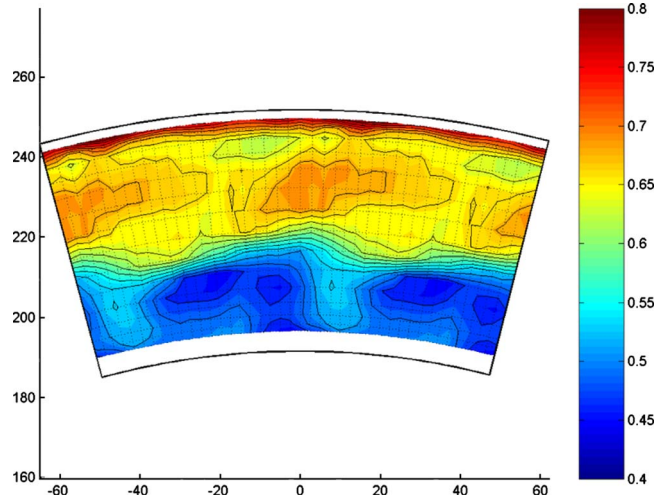


Fig. 9 Mach number distribution in plane C for the IC

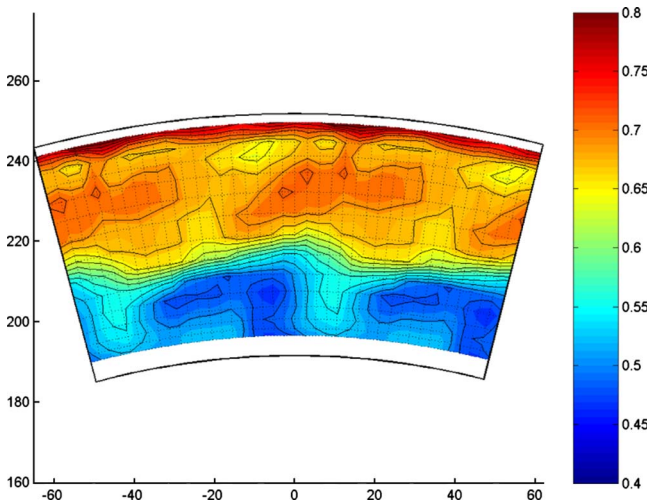


Fig. 7 Mach number distribution in plane C, base design

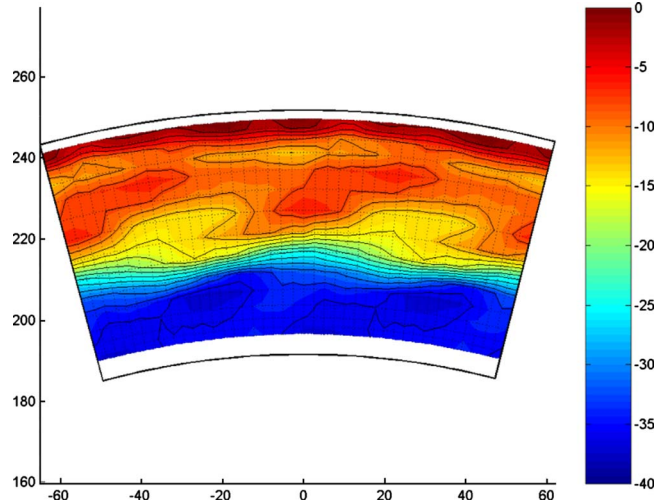


Fig. 10 Yaw angle distribution in plane C for the IC

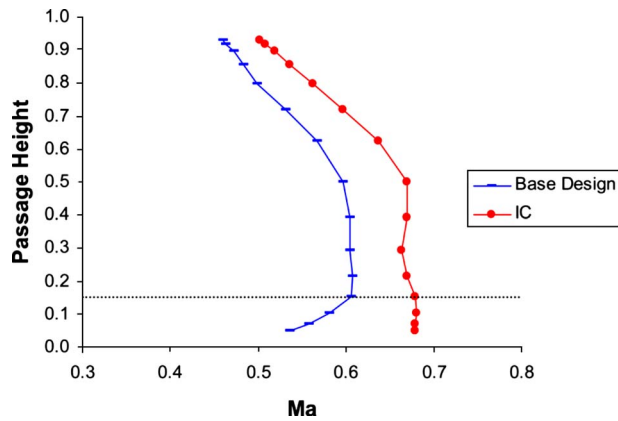


Fig. 11 Mass averaged Mach number distribution in plane E

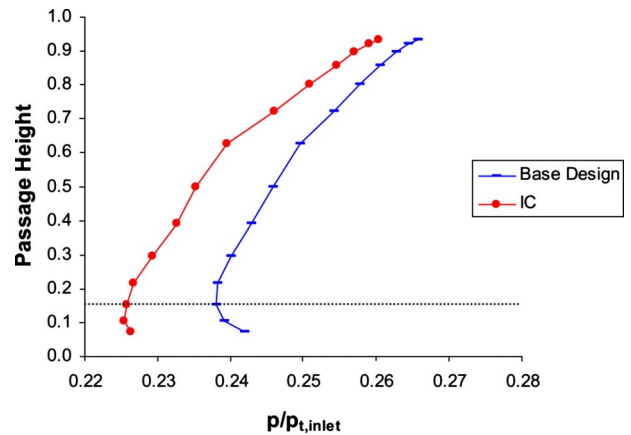


Fig. 13 Area averaged static pressure distribution in plane E

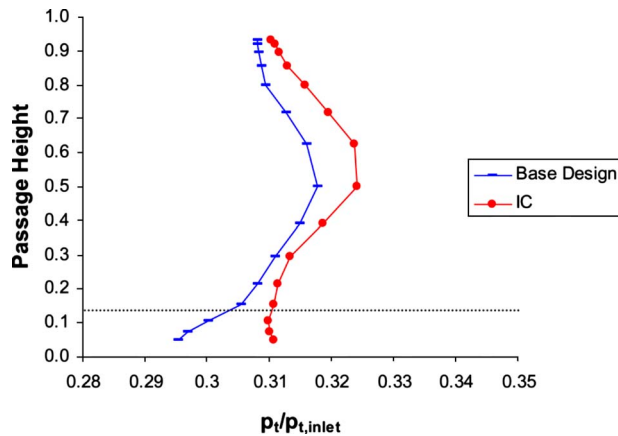


Fig. 12 Mass averaged total pressure distribution in plane E

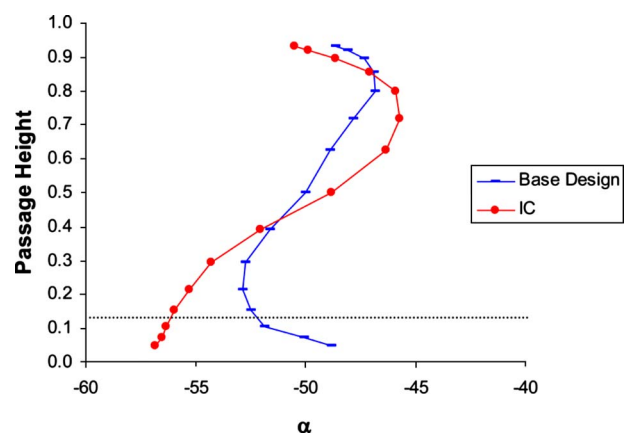


Fig. 14 Mass averaged yaw angle distribution in plane E

static pressure in plane C (see Fig. 5). The gradient is over the most part of the channel height the same except the approximately upper 15%. It seems that in this realm the different curvature of the modified outer duct wall is responsible for this difference. The yaw angle distribution is the same for both configurations (Figs. 6, 8, and 10). In the contour plots, the same structures are visible for both cases. This variation in circumferential direction is imposed by the HP-vane. At the tip region, the effect of the rotor tip clearance can be seen clearly.

Due to the fact that the strut has no influence on the flow in duct inlet, no LDV measurements have been performed for the IC. The time resolved data at duct inlet have been discussed in detail by Göttlich et al. [2].

3.1.2 Outflow of the LP-Vane and the Strut (Plane E), Respectively. In Figs. 11–14, the mass averaged results are depicted, except the static pressure distribution that has been area averaged. Figures 15–20 show the contour plots of the base design on the left and on the right side; the plots of the integrated concept are depicted. Each plot is viewed from downstream and shows a 20 deg section with the same relative stator-stator (strut) position. The periodicity of the base design is 15 deg and for the IC it is 60 deg.

The IC accelerates the flow to a higher Mach number level but the radial distribution is nearly the same except at the hub region. For the difference there, the untypical hub leakage vortex (HLV) (vortices can be identified in the yaw angle distribution as a concentration of horizontal contour lines) is responsible. This gap at the hub is necessary for circumferential traversing. Its influence is up to approximately 16% passage height. The dotted line in the figures represents this limit. If one takes a look at the contour

plots, e.g., of the Mach number (Figs. 16 and 19), one can see that for the base design three wakes (dashed line), two upper passage vortices (UPVs) and lower passage vortices (LPVs), and three HLVs have been observed in this 20 deg section, while for the IC only one wake, one UPV, one LPV, and one HLV is within the same section. This means that during the averaging of the results of the base design these features are taken into account more often. But the wakes of the base design are thinner than the wakes of the IC (compare Fig. 15 with Fig. 18). This wakes of the IC are not only thicker but even slower especially from about 20% to 80% passage height. These slow and thick wakes seem to be responsible for the higher Mach number. Due to their blockage effect, the mass has to go through a smaller effective area (geometrical areas are identical for both designs) between two neighboring wakes. It can be seen in Figs. 18 and 19 that the wake of the IC is slowest and thickest near the hub up to about 35% passage height.

The total pressure (see Fig. 12) is insignificantly higher for the IC but shows nearly the same behavior as the Mach number distribution. The static pressure gradient is the same for both configurations up to about 60% passage height. The level is lower due to the larger Mach number. The largest difference between these configurations can be seen in the yaw angle distribution. It can be seen that from the hub to about 40% passage height the IC turns the flow more or in other words the meridional component of the absolute velocity is smaller and the circumferential component is larger compared with the base design.

This indicates that less mass flows through this (geometrical) area. Furthermore, the large LPV leads to over- and underturning of the flow. From 40% passage height upward, the strut is less turning compared with the base design or again in other words the

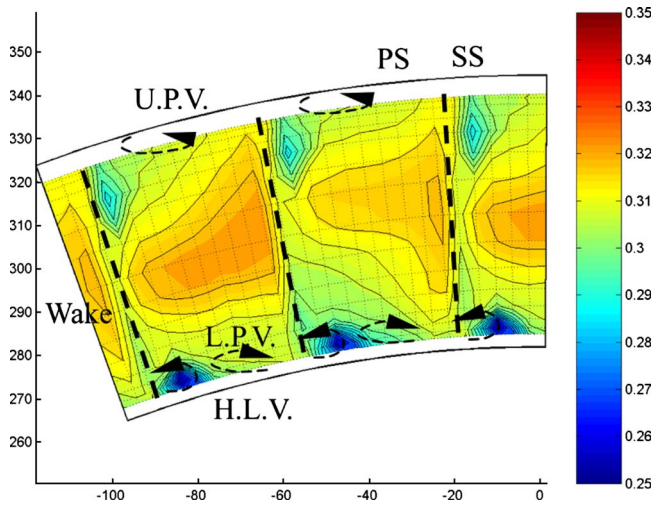


Fig. 15 Total pressure ratio distribution of the base design

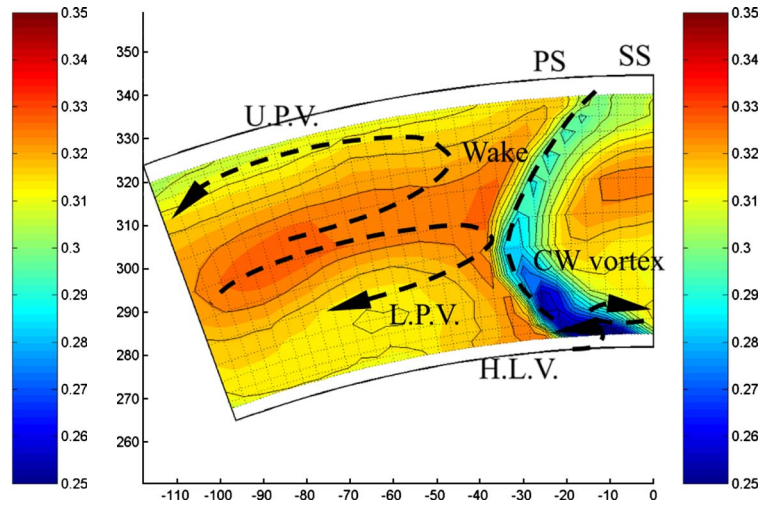


Fig. 18 Total pressure ratio distribution of the IC

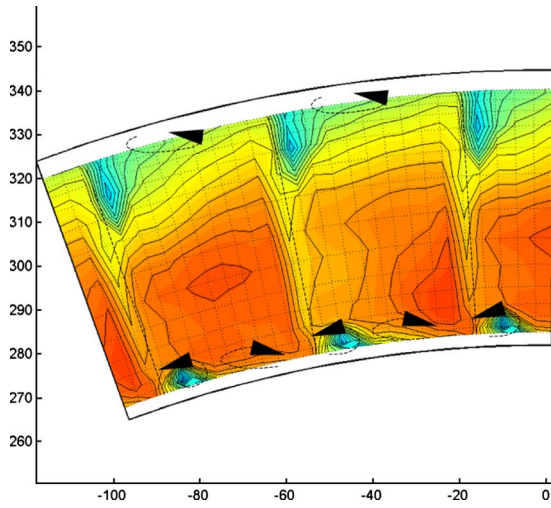


Fig. 16 Mach number distribution of the base design

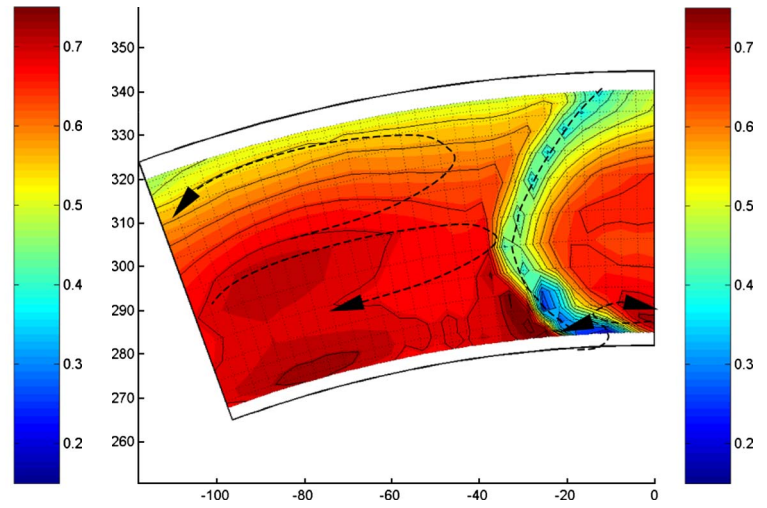


Fig. 19 Mach number distribution of the IC

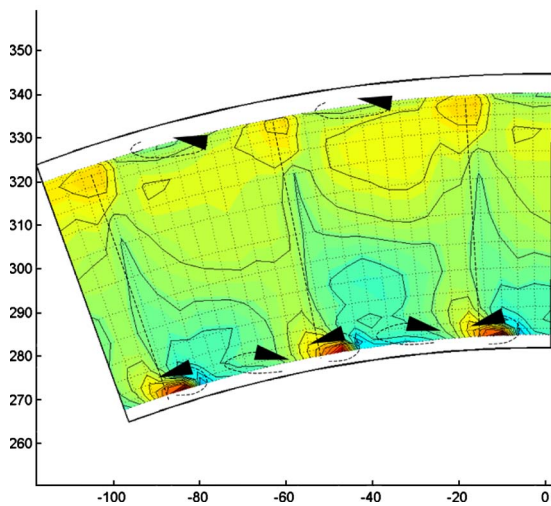


Fig. 17 Yaw angle distribution of the base design

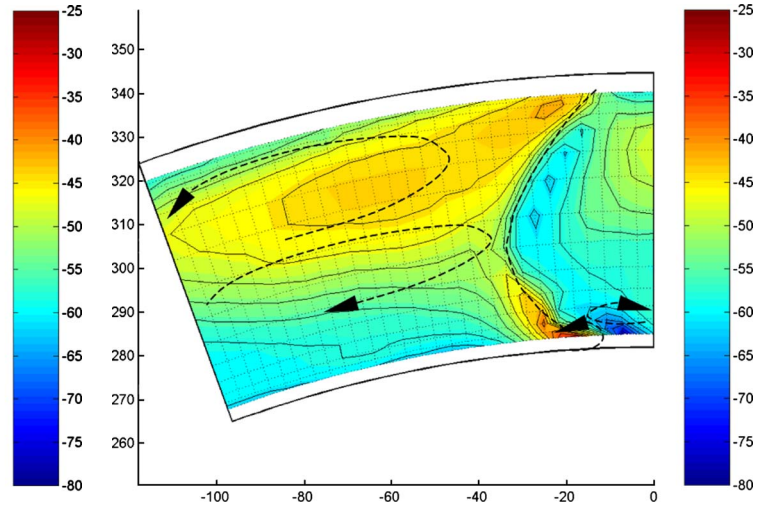


Fig. 20 Yaw angle distribution of the IC



Fig. 21 Oil coating before the surfaces are exposed to the flow

meridional component of the absolute velocity is higher (same circumferential component), which is in good agreement with the higher Mach number mentioned before. The over- and underturning of the flow due to the UPV can be observed. That means that the usually following rotor has to be designed for a larger angle variation over the passage height.

In the contour plots of the total pressure ratio (Figs. 15 and 18) and in the Mach number (Figs. 16 and 19) distribution, the influence of the HP-vanes can still be seen in both the base design and the IC. As written before within the wake, a region of low Mach number and total pressure close to the hub is visible for the IC.

This region extends up to about 35% passage height. It seems that the risk of separation is high at the suction side (SS) near the hub. This can also be seen in Fig. 24 where a region of low wall shear stress (C) has been detected. In the plots of the base design and the IC, a thickening of the wake close to the casing has been observed. The UPV and the LPV occupy nearly the whole flow channel of the IC. For the base design, the passage vortices are much smaller but there are more within the measurement plane. In the plots of the IC beside the HLV at the hub, another vortex can be observed, which rotates in the clockwise (CW) direction.

3.2 Oil Flow Visualization. A mixture of synthetic motor oil and titanium oxide is used to cover the inner and outer duct surfaces (bright). The red color is added to cover the pressure and suction surface of the struts. Figure 21 shows the surfaces of the outer duct wall and the struts before they are exposed to the flow. In this figure, the flow is from left to right. All pictures of the outer duct endwall are taken from the inner duct through removable inserts.

In Fig. 22, the flow on the outer duct wall is visualized and is nearly axial at the casing. The strong cross flow due to the pres-

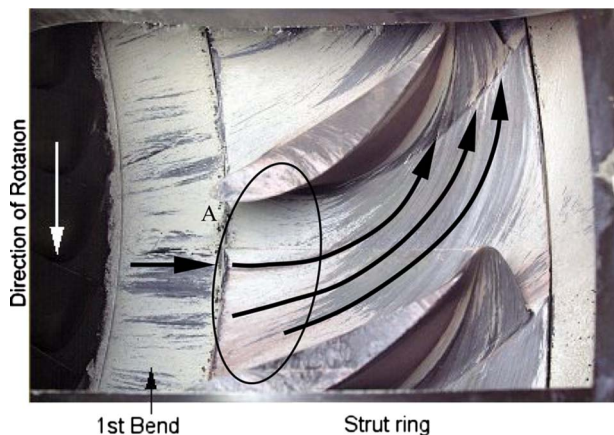


Fig. 22 Picture of the outer duct wall

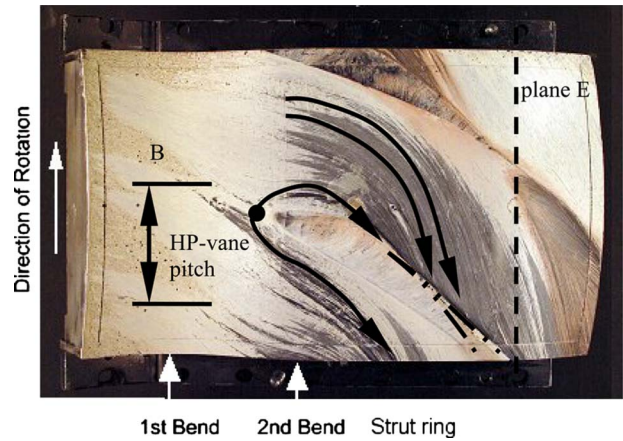


Fig. 23 Picture of the inner duct wall

sure gradient from the pressure to the suction side of the adjacent strut within the passage can be seen nicely. There is a region (A) of lower shear stress at an axial position close the leading edge. Figure 23 shows the inner duct wall. Regions (B) of low wall shear stress have been observed in the first part of the duct wall, which have a distance of one HP-vane pitch. This means that the flow is influenced by the HP-vane. The dashed line mark the 5HP measurement plane. The dot is approximately the separation point where the horseshoe vortices starts to form. Also a strong cross flow pattern can be seen. Between the two dash-dotted lines, the effect of the HLV is visible. The part of the duct between rotor exit and strut leading edge shows the same features as the base design. Figure 24 shows the oil flow visualization on the suction surface of the strut. The flow is from right to left. Due to the uncommon "hub clearance," which is necessary for circumferential traversing, the leakage flow from this hub gap can be seen on the suction surface (below the dash-dotted line). A region (C) of low wall shear stress is visible. The pressure side (PS) leg of the horseshoe vortex cannot be seen explicitly as in Refs. [5,6]. The radial inward flow due to the pressure gradient imposed by the meridional curvature of the duct (second bend at the casing) and the curvature of the trailing edge can be seen. The radial pressure gradient pushes the flow down from the outer duct wall along the suction surface of the strut to the inner duct wall. The white circle in the first third of the strut chord length indicates approximately the position where the flow starts to move downward. Between the two dotted lines, a flow with low shear stress is present. In the plot of the yaw angle (Fig. 20), it can be seen that the sense of rotation is opposite (clockwise) to the upper passage vortex.

The different color indicates that the flow is from the casing endwall (bright) and is mixed with the flow at the strut surface. It seems that the clockwise rotating vortex observed close to the HLV is the casing horseshoe vortex traveling below the UPV and pushed radially inward by the pressure gradient. The oil flow vi-

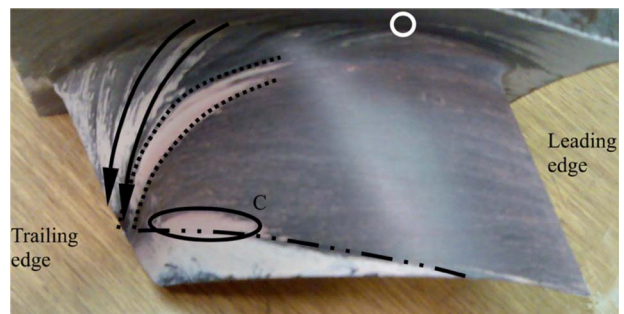


Fig. 24 Oil flow visualization on Suction Surface

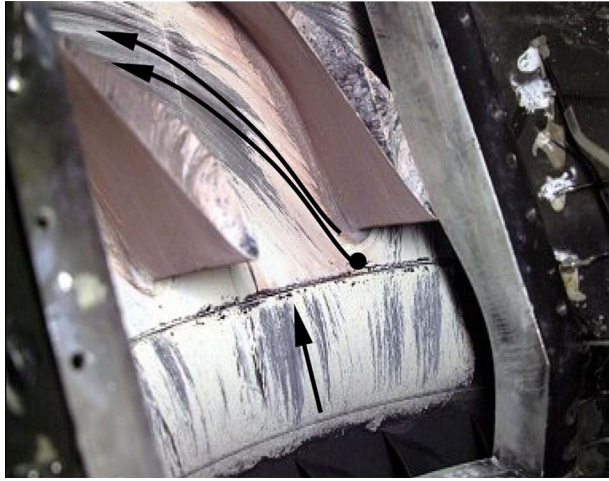


Fig. 25 Oil flow visualization on the pressure side

ualization on the pressure side can be seen in Fig. 25. The black dot marks approximately the position of the separation point at the outer duct endwall. The cross flow within the passage can be seen again.

3.3 Static Pressure Taps. Figure 26 shows the pressure distribution along the duct by means of the pressure rise coefficient, which is defined as

$$C_{pn} = (p_n - p_C) / (p_{t,C} - p_C) \quad (1)$$

where the subscript n relates to the local position and C refers to the measurement plane C near duct inlet at $x/l=0$.

At the inner wall, the static pressure distribution is exactly the same for both configurations. For the outer duct wall, the minimum in C_p was observed at $x/l=0.25$ for both configurations but it is higher for the IC.

This is due to the fact that the outer duct wall was changed to compensate the blockage of the struts and thus rises the minimum pressure as well as the blockage of the struts.

3.4 Estimation of Duct Loss and the Weight Reduction. The total pressure loss from plane C to plane E is roughly estimated by

$$\Delta p_t = \frac{p_{t,C} - p_{t,E}}{p_{t,C}} \times 100 \quad (2)$$

The total pressure loss base design is 4.4% and the total pressure loss IC is 4.3%.

Here the pressure loss of the IC is slightly smaller than for the base design. If one considers that in a real engine there would be no hub leakage, the authors estimate that the loss decreases. But

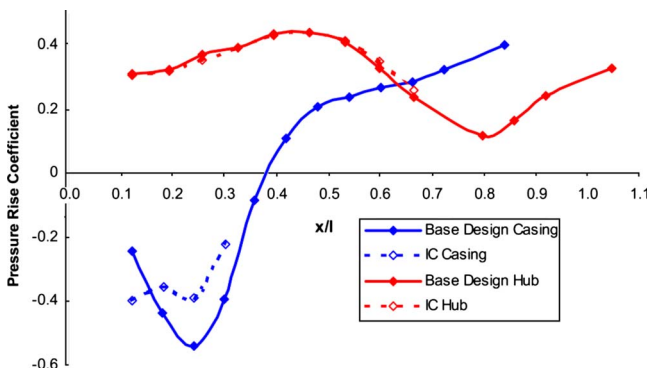


Fig. 26 Static pressure rise coefficient

here it is assumed that the losses stay in the same magnitude. It seems that it is possible to design a configuration with a strut that fulfills both functions of a strut and of a LP-vane without severe loss increase.

The following weight reduction only considers the weight of the blading. For the struts two limits can be given:

- (a) solid struts: 11.4 kg
- (b) hollow struts (approximately 2 mm wall thickness): 4.3 kg
- (c) solid LP-vanes: 2.8 kg
- (d) solid struts and LP-vanes: 14.2 kg (conventional design)
- (e) hollow struts and LP-vanes: 7.1 kg (conventional design)

That means that a weight reduction (based on the conventional design) due to the removed LP-vane row of 20% for the solid struts and 39% for the hollow struts is possible. A further reduction can be taken into account due to the shorter inner and outer casing parts and the reduced length of the shafts.

4 Conclusion

A novel concept to reduce duct length, a so called integrated concept, has been compared with a base design. The intention was to achieve similar outflow conditions. It was shown that a similar flow field can be realized with this IC as for the base design. A larger yaw angle variation over the passage height due to the large secondary flows must be taken into account. A significant weight reduction of the blading between 20% and 39% is possible.

Acknowledgment

This work was made possible by the European Union (EU) within the project AST3-CT-2003-502836, AIDA "Aggressive Intermediate Duct Aerodynamics" and the Austrian Ministry for Education, Science and Culture (BMBWK).

Nomenclature

Symbols

- α = $\tan^{-1}(c_t/c_n)$ yaw angle (deg)
- C = chord length (mm)
- c_{ax}, c_t, c_n, c_r = axial, tangential, normal, and radial velocities (m/s)
- d_{TE} = trailing edge thickness (mm)
- h = average blade height (mm)
- H = enthalpy (J/kg)
- l = axial duct length (mm)
- $l/h_{exit,blade}$ = nondimensional duct length
- T = temperature (K)
- p = pressure (bar)
- Δp_t = total pressure loss (%)
- u = circumferential velocity (m/s)
- $\Delta H/u^2$ = loading coefficient
- c_{ax}/u = flow coefficient
- Ma = Mach number
- x = axial distance (mm)

References

- [1] Marn, A., Göttlich, E., Pecnik, R., Malzacher, F. J., Schennach, O., and Pirker, H. P., 2007, "The Influence of Blade Tip Gap Variation on the Flow Through an Aggressive S-Shaped Intermediate Turbine Duct Downstream a Transonic Turbine Stage-Part I: Time Averaged Results," ASME Paper No. GT2007-27405.
- [2] Göttlich, E., Marn, A., Pecnik, R., Malzacher, F. J., Schennach, O., and Pirker, H. P., 2007, "The Influence of Blade Tip Gap Variation on the Flow Through an Aggressive S-Shaped Intermediate Turbine Duct Downstream a Transonic Turbine Stage-Part II: Time-Resolved Results and Surface Flow," ASME Paper No. GT2007-28069.
- [3] Norris G., Dominy R. G., and Smith A. D., 1998, "Strut Influences Within a Diffusing Annular S-Shaped Duct," ASME Paper No. 98-GT-425.
- [4] Norris G., Dominy R. G., and Smith A. D., 1999, "Flow Instability Within a Diffusing, Annular S-Shaped Duct," ASME Paper No. 99-GT-70.

- [5] Pullan, G., Denton, J., and Dunkley, M., 2003, "An Experimental and Computational Study of the Formation of a Streamwise Shed Vortex in a Turbine Stage," *ASME J. Turbomach.*, **125**, pp. 291–297.
- [6] Pullan, G., Denton, J., and Curtis, E., 2006, "Improving the Performance of a Turbine With Low Aspect Ratio Stators by Aft-Loading," *ASME J. Turbomach.*, **128**, pp. 492–499.
- [7] Davis, R. L., Yao J., Clark J. P., Stetson, G., Alonso, J. J., Jameson, A., Haldeman, C. W., and Dunn, M. G., 2002, "Unsteady Interaction Between a Transonic Turbine Stage and Downstream Components," ASME Paper No. GT2002-30364.
- [8] Miller, R. J., Moss, R. W., Ainsworth, R. W., and Harvey, N. W., 2003, "The Development of Turbine Exit Flow in a Swan-Necked Inter-Stage Diffuser," ASME Paper No. GT2003-38174.
- [9] Miller, R. J., Moss, R. W., Ainsworth, R. W., and Harvey, N. W., 2004, "The Effect of an Upstream Turbine on a Low-Aspect Ratio Vane," ASME Paper No. GT2004-54017.
- [10] Göttlich, E., Marn, A., and Malzacher, F. J., Schennach, O., and Heitmeir, F., 2007, "Experimental Investigation of the Flow Through an Aggressive Intermediate Turbine Duct Downstream of a Transonic Turbine Stage," *Proceedings of the Seventh ETC*, Athens, p. 383.
- [11] Göttlich, E., Malzacher, F., Heitmeir, F., Marn, A., 2005, "Adaptation of a Transonic Test Turbine Facility for Experimental Investigation of Aggressive Intermediate Turbine Duct Flows," AIAA Paper No. ISABE-2005-1132.
- [12] Erhard, J., and Gehrler, A., 2000, "Design and Construction of a Transonic Test Turbine Facility," ASME Paper No. 2000-GT-480.
- [13] Neumayer, F., Kulhanek, G., Pirker, H.P., Jericha H., Seyr, A., and Sanz, W., (2001), "Operational Behaviour of a Complex Transonic Test Turbine Facility," ASME Paper No. 2001-GT-489.
- [14] Sovran, G., and Klomp, E. D., 1967, "Experimentally Determined Optimum Geometries for Rectilinear Diffusers with Rectangular Conical or Annular Cross Section," *Fluid Mechanics of Internal Flow*, G. Sovran, ed., Elsevier, New York.

Aerothermal Performance of Streamwise and Compound Angled Pulsating Film Cooling Jets

Vipluv Aga

e-mail: vaga@ethz.ch

Michel Mansour

Reza S. Abhari

Department of Mechanical and Process
Engineering,
Institute for Energy Technologies,
ETH Zurich,
CH-8092 Zurich, Switzerland

The quantification of aerothermal loss is carried out for streamwise and compound angled film cooling jets with and without large scale pulsation. This paper reports on the simultaneous measurements of the unsteady pressure and temperature field of streamwise and a 60 deg compound angled film cooling jet, both with a 30 deg surface angle over a flat plate with no pressure gradients. Turbine representative nondimensionals in terms of the geometry and operating conditions are studied. The main flow is heated more than the injected flow to have a temperature difference and hence a density ratio of 1.3, while the blowing ratio is maintained at 2. The entropy change, derived from pressure and temperature measurements, is calculated by using modified reference conditions to better reflect the losses in both the jet and the freestream. The effects of the periodic unsteadiness associated with rotating machinery are simulated by pulsating the jets. These effects are documented through time-resolved entropy change contours. Mass-averaged entropy and kinetic energy loss coefficients seem to be apt quantities for comparing the aerothermal performance of streamwise and compound angled injections. It is observed that the mass-averaged entropy loss of a streamwise jet doubles when it is pulsed, whereas that of a compound angled jet increases by around 50%. It may be conjectured from the measurements shown in this study that streamwise oriented jets suffer most of their entropy losses at the hole exit due to separation, whereas in compound angled jets, downstream thermal mixing between the jet and the freestream is the dominant mechanism. [DOI: 10.1115/1.3072489]

1 Introduction

Film cooling of gas turbine stator and rotor airfoil surfaces has played a major role in preserving the structural integrity of these hot-section components at operating temperatures in excess of the melting temperatures of the constituent alloys. Additionally, a judicious choice of film cooling strategies can be instrumental in substantially improving engine efficiency, thus making a strong case for a cogent understanding of its flow and thermal structure. Film cooling basically comprises the use of relatively cool air extracted from the latter stages of a high pressure compressor and ejected over the airfoil to be cooled into the hot flow path through small holes in the airfoil surface. The geometry and orientation of the holes have a direct influence on the film uniformity, adiabatic effectiveness, and heat transfer coefficient of the surface. Additionally, the injected air flow would also cause significant changes in the expected aerothermal field, which would be of particular concern in some regions like turbine end walls.

Previous film cooling studies have primarily concentrated on surface heat transfer and adiabatic effectiveness measurements using various methods such as thin-film gauges and thermocouples (see, e.g., Refs. [1,2]), liquid crystals (see, e.g., Ref. [3]), and infrared cameras (see, e.g., Ref. [4]). Such studies have primarily concerned themselves with surface heat transfer information rather than the flow structure per se. These studies also took into account the effects of geometry and orientation on the surface results apart from the various flow conditions. Film cooling research of late has also started making inroads into deciphering the

complex flow structure and thermal field. Studies such as Refs. [2,5] reported steady temperature distributions within the emanating cooling jet and also provided surface measurements for the adiabatic effectiveness. It was noted that the need to understand the flow structure, which ultimately governs the surface results, is of paramount importance for future designs.

The velocity field of a streamwise film cooling jet has been studied for a range of BR and DR in Ref. [6]. In order to better understand the underlying flow physics that affect surface cooling, the velocity and thermal fields have been measured in Refs. [7,8]. Similar detailed computational measurements for compound angled jets have been carried out in detail in Refs. [9–11], whereas Ref. [12] shows particle image velocimetry (PIV) measurements of velocity and vorticity for a compound angled geometry. Hot wire measurements within a film cooling jet in Ref. [13] have shown the underlying anisotropy as well as the turbulent characteristics of film cooling flows. Studies on freestream turbulence effects on adiabatic effectiveness (see, e.g., Refs. [14,15]) have shown that the freestream turbulence is instrumental in altering the mixing and spreading of the jet, thereby significantly changing the film cooling effectiveness.

The flow physics of a film cooling jet in real turbine conditions is significantly affected by the unsteady effects due to the moving blades [1]. Many studies have incorporated jet pulsations and duty cycle variations, notably Ref. [16], wherein it was found that pulsations tend to increase effectiveness for some amplitudes, whereas the frequency did not have much effect. Recent studies [17,18] have shown the marked effect of the frequency of jet pulsation on both heat transfer and effectiveness. Unsteady PIV measurements of pulsating jets in Ref. [6] have also shown that frequency and BR are important parameters, which determine whether a pulsed jet may be considered quasisteady and equivalent, by virtue of its velocity field, to a steady jet of equivalent BR .

Contributed by the International Gas Turbine Institute of ASME for publication in the JOURNAL OF INTERNATIONAL GAS TURBINE INSTITUTE. Manuscript received August 22, 2008; final manuscript received August 31, 2008; published online July 6, 2009. Review conducted by David Wisler. Paper presented at the ASME Turbo Expo 2008: Land, Sea and Air (GT2008), Berlin, Germany, June 9–13, 2008.

It has also been established by in-depth computational studies in Ref. [19] that near-hole pressure fluctuations have significant effects on the adiabatic effectiveness of a streamwise hole. However, most of these studies are primarily for streamwise injection, and the flow physics of compound angled injection with pulsation is still the subject of intense research.

Although film cooling studies have almost always concentrated on the primary heat transfer issues, engine designers are also concerned with the aerothermodynamic losses that might be produced when film cooling injection causes mixing losses. This is of particular significance when the aerodynamics are significantly altered in contoured end walls of a turbine due to film cooling. Specifically, studies such as those in Ref. [20] have concluded that since the losses generated by film cooling ejection at end walls could be significant, the nature of the 3D flow field should be accounted for when designing end wall film cooling. The aerodynamic mixing effect due to film cooling ejection was also studied in Ref. [21], in which a mass-weighted definition for the reference pressure was used to compute the film cooling pressure loss to take into account loss from both the freestream and the injected coolant. Other studies such as Refs. [3,22] have also concentrated on the aerothermal performance of film cooling holes. These studies have recognized the need to use the kinetic energy loss coefficient, which is superior to a pressure loss coefficient or an entropy production based only on freestream conditions, as it also takes into account the losses within the film cooling holes. However, it should be noted that most of these studies were performed at conditions when coolant and freestream temperatures were equal due to the absence of simultaneous temperature and pressure measurements. Thus, the effect of thermal gradients or unsteadiness on kinetic energy loss or entropy has not been properly characterized in previous studies even though almost every film cooling hole is used in an environment where there is periodic unsteadiness due to blade passage in actual machinery.

The current study is carried out using a novel measurement technique. An in-house developed probe, the fast response entropy (FENT) probe, simultaneously measures pressure and temperature at high acquisition rates up to 40 kHz. It is built on the framework of the well established fast response aerodynamic probe (FRAP) technology developed at the ETH Zurich [23] by combining FRAP with thin-film gauge technology. Hence, it is versatile, reliable, and robust.

The results outlined in this paper capture in detail the time-resolved and averaged temperature, pressure, entropy change, and kinetic energy loss coefficient for a single operating condition, viz., $BR=2$ and $DR=1.3$ for a streamwise and 60 deg lateral angled hole over a flat plate. The effect of jet pulsation (which mimics the periodic unsteadiness in a turbine) on these derived quantities is discussed, specifically in terms of the dominant loss mechanisms for the two geometries and the time-resolved evolution of loss. The detailed flow structure in the near-hole region with respect to the thermal field would be of special interest to computational researchers. This is especially true when the comparison is to be made between a steady run and one with pulsation. Such a comparison would involve using the appropriate reference conditions and loss evaluation quantities, which are discussed in this paper. The results that compare streamwise and compound angled jets would also be of interest to designers to quantify the impact of film cooling on the aerothermodynamics in the near-hole region.

2 Experimental Methodology

2.1 Experimental Setup. The film cooling test rig, described in detail in Refs. [6,12], is powered by a centrifugal compressor, which, through insulated piping, leads to a heat exchanger wherein the freestream flow can be heated to about 120°C. This heat exchanger is fed by 7 bar saturated steam from the house heating system. A water-cooled heat exchanger extracts heat from the freestream downstream from the test section. Various pressure

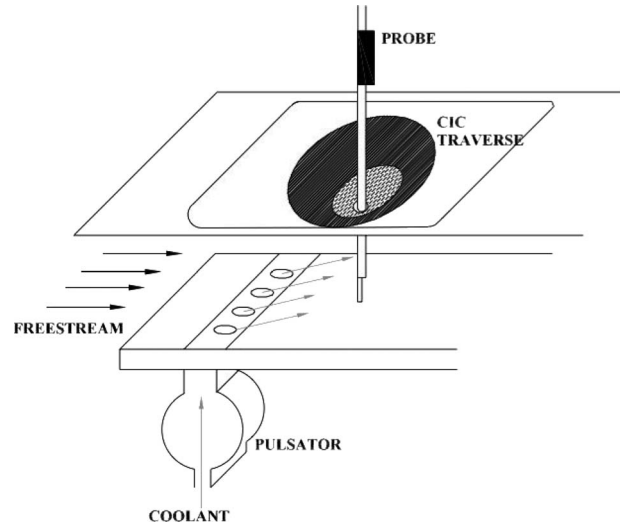


Fig. 1 Schematic of the test section for measurement with the FENT probe

and temperature probes at different points within the loop allow a real-time monitoring and measurement of the conditions within the rig. The boundary layer thickness of the main flow is controlled by a suction arrangement. A centrifugal blower drives the boundary layer suction, extracting through 327 discrete holes of 1.2 mm diameter stacked over an area of $60 \times 180 \text{ mm}^2$. The extracted air is fed back into the loop far downstream of the cooler. The secondary or the cooling flow is delivered by a shop air system with a maximum of 75 g/s mass flow rate. First a drier lowers the dew point of the air to -70°C . Solid water-absorbing particles then alternatively dry the air and recuperate within the drier. The dried air can then be cooled to about -60°C by a single cycle cooler for ejecting into the test section through MACOR inserts, which can be changed to measure different hole geometries. As Fig. 1 shows, the coolant air enters through a pulsator, which delivers steady air when switched off, but can be made to pulsate the injection at frequencies up to 500 Hz.

The test section consists of a rectangular flow path of $40 \times 181 \text{ mm}^2$ cross section. The area of main interest is near the injection site of the secondary flow. A novel traversing and probe access technique is used, henceforth referred to as the circle-in-circle (CIC) system. This traversing system is made of two circular metal plates fitted onto a flat plate. This is shown in Fig. 2. The two nonconcentric circular disks can each rotate about their own axes and thereby allow the small probe entry hole a positioning at

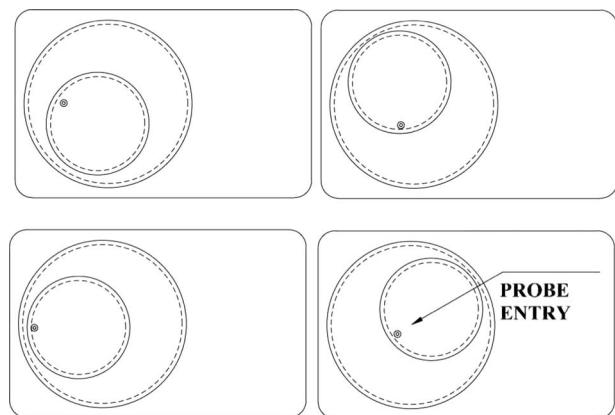


Fig. 2 CIC plane traversing system for probe access shown in different configurations allowing for flexible spatial access

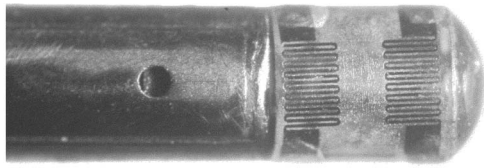


Fig. 3 Photograph of the tip of the fast entropy probe (FENT). The diameter of the head is 1.8 mm.

any point in the plane. The probe itself can be traversed perpendicular to the plane of the traversing system, as shown in Fig. 1, thereby allowing an access to any measurement point within the 3D domain. The sealing between the moving circles is effected by tight clamps. The main advantage of such a probe access system is the ease of manufacture, absolute flexibility in spatial access, and ability to move the probe without any other force except that from the four axis traversing system moving the probe assembly itself. This kind of system does not cause any intrusion at the wall, being flush with it, and allows a rapid experimental campaign.

2.2 Measurement Procedure. First the flow parameters are adjusted with the aid of the real-time monitoring system. Forty primary data channels (pressure, temperature, frequency, and mass flow) are acquired directly from their corresponding sensors. These are written to file together with ten derived flow parameters. The most relevant parameters such as main flow Mach number, blowing ratio, and density ratio are shown online, thus allowing their fast and accurate adjustment. The test rig is described in more detail in Ref. [6]. The main measurement device is the FENT probe, exhaustive details of which are presented in Ref. [24]. It primarily consists of an unsteady total temperature miniature probe mated with an established aerodynamic pressure probe technology known as FRAP [23]. The FRAP employs a miniature silicon piezoresistive chip, which is glued beneath a pressure tap on the probe tip. Polynomial calibration charts for pressure and temperature are made before every measurement. The pressure probe is attached to the unsteady total temperature probe, which consists of a pair of thin-film gauges that are deposited onto a substrate, and used as resistance thermometers, which are heated to different temperatures. This allows measurement of unsteady temperature along with total velocity derived from the pressure information. The FENT probe has a cutoff frequency of 35 kHz and an upper temperature limitation of 130°C. The temperature limitation comes from the semiconductor characteristics of the pressure sensor, which experience an exponential increase in the electromagnetic noise on the pressure signal above that temperature. Details are available in Ref. [23]. A close-up photograph of this probe is shown in Fig. 3. The flow field was measured at six planes normal to the primary freestream velocity at $X/D=0, 1, 2, 3, 4,$ and 6 . The hole center was used as the origin of the coordinate system described in Fig. 4. Each normal plane consisted of 19 wall lateral and 15 wall normal points. The closest to wall Z/D

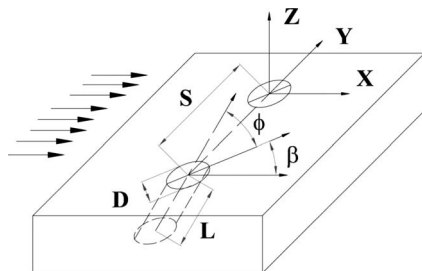


Fig. 4 Definition of the coordinate system and geometrical parameters

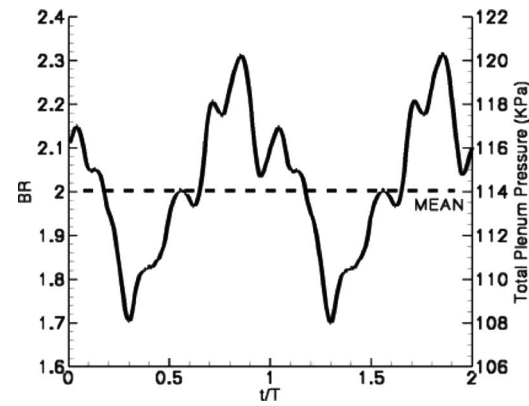


Fig. 5 Blowing ratio and pressure variation measured in the plenum with respect to time for $BR=2, DR=1.3,$ and pulsation of 400 Hz, $f_r=0.025$

measured was around 0.5 in the case of the streamwise unpulsated case as the developed probe could not penetrate owing to its size. In the other cases, as the temperature sensors were located lower than the pressure sensors, measurements closer to the wall were possible. However, the measurement of quantities derived from both pressure and temperature was limited to $Z/D=0.5$. It must be noted, however, that all derived quantities used pressure and temperature measurements from coincident points. This was done by traversing the probe with the same wall normal distance as the distance between the temperature and pressure sensor to obtain signals at coincident points. Pressure and temperature signals were acquired simultaneously at a sampling rate of 100 kHz over 2 s. The data sets are processed to obtain time-resolved total and static temperature, total and static pressure, Mach number, flow angles, and velocity by phase-lock averaging over 250 samples.

2.3 Flow Conditions. Figure 4 shows the coordinate system and symbols used henceforth. The inserts consisted of five holes of hole diameter $D=7$ mm. This hole size was sufficient for the probe diameter of 1.8 mm. The origin of the coordinate system is located at the geometric center of the injection hole in the center of the row. The hole pitch was $S=4D$, and the metering length was $L=4D$. Two geometries were tested, both having a surface angle of $\phi=30$ deg and lateral angles of $\beta=0$ deg and $\beta=60$ deg. All spatial dimensions are nondimensionalized by the hole diameter, D . The pulsation frequencies were 0 Hz and 400 Hz corresponding to a hole diameter based reduced frequency, $f_r=fD/U_{h,\infty}=0.025$, which lies in the engine range of 0.01–0.1 according to Refs. [19,17,18]. The total pressure variation in the plenum and the corresponding local BR variation are shown in Fig. 5 for the pulsations introduced. The duty cycle of the pulsations is a little above 0.5, as visible in the figure. All time axes are nondimensionalized by the time period of a single pulsation for 400 Hz.

The Mach number of the freestream, M , was held constant at 0.3, and the main flow parameters were also held constant, $BR=2, DR=1.3,$ and $IR=3.07$. This resulted in typical freestream velocities of $U_h=120$ m/s and a hole based Reynolds number, $Re_D=U_{h,\infty}D/\nu\sim 46,000$. The density ratios were obtained by maintaining the coolant at room temperature (298 K) and by heating the freestream to about 393 K. These ranges could not be extended due to the limitations on the temperature measurement of the piezoresistive chip on the probe [23].

2.4 Error Estimates. The errors in the loop pressures and temperatures, which were used to maintain the operating conditions, were always in the range of 0.1–0.3% relative to the quantities being measured. The details of the error calculations are given in Ref. [6] since the same rig was used. The relative error in the pressure measurement from the FENT probe was 0.1%, while

Table 1 Error estimates of derived quantities

Parameter	Relative uncertainty (%)
M	0.52
DR	0.26
BR	2.6
IR	5.00
f_r	0.54
Entropy change, Δs	2.5

the unsteady total temperature measurement error was 2.5% relative. These discussions are detailed in Ref. [24]. The uncertainties in the derived quantities thereof are provided in Table 1.

3 Results and Discussions

The simultaneous pressure and temperature measurements are resolved to obtain quantities such as entropy generation and a kinetic energy loss coefficient. Estimates of loss in turbomachinery applications are best described by the change in entropy [25]. The difficulty, however, arises in denoting a proper reference temperature and pressure to calculate this change for a jet in a cross-flow situation. Ascribing the reference conditions to the freestream conditions neglects the losses arising from the cooling hole. In this particular study, using the mixed-out conditions as a reference is also not possible since the domain of data acquisition did not extend far enough to record the mixed-out temperatures and pressures. A logical way to take into account this two temperature, two pressure problem is to use a reference condition that is a mass-weighted average of the two initial conditions of the hot freestream and the coolant in the plenum. Such a definition was successfully applied in Ref. [21] to reference the pressure losses from film cooling holes in a turbine. For the purposes of creating a reference baseline, from which to compute the reference temperatures and conditions downstream of the flow, P_{ref} and T_{ref} are defined by Eqs. (1) and (2), respectively. The conceptual basis for these definitions is to assume that the fluid that is measured downstream has arrived from just a single initial condition given by $P_{t,ref}$ and $T_{t,ref}$ and that the difference between the two is due to the various lossy mechanisms such as mixing, heat transfer, and viscous dissipation between the streams and separation within the hole,

$$P_{t,ref} = \frac{\dot{m}_c}{\dot{m}_c + \dot{m}_h} P_{t,c} + \frac{\dot{m}_h}{\dot{m}_c + \dot{m}_h} P_{t,h} \quad (1)$$

$$T_{t,ref} = \frac{\dot{m}_c}{\dot{m}_c + \dot{m}_h} T_{t,c} + \frac{\dot{m}_h}{\dot{m}_c + \dot{m}_h} T_{t,h} \quad (2)$$

The reference condition in Eq. (1) can now be used to define a total pressure loss coefficient, $C_{P,t}$, similar to that in Ref. [21], defined by Eq. (3), where U_∞ is the incoming freestream velocity,

$$C_{P,t} = \frac{P_{t,ref} - P_t}{\frac{1}{2}\rho U_\infty^2} \quad (3)$$

Since the traditional total pressure loss coefficient does not take into account the thermodynamics of the flow, the entropy change is a better indicator of mixing and separation losses [25]. The entropy change Δs at a point (P_t, T_t) is given by

$$s_{ref} - s = \Delta s = -C_p \ln\left(\frac{T_t}{T_{t,ref}}\right) + \mathcal{R} \ln\left(\frac{P_t}{P_{t,ref}}\right) \quad (4)$$

In order to obtain a positive number and for ease of comparison, this entropy change is nondimensionalized and plotted in subsequent figures as an entropy function, $e^{-\Delta s/\mathcal{R}}$. Thus, an area where this quantity, $e^{-\Delta s/\mathcal{R}}$, is low signifies an area of greater loss as the entropy change from the reference condition is higher. It

must be noted that such a definition of entropy change depends on the viability of assuming the mass-weighted averages of the reference conditions in the first place. As defined by Denton in Ref. [25], an entropy loss coefficient is also defined at every measurement point using the local temperature and total velocity by Eq. (5), where V is the local total velocity. This value is primarily used for comparing mass-weighted averaged values for different conditions in subsequent sections,

$$\zeta = \frac{T\Delta s}{0.5V^2} \quad (5)$$

Aerothermal performance of film cooling jets is most characteristically described by a film cooling loss coefficient. This is the ratio of the kinetic energy at a point downstream of injection, after some mixing has occurred, to the sum of the kinetic energy that the freestream and coolant flow would have had were they to isentropically arrive at the point in question. This definition is explained in detail in Refs. [3,21,26,27]. The loss coefficient, ξ , is defined in Eq. (6). The advantage of using this definition is that the losses in both the freestream and the coolant holes are considered. Additionally, an ideal reference condition, as described in Eqs. (1) and (2), need not be estimated,

$$\xi = 1 - \frac{\left(1 + \frac{\dot{m}_c}{\dot{m}_h}\right) T_t \left(1 - \frac{P_s}{P_t}\right)^{(\gamma-1)/\gamma}}{T_{t,h} \left(1 - \frac{P_s}{P_{t,h}}\right)^{(\gamma-1)/\gamma} + \frac{\dot{m}_c}{\dot{m}_h} T_{t,c} \left(1 - \frac{P_s}{P_{t,c}}\right)^{(\gamma-1)/\gamma}} \quad (6)$$

Unlike the calculation of ξ in other works such as Refs. [21,26], there exists an engine representative temperature gradient. Previous measurements of the quantity, ξ , have primarily been estimated with pressure probes in $DR=1$ conditions; however, as will be shown later, the temperature gradients have a significant effect on the thermal mixing loss generation.

3.1 Total Pressure Loss Coefficient, $C_{P,t}$. The total pressure loss coefficient, $C_{P,t}$, as defined in Eq. (3), is plotted at $X/D=6$ for streamwise and compound angled injections in the presence and absence of 400 Hz or $f_r=0.025$ pulsation in Fig. 6. The wake shows up as a region of high total pressure loss. It should be noted that since the blowing ratio is 2, the total pressure of injection is higher than that of the freestream, and unless the reference pressure, P_{ref} , is mass weight averaged, as shown in Eq. (1), there would have been regions in this plot having negative values. The total pressure loss for a compound angled injection in Fig. 6 shows the larger spread of the injected coolant in Fig. 6(d). It can be argued that the $C_{P,t}$ plot only shows the regions of pure aerodynamic loss even though other losses are taking place. The compound angled jets (Figs. 6(c) and 6(d)), both show a greater spread of loss on the windward side of the jet due to the blockage effect, which leads to some total pressure drop in the freestream.

3.2 Entropy Generation and Temperature Profiles

3.2.1 Streamwise Injection. The local temperature within a film cooling jet, T , is nondimensionalized using $\theta = (T - T_h)/(T_c - T_h)$. The entropy change is with respect to the reference conditions as described in Eqs. (1) and (2). Figures 7(a) and 7(b) show the time-averaged contours for θ for a streamwise injection at $\beta = 0$ deg. It is clear that due to time averaging, Figs. 7(a) and 7(b) are almost identical, except for the part of the flow in (a) below $Z/D=0.5$, which could not be measured due to probe access difficulties for that one case. However, at high pulsation frequency it has been shown in Ref. [6] that a pulsating flow is quasisteady to the point that it has almost the same flow structure of a nonpulsating flow when viewed in time-averaged conditions. This is not strictly true for the plots of the entropy function, $e^{-\Delta s/\mathcal{R}}$, which shows higher losses for the pulsed case especially in the wake region. The time-averaged plots thus give only a partial insight into the actual comparison because, as visible in Fig. 5, the BR

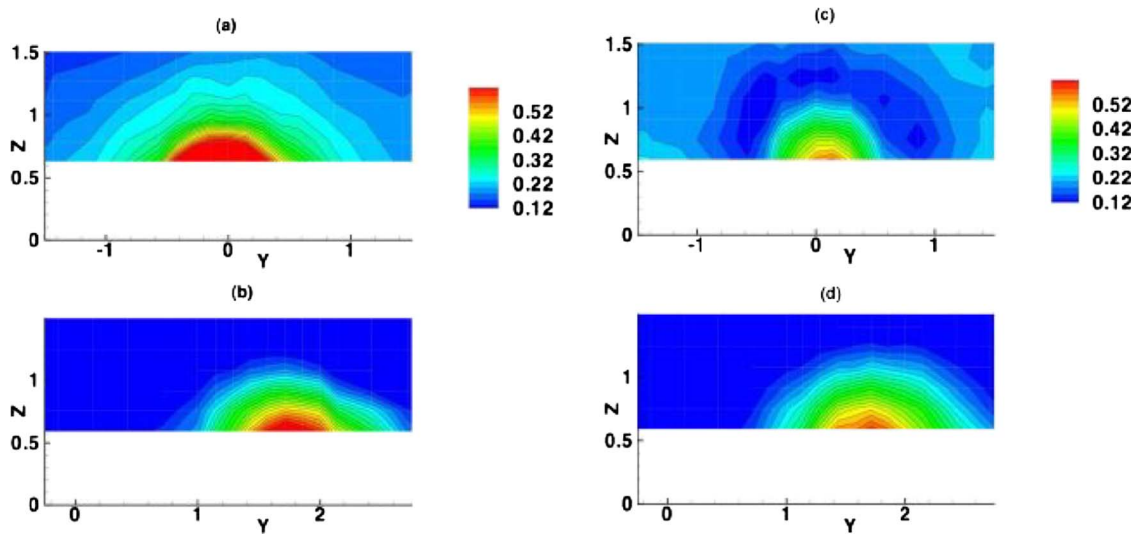


Fig. 6 Time-averaged total pressure loss coefficient, $C_{P,h}$ at $X/D=6$ for (a) $\beta=0$ deg, $f_r=0$; (b) $\beta=60$ deg, $f_r=0$; (c) $\beta=0$ deg, $f_r=0.025$; and (d) $\beta=60$ deg, $f_r=0.025$

variation over a pulsation period is almost 0.6, which would lead to quite a bit of smearing of the temperature and pressure distribution in the wake.

Since the entropy contours are closely correlated with the temperature contours, as shown in Fig. 7, only the contours of the entropy function will be considered henceforth. In Fig. 5, the trough of the pulsation is at $t/T=0.3$, but in Fig. 8, the jet appears smallest at $t/T=0.64$. Hence the crest of the jet appears at $t/T=0.08$ and the trough appears at $t/T=0.64$. Only these two phases are shown at different downstream points as the variation is quite small at other phases. The temperature distribution downstream of the hole does not disappear completely as the injection is not completely switched off due to the high frequency. It simply becomes smaller and travels closer to the wall as the effect of the jet passes through.

Figure 8 shows the entropy function contours as they vary with time during a single pulsation and their behavior with increasing

distance from the injection hole. The entropy change takes into account the change in total temperature and total pressure. The similarity of entropy contours to the temperature contours suggests the preponderance of the temperature gradients over the pressure gradients in entropy generation. The sites of high entropy change are found within the coolant core. In comparing the figures at $t/T=0.08$, $X/D=3$ and $t/T=0.64$, $X/D=3$, it can be readily concluded that as the jet becomes smaller with the pulsation trough at $t/T=0.64$, the place where entropy change is maximum in both the plots is within the coolant core, where the lowest total temperature can be found.

3.2.2 Compound Angled Injection. The time-averaged plots of θ and entropy function, $e^{-\Delta s/R}$ for the pulsated and nonpulsated jet with a $\beta=60$ deg lateral angle are shown in Fig. 9. The temperature distribution of the compound angled jet has some distinct characteristics when compared with a streamwise injection. From

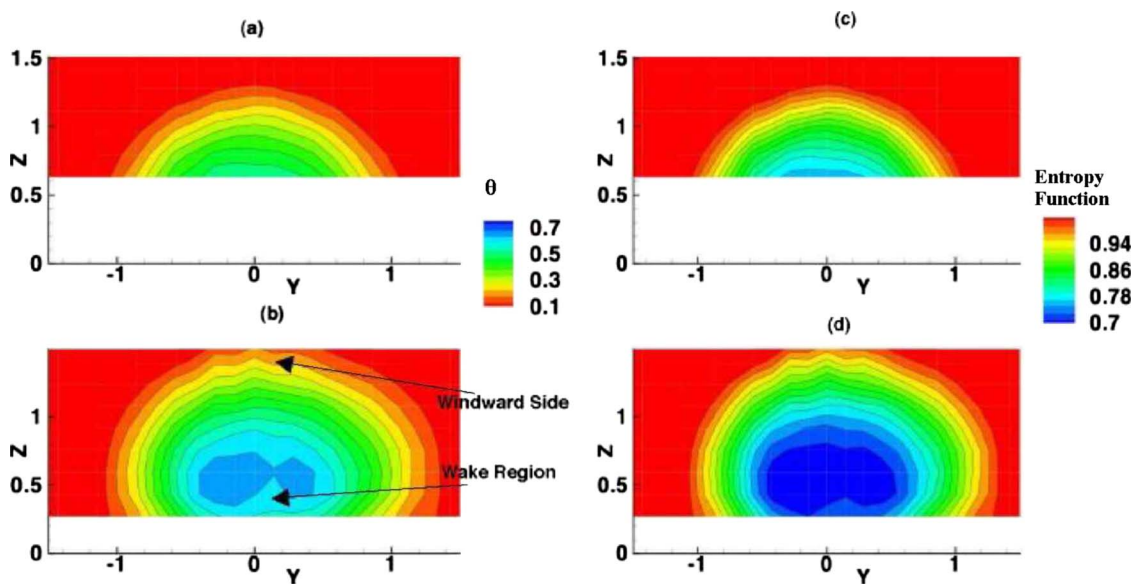


Fig. 7 Time-averaged nondimensionalized temperature, $\theta=(T-T_h)/(T_c-T_h)$, at $X/D=6$ for (a) $\beta=0$ deg, $f_r=0$ and (b) $\beta=0$ deg, $f_r=0.025$. Time-averaged contours of the entropy function, $e^{-\Delta s/R}$, shown for (c) $\beta=0$ deg, $f_r=0$ deg and (d) $\beta=0$ deg, $f_r=0.025$.

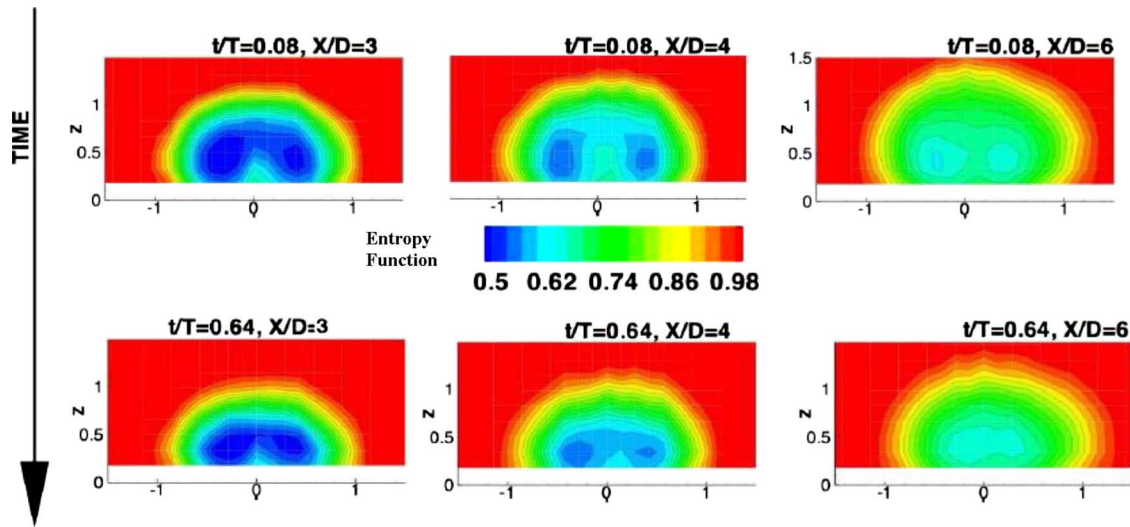


Fig. 8 Contours of the entropy function, $e^{-\Delta s/\mathcal{R}}$, of a pulsating jet at $BR=2$, $DR=1.3$, and $\beta=0$ deg shown at $X/D=3, 4, 6$, at the crest $t/T=0.08$, and at the trough $t/T=0.64$ during a pulsation

flow structure measurements of Ref. [12] and detailed simulations of the lateral angled jet of Refs. [9–11], it is known that the jet almost never lifts off even at $BR=2$ and is always attached to the wall. These studies show that the counter-rotating vortex pair (CVP) structure is replaced by only a single vortex, which is much weaker in intensity than a corresponding CVP. The temperature profiles in Fig. 9 reiterate the fact as the coolant jet has a significantly lower vertical spread and is almost squashed down to the wall laterally when compared with a streamwise jet. It is suspected that part of the boundary layer wake of the lateral angled jet is not visible since it is very close to the wall, which could not be accessed by the FENT probe. A single vortex core, which had been ejected at $Y/D=0$, piles up the boundary layer mixed with the cool fluid preferentially on one side by entrainment, causing the shape observed. The time-averaged temperature contours of the pulsated flow (Fig. 9(b)) show some differences from the steady flow. This is because the lateral penetration of the jet in the Y/D direction increases with increasing BR , so during a pulsation, the cross section of the jet boundary not only grows larger and then smaller with time when viewed in the $Y-Z$ plane but also moves from left to right in the Y direction. The ramifications of

these dynamics are visible in the entropy change contours where (d) shows a larger coolant wake with a pronounced single pile-up as compared with (c), which is smaller and spread closer to the wall. The pulsating jet, due to its lateral movement, does not allow the coherent pile-up of the boundary layer, but instead shows a larger coolant core, which is lifted slightly higher than the steady jet. The spatial extent of the regions with greater entropy change is seen to be higher in the pulsated case. A primary conclusion from the entropy contours in Fig. 9 is the good correlation with the temperature distribution. The time-resolved entropy contours in Fig. 10 show that during a pulsation, only the size of region at $X/D=6$ changes but not its shape, unlike in the plots at $X/D=3$. It can thus be concluded that the lateral sweeping effect of the jet due to pulsation is not apparent after about four diameters downstream of the injection location. The coolant spread with the compound jet is much greater laterally than that of a streamwise case, but the spread is much closer to the wall, as visible in Figs. 8 and 10.

These figures suggest that the thermal mixing of the jet with the hot fluid could take place in different ways. For a streamwise injection, it has been shown in previous literature as well as in the

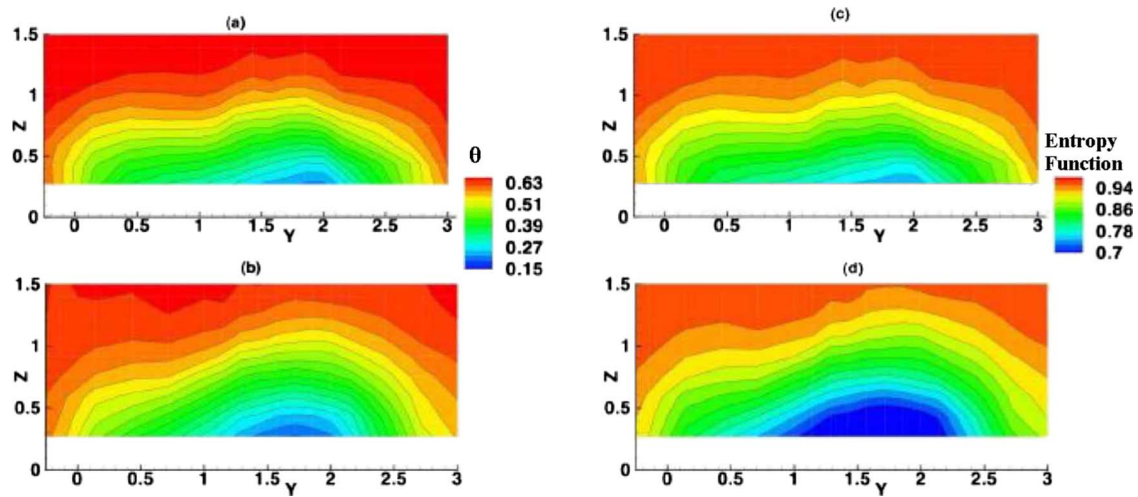


Fig. 9 Time-averaged nondimensional temperature, $\theta=(T-T_h)/(T_c-T_h)$, at $X/D=6$ for (a) $\beta=60$ deg, $f_r=0$ and (b) $\beta=60$ deg, $f_r=0.025$. Time-averaged contours of the entropy function, $e^{-\Delta s/\mathcal{R}}$, shown for (c) $\beta=60$ deg, $f_r=0$ deg and (d) $\beta=60$ deg, $f_r=0.025$.

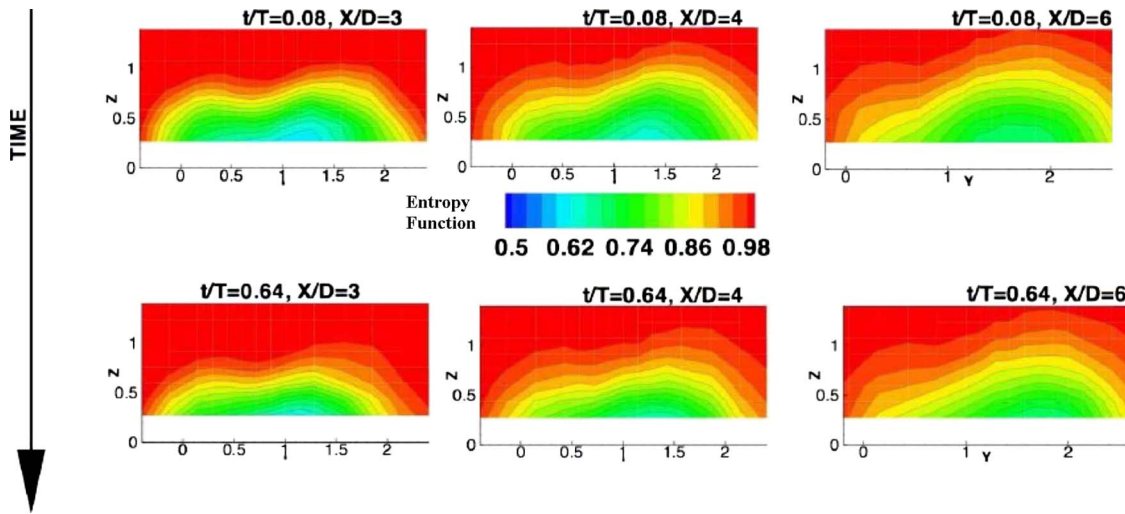


Fig. 10 Contours of the entropy function, $e^{-\Delta s/\mathcal{R}}$, of a pulsating jet at $BR=2$, $DR=1.3$, and $\beta=60$ deg shown at $X/D=3, 4, 6$, at the crest $t/T=0.08$, and at the trough $t/T=0.64$ during a pulsation

thermal contours in Fig. 7 that coolant core mixes with the hot fluid entrained from outside by the CVP, thereby getting warmer. In the context of the knowledge that a compound angled jet has most of its coolant spread within the boundary layer, not only is the coolant more spread out, but due to the absence of a strong CVP, there is little entraining of hot fluid from the freestream to within the jet. Instead a better distribution of temperature within the boundary layer occurs, which piles up on one side as the coolant spreads laterally rather than remaining confined within a vortex core.

3.3 Mass-Averaged Performance Indicators. From Figs. 7 and 9 it appears that pulsating a compound angled jet changes the local entropy and temperature distribution much more than with a streamwise jet. However it should be noted that the momentum of a streamwise jet is much higher than a compound angled jet at the same downstream distance due to the strong entrainment of its CVP, whereas the compound angled jet loses its forward momentum in the redistribution of the coolant laterally and energizing the boundary layer. In order to get averaged quantities of performance, which can be conveniently interpreted, the total pressure loss coefficient, $C_{P,t}$, the entropy loss coefficient, ζ , and the kinetic energy loss coefficient, ξ , were mass flow averaged at the measurement planes using Eq. (7), where \mathcal{F} represents the quantity being averaged,

$$\bar{\mathcal{F}} = \frac{\int \int \mathcal{F} \rho V dA}{\int \int \rho V dA} \quad (7)$$

3.3.1 Total Pressure Loss Coefficient. Figure 11 shows the mass-averaged total pressure coefficient for different conditions. It is conjectured that this quantity indicates the total pressure loss from the cooling hole as well as that suffered by the main flow during the mixing process. It must be noted, however, that for all cases, parts of the wake very close to the wall, where there could be significant pressure loss, were not measured due to the inaccessibility of the probe. It is observed in Fig. 11(a) that the mass-weighted time-averaged total pressure loss increases much more for the streamwise case for successive downstream stations than for the compound angle jets in general. Pulsating jets tend to have

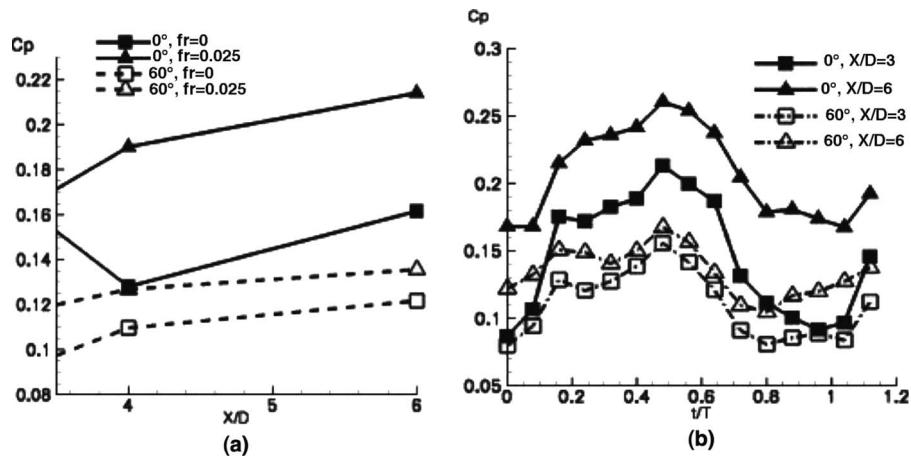


Fig. 11 Evolution of mass flow weighted average of the total pressure loss coefficient $C_{P,t}$ (a) with distance from the hole center and (b) within a single pulsation of $f_r=0.025$

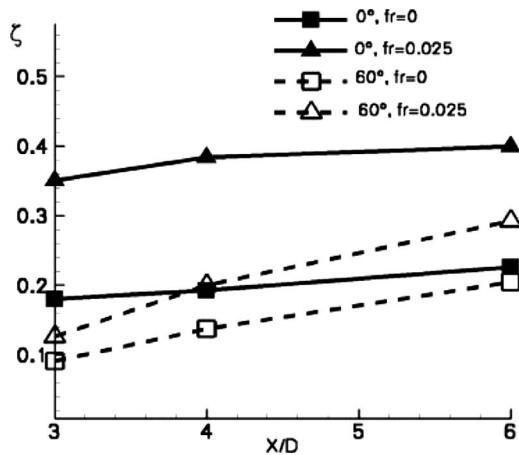


Fig. 12 Evolution of mass flow weighted average of the entropy loss coefficient ζ with distance from the hole center with and without pulsations

higher pressure losses on an average than steady jets. Total pressure losses are caused due to nonisentropic momentum mixing, which are enhanced by pulsation. A compound angled injection suffers from lesser total pressure loss, even though it can be argued that the injection with its greater cross section to the freestream would cause a larger blockage and hence greater losses in the freestream. This is due to the fact that on mass averaging, the lower losses caused in the jet body itself tend to compensate the blockage total pressure loss. Due to the lesser effective velocity difference between jet and freestream, the losses at the jet exit are lesser for a compound angled injection. Figure 11(b) shows the change in the mass-weighted pressure loss coefficient for measurement planes at $X/D=3$ and 6 at different phases within a pulsation cycle for streamwise and compound angled holes. Since the change in loss coefficient during a pulsation increases with downstream distance for the streamwise case by almost 20% but only by about 5% for the compound injection, it can be argued that the dissipation of total pressure due to mixing is higher for a streamwise injection.

3.3.2 Entropy Loss Coefficient. Entropy change has been advocated as the most physically relevant loss parameter by [25] for turbomachinery analysis. However, in Ref. [25], the explanations and models about film cooling loss are focused only on the loss undergone by the freestream and that, too, in a control volume analysis, where the final quantities are calculated after the complete mixing. The entropy loss coefficient primarily shows the losses the freestream suffers due to (a) viscous dissipation, (b) mixing of mass, momentum and energy, and (c) heat transfer. Due to the modified definition of the reference quantities described by Eqs. (1) and (2), this loss coefficient would also indicate the losses that the jet itself suffers within the hole and during ejection. It should be noted that the results in this section are an attempt to understand the near-hole loss-generating mechanisms with a somewhat different definition of entropy loss than that espoused in Ref. [25]. Owing to probe inaccessibility to far downstream positions, the fully mixed-out averaged losses could not be calculated, but rather attention is focused on the evolution of loss with downstream mixing as well as its variation at near-hole positions during a pulsation. These definitions seek to understand loss-generating mechanisms during the mixing process in detail.

The mass-averaged entropy loss coefficient as described in Ref. [25] and given by Eq. (5) is shown in Fig. 12. One notable feature is the greater slope of the $\beta=60$ deg case with distance than of the streamwise injection. This means that the entropy loss increases much faster for the compound angled case spatially downstream than for the streamwise injection. The entropy change for a

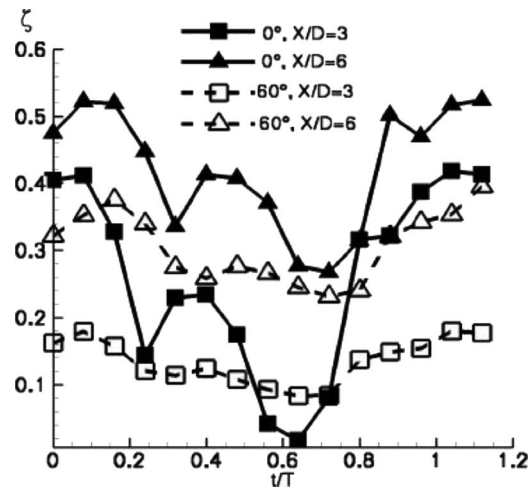


Fig. 13 Evolution of mass flow weighted average of the entropy loss coefficient ζ at two distances and pulsation of $f_r=0.025$

compound angled injection at $X/D=6$ is almost double that at $X/D=3$, whereas the same ratio for streamwise injection is only about 10–20%. This is due to greater thermal mixing during compound angled injection. However, the streamwise injection has a higher loss to begin with, say, at $X/D=3$, which does not increase as substantially because the thermal mixing is not as prominent as the jet propagates downstream. The near-hole flow-field computations of Ref. [9] show that the geometry of the incoming jet significantly affects the freestream-crossflow pressure field at the exit. This is manifested as the streamwise jet suffers most of its total temperature and pressure loss while being injected into the freestream and the viscous dissipation thereof due to the higher effective velocity difference between the jet and the freestream at every elemental area, whereas the compound angled injection being injected much closer to the wall has areas of lower momentum and therefore lower viscous dissipation due to velocity differences between the jet and freestream.

Pulsating the flow shows a marked increase in the entropy loss coefficient in both streamwise and compound angled cases. The averaged plots also show that pulsating a streamwise jet increases the entropy loss coefficient by almost 65% but only by around 10% of that for the compound angled case. Hence, it is insightful to view the change in the mass-weighted entropy loss coefficient, ζ for the pulsating flow in a time-resolved manner as shown in Fig. 13.

A few observations are noteworthy in Fig. 13. First, the relative variation in the entropy loss production over a cycle corresponds to the jet size as demarcated by the entropy contours in Figs. 8 and 10. Because of this, the trough of the entropy loss variation corresponds to around $t/T=0.64$ at which point the jet is observed to have the smallest size and shows the highest loss when the jet is at its largest. Second, the variation of the entropy loss coefficient for the streamwise case has a much larger range within a cycle than that of the compound angled case. This is because as the effective BR increases and decreases for the streamwise jet during a pulsation, it lifts away from the wall and comes closer to it, respectively. However, the compound angled jet stays more or less attached to the wall during the entire cycle but only moves laterally within a pulsation, thereby not going through as big a change in jet spatial extent as the streamwise case. This is manifest quite starkly at the point $t/T=0.64$, where for the $X/D=3$ curve, the trough of the entropy change for $\beta=0$ deg is even lower than that for $\beta=60$ deg, whereas the crest at $t/T=1.08$ is a good two and a half times larger.

3.3.3 Kinetic Energy Loss Coefficient. The kinetic energy loss

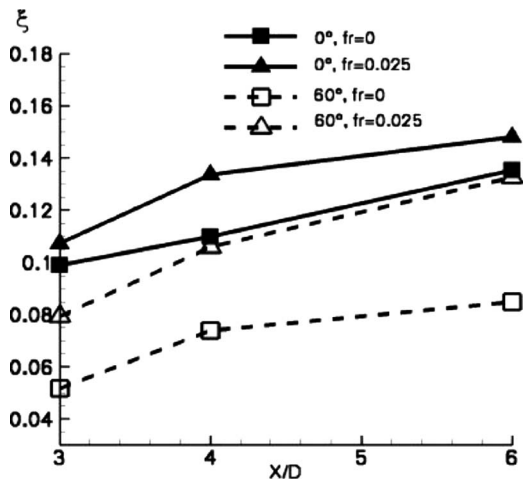


Fig. 14 Evolution of mass flow weighted average of the film cooling loss coefficient ξ with distance from the hole center with and without pulsations

coefficient, as described in Eq. (6), has often been used to describe the performance of film cooling geometries by taking into account losses in both jet and freestream.

Figure 14 shows the mass-averaged kinetic energy loss coefficient, ξ , derived from the time-averaged temperatures and pressures at different downstream points for all the conditions. This loss coefficient indicates both the mixing loss and separation losses in kinetic energy suffered by the jet and freestream in a combined manner. The trends are similar to the entropy change curve; i.e., overall the streamwise injection shows higher losses than the compound angled ones, and pulsation increases the losses of a steady jet. The relative increase in loss for the compound angled case from $X/D=3$ to $X/D=6$ is higher, which could indicate the greater mixing loss contribution due to compounding. Pulsation would tend to reduce the averaged kinetic energy anyways as during part of the cycle the high BR jet becomes smaller at all planes of measurement. As far as the average loss is concerned, the kinetic energy loss coefficient shows similar information to the entropy loss coefficient. However, this is only true because the entropy loss coefficient takes into account the losses in the jet itself and not only the freestream.

The time-resolved plots of the mass-averaged kinetic energy loss coefficients are shown in Fig. 15. The trend in the variation over a cycle is very similar to the total pressure loss coefficient

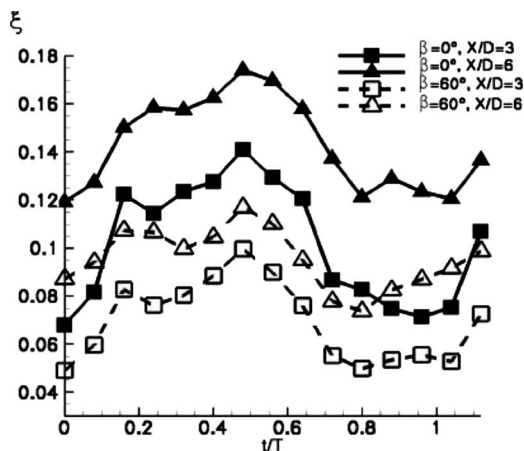


Fig. 15 Evolution of mass flow weighted average of the film cooling loss coefficient ξ at two distances and pulsation of $f_r = 0.025$

variation and somewhat different from the evolution of the entropy loss coefficient. The lowest kinetic energy loss within a cycle appears just after $t/T=0.88$ at which point the jet is at its largest size from the time-resolved entropy contours. This trend is quite different from that of the entropy loss coefficient plot in Fig. 13. It appears that the kinetic energy loss coefficient variation lags the variation of the low temperature jet regions by about half a cycle. The explanation has more to do with the definition of these quantities than with the mechanisms.

Through the discussions in Ref. [28] with regard to the air-cooled gas turbine using the basic framework of an injection into a freestream, it is understood that the entropy creation is basically divided into two terms. One is the entropy change due to the kinetic energy change of the jet and freestream as their velocities equilibrate. This is because of viscous dissipation as well as momentum mixing. The second contribution to entropy change is due to the thermal mixing. Figure 13 shows the entire loss variation, whereas Fig. 15 shows mainly the change in kinetic energy and not the associated thermal losses due to thermal mixing. It is for this reason that the entropy change variation within a cycle follows the jet growth and shrinkage closely, whereas the kinetic energy loss variation within a cycle shows a definite offset. The differences in the time scales with which a change in velocity propagates compared with the convective transport of temperature by the jet body are responsible for these offsets especially since the pulsation frequency is very high. Based on this reasoning, Fig. 15 shows that although the absolute levels of kinetic energy loss for streamwise injection are higher, the relative variation of the coefficient within a cycle is not too different for the two geometries. Compare this observation to the large difference in variation of the entropy change coefficient within a cycle. This large variation is due to the inclusion of the thermal losses, which would completely depend on the spatial extent of the low temperature fluid within the region of interest. The advantage of using a compound angled jet is therefore not only to give an increased coolant coverage but also to reduce the aerothermal losses in a high blowing ratio application. Although compound angled injection has greater thermal mixing losses, which increase with downstream distance, it cannot be ascertained whether at a point far downstream the mixing losses would be high enough to be higher than the losses in the streamwise injection.

4 Conclusion

Detailed measurements using a novel probe technique that allows simultaneous measurements of temperature and pressure have been performed. A novel probe access and traversing system has been used for a flexible and rapid experimental campaign. Streamwise and 60 deg lateral angled film cooling jets with a 30 deg inclination angle were studied, with and without engine representative pulsation of a hole diameter based reduced frequency of $f_r=0.025$. A single operating point, viz., $BR=2$, $DR=1.3$, and $IR=3.04$, was investigated in detail. Time resolved temperature and entropy change data were recorded. The presence of a thermal gradient between the freestream and the coolant led to significant observations, mainly with respect to the evolution of loss due to thermal mixing. Mass-weighted inlet total pressures and temperatures were used as reference conditions to better capture the entropy change within the incoming jet and the freestream simultaneously. The entropy change contours followed the trends of the temperature contours. It was observed that the wake of a streamwise jet had areas of high entropy change, and the cores of the counter-rotating vortex pair showed the regions of maximum entropy change. As the jet mixes with downstream propagation, the coolant spread increases and the areas of entropy generation spread over a larger region in step with the temperature mixing. The compound angled jet, in general, is closely attached to the wall even at high BR . The areas of high entropy change are again mostly confined within the coolant body. One important observation during pulsation is that a streamwise jet increases and de-

increases in size as it rises vertically above the wall, whereas a compound angled jet has a distinct lateral movement. In light of these observations, the important conclusions are as follows:

1. The compound angled jets have lower entropy losses than the streamwise ones (between 40% and 75% lesser depending on the downstream distance from the hole), which increase faster with thermal mixing as the jet propagates downstream. However a streamwise jet still leads to greater entropy change primarily due to viscous dissipation and separation losses at the hole exit.
2. The usage of a compound angled hole would seem to have the benefit that kinetic energy losses suffered by the jet itself are lower, even while having a greater coolant coverage over a larger part of the metal. A possible drawback is that thermal mixing losses keep increasing with downstream distance. However, whether at a far downstream position these losses become greater than that for a streamwise injection could not be ascertained due to limited data.
3. A pulsating jet shows a marked increase in aerothermal losses due to greater thermal mixing and enhanced shear losses due to the changing size of the jet. A streamwise pulsating jet has around double the entropy loss than that of a steady jet due to greater penetration and effective blowing ratio variation near the hole.
4. A pulsating compound angled jet suffers only about one-half times the loss of a steady jet at the same downstream position as the jet does not penetrate very much into the freestream but is forced to oscillate in a lateral direction against smaller shear forces.
5. It has been shown that an entropy loss coefficient incorporates the loss due to momentum mixing, thermal mixing, and separation losses near the hole exit.
6. The kinetic energy loss coefficient, on the other hand, will reflect the loss due to separation and momentum mixing, but the loss in thermal energy due to mixing will be underpredicted.

Acknowledgment

The authors acknowledge the technical expertise of Cornel Reshef for the instrumentation and development of FRAP technology, as well as the insightful support of Dr. Ndaona Chokani and Dr. Martin Rose in different phases of this work.

Nomenclature

X	= axial (streamwise) coordinate
Y	= lateral coordinate
Z	= vertical coordinate
U, V, W	= mean velocity components
ρ	= density
M	= Mach number
P	= pressure
T	= temperature
\mathcal{R}	= specific gas constant of dry air
C_p	= specific heat capacity at constant pressure
s	= entropy
D	= hole diameter
Re_D	= Reynolds number based on hole diameter, $U_\infty D / \nu$
S	= pitch distance between two holes
L	= length of the hole pipe
ϕ	= injection angle with respect to surface of the flat plate
β	= lateral angle of hole axis with freestream
BR	= blowing ratio, $\rho_c U_c / \rho_f U_f$
DR	= density ratio, ρ_c / ρ_f
IR	= momentum flux ratio, BR^2 / DR
f	= frequency of pulsation, Hz

f_r	= reduced frequency, fD / U_∞
\dot{m}	= mass flow rate
θ	= nondimensionalized temperature, $(T - T_h) / (T_c - T_h)$
t/T	= time nondimensionalized by the pulsation period

Subscripts

c	= coolant fluid
h	= (hot) freestream fluid
ref	= reference value
D	= hole diameter based
t	= total quantity
s	= static quantity
∞	= averaged reference value

References

- [1] Abhari, R. S., 1996, "Impact of Rotor-Stator Interaction on Turbine Blade Film Cooling," ASME J. Turbomach., **118**, pp. 123–133.
- [2] Ligrani, P. M., and Ramsey, A. E., 1997, "Film Cooling From Spanwise-Oriented Holes in Two Staggered Rows," ASME J. Turbomach., **119**, pp. 562–567.
- [3] Reiss, H., and Boelcs, A., 2000, "Experimental Study of Showerhead Cooling on a Cylinder Comparing Several Configurations Using Cylindrical and Shaped Holes," ASME J. Turbomach., **122**, pp. 161–169.
- [4] Dittmar, J., Schulz, A., and Wittig, S., 2003, "Assessment of Various Film-Cooling Configurations Including Shaped and Compound Angled Holes Based on Large-Scale Experiments," ASME J. Turbomach., **125**, pp. 57–64.
- [5] Jung, I. S., and Lee, J. S., 2000, "Effects of Orientation Angles on Film Cooling Over a Flat Plate: Boundary Layer Temperature Distributions and Adiabatic Film Cooling Effectiveness," ASME J. Turbomach., **122**(1), pp. 153–160.
- [6] Bernsdorf, S., Rose, M., and Abhari, R. S., 2006, "Modeling of Film Cooling—Part I: Experimental Study of Flow Structure," ASME J. Turbomach., **128**, pp. 141–149.
- [7] Pietrzyk, J. R., Bogard, D. G., and Crawford, M. E., 1989, "Hydrodynamics Measurements of Jets in Crossflow for Gas Turbine Film Cooling Applications," ASME J. Turbomach., **111**(2), pp. 139–145.
- [8] Rydholm, H. A., 1998, "An Experimental Investigation of the Velocity and Temperature Fields of Cold Jets Injected into a Hot Crossflow," ASME J. Turbomach., **120**(2), pp. 320–326.
- [9] McGovern, K. T., and Leylek, J. H., 2000, "A Detailed Analysis of Film-Cooling Physics: Part II—Compound Angled Injection With Cylindrical Holes," ASME J. Turbomach., **122**, pp. 113–121.
- [10] Hyams, D. G., and Leylek, J. H., 2000, "A Detailed Analysis of Film-Cooling Physics: Part III—Streamwise Injection With Shaped Holes," ASME J. Turbomach., **122**, pp. 122–132.
- [11] Brittingham, R. A., and Leylek, J. H., 2000, "A Detailed Analysis of Film-Cooling Physics: Part IV—Compound Angled Injection With Shaped Holes," ASME J. Turbomach., **122**, pp. 133–145.
- [12] Aga, V., Rose, M., and Abhari, R. S., 2008, "Experimental Flow Structure Investigation of Compound Angled Film Cooling," ASME J. Turbomach., **130**, p. 031005.
- [13] Kaszeta, R. W., and Simon, T. W., 2000, "Measurement of Eddy Diffusivity of Momentum in Film Cooling Flows With Streamwise Injection," ASME J. Turbomach., **122**(1), pp. 178–183.
- [14] Saumweber, C., Schulz, A., and Wittig, S., 2003, "Free-Stream Turbulence Effects on Film Cooling With Shaped Holes," ASME J. Turbomach., **125**(1), pp. 65–73.
- [15] Bons, J. P., MacArthur, C. D., and Rivir, R. B., 1996, "The Effect of High Freestream Turbulence on Film Cooling Effectiveness," ASME J. Turbomach., **118**(4), pp. 814–825.
- [16] Ekkad, S. V., Ou, S., and Rivir, R. B., 2006, "Effect of Jet Pulsation and Duty Cycle on Film Cooling From a Single Jet on a Leading Edge Model," ASME J. Turbomach., **128**, pp. 564–571.
- [17] Coulthard, S., Volino, R. J., and Flack, K. A., 2007, "Effect of Jet Pulsing on Film Cooling—Part I: Heat Transfer Results," ASME J. Turbomach., **129**, pp. 247–257.
- [18] Coulthard, S., Volino, R. J., and Flack, K. A., 2007, "Effect of Jet Pulsing on Film Cooling—Part II: Effectiveness and Flow-Field Temperature Results," ASME J. Turbomach., **129**, pp. 232–246.
- [19] Burdet, A., and Abhari, R. S., 2007, "Influence of Near Hole Pressure Fluctuation on the Thermal Protection of a Film Cooled Flat Plate," ASME Paper No. HT2007-321812.
- [20] Friedrichs, S., Hodson, H. P., and Dawes, W. N., 1997, "Aerodynamic Aspects of Endwall Film Cooling," ASME J. Turbomach., **119**(4), pp. 786–793.
- [21] Wilfert, G., and Fottner, L., 1996, "The Aerodynamic Mixing Effect of Discrete Film Cooling Jets With Mainstream Flow on a Highly Loaded Turbine Blade," ASME J. Turbomach., **118**(3), pp. 468–478.

- [22] Lee, S. W., Kim, Y. B., and Lee, J. S., 1997, "Flow Characteristics and Aerodynamic Losses of Film Cooling Jets With Compound Angle Orientations," *ASME J. Turbomach.*, **119**(2), pp. 310–319.
- [23] Kupferschmied, P., Koepfel, P., Gizzi, W., Roduner, C., and Gyarmathy, G., 2000, "Time-Resolved Flow Measurements With Fast-Response Aerodynamic Probes in Turbomachines," *Meas. Sci. Technol.*, **11**, pp. 1036–1054.
- [24] Mansour, M., Chokani, N., Kalfas, A. I., and Abhari, R. S., 2008, "Unsteady Entropy Measurements in a High Speed Radial Compressor," *ASME J. Eng. Gas Turbines Power*, **130**(2), p. 021603.
- [25] Denton, J. D., 1993, "Loss Mechanisms in Turbomachinery," *ASME J. Turbomach.*, **115**, pp. 621–656.
- [26] Drost, U., 1998, "An Experimental Investigation of Gas Turbine Airfoil Aero-Thermal Film Cooling Performance," Ph.D. thesis, EPF Lausanne, Switzerland.
- [27] Young, J. B., and Horlock, J. H., 2006, "Defining the Efficiency of a Cooled Turbine," *ASME J. Turbomach.*, **128**, pp. 658–667.
- [28] Young, J. B., and Wilcox, R. C., 2002, "Modeling the Air-Cooled Gas Turbine: Part II—Coolant Flows and Losses," *ASME J. Turbomach.*, **124**, pp. 214–221.

Influence of Wake Structure on Unsteady Flow in a Low Pressure Turbine Blade Passage

S. Sarkar

Department of Mechanical Engineering,
Indian Institute of Technology Kanpur,
Kanpur-208016, India
e-mail: subra@iitk.ac.in

The effect of wake structures on the evolution of the boundary layer over the suction side of a high-lift low-pressure turbine blade is studied using large-eddy simulation (LES) for a Reynolds number $Re = 7.8 \times 10^4$ (based on the axial chord and the inlet velocity). The wake data of different characteristics (defined by the wake deficit and the small-scale motion) are extracted from a precursor LES of flow past a cylinder. This replaces a moving bar that generates wakes in front of a cascade. LES results illustrate that apart from the wake kinematics, the large pressure oscillations and rollup of the separated shear layer along the rear half of the suction surface depend on the length scale of the convective wake. The transition of this rolled-up shear layer is influenced by the wake turbulence and the small-scale motion. [DOI: 10.1115/1.3072490]

1 Introduction

Aerofoils of a modern low-pressure turbine (LPT) are subjected to increasingly stronger pressure gradient as designers impose higher loading in an effort to improve efficiency and lower cost by reducing the number of blades in an engine. As the LPT is relatively heavy consisting of a large number of stages, small improvements of its efficiency have a significant effect on the overall efficiency of a jet engine and thus the fuel consumption. Therefore, there are continued efforts toward the generation of “high-lift” blade profiles. If the adverse pressure gradient on the suction side of these aerofoils becomes strong enough, the boundary layer will separate. Wakes from the upstream blade row interact with this separated boundary layer and make it highly unsteady. Under such an environment, the flow configuration depends on the receptivity to external disturbances and the internal growth mechanisms of the shear layer [1].

The unsteady wake produces an incident flow that has two distinctive features: a freestream velocity defect described by the kinematics of the wake and its velocity fluctuations. Although the kinematics of the wake is partly responsible for the character of the boundary layer developing over the downstream blade, the effect of wake turbulence and its convection through the blade passage are important for boundary layer transition. A pioneer work describing the kinematics of wake convection through a cascade passage was done by Meyer [2]. It used the potential flow solution to model the convective wake replacing each wake by a perturbation jet (the so-called “negative jet”) on a uniform flow. A considerable progress has been made over the past 3 decades in understanding the behavior of a separated boundary layer under the influence of the unsteady wakes [3–10]. If the wake frequency is reduced and the Reynolds number is high enough, one could possibly find a combination of bypass transition and separation-induced transition.

The experiments by Stieger et al. [11] and the LES performed by Sarkar and Voke [12] illustrated the appearance of coherent vortices by the rollup of the shear layer via the Kelvin–Helmholtz (KH) mechanism over the rear half of the suction surface of a high-lift LPT blade. These vortices are identified as the source of pressure fluctuations on the suction surface. Sarkar [13] further

indicated that the transition during the wake-induced path is governed by a mechanism that involves the formation and convection of coherent vortices followed by the production of turbulent kinetic energy (TKE) inside the KH rolls. It was also shown by Wissink et al. [14] that small-scale fluctuations carried by the convective wake influence the transition to turbulence of the highly diffusive boundary layer on the suction surface. Thus, the unsteady flow on the suction surface is dependent on the turbulence intensity and the length scale of passing wakes.

Most of the experimental studies on the unsteady wake-induced transition were performed by sweeping a row of wake-generating cylinders upstream of a cascade. No work has clearly specified the characteristics of generated wakes. In reality, the flow pattern, Strouhal number, and turbulent intensity of a wake generated by a cylinder are different from those of a wake that actually sheds from a turbine blade trailing edge. Unfortunately, in the experiments it is extremely difficult to differentiate between the mean effect of the wake as a negative jet and the effect of the small-scale fluctuations carried by the wake. However, the wake simulation may be manipulated to generate the data for various wake patterns such as a two-dimensional (2D) laminarlike wake and a 3D (turbulent) unsteady wake, or the fluctuations may be removed, imposing a passing wake containing no turbulence at all but only a momentum deficit equal to the time mean of the turbulent wake. These manipulations will allow us to elucidate in a very direct manner the effects of the wake eddies and the mean velocity deficit on the development of an unsteady boundary layer on the suction surface of a LPT blade. In this paper, the wake data from a 2D precursor simulation having no small-scale fluctuations in the spanwise direction and the data from a realistic 3D simulation are fed at the cascade inlet to examine the role of velocity deficit and 3D small-scale eddies in a separation-induced transition over the suction surface of a high-lift LPT blade (T106 profile) through LES.

2 Cascade Geometry and Computational Details

The cascade geometry considered here is that of the high-lift LPT blade, the T106 profile studied experimentally in different laboratories [11,15]. According to Ref. [11], the blade aspect (span-to-pitch) ratio was 1.89 with a chord of 198 mm, and thus the flow at the midspan can be considered two dimensional. This allows a three-dimensional simulation to be performed under the assumption of a homogeneous flow in the spanwise direction. The pitch-to-chord ratio was 0.799. The blade stagger angle λ , the inlet flow angle β_1 , and the exit flow angle β_2 are 30.7 deg, 37.7

Contributed by the International Gas Turbine Institute of ASME for publication in the JOURNAL OF TURBOMACHINERY. Manuscript received August 27, 2008; final manuscript received September 14, 2008; published online July 9, 2009. Review conducted by David Wisler. Paper presented at the ASME Turbo Expo 2008: Land, Sea and Air (GT2008), Berlin, Germany, June 9–13, 2008.

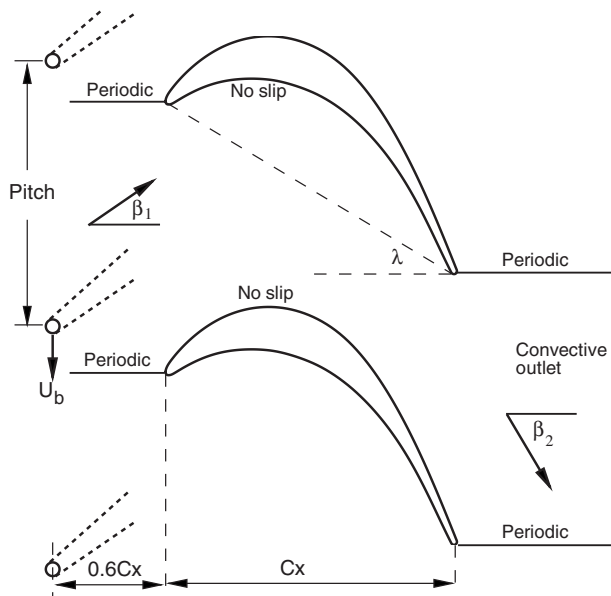


Fig. 1 Geometry of T106 low-pressure cascade and a schematic of a row of wake-generating cylinders sweeping at a speed U_b ahead of the cascade

deg, and -63.2 deg, respectively, as shown in Fig. 1. The moving cylinders ahead of the cascade are also shown in Fig. 1. LES of wake passing over the T106 profile in a cascade is performed at a Reynolds number of 7.8×10^4 (based on the axial chord and the inlet velocity) and a flow coefficient, $\phi = V_{x1}/U_b$, of 0.83. The bar pitch matches with the cascade pitch that yields a reduced blade passing frequency, $f_r = fC/V_{2is}$ of 0.68, f being the frequency. This allows the use of a single cascade channel to replace the large number of blades in a cascade by a periodic condition on the pitchwise boundaries and makes a direct numerical simulation (DNS) or LES affordable.

The moving row of wake-generating bars is replaced by a precursor LES of the flow past a thin cylinder, D being 2% of the blade chord for a Reynolds number of 1842 (based on the inlet velocity and the diameter of the cylinder). A grid of about 3×10^6 points is used to resolve the flow around the bar. The wake data are collected from a plane $5.25D$ downstream of the cylinder and are interpolated at the inlet plane of cascade considering the kinematics of flow by matching the velocity triangles. Thus, the present LES uses coupled simulations of flow around a cylinder for the generation of a wake, providing inflow conditions for successor simulations of wake interactions with the blade.

The filtered, time-dependent, incompressible mass and momentum equations in a fully covariant form are solved on a staggered grid using a symmetry-preserving finite difference scheme of second-order spatial and temporal accuracy. The details of mathematical formulations and numerical methods in general curvilinear coordinates used in the present study have already been reported [16,17]. The momentum advancement is explicit using the second-order Adams–Bashforth scheme except for the pressure term that is solved by a standard projection method. The pressure equation is discrete Fourier transformed in one dimension (in which periodicity of the flow and, hence, uniformity of the geometry are imposed) and is solved iteratively using multigrid acceleration in the other two dimensions. The LES uses $384 \times 192 \times 32$, i.e., 2.4×10^6 , points in the streamwise, cross-stream, and spanwise directions with the near wall mesh resolution as $5 < \Delta x^+ < 80$, $5 < \Delta z^+ < 20$, and $1 < \Delta y^+ < 3.5$ for the cascade. The other computational details and the subgrid model are the same as those used in an earlier study [13] that describes the unsteady pressure and the separation-induced transition on the suction sur-

face. The validation of the present LES against the experiment [11,15] and the DNS [18] was also presented in Ref. [13]. This indicated that the LES data could be qualitatively used to describe the evolution of boundary layer perturbed by passing wakes on the suction surface.

3 Results and Discussion

The objective of the present paper is to elucidate the response of the internal growth mechanisms of an inflexional layer due to a structural change in external disturbances. For the present instant, 2D and 3D unsteady simulations of flow past a cylinder (D being the same) are carried out to generate wake data of different wake patterns and thus of different eddy scales. The successor simulations of wake interactions with the blade are always three dimensional.

3.1 Characteristics of Wake Data. A realistic representation of wake data is vital for the successor simulation of wake convection through a LPT cascade passage. The cylinder diameter being very small compared with the pitch, it is wise to check the resolution with the mesh used. Spectral analysis of the streamwise component of velocities obtained from a 3D simulation of flow past the tiny bar along the centerline at $5.5D$ downstream indicates that the value of the Strouhal number ($St = fD/V_1$) is 0.212. This matches well with the Strouhal number of 0.2113 for the Reynolds number of 1842 following the empirical relations prescribed by Norberg [19]. The contours of time-averaged pressure coefficients near the cylinder along with the time-averaged turbulent stresses are presented in Fig. 2. The distributions of the pressure coefficient, its minimum value, and also the base suction pressure agree with the experiment [20] and the previous simulation [21]. The Reynolds normal stresses and the shear stress are found to be symmetric about $\eta=0$. The streamwise Reynolds normal stress $\overline{u'^2}$ presents a double-peak feature with the occurrence of a local minimum along the line of symmetry, whereas the cross-flow Reynolds normal stress $\overline{v'^2}$ reaches a local maximum along $\eta=0$. It is worth pointing out that the turbulence statistics obtained from the present LES are similar to those of earlier studies [21,22].

Figure 3 compares the instantaneous contours of vorticity from 2D and 3D simulations. The 2D simulation illustrates large organized coherent structures (Kármán vortex shedding) resembling the laminarlike flow, while the 3D simulation produces the wake structures with small-scale eddies, elucidating a more realistic picture. The levels of vorticity and Reynolds stress are found to be higher, and also vortices roll up closer to the cylinder in the 2D simulation. This is attributed to the random spanwise fluctuations that redistribute energy in the third direction, developing realistic structures, which is absent in 2D. These differences in flow characteristics of 2D and 3D simulations for a cylinder have also been reported [21]. From the time history (not shown), it was found that the peak-to-valley pressure traces in the wake are about 60% higher in the 2D simulation than in the corresponding 3D simulation. The center of the low-pressure region in the wake for the 2D simulation appears closer to the cylinder by about $0.5D$ as compared with the 3D simulation. It is also noted that the pressure at the center of the low-pressure region for the 2D simulation is lower ($\overline{C}_{p_{\min}} = -1.87$) than that for the 3D simulation ($\overline{C}_{p_{\min}} = -1.50$). The time-averaged TKE contours near the cylinder for both the simulations are presented in Fig. 4. The TKE reaches a symmetric state along the line of symmetry ($\eta=0$) of the cylinder with a local maximum. The 2D simulation produces a higher TKE as compared with the 3D with the local maximum closer to the cylinder. The 3D wake data that are kinematically transferred to the cascade inlet have a maximum mean wake deficit of $0.25V_1$, a wake half-width of $0.02C_x$, and a level of turbulence intensity of about 10% (based on the inlet velocity). The 2D data have a wake deficit of $0.475V_1$, a wake half-width of $0.02C_x$, and a level of

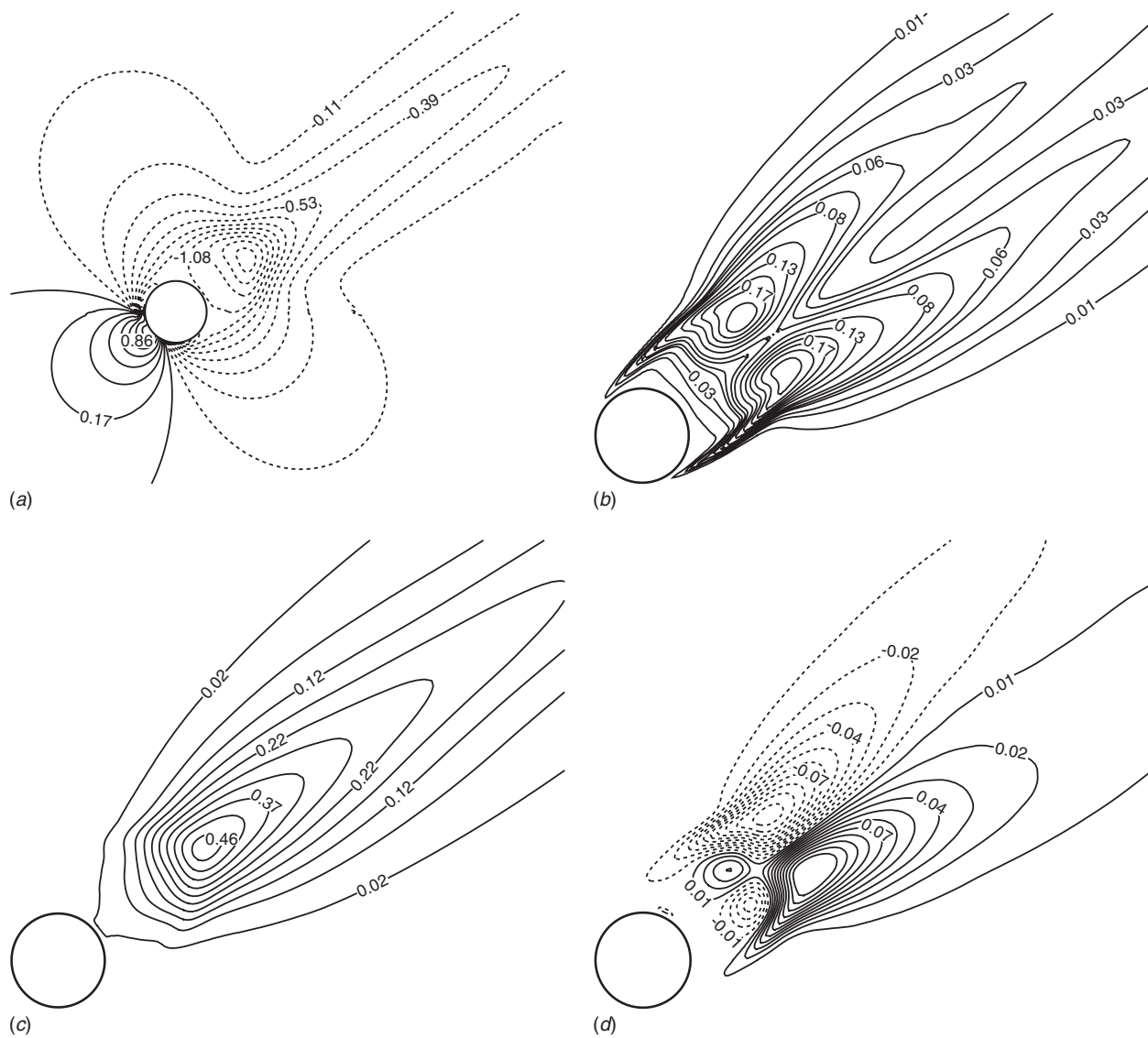
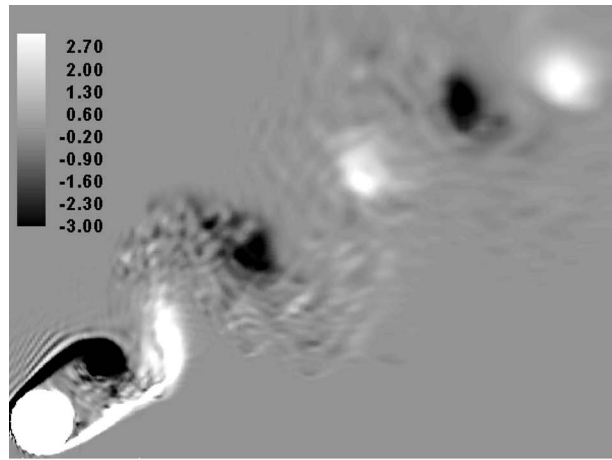


Fig. 2 Contours of time-averaged (a) pressure coefficient (dashed lines indicate negative values), (b) streamwise Reynolds normal stress \bar{u}^2 , (c) cross-flow Reynolds normal stress \bar{v}^2 , and (d) Reynolds shear stress $\bar{u}'v'$

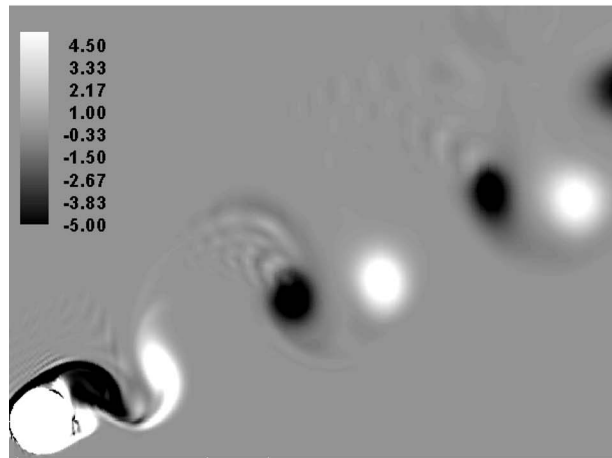
turbulence intensity of about 20% (with no fluctuations in the spanwise direction). The wake data from the 2D simulation have a larger and organized vortex structure, and thus the velocity deficit is about 90% higher, whereas the corresponding 3D simulation produces smaller eddy structures that promote more mixing, resulting in a weaker velocity deficit. 2DW refers to the simulation where the 2D wake data are fed at the cascade inlet plane, and 3DW refers to the simulation where the 3D wake data are interpolated at the cascade inlet plane for the successor 3D simulation of cascade with wake passing.

3.2 Kinematics of Wake Convection. The distortion of a wake segment as it convects within the LPT blade passage is illustrated in Fig. 5 by instantaneous isosurface of vorticity magnitude $|\omega|$ for the simulation 3DW. After being segmented at the leading edge, the suction- and pressure-side wakes behave differently. Straining of wakes near the suction surface starts from the stagnation point, but these are quickly broken down to random small-scale structures (wake 2 in Fig. 5(a)). The pressure-side wake suffers from severe stretching and thinning with the decay of turbulence (wake 2 in Fig. 5(b)). A bow forms between the pressure- and suction-side wake, owing to different convection speeds. In the apex region (Figs. 5(b) and 5(c)) of the distorted

wake, enhancement of turbulence occurs with growing random small-scale structures and loss of preferred orientation. Figure 6 shows the wake distortion inside the blade passage for the simulation 2DW. A noticeable difference in the wake structure as it convects within the blade passage is observed with 2D wake imposed at the inlet. Here also straining of wakes near the suction surface starts from the stagnation point, but the wakes maintain their 2D structures far downstream and break down to small-scale structures near the trailing edge (wake 2 in Fig. 6(c)). As shown earlier, the pressure-side wake suffers from severe stretching and thinning; however it preserves solenoidal structures with limited spanwise anisotropy even up to the trailing edge of the blade (wake 2 in Fig. 6(c)). In the apex region (Figs. 6(b) and 6(c)) of the distorted wake, enhancement of turbulence may not occur due to the absence of spanwise fluctuations. In both cases, sharp turning of the turbine passage causes the pressure-side wake to descend toward the wall over the downstream half of the pressure surface, whereas the suction-side wake after warping around the leading edge travels relatively above the surface. These highly strained wake fluids and generated vortical structures of different features interact periodically with the inflexional boundary layer



(a)

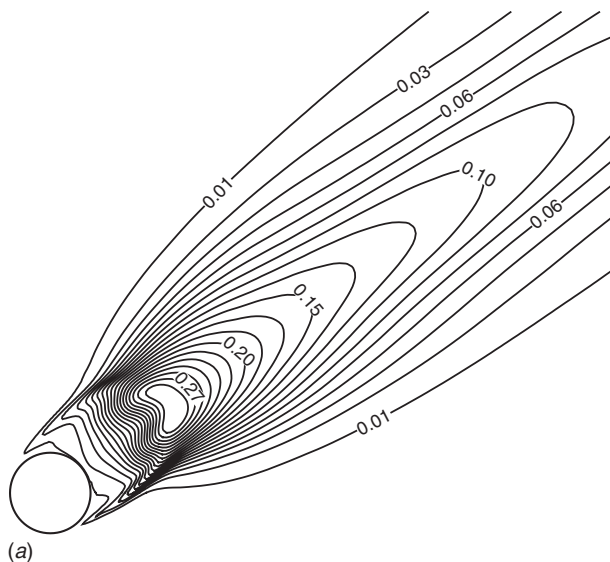


(b)

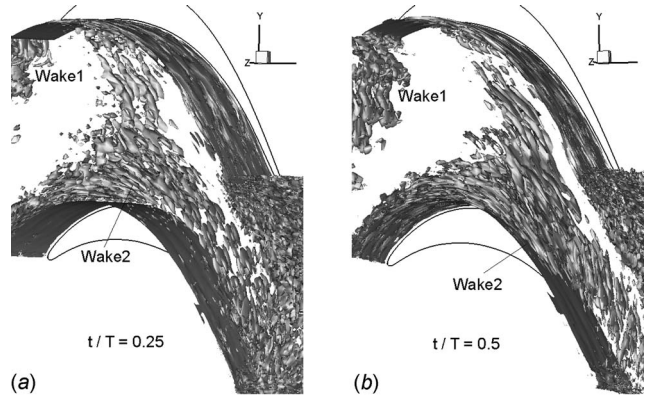
Fig. 3 Instantaneous vorticity depicting wake structure: (a) 3D simulation and (b) 2D simulation (presented in different scales)

over the suction surface, an example of complex interactions between spatial and temporal scales of turbulent eddies with an unsteady boundary layer.

Figures 7(a) and 7(b) (four points in each direction are skipped

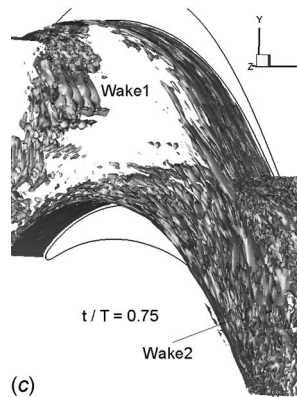


(a)

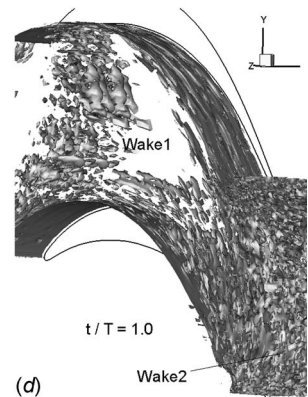


(a)

(b)



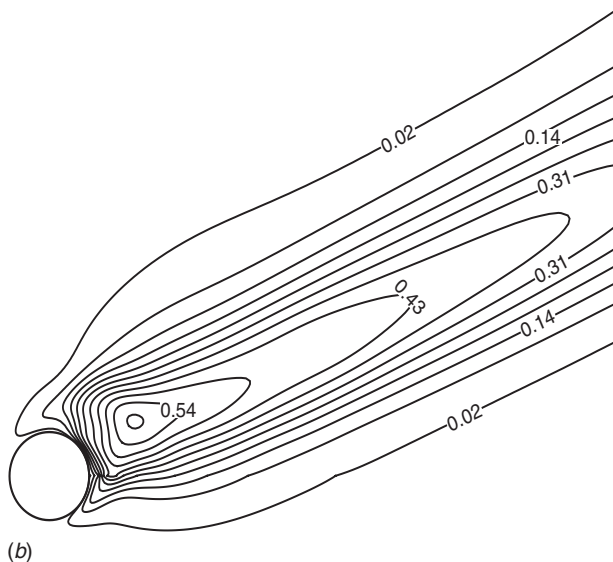
(c)



(d)

Fig. 5 Instantaneous isosurface of vorticity $|\omega|$ at four equal time intervals through the wake passing cycle for the simulation 3DW

to draw the figure) show the phase-averaged velocity perturbation vectors (the difference between a phase-averaged and a time-averaged quantity) illustrating the kinematics of wake segments within the blade passage for the simulations 3DW and 2DW, respectively. The effect of a negative jet is observed in Fig. 7. The wake segment within the blade passage is identified as a perturbation jet pointing toward the source of the wake. As the wake fluid impinges on the surface, it splits into two streams, one pointing downstream, which accelerates the flow downstream of the



(b)

Fig. 4 Contours of time-averaged TKE near the cylinder: (a) 3D simulation and (b) 2D simulation

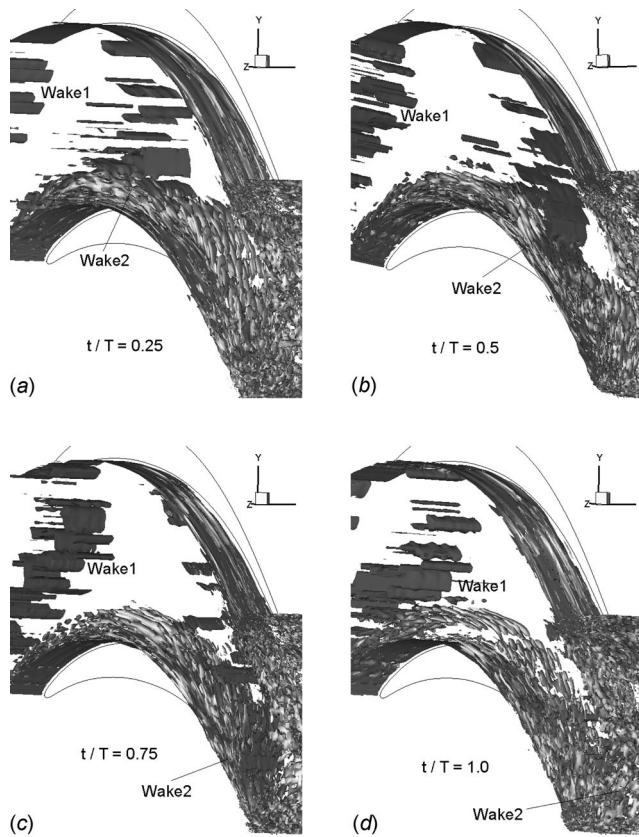


Fig. 6 Instantaneous isosurface of vorticity $|\omega|$ at four equal time intervals through the wake passing cycle for the simulation 2DW

approaching wake, and the other pointing upstream, which retards the flow after the wake has passed. The negative jet effect within the blade passage also produces a pair of counter-rotating vortices; the center of these are marked as A and B in Fig. 7. This can also be explained as a local concentration of vorticity produced by convection of the wake fluid. High wake deficit creates a stronger jet effect in the simulation 2DW (apparent from the length of velocity perturbation vector) as compared with the simulation 3DW. It, in turn, also produces a stronger rotating vortex within the blade passage. This illustrates that the kinematics of a jet is mainly governed by an inviscid phenomenon, and the effect of a negative jet on the boundary layer over the suction surface may be more pronounced for case 2DW.

Phase-averaged turbulent kinetic energies ($TKE = \frac{1}{2} \langle u_i' u_i' \rangle$) normalized by the isentropic exit velocity at two representative time instants during the wake passing cycle are presented in Fig. 8 for the simulations 3DW and 2DW. These are compared with the measured TKE [23] at nearly corresponding phases. The kinematics of wake convection described earlier is apparent from the elevated regions of TKE. As compared with the simulation 2DW, the simulation 3DW resolves better the wake deformation and turbulence augmentation in space and time. However in both cases, there are discrepancies with the experiment. The high levels of TKE, as seen in case 2DW (presented in a different scale), are due to the convection of high imposed inlet wake turbulence. For the simulation 3DW, a gradual decay in the wake turbulence near the pressure surface and also over the front part of the suction surface is attributed to the stretching of the wake. The enhancement of turbulence in the region of the bow-apex near the suction surface can be correlated with growing irregularity and small-scale structures, as seen in Fig. 5. This is due to the accumulation of wake fluid in the region and the wake being in a state of

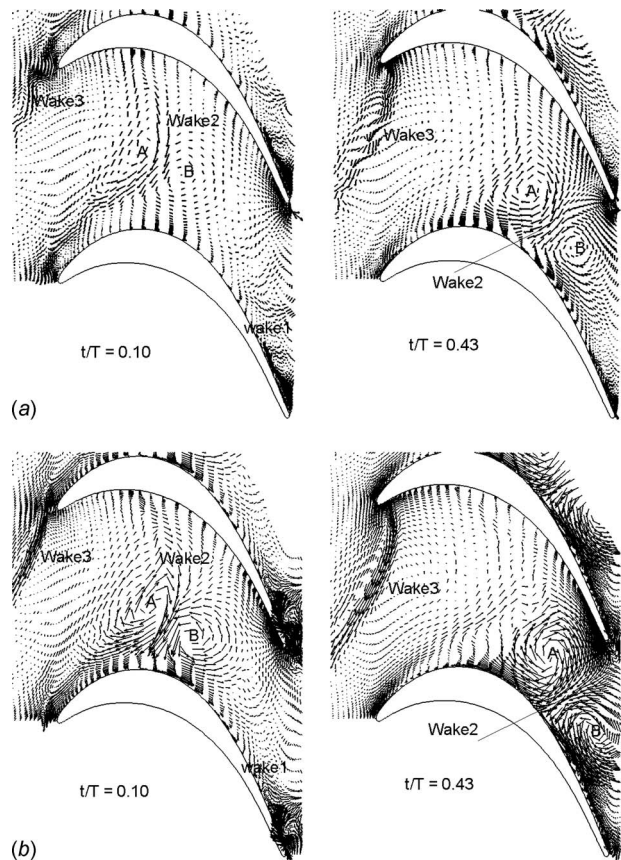


Fig. 7 Phase-averaged perturbation of velocity vectors at two time intervals through the wake passing cycle: simulations (a) 3DW and (b) 2DW

compression. If perturbation velocity vectors are superimposed, it is revealed that high levels of TKE occur slightly below the centers of a counter-rotating vortex pair, an observation consistent with the experiment. In the region of bow-apex near the suction surface, the highest level of resolved turbulence intensity based on the isentropic exit velocity is about 6.3% for the simulation 3DW and 7.5% for the simulation 2DW, whereas the experimental value of turbulence intensity is about 7%. These discrepancies may be attributed to the differences in wake characteristics. Thus, the wake turbulence intensity and length scale have a remarkable effect.

Contours of the normalized phase-averaged production of TKE ($P_{TKE} = -\langle u_i' u_j' \rangle (\partial u_i' / \partial x_j)$) at a particular phase (which is characteristic of all the phases) are shown in Fig. 9 for the simulations 3DW and 2DW. The simulation 3DW predicts the trend and high production regions in a good degree of confidence. It is seen in Fig. 9 that the production throughout the wake passing cycle is confined to the path of the wake, owing to the coexistence of turbulent stress and shear in the wake fluid. The high production in the bow-apex region near the suction surface, which corresponds to the zone of high TKE, is resolved better by simulation 3DW when compared with the experiment [23]. This is attributed to the combined effect of a local concentration of vorticity by convection and a high level of turbulence. The simulation 2DW produces an inappropriate distribution with discrete and concentrated high levels of production, particularly in the apex region. This is due to a 2D solenoidal structure with very limited spanwise variation in migrating wakes within the blade passage, as seen in Fig. 6. Thus, the small-scale disturbances carried by the wake are needed to seed the production of TKE as in case 3DW. A very high level of TKE and production appears in the boundary

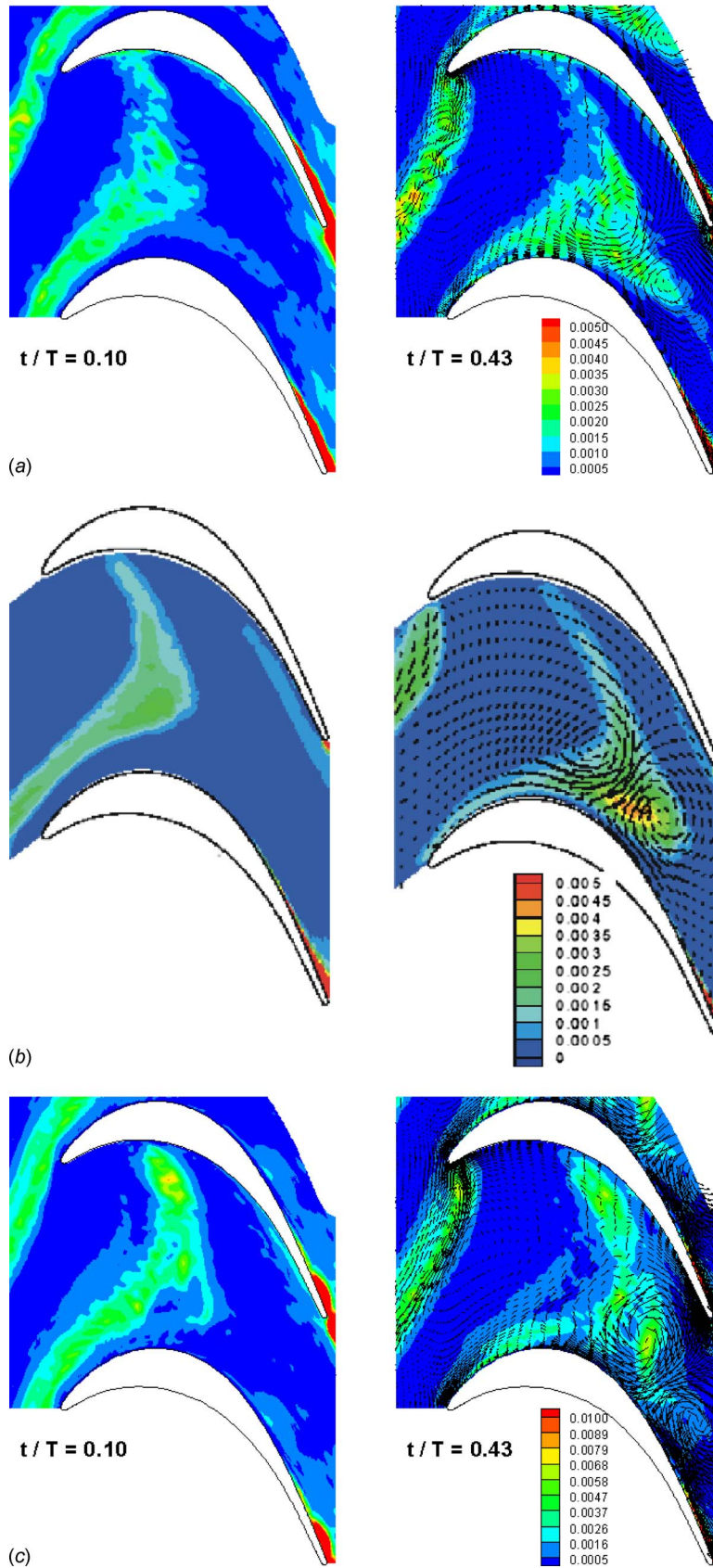


Fig. 8 Phase-averaged contours of nondimensional turbulent kinetic energy: (a) simulation 3DW, (b) experiment by Stieger and Hodson [23], and (c) simulation 2DW

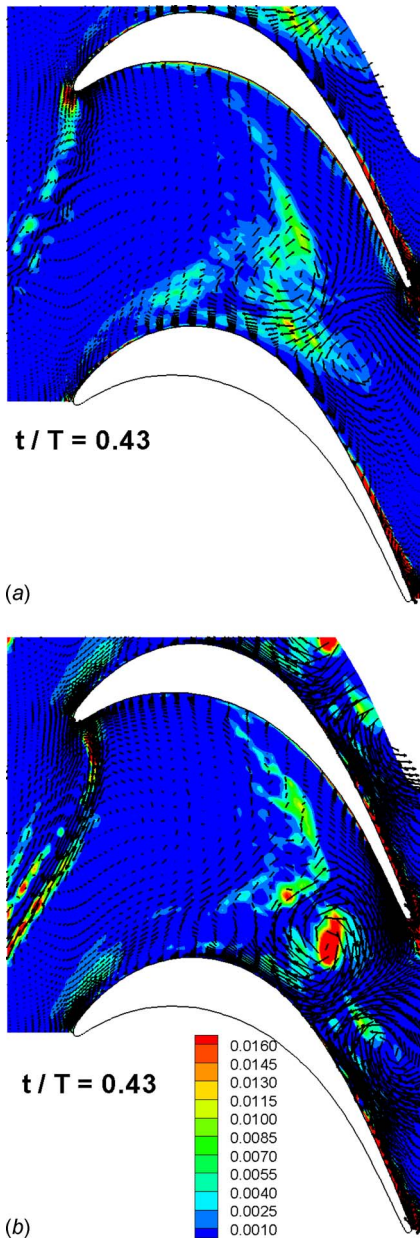


Fig. 9 Phase-averaged contours of production: simulations (a) 3DW and (b) 2DW

layer over the rear part of the suction surface: the effects of wake kinematics on the development of unsteady boundary layer. In the following sections, the growth mechanism of the shear layer due to receptivity to the external disturbances along the suction side of a LPT will be described.

3.3 Unsteady Boundary Layer. The distributions of time-averaged surface pressure coefficient [$C_p = (\bar{P}_{01} - \bar{P}) / (\bar{P}_{01} - \bar{P}_2)$] with the wake passing over the LPT blade from the simulations 3DW and 2DW are compared with the experiment [11] in Fig. 10. The agreement is good except near the leading edge of the suction surface for both cases. This may be attributed to the uncertainties of inflow angle due to the presence of wake-generating bars [15]. Experimental data reveal the existence of a laminar separation bubble over the rear part of the suction surface for flow without passing wakes. The bubble starts at $S/S_o = 0.6$ and extends to $S/S_o = 0.8$, where the separated layer undergoes a transition and reattaches by $S/S_o = 0.9$. The work of Schulte and Hodson [24]

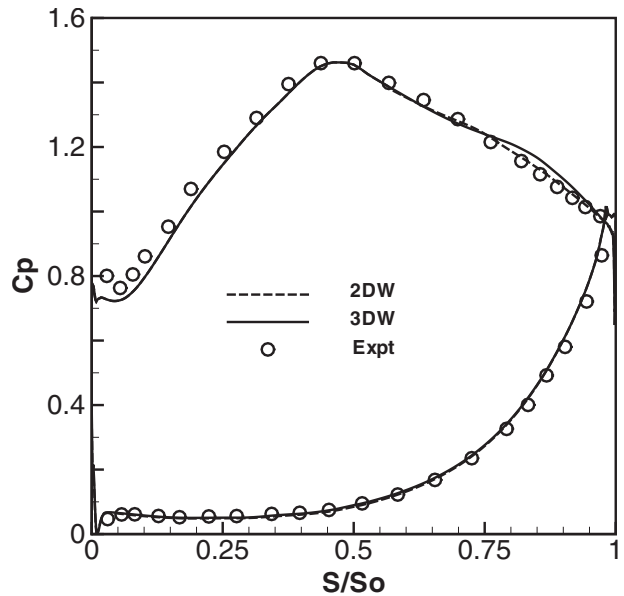


Fig. 10 Time-averaged C_p distributions on the T106 blade: present LES and experiment by Stieger et al. [11]

further indicated that the mean flow suggests a suppression of the flow separation due to the jet effect of passing wakes. The time-mean pressure distributions obtained from the simulation 3DW support the experiment [24]; however a trace of separation is felt over the region $0.75 < S/S_o < 0.90$. The suppression of the flow separation as a result of wake passing is very evident from the simulation 2DW that depicts a more close agreement with the experiment over the rear half of the suction surface.

To investigate the nature of the boundary layer in this region, the time-averaged velocity profiles with their derivatives at different streamwise locations along the rear half of the suction surface are shown in Fig. 11 for both the simulations. The simulation 3DW detects that the mean flow tends to be inflexional over the

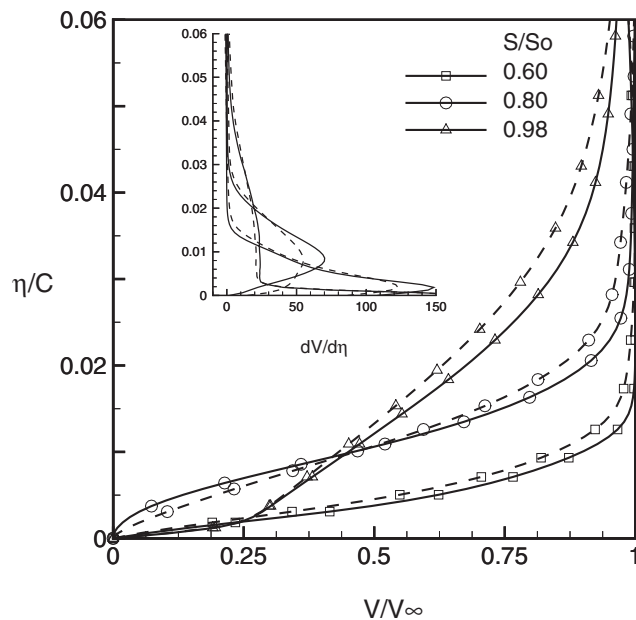


Fig. 11 Time-averaged velocity profiles and their derivatives at three sections along the suction surface: the firm line represents the simulation 3DW, and the dashed line represents the simulation 2DW

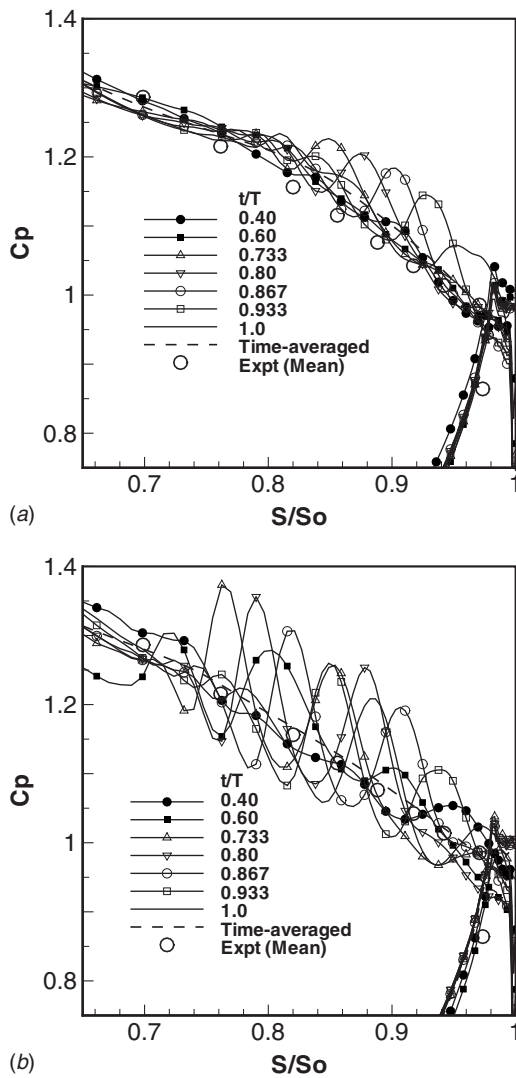


Fig. 12 Phase-averaged $\langle C_p \rangle$ distributions on the rear half of the suction surface: present LES and experiment by Stieger et al. [11], simulations (a) 3DW and (b) 2DW

region $0.70 < S/S_o < 0.85$, and then it becomes a fully developed turbulentlike flow downstream. Although the nature of the mean flow appears the same, the simulation 2DW predicts an attached layer along the rear half of the suction surface. Thus, the mean pressure distributions on the suction surface are in conformity with the velocity profiles.

To illustrate the unsteady surface pressure, the phase-averaged distributions of pressure coefficients [$\langle C_p \rangle = (\langle P_{01} \rangle - \langle P \rangle) / (\langle P_{01} \rangle - \langle P_2 \rangle)$] over the rear half of the suction surface at a series of time instants through the wake passing cycle are shown in Figs. 12(a) and 12(b) for the simulations 3DW and 2DW. The time-averaged values of C_p from the experiment [11] are also superimposed. A remarkable change occurs in the distributions of $\langle C_p \rangle$ as the wake convects over the steady-flow separation region on the suction surface. A series of large-amplitude pressure oscillations are observed on the suction surface for $t/T > 0.65$. The peak-to-valley amplitude of these pressure fluctuations is about $\Delta \langle C_p \rangle = 0.15$ for the simulation 3DW, whereas $\Delta \langle C_p \rangle = 0.29$ for the simulation 2DW. The corresponding experimental value is 0.3. Thus, these large-amplitude pressure fluctuations occurring on the suction surface are dependent on the wake deficit and, so, on the length scale of the passing wake. Furthermore, the process of phase averaging

eliminates random fluctuations, and thus, the pressure oscillations reflected in the phase-averaged results are due to deterministic coherent structures in the flow.

Contours of the phase-averaged spanwise vorticity illustrating the difference in flow structures are presented in Figs. 13(a) and 13(b) for the simulations 3DW and 2DW as the wake passes over the rear half of the suction surface. The negative jet effect of the wake initiates a rollup of the separated boundary layer via the KH mechanism, and a large vortex associated with instantaneous backflow appears. Once a vortex appears, it convects downstream at a speed lower than the local freestream that generates further rollup vortices downstream, which is very evident in Fig. 13(b) (the convection of a vortex is marked by 1, 2, and 3). In the simulation 2DW with high wake deficit, the rollup of the separated shear layer starts earlier as compared with the simulation 3DW. This may cause a shift in phase for the corresponding events in the boundary layer evolution on the suction surface between the two simulations. It also appears that the vortex rolls are bigger in case 2DW, resulting in higher oscillation of pressure distribution.

To illustrate further the effect of wake structure on the evolution of boundary layer, the streamwise periodic velocity fluctuations $\langle u \rangle - \bar{u}$ along the rear half of the suction surface at a section within the inner part of the boundary layer ($\eta/C = 0.003$) are presented in Fig. 14 for both the simulations. The appearance of dips in the profile of $\langle u \rangle - \bar{u}$ can be related to the coherent vortices and the magnitude of pressure oscillations ($P \approx V^2$) on the suction surface. The larger dips in the profile of $\langle u \rangle - \bar{u}$ for the simulation 2DW confirm the formation of bigger rollup vortices resulting in higher pressure oscillations, as seen in Fig. 12. For the simulation 3DW, a dip in $\langle u \rangle - \bar{u}$ appears near $S/S_o = 0.8$ at $t/T = 0.6$, which is the initiation of a rollup vortex. Whereas for the simulation 2DW, two vortices appear at the same phase near $S/S_o = 0.72$ and 0.8 . By the time $t/T = 0.8$, three prominent vortices are created for the simulation 2DW, while two vortices are formed for the simulation 3DW. As the wake moves past the rear half, three rollup vortices are finally appreciable for the simulation 3DW. Thus, the discussion linking Figs. 12–14 confirms that the KH instability of the shear layer along the rear half of the suction surface is induced by the low-frequency disturbances associated with the mean part of the impinging wake. The formation and strength of these vortices and thus the amplitude of pressure fluctuations can be related to the strength of the negative jet illustrating an inviscid phenomenon.

The growth of disturbances and development of three-dimensional motions can be monitored by the evolution of velocity fluctuations. The streamwise, blade-normal, and spanwise components of the time-averaged velocity fluctuations (rms) at two sections of the boundary layer along the rear half of the suction surface are shown in Fig. 15 for both simulations. It should be noted that the mean boundary layer thickness over the rear half of the suction surface varies from 3% to 5% of the chord. Few representative phase-averaged velocity fluctuations (streamwise) at $t/T = 0.6, 0.8$, and 0.933 as the wake convects over the inflexional region are superimposed. Upstream of $S/S_o = 0.75$, the rms values of velocity fluctuations tend to have the same level of the freestream, indicating the flow to be laminar for both cases. For the simulation 3DW, the velocity fluctuations increase rapidly in the second half of the steady-flow separation $0.80 < S/S_o < 0.90$, reaching a maximum at $S/S_o = 0.92$, near the point of mean reattachment, indicating that three-dimensional motion and nonlinear interaction lead to breakdown to turbulence in the second half of the separated boundary layer. The velocity fluctuations tend to drop slowly downstream of $S/S_o = 0.92$, reflecting the end of transition [3,9]. The trend is the same for the simulation 2DW, although enhancement of streamwise velocity fluctuations is less severe, which may be due to the 2D wake turbulence. Anisotropy is high within the inner part of the shear layer with a very promi-

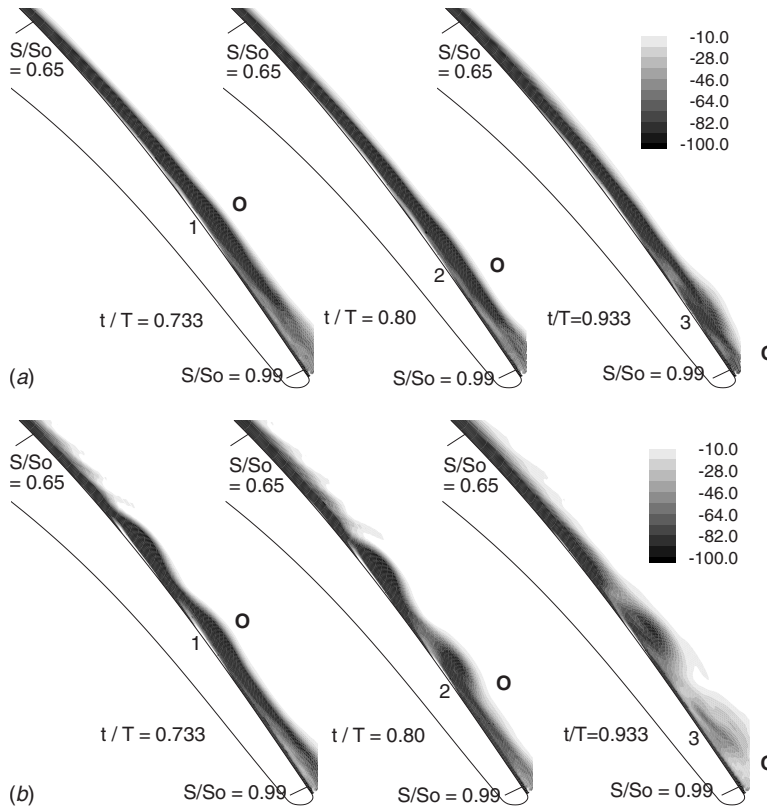


Fig. 13 Phase-averaged spanwise vorticity on the rear half of the suction surface: simulations (a) 3DW and (b) 2DW (the location of the wake centerline is marked by a circle)

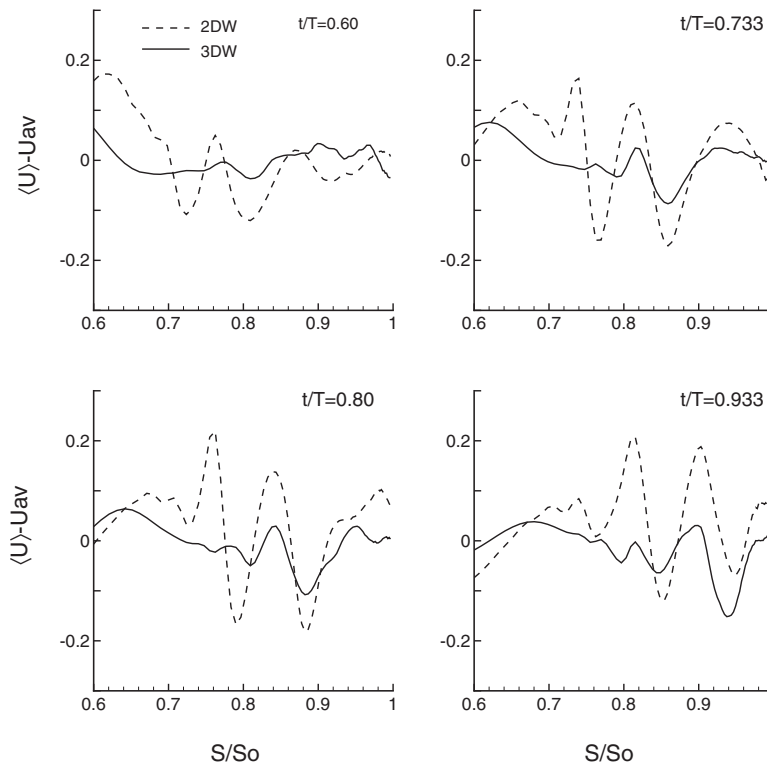


Fig. 14 Streamwise component of phase-averaged velocity perturbations $\langle u \rangle - \bar{u}$ along a section of boundary layer on the suction surface

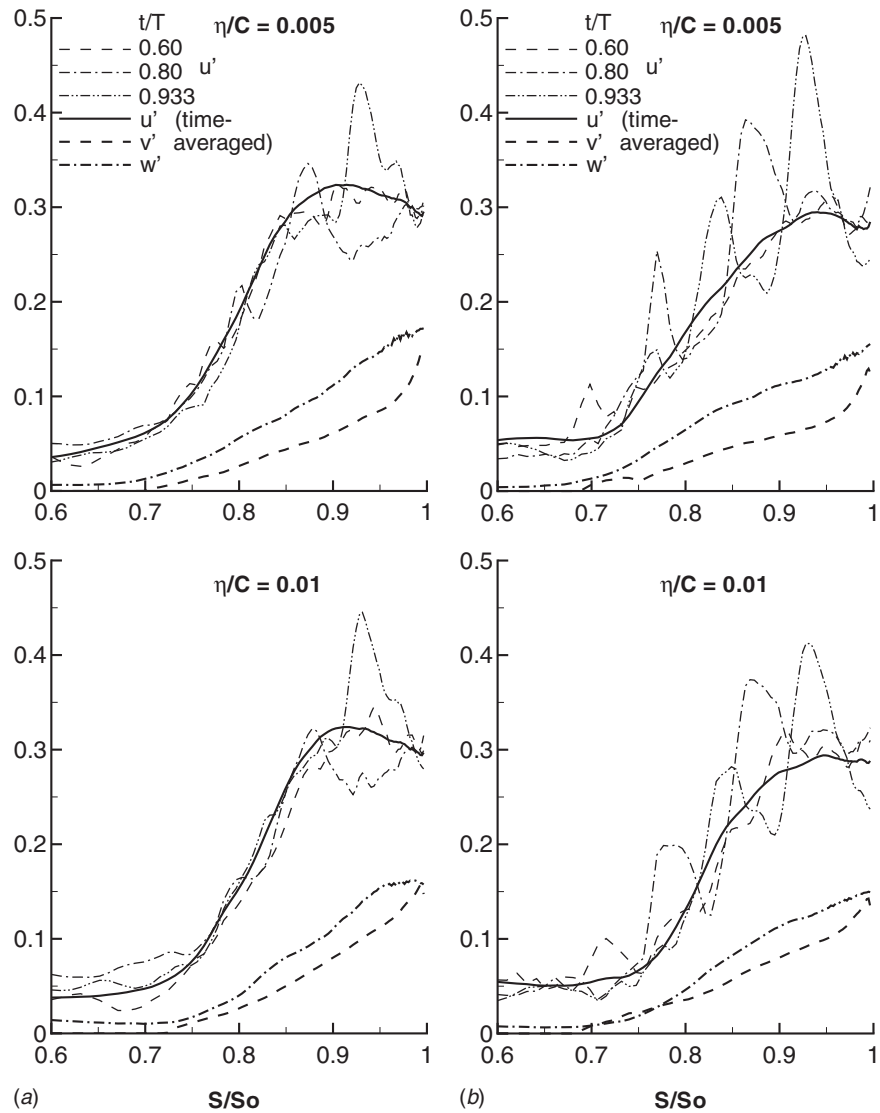


Fig. 15 Velocity fluctuations (rms and phase averaged) at two sections of boundary layer along the rear half of the suction surface: simulations (a) 3DW and (b) 2DW

nent streamwise component of velocity fluctuation; a similar trend was reflected in a DNS [10]. What is interesting is that the streamwise evolutions of phase-averaged velocity fluctuations demonstrate large oscillations as the wake migrates over the steady-flow separated region. This is attributed to the appearance of the large-scale rollup vortices via excitation of the shear layer. The simulation 2DW produces larger oscillation, illustrating the formation of bigger KH rolls resulting from combined effects of high wake turbulence and velocity deficit.

The isosurface of the spanwise component of instantaneous vorticity is plotted in Figs. 16(a) and 16(b) for the two simulations to visualize the three-dimensional flow structures and the internal growth mechanism of shear layer over the rear half of the suction surface. When the wake is ahead of the separation region, a number of longitudinal streaky structures appear, as reported earlier [13]. Downstream of $S/S_o=0.9$, they break down into small and irregular structures. Very similar flow structures were observed while studying the transition mechanism of a laminar separation bubble through a DNS [25]. Thus, small perturbations are amplified due to the separated boundary layer, and then the nonlinear interactions and the vortex stretching process create these streaks, which are characteristics of transition. When the wake crosses over the rear half of the suction surface ($t/T > 0.7$), Figs. 16(a)

and 16(b) illustrate the formation of 3D vortex loops via excitation of the separated layer by the impinging wake. It is interesting to note the spanwise distortion of a vortex loop during its streamwise movement. Once formed, they convect downstream and grow owing to nonlinear interactions before breaking down to small structures. These 3D vortex loops influence the transition that becomes time dependent. It should be noted that in contrast to the wake structure within the blade passage for the simulation 2DW, the 2D turbulence in the wake is able to seed the small-scale fluctuations within the boundary layer in the spanwise direction on the rear half of the suction surface although the levels of fluctuation, flow structures, and the locations of vortices are different in minute details for the two cases.

Figures 17(a) and 17(b) show the phase-averaged contours of nondimensional TKE on the rear half of the suction surface as the wake migrates over the steady-flow separated region for both simulations. The levels of TKE illustrate that the boundary layer is transitional in the region $0.75 < S/S_o < 0.90$, and then it becomes turbulent. Further at $t/T=0.733$, the phase-averaged vorticity (Fig. 13(a)) depicts the appearance of a rollup vortex via the KH instability of the shear layer (position marked by 1) for the simulation 3DW, whereas the simulation 2DW creates two KH rolls at the same time (Fig. 13(b)). The corresponding contours of TKE (Fig.

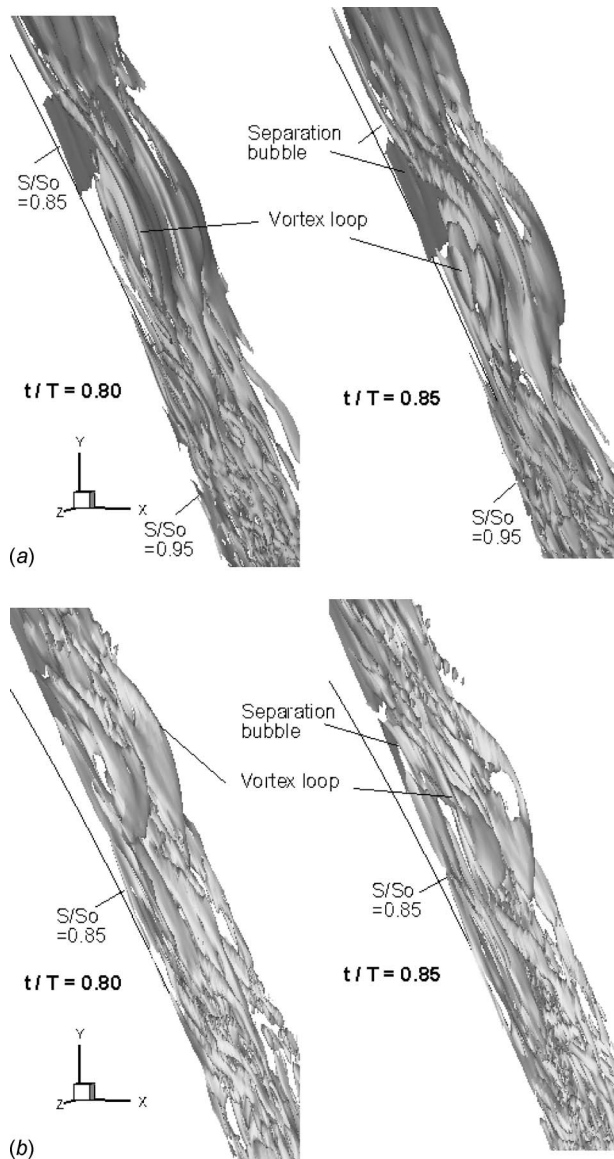


Fig. 16 Instantaneous isosurface of spanwise component of vorticity illustrating the formation of 3D vortex loops on the rear half of the suction surface: simulations (a) 3DW and (b) 2DW

17) do not show elevated values at the locations, illustrating that rollup of shear layer initiates with the laminar/transitional boundary layer. However, TKE contours for the simulation 2DW reflect the formation of larger rolls. At $t/T=0.80$ and 0.933 , the convection and growth of vortices are observed by the corresponding TKE contours with local concentration (the locations marked 2 and 3). As anticipated the simulation 2DW depicts larger oscillation in TKE, illustrating the formation of bigger KH rolls because of high velocity deficit and inlet turbulence. Thus, the wake structure has a strong influence on the rollup vortices and generation of turbulence along the suction surface of a high-lift LPT blade, the effect of the interaction of the passing wake with the separated boundary layer.

The phase-averaged contours of the production of TKE on the rear half of the suction surface are depicted in Figs. 18(a) and 18(b) for both simulations. Similar to the evolutions of TKE, as seen in Fig. 17, the production contours illustrate local concentration of high values in the corresponding location. The production occurs when turbulence extracts work from the mean flow. This

occurs in regions of high turbulent stress and high spatial velocity gradient, which are aligned in the same direction. Hence, high production on the suction surface can be considered as the combined effect of a local concentration of vorticity by the KH rolls and a growing level of turbulence in the boundary layer. For $t/T \geq 0.8$, the simulation 2DW shows discrete nature of high local production conforming to the locations of rollup vortices and illustrates lack in uniformity over the last 20% of the rear half as compared with the simulation 3DW. The enhanced production in the case of the 2D wake is mainly because of local concentration of vorticity associated with larger rollups. Although in the absence of spanwise anisotropy, the 2D wake triggers turbulence in the boundary layer, the nature of small-scale eddy motion has not been resolved properly. The simulation 3DW produces an appropriate distribution of production, illustrating the appearance of rollup vortices followed by the production of TKE inside the KH rolls. It further reflects that the boundary layer is transitional over the last 20% of the suction surface.

To illustrate further, the time-mean profiles of TKE and the production at different locations over the rear half of the blade are presented in Fig. 19 for both simulations. The peak of production occurs in the central region of the boundary layer, i.e., away from the wall. The high production in the central region of the boundary layer is attributed to the locus of concentration of spatial velocity gradient due to migrating rollup vortices. Downstream of $S/S_o=0.95$, the time-averaged peak of production and TKE shifts toward the wall and drops a bit, illustrating the end of transition. Wu et al. [9] observed a similar trend while studying boundary layer transition by periodic migrating wakes over a flat plate through DNS. What is interesting is that even with lower wake deficit and inlet turbulence level, the simulation 3DW produces higher values (maximum level) of mean TKE by 17% and production by 35% as compared with the simulation 2DW. Thus, the small-scale eddies play a vital role in generating turbulence and transition of boundary layer.

4 Conclusions

The response of an inflexional boundary layer over the suction surface of a high-lift LPT blade subjected to the periodic passing wake of different eddy structures is presented through LES. A periodic wake has a mean effect, which can be described by the low-frequency velocity deficit, and the effect of small-scale fluctuations. Two different wake patterns—one with a wake deficit of $0.25V_1$ and a level of turbulence intensity of about 10%, and the other with a wake deficit of $0.475V_1$ having no fluctuations in the spanwise direction—are used at the cascade inlet plane for the successor 3D simulation of cascade with wake passing. The kinematics of the wake illustrates that even after severe distortion and stretching, it preserves the solenoidal structures when a 2D wake is imposed at the cascade inlet. The resolved level of TKE and production within the blade passage agrees relatively well with the experiment when a wake with 3D fluctuations is used.

The KH instability of the separated shear layer, which evolves the large-scale vortex loops over the rear half of the suction surface, is triggered by the low-frequency mean effect of the convective wake. Thus, the magnitude of the pressure oscillations along the rear half of the suction surface depends on the velocity deficit of the migrating wake and has no relation to the small-scale fluctuations. After instability, the transition to turbulence of the boundary layer, which is the result of nonlinear interactions of wake turbulence and the generation of production inside the KH rolls, largely depends on the small-scale fluctuations carried by the wake.

Nomenclature

- C = chord
- C_x = axial chord
- D = bar diameter

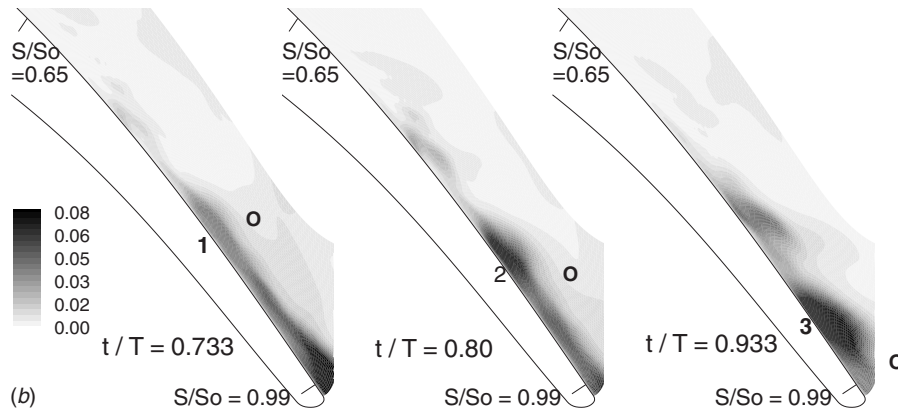
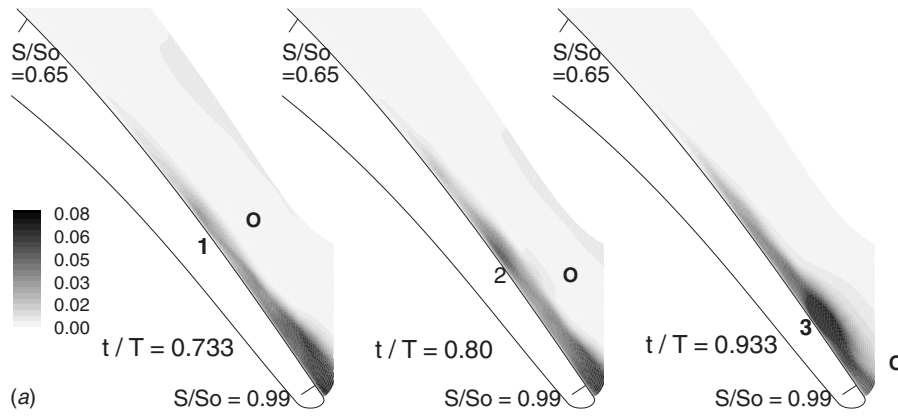


Fig. 17 Phase-averaged contours of nondimensional TKE on the rear half of the suction surface during the interaction of wake and separated boundary layer: simulations (a) 3DW and (b) 2DW (the location of the wake centerline is marked by a circle)

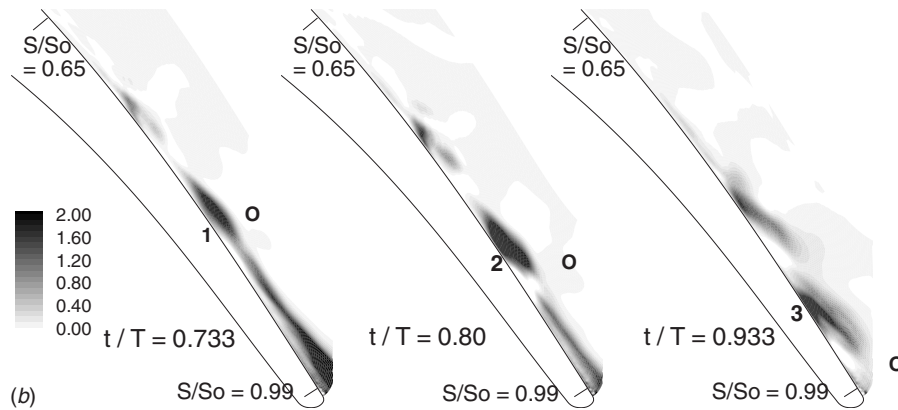
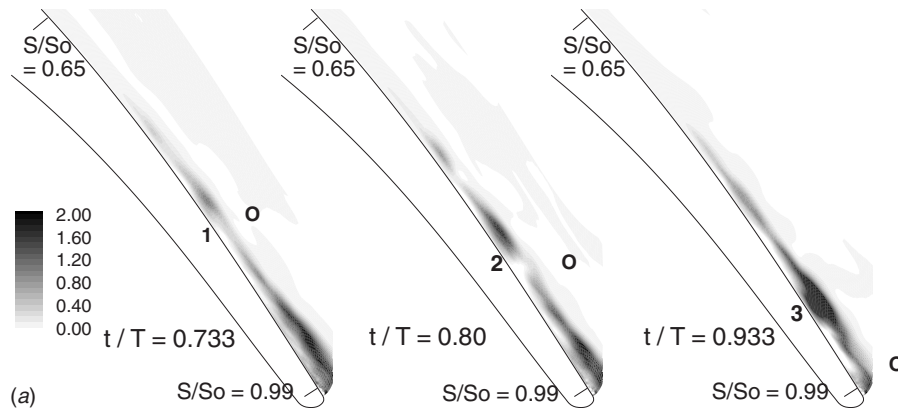


Fig. 18 Phase-averaged contours of nondimensional production on the rear half of the suction surface during the interaction of wake and separated boundary layer: simulations (a) 3DW and (b) 2DW

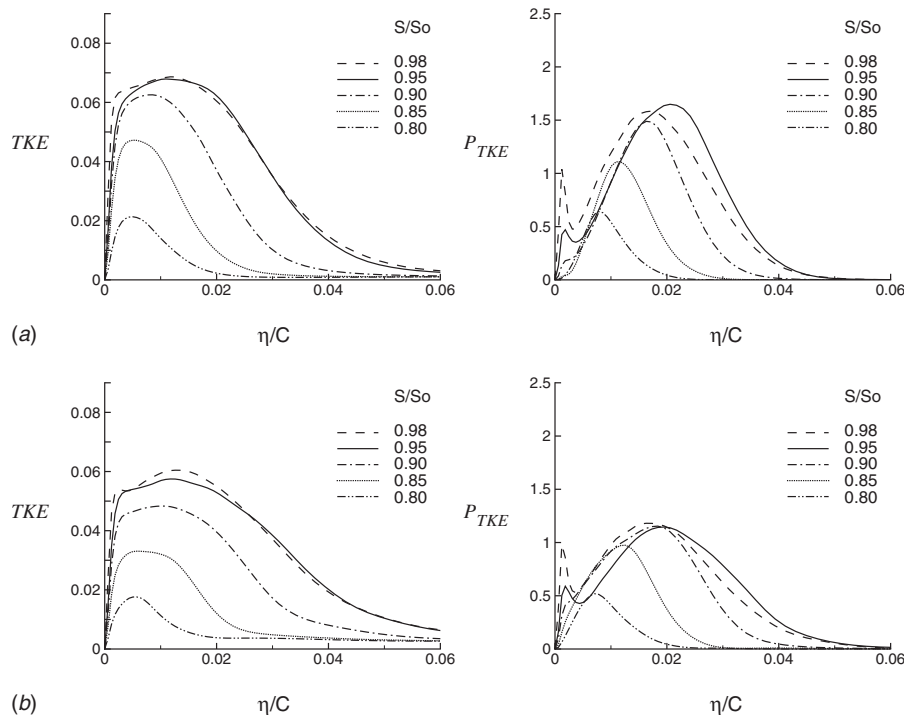


Fig. 19 Time-averaged profiles of TKE and production on the rear half of the suction surface: simulations (a) 3DW and (b) 2DW

f = bar passing frequency
 Re = Reynolds number = $V_1 C_X / \nu$
 S = distance along the blade surface
 So = suction surface length
 t = time
 T = bar passing period
 u', v', w' = velocity fluctuations (rms)
 U_b = bar speed or blade speed
 V = velocity
 V_x = axial velocity
 x, y, z = Cartesian coordinates
 $\Delta x^+, \Delta y^+, \text{ and } \Delta z^+$ = mesh size in wall units
 η = wall-normal axis
 ν = kinematic viscosity

Subscripts

0 = total
 1 = inlet
 2 = exit
 is = isentropic
 ∞ = freestream

References

- [1] Hunt, J. C. R., and Durbin, P. A., 1999, "Perturbed Vortical Layers and Shear Sheltering," *Fluid Dyn. Res.*, **24**, pp. 375–404.
- [2] Meyer, R. X., 1958, "The Effects of Wakes on the Transient Pressure and Velocity Distributions in Turbomachines," *ASME J. Basic Eng.*, **80**, pp. 1544–1552.
- [3] Mayle, R. E., 1991, "The Role of Laminar Turbulent Transition in Gas Turbine Engines," *ASME J. Turbomach.*, **113**, pp. 509–537.
- [4] Walker, G. J., 1993, "The Role of Laminar Turbulent Transition in Gas Turbine Engines: A Discussion," *ASME J. Turbomach.*, **115**, pp. 207–217.
- [5] Halstead, D. E., Wisler, D. C., Okiishi, T. H., Walker, G. J., Hodson, H. P., and Shin, H.-W., 1997, "Boundary Layer Development in Axial Compressors and Turbines—Part 1: Composite Picture," *ASME J. Turbomach.*, **119**, pp. 114–127.
- [6] Halstead, D. E., Wisler, D. C., Okiishi, T. H., Walker, G. J., Hodson, H. P., and Shin, H.-W., 1997, "Boundary Layer Development in Axial Compressors and Turbines—Part 2: Compressors," *ASME J. Turbomach.*, **119**, pp. 426–444.
- [7] Halstead, D. E., Wisler, D. C., Okiishi, T. H., Walker, G. J., Hodson, H. P., and Shin, H.-W., 1997, "Boundary Layer Development in Axial Compressors and Turbines—Part 3: LP Turbines," *ASME J. Turbomach.*, **119**, pp. 225–237.
- [8] Halstead, D. E., Wisler, D. C., Okiishi, T. H., Walker, G. J., Hodson, H. P., and Shin, H.-W., 1997, "Boundary Layer Development in Axial Compressors and Turbines—Part 4: Computations and Analyses," *ASME J. Turbomach.*, **119**, pp. 128–139.
- [9] Wu, X., Jacobs, R. G., Hunt, J. R. C., and Durbin, P. A., 1999, "Simulation of Boundary Layer Transition Induced by Periodically Passing Wakes," *J. Fluid Mech.*, **398**, pp. 109–153.
- [10] Wu, X., and Durbin, P. A., 2001, "Evidence of Longitudinal Vortices Evolved From Distorted Wakes in Turbine Passage," *J. Fluid Mech.*, **446**, pp. 199–228.
- [11] Stieger, R., Hollis, D., and Hodson, H., 2003, "Unsteady Surface Pressures Due to Wake Induced Transition in Laminar Separation Bubble on a LP Turbine Cascade," *ASME Paper No. GT2003-38303*.
- [12] Sarkar, S., and Voke, P. R., 2006, "Large-Eddy Simulation of Unsteady Surface Pressure Over a LP Turbine Due to Interactions of Passing Wakes and Inflectional Boundary Layer," *ASME J. Turbomach.*, **128**, pp. 221–231.
- [13] Sarkar, S., 2007, "The Effects of Passing Wakes on a Separating Boundary Layer Along a Low-Pressure Turbine Blade Through Large-Eddy Simulation," *Proc. Inst. Mech. Eng., Part A*, **221**, pp. 551–564.
- [14] Wissink, J. G., Rodi, W., and Hodson, H., 2006, "Influence of Disturbances Carried by Periodically Incoming Wakes on the Separating Flow Around a Turbine Blade," *Int. J. Heat Fluid Flow*, **27**, pp. 721–729.
- [15] Stadtmüller, P., 2001, "Investigation of Wake-Induced Transition on the LP Turbine Cascade T106 A-EIZ," *DFG-Verbundprojekt Fo 136/11, Version 1.0*, University of the Armed Forces Munich, Germany.
- [16] Yang, Z., and Voke, P. R., 2000, "Large-Eddy Simulation of Separated Leading-Edge Flow in General Coordinate," *Int. J. Numer. Methods Eng.*, **49**, pp. 681–696.
- [17] Yang, Z. Y., and Voke, P. R., 2001, "Large-Eddy Simulation of Boundary Layer Separation and Transition at a Change of Surface Curvature," *J. Fluid Mech.*, **439**, pp. 305–333.
- [18] Wissink, J. G., 2003, "DNS of Separating, Low Reynolds Number Flow in a Turbine Cascade With Incoming Wakes," *Int. J. Heat Fluid Flow*, **24**, pp. 626–635.
- [19] Norberg, C., 2003, "Fluctuating Lift on a Circular Cylinder: Review and New Measurements," *J. Fluids Struct.*, **17**, pp. 57–96.
- [20] Williamson, C. H. K., and Roshko, A., 1990, "Measurements of Base Pressure in the Wake of a Cylinder at Low Reynolds Number," *Z. Flugwiss. Weltraumforsch.*, **14**, pp. 38–46.
- [21] Mittal, R., and Balachandrar, S., 1995, "Effect of Three-Dimensionality on the Lift and Drag of Nominally Two-Dimensional Cylinders," *Phys. Fluids*, **7(8)**, pp. 1841–1865.

- [22] Ghosal, S., and Rogers, M. M., 1997, "A Numerical Study of Self-Similarity in a Turbulent Plane Wake Using Large-Eddy Simulation," *Phys. Fluids*, **9**, pp. 1729–1739.
- [23] Stieger, R. D., and Hodson, H. P., 2005, "The Unsteady Development of a Turbulent Wake Through a Downstream Low-Pressure Turbine Blade Passage," *ASME J. Turbomach.*, **127**, pp. 388–394.
- [24] Schulte, V., and Hodson, H. P., 1998, "Unsteady Wake-Induced Boundary Layer Transition in High Lift LP Turbine," *ASME J. Turbomach.*, **120**, pp. 28–35.
- [25] Alam, M., and Sandham, N. D., 2000, "Direct Numerical Simulation of Short Laminar Separation Bubbles With Turbulent Reattachment," *J. Fluid Mech.*, **410**, pp. 1–28.

Yao-Hsien Liu

Michael Huh

Turbine Heat Transfer Laboratory,
Texas A&M University,
College Station, TX 77843-3123

Dong-Ho Rhee

Korea Aerospace Research Institute,
Daejeon 305-333, Korea

Je-Chin Han

Turbine Heat Transfer Laboratory,
Texas A&M University,
College Station, TX 77843-3123
e-mail: jc-han@tamu.edu

Hee-Koo Moon

Solar Turbines Inc.,
San Diego, CA 92186

Heat Transfer in Leading Edge, Triangular Shaped Cooling Channels With Angled Ribs Under High Rotation Numbers

The gas turbine blade/vane internal cooling is achieved by circulating compressed air through the cooling channels inside the turbine blade. Cooling channel geometries vary to fit the blade profile. This paper experimentally investigated the rotational effects on heat transfer in an equilateral triangular channel ($D_h = 1.83$ cm). The triangular shaped channel is applicable to the leading edge of the gas turbine blade. Angled 45 deg ribs are placed on the leading and trailing surfaces of the test section to enhance heat transfer. The rib pitch-to-rib height ratio (P/e) is 8 and the rib height-to-channel hydraulic diameter ratio (e/D_h) is 0.087. Effect of the angled ribs under high rotation numbers and buoyancy parameters is also presented. Results show that due to the radially outward flow, heat transfer is enhanced with rotation on the trailing surface. By varying the Reynolds numbers (10,000–40,000) and the rotational speeds (0–400 rpm), the rotation number and buoyancy parameter reached in this study are 0–0.58 and 0–1.9, respectively. The higher rotation number and buoyancy parameter correlate very well and can be used to predict the rotational heat transfer in the equilateral triangular channel. [DOI: 10.1115/1.3072493]

1 Introduction

Modern gas turbine blades operate at high temperatures to improve efficiency. Figure 1 shows that the internal cooling passage geometry varies along the blade span. Rib turbulators are typically placed on the cooling passage leading and trailing surfaces to enhance heat transfer. Many modern cooling techniques are discussed in Ref. [1]. The study of the gas turbine blade internal cooling began with stationary rectangular cooling channels with the ribs placed on the walls of the cooling passage. Rib turbulators are widely used inside the blade cooling passages. Ribs trip the boundary layer of the coolant flow and enhance heat transfer at the cost increased pressure drop. The rib effects in the stationary channel as well as in the rotating channels have been studied by several research groups. Rib spacing, rib height, rib angle, and the geometry of the ribs all affect the rib performance. Han [2] measured the heat transfer and friction factor in a square duct with several rib configurations. Han [3] then extended the study to the heat transfer and pressure drop in ribbed channels with five different aspect ratios ($AR=4:1$, $2:1$, $1:1$, $1:2$, and $1:4$). The results in the rectangular channel are comparable to the Dittus–Boelter correlation for the turbulent flow in a smooth tube by using the hydraulic diameter of the rectangular channel. Han and Zhang [4] studied the effect of rib-angle orientation on local mass transfer distribution in a three-pass rib-roughened square channel. They concluded that the angled ribs generally provide higher mass transfer coefficients than the transverse ribs. Moreover, the parallel ribs give higher mass transfer than the crossed ribs. Taslim and Lengkon [5] investigated the staggered 45 deg angled ribs in a square channel. Three rib spacing-to-height ratios (5, 8.5, and 10), each with three height-to-passage hydraulic diameter ratios (0.133, 0.167, and 0.25), were tested. They found that for the 45

deg angled ribs in the staggered arrangements, the case for $P/e = 10$ and $e/D_h = 0.133$ had the best thermal performance. Taslim and Spring [6] used a liquid crystal technique to study the effects of rib profile, spacing, and blockage on the heat transfer coefficients in two rectangular channels with $AR=0.5$ and 0.55 . They found that the sensitivity of the Nusselt number on P/e decreases as e/D_h increases. Liu et al. [7] studied the rib spacing effects ($P/e=10, 7.5, 5$, and 3) in a rotating rectangular ($AR=1:2$) channel. They found that the very close spacing of $P/e=3$ had the best thermal performance.

The triangular cooling channel is normally applied near the leading edge of the turbine blade to fit the blade profile. The measurements are also in good agreement with the correlations developed for the turbulent tube flow in the smooth tube. Metzger and Vedula [8] experimentally measured the heat transfer in triangular channels with angled ribs on two walls. They studied three different rib angles and three different sets of rib orientations. For all the test configurations, 60 deg angled ribs produce higher heat transfer than the 30 deg angled ribs, and $P/e=7.5$ rib spacing yield the best thermal performance. Ahn and Son [9] studied the heat transfer and pressure drop in a roughened equilateral triangular channel with $P/e=4, 8$, and 16 . They concluded that the $P/e=8$ has the best thermal performance with the Reynolds numbers from 10,000 to 70,000. Haasenritter and Weigand [10] performed a computational study of the heat transfer in a rib-roughened triangular channel. The results show good agreement with the experimental data from Ref. [8]. Lee et al. [11] measured the heat transfer and pressure drop in a rotating equilateral triangular channel with three different rib arrangements: 45 deg, 90 deg, and 135 deg. They showed that the thermal performance for 45 deg and 135 deg angled ribs is very similar and both higher than the 90 deg ribs. Dutta et al. [12] studied the heat transfer in a two-pass rotating triangular duct. They studied two channel orientations to the direction of rotation. For the radially outward flow in the first pass, the Nusselt number ratios increase with rotation on the trailing wall and reduce on the leading wall. Zhang et al. [13] tested the heat transfer in a triangular duct with full and partial

Contributed by the International Gas Turbine Institute of ASME for publication in the JOURNAL OF TURBOMACHINERY. Manuscript received August 29, 2008; final manuscript received September 21, 2008; published online July 9, 2009. Review conducted by David Wisler. Paper presented at the ASME Turbo Expo 2008: Land, Sea and Air (GT2008), Berlin, Germany, June 9–13, 2008.

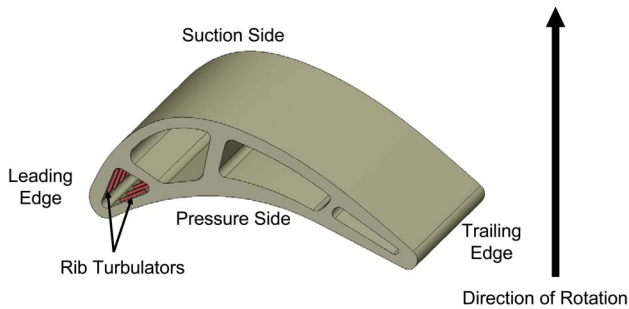


Fig. 1 Internal gas turbine blade cooling passage

ribbed walls. They found that the heat transfer coefficients and friction factors in triangular ducts with partial ribbed walls (90 deg or 45 deg ribs) were 10% higher than those with fully ribbed walls.

The entrance geometry also affects the heat transfer distribution inside cooling channels. Kays and Crawford [14] summarized the works that consider the heat transfer in tubes with various entrance conditions. The Nusselt number in tubes with fully developed turbulent flow is also included. The widely accepted Dittus/Boelter–McAdams correlation for the fully developed turbulent flow in circular tubes can also be applied to the flow through channels with noncircular cross section. Wright et al. [15] studied the effect of entrance geometry on the heat transfer enhancement in a rotating rectangular channel (AR=4:1). They showed that with the simultaneous development of both the hydrodynamic and thermal boundary layers, the Nusselt number ratios may not reach the fully developed values predicted by the Dittus/Boelter–McAdams correlation. The entrance geometry with redirected sharp bend by Liu et al. [16] and the sudden contraction by Wright et al. [17] both showed that the heat transfer enhancement is higher than the fully developed flow condition.

In the actual turbine, the blade is rotating and the effect of rotation in the cooling channels should be considered. The secondary flow induced by rotation has a great impact in the smooth channel as well as in the ribbed channel. Wagner et al. [18] performed heat transfer measurements inside a smooth square channel with radial outward flow in the first pass. The rotation number ranged from 0.00 to 0.48 in their studies. Wagner et al. [19] continued to investigate the heat transfer inside the second and third passages of the smooth square channel. The results from Refs. [18,19] showed that both the rotation number and density ratio caused large changes in heat transfer for radially outward flow but relatively small changes for radially inward flow. Johnson et al. [20] performed the heat transfer measurement in a rotating square channel with ribs skewed to the flow and compared the results from the smooth channel. They showed that the heat transfer with skewed ribs is less sensitive to the buoyancy than the heat transfer inside the smooth channel or normal ribbed channel. Fu et al. [21] studied the buoyancy effects in five different aspect ratio channels (AR=4:1, 2:1, 1:1, 1:2, and 1:4) with two channel orientations (90 deg and 45 deg or 135 deg). The rotation numbers varied from 0.0 to 0.3. They showed that increasing the local buoyancy parameter increases the Nusselt number ratio on the trailing surface and decreases the Nusselt number ratio on the leading surface in the first pass for all channels.

The effect of rotation needs to be tested under high rotation numbers in order to simulate the actual engine condition. Zhou et al. [22] investigated the heat transfer in a 4:1 channel under high rotation numbers from 0 to 0.6. They concluded that there is a critical rotation number where the trend of the heat transfer enhancement begins to reverse. Liou et al. [23] investigated the heat transfer in a rectangular channel (AR=1:2) with 45 deg angled ribs under high rotation numbers from 0 to 2. They found that the 45 deg staggered ribs generated overall heat transfer enhancement

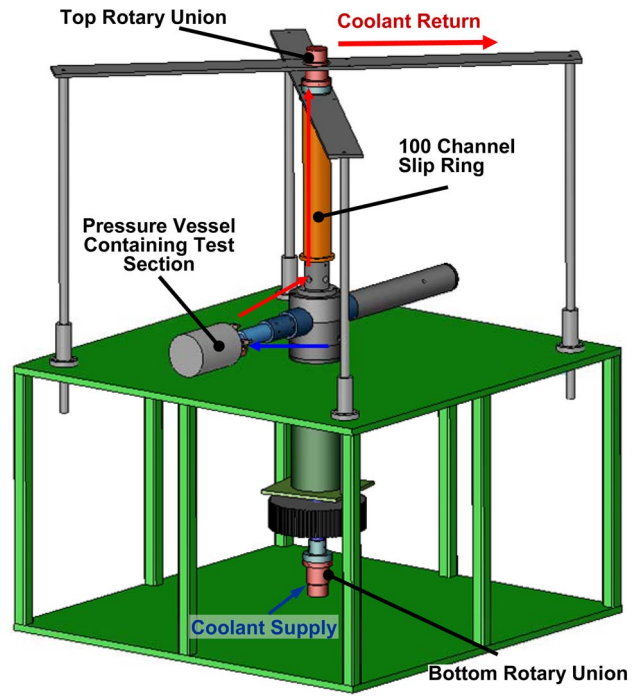


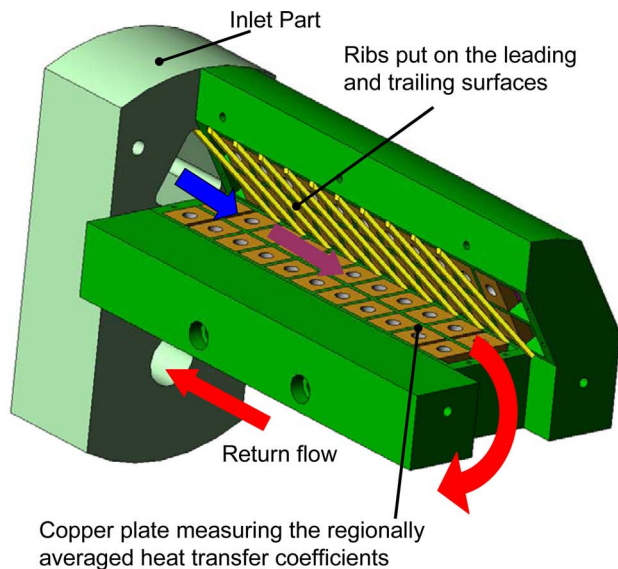
Fig. 2 Rotating facility with the test section

of 1.6–4.3 times higher than the Dittus–Boelter correlation in the Reynolds number range of 5000–15,000. Liu et al. [16] also studied the heat transfer in a two-pass rectangular (AR=1:4) channel under high rotation numbers from 0 to 0.67. They found that the buoyancy parameter is also good to quantify the effect of rotation. Wright et al. [17] conducted the heat transfer measurements in a wedge-shaped trailing edge channel under high rotation numbers from 0 to 1.0. It shows that the nondimensional rotation number and buoyancy parameter not only can be used in the rectangular channel but also valid in this wedge-shaped channel.

Based on the data available in open literature, the objective of the current study is to investigate the heat transfer distribution in the equilateral triangular channel under stationary and rotating conditions. Since the thermal load varies near the leading edge of the turbine blade, each surface of the channel is divided into two regions to provide individual heat transfer distribution during the tests. The ribs are skewed 45 deg to the mainstream flow and this configuration provides higher heat transfer enhancement near the leading edge of the blade where the thermal load is high. Although the effect of rotation has been studied by several groups, however, most of the data available in open literature are low rotation number and low buoyancy parameter. The results on the high rotation number and buoyancy parameter are still very limited. This study also investigates the heat transfer in the rotating equilateral triangular channel under high rotation numbers and high buoyancy parameters. Correlation functions will be generated to predict the heat transfer enhancement.

2 Experimental Setup

2.1 Rotating Facility. The study of the heat transfer inside the triangular channel is performed in a rotating facility, as shown in Fig. 2. The coolant air comes in from the bottom of the rig through a rotary union into the hollow shaft. The air continues to travel through the hub to a rubber hose and comes into the pressure vessel containing the triangular test section. After the air passes through the heated test section, the air goes through another rubber hose to a copper tubing inside the slip ring. The copper tubing is connected to the second rotary union at the top of



Copper plate measuring the regionally averaged heat transfer coefficients

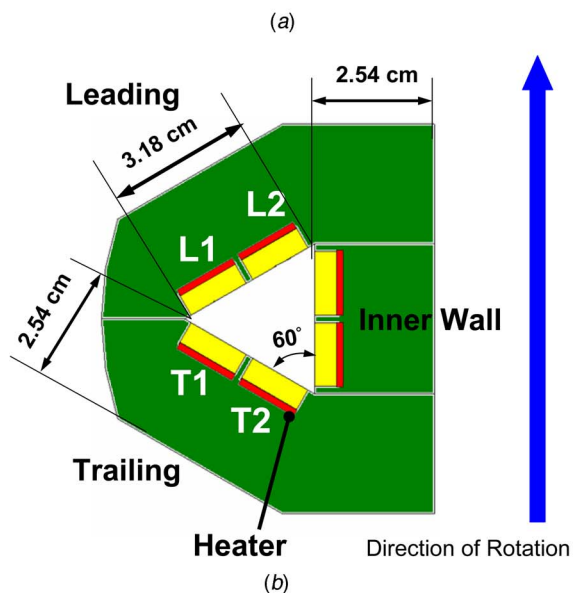


Fig. 3 (a) Details of the triangular test section and (b) cross section view of the test section

the slip ring. The coolant air then expels to the outside through an aluminum pipe. A needle valve is attached to the pipe to adjust the pressure of the flow loop. A motor is used to drive the shaft with a frequency controller to control the rotational speeds from 0 rpm

to 400 rpm. A 100 channel slip ring is used as an interface to transfer the data reading from the rotating test section to the data acquisition system.

2.2 Equilateral Triangular Test Section. The equilateral triangular test section used in the current study is shown in Fig. 3(a). The coolant air goes from a 1.27 cm diameter pipe to the inlet part. Two mesh screens are placed on the inlet part to help spread the flow. The thickness of the inlet part is 3.81 cm with the $L_e/D_h=2.09$. The inlet part has an equilateral triangular shaped slot with the same dimension as the triangular test section and is fully attached to the test section parts. The flow goes radially outward into the test section and discharges into the cavity of the pressure vessel then back to the flow loop.

The equilateral triangular test section consists of three parts: leading, trailing, and the inner walls, as shown in Fig. 3(b). These three pieces are made of garolite and the thickness of the three walls is 2.54 cm. Two rows of copper plates are instrumented in each wall. The size of each copper plate is 1.35 cm wide \times 1.11 cm high and the thickness is 0.476 cm. The copper plates on the leading and trailing surfaces are in staggered arrangement. The gaps between the copper plates are filled with silicon. A blind hole is drilled in each copper plate and the thermocouple is glued in each hole by the epoxy. Electric resistant heaters are placed beneath the copper plates in each row. In other words, a total of six heaters are used to heat up L1, L2, T1, T2, and two inner wall regions, respectively. The insulating material of the test section reduces the heat loss from the heaters to the supporting material.

In the current study, the ribs are only glued on the leading and trailing surfaces by the super glue. The square ribs are made of brass and the cross section is 1.59×1.59 mm². The P/e ratio in the current study is 8 and the e/D_h ratio is 0.087. The ribs are skewed to the mainstream flow with a 45 deg angle of attack, as shown in Fig. 4. Due to the staggered arrangement of the copper plates, the ribs on the trailing surface and leading surface are also staggered. In order to eliminate the conduction effects caused by the continuous ribs across surfaces, insulation (super gel) is filled between the ribs continuous across the entire surface, as shown in Fig. 4.

The coolant air inside the pressure vessel is pressurized at six times of the atmospheric pressure for both the stationary and rotating cases. The Reynolds number varies from 10,000 to 40,000 and the rotational speeds vary from 0 rpm to 400 rpm. The channel orientation is 90 deg to the direction of rotation.

3 Data Reduction

This study experimentally measured the regionally averaged heat transfer coefficient (h) within the rotating triangular channel, as shown in Eq. (1).

$$h = \frac{\dot{Q}_{in} - \dot{Q}_{loss}}{A(T_{w,x} - T_{b,x})} \quad (1)$$

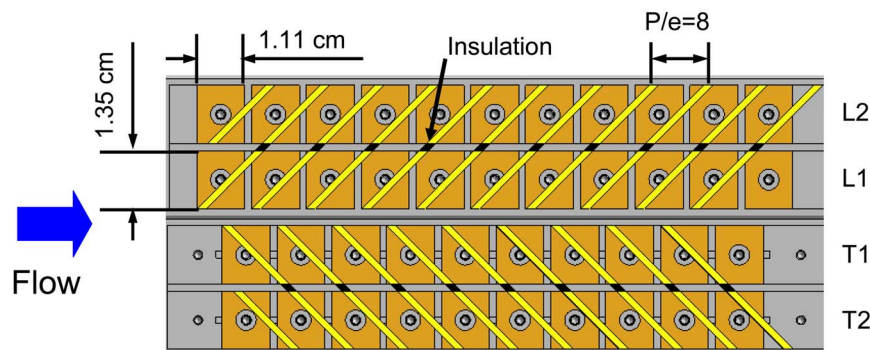


Fig. 4 Rib configurations of the current study

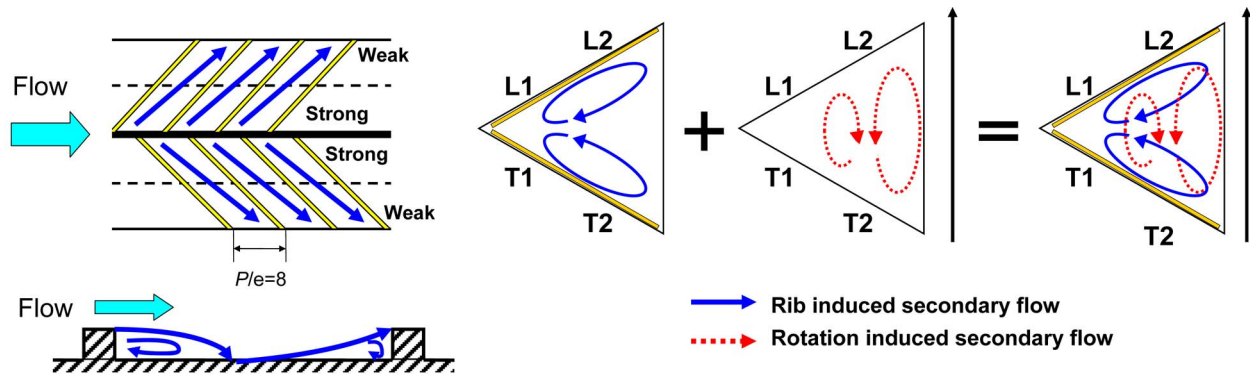


Fig. 5 Conceptual view of the secondary flow due to rotation and ribs

The heat input supplying to the copper plates is determined by the voltage and current from each etched foil heater. A total of six heaters are used to maintain the uniform wall temperatures in the circumferential direction. In order to determine the heat loss, the insulation material is filled inside the test section and the heat is supplied without coolant flow until a series of given temperatures is reached. The heat supplied during this calibration is equal to the heat loss from the system during the experiment. The heat loss test is performed under each rotational speed. The regionally averaged wall temperature is measured by the thermocouple beneath each copper plate. Two thermocouples are placed at the inlet and outlet of the test section to obtain the air temperature. The bulk temperature at each location is obtained by the linear interpolation of the inlet and outlet air temperatures.

The nondimensional Nusselt number (Nu) can be obtained by the measured heat transfer coefficient. The Nusselt number (Nu_o) from the turbulent flow in a smooth tube developed by Dittus/Boelter–McAdams is used to evaluate the heat transfer enhancement, as shown in Eq. (2).

$$\frac{Nu}{Nu_o} = \left(\frac{hD_h}{k} \right) \left(\frac{1}{0.023 Re^{0.8} Pr^{0.4}} \right) \quad (2)$$

All air properties are based on the bulk air temperature. An uncertainty analysis was performed based on Kline and McClintock [24]. The uncertainty for the temperature measurement is 0.3°C . The uncertainty of the local heat transfer coefficient is affected by the local wall to coolant temperature difference and the net heat flux from each copper plate. The uncertainty of the Nusselt number ratio is approximately 4.9% at the highest Reynolds number ($Re=40,000$). At the lowest Reynolds number ($Re=10,000$), the maximum uncertainty is approximately 9.8%.

4 Results and Discussion

Through the results and discussion, only the data on the leading and trailing surfaces are reported. The leading and trailing surfaces are divided into four regions in the spanwise direction, as shown in Fig. 3(b). The results in the stationary channel will be discussed first to provide the baseline data before the effect of rotation is considered in this study.

4.1 Heat Transfer in the Stationary Channel. Heat transfer inside the stationary channel is influenced by the channel geometry and the flow behavior. Figure 5 shows the secondary flow structures in this triangular channel. The angled rib induced secondary flow goes from the rib leading region (L1 and T1) toward the rib trailing (L2 and T2) region. The strength of this secondary flow decreases along the rib orientation. The heat transfer is enhanced on the rib leading region (L1 and T1) because the rib induced secondary flow is strong. As the secondary flow goes toward the rib trailing region (L2 and T2), it tends to turn around the corner. In the current study, the coolant flow goes through an

unheated entrance ($L_e/D_h=2.09$) and then into the heated triangular test section. The entrance length is very short and the flow is not fully developed. In order to study the heat transfer enhancement, the Nusselt number ratio (Nu/Nu_o) is considered.

Figure 6 shows the Nusselt number ratio comparisons in the stationary triangular channel with smooth walls and ribbed walls at $Re=20,000$. Each data point of the current study is the average of the two points on the leading or trailing surfaces. The data from Metzger and Vedula [8] were also tested in an equilateral triangle channel with 60 deg angled ribs and $P/e=7.5$. An identical smooth channel with $L_e/D_h=10.39$ was installed upstream of their test section as a flow-developing section. However, the unheated region in the current study is much shorter ($L_e/D_h=2.09$). The coolant flow is in the developing condition and the boundary layer is much thinner. Therefore, the Nusselt number ratios (Nu/Nu_o) in the current study are higher than the results from Metzger and Vedula [8] but the trends of these two are very similar. As stated in Ref. [8], the angled rib induced secondary flow grows in strength as the flow encounters several additional ribs in the streamwise direction and the heat transfer is enhanced gradually. For the ribbed cases, both results show that the Nusselt number ratio increases along the streamwise direction. For the smooth cases, the Nusselt number ratio of the current study shows gradual decreases in the streamwise direction. While the data from Metzger and Vedula [8] maintain the same level due to the fully developed flow condition.

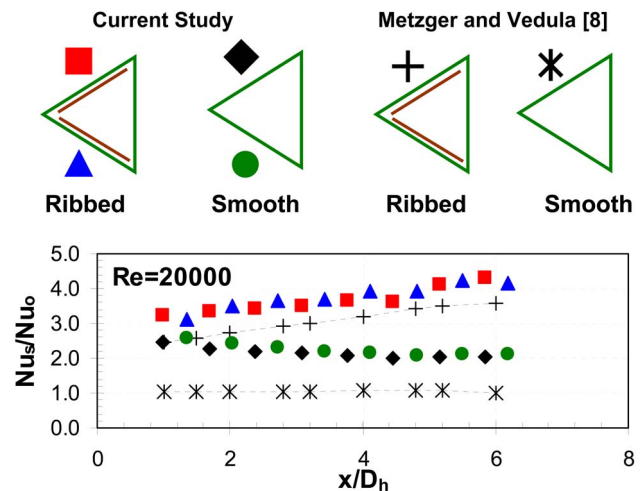


Fig. 6 Nusselt number ratio (Nu/Nu_o) comparison in the stationary channel ($Re=20,000$)

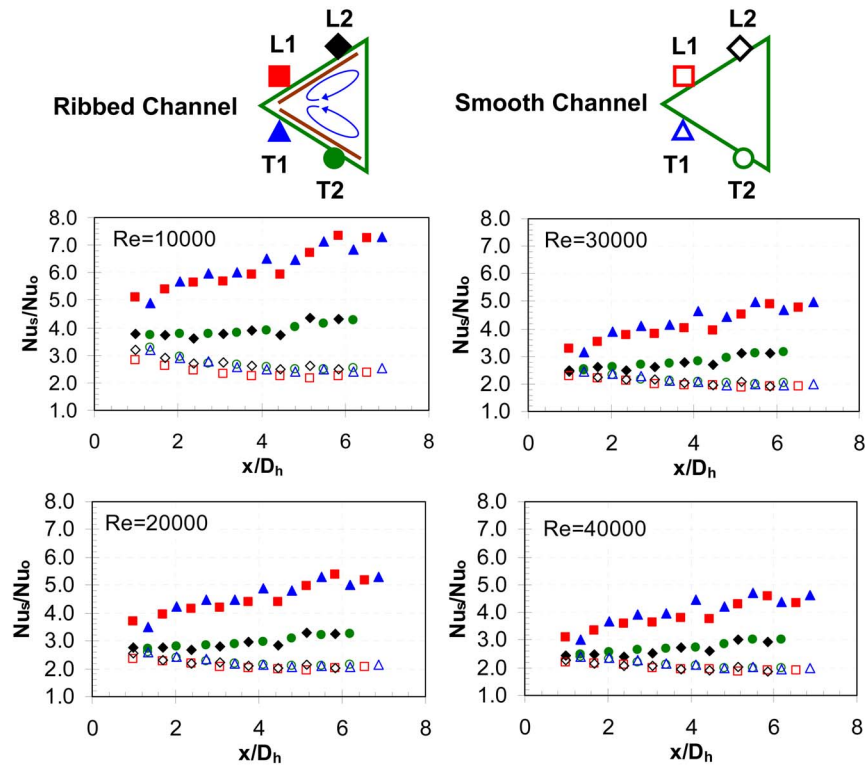


Fig. 7 Nusselt number ratios (Nu_s/Nu_o) in the stationary channel

Figure 7 shows the Nusselt number ratios (Nu/Nu_o) in the stationary channel with smooth walls and ribbed walls. Four different Reynolds numbers from 10,000 to 40,000 are reported. The results on the smooth walls will be discussed first. Due to the symmetric geometry of the channel, the heat transfer enhancement on these four regions is very close. The Nusselt number ratio decreases along the streamwise direction due to the boundary layer development. The Nusselt number ratio decreases from about 3.0 to 2.2 when Reynolds number is 10,000. The Nusselt number ratio decreases from 2.3 to 2.0 when Reynolds number is 40,000. It shows that the Dittus–Boelter–McAdams correlation can still be applied to the smooth triangular channel with the hydraulic diameter replacing the tube diameter.

When ribs are put on the channel surface, they trip the boundary layer and the heat transfer is enhanced at the cost of the higher pressure drop. When the leading and trailing surfaces are roughened with ribs, the heat transfer enhancement is greater than the smooth cases. The angled ribs are generally considered better than the orthogonal ribs and they produce the secondary flow along the rib orientations. The rib induced secondary flow goes along the surface of L1 and T1 toward L2 and T2 regions. In L2 and T2 regions, the secondary flow starts to turn around due to the channel geometry. The secondary flow induced by the 45 deg angled ribs tends to impinge on the region (L1 and T1), as shown in Fig. 5. The heat transfer enhancement on the rib leading region (L1 and T1) is higher than the rib trailing region (L2 and T2). For the lowest Reynolds number of 10,000, the heat transfer enhancement near the rib leading region (L1 and T1) is about 1.7 times higher than the smooth cases near the entrance and 3.5 times higher than the smooth cases near the exit of the channel. While on the rib trailing region (L2 and T2), the heat transfer enhancement from the entrance to the exit is only about 1.3–2.0 times higher than the smooth cases at $Re=10,000$. The entire ribbed leading and trailing surfaces both have higher heat transfer enhancement than the smooth cases. However, as the Reynolds number increases, the heat transfer enhancement by the ribs decreases. The heat transfer

enhancement by the ribs decreases as the Reynolds number increases from 10,000 to 40,000. This figure shows that the stationary heat transfer enhancement due to ribs is higher near the rib leading region (L1 and T1) than the rib trailing region (L2 and T2).

4.2 Heat Transfer in the Rotating Channel. Before the detailed discussion of the rotating results, it is necessary to describe the effect of rotation inside cooling channels. The rotational behavior inside the traditional rectangular channel has been studied by several groups. Two counter-rotating vortices are formed inside the rotating channel. These two counter-rotating vortices vary depending on the channel geometry and the direction of rotation. This secondary flow pattern induced by rotation in this triangular channel is shown in Fig. 5, which also involves the formation of the two counter-rotating vortices. In the ribbed channel, the rotating vortex is allowed to develop more freely due to the larger space near the rib trailing region (L2 and T2). The rotating vortex near the rib leading region (L1 and T1) is relatively small because the space is small and restricts the development of the rotating vortex. For the radially outward flow in the current study, the two counter-rotating vortices enhance heat transfer on the trailing surface, while decrease the heat transfer on the leading surface.

Figure 8 shows the Nusselt number ratio distributions with smooth walls. The stationary results and rotating results are plotted in the same figure to study the effect of rotation. Four Reynolds number cases, each under stationary condition and the highest rotational speed (400 rpm), are presented. The effect of rotation enhances the heat transfer on the trailing surface (both T1 and T2). On the leading surface, the Nusselt number ratio in the L2 region is smaller than the stationary case. While in the L1 region, the Nusselt number ratio is very close to the stationary case from $Re=20,000$ to $Re=40,000$. The heat transfer enhancement/declination due to rotation decreases when Reynolds number increases. The heat transfer enhancement due to rotation is smallest at the highest Reynolds number of 40,000.

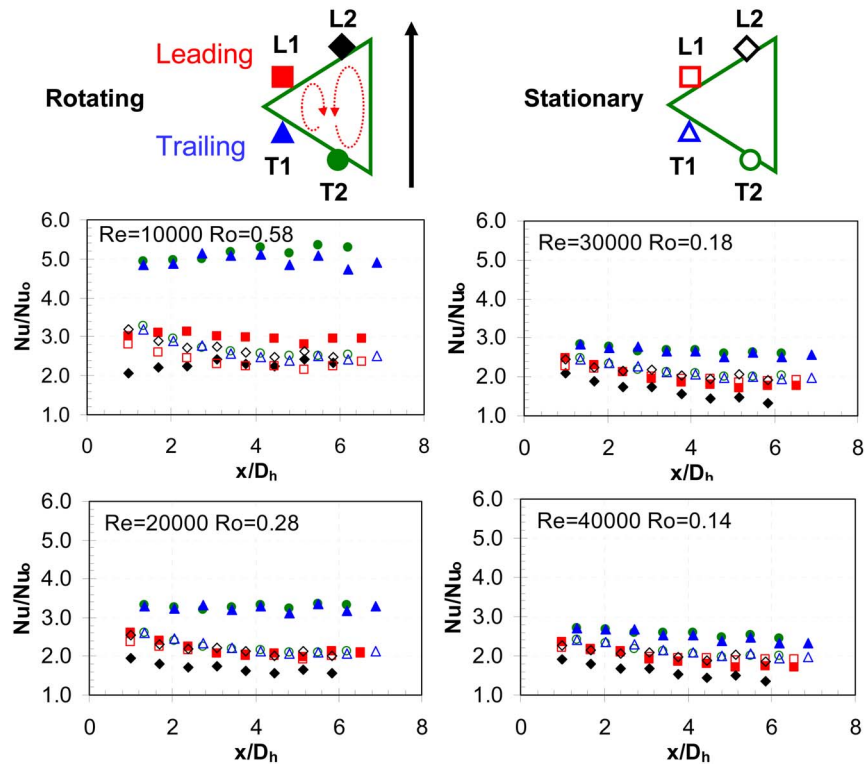


Fig. 8 Nusselt number ratios (Nu/Nu_0) in a smooth channel

When considering the effect of rotation with ribs, the rib induced secondary flow is going to interact with the rotation induced secondary flow, as shown in Fig. 5. When the ribs are put on the leading and trailing surfaces, the Nusselt number ratio distributions in both the stationary and rotating channels are shown

in Fig. 9. In the ribbed channel, the heat transfer enhancement/declination due to effect of rotation is smaller than the smooth cases. Near the rib leading region (L1 and T1), the rib induced secondary flow dominates over the smaller rotation induced secondary flow and the effect of rotation does not have a significant

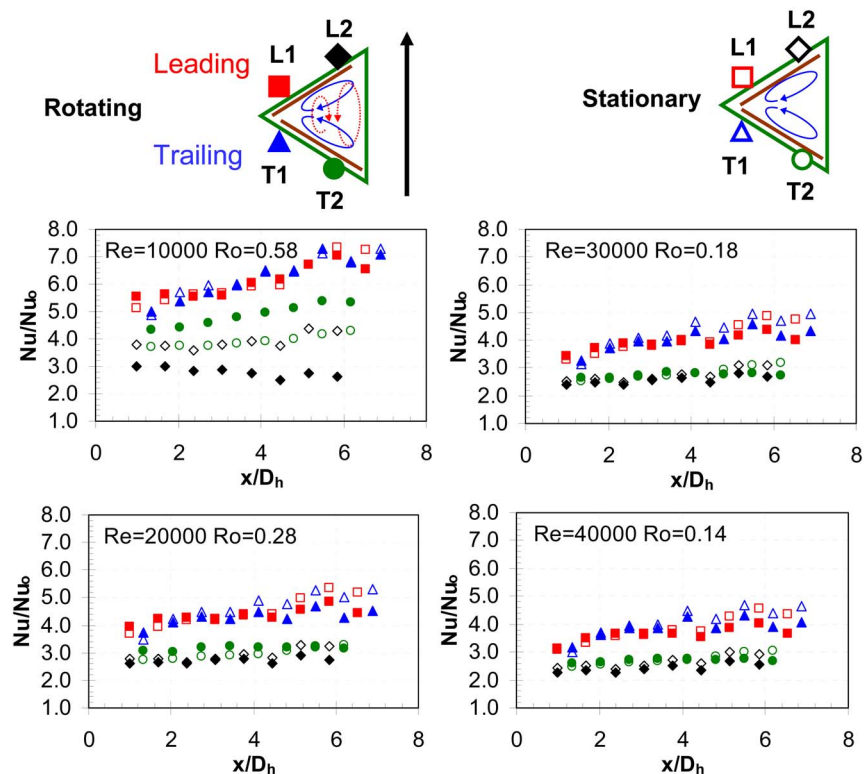


Fig. 9 Nusselt number ratios (Nu/Nu_0) in a ribbed channel

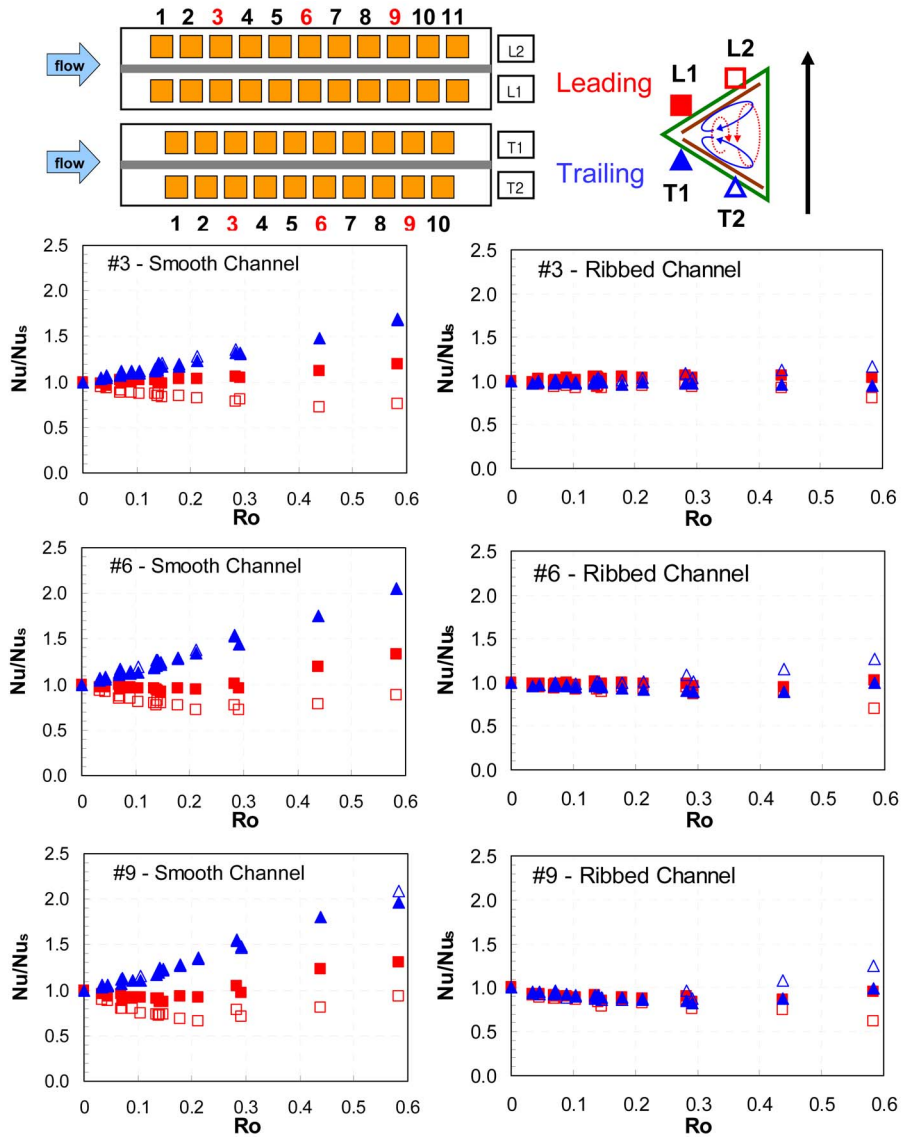


Fig. 10 Effect of rotation number on three different regions

impact on heat transfer. The Nusselt number for the rotating cases is fairly close to the stationary cases at the beginning of the channel and starts to diverge at the end of the channel. While on the rib trailing region (L2 and T2), the effect of rotation is more obvious and enhances heat transfer on the trailing surface while decreases heat transfer on the leading surface. In the L2 region, the rib induced secondary flow opposes the rotation induced secondary flow and produces low heat transfer. The lowest heat transfer enhancement occurs in the L2 region. Again, the effect of rotation decreases as the Reynolds number increases. At $Re = 40,000$, the effect of rotation on heat transfer enhancement is very small.

4.3 Rotation Number Effects. The rotation number is a relative measure of the Coriolis force to the bulk flow inertia force, as shown in Eq. (3).

$$Ro = \frac{\Omega D_h}{V} \quad (3)$$

This nondimensional parameter is widely used to quantify the effect of rotation in industry and academia. In order to study the heat transfer enhancement due to rotation, the Nusselt number ratio (Nu/Nu_s) has been plotted with the rotation number, as

shown in Fig. 10. Results on three different regions (3, 6, and 9) are chosen to study the effect of rotation along the streamwise direction. The data for the smooth cases and ribbed cases are both reported.

The discussion begins with the smooth cases. In region 3, the flow develops due to the short entrance. The Nusselt number ratios (Nu/Nu_s) increase with the rotation number on the trailing surfaces. Both T1 and T2 regions have the similar heat transfer enhancement. However, on the leading surface, the Nusselt number ratios (Nu/Nu_s) in the L1 region did not vary significantly until a rotation number of 0.3, and then gradually increase. The Nusselt number ratios in the L2 region decrease with the rotation number until a rotation number of 0.44, and then start to increase. The Nu/Nu_s declination in the L2 region is larger than the L1 region. It shows that the rotation induced secondary flow has a greater impact in the L2 region and the heat transfer is low.

When the flow moves to region 6, the boundary layer grows thicker on the smooth wall. The highest Nusselt number ratio (Nu/Nu_s) on the trailing surfaces increases from 1.6 (in region 3) to 2.0. The Nusselt number ratios (Nu/Nu_s) in the L2 region decrease with rotation number up to 0.3, and then gradually increase with the rotation number. While in the L1 region, the Nusselt

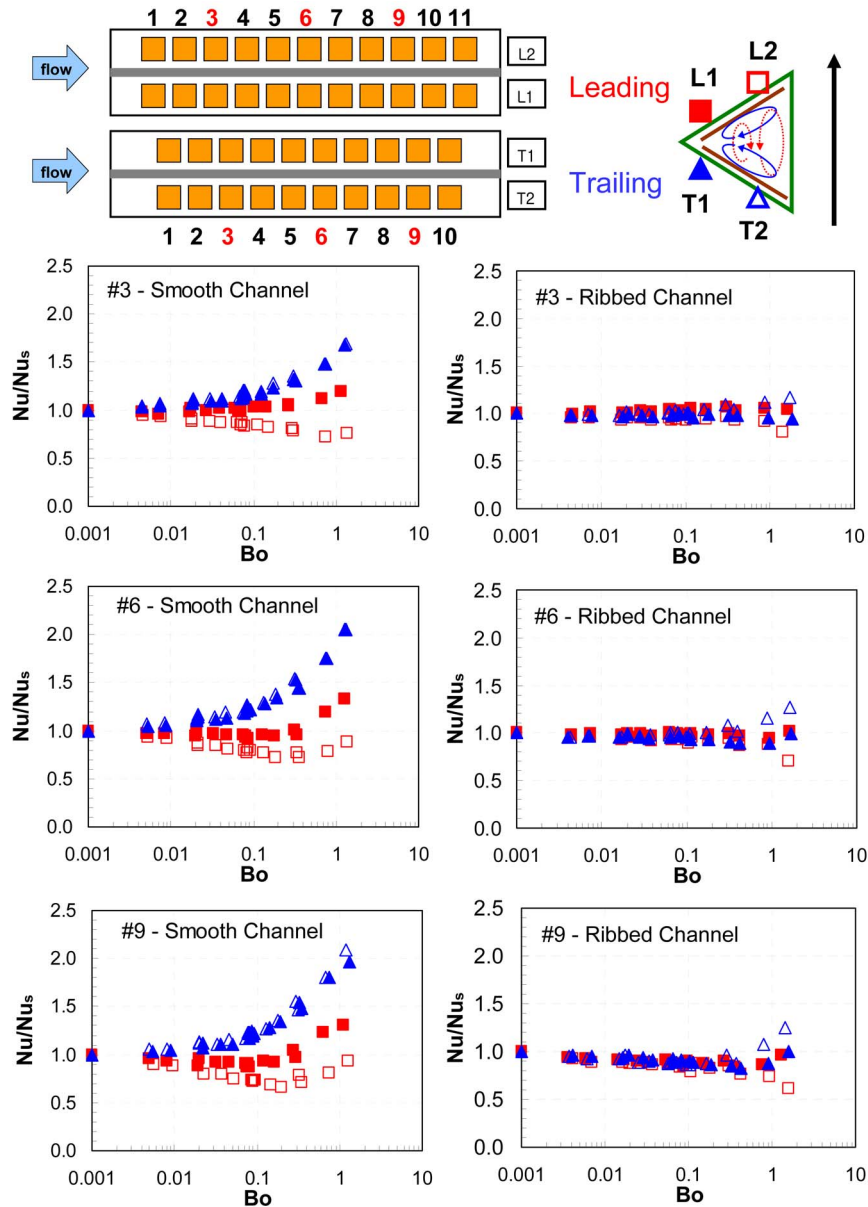


Fig. 11 Effect of buoyancy parameter on three different regions

number ratios (Nu/Nu_s) did not vary significantly until a rotation number of 0.3, and then gradually increase. As the flow goes further downstream to region 9, the trend and the level of Nusselt number ratios are very similar to region 6.

As discussed before, the effect of rotation is reduced on the ribbed surfaces. The Nusselt number ratios (Nu/Nu_s) with rotation number on the ribbed surfaces are also presented in these three regions. The deviation of Nusselt number ratios on the ribbed surfaces is smaller than the smooth surfaces. In region 3, the Nu/Nu_s of T2 region gradually increases with the rotation number up to about 1.2, which is much smaller than the smooth wall case. In the L1 and T1, the heat transfer enhancement due to rotation is very small, which indicates that the rib induced secondary flow behavior dominates. In the L2 region, the (Nu/Nu_s) decreases with the rotation number to about 0.8 only. When the flow moves further downstream to regions 6 and 9, the heat transfer enhancement/declination is larger than region 3.

4.4 Buoyancy Parameter Effects. The buoyancy parameter is also a widely used nondimensional parameter to quantify the

effect of rotation inside the gas turbine blade. The buoyancy parameter due to the centrifugal force and temperature difference is important because of the high rotating speed and large temperature difference in the actual engines. The buoyancy parameter considers all factors affecting the effect of rotation: the density ratio (temperature difference), the rotation number, and the rotating radius. It is shown in Eq. (4).

$$Bo_x = \left(\frac{\Delta\rho}{\rho} \right)_x (Ro)^2 \frac{R_x}{D_h} = \frac{T_{w,x} - T_{b,x}}{T_{f,x}} (Ro)^2 \frac{R_x}{D_h} \quad (4)$$

The local film temperature is defined as the average of the local wall temperature and the local bulk temperature, as shown in Eq. (5).

$$T_{f,x} = (T_{w,x} + T_{b,x})/2 \quad (5)$$

Figure 11 shows the Nusselt number ratios (Nu/Nu_s) with the buoyancy parameter in regions 3, 6, and 9. Again, the results on the smooth walls and the ribbed walls are reported. Similar trends can be observed as in the rotation number plots. It also shows that

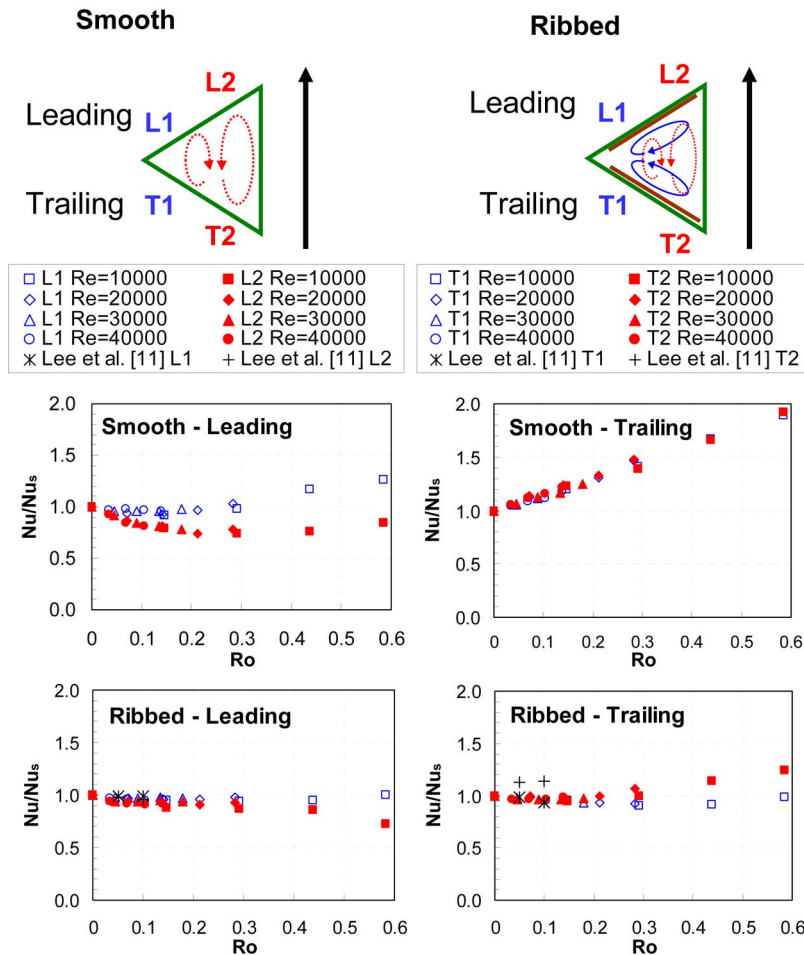


Fig. 12 Streamwise averaged Nusselt number ratio (Nu/Nu_s) with rotation number

the Nusselt number ratio increases with the buoyancy parameter on the trailing surface. For the L1 region in regions 3 and 6, the Nusselt number ratio increases with the buoyancy parameter. While in the L1 region of region 9, the Nusselt number ratio decreases with the buoyancy parameter until a critical buoyancy parameter of 0.3 and then increases. In the L2 region, the Nusselt number ratio decreases with the buoyancy parameter and then gradually increases. While for the ribbed cases, the heat transfer enhancement/declination is smaller than the smooth cases. This figure shows that the heat transfer enhancement due to rotation can be quantified by the local buoyancy parameter on both the smooth walls and the ribbed walls.

4.5 Average Heat Transfer. Figure 12 shows the average Nusselt number ratios (Nu/Nu_s) with rotation number on the leading and trailing surfaces. Each data point is the average of nine points in the streamwise direction of each region. Four Reynolds numbers and five rotational speeds are presented in this figure for both the smooth cases and the ribbed cases. The data from Lee et al. [11] are also plotted as a comparison for the ribbed cases. It shows that on the leading surface, the Nusselt number ratios (Nu/Nu_s) are very similar; while on the trailing surface, the deviation of Nusselt number ratio (Nu/Nu_s) due to rotation is smaller than the data from Lee et al. [11]. This indicates that the effect of rotation is stronger for the flow in the fully developed channel than in the flow-developing channel. The current study is to extend the data available in the lower rotation number domain to a higher one. For the ribbed case, it shows that in the L1 region,

the average Nusselt number ratios remain the same level. In the L2 region, it decreases with the rotation number. On the trailing surface, Nusselt number ratios increase with the rotation number in the T2 region but remain the similar level in the T1 region. For the smooth case, the heat transfer enhancement/declination occurs at a lower rotation number than the ribbed case. On the leading surface, Nusselt number ratios decrease with the rotation number and then gradually increase with the rotation number. On the trailing surface, Nusselt number ratios increase with the rotation number. Figure 13 proves that the average buoyancy parameters can also be used to quantify the effect of rotation with the contribution from different Reynolds numbers and rotational speeds.

The average Nusselt number ratios (Nu/Nu_s) on the leading and trailing surfaces are plotted in Fig. 14. Each data point is now the average of 18 points over the entire leading and trailing surfaces. The results are plotted with the rotation number and the average buoyancy parameter. The heat transfer enhancement due to rotation on the smooth walls is higher than the ribbed walls. The heat transfer enhancement/declination for the smooth cases occurs at a lower rotation number and buoyancy parameter than the ribbed cases. The Nu/Nu_s on the smooth trailing surface increases with rotation number to about 1.9. While on the smooth leading surface, the Nu/Nu_s decreases to about 0.85 at a rotation number of 0.2, and then gradually increases with the rotation number. For the ribbed cases, the Nu/Nu_s values on the leading and trailing surfaces are very close when the rotation number is smaller than 0.3. After that, the Nusselt number ratios on the

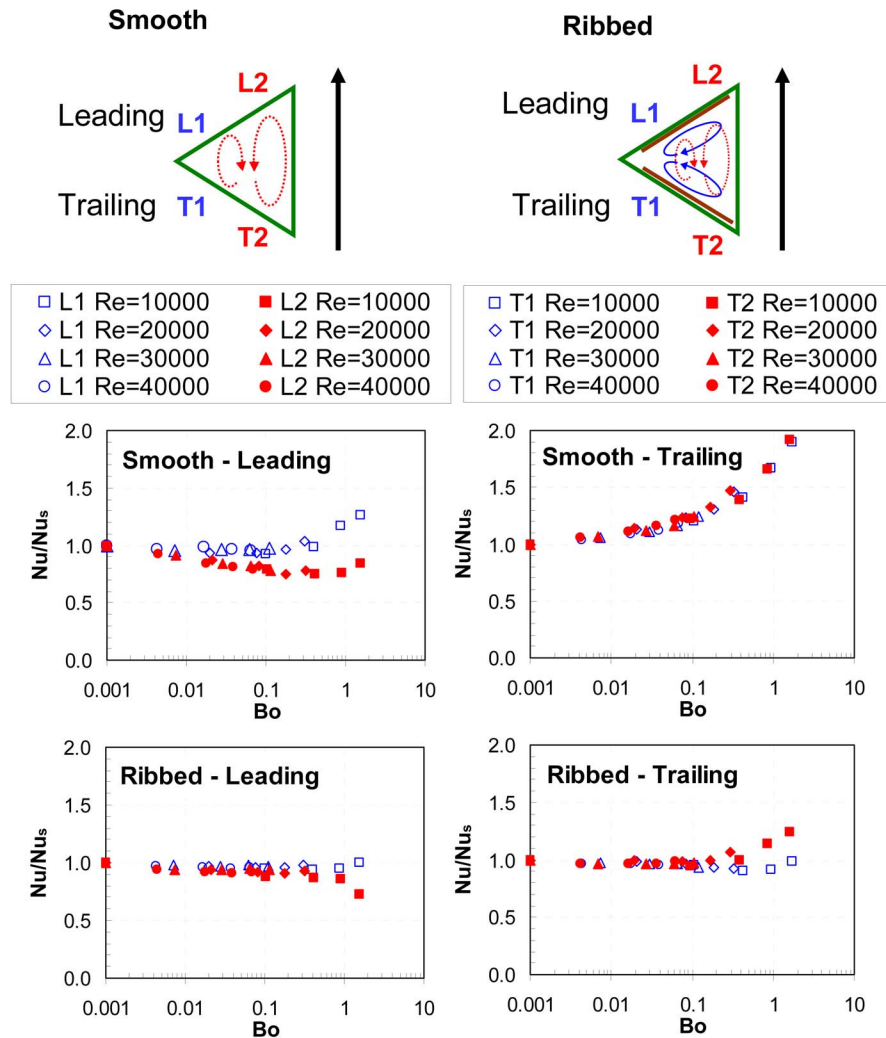


Fig. 13 Streamwise averaged Nusselt number ratio (Nu/Nu_s) comparison with buoyancy parameter

leading and trailing surfaces begin to diverge. Figure 14 also shows the Nu/Nu_s with the average buoyancy parameters. The trends are very similar to the plots with the rotation number. The data can be correlated with a power function with the rotation number as well as the buoyancy parameter, as shown in the figure. The deviation of the correlation data to the experimental data is within $\pm 6.8\%$. The constants for the correlation functions are also shown in the figure. This figure shows that the nondimensional rotation number and buoyancy parameter can be used to correlate the data in the equilateral triangular channel even in the extended range.

5 Conclusion

This paper studied the heat transfer distribution in a rotating equilateral triangular channel under high rotation numbers. The results on the leading and trailing surfaces of the channel have been reported. Four Reynolds numbers from 10,000 to 40,000, each with the rotational speeds from 0 rpm to 400 rpm, were tested. The smooth wall cases as well as the ribbed cases were investigated for comparison. This rib configuration is chosen in order to provide better heat transfer near the leading edge of the gas turbine blade. The tests are done under high rotation number and high buoyancy parameters to simulate the actual engine condition. Based on the results reported, the following conclusion can be made.

1. In the stationary channel, the 45 deg angled ribs enhance heat transfer. The Nu/Nu_o is higher on the rib leading region (L1 and T1) than the rib trailing region (L2 and T2). This is a good design near the blade leading edge region only. When Reynolds number increases, the rib enhanced heat transfer decreases.
2. In the rotation smooth channel, the heat transfer increases on the trailing surface, while the heat transfer decreases on the leading surface. The channel wide side region (L2 and T2) has the largest heat transfer declination.
3. In the rotating ribbed channel, the rib induced secondary flow interacts with the rotation induced secondary flow. The rib induced secondary flow in the rib leading region (L1 and T1) is much stronger, and the effect of rotation is small and does not have a significant impact on heat transfer of the rib leading region. While near the rib trailing region (L2 and T2), the wide space allows the rotation induced secondary flow to develop freely and the effect of rotation is more obvious. In general, the effect of rotation in the ribbed channel is smaller than the smooth channel.
4. The rotation number and buoyancy parameter are still good parameters to quantify the effect of rotation in this equilateral triangular channel with smooth walls and ribbed walls. Both of these two nondimensional parameters are extended to the range close to the actual engine application.

Ro	A	m	B	n
Leading - rib	1.19	0.035	1.6	1.45
Trailing - rib	0.99	0.01	1.9	5.5
Leading - smooth	0.97	0.02	-5.5	7.5
Trailing - smooth	0.5	-0.2	0.8	0.95

Bo	A	m	B	n
Leading - rib	1.21	0.04	0.55	0.8
Trailing - rib	0.98	0.01	0.02	2
Leading - smooth	0.8	-0.02	0.18	1.1
Trailing - smooth	1.1	0.02	-0.2	0.25

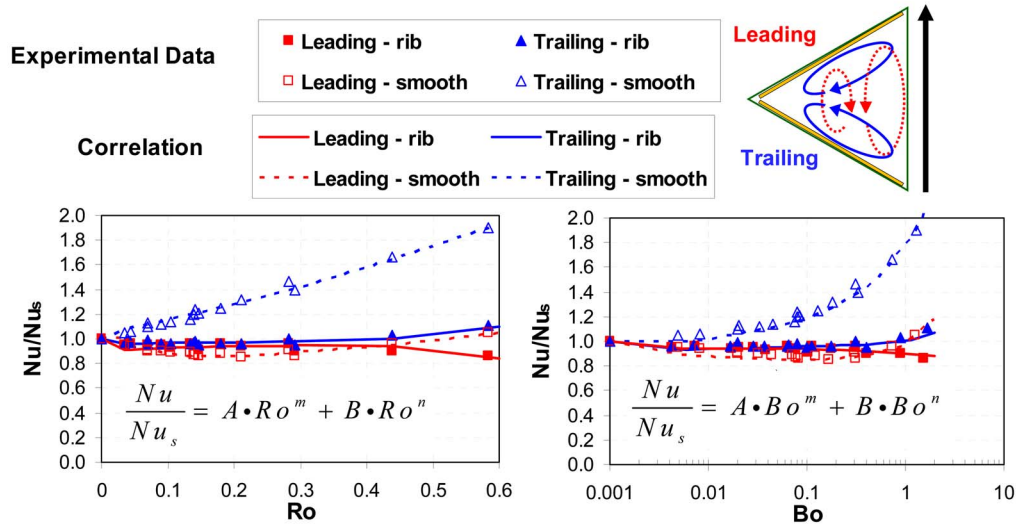


Fig. 14 Average Nu ratio (Nu/Nu_s) for the leading and trailing surfaces and the correlation

Acknowledgment

This work has been funded through the Solar Turbines Inc.

Nomenclature

- A = area of the copper plate
 AR = channel aspect ratio, $W:H$
 Bo_x = local buoyancy parameter
 D_h = channel hydraulic diameter
 e = rib height
 H = channel height
 h = regionally averaged heat transfer coefficient
 k = thermal conductivity of the coolant
 L = length of the rib-roughened portion of the test section
 L_u = length of the unheated portion of the inlet part
 Nu = regionally averaged Nusselt number
 Nu_o = Nusselt number of the fully developed turbulent flow in nonrotating smooth tube
 P = rib spacing
 Pr = Prandtl number of the coolant
 Q_{loss} = heat loss through the wall
 Q_{in} = heat input at the wall
 R_x = local radius of rotation
 Re = Reynolds number, $\rho V D_h / \mu$
 Ro = rotation number, $\Omega D_h / V$
 $T_{w,x}$ = local wall temperature
 $T_{b,x}$ = local coolant bulk temperature
 $T_{f,x}$ = local film temperature $(= (T_{w,x} + T_{b,x}) / 2)$
 V = bulk velocity in the streamwise direction
 W = channel width
 α = rib angle of attack
 β = angle of channel orientation with respect to the axis of rotation
 μ = viscosity of the coolant
 ρ = density of the coolant
 $(\Delta\rho/\rho)_x$ = local coolant-to-wall density ratio $(= (T_{w,x} - T_{b,x}) / T_{f,x})$
 Ω = rotational speed

References

- [1] Han, J. C., Dutta, S., and Ekkad, S. V., 2000, *Gas Turbine Heat Transfer and Cooling Technology*, Taylor & Francis, New York.
- [2] Han, J. C., 1984, "Heat Transfer and Friction in Channels With Two Opposite Rib-Roughened Walls," *ASME J. Heat Transfer*, **106**, pp. 774–781.
- [3] Han, J. C., 1988, "Heat Transfer and Friction Characteristics in Rectangular Channels With Rib Turbulators," *ASME J. Heat Transfer*, **110**, pp. 321–328.
- [4] Han, J. C., and Zhang, P., 1991, "Effect of Rib-Angle Orientation on Local Mass Transfer Distribution in a Three-Pass Rib-Roughened Channel," *ASME J. Turbomach.*, **113**, pp. 123–130.
- [5] Taslim, M. E., and Lengkon, A., 1998, "45 deg Staggered Rib Heat Transfer Coefficient Measurements in a Square Channel," *ASME J. Turbomach.*, **120**, pp. 571–580.
- [6] Taslim, M. E., and Spring, S. D., 1994, "Effects of Turbulator Profile and Spacing on Heat Transfer and Friction in a Channel," *J. Thermophys. Heat Transfer*, **8**(3), pp. 555–562.
- [7] Liu, Y. H., Wright, L. M., Fu, W. L., and Han, J. C., 2007, "Rib Spacing Effect on Heat Transfer in Rotating Two-Pass Ribbed Channel ($AR=1:2$)," *J. Thermophys. Heat Transfer*, **21**(3), pp. 582–595.
- [8] Metzger, D. E., and Vedula, R. P., 1987, "Heat Transfer in Triangular Channels With Angled Roughness Ribs on Two Walls," *Exp. Heat Transfer*, **1**, pp. 31–44.
- [9] Ahn, S. W., and Son, K. P., 2002, "Heat Transfer and Pressure Drop in the Roughened Equilateral Triangular Duct," *Int. Commun. Heat Mass Transfer*, **29**, pp. 479–488.
- [10] Haasenritter, A., and Weigand, B., 2001, "Heat Transfer in Triangular Rib-Roughened Channels," *ASME Paper No. NHTC 2001-20245*.
- [11] Lee, D. H., Rhee, D. H., and Cho, H. H., 2006, "Heat Transfer Measurements in a Rotating Equilateral Triangular Channel With Various Rib Arrangements," *ASME Paper No. GT 2006-90973*.
- [12] Dutta, S., Han, J. C., and Lee, C. P., 1995, "Experimental Heat Transfer in a Rotating Triangular Duct: Effect of Model Orientation," *ASME J. Heat Transfer*, **117**, pp. 1058–1061.
- [13] Zhang, Y. M., Gu, W. Z., and Han, J. C., 1994, "Augmented Heat Transfer in Triangular Ducts With Full and Partial Ribbed Walls," *J. Thermophys. Heat Transfer*, **8**(3), pp. 574–579.
- [14] Kays, W. M., and Crawford, M. E., 1993, *Convective Heat and Mass Transfer*, 3rd ed., McGraw-Hill, New York, pp. 311–349.
- [15] Wright, L. M., Fu, W. L., and Han, J. C., 2005, "Influence of Entrance Geometry on Heat Transfer in Rotating Rectangular Cooling Channels ($AR=4:1$) With Angled Ribs," *ASME J. Heat Transfer*, **127**, pp. 378–387.
- [16] Liu, Y. H., Huh, M., Han, J. C., and Chopra, S., 2007, "Heat Transfer in a Two-Pass Rectangular Channel ($AR=1:4$) Under High Rotation Numbers," *ASME Paper No. GT 2007-27067*.
- [17] Wright, L. M., Liu, Y. H., Han, J.-C., and Chopra, S., 2007, "Heat Transfer in a Trailing Edge, Wedge-Shaped Cooling Channels Under High Rotation Numbers," *ASME Paper No. GT 2007-27093*.
- [18] Wagner, J. H., Johnson, B. V., and Hajek, T. J., 1991, "Heat Transfer in Rotating Passages With Smooth Walls and Radial Outward Flow," *ASME J.*

Turbomach., **113**, pp. 42–51.

- [19] Wagner, J. H., Johnson, B. V., and Kopper, F. C., 1991, "Heat Transfer in Rotating Serpentine Passages With Smooth Walls," *ASME J. Turbomach.*, **113**, pp. 321–330.
- [20] Johnson, B. V., Wagner, J. H., Steuber, G. D., and Yeh, F. C., 1994, "Heat Transfer in Rotating Serpentine Passages With Trips Skewed to the Flow," *ASME J. Turbomach.*, **116**, pp. 113–123.
- [21] Fu, W. L., Wright, L. M., and Han, J. C., 2005, "Buoyancy Effects on Heat Transfer in Five Different Aspect-Ratio Rectangular Channels With Smooth Walls and 45-Degree Ribbed Walls," *ASME Paper No. GT 2005-68493*.
- [22] Zhou, F., Lagrone, J., and Acharya, S., 2004, "Internal Cooling in 4:1 AR Passages at High Rotation Numbers," *ASME Paper No. GT 2004-53501*.
- [23] Liou, T. M., Chang, S. W., Hung, J. H., and Chiou, S. F., 2007, "High Rotation Number Heat Transfer of 45° Rib-Roughened Rectangular Duct With Two Channel Orientations," *Int. J. Heat Mass Transfer*, **50**, pp. 4063–4078.
- [24] Kline, S. J., and McClintock, F. A., 1953, "Describing Uncertainty in Single-Sample Experiments," *Mech. Eng. (Am. Soc. Mech. Eng.)*, **75**, pp. 3–8.

The Effects of Manufacturing Tolerances on Gas Turbine Cooling

Ronald S. Bunker

GE Global Research Center,
Niskayuna, NY 12309

This study presents a summary of the effects of manufacturing methods and processing steps upon the resulting thermal boundary conditions for typical highly cooled turbine airfoils. Specific emphasis is placed on the conservatism that must be “designed into” the component for survival due to realistic manufacturing tolerances. Using the features of a typical blade design, the main geometric factors that can influence the blade heat transfer capability through manufacturing variability are enumerated. The tolerances on those geometric factors are provided, and the approximate quantitative impact on thermal boundary conditions is summarized. A simple example of airfoil cooling for a representative wall section is used to tabulate the variations with the resulting changes in the most affected thermal boundary conditions. Each of the main geometric factors is then evaluated in terms of its possible effect on maximum metal temperature. Pareto's of the effects of manufacturing factors exhibit which factors are key and where tighter tolerances may help. Monte Carlo analysis results show the probability distributions associated with overall cooling changes tied to the tolerances. [DOI: 10.1115/1.3072494]

1 Introduction

The technology of cooling gas turbine components, most notably the high-pressure turbine (HPT) airfoils, has developed over the years from simple smooth cooling passages to very complex internal and external geometries. The fundamental aim of this technology area is to obtain the highest overall cooling effectiveness with the lowest possible penalty on the thermodynamic cycle performance. In parallel with the cooling technology developments of the last 40 years there has necessarily occurred an equal development and maturing of the manufacturing technologies enabling such complex cooled airfoils to be produced. These manufacturing technologies span the entire process of fabrication from investment casting to the application of protective coatings. Manufacturing processes include the machining of wax and core molds and dies, the ceramic core formation, the casting of metal parts, the removal of slag residue from the casting, external machining (e.g., milling or electrodischarge machining (EDM)) for finished dimensions, internal machining (e.g., EDM or electrochemical machining (ECM)) of specific holes or channels, the drilling of film holes (laser, EDM, or water jet), the application of internal and/or external protective coatings such as bondcoat and ceramic thermal barrier coating (TBC) (physical vapor deposition, air plasma spray, and chemical vapor deposition), as well as various joining operations (brazing and welding).

An example of a typical aviation HPT cross section is shown in Fig. 1. Also shown are photos of a highly cooled HPT vane and blade manufactured using the investment casting process (the blade is shown with thermal barrier coating). All of the HPT and combustor components shown here are the product of sophisticated fabrication processes and are subject to manufacturing constraints and variations that affect the cooling of the parts. Figure 2 provides an overview of the design process, or design cycle, typical of highly cooled airfoils. Every aspect of this design process from the initial engine cycle objectives to the life of the final component is affected by the manufacturing methods by the fact

that process variability (statistical mean and standard deviation) must be “designed into” the final component to assure survival and guarantee lifetime economics. By direct association, many of the same manufacturing variations will affect the repair processes used to refurbish these components for extended life. A more detailed view of the design process specific to the cooling design is shown in Fig. 3. Here the principle design factors affecting heat transfer and cooling of HPT airfoils are linked to the cooling design analysis as required boundary conditions; also shown are the major turbine design elements that are linked to the cooling design and therefore directly impacted. The impact of the uncertainty in these thermal boundary conditions upon the resulting design and life of the cooled airfoils is depicted in Fig. 4 for a HPT blade. This Pareto chart shows the notional percentage of overall impact that these key boundary conditions might have on the design (e.g., bulk temperature or life) considering each to have a design uncertainty due to available experimental data, scaling effects, predictive accuracy, or unknowns. Included in these overall uncertainties and impacts are the tolerances derived from or due to the manufacturing processes.

The present study seeks to identify and quantify the effects of manufacturing, as dictated by the tolerances allowed in the finished product, upon the resulting cooling design of a HPT airfoil. Using the features of a typical blade design, the main geometric factors that can influence the blade heat transfer capability through variability are enumerated. The tolerances on those geometric factors are provided, and the qualitative impact on thermal boundary conditions is summarized. A simple example of airfoil cooling for a representative wall section is used to tabulate the variations with the resulting changes in the most affected thermal boundary conditions. Each of the main geometric factors is then evaluated in terms of its possible effect on maximum metal temperature. Only the heat transfer and cooling aspects of the blade design are considered in detail here, not the flow rate or internal pressure losses. Since the heat transfer and flow are intimately related though, many of the thermal results can easily be translated to effects on cooling flows.

This study will not go into operational factors, such as combustor profile and pattern factors, or in-service changes, such as surface erosion and debris deposition. Only the manufacturing tolerances for parts entering service will be treated. To maintain a clear

Contributed by the International Gas Turbine Institute of ASME for publication in the JOURNAL OF TURBOMACHINERY. Manuscript received August 30, 2008; final manuscript received October 10, 2008; published online July 13, 2009. Review conducted by David Wisler. Paper presented at the ASME Turbo Expo 2008: Land, Sea and Air (GT2008), Berlin, Germany, June 9–13, 2008.

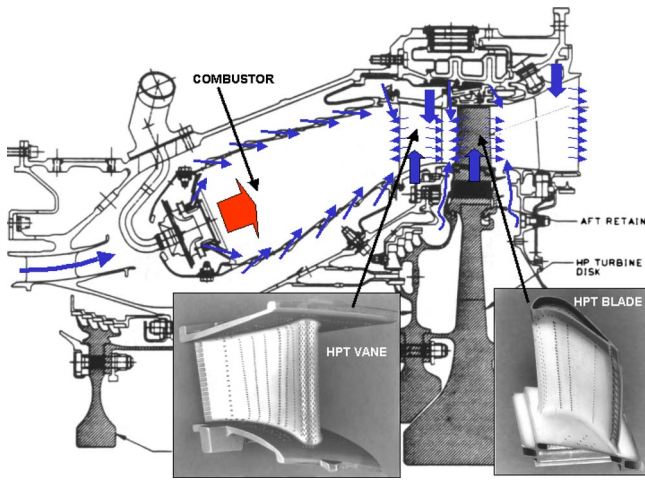


Fig. 1 Typical aviation high-pressure turbine cross section with vane and blade

focus, possible combined effects will also not be included, as these would be too numerous to account for here, for example, the placement of film holes relative to turbulators, the location of impingement jets near film hole entries, and the radius of turbu-

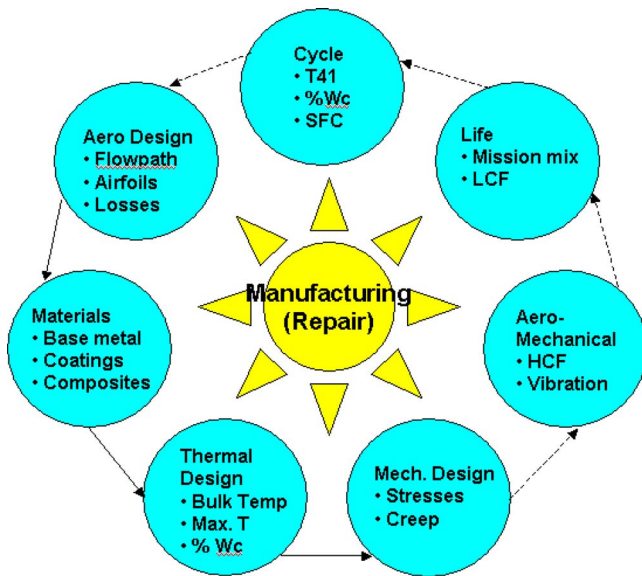


Fig. 2 Design cycle for highly cooled turbine airfoils

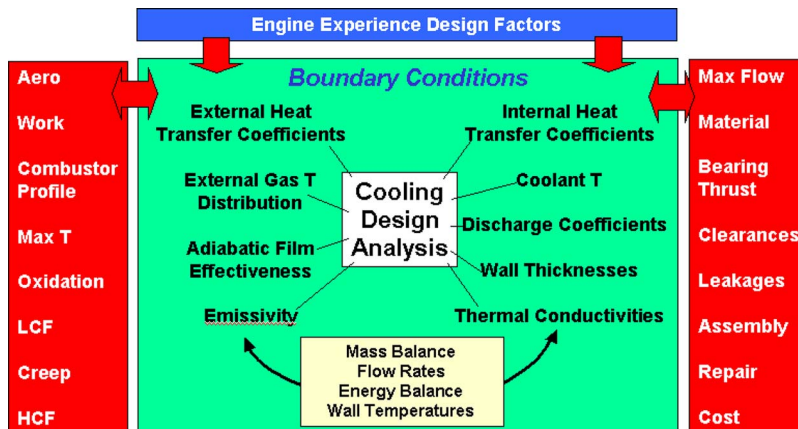


Fig. 3 Detailed design process for cooled airfoils

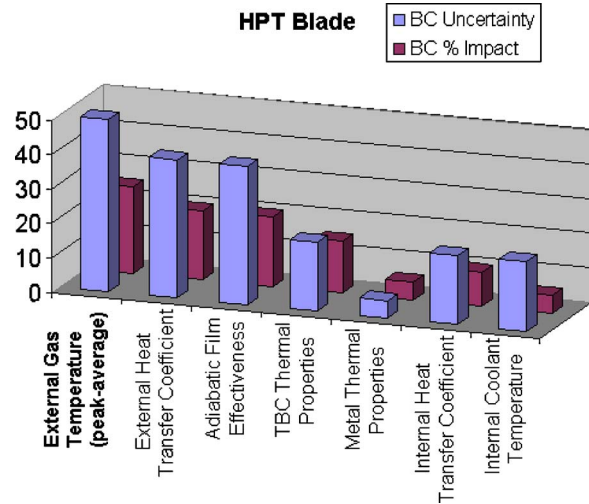


Fig. 4 Example of thermal boundary condition uncertainty and impact levels

lators in passages of differing aspect ratios. Such combined factors can have magnified effects, but these are generally only highly localized.

Material property variations will not be explicitly addressed. Generally, key properties for mechanical strength are considered to have $\pm 3\sigma$ variation in design. These variations are included in the thermal design in as much as that design must account for $\pm 3\sigma$ conditions. Properties affecting airfoil heat transfer and cooling include the thermal conductivity, thermal diffusivity, emissivity, and heat capacity. These thermal properties are usually considered constant at any particular pressure and temperature. Exceptions are made for oxidation of metal and bondcoat and also densification of TBC.

Finally, a note is worthwhile about what can or cannot be detected under inspections. If something cannot be detected by inspection then the design must conservatively account for the possible effects. If it can be detected, then conservatism may be reduced, but obtaining sufficiently detailed information on each and every part is time consuming and costly. Unless every part can be inspected, standard deviations must still be allowed for in the batch population. In-process inspections of the first batches of parts are used to check on more details than final inspections and to adjust the process to achieve the desired parameter means and standard deviations. Only after this adjustment is made are inspections of the parts reduced to an after-process level. Defects will not be treated here.

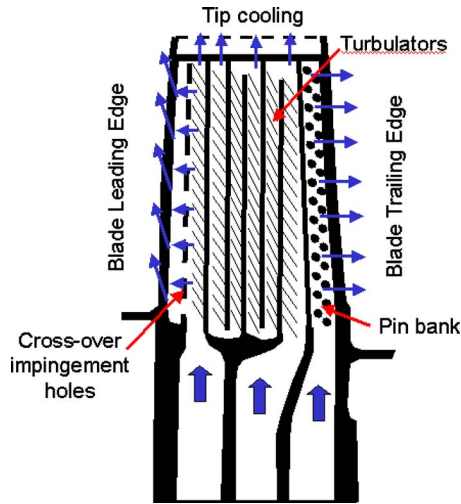


Fig. 5 Sample cooling design for a high-pressure turbine blade

2 Manufacturing Factors and Effects

In the turbine airfoil design community and among the various manufacturers there are a very large number of cooled airfoil designs and an even larger number of individual cooling features. This study will not attempt to examine all cooling features and their variations, but will instead utilize a generic representative cooled blade that incorporates many of the most commonly used

cooling technologies. Figure 5 depicts a typical turbine blade (or bucket) having three distinct internal cooling circuits, similar to the blade shown in Fig. 1. The airfoil forward region is cooled by a radial passage that delivers impingement air to the leading edge through crossover holes, while the lead edge discharges showerhead film cooling. The airfoil midchord region is cooled by a five-pass serpentine with turbulated channels and 180 deg turns. The airfoil trailing edge region utilizes a radial passage with pin bank that feeds a distribution of small axial flow channels ending in pressure side bleed slots (see Fig. 1). The blade tip section has passage dust holes and dedicated coolant holes exiting into a squealer tip. In addition, rows of film holes other than the showerhead may be located to draw from any or all of the passages to refresh the film cooling.

Thirty-two separate manufacturing factors have been selected as having definite effects upon the resulting cooling effectiveness of the blade. These factors are by no means an exhaustive list, but do represent readily identified elements of the finished product that cooling designs must account for in analyses. Table 1 provides this list of factors, the nominal tolerances for each factor, and an approximate evaluation of the influence of each factor on the cooling design parameters. The influence or effect is given as high (H), medium (M), or low (L) for simplicity and is a subjective measure that may differ among designers or have various weighting for differing designs. This measure is provided only as a general guideline here; it is not quantitatively used. The main cooling design parameters noted include the external heat transfer coefficient (EHTC), internal heat transfer coefficient (IHTC), and adiabatic film effectiveness (Film). Also noted are the discharge coefficients, friction factors, and aerodynamic loading/losses as flow parameters that influence the cooling design but are not di-

Table 1 Summary of manufacturing factors and their effect levels on cooling

Code	Factor	Tolerance	Effect of factors on cooling design parameter						
			Discharge coefficient	Internal HTC	Friction factor	External HTC	Film effectiveness	Aero load or loss	External heat flux
A1	Aerodynamic profile/shape	±0.05 mm	L	L	L	M	M	M	M
A2	Airfoil incidence angle	±2 deg	L	L	L	M	M	M	M
A3	Surface roughness (initial)	+1 μm	L	L	L	H	M	M	H
B1	Bondcoat thickness	±0.025 mm	L	L	L	L	L	L	L
B2	TBC thickness	±0.05 mm	L	L	L	L	L	M	H
B3	Local wall thickness	±0.125 mm	L	L	L	L	L	L	L
C1	Film hole diameter (effective)	±10%	M	L	L	M	H	M	M
C2	Film hole L/D	±6%	M	L	L	L	M	L	M
C3	Film hole angle to surface tangent	±5 deg	M	L	L	M	H	M	M
C4	Film hole orientation to external flow	±5 deg	M	L	L	M	H	M	M
C5	Film hole orientation to internal flow	±5 deg	H	L	L	L	M	M	M
C6	Film hole P/D	±10%	L	M	L	M	H	M	H
C7	Film hole shaped exit spec	±30%	H	L	L	H	H	H	H
D1	Impingement hole diameter	±10%	L	L	L	L	L	L	L
D2	Impingement array X/D or Y/D	±10%	L	H	M	L	L	L	L
D3	Impingement Z/D	±20%	L	H	M	L	L	L	L
D4	Crossover hole diameter	±10%	H	H	L	L	L	L	L
E1	Cooling passage turn aspect ratios	±10%	L	H	H	L	L	L	L
E2	Passage H/W (or aspect ratio)	±10%	L	M	H	L	L	L	L
F1	Turbulator e/D (blockage)	±20%	M	H	H	L	L	L	L
F2	Turbulator radius r/e	±50%	L	M	H	L	L	L	L
F3	Turbulator P/e	±20%	L	M	H	L	L	L	L
F4	Turbulator angle	±5 deg	M	H	H	L	L	L	L
F5	Turbulator end wrap-around	±50%	L	M	M	L	L	L	L
F6	Turbulator lean	±5 deg	L	M	M	L	L	L	L
G1	Pin diameter	±20%	L	L	M	L	L	L	L
G2	Pin fillet r/H	±20%	L	M	H	L	L	L	L
G3	Pin array S/D	±10%	L	H	H	L	L	L	L
G4	Pin H/D	±20%	L	M	H	L	L	L	L
H1	TE channel blockage e/H	±20%	L	M	M	L	H	M	M
H2	TE exit slot or hole H/W (aspect ratio)	±10%	M	M	H	M	M	M	M
H3	TE lip thickness to slot height ratio t/H	±25%	H	L	L	H	H	M	H

rectly specified in the thermal boundary conditions. The external heat flux is also shown since this is related to the aerodynamics, cooling flows, and the airfoil materials/construction, and affects the cooling requirement.

The several groups of factors will be briefly described here including the tolerance for each, the nominal design value for the present example, and the known effect of the factor as it influences the main cooling parameters. Nominal design values in this example are those for a stage 1 blade of a large heavy frame gas turbine in the 150 MW class. For each factor, only the most-influenced cooling parameter (EHTC, IHTC, or Film) will be discussed, as this will dominate the subsequent estimates of overall cooling effectiveness. The tolerances provided for each factor should also be viewed as approximate. In fact, the results of this study can be used to provide a means for the assessment of the tolerances and their adequacy.

2.1 External Aerodynamics. The airfoil aerodynamic profile or shape (A1), the incidence angle for the nominal operating condition (A2), and the surface roughness (A3) are the three manufacturing factors affecting primarily the EHTC. The airfoil surface coordinates are generally specified with tight tolerances since the aerodynamic performance can be very sensitive to small changes. The aft region of the airfoil and most especially the throat diameter are tightly controlled due to the potential for flow separations and variable turbine flow rates. A tolerance of 0.05 mm for the throat diameter is desired. While the aerodynamic effects of small profile changes are continuously under study, there is no available investigation of such changes on the external heat transfer. The effect of airfoil shape will be taken as equal to that of incidence angle.

The effect of incidence angle, however, has been studied with respect to EHTC. Giel et al. [1] performed full-surface heat transfer coefficient (HTC) measurements in a linear cascade for a representative power turbine blade shape and varied the incidence angle by the tolerance amount of ± 2 deg. Effects were noted in the stagnation region, slight changes in the pressure side forward diffusion region, and in an earlier boundary layer transition to turbulent flow. Overall, a +2 deg change resulted in about 6% higher airfoil heat transfer, while a -2 deg change did not appreciably alter heat transfer. For a more aggressive ± 5 deg incidence angle change, Arts et al. [2] showed similar but stronger effects, albeit on a differing airfoil shape.

In the present context, airfoil surface roughness is the initial manufactured roughness as the airfoil is first put into service. Most high-pressure turbine blades now employ TBCs, which are typically polished from a very rough condition (e.g., for air plasma sprayed TBC) to a smoother condition. External surface roughness is known to have potentially large effects on EHTC. Operational evidence suggests that an airfoil with initially smoother surface will not become as rough in service, or at least will not roughen as quickly, due to deposits, erosion, or corrosion. The study of Bunker [3] specifically measured heat transfer coefficients on TBC coated surfaces for as-sprayed roughness and various degrees of polishing. A typical specification for nominal initial roughness is 2.5 μm (roughness average value), while the tolerance is about ± 1 μm . At these values, the rougher surface led to a 2% increase in EHTC as interpolated from the data of Bunker [3], while the smoother surface provided no decrease.

2.2 Airfoil Wall Construction. The typical cooled blade wall section is simply composed of an investment cast nickel or cobalt alloy base metal (B3), a metallic bond coat (B1), and a layer of TBC (B2). The base metal structural design and thickness are an integral part of the overall thermal-mechanical design. The base metal thickness provided as a product of the casting will have a tolerance of about ± 0.125 mm on a nominal value of 2 mm, with limits set on the thermal stresses, low cycle fatigue life, and creep rupture life. The bond coat is only about 0.2 mm thick with a tolerance of ± 0.025 mm. The bond coat is only present to provide

strain matching and bonding augmentation for the TBC. Base metal and bond coat have only minor effects on the heat transfer via thermal conductivity. It is the TBC layer that has come to be relied upon as a heat load mitigation technology. With a nominal thickness of 0.5 mm and a tolerance of ± 0.05 mm, TBC thickness variations can have a substantial effect on the external heat flux and the resulting maximum base metal and bond coat temperatures. This effect is contained in the TBC thermal conductivity, taken here as 0.173 W/m K.

2.3 Film Cooling. Film cooling in all of its various formats has become a mainstay of cooling technology today. To fully characterize film cooling behavior one would need a multitude of parameters concerning the film injection, hot gas flow, geometry, and interaction effects. Manufacturing constraints influence and limit the geometry of the film holes and the part. These factors include the effective film hole diameter (C1), film hole length-to-diameter ratio L/D (C2), film hole axis angle to the external surface tangent (C3), film hole orientation to the external (C4) and internal flow (C5), film hole pitch-to-diameter ratio P/D (C6), and the specification of the hole exit shaping (C7). All of these factors primarily affect the adiabatic film cooling, or do so indirectly by affecting the discharge coefficients.

The effective film hole diameter refers to the combination of a measurable hole throat area and a discharge coefficient. This combination varies with the manufacturing method used to drill film holes. EDM uses a high electrical conductivity shaped tool to burn away the desired material within an electrolyte bath by electrical discharge. For a round hole the tool is shaped as a cylinder slightly undersized from the final desired hole diameter. Burn rates are somewhat slow to avoid damage of the part and to maintain good consistency of the resulting film hole. A shaped film hole is made with a negatively shaped tool. A typical EDM film hole has a very uniform internal surface finish with an average roughness of about 2.5 μm . A round EDM film hole can usually be counted on to have a discharge coefficient of about 0.8 for plenum supply conditions. Abrasive water jet machining is a relatively new process gaining popularity in small and microdrilling operations. Water-jet drilling can be applied by continuous or pulsed operation, percussion, or trepanning operation. Water jet can be employed to produce virtually any of the film hole sizes and shaped in use today. Under well controlled conditions, water jet can produce very clean and tailored holes, including shaped exits. Laser drilling is perhaps the most common technique employed due to its rapid processing, ready programming on multi-axis machines, and low cost. Laser drilling can also be applied by continuous or pulsed operation, percussion, or trepanning operation. Film holes are usually drilled by the percussion method. In this method, a molten metal zone is formed as the laser energy is deposited in the metal; the metal is carried off as a vapor and also forms a plasma in the trapped region. As a result, laser drilling results in a somewhat irregular internal hole diameter and finish. For smaller holes this effect can be magnified to the extent that a significant percentage of the flow area cannot be measured by a simple pin gauge. A typical laser hole discharge coefficient is larger than that of an EDM hole, closer to 0.9. Manufacturing variations in the effective film hole area for any of these processes act as an equivalent blockage on the ideal flow area, or in terms of measurable geometry an equivalent shift in P/D . Film hole nominal diameters of 1 mm are allowed a tolerance of $\pm 10\%$. An example of the effect of such blockages on film cooling performance is shown in the study of Bunker [4] where adiabatic effectiveness changed by 20%.

The component wall thickness also has an effect on the resulting film cooling performance. Film hole sizing is usually desired to be as small as reasonably possible, such that better distribution of the coolant is obtained across a region. Small sizing also helps with issues of boundary layer disturbance. However, there are real practical limits to hole sizes due to manufacturing and debris plugging. For a given wall thickness, combined with limited mini-

imum hole diameters, a certain range of hole length-to-diameter ratios will result. As a rule, the minimum acceptable hole L/D ratio is about 1.5 for the circular metering portion of the hole. This minimum comes from the requirement that the film hole still acts as a short tube, and not as a "port" hole with overlapping inlet and exit (i.e., orifice). The study of Lutum and Johnson [5] measured film effectiveness downstream of a row of round axial holes with 35 deg angle and pitch spacing of about 3. From the data of Lutum and Johnson [5] it is clear that film hole L/D ratios of 5 or greater are desired to avoid decreased effectiveness magnitudes. Tolerances of $\pm 6\%$ may be allowed for a nominal L/D value of 5, which according to Lutum and Johnson [5] will result in a 20% decrease in film effectiveness for shorter holes. This is a substantial change in film effectiveness, which may raise the question of simply increasing the hole L/D to reduce this variation. Greater L/D can be achieved by thicker walls, but this adds weight and may increase thermal resistance and stress. Greater L/D could also be achieved by a more shallow hole angle, but here again limitations are present for manufacturing, such as the very real bouncing of the laser off a surface at small angles.

Factors C3, C4, and C5 concern the various angles of the film holes relative to the external surface tangent, external flow direction, and internal flow direction, respectively. The orientation angles relative to the external and internal flows are those predicted for the design and so are referenced to engine axial and radial directions or against some convenient data on the part. Nominally, a typical angle to the surface tangent is 30 deg, and an orientation to the expected external flow is 0 deg to minimize aerodynamic losses (though not always). Orientation to the internal flow is taken as an average of 45 deg because the internal designs of cooled airfoils contain a wide variety of geometries and resulting local flow characteristics surrounding the entry regions of film holes. Film cooling hole entries may in all cases be integrated with these complex internal geometries, creating a vast diversity of possible entry flow conditions to the holes. For each of these three angle factors a variation of ± 5 deg may be allowed. The existing literature concerning the effect of surface angle on film effectiveness contains only a few discrete values of angles, i.e., 30 deg, 35 deg, 45 deg, and 60 deg, and furthermore the data are scattered over many differing experiments and conditions, making clear interpretation of the effect magnitude for only ± 5 deg very difficult. As a consequence, the typical experimental uncertainty for such experiments, about $\pm 10\%$ for average film effectiveness, will be used to represent the variation for this factor. The literature surrounding the effect of orientation to the external flow is even more spread out in angular values, i.e., 0 deg, 45 deg, 60 deg, and 90 deg. Since this factor is simply a deviation from predicted design intent, a lesser variation of $\pm 5\%$ will be used. Likewise for the internal flow orientation, as the available data are far less, a variation of $\pm 5\%$ will be assumed from the design intent.

The film hole pitch-to-diameter ratio P/D , or surface spacing, is a straightforward factor that adjusts the average film effectiveness according to the coverage of the film row. For example, if the nominal P/D is 3 and the film holes are round, the coverage is 0.33 and the resulting average peak film effectiveness is also 0.33 (aside from other effects such as film blowoff). If then the P/D is allowed a variation of $\pm 10\%$, the local coverage and film effectiveness could be as high as 0.36 or as low as 0.27. This general rule of coverage effect is well established in literature.

Film hole exit shaping, such as fan-shaped diffusers, is now a common practice for all film holes where this provides a cost-effective performance benefit. The shaped footprint is provided a specification, which may change according to the location on the cooled airfoil, for example, to account for the effects surface curvature may impose on the manufacturing method. Generally, the actual execution of applying shaped film hole exits results in a considerable variation, as much as 30% alteration of the diffuser side angle from a nominal value of 15 deg. The effect on film

effectiveness is again contained in the surface coverage value of the exit of the diffuser. Accounting for the angle changes, this leads to changes of $+16\%/-13\%$ to the average effectiveness.

2.4 Impingement Cooling. Impingement jet cooling of the interior of cooled airfoils is commonly employed for its very high heat transfer coefficients. Vanes typically utilize internal sheet metal impingement baffles to deliver arrays of jets, while blades make use of leading edge and trailing edge crossover impingement holes in the castings. By the intent of impingement cooling, it is the IHTC that is most affected by manufacturing variations. Whether in an array format or a single row of impinging jets, the main factors influenced by manufacturing include the jet diameter D (D1), the jet center-to-center spacing X/D and Y/D (D2), and the target distance Z/D (D3).

In an impingement array, the jet diameter variation impacts the nondimensional target distance Z/D , which is known to have a local and array-averaged effect on the resulting IHTC. For a nominal jet diameter of 0.75 mm, the variation allowed is about $\pm 10\%$. Even if the jet diameters might be controlled more precisely, other manufacturing aspects contribute to this variation, such as the positioning of baffles within castings by offset pins on the baffle or on the casting wall. The study of Bailey and Bunker [6] covered a substantial range of impingement array parameters from $x/D=y/D$ from 3 to 9, z/D from 1.25 to 5.5, and jet-averaged Reynolds numbers of 14,000–65,000. Their results were very much in agreement with established correlations such as that of Florschuetz et al. [7], but with broader range. The present effect on IHTC is about $\pm 10\%$ for typical Z/D ranges.

The factor of jet array spacing, X/D and Y/D , is also allowed a variation of $\pm 10\%$ on a nominal value of 6 for each. Using the correlation developed in Ref. [6] this variation results in as much as 20% change to the IHTC.

Jet target distance Z/D is treated separately from the jet diameter since both may be affected due to the use of multiple parts in the cooled airfoil. As noted above, factor and IHTC variation are each $\pm 10\%$. The nominal target spacing Z/D is about 2.5.

Crossover impingement jet holes are either formed as part of the castings or machined after casting if access is available. Though a cast feature may appear to be less accurate than a hole formed in a sheet metal plate, the tolerances allowed for crossover holes are maintained fairly tight, about $\pm 10\%$ on diameter again. As these holes are the dedicated cooling for more sensitive regions like the leading edge stagnation region, it is very important that they not vary too much. As with the arrays of jets, the effect on IHTC is about 10%, controlled by the Z/D . In some designs, directionality of these holes can also be important, for example, if the concave leading edge changes in shape along the radial direction.

2.5 Internal Cooling Passages. The number of possible cooling passage designs, shapes, orientations, and augmentations is nearly limitless, but for the present purposes an average cooling passage definition for a multipass serpentine cooled blade is considered. This average cooling passage is nominally square and oriented with lead and trail surfaces transverse to the direction of rotation. Manufacturing variations may affect the passage turn region aspect ratio at the tip and root sections (E1) and also the main passage aspect ratio or height-to-width ratio (E2). Such changes come about primarily from the ceramic core fabrication process and also from finishing steps involving the cleaning of castings, and tip region machining and brazing. The nominal allowed variation is at most $\pm 10\%$ for each aspect ratio factor. The nominal aspect ratio for the average passage considered is 1, and the usual design value for turn aspect ratios is also 1. In neither case are there any literature data that would provide the effect upon IHTC for such small changes. There are considerable data concerning passage aspect ratio effects for greater geometry differences. The summary of Han et al. [8] suggests that only a very minor change of 1% to the IHTC would result.

2.6 Turbulated Channels. A major portion of the turbine blade internal cooling is augmented through the use of various definitions of turbulators, also known as repeating rib rougheners. The main geometric parameters that are specified for cooling passages with turbulators include the turbulator height-to-channel hydraulic diameter ratio e/D (F1), sometimes known as channel blockage, the edge radius ratio r/e at the top of the turbulator (F2), the pitch-to-height ratio P/e of the repeating turbulators (F3), the turbulator angle relative to the bulk channel flow direction (F4), the wrap-around extent of the ends of the turbulators on the adjacent walls (F5), and the turbulator lean from the desired normal orientation (F6). Factors that include the turbulator height are affected by the wear of the core die and consequently result in unavoidable variations through the life of the die. Each of the factors noted may experience variation due to improper processing in one or more steps of the investment casting process.

The first of these factors, the relative turbulator height or channel blockage, has a nominal value of 0.1 on a single turbulated side of the channel. Since the majority of channels are turbulated on two opposite walls, the total local channel area blockage can be 20% or more, but this is generally avoided by staggering the turbulators on the opposed walls. The e/D value has a fairly wide range depending on the desired heat transfer augmentation, but a value of 0.1 is average. Considering that the actual dimension for the turbulator height is about 1 mm, the tolerance allowed will be about $\pm 20\%$. Among several studies, the investigation of Taslim and Spring [9] determined that this modification to e/D results in a $\pm 7\%$ change to the IHTC.

The relative turbulator radius is a requirement of the casting process in that no sharp corners can be obtained. There is, in fact, a radius at both the base fillets of the turbulators and on the top corners, but it is the top radius that has a greater impact on flow resistance and heat transfer. This top radius is also the portion of the geometry most affected by die wear. A generous allowance of $\pm 50\%$ is provided on a nominal r/e value of 0.25, keeping in mind that most turbulators are defined to have equal width and height. This allowance still avoids the turbulator top becoming a fully rounded feature. The study of Taslim and Lengkon [10] focused on the provision of turbulator radius and observed about $\pm 2\%$ effect on IHTC for this range of variation.

Turbulator pitch-to-height ratio is another variable that may be specified to deliberately alter the average channel internal heat transfer, but when this ratio becomes too large the surface variation in IHTC also increases. Several studies have shown that peak IHTC results for P/e values in the range of 8–12, and so the usual nominal value selected is 10 with a tolerance up to $\pm 20\%$. Based on the works of Taslim and Lengkon [10] and also Han et al. [11] this variation can lead to a $\pm 5\%$ change to the average IHTC. For this factor, a lesser P/e results in higher IHTC and the greater P/e yields a lower IHTC.

Turbulator angle relative to the bulk flow direction, not accounting for buoyancy or rotational complexities, is well known to have a balanced performance of good heat transfer with moderate friction coefficient when the angle is 45 deg. This angle will only be allowed to vary slightly, about ± 5 deg. From the study of Park et al. [12] the effect of this small variation on IHTC is only about $\pm 2.5\%$.

The definition of the ends of the turbulators is sometimes problematic. It is desirable that the turbulators not terminate prior to the end walls in order to avoid zones of dead flow in the corners. It is also desirable to get the most out of the heat transfer augmentation of turbulators, yet investment casting processes and geometries do not allow turbulators to be placed fully on the interior channel walls (i.e., the cold ribs). Some partial wrap-around through the corners is desired, but there is no firm nominal value. Tolerances of 50% can be allowed as long as the feature is still present. The investigation of Taslim et al. [13] considered so-called J-ribs in turbulated channels, which to some degree mimics

the wrap-around intent. They found no change to IHTC for more feature, but a 12.5% reduction for a reduced extent feature.

Turbulators are nominally desired to project normal to the surface, i.e., to have no lean at all. Depending on the required pull planes of the casting, turbulator lean can result. No more than a ± 5 deg lean is allowed. The study of Bunker and Osgood [14] obtained heat transfer measurements for a range of positive and negative turbulator lean values up to 45 deg. For a lean of only 5 deg no change in the IHTC is indicated.

2.7 Internal Pin Banks. The use of pin banks, or arrays of pin fins, connecting the internal pressure and suction sides of an airfoil is more selective and limited than turbulators. Pin banks are normally only used in the trailing edge portions of airfoils to provide enhanced internal heat transfer with mechanical integrity. As a consequence of this thermal-mechanical role, there are definite geometry constraints placed on the pins in terms of size and spacing. The strength of ceramic cores desires larger spacing and the fill of molten metal desires larger pins, so there must be compromises. The main geometric quantities include the pin diameter (G1), the pin fillet radius-to-pin height ratio r/H (G2), the pin array center-to-center spacing ratio S/D (G3), and the pin height-to-diameter ratio H/D (G4). Since the basic function of the pin array can be obtained with fairly generous variations on any of these factors, each is allowed a $\pm 20\%$ tolerance with the exception of $\pm 10\%$ for S/D .

The pin diameter for the present case has a nominal value of 2 mm. A variation in this diameter amounts to a change in the relative spacing S/D . Holding the spacing constant, if the diameter is allowed to vary by 20% then the effect on S/D is about $-20\%/+32\%$. Using the study of Metzger et al. [15] for row-resolved heat transfer in pin bank arrays, the effect on average IHTC is about $+6\%/-8\%$.

The pin fillet radius is another requirement of casting, just as in the case of turbulators. A nominal value for r/H is 0.25 meaning that fully half of the pin channel height (top+bottom) is involved with the fillets, and only the middle half of each pin is actually a cylinder of constant diameter. The investigation of Wang et al. [16] showed that essentially equal heat transfer performance was obtained with and without such fillets.

The pin array relative spacing S/D , now holding the diameter constant, has a typical value of 2.5. As noted above, the allowed tolerance on this factor is only $\pm 10\%$. This is due to the need to maintain more precision on pin placement within the restricted overall geometry of an airfoil trailing edge region. Using the same data of Metzger et al. [15], this variation leads to half of the effect of the pin diameter or an effect of $+3\%/-4\%$ on IHTC.

Pin height-to-diameter variations are primarily the result of changes in the pin diameter since the trailing edge channel height is controlled to a greater degree. The study of Brigham and Van-Fossen [17] concerning this parameter shows that a 20% change produces a 10% change in the average IHTC.

2.8 Airfoil Trailing Edge Cooling. Finally, the airfoil trailing edge is provided some special attention as a region that proves very difficult to maintain from both the cooling and mechanical integrity viewpoints. The trailing edge is extremely limited in geometry and cooling options. For the very common configuration of internal cooling channels feeding a series of pressure side bleed slots, the three main manufacturing factors are the internal cooling channel blockage e/H (H1), the channel exit slot aspect ratio H/W (H2), and the bleed slot upper lip thickness-to-slot height ratio t/H (H3).

The internal cooling channels within the aftmost trailing edge of an airfoil are necessarily the smallest in the entire airfoil and also very likely to have the largest length-to-diameter ratio. These facts make the channels a severe challenge for investment casting, so much so that the channels are sometimes separately machined after casting. To maintain the aerodynamically thin trailing edge as well as the required minimum wall thickness, the channel

Table 2 Manufacturing factor tolerances and nominal values for a large industrial turbine blade

Code	Factor	Tolerance	Nominal value	Units	Design tolerance	Comment
A1	Aerodynamic profile/shape	± 0.05 mm	na	mm	± 0.05 mm	Throat area; flow separation
A2	Airfoil incidence angle	± 2 deg	na	deg	± 2 deg	Separation; transition
A3	Surface roughness (initial)	$+1$ μ m	2.5	μ m	3.5	No penalty for smoother
B1	Bondcoat thickness	± 0.025 mm	0.2	mm	0.175–0.225	
B2	TBC thickness	± 0.05 mm	0.5	mm	0.45–0.55	
B3	Local wall thickness	± 0.125 mm	2	mm	1.875–2.125	Thermal stresses
C1	Film hole diameter (effective)	$\pm 10\%$	1	mm	0.9–1.1	Coating blockage
C2	Film hole L/D	$\pm 6\%$	5	**	4.7–5.3	Derived from other factors
C3	Film hole angle to surface tangent	± 5 deg	30	deg	25–35	
C4	Film hole orientation to external flow	± 5 deg	0	deg	–5–5	Nominal is axial orientation
C5	Film hole orientation to internal flow	± 5 deg	45	deg	40–50	Average orientation used
C6	Film hole P/D	$\pm 10\%$	3	**	2.7–3.3	
C7	Film hole shaped exit spec	$\pm 30\%$	15	deg	10.5–19.5	Fan-shaped hole
D1	Impingement hole diameter	$\pm 10\%$	0.75	mm	0.675–0.825	
D2	Impingement array X/D or Y/D	$\pm 10\%$	6	**	5.4–6.6	
D3	Impingement Z/D	$\pm 10\%$	2.5	**	2.25–2.75	
D4	Crossover hole diameter	$\pm 10\%$	1	mm	0.9–1.1	
E1	Cooling passage turn aspect ratios	$\pm 10\%$	1	**	0.9–1.1	Average of a multipass circuit
E2	Passage H/W (or aspect ratio)	$\pm 10\%$	1	**	0.9–1.1	Average of a multipass circuit
F1	Turbulator e/D (blockage)	$\pm 20\%$	0.1	**	0.08–0.12	
F2	Turbulator radius r/e	$\pm 50\%$	0.25	**	0.125–0.375	
F3	Turbulator P/e	$\pm 20\%$	10	**	8–12	
F4	Turbulator angle	± 5 deg	45	deg	40–50	
F5	Turbulator end wrap-around	$\pm 50\%$	Partial	**	0.5–1.0	No firm nominal value
F6	Turbulator lean	± 5 deg	0	deg	–5–5	
G1	Pin diameter	$\pm 20\%$	2	mm	1.6–2.4	
G2	Pin fillet r/H	$\pm 20\%$	0.25	**	0.2–0.3	
G3	Pin array S/D	$\pm 10\%$	2.5	**	2.25–2.75	
G4	Pin H/D	$\pm 20\%$	3	**	2.4–3.6	Derived from other factors
H1	TE channel blockage e/H	$\pm 20\%$	0.25	**	0.2–0.3	High blockage turbulators
H2	TE exit slot or hole H/W (aspect ratio)	$\pm 10\%$	0.4	**	0.36–0.44	
H3	TE lip thickness to slot height ratio t/H	$\pm 25\%$	0.5	**	0.375–0.625	

height must be very small. As a consequence, any heat transfer augmentation such as the use of turbulators results in very high blockage ratios compared to other passages in the airfoil. It is not uncommon to find e/H blockages of 25% or greater, while the same limitations and $\pm 20\%$ tolerance apply as in the case of turbulated channels. The study of Bailey and Bunker [18] examined the heat transfer coefficients in a turbulated channel with such very high blockages. For the indicated tolerances, the IHTC would vary by about $\pm 4\%$. This factor impacts both the IHTC and the subsequent slot film effectiveness, but here the IHTC is the main concern.

The exit of the trailing edge channels must conform well to the geometry of the thin radial base of the airfoil. To do this, the exits are typically in the form of rectangular slot openings with nominal H/W aspect ratio of 0.4, where the width is the radial dimension. These slot openings need to be closely controlled due to the positional tolerances and wall thickness requirements in the restricted geometry. A tolerance of $\pm 10\%$ is allowed for this aspect ratio. There is no available study of the effect of this aspect ratio on the resulting slot film effectiveness, but in general as the aspect ratio increases the film cooling acts less like a protective layer and more like a film hole, leading to less cooling effectiveness. An equivalent 10% reduction in film effectiveness is assumed for the 10% change in aspect ratio. However, if the aspect ratio decreases from nominal, no added benefit is assumed since the slot is already provided good film cooling.

The pressure side relative lip thickness is known to have an impact on the resulting slot film effectiveness. Some structural wall thickness is required to avoid cracking and creep issues, yet it is desired to have a very thin lip thickness compared to the slot height to minimize aerodynamic losses and coolant mixing effects with the hot gases. The nominal t/H value is 0.5. A tolerance of $\pm 25\%$ is allowed that accounts mostly for the change in lip thick-

ness due to core shifts. The study of Kacker and Whitelaw [19] indicates that this variation in relative lip thickness yields a $\pm 6\%$ effect on the slot film effectiveness. In this case, a lesser relative lip thickness results in greater film effectiveness.

3 Tolerances on Nominal Cooling Design Conditions

The foregoing discussion of 32 manufacturing factors and tolerances is summarized in Table 2 with the nominal values for each factor, as well as the resulting range of parameter values due to the allowed tolerances. As a reminder, the parameter values and ranges noted do not include the effects of operational factors, such as combustor profile and pattern factors, or in-service changes, such as surface erosion and debris deposition. Only the manufacturing tolerances for parts entering service have been considered.

4 Simplified Cooled Airfoil Model

For the purpose of calculating the blade wall metal temperature changes due to each of the manufacturing factor variations, a very simplified model of a cooled airfoil is used. Figure 6 shows the level of simplification from the entire blade to only a radial section of the airfoil containing all of the cooling passages, then to a flat plate representation with hot gas flow on one side and coolant flow on the other (film holes not shown). This simplified analysis approach is explained in detail in the handbook solution of Bunker [20]. Each side of the airfoil is considered as a flat plate with leading edge starting point at $X=0$. The external heat transfer coefficient distribution is calculated along the entire length of the plate, including laminar and turbulent regions if applicable, using standard correlations for boundary layer heat transfer in a zero pressure gradient flow, namely, per Kays and Crawford [21],

$$\text{laminar } H_{\text{gas}}(x) = 0.332(k/x) \times \text{Re}^{0.5} \text{Pr}^{1/3}$$

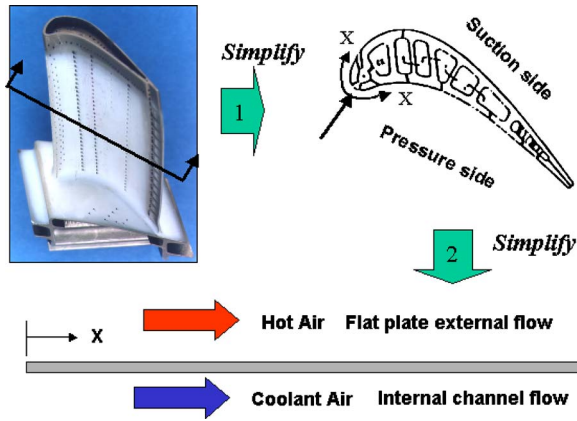


Fig. 6 Simplified model for estimation of blade cooling effects

$$\text{turbulent } H_{\text{gas}}(x) = 0.0287(k/x) \times \text{Re}^{0.8} \text{Pr}^{0.6}$$

The hot gas Mach number is taken as an average of 0.6 for the entire airfoil, but the local boundary layer Reynolds number still varies with distance and property changes over an appropriate magnitude range. The internal cooling flow can be estimated either as a turbulent channel heat transfer or as an impingement array heat transfer. The germane result for the coolant side is that the internal heat transfer coefficient is a realistic augmented magnitude over that of smooth fully developed turbulent duct flow heat transfer. In the present nominal calculation this augmentation factor is 4, which is representative of impingement cooling or rotational turbulent channel flow. At each location of the blade wall along the surface the one-dimensional model of Fig. 7 is employed to calculate material temperatures. This one-dimensional analysis captures the primary effect of each considered parameter without masking due to design-specific geometry. An iterative solution provides the metal temperatures along the entire blade length accounting for internal and external fluid property changes. Thermal radiation is not included in this model. Table 3 shows the input conditions for gas and coolant as well as the wall and coating thicknesses. The surface average nominal conditions of the airfoil include an aerodynamically smooth surface (as manufactured) and an adiabatic film effectiveness of 0.4. The nominal factor values result in a blade row total cooling flow rate of 5.2% of the compressor discharge flow for an appropriately sized blade. Table 3 also provides the surface averaged values of heat flux, IHTC, and EHTC under nominal conditions.

5 Results and Discussion

When used with completely nominal values, the simplified yet representative blade cooling estimation described above leads to an average IHTC of 2600 W/m² K and an average EHTC of 5850 W/m² K. The average film effectiveness is assumed to be 0.4 everywhere except in the trailing edge pressure side bleed slots where a value of 0.8 is used due to the very short and tan-

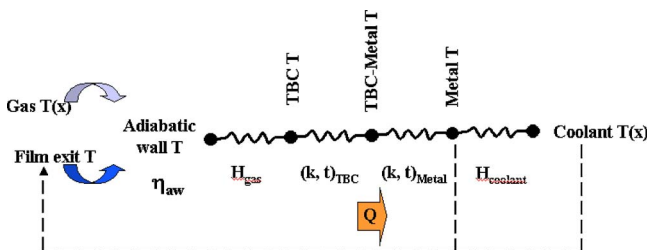


Fig. 7 One-dimensional heat transfer model applied to each blade surface location

Table 3 Blade analysis input conditions

Inlet gas P total	20.4 bars (300 psi (absolute))
Inlet gas T total	1510 °C (2750 °F)
Coolant P	21.8 bars (320 psi (absolute))
Coolant T	483 °C (900 °F)
Average gas Mach	0.6
Average film effectiveness	0.4
Wall thickness	2 mm (0.080 in.)
Bond coat thickness	0.2 mm (0.008 in.)
TBC thickness	0.5 mm (0.020 in.)
Surface average roughness	2.5 μm (100 μin.)
Internal cooling Re	30,000
Blade row cooling W_c (%)	5.2
Wall heat flux	648.4 kW/m ²
Internal average HTC	2600 W/m ² K
External average HTC	5850 W/m ² K

gential nature of the flow. In calculating the effect of factors H2 and H3 on metal temperature, the internal cooling was removed since it does not exist on the exposed trailing edge. Table 4 summarizes all of the manufacturing factors again, the main boundary condition impacted, the previously described ranges of variations on the factors normalized to the nominal values, and the resulting ranges for the heat transfer boundary conditions. Wall thickness and bond coat thickness variations are not considered at this point as the resulting changes in thermal boundary conditions are negligible. TBC thickness is included due to its significant influence on heat flux (HF). The TBC factor shown is the thermal conductivity, the nominal cooling value is the temperature drop across the TBC, and the cooling range is the resulting metal temperature range.

The last column of Table 4 is the change in maximum metal temperature from nominal, as estimated by the model, due to the individual effect of each of the manufacturing factors. These metal temperature changes are compared in the Pareto chart of Fig. 8. Factors resulting in zero change are not included in the Pareto. Looking at the overall groups of factors, the external aerodynamic factors have little impact on blade temperature due to the very tightly controlled tolerances required. TBC thickness is a well recognized factor affecting blade temperature; thus even fractions of a millimeter in variation can have substantial impact. The application of TBC should therefore always err on the "more is better" side, but the overall design must stay within experience limits for TBC strain and durability.

Film cooling factors are all shown to be significant, which is understandable by the high degree of heat flux reduction provided for the entire airfoil by this technology. Two factors especially, the film hole diameter and the L/D ratio, stand out as the maximum factors for the entire Pareto with up to 40 °C metal change. This seems a magnitude of change that would be difficult to overcome without far tighter tolerances being enforced. In reality though, quality specifications will not allow more than a fraction of the film holes to be out-of-spec. Flow checks for the airfoils and the flow circuits will catch cases where the flow is too low (or too high), indicative of too many holes being undersized or plugged. The high magnitude of these effects, and all of the film cooling factors, is also due to the global or full-surface nature of film cooling. Maximum effects, for example, three to five adjacent film holes flowing low, will be felt mostly in that local region. This is, however, still a significant impact, hence the attention on quality inspections for all film cooled airfoils. Film hole angles and orientations are also potentially significant factors, but there are less definitive data to support tighter tolerances on these. The general rule is to use shallow angles wherever possible. External flow orientation can be a tricky business without engine testing confirmation. Internal flow orientation relies on achievable manufacturing (e.g., no damage to the airfoil interior due to drilling) and normally distributed effects of internal flows (statistically). The

Table 4 Primary thermal boundary condition ranges and resulting metal temperature changes

Code	Factor	Main effect	Factor relationship	Nominal cooling value	Cooling value range	Max metal T deltas (°C)
A1	Aerodynamic profile/shape	EHTC	0.94/1.06	5850 W/m ² K	5500–6200	1.9
A2	Airfoil incidence angle	EHTC	1.06/1.0	5850 W/m ² K	5850–6200	1.9
A3	Surface roughness (initial)	EHTC	1.02	5850 W/m ² K	5967	0.6
B1	Bondcoat thickness	None	None	**	**	**
B2	TBC thickness	HF	0.173 W/m K	397 K/mm	849–874 °C	12.8
B3	Local wall thickness	None	None	**	**	**
C1	Film hole diameter (effective)	Film	0.8/1.2	0.4	0.32–0.48	39.4
C2	Film hole L/D	Film	0.8/1.0	0.4	0.32–0.4	39.4
C3	Film hole angle to surface tangent	Film	1.1/0.9	0.4	0.36–0.44	19.4
C4	Film hole orientation to external flow	Film	0.95	0.4	0.38	10.0
C5	Film hole orientation to internal flow	Film	0.95	0.4	0.38	10.0
C6	Film hole P/D	Film	0.9/1.1	0.4	0.36–0.44	19.4
C7	Film hole shaped exit spec	Film	0.87/1.16	0.4	0.35–0.46	24.4
D1	Impingement hole diameter	IHTC	1.09/0.9	2600 W/m ² K	2340–2834	22.2
D2	Impingement array X/D or Y/D	IHTC	1.2/0.8	2600 W/m ² K	2080–3120	36.1
D3	Impingement Z/D	IHTC	1.09/0.9	2600 W/m ² K	2340–2834	22.2
D4	Crossover hole diameter	IHTC	1.09/0.9	2600 W/m ² K	2340–2834	22.2
E1	Cooling passage turn aspect ratios	IHTC	1	2600 W/m ² K	2600	0.0
E2	Passage H/W (or aspect ratio)	IHTC	0.99/1.01	2600 W/m ² K	2574–2626	2.2
F1	Turbulator e/D (blockage)	IHTC	0.93/1.07	2600 W/m ² K	2418–2782	10.0
F2	Turbulator radius r/e	IHTC	0.98/1.02	2600 W/m ² K	2548–2652	2.8
F3	Turbulator P/e	IHTC	1.05/0.95	2600 W/m ² K	2470–2730	6.7
F4	Turbulator angle	IHTC	0.975/1.025	2600 W/m ² K	2535–2665	3.9
F5	Turbulator end wrap-around	IHTC	1.0/0.875	2600 W/m ² K	2275–2600	16.1
F6	Turbulator lean	IHTC	1	2600 W/m ² K	2600	0.0
G1	Pin diameter	IHTC	0.92/1.06	2600 W/m ² K	2392–2756	11.1
G2	Pin fillet r/H	IHTC	1	2600 W/m ² K	2600	0.0
G3	Pin array S/D (or X/D)	IHTC	0.96/1.03	2600 W/m ² K	2496–2678	6.1
G4	Pin H/D (connected)	IHTC	0.9/1.1	2600 W/m ² K	2340–2860	13.9
H1	TE channel blockage e/H	IHTC	0.96/1.04	2600 W/m ² K	2496–2704	6.1
H2	TE exit slot or hole H/W (aspect ratio)	Film	0.9/1.0	0.8	0.72–0.8	20.0
H3	TE lip thickness to slot height ratio t/H	Film	1.06/0.94	0.8	0.85–0.75	12.8

film hole P/D and exit shaping specification factors impact the film surface coverage and so have significant effect on metal temperature. Controlling P/D is easier than the exit shaping, but manufacturing processes that remove the element of operator variation or error can minimize these factors.

Impingement cooling factors show the next strongest effects on blade temperature as a whole after film cooling. Impingement hole size, spacing, and distance all have large possible impact. As with film cooling, the quality checks should assure that only localized increases (or decreases) in metal temperature occur, not airfoil-wide changes. Since impingement cooling factors are constrained to the blade internal geometry, not involving any external flow interactions, it should in practice be easier to assure (bias) variations that favor decreased metal temperatures compared to the nominal target value.

Cooling passage aspect ratio has little impact on blade temperature, but the factors associated with cooling augmentation, turbulation, and pin banks do have moderate effects. Overall, turbulated channels have remarkable robustness with respect to manufacturing. The e/D blockage factor is immediately recognized as a key factor. The turbulator end wrap-around factor is frankly not well known and in the present estimation somewhat speculative. The fact that channels having two walls turbulated versus all four walls turbulated leads to large differences in IHTC on the primary surface is telling though. The strong effect of turbulator end geometry shown here is at a minimum a signal that more understanding is of this factor would be beneficial. Pin array factors are seen to have more impact on blade temperatures than turbulators. This can be attributed to the regions where pin banks are generally employed, these regions having much more constrained geometry and hence higher variations due to achievable tolerances.

Trailing edge cooling passage blockage is seen to be a similar effect to that of turbulated channel blockage. The other two trailing edge factors, exit slot aspect ratio and lip thickness, are moderate to sizable effects on blade temperature, albeit very localized to the trailing edge. These two factors are more closely associated with film effectiveness behavior. The fact that airfoil trailing edges are typically troublesome to maintain to desired metal temperatures, despite the high amount of coolant flow used for this purpose, attests to the sensitivity of these factors.

The Pareto of Fig. 8 is single sided, that is, it shows only the maximum metal temperature changes due to one side of the variations in the manufacturing factors. There is a nearly equal opposite side where metal temperatures are reduced. In a completely random normal distribution of all factors, most of these variations would balance out to a great degree. The simplified blade model used for analysis here does not have the detail to model all 32 factors independently at the same time. Instead, the average film effectiveness and average internal heat transfer coefficient have been given normal distributions ($\pm 3\sigma$) covering the range of 0.9–1.1 of their nominal values. A CRYSTAL BALL® Monte Carlo simulation was run with 20,000 trials to determine the distribution of resulting maximum metal temperature change. Figure 9 shows that the resulting distribution for change in metal temperature covers the range of roughly $\pm 20^\circ\text{C}$. On the high side, an increase of $+20^\circ\text{C}$ could in severe cases decrease blade life by nearly 33%. This is the magnitude of potential variation that must be accommodated in the cooling design due to manufacturing tolerances.

Having noted the importance of quality inspections, and in particular that of flow checks for cooled airfoils, the same simulation was run, but this time providing a 0.9–1.1 range on coolant flow

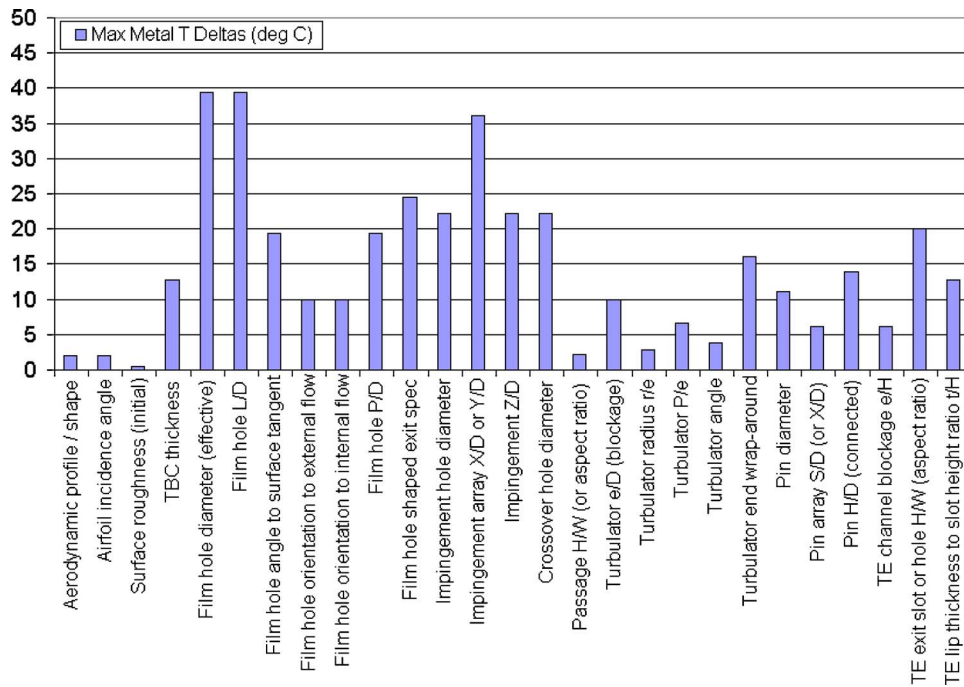


Fig. 8 Pareto of blade metal temperature changes for manufacturing factors (°C)

rate rather than IHTC. This flow rate variation would be the result of one or many manufacturing variations leading to an effective flow area change of $\pm 10\%$ (see Table 2). Figure 10 shows the resulting cumulative distribution chart for blade row cooling flow as percent of engine core flow. The blade cooling flow varies from 4.69% to 5.73% core flow in this example. More importantly, if a blade flow rate variation of $\pm 5\%$ of the average value is allowed in flow check specifications, then about 13.5% of the airfoils would be rejected. This projected result imposes a severe loss to

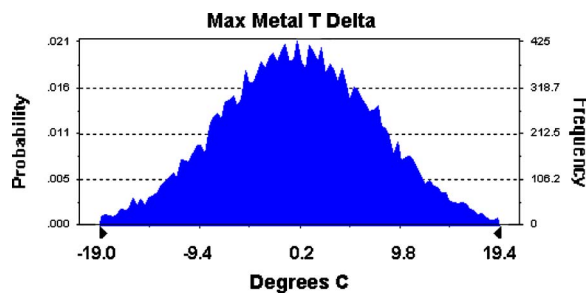


Fig. 9 Monte Carlo simulation frequency chart for blade metal temperature changes

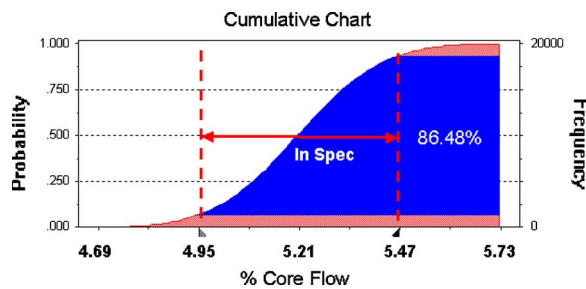


Fig. 10 Cumulative distribution of effect on blade row cooling flow rate

manufacturing yield and productivity as well as economic viability. The importance of controlling variability factors that influence the blade flow (and heat transfer) becomes very compelling.

Finally, the impact of airfoil cooling design practice may be assessed by adjusting the overall average film effectiveness and IHTC values and by repeating the simulation. Figure 11 shows the new Pareto results when an average film effectiveness of 0.6 is used with a lower average IHTC (note that the ordinate scale is double that of Fig. 8). The same coolant flow rate is maintained to provide the same film coverage, and the IHTC is lowered to provide the same nominal value metal temperatures. This adjustment shows the sensitivity of a cooling design that emphasizes film cooling over internal cooling, yet leads to the same flow and metal temperatures. Not surprisingly, the effect is to double the magnitudes of the film cooling factors, while decreasing those of internal cooling by about two-thirds.

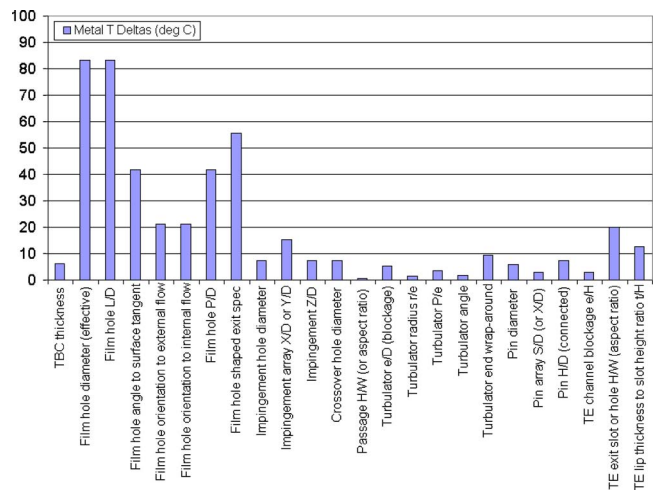


Fig. 11 Pareto of metal temperature changes for predominantly film cooled blade (°C)

6 Conclusions

The present study has identified and quantified the effects of manufacturing, as dictated by the tolerances allowed in the finished product, upon the resulting cooling design of a HPT blade. Using the features of a typical blade design, the main geometric factors that can influence the blade heat transfer capability through variability have been discussed in detail. A simple example of airfoil cooling for a representative wall section has been used to tabulate the variations with the resulting changes in the primary thermal boundary condition affected by each factor. Each of the main geometric factors has been evaluated in terms of its possible effect on maximum metal temperature. Potentially large metal temperature changes of up to $\pm 40^\circ\text{C}$ are estimated for critical film cooling geometry factors, while most of the factors associated with film cooling and impingement cooling average about $\pm 20^\circ\text{C}$ effect. Other factors such as turbulated passages tend to be more moderate in effect. A Monte Carlo simulation for typical average blade cooling shows $\pm 20^\circ\text{C}$ metal temperature variation with tolerances of $\pm 10\%$ on average film cooling effectiveness and internal heat transfer coefficient. Specification of a flow check target of $\pm 5\%$ leads to as much as 13.5% rejection of parts, a very significant level. This points to the necessity for greater understanding of the effects of manufacturing tolerances on the resulting cooling capability as well as the need for more accurate and detailed levels of quality inspections to reduce variability in final parts. In particular, for a conventionally designed cooled airfoil, additional research and development into the effects of film hole effective diameter, shape, and L/D ratio changes is needed for as-manufactured film holes and engine representative conditions. Improved understanding in this area also carries the greatest potential cost benefit, due to the relatively large fraction of cost invested in forming film holes, provided manufacturing variations can be controlled. Further research into the effects of impingement hole size and spacing is also indicated, despite the typically lower relative cost benefit, since future designs are expected to utilize more investment cast impingement with higher sensitivity to manufacturing variations.

Nomenclature

D	= film hole diameter, impingement hole diameter, pin diameter, or channel hydraulic diameter
e	= turbulator height
e/D	= relative turbulator height in rectangular duct
e/H	= relative turbulator height in trailing edge channel
H_{coolant}	= coolant side heat transfer coefficient
H_{gas}	= hot gas side heat transfer coefficient
H/W	= channel height-to-width aspect ratio
H/D	= pin height-to-diameter ratio
k	= thermal conductivity
L/D	= film hole length-to-diameter ratio
P	= pressure, or film hole pitch, or turbulator pitch
P/D	= film hole pitch-to-diameter ratio
P/e	= turbulator pitch-to-height ratio
Re	= Reynolds number
r/e	= turbulator corner radius-to-height ratio
r/H	= pin fillet radius-to-pin height ratio
S/D	= pin center spacing-to-diameter ratio
t	= material thickness
T	= temperature

W_c	= cooling fluid flow rate
x	= location on the surface from the leading edge
X/D	= impingement hole axial spacing-to-diameter ratio
Y/D	= impingement hole lateral spacing-to-diameter ratio
Z/D	= impingement hole target spacing-to-diameter ratio
η_{aw}	= adiabatic film effectiveness

References

- [1] Giel, P. W., Bunker, R. S., VanFossen, G. J., and Boyle, R. J., 2000, "Heat Transfer Measurements and Predictions on a Power Generation Gas Turbine Blade," ASME Paper No. 2000-GT-209.
- [2] Arts, T., Duboue, J.-M., and Rollin, G., 1998, "Aerothermal Performance Measurements and Analysis of a Two-Dimensional High Turning Rotor Blade," ASME J. Turbomach., **120**(3), pp. 494–499.
- [3] Bunker, R. S., 2003, "The Effect of Thermal Barrier Coating Roughness Magnitude on Heat Transfer With and Without Flowpath Surface Steps," International Mechanical Engineering Conference, Washington DC, Paper No. IMECE2003-41073.
- [4] Bunker, R. S., 2000, "Effect of Partial Coating Blockage on Film Cooling Effectiveness," ASME Paper No. 2000-GT-244.
- [5] Lutum, E., and Johnson, B. V., 1998, "Influence of the Hole Length-to-Diameter Ratio on Film Cooling With Cylindrical Holes," ASME Paper No. 98-GT-10.
- [6] Bailey, J. C., and Bunker, R. S., 2002, "Local Heat Transfer and Flow Distributions for Impinging Jet Arrays of Both Sparse and Dense Extent," ASME Paper No. GT-2002-30473.
- [7] Florschuetz, L., Truman, C., and Metzger, D., 1981, "Streamwise Flow and Heat Transfer Distributions for Jet Array Impingement With Crossflow," ASME J. Heat Transfer, **103**, pp. 337–342.
- [8] Han, J. C., Dutta, S., and Ekkad, S. V., 2000, *Gas Turbine Heat Transfer and Cooling Technology*, Taylor & Francis, New York, p. 295.
- [9] Taslim, M. E., and Spring, S. D., 1988, "Experimental Heat Transfer and Friction Factors in Turbulated Cooling Passages of Different Aspect Ratios, Where Turbulators Are Staggered," AIAA/ASME/SAE/ASEE 24th Joint Propulsion Conference, Boston, MA, Paper No. AIAA-88-3014.
- [10] Taslim, M. E., and Lengkong, A., 1998, "45-deg Round Corner Rib Heat Transfer Coefficient Measurements in a Square Channel," ASME Paper No. 98-GT-176.
- [11] Han, J. C., Glicksman, L. R., and Rohsenow, W. M., 1978, "An Investigation of Heat Transfer and Friction for Rib-Roughened Surfaces," Int. J. Heat Mass Transfer, **21**, pp. 1143–1156.
- [12] Park, J. S., Han, J. C., Huang, Y., Ou, S., and Boyle, R. J., 1992, "Heat Transfer Performance Comparisons of Five Different Rectangular Channels With Parallel Angled Ribs," Int. J. Heat Mass Transfer, **35**, pp. 2891–2903.
- [13] Taslim, M. E., Li, T., and Spring, S. D., 1998, "Measurements of Heat Transfer Coefficients and Friction Factors in Passages Rib-Roughened on All Walls," ASME J. Turbomach., **120**, pp. 564–570.
- [14] Bunker, R. S., and Osgood, S. J., 2003, "The Effect of Turbulator Lean on Heat Transfer and Friction in a Square Channel," ASME Paper No. GT2003-38137.
- [15] Metzger, D. E., Shepherd, W. B., and Haley, S. W., 1986, "Row Resolved Heat Transfer Variations in Pin-Fin Arrays Including Effects of Non-Uniform Arrays and Flow Convergence," ASME Paper No. 86-GT-132.
- [16] Wang, Z., Ireland, P., Jones, T., and Kohler, S. T., 1994, "Measurements of Local Heat Transfer Coefficient Over the Full Surface of a Bank of Pedestals With Fillet Radii," ASME Paper No. 94-GT-307.
- [17] Brigham, B. A., and VanFossen, G. J., 1984, "Length to Diameter Ratio and Row Number Effects in Short Pin Fin Heat Transfer," ASME J. Eng. Gas Turbines Power, **106**, pp. 241–245.
- [18] Bailey, J. C., and Bunker, R. S., 2003, "Heat Transfer and Friction in Channels With Very High Blockage 45-deg Staggered Turbulators," ASME Paper No. GT2003-38611.
- [19] Kacker, S. C., and Whitelaw, J. H., 1969, "An Experimental Investigation of Slot Lip Thickness on the Impervious Wall Effectiveness of the Uniform Density, Two-Dimensional Wall Jet," Int. J. Heat Mass Transfer, **12**, pp. 1196–1201.
- [20] Bunker, R. S., 2006, "Solution for the Heat Transfer Design of a Cooled Gas Turbine Airfoil," *Handbook of Heat Transfer Calculations*, M. Kutz, ed., McGraw-Hill, New York.
- [21] Kays, W. M., and Crawford, M. E., 1980, *Convective Heat and Mass Transfer*, 2nd ed., McGraw-Hill, New York.

Windage Power Losses From Spiral Bevel Gears With Varying Oil Flows and Shroud Configurations

Graham Johnson

Budi Chandra

Colin Foord

Kathy Simmons¹

University Technology Centre in Gas Turbine
Transmission Systems,
University of Nottingham,
University Park,
Nottingham NG7 2RD, UK

In many aero-engines, the power to drive accessories is transmitted through high speed bevel gears in a chamber in the center of the engine. The windage power loss (WPL) associated with these gears makes a significant contribution to the overall heat generation within the chamber. Shrouding the gears provides an effective method of reducing this WPL and managing the flow of lubricating oil. Experimental and computational programs at the University of Nottingham Technology Centre in Gas Turbine Transmission Systems are providing an improved understanding of shroud performance and design. This paper presents the results from a pair of shrouded meshing gears run at representative speeds and oil flow in a rig with speed and torque measurement. A previously published study of a single bevel gear operating in air (Johnson et al., 2007, "Experimental Investigation Into Windage Power Loss From a Shrouded Spiral Bevel Gear" ASME Paper No. GT2007-27885) found a reduction in torque of up to 70% from shrouding. In this work, the addition of oil and the pinion gear did not lead to high torque due to the buildup of oil under the shrouds, but the reduction in torque due to fitting the shrouds is significantly less than was found for the same gear in air alone. In order to isolate the various parameters, further testing with a single gear was carried out. A fully (360 deg) shrouded gear shows a big improvement over an unshrouded gear when running in air alone, but much of this benefit disappears as soon as a very small amount of oil is introduced under the shroud. This implies that the oil is recirculating under the shroud. Increasing the oil flow beyond this initial level increases the torque by the amount required to accelerate the oil mass flow up to the peripheral speed of the gear. Providing a full width slot in the shroud downstream of the oil jet allows the oil to escape without any recirculation and restores much of the benefit of the shroud. Further insight into the oil behavior is obtained from torque measurements and observations through a transparent shroud and with various slot configurations. Video observation shows evidence of a vortex flow under the shroud that carries some of the oil toward the inner diameter of the gear. The three main windage contributors, air alone, recirculation of oil under the shroud, and acceleration of the feed oil, are quantified and methods for achieving the optimum design are discussed. [DOI: 10.1115/1.3072519]

1 Introduction

Gear windage is the phenomenon where fluid near a gear is accelerated due to the gear's motion. Gear windage power loss is the power required to rotate a gear in the surrounding fluid and acts in addition to the power dissipated in the gear mesh. This power represents a loss to the gear system and is manifested as increased turbulence and heat generation in the fluid. The University of Nottingham Technology Centre in Gas Turbine Transmission Systems is currently partway through a program of computational and experimental research aimed to reduce the windage power loss for a typical aero-engine high speed spiral bevel gear. The two-phase (oil/air) flows related to meshing gear lubrication, shrouding, and scavenging are complex and so the approach taken has been to separate the various physical phenomena and to conduct a staged investigation. The first stage [1,2] studied the windage losses associated with an unmeshed spiral bevel gear rotating in air. These papers studied the pumping effect of the bevel gear

and showed the value of restricting the air flow. A good understanding of this behavior is a prerequisite to understanding meshing gear and two-phase performance. Previously published studies have investigated the windage power loss from spur gears [3,4] and a spiral bevel gear [5].

The investigations into the windage losses from bevel gears by Winfree [5] provide a comprehensive source of data. A single gear having a diameter of 380 mm, rotating at speeds up to 6500 rpm, was used for the study. Measurements showed that shrouding reduces losses by up to 79%.

This paper describes the results of an experimental study into the windage power losses associated with a pair of meshing spiral bevel gears, which are fully shrouded. In order to isolate the various parameters, further testing with a single gear was carried out. This includes the effect of various oil flows and shroud configurations. A transparent shroud allows observation of the oil behavior under the shroud.

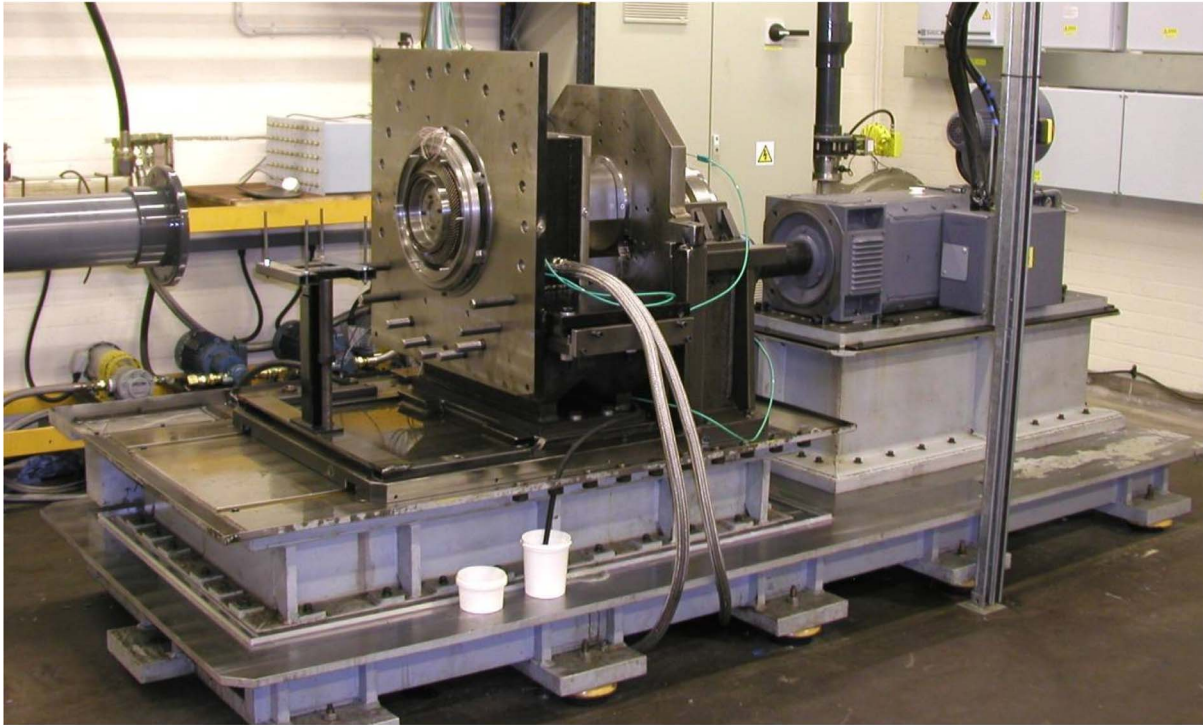
2 Experimental Details

2.1 Test Facility. The test facility, shown in Fig. 1, was designed and built around an existing test bed, gearbox, and 130 kW dc motor and is capable of driving the working section shaft at speeds up to 15,000 rpm in either direction.

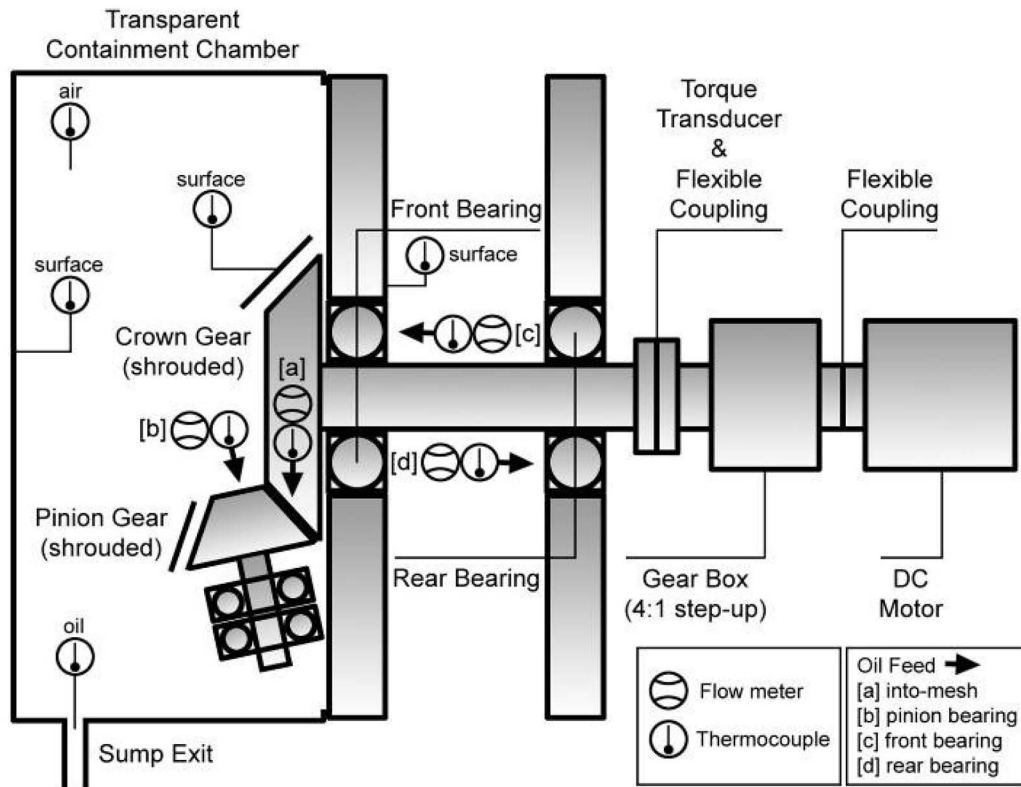
A proprietary torque transducer, which includes a shaft speed

¹Present address: Rolls-Royce plc, P.O. Box 31, Derby DE24 8BJ, UK.

Contributed by the International Gas turbine Institute of ASME for publication in the JOURNAL OF TURBOMACHINERY. Manuscript received September 3, 2008; final manuscript received October 24, 2008; published online July 13, 2009; Review conducted by David Wisler. Paper presented at the ASME Turbo Expo 2008: Land, Sea and Air (GT2008), Berlin, Germany, June 9–13, 2008.



(a) Experimental facility



(b) Experimental facility schematic

Fig. 1 (a) Experimental facility. (b) Experimental facility schematic.

sensor, is fitted between the gearbox and working section. Pumps, heaters, and coolers for the oil supply and scavenge provide Mil L 7808 type gas turbine oil at up to 5 l/min flow and 120°C temperature. This oil was chosen as it has a lower viscosity than the now more widely used Mil L 23699 and enables typical operating viscosity to be achieved at a temperature approximately 20°C lower. This is important, as the use of transparent polycarbonate shrouds for some testing imposes a limit on rig temperature.

NI LABVIEW™ code was written to control and monitor the rig and to acquire all measurement data. The data consist of torque, shaft speed, various temperatures, and oil flows.

2.2 Measurement. Figure 1(b) is a schematic of the complete test facility showing the location and type of all measurement points.

Windage torque. The torque measured by the transducer includes the parasitic torque from the rig bearings and windage from the rig shaft. The rig was designed with two small diameter angular contact ball bearings, which are spring loaded in order to keep this torque consistent and as low as possible. Tare runs were carried out with the gear removed, in order to obtain values of the parasitic torque over the speed range. These values are subtracted from the test measurements. It was noticed during the tare runs that the bearing torque drifted slightly with running time, evidence of a slight sensitivity to bearing temperature. The potential uncertainty in measured torque caused by this sensitivity was minimized during test runs by always running the rig to a repeated time history determined to be sufficient to allow the rig bearing temperatures to reach a near stabilized state. In this manner, repeatability and accuracy of torque measurements to better than 0.1 N m were achieved.

Shaft speed. All reported shaft speeds are motor set points, which are within 10 rpm of the actual speed measured with an optical transducer integral to the torque transducer.

Oil flow. Flows are measured with a positive displacement flow meter, calibrated with the oil used for the testing. Accuracy is within 2% of reading.

Temperatures. Temperatures were measured at a number of locations for control and safety monitoring purposes, as indicated in Fig. 1(b).

Vibration. Bearing housing vibration levels are measured for safety monitoring purposes and also to provide data for trim balancing the rotor.

3 Test Program and Results

3.1 Crown Gear Plus Pinion. The test gear shown in Fig. 2 has an outer diameter of 264 mm. Figure 3 is a photograph of the test setup, which shows the shrouded bevel gear and pinion. The oil to lubricate the mesh is directed from the jet (5) on the right hand side of the picture through a hole in the shroud on to the crown gear as it enters the mesh. The pinion, which runs at 2.22 times the main shaft speed, is mounted on two roller bearings and an angular contact ball bearing. Oil from the jet (6) is fed into the center of the pinion shaft and flows out through the radial holes to lubricate the bearings.

The pinion is unloaded, except for windage and pinion bearing friction. The loss torque of the pinion bearings contributes to the torque measured by the torque transducer and must be removed in order to obtain an accurate value for gear windage. This bearing torque is predicted using an established proprietary correlation and subtracted from the measured torque after allowing for the gear ratio. As a further refinement, torque is measured and predicted at a range of pinion oil flows, while all other conditions remained constant. The results for 10,000 rpm main shaft speed are shown in Fig. 4.

Rolling contact bearing torque comprises two main terms, friction within the contact zone and churning of the oil, which passes through the bearing. The contact friction term depends on bearing load and oil chemistry but does not depend on bearing oil flow



Fig. 2 Test gear

beyond the very small amount needed to establish an elastohydrodynamic film. The churning term depends primarily on bearing oil flow, viscosity, and method of supply. The slopes of the lines in Fig. 4 represent the pinion bearings churning term because nothing other than pinion bearing oil flow was changed during this test. The most accurate assessment is obtained by using the slope of the measured data and the predicted contact friction. The size of contact friction term can be seen by extrapolating the prediction line back to zero pinion oil flow.

Torque distribution obtained in this way is shown in Fig. 5. The increase in pinion bearing torque with speed is as expected because the speed dependent churning term is dominant at the high oil flow in this test. The rig bearings have a very low oil flow in order to minimize bearing torque and avoid the need for oil seals. Their torque is therefore dominated by contact friction. The measured small reduction with increasing speed is repeatable and probably caused by the increase in elastohydrodynamic oil film thickness and shear rate.

The main reason for carrying out these tests on the complete



Fig. 3 Shrouded crown gear and pinion. 1. Crown gear; 2. Crown shroud; 3. pinion gear; 4. Pinion - shroud; 5. Into mesh oil jet; 6. Pinion bearing oil jet.

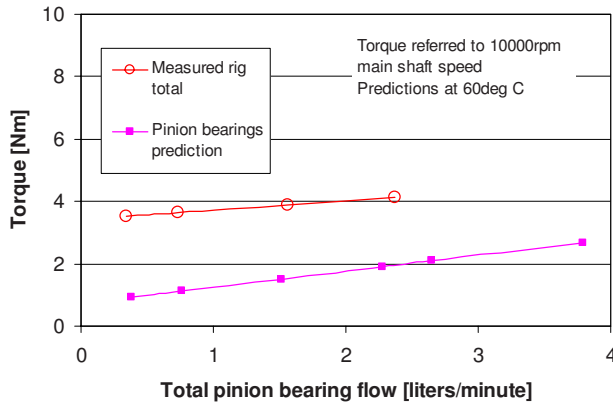


Fig. 4 Effect of pinion bearing oil flow on torque at 10,000 rpm main shaft speed

assembly early in the test program was to check the system operation and to answer a concern that oil may build up under the shroud, leading to very high torque. The density of oil is approximately 950 times that of air, so the potential increase in torque is a factor of 950 if all the air were replaced by oil. Even localized pools of oil would lead to much increased torques. Visual observation shows that the oil is carried through the gap at the rear of the shroud and no very high torques were measured. Figure 5 shows that gear windage is the largest component at high speed, but the values are consistent with pumping air and a little oil. Subsequent testing examines the factors that contribute to the total windage.

3.2 Crown Gear Alone. The pinion assembly and shrouds were removed, leaving just the crown gear and oil jet. The measured results in Fig. 6 show a linear increase in torque with oil flow. The increase due to oil flow is modeled by analogy with a turbo machine. The tangential force on the gear is equal to the oil mass flow rate times the change in whirl velocity. The whirl velocity is the tangential component of the velocity of the working fluid. In this case, the inlet whirl velocity is assumed to be zero and the outlet whirl velocity is the peripheral speed of the gear at its outer radius. The force calculated in this way also acts at the outer radius, which gives the following equation:

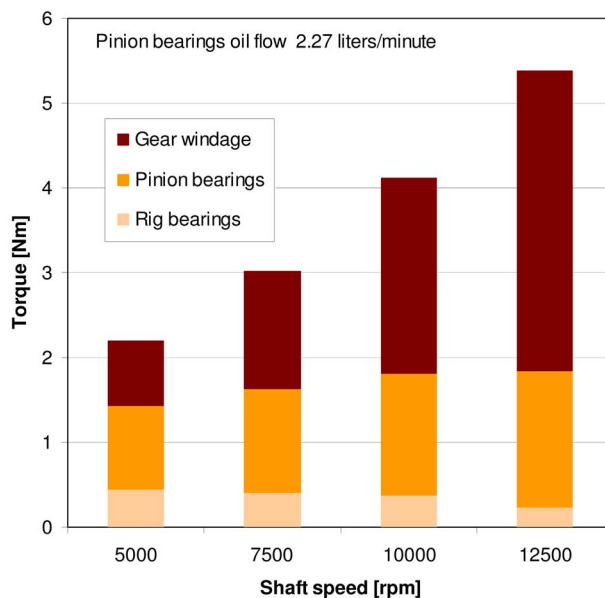


Fig. 5 Torque distribution with shrouded gear and pinion

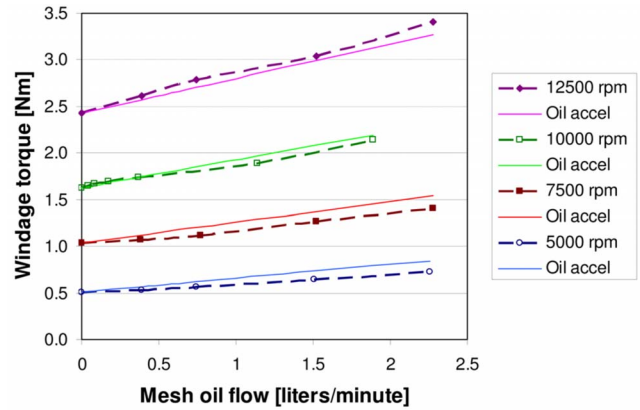


Fig. 6 Windage torque for unshrouded gear

$$T_{oil} = m\omega r^2$$

This simple model shows remarkably good agreement with the measured data and is referred to as the oil acceleration term. It is added to the torque measured with zero oil flow to produce the "Oil accel" lines in Fig. 6.

3.3 Shrouded Crown Gear. A transparent crown gear shroud, which covers the full circumference of the gear, was fitted. The cross section is shown in Fig. 7.

Figure 8 shows a large reduction in windage torque due to the shroud at zero oil flow, which is in line with the measurements in Ref. [1]. However, the benefit of shrouding is much reduced as soon as a small quantity of oil is introduced. This is due to a new component of windage torque, which adds to the air alone and oil acceleration terms.

As observed in Sec. 3.1, the majority of oil delivered by the jet exits the undershroud space through the outlet clearance between the shroud and gear and consequently no very high torque levels were measured. However, observations through the transparent shroud show that some oil is trapped under the shroud and that this oil flows inboard along the inner surface of the shroud. The

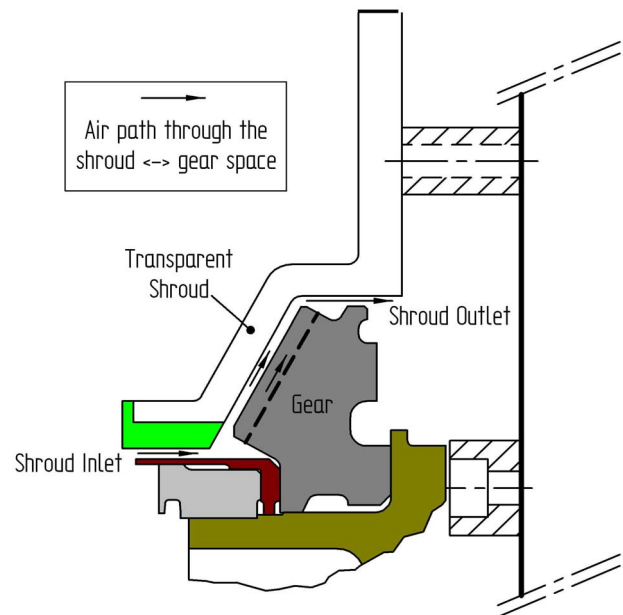


Fig. 7 Shroud cross section

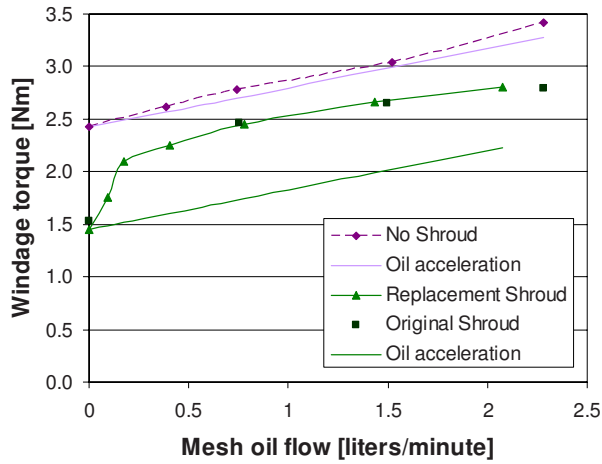


Fig. 8 Windage torque at 12,500 rpm

inboard flow of oil is driven by a toroidal vortex in the air flow. Recirculation of this oil between the inner radius and the outer radius of the gear leads to the additional torque identified in Fig. 8.

Two types of shroud with the same geometry but different construction were used at different times in the test program. Tests show excellent agreement between the original and replacement shrouds in Fig. 8.

Having identified a component of torque associated with oil retained under the shroud, testing progressed to examine the scavenge effect of slots in the shroud.

3.4 Effect of Slots in the Shroud. The aim of these tests was to gain a better understanding of the oil recirculation and the potential for reducing the recirculation losses through the use of a scavenge slot.

The segments in the transparent shroud can be rearranged to provide slots of several widths and positions. Figure 9 shows a typical slot and Fig. 10 shows the extent and position of the alternatives tested. The start angle of the slots in Fig. 10 is measured from the oil jet in the direction of rotation. The results of the slotted shroud tests are shown in Fig. 11. All of the slotted shrouds show lower torque than the full 360 deg shroud over most of the oil flow range.

The lowest torque is for the slots A and C, which allow the oil to escape soon after the oil jet. Moving the slot to B, which is almost opposite to the jet, allows more recirculation and generates some increase in torque. A further move to E, just ahead of the oil jet, has little additional effect. Slot D is in reality a short shroud, which covers 36% of the gear circumference. The trend of the windage torque curve for slot D is similar to the unshrouded case but at a lower absolute torque level. This reduction in torque reflects the reduction in the air alone component due to the portion of the gear, which is shrouded.

3.5 Flow Visualization. The transparent shrouds and containment vessel allow direct visual observation, video recording, and still photography.

Figure 12 is a long exposure photograph of the oil streak just after the injection point. The oil jet can be seen entering through the hole in the shroud on the right of the picture. The oil is thrown to the outside of the shroud by the action of the gear but then curves inward and flows back toward the inner radius on the inside surface of the shroud. The oil flow is 0.25 l/min and the shroud is in the slot E configuration. Internal crazing of the shroud

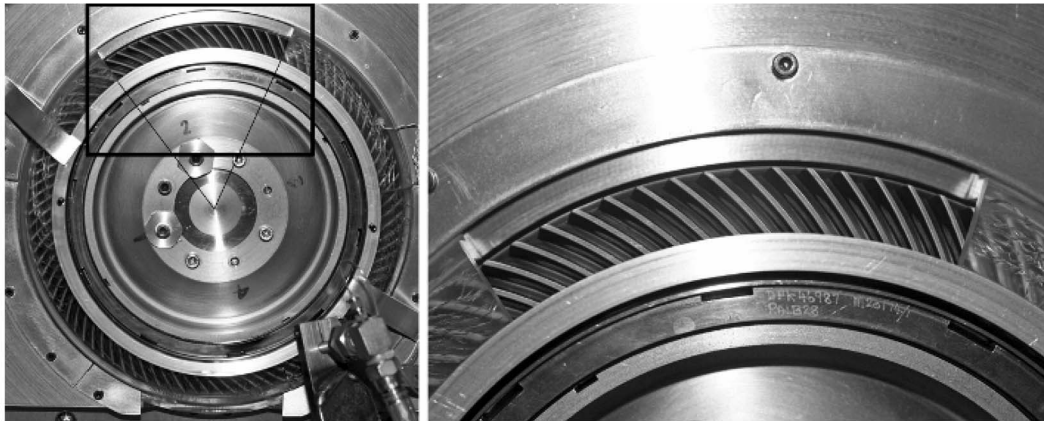


Fig. 9 Shroud with slot B

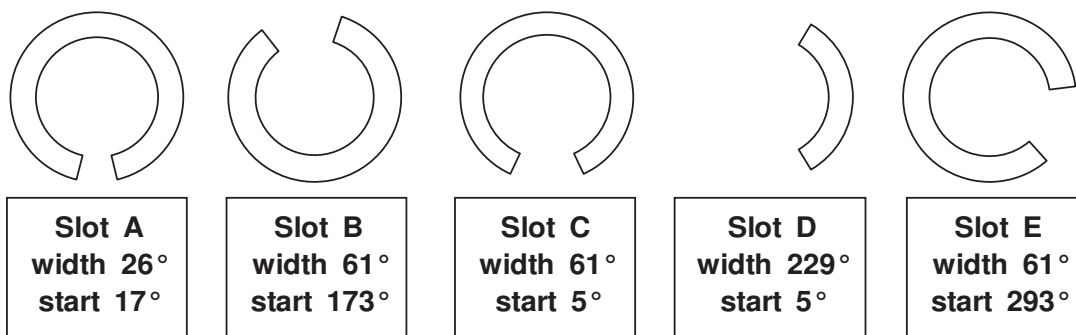


Fig. 10 Extent and position of slots

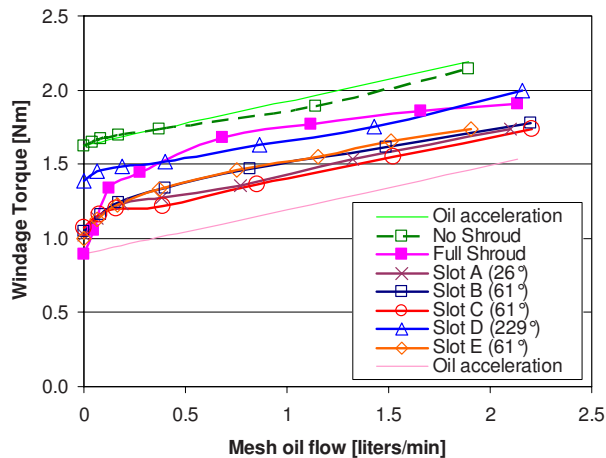


Fig. 11 Slotted shrouds at 10,000 rpm

due to thermal stressing is visible, but has no effect on the flow.

Figure 13 is a still frame from a video that shows the oil leaving the shroud through slot B. Most of the oil is ejected from the inner radius. The oil flow is 1.5 l/min.

The oil behavior at speeds higher than 5000 rpm is similar. Photography becomes progressively more difficult as speed increases because of the oil mist within the chamber, but information can still be obtained by direct viewing.

4 Discussion of Results

4.1 Torque Breakdown. The windage torque can be considered as the sum of three main terms, single-phase air alone, oil acceleration, and a third “oil recirculation” component representing the additional windage term identified in Sec. 3.3. This is shown in Fig. 14, which is a typical result.

The separation into three terms is highly significant. The air alone term, which is the largest in this case, can be estimated and optimized using single-phase computational fluid dynamics (CFD) analysis, which is well established [2]. The oil acceleration term is easily calculated as in Sec. 3.2. The oil recirculation term still has to be determined empirically but, with an effective slot in the shroud, it is a small term.

The oil recirculation term has been so named on the basis of the visual evidence shown in Figs. 12 and 13, which show that the bulk of the oil that remains under the shroud (i.e., has not exited

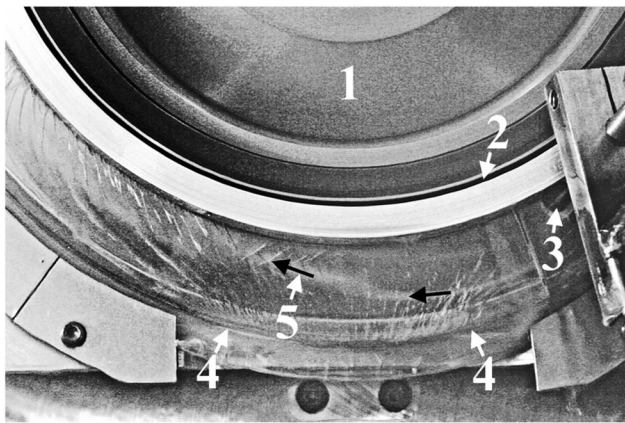


Fig. 12 Oil streak under the shroud at 5000 rpm. 1. Crown gear; 2. Shroud inlet; 3. Into mesh oil jet; 4. Gear outer diameter; 5. Path of oil under the shroud.

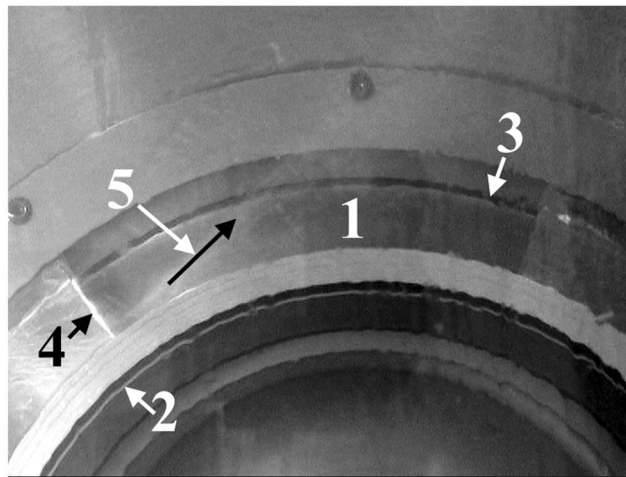


Fig. 13 Oil leaving slot B at 5000 rpm. 1. Face of crown gear; 2. Shroud inlet; 3. Shroud exit space; 4. Start of shroud slot; 5. Path of oil exiting the shroud.

the shroud space via the rear shroud-gear clearance) is concentrated at the inner radius of the gear having been recirculated from the outer diameter.

Although shown as constant, it is likely that the single-phase term does exhibit some sensitivity to oil flow. The presence of oil under the shroud in the form of a mist will increase the effective density of the air, which will to some extent increase the single-phase term. Conversely the presence of oil under the shroud in “solid” form could restrict the pumping of air through the shroud thereby reducing the single-phase windage term. In practice, the combined effect is small.

4.2 Extent of Shroud. The single-phase air alone term can be obtained experimentally by turning off the mesh oil flow. This term is found to be linearly proportional to the shroud open fraction. Figure 15 shows this linear behavior for a shaft speed of 10,000 rpm. The crown gear without a shroud (open fraction=1) gives the highest single-phase term, whereas the complete 360 deg shroud without any slots (open fraction=0) gives the lowest single-phase term. This linear relation allows prediction of single-phase term at various shroud open fractions.

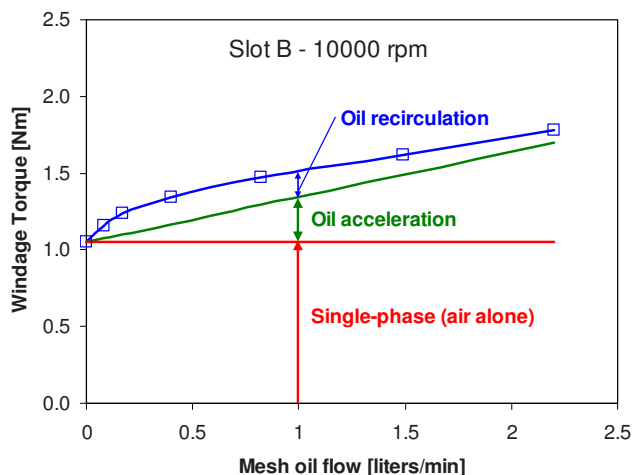


Fig. 14 Breakdown of terms that determine windage torque level

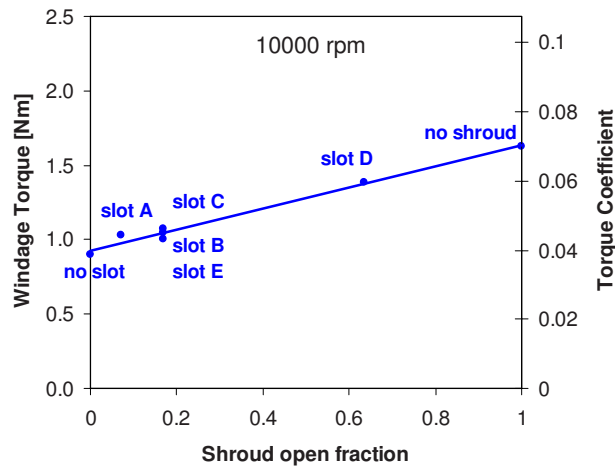


Fig. 15 Air alone windage torque and torque coefficient C_m

4.3 Oil Recirculation. The dimensionless torque coefficient C_m in Fig. 15 is useful for scaling to other conditions in single-phase flow and is described in Ref. [1]. It has been suggested that use of this coefficient can be extended to two-phase flow by using a modified density, which depends on oil and air flow rates. However, visual observations show that the phases tend to remain separate and also the air flow rate and the proportion of oil recirculated are difficult to determine. It is therefore more effective to assess the large *air alone* and *oil acceleration* terms independently and consider the air oil interaction as the relatively small *oil recirculation* term.

4.4 Effect of the Pinion. In the real application with meshing gears, there must be a slot in the shroud to accommodate the pinion, but the pinion tends to block the movement of air and oil in the circumferential direction. A good shroud design must ensure that oil ejected from the mesh is effectively scavenged and not re-ingested.

5 Concluding Remarks

Shrouding a high speed bevel gear can show a significant reduction in windage losses, but careful design is necessary to ensure the potential benefits are realized.

Visualization through a transparent shroud shows that the oil and air phases remain separate, which means that analysis cannot be based on an averaged density.

Analyzing the windage in terms of three components provides an effective method of prediction and also emphasizes the need to achieve good single-phase (air alone) performance.

Acknowledgment

The authors would like to thank Rolls-Royce plc for their financial support of this work. We also thank Neil Fomison of Rolls-Royce and Carol Eastwick of Nottingham University for their technical support and encouragement during this project and Bob Stables of Nottingham for designing and organizing the manufacture of the rig.

Nomenclature

- T = gear windage torque (N m)
- ρ = density of air exiting the shrouded gear (kg/m^3)
- m = oil mass flow rate (kg/s)
- r = outer radius of the gear (m)
- ω = gear rotational speed (rad/s)
- C_m = nondimensional gear torque $C_m = T / \frac{1}{2} \rho r^5 \omega^2$

References

- [1] Johnson, G., Simmons, K., and Foord, C., 2007, "Experimental Investigation Into Windage Power Loss From a Shrouded Spiral Bevel Gear," ASME Paper No. GT2007-27885.
- [2] Rapley, S., Eastwick C., and Simmons, K., 2007, "The Application of CFD to Model Windage Power Loss From a Spiral Bevel Gear," ASME Paper No. GT2007-27879.
- [3] Dawson, P. H., 1984, "Windage Loss in Large High-Speed Gears," Proc. Inst. Mech. Eng., Part A: Power and Process Engineering, **198**(1), pp. 51–59.
- [4] Diab, Y., Ville, F., Changenet, C., and Vexel, P., 2003, "Windage Losses in High Speed Gears—Preliminary Experimental and Theoretical Results," DETC'03, ASME 2003 Design Engineering Technical Conferences and Computers and Information in Engineering Conference, Vol. 4B, pp. 941–947.
- [5] Winfree, D. D., 2000, "Reducing Gear Windage Losses From High Speed Gears," *Proceedings of DETC'00, ASME Power Transmission and Gearing Conference*, Baltimore, MD, Sept. 10–13, pp. 747–756.

Simplified Approach to Predicting Rough Surface Transition

R. J. Boyle

NASA Glenn Research Center,
Cleveland, OH 44135
e-mail: robert.j.boyle@grc.nasa.gov

M. Stripf

Universität Karlsruhe,
76128 Karlsruhe, Germany
e-mail: matthias.stripf@its.uni-karlsruhe.de

Turbine vane heat transfer predictions are given for smooth and rough vanes where the experimental data show transition moving forward on the vane as the surface roughness physical height increases. Consistent with smooth vane heat transfer, the transition moves forward for a fixed roughness height as the Reynolds number increases. Comparisons are presented with published experimental data. Some of the data are for a regular roughness geometry with a range of roughness heights, Reynolds numbers, and inlet turbulence intensities. The approach taken in this analysis is to treat the roughness in a statistical sense, consistent with what would be obtained from blades measured after exposure to actual engine environments. An approach is given to determine the equivalent sand grain roughness from the statistics of the regular geometry. This approach is guided by the experimental data. A roughness transition criterion is developed, and comparisons are made with experimental data over the entire range of experimental test conditions. Additional comparisons are made with experimental heat transfer data, where the roughness geometries are both regular and statistical. Using the developed analysis, heat transfer calculations are presented for the second stage vane of a high pressure turbine at hypothetical engine conditions. [DOI: 10.1115/1.3072521]

1 Introduction

Surface roughness adversely affects turbomachinery performance by increasing external heat transfer and by increasing loss. Measured surface roughness for in service blades show a high degree of variability. It is useful to the designer to have an estimate of the effects of surface roughness on both heat transfer and aerodynamic performance. Data show that as the roughness height progressively increases, the turbine vane transition moves forward on both the suction and pressure surfaces of the vane. Data, such as those of Arts [1], show that a smooth vane can have laminar flow over much of the vane at moderate Reynolds numbers, even with relatively high inlet turbulence. When the boundary layer is not forced to be turbulent due to film cooling, understanding the interaction of surface roughness and transition is important. The change in blade surface heat transfer with transition is a very good indicator of transition start and length. Tests of a solid high pressure turbine vane are therefore valuable, even if the vane is film cooled when installed in an engine. Transition is typically not an issue for the first turbine stage, since the blades are generally film cooled. Arts [2] showed that just the presence of film cooling holes causes transition to turbulent flows on the blade surfaces. In later stages, film cooling may not be used, and the Reynolds numbers are lower. Heat transfer may remain a concern if blades have only internal cooling. Hourmouziadis [3] showed nearly an order of magnitude decrease in Reynolds numbers between the high pressure turbine inlet and the last low pressure turbine stage. Predicting the performance of low pressure turbines is highly dependent on understanding transition, especially at cruise conditions, where laminar separation can cause severe loss penalties.

Surface roughness generally adversely affects blade row aerodynamic efficiency. Kind et al. [4], Boynton et al. [5], and Bamert and Stansted [6,7] reported decreases in turbine efficiencies of up to several points due to surface roughness. Abuaf et al. [8] and Stabe and Liebert [9] showed that just polishing blade surfaces can improve efficiency. On the other hand, Harbecke et al. [10] showed that profile loss was not increased until a critical

roughness height was reached. Boyle and Senyitko [11] showed that high Reynolds number surface roughness doubled vane loss, but at low Reynolds numbers roughness improved aerodynamic efficiency. Roughness modified the Reynolds number and surface location at which separation occurred. To utilize surface roughness to improve low pressure turbine aerodynamic efficiency requires understanding of the effects of roughness on transition. To predict the efficiency decrement due to roughness at higher Reynolds numbers also requires understanding of the effects of roughness on the surface boundary layers.

There are two approaches to calculating rough surface boundary layers. The first is the discrete element method and is ideally suited to situations where the roughness geometry is known, and is regular and periodic. This method has been used by a number of researchers, and shown to give accurate results. Taylor et al. [12], Hosni et al. [13], and Stripf et al. [14] used this method to calculate rough surface heat transfer. McClain [15] extended the discrete element model to account for random roughness, and McClain et al. [16] presented friction factor and heat transfer comparisons with data developed using roughness determined from actual blade measurements. The characteristics of measured turbine blade roughness vary widely, and a priori discrete element model calculations need detailed information regarding the roughness characteristics.

The second, and older, approach to calculating rough surface boundary layers is to calculate the equivalent sand grain roughness. Several authors proposed correlations to obtain the equivalent sand grain roughness. Among these are Sigal and Danberg [17], Dvorak [18], Simpson [19], Dirling [20], van Rij [21], and Waigh and Kind [22]. Common to all these correlations is the requirement that the roughness image or trace be modeled as a roughness geometry, in order to obtain values for projected and windward areas. The correlation of Koch and Smith [23] only uses a statistical value from the roughness trace or image.

The Koch and Smith [23] correlation provides the simplest way of determining the equivalent sand grain roughness from the roughness image. The suitability of this correlation can be determined by using the statistical parameters of regular roughness geometries. A regular roughness geometry is one that is suitable for the discrete element method. It was found that better agreement with the experimental data was achieved by a modification to the Koch and Smith correlation.

Contributed by the International Gas Turbine Institute of ASME for publication in the JOURNAL OF TURBOMACHINERY. Manuscript received September 12, 2008; final manuscript received October 28, 2008; published online July 13, 2009. Review conducted by David Wisler. Paper presented at the ASME Turbo Expo 2008: Land, Sea and Air (GT2008), Berlin, Germany, June 9–13, 2008.

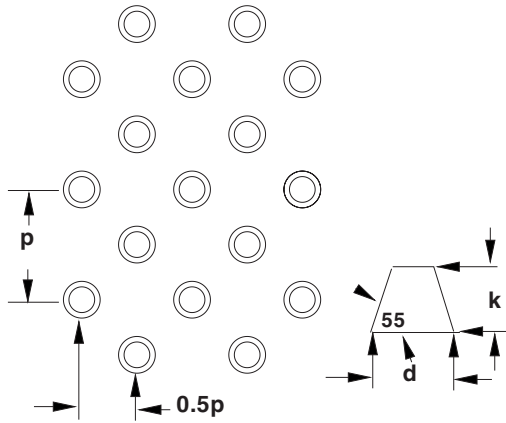


Fig. 1 Arrangement of truncated cone roughness elements

There are four parts to the work presented herein. The first determines a correlation for the equivalent sand grain roughness, k_s , that is consistent with the experimental data of Stripf et al. [24]. The second part determines modifications to transition start and relaminarization criteria to yield heat transfer predictions consistent with the same experimental data. The third part compares heat transfer predictions using the proposed modifications with data to determine the applicability of the modeling to other data sets. The fourth part shows heat transfer and aerodynamic loss calculations at a unit Reynolds number consistent with current engine operating conditions. Even though both the determination of the equivalent sand grain roughness and the transition criteria are derived from the same data they are not wholly dependent on each other. If the reader prefers a different method of calculating k_s , the coefficients in the transition criteria could be changed to yield the same results with different values for k_s .

2 Discussion of Results

2.1 Equivalent Sand Grain Roughness. The roughness geometry used in the test of Stripf et al. [24] to measure vane heat transfer coefficients is shown in Fig. 1. In their tests the height of the truncated cones and the spacing between cones were varied. The dimensions of the roughness geometry is given in Table 1. For all tests the vane axial and true chords were 53 mm and 94 mm, respectively. Data were obtained for variations in inlet turbulence intensity and Reynolds numbers. Figure 2 shows their measured heat transfer coefficients at an inlet true chord Reynolds number of 250,000. As the roughness height increases, the transition moves forward, toward the leading edge, for both the suction and pressure surfaces. Only at the highest roughness does the heat transfer appear to be fully turbulent over the entire vane surface. An important feature of these data is that roughness spacing has a very minor effect on heat transfer.

Table 1 Dimension of roughness elements

Label	k (μm)	d (μm)	p (μm)
r10m	10	25	55
r10s	10	25	70
r20m	20	50	110
r20s	20	50	140
r30m	30	75	165
r40m	40	100	220
r40s	40	100	300
r50s	48	100	300
r80m	80	200	440
r80s	80	200	600

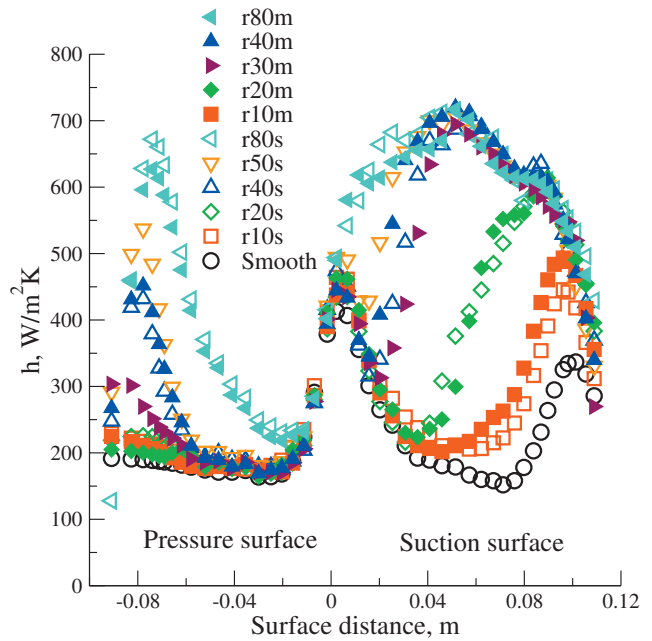


Fig. 2 Heat transfer coefficients, $Re_{in}=2.5 \times 10^5$, $Tu=8\%$

A number of correlations have been proposed to calculate the equivalent sand grain roughness, k_s . These correlations show that k_s is strongly dependent on roughness spacing. These correlations for the ratio of k_s to physical height are triangular in shape, with a spacing parameter that gives a maximum ratio. Closely spaced roughness elements are required to achieve the maximum value for k_s . Stripf et al. [24] gave k_s values using the correlation of Waigh and Kind [22]. This correlation predicted a strong effect due to spacing, such that the widely spaced roughness would have to have nearly twice the roughness height to achieve the same value for k_s . Figure 2 shows that this is inconsistent with the experimental data. The correlation of Sigal and Danberg [17] has three regions, where a plateau separates the two legs of the triangle. At this plateau the ratio of $k_s/k=8$. When applied to roughness measurements of in service blades, a common feature of these correlations is that the roughness image or traces have to be transformed into a model geometry.

The correlation of Koch and Smith [23] uses only a statistical measure of the surface roughness, without requiring that a model geometry be constructed. This correlation gives $k_s=6.2R_a$. Table 2 gives statistical quantities R_a , R_{rms} , and skewness (S_k) of the roughness tested by Stripf et al. [24]. Also shown are the k_s values determined from the correlations of Waigh and Kind [22], Koch and Smith [23], and the present proposed correlation. Since the spacing affects the value of R_a , the correlation of Koch and Smith [23] shows a spacing effect not seen in the data. Table 2 also shows that as the spacing increases R_a increases, the skewness of the roughness decreases. The three statistical quantities given in Table 2 are defined as

$$R_a = \frac{\sum_{i=1}^n |y_i - \bar{y}|}{n}$$

where n equals the number of points in the roughness measurement, and is generally very large.

$$R_{rms} = \sqrt{\frac{\sum_{i=1}^n (y_i - \bar{y})^2}{n-1}}$$

and

$$S_k = \frac{\sum_{i=1}^n (y_i - \bar{y})^3}{nR_{rms}^3}$$

Table 2 Roughness characteristics

Label	k (μm)	\bar{y} (μm)	R_a (μm)	R_{rms} (μm)	S_k	k_S		
						Waigh and Kind (μm)	Koch and Smith (μm)	Present (μm)
r10m	10	1.8	2.5	3.2	1.65	48	15	37
r10s	10	1.1	1.8	2.7	2.44	25	11	40
r20m	20	3.5	5.0	6.4	1.65	96	31	73
r20s	20	2.2	3.5	5.3	2.44	51	22	79
r30m	30	5.3	7.5	9.6	1.65	144	46	110
r40m	40	7.1	10.0	12.8	1.65	192	62	147
r40s	40	3.8	6.3	10.0	2.69	89	39	160
r50s	48	4.0	6.7	10.8	2.87	106	42	181
r80m	80	14.1	20.0	25.5	1.65	384	124	293
r80s	80	7.6	12.7	20.0	2.69	177	79	320

Since the skewness, S_k , is related to R_{rms} , the Koch and Smith [23] correlation was modified to give a k_S consistent with the data shown in Fig. 2. The revised correlation for k_S is

$$k_S = 4.3R_{\text{rms}}(1 + C_{\text{sk}}S_k) \quad \text{for } S_k > 0$$

The coefficient of 6.2 was reduced to 4.3 based on the ratio of R_a to R_{rms} . The data in Fig. 2 and the statistics in Table 2 suggest that C_{sk} is slightly less than 1. However, for simplicity, the constant C_{sk} was set to 1.0. The requirement that $S_k > 0$ is not expected to be a difficulty. The measurements of Taylor [25] for the roughness of in service blades showed positive skewness for many cases. Bons et al. [26] measured vane surface roughness and, except for spalled regions, generally found positive skewness values. Spalled regions gave negative skewness. A conservative approach would be to take k_S as the maximum of $k_S = 4.3R_{\text{rms}}(1 + S_k)$, Koch and Smith [23] criterion of $k_S = 6.2R_a$, or $k_S = 4.3R_{\text{rms}}$.

The reasonableness of this correlation is shown in Fig. 3 where the data shown in Fig. 2 are compared with fully turbulent calculations for several different equivalent sand grain roughness heights using the above expression for k_S . Since the calculations

are for fully turbulent flow, comparisons are meaningful only after transition is complete. Overall, the agreement in this region is good. The comparison for the highest roughness, where the measurements indicate nearly fully turbulent flow, shows very good agreement for both the pressure and suction surfaces.

A question that arises from the data in Table 2 is whether an equivalent roughness height of nearly a third of a millimeter is too high compared with actual measurements. Most data in the literature give the roughness height in terms of R_a , and for comparison with Table 2 entries the Koch and Smith conversion to k_S will be used. Tarada and Suzuki [27] reported a wide variation in R_a values. They were between 25 μm and 150 μm (k_S between 155 μm and 930 μm) and depended on the engine's operating environment. Taylor [25] measured R_a values between 2 μm and 11 μm (k_S between 12.4 μm and 68 μm). Bogard et al. [28] extensively measured surface roughness on two vanes. The first had R_a values between 9 μm and 22 μm , and the second ranged from 21 μm to 46 μm . This represents a range of k_S between 56 μm and 285 μm . Bons et al. [26] measured surface roughness on a variety of turbine blades. For deposition and corrosion, they measured the R_a values between 3 μm and 33 μm , giving a k_S range between 19 μm and 205 μm . Zhang and Ligrani [29] calculated a k_S value of 62 μm for a turbine blade used in a utility power application. Just in terms of roughness height, the answer is that a roughness height of nearly a third of a millimeter is not excessive.

When the Reynolds number effects are accounted for, even the highest roughness may not be sufficiently high. Bogard et al. [28], in a low Reynolds number experiment, scaled up the measured roughness by a factor of 25 to account for the Reynolds number effects. Since the roughness parameter, H^+ (sometimes referred to as Re_k), increases almost linearly with unit Reynolds number in turbulent flow regime, engine unit Reynolds numbers should be matched if the roughness height scale factor is 1. The data of Stripf et al. [24] were obtained at maximum unit Reynolds number less than typically seen by the first stage vane at takeoff or in an utility application. On the other hand, the unit Reynolds number decreases in later stages, where roughness transition is more likely to be a factor.

2.2 Heat Transfer Modeling Assumptions. The data in Fig. 2 clearly show transition occurring for both the suction and pressure surfaces of the vane. The locations for transition are strongly dependent on the roughness height. Three modeling issues with respect to transition were investigated. The first was the start of transition. The second was the length of transition. The third was relaminarization. A number of approaches were examined for each of these modeling issues. Rather than detail all of the approaches taken, the modeling that gave the best agreement with all of the data is presented.

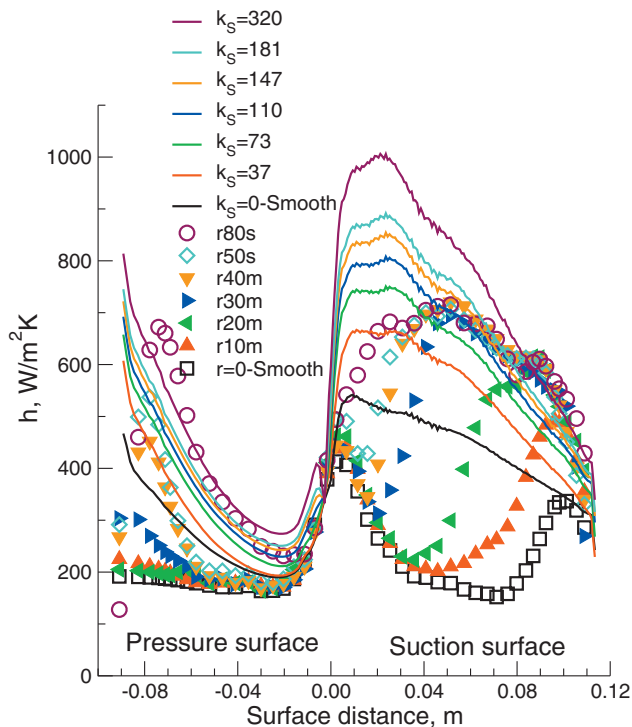


Fig. 3 Comparison of fully turbulent calculations with data $Re_{in} = 250,000$, $Tu = 8\%$

Start of transition. Mayle's [30] transition start model was modified to account for roughness effects. In this model when the momentum thickness Reynolds number, Re_θ , exceeds a critical Reynolds number, Re_{crit} , transition begins. For smooth surfaces $Re_{crit}=400Tu^{-0.625}$. The critical Reynolds number for rough surface transition is

$$Re_{rough} = \frac{Re_{smooth}}{1 + Tu^{-0.625}(C_{st}(H^+ - 5))^{1.25}}$$

Unless stated otherwise $C_{st}=0.05$. H^+ is calculated from $H^+ = k_S U_{fs} \rho \sqrt{C_f/2} / \mu$. The term $H^+ - 5$ occurs because a surface roughness that gives H^+ less than 5 is considered hydraulically smooth. Comparisons are made for two inlet turbulence intensities, and including the term $Tu^{-0.625}$ gave better agreement with data. This term means that at high H^+ values, the start of transition is independent of the local turbulence intensity. The roughness term was raised to the 1.25 power based on comparisons with the data, which show suction surface transition moving from near the trailing edge to near the leading edge as the roughness height increases by a factor of 8.

The local turbulence intensity used in the transition start criteria was calculated using the work of Steelant and Dick [31], where the local Tu is calculated from

$$Tu = Tu_{in} (U_{in}/U_{fs})^{3/2}$$

Calculations of the turbulence distribution within the vane passage using a $k-\omega$ turbulence model was consistent with this approximation for the local turbulence intensity when the inlet length scale used in the calculations was small. Because of the accelerations through the vane passage, the maximum local turbulence intensity at the start of transition for the smooth vane was less than 1%. The data showed that this low turbulence intensity in the transition criteria was appropriate.

Transition length. In the base cases, the transition length model was not modified to account for roughness effects. When modifications were made the spot production parameter, N , was increased by

$$N_{rough} = N_{smooth} \exp(C_{LT}(H^+ - 5))$$

With $C_{LT}=0$ there is no modification to the transition length. The transition length model is the one detailed by Boyle and Simon [32]. It is a modification of the transition length model of Solomon et al. [33] to account for Mach number effects. It was shown to give good agreement with smooth blade heat transfer data for both stator [1,34] and rotor test cases [35]. It was found that the length of transition, as evidenced by the rough surface heat transfer data, was reasonably well predicted for many, but not all, cases without modifying the spot production parameter, N .

Relaminarization. Because much of the comparisons are at flow conditions where the favorable pressure gradients are strong enough to cause relaminarization, it was necessary to modify the relaminarization criteria. For smooth surfaces, it is accepted that when the pressure gradient parameter, $K=3.0 \times 10^{-6}$ a turbulent boundary will relaminarize. Since data show that as the height of the roughness increases, the laminar pressure surface boundary layer becomes turbulent sooner. Calculations without a relaminarization model showed early pressure surface transition for many cases. The calculation of the critical value of K for relaminarization is

$$(K_{crit})_{rough} = \frac{(K_{crit})_{smooth}}{\exp(-C_{rlm}(H^+ - 5))^{1.25}}$$

where $C_{rlm}=0.0354$, and $(K_{crit})_{smooth}=3.0 \times 10^{-6}$. The local value for K is calculated from the local inviscid velocity gradient as

$$K = \frac{\nu}{U_{fs}^2} \frac{dU_{fs}}{dS}$$

where S is the streamwise distance from the stagnation point.

Heat transfer calculations. Comparisons are made with mid-span heat transfer data, so that a two dimensional analysis is appropriate. Heat transfer and loss calculations were done using a quasi-3D Navier-Stokes analysis. The solver used was the quasi-3D Navier-Stokes code RVCQ3D, run as a two dimensional analysis. This code has been documented by Chima [36]. C-type grids, typically 377×55 , were used. Boyle and Simon [32] gave a more detailed description of the analysis. The solutions were monitored to assure that convergence was achieved.

An algebraic turbulence model described by Chima et al. [37] was used. It is a two layer model and incorporates the Cebeci-Chang roughness model described in Ref. [38]. This model increases the mixing length to account for roughness. The distance increment is given by

$$\Delta y^+ = 0.9(\sqrt{H^+} - H^+ \exp^{-0.167H^+})$$

and

$$\Delta y = \Delta y^+ \mu / (U_{fs} \rho \sqrt{C_f/2})$$

In the algebraic models, the increment in y is only applied in the inner region. The turbulent eddy viscosity in the inner region, $\mu_{t,i}$ is given by

$$\mu_{t,i} = \rho(dU/dy)[\kappa(y + \Delta y)(1 - \exp^{-(y^+ + \Delta y^+)/A^+})]^2$$

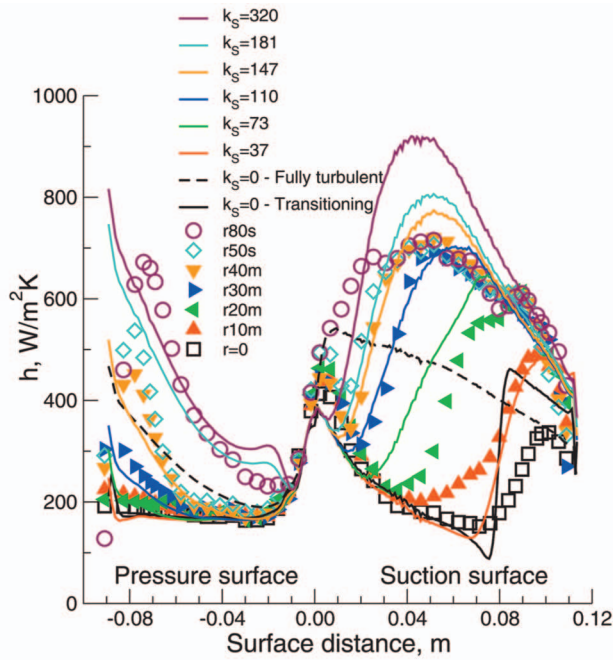
In the two equation $k-\omega$ turbulence model, roughness effects are accounted for by modifying the wall boundary condition on ω . Two equation models are most applicable when flows are turbulent. Calculations were done using the $k-\omega$ turbulence model only for fully turbulent cases. Calculations using the $k-\omega$ model were similar to those shown in Fig. 3, using the algebraic model. For each k_S value the increase in heat transfer over the smooth calculation was nearly the same for both turbulence models.

When the flows were predicted to not be fully turbulent, the laminar viscosity was increased to account for the effects of high freestream turbulence. Ames et al. [39] described two turbulence models to augment laminar viscosity. Based on the results presented by Boyle et al. [40], the Ames model without a leading edge correction was used.

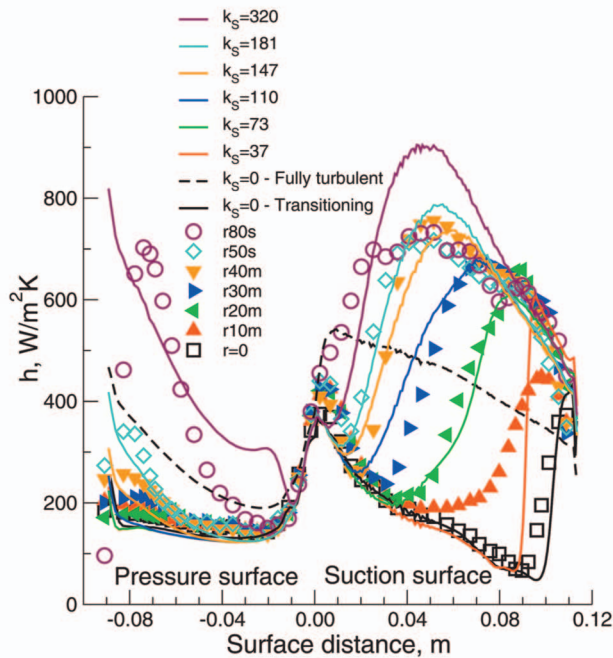
2.3 Baseline Heat Transfer Comparisons. In this section, heat transfer comparisons are made with the cases used to determine the rough surface heat transfer modeling. In Sec. 2.4, comparisons are shown for cases that were not used to determine the transition modeling. The models for rough surface transition and relaminarization have only a few parameters. The number is far less than the number of cases that will be shown in this section. The goal of the work is reasonable agreement for a wide range of cases. Because of the large number of cases, and the small number of parameters, it is unreasonable to expect perfect agreement for all cases.

Comparisons of predicted and measured heat transfer coefficients are given for three Reynolds numbers and two inlet turbulence intensities. Figure 4 compares the predicted and measured heat transfer coefficients for an inlet true chord Reynolds number of 250,000 at inlet turbulence intensities of 4% and 8%. Since the transition modeling uses only a few parameters, it is noteworthy that the agreement for the start of transition is good over the entire range of roughness heights. The agreement is reasonable for both the suction and pressure surfaces, where the streamwise pressure gradients are very different. The second highest roughness shows transition close to the leading edge for the suction surface, but nearly halfway back on the pressure surface.

The analysis underpredicts the heat transfer in the leading edge region. However, the predictions are in good agreement with pressure surface data, where the flow is laminar. The underprediction in the leading edge region is not due to roughness. Here the analysis underpredicts the smooth surface heat transfer by more than the small increase in heat transfer due to roughness.



a) $Tu_{IN} = 8\%$



b) $Tu_{IN} = 4\%$

Fig. 4 Transition modeling predictions, $Re_{in} = 250,000$

Figure 4 also shows a fully turbulent calculation for a smooth vane. The data show that the heat transfer rates for the highest roughness can be nearly twice as great as those calculated using the smooth fully turbulent assumption. However, at low to moderate roughness, a fully turbulent calculation can significantly overestimate the heat transfer rate.

Comparing Figs. 4(a) and 4(b) shows that the heat transfer distributions do not change significantly, even when the turbulence level doubles. The critical Reynolds number for the start of smooth surface transition decreases by nearly 50% when the turbulence level doubles. By multiplying the roughness term for the start of transition by a turbulence intensity factor, the agreement

with data is improved. However, pressure surface transition at the highest roughness is predicted to occur further downstream than the data. This suggests that the exponent on the Tu term in the denominator for the start of transition should be more negative.

The question of whether the transition length correlation should be modified to account for roughness is complicated by the failure of the transition model to accurately predict smooth surface transition. For the smooth vane suction, surface transition occurs in regions where the pressure gradient is very negative. At this Reynolds number, the pressure gradient at the start of transition for the smooth surface is more negative than the pressure gradient data of Gostelow et al. [41], which was used by Solomon et al. [33] to determine the value of the spot production parameter, N . The length of transition is very sensitive to negative pressure gradients. Figure 4(a) shows that an abrupt smooth suction surface transition was calculated for the 8% turbulence level. The transition length would increase if N were limited to a smaller value. The data of Gostelow and Walker [42] strongly indicate that extrapolating the correlation of Gostelow et al. [41] to more negative pressure gradients would overestimate the value for N . At the lower turbulence intensity (Fig. 4(b)), the start of suction surface transition is at an even more negative pressure gradient because the critical Reynolds number for the start of transition is increased. At the lower pressure gradient, the rapid increase in intermittency is appropriate. Fortunately, the question of whether the transition model should be modified to account for surface roughness is not dependent on extrapolating the database for the correlation of N . Where rough surface transition is seen for negative pressure gradient values, they are within the database used to correlate N . The form of the correlation for N is asymptotic for large positive values of the pressure gradient.

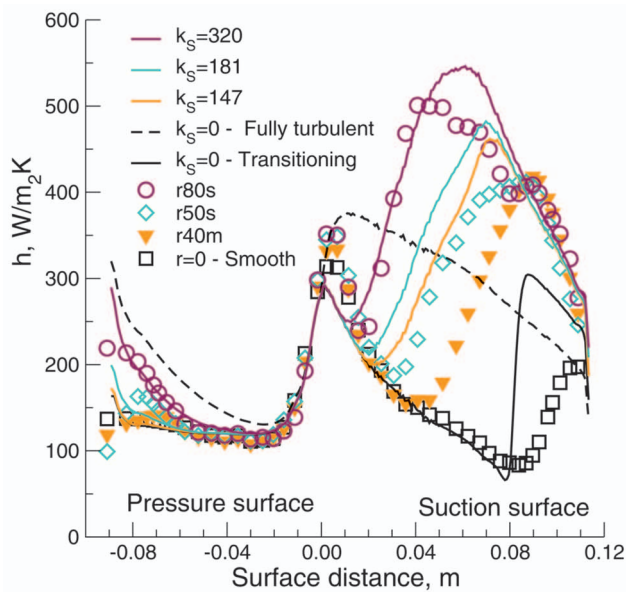
Figure 5 shows the heat transfer comparisons for a lower inlet Reynolds number of 140,000 for the same two inlet turbulence intensities. Here the analysis shows the same trends as the data and overall is in reasonably good agreement with the data. Transition is predicted somewhat earlier than is seen in the data, especially at the higher Tu_{in} . Improved agreement with the data would be achieved by changing the coefficient in the transition start model, C_{ST} , from 0.05 to 0.033. However, the agreement with the data in Fig. 4 for the higher Reynolds number would not be as good.

Figure 6 shows the heat transfer comparisons for the lowest inlet Reynolds number of 90,000. The comparison is at a turbulence intensity of 8%. The agreement is very similar to that in Fig. 5 for the intermediate roughness. The results in Figs. 5 and 6 indicate that the 1.25 exponent on roughness term should be increased. However, when this was done, either in isolation or in combination with changing the coefficient, C_{ST} , in the transition start model, overall agreement with data was not improved.

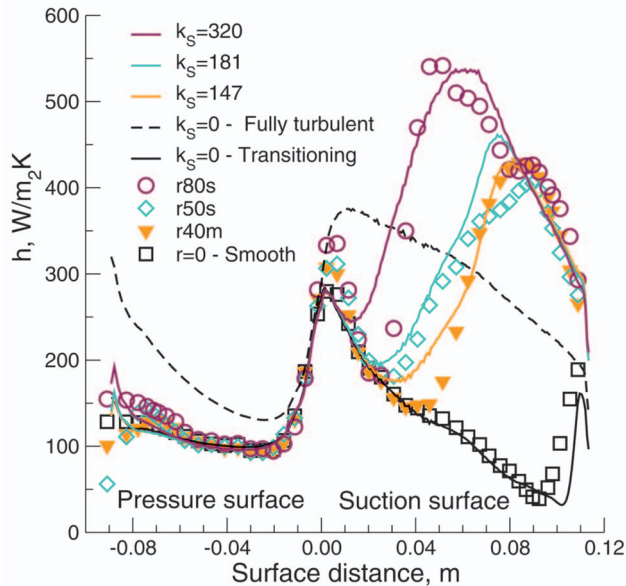
2.4 Other Rough Surface Heat Transfer Comparisons.

Heat transfer comparisons were made for three other data sets, which were not used to determine the modeling for transition. Each data set shows transition behavior in the heat transfer results.

Turbine rotor of Blair. Figure 7 compares Stanton number predictions with those measured by Blair [43] at the midspan of a turbine rotor. Data were obtained in a large scale rotating turbine test facility. Figure 7 shows comparisons at the highest inlet Reynolds number of 580,000. Stanton numbers were given for a smooth surface, a near smooth surface, and a rough surface. Table 3 shows the roughness measurements from the reference both as absolute numbers and as a fraction of axial chord. Only R_{rms} and the maximum-to-minimum roughness heights were given. At this Reynolds number, the smooth data show that the pressure surface is laminar. The predictions for the smooth suction surface are lower than the data. The inlet turbulence intensity was estimated to be 5%. Increasing Tu_{in} improved agreement for the smooth suction surface but increased pressure surface heat transfer.



a) $Tu_{IN} = 8\%$



b) $Tu_{IN} = 4\%$

Fig. 5 Transition modeling predictions, $Re_{in} = 1.4 \times 10^5$

The near smooth data showed transition occurring midway along the pressure surface. A k_S of 27 gave H^+ values less than 5 so that the predicted heat transfer did not change from the smooth surface prediction. Since increased heat transfer is seen in the

Table 3 Roughness characteristics for Blair's rotor

Label	R_{rms} (μm)	$R_{max-to-min}$ (μm)	$R_{max-to-min}/C_x$ (%)
Smooth	0.33	7.6	0.0047
Near smooth	6.4	51	0.032
Rough	N. A.	660	0.41

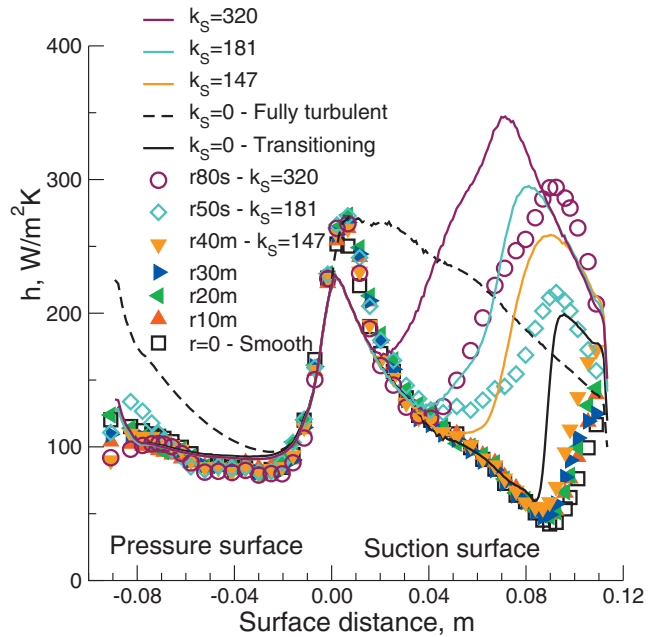


Fig. 6 Transition modeling predictions, $Re_{in} = 0.9 \times 10^5$, $Tu_{in} = 8\%$

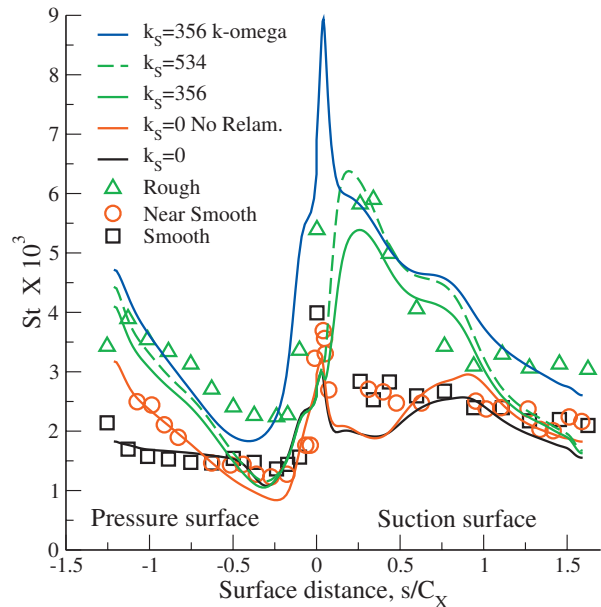


Fig. 7 Comparison with rotor data of Blair [43]

data, $k_S > 4.3R_{rms}$ should have been used. Perhaps the near smooth roughness had positive skewness. Interestingly, good agreement with the near smooth data is achieved when relaminarization is suppressed.

The rough surface data and predictions show that transition occurred close to the leading edge. The rough surface k_S value was estimated using the near smooth R_{rms} value and the ratio of maximum to minimum heights. Clearly, this is a somewhat crude approximation. Nevertheless, the agreement is reasonably good and improves when k_S is increased by 50%. A prediction is also shown using the k - ω turbulence model. Except for the leading edge region, these results agree well with the data and are an improvement for the rear portion of the suction surface.

Turbine vane of Boyle and Senyitko. Figure 8 compares the measured and predicted Nusselt numbers for the data of Boyle and

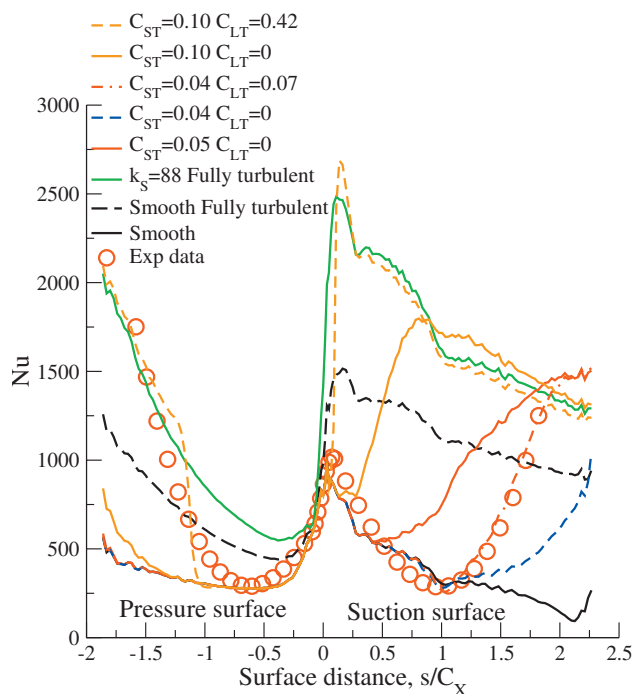


Fig. 8 Comparison with vane data of Boyle and Senyitko [44]

Senyitko [44]. The roughness characteristics for four measurements are given in Table 4. Calculations were done with $k_S = 88 \mu\text{m}$. The data in Fig. 8 clearly show the transition occurring midway along both the pressure and suction surfaces. The axial chord was 52 mm. Even though the axial chord Reynolds number is over a million, and the average R_{rms}/C_X was 0.00036, the measured inlet turbulence was only 1%. Figure 8 shows that at this low turbulence intensity smooth surface calculations predicted laminar flow for all of the pressure and suction surfaces. A smooth fully turbulent calculation gave heat transfer rates much greater than seen in the rough surface data over the forward portion of both the suction and pressure surfaces. The fully turbulent rough surface calculation gave heat transfer rates much greater than the data over most of the suction and pressure surfaces. Toward the rear of both surfaces, the agreement between the calculations and

Table 4 Rough vane roughness characteristics

Trace	R_{rms} (μm)	R_a (μm)	Skewness	k_S (μm)
1	17.7	14.0	0.206	92
2	20.5	15.9	-0.441	99
3	17.5	13.9	-0.010	86
4	17.0	13.0	-0.085	81
Avg.	18.2	14.2		88

Table 5 Roughness characteristics of LPT blade

Label	k (μm)	\bar{y} (μm)	R_a (μm)	R_{rms} (μm)	S_k	k_S	
						Koch and Smith (μm)	Present (μm)
L17	17	5.2	6.1	6.9	0.83	38	77
L27a	27	6.8	8.6	10.0	1.12	53	121
L27b	27	3.0	5.0	7.5	2.42	31	127
L27c	27	1.7	3.1	5.8	3.54	19	131
L50a	50	8.0	12.5	16.8	1.84	78	223
L90	90	14.7	20.8	27.0	1.74	129	395

data is good. This indicates that the k_S value determined from the roughness statistics is appropriate.

Rough surface heat transfer predictions using the baseline value $C_{ST}=0.05$ showed early suction surface transition and no pressure surface transition. Decreasing C_{ST} by 20% gave good agreement with the start of suction surface transition. The variations of k_S seen in Table 4 are about 10%. Decreasing C_{ST} by 20% was the equivalent of decreasing k_S by 21%.

Even with $C_{ST}=0.04$ the calculated suction surface transition length was longer than seen in the data. Increasing C_{LT} from 0 to 0.071 showed good agreement for the suction surface transition length. However, this calculation still did not show pressure surface transition consistent with data. A $C_{LT}=0.42$ was needed to yield pressure surface heat transfer consistent with the experimental data. However, this same calculation gave very poor agreement with the suction surface data due to the rapid transition near the leading edge. The start of transition was not changed. But, suction surface transition began in a region of strong favorable pressure gradients. Consequently, the calculated transition length with $C_{LT}=0$ was very long.

Turbine blade of Stripf. A second series of tests was run with roughness elements similar to those in the tests used to determine the roughness transition models [45]. Table 5 gives roughness characteristics for the cases. The cases labeled L27a, L27b, and L27c had the same roughness heights but different spacings between the elements. The different spacings result in different values of the roughness statistics.

Figure 9 compares the measured and predicted heat transfers for this case. Even though these data were not used to develop the roughness transition models, the agreement between the calculations and measured data is good. The calculations were done with no modification of the transition length due to roughness. The results indicate that none was needed.

Figure 10 compares the results for different roughness spacings. As seen in Table 5, the proposed correlation for k_S has little variation among the three cases with the same roughness height. The data in Fig. 10 show a dependency on roughness spacing. As seen in Table 5, the variation in R_a values is consistent with the experimental data, in that smaller R_a values give lower heat transfer. However, just using $k_S=6.2R_a$ does not give good agreement with the data. The value of H^+ are too low. Increasing C_{ST} from 0.05 to 0.10 to adjust the start of transition when using the Koch and Smith correlation does not give good agreement with the data. It could be argued that a coefficient slightly less than 1 should be applied to the skewness term. If this is done the coefficients in the roughness models should also be adjusted. Except for specialized test cases, roughness typically exhibits noticeable variations when measured at different blade surface locations.

2.5 Extension to Higher Reynolds Numbers. In typical engine applications, the Reynolds number may be significantly higher than those used for data comparisons. A series of calculations was done with the same physical roughness but at a higher Reynolds number. When the Reynolds number was increased, calculations were done for two exit Mach numbers. The lower one

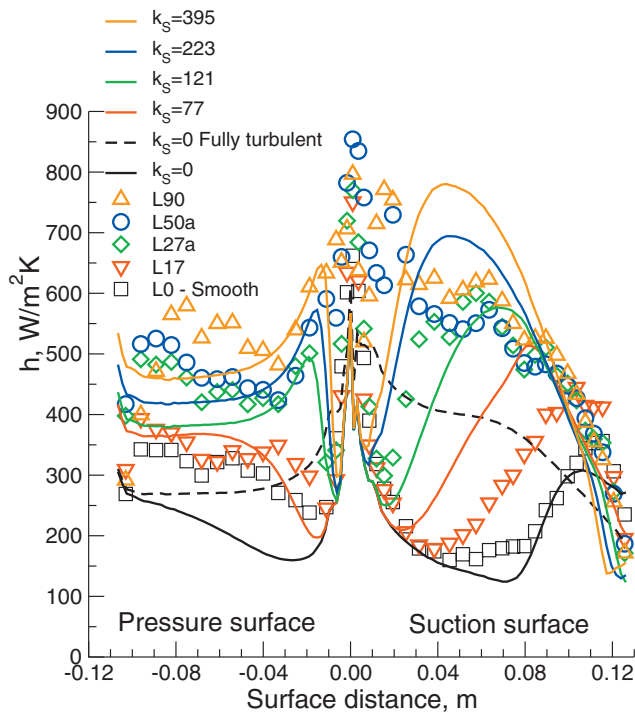


Fig. 9 Comparison with LPT blade data of Stripf [45]

($M_2=0.55$) is the same as for the highest Reynolds number tested by Stripf et al. [24]. Since the same geometry was used, the vane loading moved aft as the Mach number increased. The vane isentropic Mach number distributions for both exit Mach numbers are shown in Fig. 11. The higher Mach number results in a very aft loaded vane. This is a consequence of the vane not being designed for this high subsonic Mach number. The results for $M_2=0.9$ are presented because the distribution is not unlike the midspan distribution seen when there is an appreciable decrease in the span

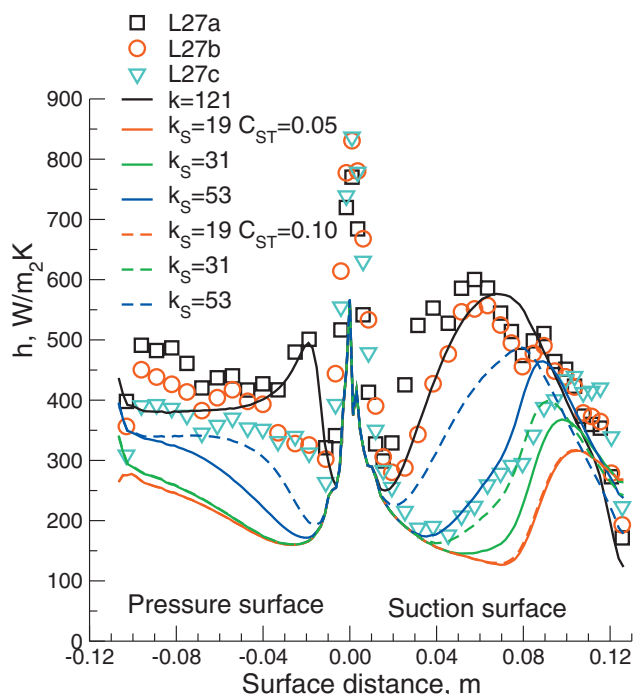


Fig. 10 Effect of roughness spacing on heat transfer

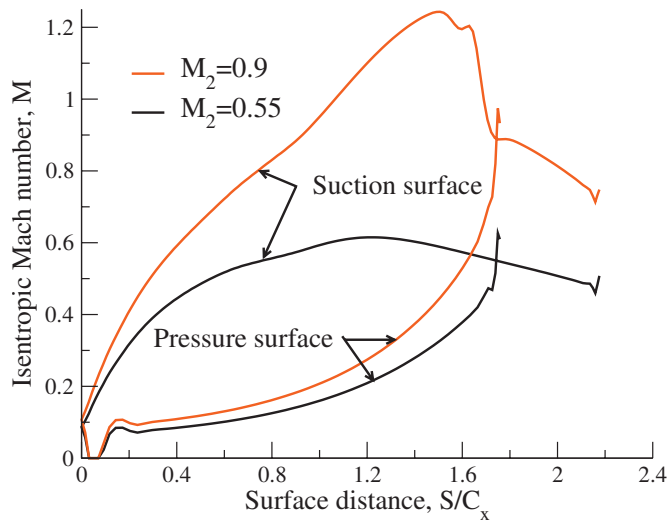


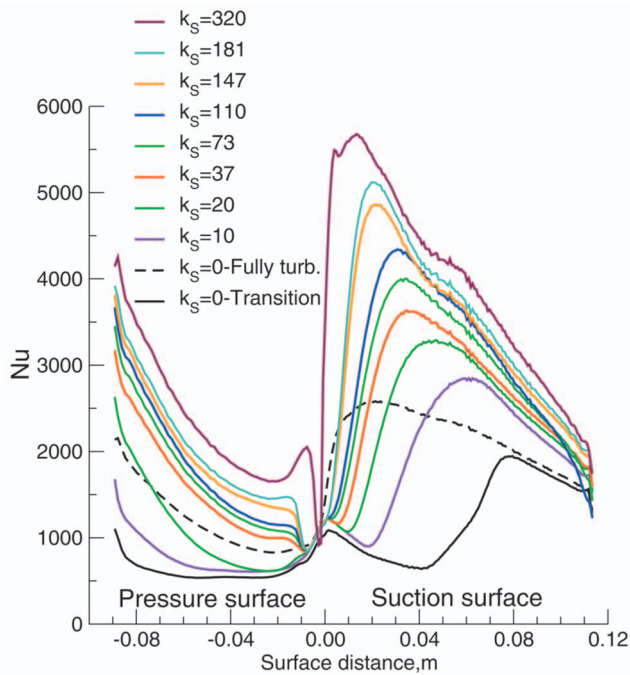
Fig. 11 Mach number distributions

between the leading and trailing edges. The rapid shocklike decrease in Mach number, and consequently rapid diffusion, is a result of the blade profile.

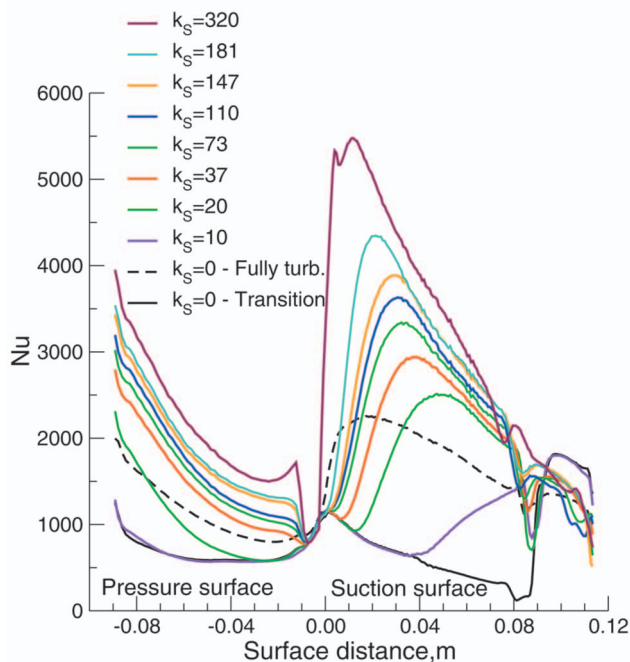
The axial chord Nusselt number distributions for a range of roughness heights are shown in Fig. 12. The Nusselt numbers are shown for a vane exit unit Reynolds number of $300,000 \text{ cm}^{-1}$. The value is less than what is typical for a first stage vane of a high pressure turbine. A unit Reynolds number in this range is appropriate for the second stage vane, which may or may not be film cooled. The unit Reynolds number of $300,000 \text{ cm}^{-1}$ is nearly twice as great as the highest Reynolds number tested by Stripf et al. [24]. For the smooth surface, the distance from the leading edge at which suction surface transition is seen nearly doubles as the exit Mach number is increased. This is the result of the aft loading at the higher exit Mach number. At both exit Mach numbers, the smooth pressure surface remained almost entirely laminar.

At both exit Mach numbers, the effect of increasing surface roughness is to move the location of the start of suction surface transition forward, toward the leading edge. The high exit Mach number with the aft loading shows that a higher k_s value is required for transition to start at the same surface location. Except for the smallest roughness heights, pressure surface transition is very similar at both Mach numbers. Relaminarization is not an issue, and once a critical roughness height is reached, transition to turbulent flow occurs close to the leading edge. For small roughness heights, pressure surface transition behaves similar to suction surface transition.

Because the calculations shown in Fig. 12 are not compared with experimental data, it is useful to relate these results to those presented in the literature in a qualitative manner. This is done to show the reasonableness of the modeling presented herein. Abuaf et al. [8] examined the effects of small roughness on vane heat transfer and aerodynamic efficiency. Their exit vane axial chord Reynolds number varied between 6.8×10^5 and 2.3×10^6 . The inlet turbulence intensity was 14%. Their maximum R_a value was $2.33 \mu\text{m}$, but the axial chord was only 4.8 cm. The vane was forward loaded, and at the lowest Reynolds number suction surface transition occurred just upstream of the peak isentropic Mach number. Roughness was not a factor in transition at the lowest Reynolds number. As the Reynolds number increased, the vane with $R_a=2.33 \mu\text{m}$, ($k_s \approx 15$), was seen to move transition closer to the leading edge. At the highest Reynolds number, transition was seen at the leading edge. Pressure surface transition was not affected by roughness, but was turbulent for nearly 80% of the



a) $M_2 = 0.55$



b) $M_2 = 0.9$

Fig. 12 Nusselt numbers at $Re_1=300,000 \text{ cm}^{-1}$, $Tu=8\%$

surface distance. In the turbulent region, the heat transfer rates increased approximately 10–15% as a result of surface roughness.

The importance of roughness in terms of aerodynamic losses is illustrated in Fig. 13. The loss coefficient, Y , is calculated from

$$Y = \frac{P_{in,t} - P_{2,t}}{P_{ni,t} - P_2}$$

Figure 13 shows the loss coefficient, Y , as a function of k_S . At the highest equivalent height, the loss coefficient nearly doubles

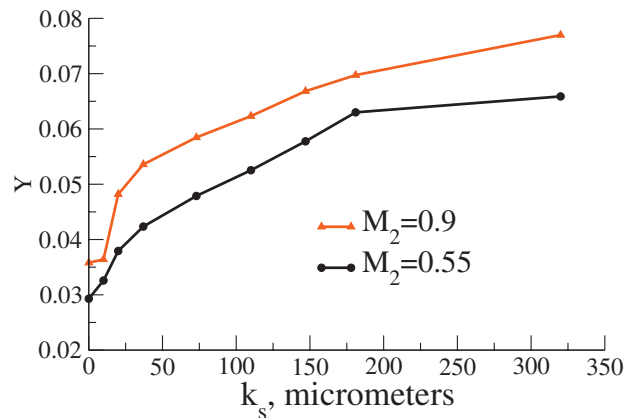


Fig. 13 Calculated losses at $Re_1=300,000 \text{ cm}^{-1}$

and approaches an asymptotic value. The increase in smooth surface loss for the higher exit Mach number remains even as the surface roughness increases.

The data show that an important parameter is H^+ . In fully turbulent flow, H^+ is nearly proportional to the Reynolds number. Therefore, doubling the unit Reynolds number results in a similar loss distributions, but with the abscissa in Fig. 13 reduced by half.

3 Concluding Remarks

An approach to calculating an equivalent sand grain roughness has been given. This approach is consistent with experimental data in that the weak effect of roughness spacing is accounted for. This approach uses only statistical quantities, which are readily available from roughness measurements. When the calculated k_S values were used with either an algebraic or a $k-\omega$ turbulence model, heat transfer rates were in good agreement with data in the fully turbulent regions.

Two-dimensional calculations were done to determine criteria for transition and relaminarization that were reasonably consistent with experimental data. Both calculations and data show heat transfer rates much less than for fully turbulent flow at small roughness heights. For high roughness heights, heat transfer rates were nearly double those for the fully turbulent smooth flow. This simplified approach gave reasonable agreement with data for most of the cases examined. There were two prominent exceptions. Both involved the blade pressure surface. The data for the near smooth case of Blair showed that a roughness with a calculated $H^+ < 5$ appeared to cause a laminar boundary to become turbulent. In the second case, a vane tested with low inlet turbulence exhibited rapid transition midway along the pressure surface. This was not predicted by the analysis, and further work in this area is needed.

Using the modification to account for roughness on the start of transition, calculations were then done for a unit Reynolds number of $300,000 \text{ cm}^{-1}$. This is representative of the second stage of a high pressure turbine. For good cycle efficiency, the second stage vane might not be film cooled, and accurate transition predictions would be important. Vane loading was seen to be an important parameter. Aft loading delayed transition, both for smooth and slightly rough surfaces. Even at this moderately high Reynolds number, smooth and slightly rough surfaces had heat transfer rates significantly less than for the fully turbulent calculations. On the other hand, high roughness levels showed heat transfer rates far greater than those calculated for fully turbulent flow.

The effects of surface roughness on losses were also examined. The smooth aft loaded vane had a greater predicted loss than the forward loaded vane. Loss levels approached asymptotic values nearly twice that of the smooth vane as k_S increased.

Nomenclature

A^+	= near wall damping coefficient
C	= modeling constant
C_x	= axial chord
$C_f/2$	= friction coefficient
d	= base diameter
H^+	= normalized roughness height
h	= heat transfer coefficient
K	= acceleration parameter
k	= physical roughness height
k_S	= equivalent sand grain roughness
M	= Mach number
n	= number of points in roughness calculation
N	= spot production parameter
Nu	= Nusselt number
P	= pressure
p	= pitch
R_a	= absolute roughness height
R_{rms}	= root mean square roughness height
Re	= Reynolds number
Re_1	= unit Reynolds number
S	= surface distance
S_k	= skewness
St	= Stanton number
Tu	= turbulence intensity
U	= velocity
Y	= loss coefficient
y	= measured height distance from surface
\bar{y}	= average height
Δy	= increase in mixing length due to roughness
Δy^+	= normalized value for Δy
θ	= momentum thickness
κ	= mixing length constant
μ	= dynamic viscosity
$\mu_{t,i}$	= inner region eddy viscosity
ρ	= density

Subscripts

2	= vane exit
fs	= local freestream
in	= vane inlet
rlm	= relaminarization
rough	= rough
smooth	= smooth
sk	= skewness
SL	= length
st	= transition start
t	= total

References

- [1] Arts, T., Lambert de Rouvroit, M., and Rutherford, A. W., 1990, "Aero-Thermal Investigation of a Highly Loaded Transonic Linear Turbine Guide Vane Cascade," VKI Technical Note 174.
- [2] Arts, T., 1995, "Thermal Investigation of a Highly Loaded Transonic Turbine Film Cooled Guide Vane," First European Conference on Turbomachinery—Fluid Dynamic and Thermodynamic Aspects, Erlanger, Germany, VKI Preprint No. 1995-11.
- [3] Hourmouziadis, J., 1989, "Aerodynamic Design of Low Pressure Turbines," AGARD Lecture Series No. 167.
- [4] Kind, R. J., Serjak, P. J., and Abbott, M. W. P., 1998, "Measurements and Prediction of the Effects of Surface Roughness on Profile Losses and Deviation in a Turbine Cascade," ASME J. Turbomach., **120**, pp. 20–27.
- [5] Boynton, J. L., Tabibzadeh, R., and Hudson, S. T., 1993, "Investigation of Rotor Blade Roughness Effects on Turbine Performance," ASME J. Turbomach., **115**, pp. 614–620.
- [6] Bammert, K., and Stansted, H., 1972, "Measurements Concerning the Influence of Surface Roughness and Profile Changes on the Performance of Gas Turbines," ASME J. Eng. Power, **94**, pp. 207–213.
- [7] Bammert, K., and Stansted, H., 1976, "Influences of Manufacturing Tolerances and Surface Roughness of Blades on the Performance of Turbines," ASME J. Eng. Power, **98**, pp. 29–36.
- [8] Harbecke, U. G., Riess, W. and Seume, J. R., 2002, "The Effect of Milling Process Induced Coarse Surface Texture on Aerodynamic Turbine Profile Losses," ASME Paper No. GT-2002-3033.
- [9] Abuaf, N., Bunker, R. S., and Lee, C. P., 1998, "Effects of Surface Roughness on Heat Transfer and Aerodynamic Performance of Turbine Airfoils," ASME J. Turbomach., **120**, pp. 522–529.
- [10] Stabe, R. G., and Liebert, C. H., 1975, "Aerodynamic Performance of a Ceramic-Coated Core Turbine Vane Tested With Cold Air in a Two-Dimensional Cascade," NASA Report No. TMX-3191.
- [11] Boyle, R. J., and Senyitko, R. G., 2003, "Measurements and Predictions of Surface Roughness Effects on Turbine Vane Aerodynamics," ASME Paper No. GT-2003-38580.
- [12] Taylor, R. P., Coleman, H. W., and Hodge, B. K., 1985, "Predictions of Turbulent Rough-Wall Skin Friction Using a Discrete Element Approach," ASME J. Fluids Eng., **107**, pp. 251–257.
- [13] Hosni, M. H., Coleman, H. W., and Taylor, R. P., 1991, "Measurements and Calculations of Rough Wall Heat Transfer in the Turbulent Boundary Layer," Int. J. Heat Mass Transfer, **34**, pp. 1067–1082.
- [14] Stripf, M., Schulz, A., and Bauer, H.-J., 2008, "Modeling of Rough Wall Boundary Layer Transition and Heat Transfer on Turbine Airfoils," ASME J. Turbomach., **130**, p. 021003.
- [15] McClain, S. T., 2002, "A Discrete Element Method for Turbulent Flows Over Randomly Rough Surfaces," Ph.D. thesis, Mississippi State University, Mississippi State, MS.
- [16] McClain, S. T., Hodge, B. K., and Bons, J. P., 2003, "Predicting Skin Friction and Heat Transfer for Turbulent Flow Over Real Gas Turbine Surface Roughness Using the Discrete Element Method," ASME Paper No. GT2003-38813.
- [17] Sigal, A., and Danberg, J. E., 1990, "New Correlation of Roughness Density Effect on the Turbulent Boundary Layer," AIAA J., **28**(3), pp. 554–556.
- [18] Dvorak, F. A., 1969, "Calculation of Turbulent Boundary Layers on Rough Surfaces in Pressure Gradient," AIAA J., **7**(9), pp. 1752–1759.
- [19] Simpson, R. L., 1973, "A Generalized Correlation of Roughness Density Effects in the Turbulent Boundary Layer," AIAA J., **11**(2), pp. 242–244.
- [20] Dirling, R. B., 1973, "A Method for Computing Roughwall Heat Transfer Rates on Re-Entry Nostetips," AIAA Paper No. 73-763.
- [21] van Rij, J. A., Belnap, B. J., and Ligrani, P. M., 2002, "Analysis and Experiments on Three-Dimensional, Irregular Surface Roughness," ASME J. Fluids Eng., **124**, pp. 671–677.
- [22] Waigh, D. R., and Kind, R. J., 1998, "Improved Aerodynamic Characterization of Regular Three-Dimensional Roughness," AIAA J., **36**(6), pp. 1117–1119.
- [23] Koch, C. C., and Smith, L. H., 1976, "Loss Sources and Magnitudes in Axial-Flow Compressors," ASME J. Eng. Power, **98**, pp. 411–424.
- [24] Stripf, M., Schulz, A., and Wittig, S., 2005, "Surface Roughness Effects on External Heat Transfer of a HP Turbine Vane," ASME J. Turbomach., **127**, pp. 200–208.
- [25] Taylor, R. P., 1990, "Surface Measurements on Gas Turbine Blades," ASME J. Turbomach., **112**, pp. 175–180.
- [26] Bons, J. P., Taylor, R. P., McClain, S. T., and River, R. B., 2001, "The Many Faces of Turbine Surface Roughness," ASME J. Turbomach., **123**, pp. 739–748.
- [27] Tarada, F., and Suzuki, M., 1993, "External Heat Transfer Enhancement to Turbine Blading Due to Surface Roughness," ASME Paper No. 93-GT-74.
- [28] Bogard, D. G., Schmidt, D. L., and Tabbita, M., 1998, "Characterization and Laboratory Simulation of Turbine Airfoil Surface Roughness and Associated Heat Transfer," ASME J. Turbomach., **120**, pp. 337–342.
- [29] Zhang, Q., and Ligrani, P. M., 2004, "Mach Number/Surface Roughness Effects on Symmetric Transonic Turbine Airfoil Aerodynamic Losses," J. Propul. Power, **20**(6), pp. 1117–1125.
- [30] Mayle, R. E., 1991, "The Role of Laminar-Turbulent Transition in Gas Turbine Engines," ASME J. Turbomach., **113**, pp. 509–537.
- [31] Steelant, J. and Dick, E., 1999, "Prediction of By-Pass Transition by Means of a Turbulence Weighting Factor—Part I: Theory and Validation," ASME Paper No. 99-GT-29.
- [32] Boyle, R. J., and Simon, F. F., 1999, "Mach Number Effects on Turbine Blade Transition Length Prediction," ASME J. Turbomach., **121**, pp. 694–702.
- [33] Solomon, W. J., Walker, G. J., and Gostelow, J. P., 1996, "Transition Length Prediction For Flows With Rapidly Changing Pressure Gradients," ASME J. Turbomach., **118**, pp. 744–751.
- [34] Hylton, L. D., Mihelc, M. S., Turner, E. R., Nealy, D. A., and York, R. F., 1983, "Analytical and Experimental Evaluation of the Heat Transfer Distribution Over the Surfaces of Turbine Vanes," NASA Report No. CR-168015.
- [35] Arts, T., Duboue, J.-M., and Rollin, G., 1997, "Aero-Thermal Performance Measurements and Analysis of a Two-Dimensional High Turning Rotor Blade," ASME Paper No. 97-GT-120.
- [36] Chima, R. V., 1987, "Explicit Multigrid Algorithm for Quasi-Three-Dimensional Flows in Turbomachinery," J. Propul. Power, **3**(5), pp. 397–405.
- [37] Chima, R. V., Giel, P. W., and Boyle, R. J., 1993, "An Algebraic Turbulence Model for Three-Dimensional Viscous Flows," AIAA Paper 93-0083.
- [38] Becchi, T., and Chang, K. C., 1978, "Calculation of Incompressible Rough-Wall Boundary Layer Flows," AIAA J., **16**(7), pp. 730–735.
- [39] Ames, F. E., Wang, C., and Barbot, P. A., 2003, "Measurement and Prediction of the Influence of Catalytic and Dry Low NO_x Combustor Turbulence on Vane Surface Heat Transfer," ASME J. Turbomach., **125**, pp. 221–231.

- [40] Boyle, R. J., Giel, P. W., and Ames, F. E., 2004, "Predictions for the Effects of Freestream Turbulence on Turbine Blade Heat Transfer," ASME Paper No. GT2004-54332.
- [41] Gostelow, J. P., Blunden, A. R., and Walker, G. J., 1994, "Effects of Free-Stream Turbulence and Adverse Pressure Gradients on Boundary Layer Transition," ASME J. Turbomach., **116**, pp. 392–404.
- [42] Gostelow, J. P., and Walker, G. J., 1991, "Similarity Behavior in Transitional Boundary Layers Over a Range of Adverse Pressure Gradients and Turbulence Levels," ASME J. Turbomach., **113**, pp. 617–625.
- [43] Blair, M. F., 1994, "An Experimental Study of Heat Transfer in a Large-Scale Turbine Rotor Passage," ASME J. Turbomach., **116**, pp. 1–13.
- [44] Boyle, R. J., and Senyitko, R. G., 2005, "Effects of Surface Roughness on Turbine Vane Heat Transfer," ASME Paper No. GT2005-69133.
- [45] Stripf, M., 2007, "Einfluss der Oberflächenrauigkeit auf die transitionale Grenzschicht an Gasturbinenschaufeln," *Forschungsberichte aus dem Institut für Thermische Strömungsmaschinen*, Vol. 38, Logos, Berlin.

Experimental Study of Heat Transfer Augmentation Near the Entrance to a Film Cooling Hole in a Turbine Blade Cooling Passage

Gerard Scheepers

e-mail: gerard@qfin.net

R. M. Morris

Department of Mechanical Engineering,
University of Pretoria,
Pretoria 0002, South Africa

Film cooling is extensively used by modern gas turbine blade designers as a means of limiting the blade temperature when exposed to extreme combustor outlet temperatures. The following paper describes an experimental study of heat transfer near the entrance to a film cooling hole in a turbine blade cooling passage. Steady state heat transfer results were acquired by using a transient measurement technique in a 40 times actual rectangular channel, representative of an internal cooling channel of a turbine blade. Platinum thin film gauges were used to measure the inner surface heat transfer augmentation as a result of thermal boundary layer renewal and impingement near the entrance of a film cooling hole. Measurements were taken at various suction ratios, extraction angles, and wall temperature ratios with a main duct Reynolds number of 25,000. A numerical technique based on the resolution of the unsteady conduction equation, using a Crank-Nicholson scheme, is used to obtain the surface heat flux from the measured surface temperature history. Computational fluid dynamics predictions were also made to provide better understanding of the near-hole flow. The results show extensive heat transfer enhancement as a function of extraction angle and suction ratio in the near-hole region and demonstrate good agreement with a corresponding study. Furthermore it was shown that the effect of a wall-to-coolant ratio is of a second order and can therefore be considered negligible compared with the primary variables such as the suction ratio and extraction angle.

o [DOI: 10.1115/1.3066294]

Keywords: film cooling, coolant extraction, turbine blade, heat transfer enhancement, extraction angle, suction ratio

1 Introduction

Growing commercial pressure and environmental regulations are putting ever increasing demands on engine designers to obtain higher levels of fuel efficiency and to minimize combustion emissions. Consequently there is a strong drive to increase the compression ratio and turbine inlet temperature (TIT), thereby improving the overall efficiency of the engine. However, increasing the turbine inlet temperature enhances the thermal load on hot-end components such as rotor blades, nozzle guide vanes, and turbine disks. This problem is further aggravated by an increasing compressor outlet air temperature, analogous with higher compression ratios, which is also used to cool down these hot-end components.

Hence, more sophisticated cooling techniques and advanced thermal boundary coatings are implemented to cool down the

nozzle guide vanes and first stage rotor blades. Generally the cooling techniques that are implemented consist of a combination of convective internal cooling, such as ribbed cooling channels and impinging cooling, as well as external film cooling.

Although the cooling system provides increased cycle efficiency, it introduces various losses, which requires its design to be efficient in minimizing the quantity of air used for cooling purposes while at the same time maintaining optimum functionality of the engine and acceptable component life. For this reason an extensive amount of experimental and computational research has been done over the past couple of decades to quantify the effectiveness of coolant injection on the external surface of the blade and the influence of convective cooling on internal cooling passages [1–4].

Various correlations have been developed to predict the adiabatic film cooling effectiveness and heat transfer augmentation with regard to a variety of film cooling parameters on the external surface of the blade. These parameters include the injection of coolant from various blade surfaces with different cooling hole geometries, blowing ratios, and mainstream turbulence effects [5]. Likewise an extensive amount of research has been done with regard to augmented convective cooling in cooling channels inside the blade structure. These studies have considered the influence of different turbulator geometries and turbulator layouts on the channel heat transfer and pressure drop with and without rotation [6–8].

From the research that has been done with regard to internal cooling channels, only a limited number considered the influence of coolant extraction, to aid with external film cooling, on the internal channel wall heat transfer augmentation. Apart from the relation between the improvement of internal heat transfer augmentation and external film cooling efficiency, a greater degree of uniformity with regard to internal cooling is also required to prohibit current stress-strain limitations. This may imply that a component must be cooled more efficiently in specific local regions rather than on improved global performance [9].

Studies that have considered coolant extraction have shown that the withdrawal of air from the cooling channel induces extensive local heat transfer enhancement downstream of the coolant extraction hole [10–15]. The amount of enhancement is quantified by a nondimensional enhancement factor, which describes the amount of heat transfer augmentation and is defined as

$$EF = \frac{h}{h_0} \quad (1)$$

Furthermore research has shown that the local augmentation is fairly insensitive to the channel Reynolds number and upstream flow conditions, as well as the interaction between supplementary holes [11,12]. Studies that have considered the interaction between rib turbulators and extraction holes have shown that the position of the extraction hole relative to the rib reduces the amount of separation downstream of the turbulator and also influences the discharge coefficient of the hole [12,14,16]. Most of these experimental studies were, however, conducted in single and multiple cooling passages with multiple extraction holes, which considered the influence of coolant extraction on the average channel heat transfer enhancement. Only a limited amount of research has focused on the local influence of extraction hole parameters such as the suction ratio, or blowing ratio, defined as

$$SR = \frac{\bar{V}_{\text{hole}}}{\bar{V}_{\text{channel}}} \quad (2)$$

Another variable or parameter that has not received much attention is the angle at which the coolant is extracted.

The first, and to the knowledge of the author, the only study that considered the influence of these parameters on the near-hole heat transfer augmentation in a cooling passage was conducted by Beyerley [17]. Apart from experimental heat transfer measure-

Contributed by the Turbomachinery Division of ASME for publication in the JOURNAL OF TURBOMACHINERY. Manuscript received December 7, 2007; final manuscript received August 31, 2008; published online June 30, 2009. Review conducted by Ronald S. Bunker.

ments, making use of liquid crystal thermography, smoke flow visualization studies near the entrance to the extraction hole were also considered. The study made use of a one pass cooling channel with a single coolant extraction hole. Tests were conducted primarily at a channel Reynolds number of 25,000 and coolant extraction angles of 30 deg, 90 deg, and 150 deg. A 60 deg orthogonal or sideways extraction angle was also considered. The suction ratio of the coolant extraction hole was varied from 0 to 8.

The results showed that the local heat transfer augmentation downstream of the coolant extraction hole is induced by a complex combination of boundary layer renewal and three-dimensional flow features, such as impingement and vortex downwash, which are primarily dependent on the suction ratio. The study also showed that the amounts of heat transfer enhancement with regard to the different extraction angles were relatively similar (pertaining to the suction ratio), except for the 150 deg extraction hole, which was considerably lower at higher suction ratios.

The study conducted by Byerley [17] obtained valuable and comprehensive results of the heat transfer downstream of a coolant extraction hole. However, although the liquid crystal thermography technique used provides detailed contours of surface heat transfer, it limits the maximum wall temperature at which tests can be conducted. For this reason heated air was blown in a cooled channel, which implies that the coolant boundary layer density in the near wall region was higher than that of the mainstream flow field. Assuming that the $T_{wall}/T_{coolant}$ gradient is representative of an actual cooling passage, this method should provide an adequate approximation of the absolute convective heat transfer enhancement in a channel without coolant extraction. However, the heat transfer augmentation near the entrance to a coolant extraction hole is influenced by boundary layer renewal and vortex downwash further downstream of the extraction hole, which may be affected by the inverse density gradient in the near-wall region. Furthermore, the study conducted by Byerley [17] made use of a rectangular experimental channel with sidewalls, which were widened to neglect any interaction between the channel sidewalls and the coolant flow. Whether the sidewalls will influence the downstream heat transfer augmentation is uncertain.

The objective of the present paper is to contribute to the work that was conducted by Byerley [17] and to consider the local heat transfer augmentation near the entrance to a coolant extraction hole at varied suction ratios and extraction angles. Consequently tests were performed within the same scope; however, in the present study a thin film measuring technique was adopted. Although this technique will provide less details compared with liquid crystal thermography, it provides the ability to test at higher wall-to-coolant temperature ratios, which are representative of a gas turbine cooling channel. Tests were also conducted in a square channel to assess the influence of the channel sidewalls on the heat transfer enhancement downstream of the coolant extraction hole.

In addition to the experimental investigation, a commercial finite volume code was also used to numerically simulate the experimental domain at different suction ratio and extraction angle test cases. The purpose of the numerical investigation was to provide better understanding with regard to the flow field near the extraction hole.

2 Experimental Setup

A schematic layout of the experimental rig is displayed in Fig. 1. For the purpose of this study, a square channel with a single extraction hole was manufactured. The channel is representative of an internal cooling channel of a turbine blade, scaled 40 times, with a hydraulic diameter of 25 mm. The channel walls were made from Ertalyte, a nylon compound, and Macor ceramic plates, which were then sealed and clamped together within an aluminum casing. The Macor and Ertalyte wall sections were chosen due to their low thermal conductivity and hence to minimize lateral conduction in the substrate. This is necessary to ensure that

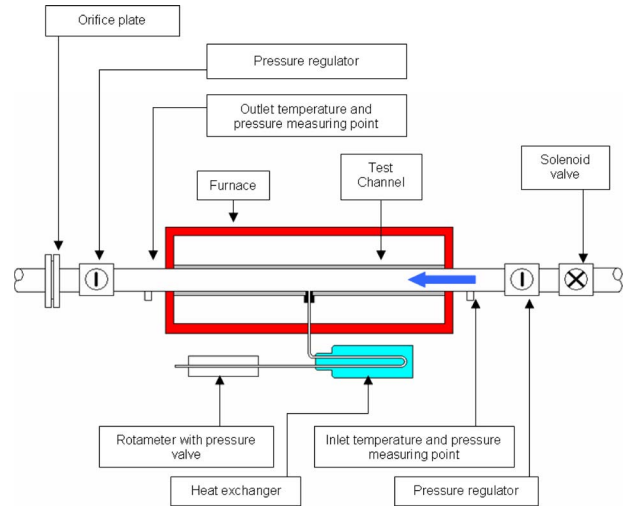


Fig. 1 Schematic layout of the experimental setup

the walls can be assumed to represent a semi-infinite substrate during the short experimental measurement period. The Macor ceramic wall section provides the substrate onto which the platinum thin film gauges are fired and also serves as a housing for the instrumentation connections and the bleed hole geometry plug connection.

An interchangeable bleed hole geometry plug, of the required hole diameter and extraction angle, is inserted, fastened, and sealed in the connecting hole of the ceramic substrate. The plug fits flush with the channel surface. The bleed hole geometry plug has a channel hydraulic diameter of 5 mm with a bleed hole length to diameter ratio of 8. This ratio is representative of the range used on actual blades. Bleed hole angles of 90 deg and 150 deg were used. The inlet of the extraction hole is sharp edged.

The experimental channel is mounted within a furnace, which provides the ability to control the wall temperature of the test channel. Coolant flow is provided by a compressor, delivering air at a maximum pressure of 600 kPa and a constant mass flow rate of 2 kg/s. The feed from the compressor is controlled using a solenoid valve, placed upstream of the channel section. The solenoid valve is a high speed open/shut valve, which provides a step change in the flow when required. Flow regulators were fitted at the inlet and outlet of the main channel, providing the ability to adjust the mass flow rate and pressure inside the channel to the required state.

The mass flow rate in the main channel was measured with an orifice plate, designed according to BS 1042, situated downstream of the experimental channel. The amount of coolant extracted from the bleed hole was controlled and measured by a rotameter on the extraction channel outlet. The extracted air flows through a heat exchanger, cooling the bleed air down to the prescribed temperature at which the rotameter is calibrated. Pressure measuring points and temperature sensors were placed at the inlet and outlets of the main channel to provide the channel pressure drop and bulk temperature measurements.

Surface temperature measurements were made downstream and upstream of the coolant extraction hole, as shown in Fig. 2. The measurement area downstream of the coolant extraction hole is concentrated near the entrance of the hole to provide line averaged measurements of the surface heat transfer enhancement induced by the extraction of the coolant. This measurement area has a length of five bleed hole diameters downstream of the extraction hole and a width of two bleed hole diameters. The size of the measurement area was chosen to provide line averaged results, which can be compared with the near-hole heat transfer contours provided by Byerley [17].

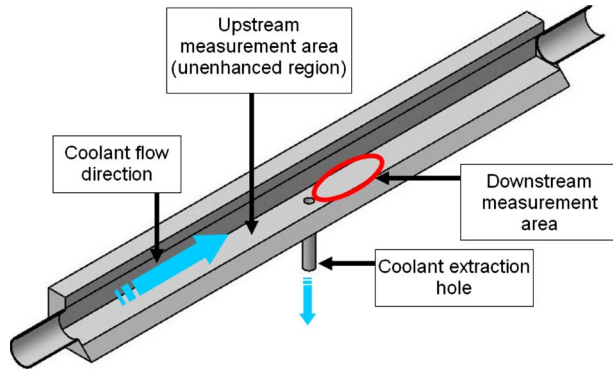


Fig. 2 Schematic cut-away of the experimental channel

The upstream measurement is used to calculate a reference surface temperature measurement in an unenhanced region, i.e., a region with fully developed hydrodynamics not directly influenced by the extraction of coolant. The purpose of the reference measurement is to provide a dimensionless representation of the near-hole heat transfer enhancement as defined by the enhancement factor.

3 Measuring Technique and Data Reduction

A transient measurement technique was used to measure the steady state heat transfer on the substrate surface upstream and downstream of the coolant extraction hole. This technique makes use of thin film gauges to measure the transient surface temperature during testing. Each gauge acts as a resistance temperature device (RTD), consisting of a very thin platinum metal element with negligible heat capacity, which is painted onto the substrate. The gauge thickness is so small, in the region of 0.1–1 μm , and its conductivity so high, in comparison with the substrate, that its influence on the flow field and heat transfer can be neglected [18].

A numerical data reduction technique was used to obtain the surface heat flux from the surface temperature measurement. This numerical method has been validated by Denos et al. [19] against the established analog heat flux measurement technique described by Schulz and Jones [20]. With this technique the wall heat flux is calculated using Eq. (3), which represents one-dimensional unsteady conduction,

$$\frac{\partial T(x,t)}{\partial x^2} = \frac{1}{\alpha(x)} \frac{\partial T(x,t)}{\partial t} \quad (3)$$

Equation (3) computes the spatiotemporal propagation of temperature into the substrate by using the experimentally measured temperature history at the exposed surface and at a given depth as boundary conditions. The initial temperature distribution within the substrate can be assumed to be uniform since the substrate is under thermal equilibrium before blowdown,

$$T(x,0) = T_0 \quad (4)$$

Furthermore it can be shown that if the transient time of the experiment is less than 1.5 s, the substrate can be considered to represent a semi-infinite substrate, yielding

$$t < \frac{L^2}{4\alpha} \Rightarrow T(\infty, t) = T_0 \quad (5)$$

This provides the ability to determine the temperature distribution history within the substrate itself, which can then be used to determine the surface heat flux by means of

$$\dot{q}_w(t) = -k \left(\frac{\partial T}{\partial x} \right)_{x=0} \quad (6)$$

To solve Eq. (3) an implicit Crank–Nicholson scheme was used, which can be outlined as

$$\frac{T_i^{n+1} - T_i^n}{\Delta t} = \frac{[\eta(T_{i+1}^{n+1} - 2T_i^{n+1} + T_{i-1}^{n+1}) + (1 - \eta)(T_{i+1}^n - 2T_i^n + T_{i-1}^n)]}{\Delta x^2} \quad (7)$$

By expressing the unknowns at time $n+1$, in Eq. (7), as a function of the computed solution at time n , a tridiagonal system is obtained, which can be solved to attain the distribution of temperature in the substrate at time step $n+1$. The temporal domain displayed in Eq. (7) represents the experimental sampling rate, while the spatial domain is the discretized substrate. The substrate discretization depth was 7 mm and was discretized with 5000 node points clustered toward the surface where the higher gradients are expected. This data reduction technique was validated against an analytical test case describing the temperature change within a substrate exposed to a step change of constant heat flux. The numerical discretization was adapted to obtain a difference of less than 0.1% with regard to the analytical solution.

4 Experimental Uncertainty

The gauge firing process, used during the application of the gauges, may cause diffusion of platinum into the substrate, thereby altering the original thermal characteristics of the ceramic [21]. Knowledge regarding the thermal product ($\sqrt{\rho C_p k}$) of the ceramic is required to accurately predict the temperature profile within the substrate. For this a Joule heating technique, suggested by Denos et al. [19], was implemented with which a gauge is subjected to a pulse of known constant heat flux. The initial parabolic change in surface temperature during this process is measured and used to determine the thermal product.

The uncertainty regarding the measuring technique was estimated with a single sample uncertainty analysis based on the method proposed by Kline and McClintock [22]. The experimentally determined thermal product provided a dispersion of 7%, which represents a surface flux uncertainty of approximately 2%. The maximum uncertainty of the temperature difference between the wall temperature and gas temperature can be considered to be $\pm 1.1^\circ\text{C}$. This provided a conservative surface heat transfer coefficient uncertainty of less than 3%, which is considered acceptable for the current application.

5 Numerical Model

In addition to the experimental investigation, test cases were numerically modeled at different suction ratios and extraction angles. The purpose of the numerical investigation was to provide better understanding with regard to the flow field near the extraction hole.

A fully three-dimensional steady state computational fluid dynamics (CFD) analysis was conducted using a commercial finite volume package (FLUENT 6.3.26). Although promising studies have been performed with large eddy simulation (LES) turbulence models on internal cooling passages without coolant extraction [23,24], it is not yet employed in routine design simulations [25]. Consequently, in this study it was decided to solve the Reynolds averaged Navier–Stokes (RANS) equations with the two-layer re-normalisation group (RNG) $k-\varepsilon$ turbulence model and a second order volume discretization scheme. The RNG $k-\varepsilon$ turbulence model was chosen since it is currently one of the more common turbulence models used in the industry [26].

An unstructured hexahedral mesh was used to discretize the numerical domain, which represented the experimental channel section. To reduce the computational effort, a symmetry boundary was used along the length of the channel, as shown in Fig. 3, to decrease the size of the model. The number of cells that were implemented totaled to 5,400,000 and was determined through a mesh independence study. The study considered mesh sizes with different degrees of nonuniform grid spacing in the main channel

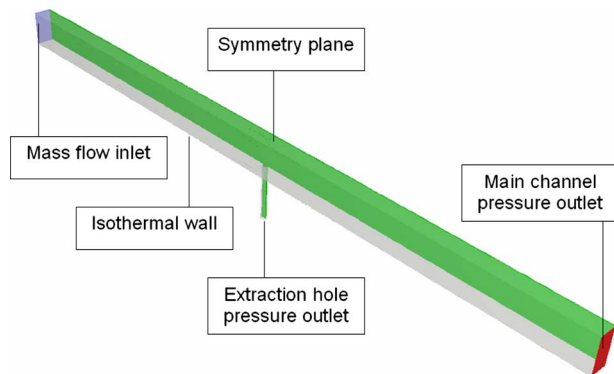


Fig. 3 Numerical domain with boundary conditions

and a constant boundary layer cell size, which provided a y^+ value of approximately 1. The grid spacing was dense in the region of the extraction hole where the higher flow gradients were expected and gradually increased further away where the flow properties were assumed to be more uniform. Figure 4 illustrates the near-hole mesh configuration and cell distribution of the 90 deg extraction model.

A mass flow boundary condition was used at the channel inlet, and pressure boundaries were used at the channel and bleed hole outlets. Experimentally measured mass flow and extraction hole outlet pressure values were implemented as flow boundary conditions to the numerical model. The channel walls were modeled as isothermal with a wall temperature equivalent to that of the ex-

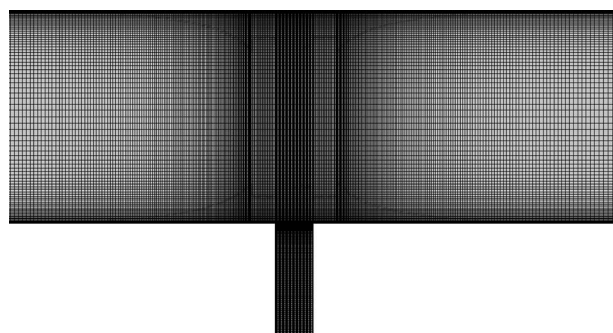


Fig. 4 Near-hole mesh configuration

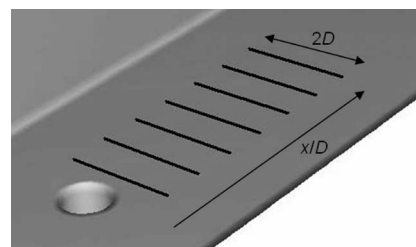


Fig. 5 Line averages downstream of the extraction hole

perimental setup. This is done to replicate the isothermal substrate walls approximated by the transient experimental technique. Convergence was determined from the residuals and by monitoring the mass flow rate at the channel and bleed outlets.

6 Results and Discussion

Transient experimental measurements were made with a channel Reynolds number of 25,000 and extraction angles of 90 deg and 150 deg. The SR ratio was varied between 0 and 5, and wall-to-coolant temperature ratios (T_w/T_c) of 1.3 and 1.4 were considered.

The experimentally measured data are presented as line averaged heat transfer enhancement values downstream of the extraction hole. The position of each measurement is defined as the ratio between the distance downstream of the extraction hole, x , and the diameter of the hole, D , as illustrated in Fig. 5. The width used for averaging is a distance of two extraction hole diameters ($2D$) and was chosen to superimpose the footprint area of heat transfer enhancement downstream of the hole.

Although the purpose of this study was to consider the heat transfer augmentation near the entrance to the coolant extraction hole, numerically predicted flow vectors are also presented to provide better understanding with regard to the experimentally measured enhancement results.

6.1 Case 1. Heat transfer enhancement profiles downstream of the 90 deg extraction hole, for $SR=5$ and $SR=2.5$, are compared in Fig. 6 with the measurements obtained by Byerley [17]. The enhancement profiles acquired from the analogous study were calculated from heat transfer enhancement contours measured with the use of liquid crystal thermography. The measurements show extensive heat transfer augmentation in the near-hole region

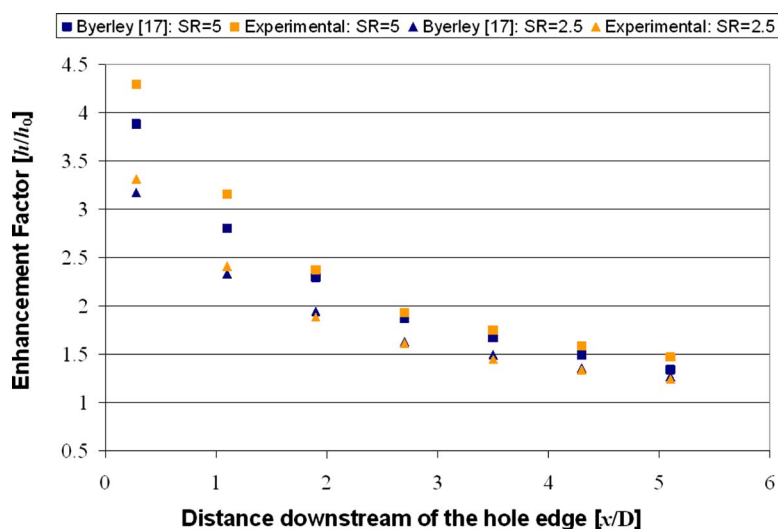


Fig. 6 Line averages downstream of the 90 deg extraction hole

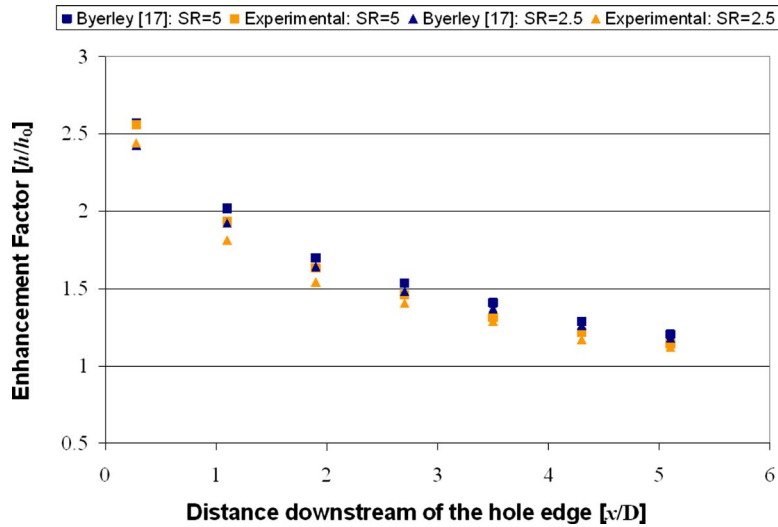


Fig. 7 Line averages downstream of the 150 deg extraction hole

for both suction ratios.

The near-hole enhancement profile for $SR=5$ shows a difference of less than 10% when compared with the profile obtained by Byerley [17]. Good agreement between the two sets of results is obtained further downstream. The enhancement profile for a $SR=2.5$ provides a better comparison, although a small difference is also observed closer to the extraction hole.

The relevant difference between the two data sets with regard to the near-hole enhancement appears to be greater at the higher suction ratio where impingement is a more dominant enhancement mechanism [17]. Although the difference can be assumed to be negligible, this observation may also indicate that the enhancement induced by impingement is influenced by the thermal gradient in the boundary at the near-hole region.

The heat transfer enhancement profiles downstream of the 150 deg extraction hole, for $SR=5$ and $SR=2.5$, are compared in Fig. 7. The comparison shows excellent agreement in the near-hole region and further downstream at both high and moderate suction ratios.

In contrast to the 90 deg extraction hole comparison, the 150

deg extraction hole enhancement profiles do not show any significant difference in the near-hole region with regard to suction ratio. It is believed that the higher angle of flow deviation, induced by the backward slanted 150 deg hole, extensively limits the amount of coolant impingement directly downstream when compared with the perpendicular extraction hole. This implies that contrary to the 90 deg extraction hole, the near-hole enhancement, which is obtained with the 150 deg extraction hole, is primarily influenced by boundary layer renewal at both high and moderate suction ratios.

This observation is further supported when considering numerically predicted velocity vectors in the near-hole region of the 90 deg and 150 deg extraction holes. Velocity vectors of the 90 deg extraction hole at suction ratios of 2.5 and 5 are displayed in Figs. 8 and 9. The encircled area shows the location of flow impingement induced by coolant extraction. When comparing the position of impingement downstream of the perpendicular hole between the two suction ratios, it should be noted that the point of impingement moves further downstream (a distance of approximately $0.5D$) with increased suction and that flow reversal takes place near the hole edge at a suction ratio of 5. At the lower

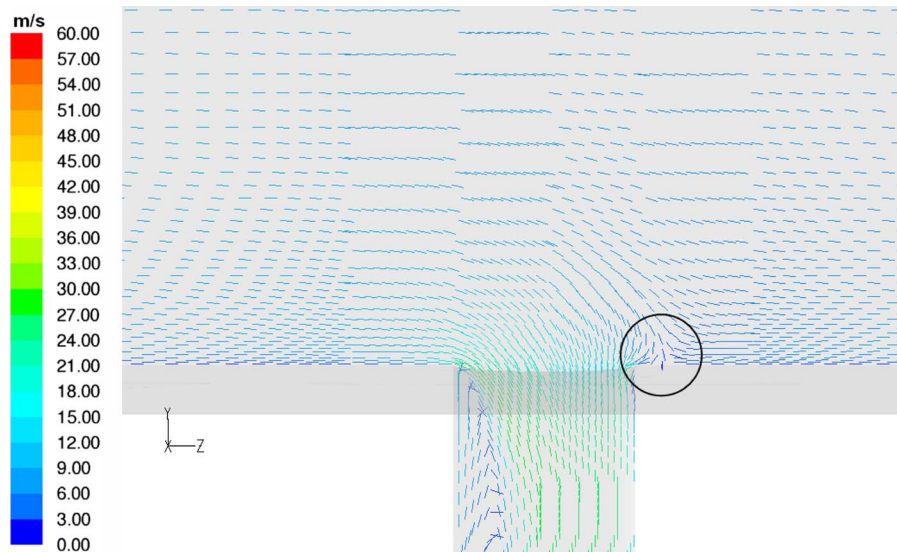


Fig. 8 Velocity vectors near the entrance to the 90 deg extraction hole at $SR=2.5$ (encircled area indicates coolant impingement)

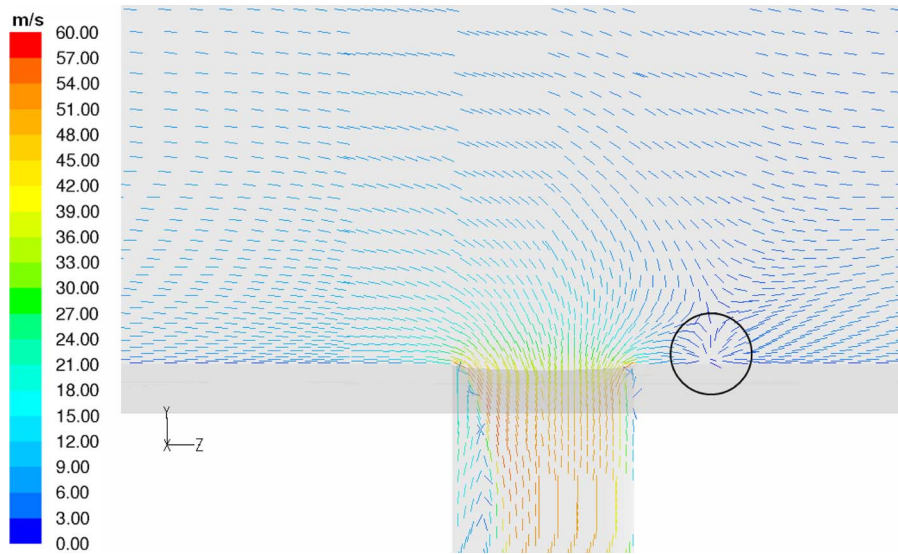


Fig. 9 Velocity vectors near the entrance to the 90 deg extraction hole at $SR=5$ (encircled area indicates coolant impingement)

suction ratio, the point of impingement is on the edge of the extraction hole. These observations relate strongly with the findings of Byerley [17], who conducted smoke visualization studies in the near-hole region of a 90 deg extraction hole. Furthermore, it indicates that the current numerical model provided qualitative agreement with regard to predicting the near-hole flow field.

Velocity vectors near the entrance of the 150 deg hole at suction ratios of 2.5 and 5 are displayed in Figs. 10 and 11. The velocity vectors of the 150 deg hole indicate that the impingement area is situated inside the extraction channel at both moderate and higher suction ratios and not downstream, as is the case with the perpendicular hole. This confirms that heat transfer augmentation downstream of the 150 deg extraction hole is to a lesser extent dependent on coolant impingement and to a greater extent on boundary layer renewal. Therefore the heat transfer augmentation downstream of the 150 deg extraction hole is extensively lower and reaches a stagnation point, regarding enhancement, at a lower suction ratio when compared with the 90 deg extraction hole. Fur-

thermore the comparison between Figs. 10 and 11 indicates an increased amount of recirculation within the cooling passage in comparison with the 90 deg extraction hole.

The good agreement, which was obtained between the enhancement profiles further downstream ($x/D > 2$), at multiple suction ratios and extraction angles, also indicates that the width of the channel has a negligible influence on the heat transfer enhancement induced by coolant extraction. This conclusion can be made since the current study was conducted in a square channel, whereas the channel used by Byerley [17] was rectangular, with the sidewalls widened intentionally to neglect any wall effects. Additionally, it should be noted that this observation is made with reference to a channel with a width that is equal to or larger than its height.

Considering that two different measuring techniques were used, with the density ratio of the present study within an engine representative range, good overall agreement was obtained. Further-

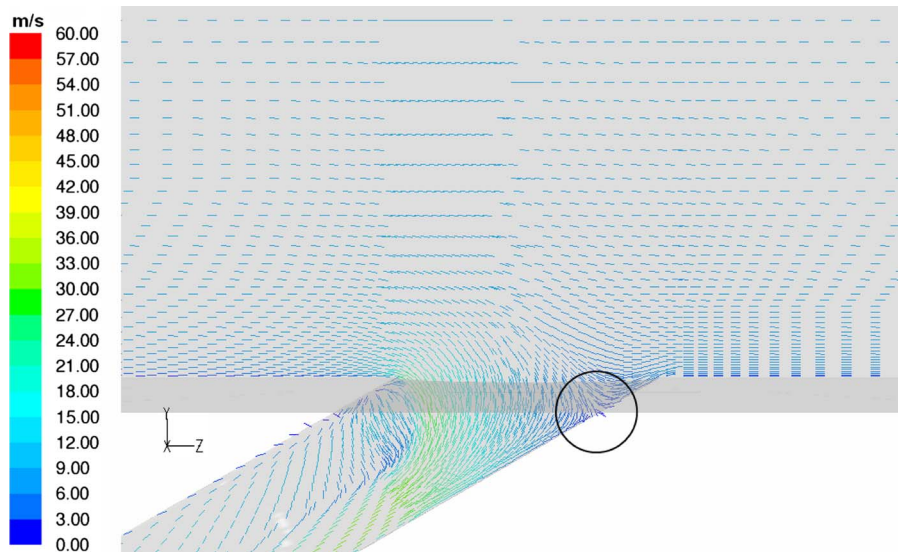


Fig. 10 Velocity vectors near the entrance to the 150 deg extraction hole at $SR=2.5$ (encircled area indicates coolant impingement)

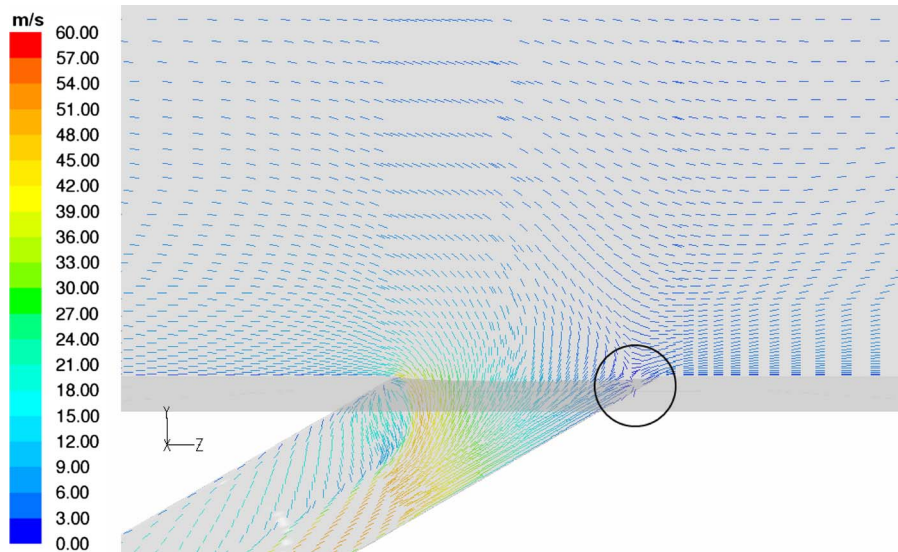


Fig. 11 Velocity vectors near the entrance to the 150 deg extraction hole at $SR=5$ (encircled area indicates coolant impingement)

more, this observation contributes to the validity of the experimental technique, which was implemented in the current study and may indicate that the wall-to-coolant temperature ratio has a negligible influence on the heat transfer augmentation induced by boundary layer renewal and flow impingement downstream of the extraction hole.

6.2 Case 2. To assess the influence of suction ratio on heat transfer enhancement, measurements were obtained at various suction ratios. Line averaged enhancement profiles downstream of the 90 deg extraction hole at multiple suction ratios, ranging from $SR=0$ to $SR=5$, are displayed in Fig. 12. Although no coolant is extracted at the zero suction ratio profile, a small amount of near-hole enhancement is observed. This can be attributed to turbulence enhancement in the boundary layer, which is induced by flow tripping across the hole edge.

The enhancement profiles show extensive enhancement near the extraction hole, even for a fairly small suction ratio of 1. When considering the amount of enhancement across the suction

ratio spectrum, the profiles indicate that the net amount of enhancement decreases exponentially with an increasing suction ratio.

6.3 Case 3. To assess the influence of the extraction angle, the line averaged enhancements downstream of the 150 deg extraction hole at $SR=5$ and $SR=2.5$ are compared with the profiles obtained with the 90 deg extraction hole, as shown in Figs. 13 and 14. Although the 150 deg extraction hole shows extensive augmentation, it is much less compared with the 90 deg extraction hole, especially at higher suction ratios. This observation correlates with the findings of Byerley [17]. The comparison shows a decrease in enhancement of approximately 45% in the near-hole region at $SR=5$, which decreases to approximately 25% in the same region for $SR=2.5$.

The difference in enhancement between the two extraction angles can be attributed to the amount of impingement downstream of the extraction hole, which has been shown to be exten-

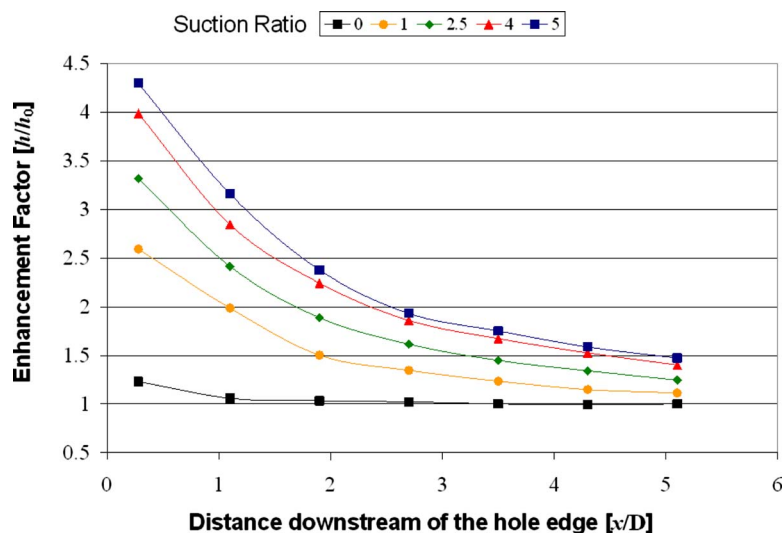


Fig. 12 Line averages downstream of the 90 deg extraction hole

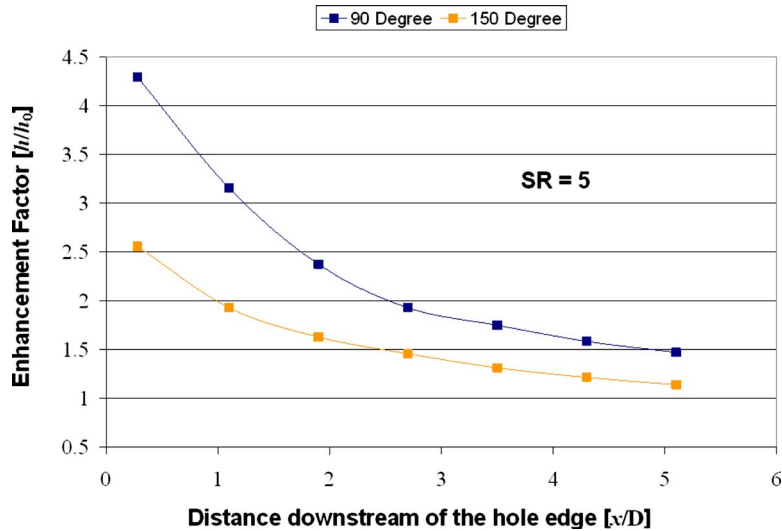


Fig. 13 Line averages downstream of different angled extraction holes

sively limited by the backward slanted 150 deg extraction hole. This observation is further illustrated when considering that the enhancement downstream of the 150 deg extraction hole is quite similar at high and moderate suction ratios in contrast to the enhancement observed with the 90 deg extraction hole at different suction ratios.

Further downstream ($x/D > 3$) the comparison shows a decreasing difference between the two enhancement profiles, although the difference is still significant. This can be expected since the extent of near-hole impingement contributes to the amount of downwash and turbulence downstream of the extraction hole.

The enhancement profiles downstream of the 150 deg extraction hole at multiple suction ratios ranging from $SR=0$ to $SR=5$ are displayed in Fig. 15. The enhancement profiles indicate that the amount of heat transfer enhancement reaches a stagnation point at a lower suction ratio when compared with the 90 deg extraction hole.

Consequently the rate of enhancement stagnation is extensively more for the slanted hole in comparison with the perpendicular hole. This is illustrated in Fig. 16, which shows a comparison between the average enhancement factors with regard to the suc-

tion ratio for the two extraction angles. The comparison shows a difference of approximately 30% with regard to the average heat transfer enhancement value at $SR=5$.

6.4 Case 4. Heat transfer enhancement at a higher wall-to-coolant temperature ratio was considered to further establish the sensitivity of near-hole enhancement with regard to a decreasing boundary layer density induced by the higher wall temperature. The absolute wall temperature was increased by approximately 10%, which is equal to a wall temperature increase of 30 K or wall-to-coolant temperature ratio of 1.4. Measurements were taken at $SR=2.5$ and $SR=5$. It was expected that if the difference in wall temperature was to influence the amount of enhancement, the discrepancy will most likely occur in the near-hole region where impingement is the primary contributor to enhancement. The enhancement profiles downstream of the 90 deg extraction hole at wall-to-coolant temperature ratios of 1.3 and 1.4 and suction ratios of 2.5 and 5 are displayed in Fig. 17. The profiles show good agreement at both suction ratios, although a small difference is present near the edge of the hole ($x/D < 2$) at the higher suction ratio. This difference is less than 2% and indicates that the effect of a varied T_w/T_c ratio on the downstream enhancement is of a

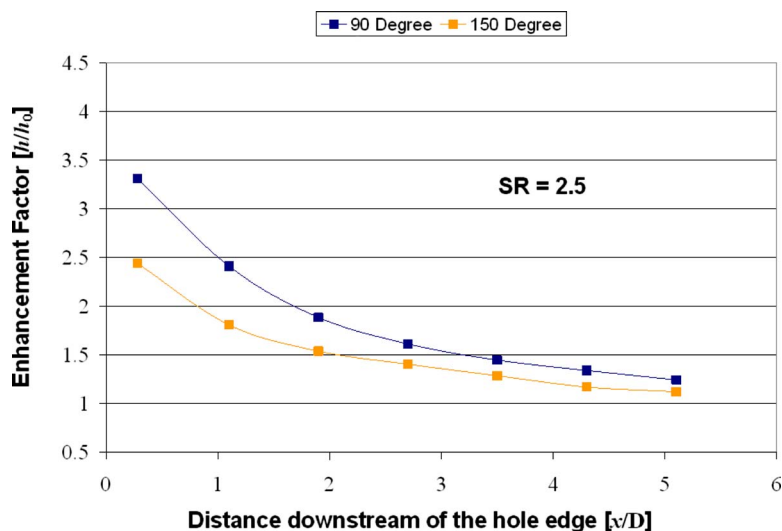


Fig. 14 Line averages downstream of different angled extraction holes

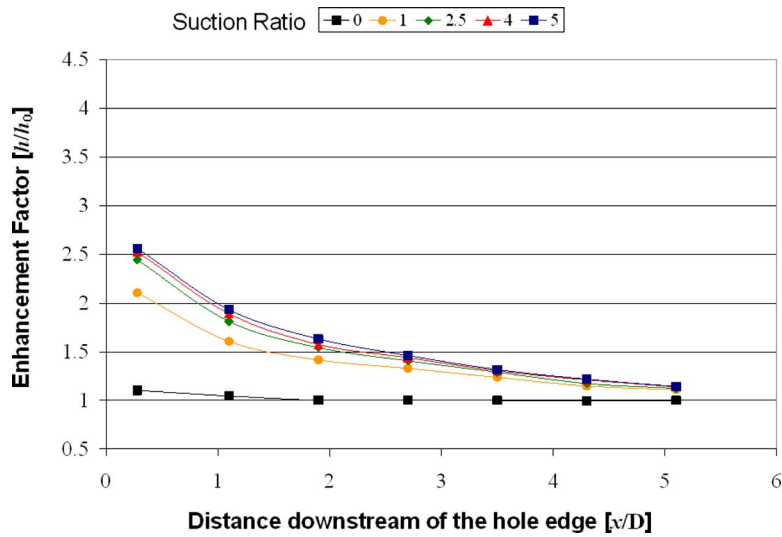


Fig. 15 Line averages downstream of the 150 deg extraction hole

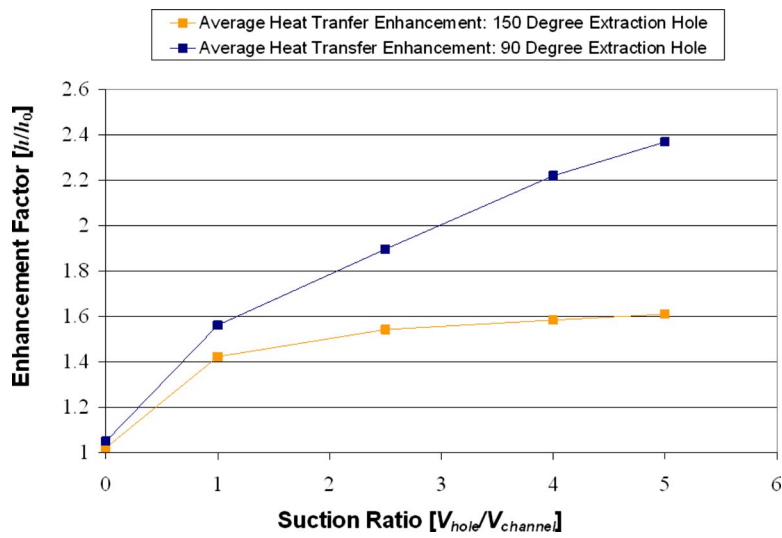


Fig. 16 Average heat transfer enhancement downstream of the 90 deg and 150 deg extraction holes at various SR ratios

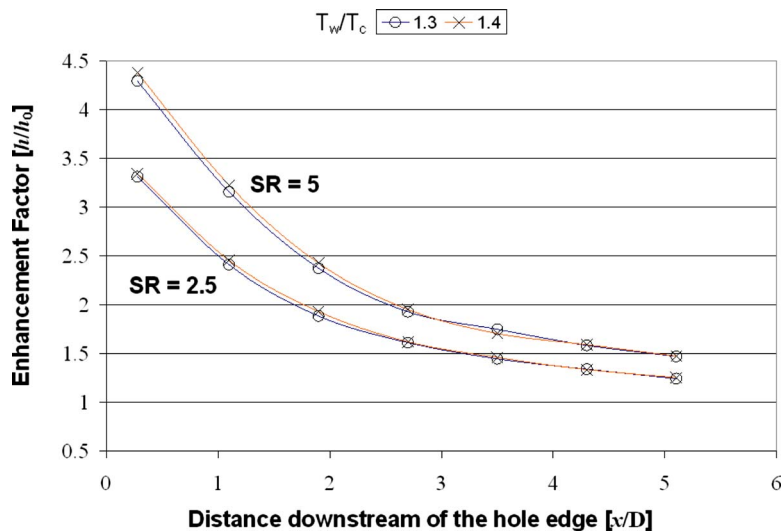


Fig. 17 Average heat transfer enhancement downstream of the 90 deg extraction hole at different T_w/T_c ratios

second order and can therefore be considered negligible compared with the primary variables such as the suction ratio and extraction angle.

7 Conclusion

In this paper an experimental study of heat transfer near the entrance to a film cooling hole in a turbine blade cooling passage was described. The study made use of platinum thin film gauges and a dedicated numerical data reduction technique to determine the amount heat transfer augmentation induced by coolant extraction. The influence of various extraction parameters such as extraction angle, suction ratio, and different wall-to-coolant temperature ratios was considered. Furthermore a numerical model of the test cases was done to provide better understanding of the near-hole flow.

Initially, the experimental setup was calibrated against a previously published study. Contrary to the corresponding study, cooled air was blown through a heated channel wall. Furthermore, use was made of platinum thin film heat flux gauges, as opposed to liquid crystal thermography to measure the thermal enhancement. Despite these differences, good overall agreement was obtained between the experimental results.

The experimental investigation showed that the primary variables that influenced the heat transfer augmentation constitute the suction ratio and extraction angle of the film cooling hole. The 90 deg extraction hole showed significant augmentation in the near-hole region with regard to an increasing suction ratio. The net amount of enhancement appeared to stagnate with an increasing amount of coolant extraction.

Although the 150 deg extraction hole also showed extensive near-hole augmentation, it was comprehensively lower compared with the 90 deg extraction hole, especially at higher suction ratios. This observation correlates with previous findings. The comparison shows a decrease in enhancement of approximately 45% in the near-hole region at $SR=5$, which decreases to approximately 25% in the same region for $SR=2.5$. Numerical flow results showed that this reduction in enhancement can be attributed to the higher angle of coolant deviation, which limits the amount of downstream impingement.

The good agreement that was obtained further downstream of the extraction hole with previously published results indicates that the channel width has a negligible influence on the heat transfer augmentation induced by coolant extraction. In this study a square channel was used as opposed to previous studies where the side-walls were widened to exclude any wall effects.

The enhancement that was obtained at a higher $T_{wall}/T_{coolant}$ ratio showed a difference of less than 2% in the near-hole region. This indicates that this variable, which was considered, does not primarily influence heat transfer augmentation and can therefore be considered to be negligible within the chosen experimental conditions.

Acknowledgment

The authors would like to acknowledge T.H. Roos and G. Sneden for their contribution to the experimental study.

Nomenclature

Roman

EF	= enhancement factor
h	= convective heat transfer coefficient ($W/m^2 K$)
h_0	= reference convective heat transfer coefficient ($W/m^2 K$)
k	= thermal conductivity ($W/m K$)
L	= wall thickness (m)
\dot{q}	= heat transfer rate (W)
SR	= suction ratio
T	= temperature (K)

t = time (s)

\bar{V} = mean velocity (m/s)

x = spatial coordinate (m)

Greek

α = thermal diffusivity (m^2/s)

η = weighting factor

ρ = density (kg/m^3)

Subscripts

c = coolant

w = wall

References

- [1] Han, J. C., Dutta, S., and Ekkad, V., 2000, *Gas Turbine Heat Transfer and Cooling Technology*, Taylor & Francis, New York.
- [2] Dunn, M. G., 2001, "Convective Heat Transfer and Aerodynamics in Axial Flow Turbines," ASME Paper No. 2001-GT-0506.
- [3] Han, J. C., 2004, "Recent Studies in Turbine Blade Cooling," *Int. J. Rotating Mach.*, **10**(6), pp. 443–457.
- [4] Han, J. C., and Dutta, S., 1995, *Heat Transfer and Cooling in Gas Turbines* (VKI Lecture Series 1995-05), von Karman Institute for Fluid Dynamics, Brussels, Belgium.
- [5] Goldstein, R. J., 2001, *Heat Transfer in Gas Turbine Systems*, Vol. 934, New York Academy of Sciences, New York.
- [6] Gritsch, M., Schulz, A., and Wittig, S., 2001, "Effects of Crossflows on the Discharge Coefficient of Film Cooling Holes With Varying Angles of Inclination and Orientation," *ASME J. Turbomach.*, **123**, pp. 781–787.
- [7] Goldstein, R. J., and Seol, W. S., 1991, "Heat Transfer to Row of Impinging Circular Air Jets Including the Effect of Entrainment," *Int. J. Heat Mass Transfer*, **34**(8), pp. 2133–2147.
- [8] Hay, N., and Lampard, D., 1998, "Discharge Coefficient of Turbine Cooling Holes: A Review," *ASME J. Turbomach.*, **120**, pp. 314–319.
- [9] Bunker, R. J., 2007, "Gas Turbine Heat Transfer: Ten Remaining Hot Gas Path Challenges," *ASME J. Turbomach.*, **129**, pp. 193–201.
- [10] Han, J. C., and Zhang, Y. M., 1992, "High Performance Heat Transfer Ducts With Parallel Broken and V-Shaped Broken Ribs," *Int. J. Heat Mass Transfer*, **35**(2), pp. 513–523.
- [11] Shen, J. R., Wang, Z., Ireland, P. T., Jones, T. V., and Byerley, A. R., 1991, "Heat Transfer Coefficient Enhancement in a Gas Turbine Blade Cooling Passage Due to Film Cooling Holes," *Proceedings of the Institution of Mechanical Engineers European Conference on Turbomachinery: Latest Developments in a Changing Scene*, Bird Cage Walk, London, pp. 219–226.
- [12] Shen, J. R., Wang, Z., Ireland, P. T., Jones, T. V., and Byerley, A. R., 1996, "Heat Transfer Enhancement Within a Turbine Cooling Passage Using Ribs and Combinations of Ribs With Film Cooling Holes," *ASME J. Turbomach.*, **118**, pp. 428–434.
- [13] Ekkad, S. V., Huang, Y., and Han, J. C., 1998, "Detailed Heat Transfer Distributions in Two Pass Smooth and Turbulated Square Channels With Bleed Holes," *Int. J. Heat Mass Transfer*, **41**(23), pp. 3781–3791.
- [14] Taslim, M. E., Li, T., and Spring, S. D., 1995, "Experimental Study of the Effects of Bleed Holes on Heat Transfer and Pressure Drop in Trapezoidal Passages With Tapered Turbulators," *ASME J. Turbomach.*, **117**, pp. 281–289.
- [15] Thurman, D., and Poinsatte, P., 2000, "Experimental Heat Transfer and Bulk Air Temperature Measurements for a Multipass Internal Cooling Model With Ribs and Bleed," ASME Paper No. 2000-GT-233.
- [16] Bunker, R. J., and Bailey, J. C., 2001, "Film Cooling Discharge Coefficient Measurements in a Turbulated Passage With Internal Crossflow," *ASME J. Turbomach.*, **123**, pp. 774–780.
- [17] Byerley, A. R., 1989, "Heat Transfer Near the Entrance to a Film Cooling Hole in a Gas Turbine," Ph.D. thesis, Department of Engineering Science, University of Oxford, UK.
- [18] Ligrani, P. M., Camci, C., and Grady M. S., 1982, "Thin Film Heat Transfer Gage Construction and Measurement Details," VKI Technical Memoranda No. 33.
- [19] Denos, R., Billiard, N., Iliopoulou, V., and Ferrara, F., 2002, "Data Reduction and Thermal Product Determination for Single and Multi-Layered Substrate Thin-Film Gauges," The 16th Symposium on Measuring Techniques in Transonic and Supersonic Flow in Cascades and Turbomachines, Cambridge, UK, Sept. 23–24, VKI Paper No. RP 2002-47.
- [20] Schulz, D. L., and Jones, T. V., 1973, "Heat Transfer Measurements in Short Duration Hypersonic Facilities," AGARDograph Report No. 165.
- [21] Dunn, M. G., 1995, *Measurement Techniques: The Thin Film Gauge* (VKI Lecture Series 1995-01), von Karman Institute for Fluid Dynamics, Brussels, Belgium.
- [22] Kline, S. J., and McClintock, F. A., 1953, "Describing Uncertainty in Single Sample Experiments," *Mech. Eng. (Am. Soc. Mech. Eng.)*, **75**, pp. 3–8.

- [23] Abdel-Wahab, S., and Tafti, D. K., 2004, "Large Eddy Simulations of Flow and Heat Transfer in a 90° Ribbed Duct With Rotation—Effect of Coriolis Forces," ASME Paper No. GT-2004-53796.
- [24] Sewall, E., and Tafti, D. K., 2004, "Large Eddy Simulation of the Developing Region of a Stationary Ribbed Internal Turbine Blade Cooling Channel," ASME Paper No. GT-2004-53832.
- [25] He, G., Guo, Y., and Hsu, A. T., 1999, "The Effect of Schmidt Number on Turbulent Scalar Mixing in a Jet-in-Crossflow," *Int. J. Heat Mass Transfer*, **42**, pp. 3727–3738.
- [26] Colban, W., Thole, K. A., and Haendler, M., 2007, "Experimental and Computational Comparisons of Fan-Shaped Film Cooling on a Turbine Vane Surface," *ASME J. Turbomach.*, **129**, pp. 23–31.